Natural satellites ephemerides
The Galilean moons' dynamics in the JUICE-Europa Clipper era

Fayolle, Sam

DOI
10.4233/uuid:667192b7-5555-49df-b2c6-2479942fc5f2

Publication date
2025

Document Version
Final published version

Citation (APA)
Fayolle, S. (2025). *Natural satellites ephemerides: The Galilean moons' dynamics in the JUICE-Europa Clipper era* . [Dissertation (TU Delft), Delft University of Technology]. https://doi.org/10.4233/uuid:667192b7-5555-49df-b2c6-2479942fc5f2

Natural satellites ephemerides

The Galilean moons' dynamics in the JUICE-Europa Clipper era

Natural satellites ephemerides

The Galilean moons' dynamics in the JUICE-Europa Clipper era

Dissertation

for the purpose of obtaining the degree of doctor
at Delft University of Technology
by the authority of the Rector Magnificus, prof. dr. ir. T.H.J.J. van der Hagen,
chair of the Board for Doctorates
to be defended publicly on Friday 24, January 2025 at 12:30 o'clock

by

Sam Liam FAYOLLE

Master of Science in Aerospace Engineering, Delft University of Technology, Netherlands
born in Pierre-Benite, France

Composition of the doctoral committee:

Rector Magnificus,	chairperson
Prof. dr. L.L.A. Vermeersen,	Delft University of Technology, *promotor*
Prof. dr. ir. P.N.A.M. Visser,	Delft University of Technology, *promotor*
Dr. ir. D. Dirkx,	Delft University of Technology, *copromotor*

Independent members:

Dr. ir. S.J. Goosens,	NASA, United States
Prof. dr. M.J. Van Hoolst,	KU Leuven / Royal Observatory Belgium, Belgium
Prof. dr. M. Kotsonis,	Delft University of Technology
Dr. habil. N.A.S. Rambaux,	Sorbonne Universite, France
Prof. dr. E.K.A. Gill,	Delft University of Technology, *reserve member*

The work presented in this dissertation was partially funded by an OSIP (Open Space Innovation Platform) grant.

Keywords: ephemerides, natural satellites, Galilean system, radio-science, astrometry, JUICE, Europa Clipper

Printed by: Ipskamp printing

Cover by: V. A. Bejach

ISBN 978-94-6384-713-1

An electronic copy of this dissertation is available at
https://repository.tudelft.nl/.

CONTENTS

SUMMARY

Since Galileo Galilei's first discovery of natural satellites orbiting around other planets, observing and reconstructing their dynamics has been at the core of our efforts to understand and characterise these distant worlds. Far from following perfect, frozen in time Keplerian orbits, the dynamics of these satellites keep evolving, with tides as driving mechanism. The dissipation of energy in natural bodies due to their visco-elastic response to tidal forcing both heats up the moons' interiors and causes their orbits to expand or shrink, as well as to become more circular or elliptical. Refining the moons' ephemerides (i.e., tabulated solutions of their motion as a function of time) is thus key to studying not only their present-day dynamics, but also the long-term thermal-orbital evolution of planetary systems.

The progressive improvement of our ephemerides solutions, initially based on ground-based astrometric observations only, has made it possible to plan direct flybys around some of Jupiter and Saturn's moons by the Galileo and Cassini spacecraft, respectively. In addition to initiating a new phase in our exploration of the outer system's natural satellites, both missions brought back evidence of the presence of subsurface liquid water oceans on some Jovian and Saturnian icy moons. This has sparked our interest in these fascinating objects, now known not to be dead icy bodies, but active ocean worlds. However, the subsistence of liquid water on these satellites - some of them very small - at such great distances from the Sun remains challenging to explain. For some of these icy moons, tidal heating is actually expected to be a key contributor to the heat budget. This places the improvement of the moons' ephemerides at the centre of our investigations of these internal oceans' stability and potential habitability: a more accurate and detailed characterisation of the tidal dissipation parameters driving the system's long-term evolution - primarily achievable via a refined solution of the moons' current orbits - indeed becomes essential.

In the coming decade, two dedicated missions will visit the three outermost of Jupiter's four Galilean satellites (Io, Europa, Ganymede, and Callisto in increasing distance to Jupiter). The Galilean moons form a fascinating system and a promising mission target to advance our understanding of planetary evolution processes. The three outer icy Galilean satellites are indeed all putative or confirmed ocean worlds, exhibiting different levels of differentiation and tidal heating intensity. On the other hand, the extreme tidal heating experienced by the innermost satellite, Io, makes it the most volcanically active object of the Solar System and places this moon at the other end of the moons' diversity spectrum. ESA's JUpiter ICy moons Explorer (JUICE) is already on its eight year-long journey to the Jovian system, and will arrive shortly after NASA's Europa Clipper spacecraft, to be launched in August 2024. Both missions will specifically study the Galilean moons: Europa Clipper will mostly focus on Europa, while JUICE will perform a series of flybys around the three icy moons before entering into orbit around Ganymede. A better

characterisation of the Galilean system's origin and history, including a refined understanding of the formation and stability of the moons' internal oceans, lies at the core of both missions' main scientific objectives.

Both JUICE and Europa Clipper radio-science tracking measurements will be instrumental in this respect, and can bring the quality of the moons' ephemerides solution to unprecedented accuracy levels (see below). Nonetheless, this ground-breaking improvement is contingent upon resolving a number of challenges arising in this new era of natural satellites' ephemerides determination. In particular, it requires exploiting synergies between extremely diverse data sets (i.e., long-term astrometry vs. very accurate, but spacecraft-focussed, radio-science) and developing adapted estimation strategies. In this context, this research investigates the quality of the ephemerides solution attainable after the JUICE and Europa Clipper missions, as part of the ongoing preparation for these two missions and, more generally, our continued exploration of other Solar System's moons. In addition to quantifying the expected contribution of JUICE and Europa Clipper radio-science, we examine the influence of the adopted estimation method, and explore promising observation synergies to further improve and stabilise the solution.

In a moons' ephemerides determination context, radio-science measurements are indirect observations: they constrain the spacecraft's orbits which, during close encounters such as flybys, also provide information on the moons' dynamics. The incorporation of such data in the moons' state estimation thus requires solving for both the spacecraft's and moons' orbits. This is traditionally achieved by first solving for the spacecraft's and flyby moon's dynamics in an arc-wise manner, determining an independent solution for each flyby. A global solution for the moons' dynamics can then be reconstructed, by reconciling the local state estimates obtained in the first step. This two-step, decoupled estimation facilitates the state determination by handling the spacecraft's and moons' dynamics separately. An alternative approach, however, consists in concurrently solving for both the moons and spacecraft's dynamics in a single inversion. We advocate that such a coupled model, by automatically accounting for all spacecraft-moons dynamical couplings, should yield the most statistically realistic representation of the estimation solution. We moreover compare the Galilean moons' ephemerides obtained from JUICE radio-science with both decoupled and coupled models, and show that adopting a coupled approach can indeed improve the solution, most notably in the radial direction.

A coupled estimation philosophy nonetheless imposes a tighter requirement on the consistency and exactitude of our dynamical models. Any mismodelled effect in either the spacecraft or moons' dynamics, as well as possible errors in noise modelling, can eventually affect both the spacecraft and moons' state solutions. Moreover, concurrently solving for two types of dynamics (i.e., spacecraft's states estimated locally, moons' states determined globally over the entire mission timeline) requires our models to be consistent over different timescales. This enhances the sensitivity of the coupled estimation to dynamical mismodelling, strengthening the need for additional, independent data sets.

In this perspective, we therefore examine the contribution of PRIDE (Planetary Radio Interferometry and Doppler Experiment) to the joint JUICE-Europa Clipper classical radio-science solution. The latter is based on range and Doppler data (i.e., measurements of the spacecraft relative position and velocity with respect to telescopes on Earth, in the line-of-sight direction). In particular, we quantify the moons' ephemerides improvement achievable with JUICE PRIDE VLBI (Very Long Baseline Interferometry) measurements of the spacecraft's lateral position in the plane-of-the-sky. We show that this improvement will be limited if a coupled state estimation can be successfully completed: the solution achievable with only Doppler and range already achieves such accuracy levels that adding VLBI cannot bring any significant improvement. However, PRIDE VLBI data can noticeably reduce the uncertainties of the moons' arc-wise state solutions. VLBI can therefore be exploited to progressively validate the radio-science solution, starting from local, per-flyby state estimation to gradually reconstruct a global solution. We explore this possibility further, by proposing a validation strategy successively capitalising on VLBI's role as an independent data set and on the refined local state solutions it can help achieve for the flyby moons.

In parallel to the critical importance of fostering promising validation opportunities for the radio-science solution, significant development efforts will still be essential to improve the consistency of our dynamical model. In particular, we demonstrate that the coherent modelling of tidal effects and rotational dynamics strongly affects the evolution of the moons' orbits caused by tidal dissipation. It will therefore be critical to upgrade our current models to ensure the robust determination of tidal dissipation and libration parameters. These are indeed crucial for our characterisation of the moons' present interior and orbital migration rate, holding the key to the system's long-term thermal-orbital evolution.

Finally, the aforementioned analyses, once combined, provide an indication of the ephemerides accuracy attainable from JUICE and Europa Clipper radio-science. The radial position of all four Galilean satellites can be determined at the meter or sub-meter level, Ganymede's formal position uncertainties even reaching down to a few centimetres during JUICE's orbital phase. The tangential errors are larger and comprised in the 1-10 m range for all moons but Io (few tens of metres). The satellites' out-of-plane positions, on the other hand, are slightly less tightly constrained (10-100 m).

An important challenge of a radio-science-only inversion lies in the stability of the ephemerides solution. JUICE and Clipper radio-science data sets spread over a limited time span, inherently bound by the missions' timelines (about 5 years). Furthermore, the lack of direct constraints on Io's orbit from radio-science yields a less robust determination of its dynamics, combined with a poor characterisation of the tidal quality factors of Io and of Jupiter, due to the entanglement of these two parameters. Given the key role of Io in the other moons' dynamics via the resonance Laplace, this has repercussions for the evolution of the entire Galilean system.

Future moons' ephemerides will, however, not only rely on upcoming radio-science from planetary missions. Recent developments in the field of astrometry also offer new opportunities to push the boundaries of ground-based measurement techniques. First, mutual approximations overcome an important limitation of the observations of mutual events (i.e., occultations and eclipses), which play a key role in current ephemerides solutions: the former indeed occur much more frequently, as they do not require a perfect alignment of the two moons with the Sun (eclipses) or Earth (occultations). We develop the missing analytical framework required to exploit mutual approximations for moons' state estimations. Moreover, we show that this analytical formulation can be used to extract additional information on the moons' relative dynamics from mutual approximation observations, and would be equally applicable to mutual events. This therefore also augments the information content accessible via past mutual event observations, with possible benefits for ephemerides determination.

Nonetheless, stellar occultations currently represent the most promising and accurate ground-based astrometric observations for natural satellites. In particular, the unprecedented accuracy of such observations (a few milliarcseconds), if combined with tracking of in-situ spacecraft, offers unique opportunities. First, radio-science enhances the effective accuracy of the moon's position measurement derived from the occultation by reducing the contribution of the planet ephemeris to the observation's error budget. Second, this strategy would help us test and possibly characterise the planetary ephemeris error, and disentangle it from moons' ephemerides uncertainties. While we investigate this synergistic experiment in the context of the Juno mission, such a unique combination of ground- and space-based observations can furthermore also be implemented during the course of the JUICE and Europa Clipper missions.

After investigating the aforementioned data sets separately, we finally quantify the potential synergy between JUICE and Europa Clipper radio-science and existing astrometric observations. The combined analysis of both data sets confirms that old astrometric measurements and direct observations of Io offer the most promising opportunities to improve the robustness of the radio-science solution, along with the determination of the tidal quality factors of Io and Jupiter at Io's frequency. This clearly demonstrates the importance of exploiting inter-data set synergies in a global inversion framework to attain the best ephemerides for the Galilean moons, and eventually reconstruct a robust picture of the system's current state and thermal orbital evolution.

In the upcoming decade, the extremely accurate JUICE and Europa Clipper radio-science measurements, enhanced by the complementarity of the missions' Jovian tour and research foci, will revolutionise the quality of the ephemerides solution for the Galilean satellites. Fully exploiting the potential of this unique data set will however require us to significantly improve the consistency and realism of our dynamical models, to match the accuracy levels predicted by the radio-science analyses presented in this dissertation, as well as to capitalise on promising existing and future synergies with other data sets and data types. Overcoming these challenges has the potential to provide a robust and ground-breaking picture of the present-day dynamics and dissipation in the Galilean system. We specifically reflect on how a refined state estimation for the Galilean satellites will contribute to advancing our understanding of the system's dynamical history and characterisation of the moons' present and past interiors. We moreover argue that the methods we developed and the resulting insights gained into moons' ephemerides determination are directly relevant for other planetary systems. The implications of the conducted research are not limited to the scope of JUICE and Europa Clipper's visit to the Galilean moons, and expand to the upcoming exploration of the Uranian system and next phases of our investigation of Jupiter and Saturn's icy satellites.

SAMENVATTING

Sinds Galileo Galilei voor het eerst manen ontdekte die rond andere planeten draaien, vormt het observeren en reconstrueren van hun dynamica de kern van onze inspanningen om deze verre werelden te begrijpen en te karakteriseren. Deze satellieten volgen geen perfecte Keplerbanen, maar hun banen evolueren in de tijd, met getijden als drijvend mechanisme. De dissipatie van energie in hemellichamen als gevolg van hun visco-elastische reactie op getijdekrachten zorgt ervoor dat het binnenste van de manen opwarmt, en dat hun banen uitzetten of krimpen, en cirkelvormiger of ellipsvormiger worden. Het verfijnen van de efemeriden van de manen (d.w.z. getabelleerde oplossingen van hun beweging als functie van de tijd) is dus essentieel om niet alleen hun huidige dynamica te bestuderen, maar ook voor het begrijpen can de thermisch-orbitale evolutie van planetenstelsels op de lange termijn.

De geleidelijke verbetering van onze efemeriden, die aanvankelijk alleen gebaseerd waren op astrometrische waarnemingen vanaf de grond, heeft het mogelijk gemaakt om ruimtemissies te plannen rond een aantal manen van Jupiter en Saturnus door respectievelijk de Galileo en Cassini satelliet. Niet alleen startten beide missies een nieuwe fase in onze verkenning van de natuurlijke satellieten aan de rand van ons zonnestelsel, maar ze leverden ook bewijs voor de aanwezigheid van oceanen met vloeibaar water onder het oppervlak van sommige ijzige manen van Jupiter en Saturnus. Dit heeft onze interesse in deze fascinerende objecten verder opgewekt, doordat we nu weten dat het geen dode ijzige hemellichamen zijn, maar actieve oceaanwerelden. Het bestaan van vloeibaar water op al deze satellieten - waarvan sommige heel klein zijn - op zo'n grote afstand van de zon blijft echter moeilijk te verklaren. Voor sommige van deze ijzige manen wordt zelfs verwacht dat getijde opwarming een belangrijke bijdrage levert aan het warmtebudget. Dit plaatst de verbetering van de efemeriden van de manen in het middelpunt van ons onderzoek naar de stabiliteit en potentiële bewoonbaarheid van deze interne oceanen. Een nauwkeurigere en gedetailleerdere karakterisering van de dissipatie parameters die de evolutie van het systeem op de lange termijn bepalen – die voornamelijk te bepalen zijn met betere schattingen van de huidige banen van de manen – is essentieel

In het komende decennium zullen twee missies de drie buitenste van Jupiters vier Galileïsche satellieten (Io, Europa, Ganymedes en Callisto in toenemende afstand tot Jupiter) bezoeken. De Galileïsche manen vormen een fascinerend systeem en een veelbelovend missiedoel om ons begrip van planetaire evolutieprocessen te vergroten. De drie buitenste, ijzige Galileïsche satellieten zijn allemaal vermoedelijke of bevestigde oceaanwerelden, die verschillende niveaus van differentiatie en mate van getijdeverwarming vertonen. Tegelijkertijd is de binnenste satelliet, Io, door zijn extreme getijdenverwarming het meest vulkanisch actieve object van het zonnestelsel. ESA's JUpiter ICy moons Explorer (JUICE) is al begonnen aan zijn acht jaar durende reis naar het Joviaanse stelsel en zal kort na NASA's Europa Clipper satelliet aankomen. Die laatste zal in augustus 2024 worden gelanceerd. Beide missies zullen specifiek de Galileïsche manen bestuderen: Europa Clipper zal zich voornamelijk richten op Europa, terwijl JUICE een reeks vluchten rond de drie ijzige manen zal uitvoeren voordat het in een baan rond Ganymedes komt. Een betere karakterisering van de oorsprong en geschiedenis van het Galileïsche systeem, inclusief een verfijnd begrip van de vorming en stabiliteit van de interne oceanen van de manen, vormt de kern van de belangrijkste wetenschappelijke doelstellingen van beide missies.

Metingen met het radiosysteem van zowel JUICE als Europa Clipper zullen in dit opzicht van groot belang zijn. De kwaliteit van de efemeriden van de manen zal er mee tot ongekende nauwkeurigheid worden gebracht (zie hieronder). Om deze baanbrekende verbetering te behalen, is het echter van cruciaal belang omossingen voor een aantal uit grotedagingen diet vereist in het bijzonder het benutten van synergiën tussen extreem verschillende datasets (d.w.z. astrometrie op lange termijn versus zeer nauwkeurige, maar op kunstsatellieten gerichte, radiometingen) en het ontwikkelen van verbeterde strategieën om het statistische schattingsprobleem op te lossen. In deze studie de kwaliteit van de efemeriden die haalbaar is na de JUICE- en Europa Clipper-missies, als onderdeel van de lopende voorbereiding voor deze twee missies en, meer algemeen, onze voortdurende verkenning van andere manen van het Zonnestelsel. Naast het kwantificeren van de verwachte bijdrage van de radiometingen van JUICE en Europa Clipper, onderzoeken we de invloed van de gekozen schattingsmethode en verkennen we veelbelovende observatiesynergieën om de oplossing verder te verbeteren en te stabiliseren.

In de context van de bepaling van de efemeriden van manen zijn radiometingen indirecte waarnemingen: ze leggen de banen van de kunstmaan vast die, bijvoorbeeld tijdens flybys, ook informatie geven over de dynamica van de manen. Het opnemen van zulke gegevens in de schatting van de banen van de manen vereist dus het oplossen van zowel de banen van de kunstsatelliet als die van de manen. Dit wordt traditioneel gedaan door eerst de dynamica van de kunstsatelliet en de desbetreffende maan per arc op te lossen, waarbij voor elke flyby een onafhankelijke oplossing wordt bepaald. Vervolgens kan een globale oplossing voor de dynamica van de manen worden gereconstrueerd door de lokale baanschattingen die in de eerste stap zijn verkregen met elkaar in overeenstemming te brengen. Deze ontkoppelde schatting vergemakkelijkt de baanbepaling door de dynamica van de kunstsatelliet en de manen apart te behandelen. Een alternatieve benadering is om tegelijkertijd de dynamica van zowel de manen als de kunstsatelliet in een enkele inversie op te lossen. Een dergelijk gekoppeld model geeft, door automatisch rekening te houden met alle dynamische koppelingen tussen de kunstsatelliet en de manen, de statistisch meest realistische oplossing van het schattingsprobleem. We vergelijken de efemeriden van de Galileïsche manen verkregen uit de metingen van het radiosysteem van JUICE met zowel ontkoppelde als gekoppelde modellen, en laten zien dat een gekoppelde aanpak de oplossing inderdaad kan verbeteren, met name in de radiale richting.

Een gekoppelde schattingsfilosofie stelt echter hogere eisen aan de consistentie en nauwkeurigheid van onze dynamische modellen. Elk verkeerd gemodelleerd effect in de dynamica van de kunstsatelliet of de manen, evenals mogelijke fouten in het modelleren van ruis op de data, kunnen uiteindelijk zowel de oplossingen van de kunstsatelliet als die van de manen beïnvloeden. Bovendien vereist het gelijktijdig oplossen van twee soorten dynamica (d.w.z. de toestanden van de kunstsatelliet die lokaal worden geschat en de toestanden van de manen die globaal worden bepaald over de hele tijdlijn van de missie) dat onze modellen consistent zijn over verschillende tijdschalen. Dit verhoogt de gevoeligheid van de gekoppelde schatting voor fouten in de dynamische modellen, wat de behoefte aan extra, onafhankelijke datasets versterkt.

Vanuit dit perspectief onderzoeken we de bijdrage van PRIDE (Planetary Radio Interferometry and Doppler Experiment) aan de gezamenlijke JUICE-Europa Clipper oplossing voor de metingen van het radiosysteem. Dit laatste is gebaseerd op afstands- en dopplergegevens (d.w.z. metingen van de relatieve afstand en snelheid van de kunstsatelliet ten opzichte van telescopen op aarde, in de zichtlijnen). In het bijzonder kwantificeren we de verbetering van de efemeriden van de manen die haalbaar is met JUICE PRIDE VLBI (Very Long Baseline Interferometry) metingen van de laterale positie van de kunstsatelliet in het hemelvlak. We laten zien dat deze verbetering beperkt zal zijn als een gekoppelde toestandsschatting volledig succesvol kan worden voltooid: de oplossing die haalbaar is met alleen Doppler en afstandsmetingen bereikt al een dergelijke mate van nauwkeurigheid dat de toevoeging van VLBI geen significante verbetering oplevert. De PRIDE VLBI-gegevens kunnen echter de onzekerheden van de lokale (per arc) baanbepalingen van de manen aanzienlijk verkleinen. VLBI kan daarom worden gebruikt om de oplossing voor metingen door het radiovysteem stapsgewijs te valideren, te beginnen met lokale toestandsschattingen per flyby om geleidelijk een globale oplossing te reconstrueren. We onderzoeken deze mogelijkheid verder door een validatiestrategie voor te stellen die achtereenvolgens gebruikt maakt van de rol van VLBI als onafhankelijke dataset en van de verfijnde lokale toestandsoplossingen die het kan helpen bereiken voor de flyby-manen.

Behalve het stimuleren van veelbelovende validatiemogelijkheden voor baanoplossingen van radio data, blijft het belangrijk dat aanzienlijke ontwikkelingsinspanningen worden gestopt in het verbeteren van de consistentie van ons dynamische model. In het bijzonder tonen we aan dat he coherente modelleren van getijde-effecten en rotatiedynamica de evolutie van de banen van de manen ten gevolge van getijdendissipatie sterk beïnvloedt. Het zal daarom van cruciaal belang zijn om onze huidige modellen te verbeteren om een robuuste bepaling van getijdendissipatie en libratieparameters te garanderen. Deze zijn namelijk cruciaal voor onze karakterisering van de huidige interne structuur van de manen en de evolution van de baanparameters, en vormen de sleutel tot de thermisch-orbitale evolutie van het systeem op de lange termijn.

Tot slot geven de bovengenoemde analyses gecombineerd een indicatie van de nauwkeurigheid van efemeriden die haalbaar is met de radiometingen van JUICE en Europa Clipper. De radiale positie van alle vier Galileïsche satellieten kan op meter- of submeterniveau worden bepaald, waarbij de formele positieonzekerheid van Ganymedes tijdens de omloopfase van JUICE zelfs enkele centimeters bereikt. De tangentiële fouten zijn groter en liggen in het bereik van 1-10 m voor alle manen behalve Io (enkele tientallen meters). De posities van de satellieten loodrecht op hun baanvlak zijn daarentegen iets minder nauwkeurig begrensd (10-100 m).

Een belangrijke uitdaging van een inversie die alleen gebaseerd is op radiometingen ligt in de stabiliteit van de efemeridenoplossing. De metingen van het radiosysteem van JUICE en Clipper strekken zich uit over een beperkt tijdsinterval, inherent gebonden aan de tijdlijnen van de missies (ongeveer 5 jaar). Bovendien leidt het gebrek aan directe metingen van Io's baan door radiometingen tot een minder robuuste bepaling van zijn dynamica, gecombineerd met een slechtere karakterisering van de getijdedissipatie van Io en Jupiter, vanwege de verstrengeling van deze twee parameters. Gezien de sleutelrol van Io in de dynamica van de andere manen via de Laplace resonantie, heeft dit gevolgen voor de evolutie van het hele Galileïsche stelsel.

De efemeriden van toekomstige manen zullen echter niet alleen afhankelijk zijn van radiometing van de komende planetaire missies. Recente ontwikkelingen op het gebied van astrometrie bieden ook nieuwe mogelijkheden om de meettechnieken vanaf de grond te verbeteren. Ten eerste ondervangen 'mutual approximations' een belangrijke beperking van de waarnemingen van 'mutual events' (d.w.z. occultaties en verduisteringen), die een sleutelrol spelen in de huidige oplossingen van efemeriden: de eerstgenoemde komen veel vaker voor, omdat ze geen perfecte uitlijning van de twee manen met de Zon (verduisteringen) of Aarde (occultaties) vereisen. We ontwikkelen het ontbrekende analytische raamwerk dat nodig is om deze metingen te gebruiken voor het schatten van de toestand van manen. Bovendien laten we zien dat deze analytische formulering kan worden gebruikt om aanvullende informatie over de relatieve dynamica van de manen te extraheren uit de data, en evenzeer van toepassing zou zijn op wederzijdse gebeurtenissen. Dit vergroot dus ook de informatiedichtheid uit mutual events in het verleden, met mogelijke voordelen voor de bepaling van efemeriden.

Sterbedekkingen vormen momenteel de meest veelbelovende en nauwkeurige astrometrische waarnemingen vanaf de grond voor natuurlijke satellieten. Met name de ongekende nauwkeurigheid van dergelijke waarnemingen (enkele milliboogseconden), indien gecombineerd met het volgen van in-situ kunstsatellieten, biedt unieke mogelijkheden. Ten eerste verbeteren radiometingen de effectieve nauwkeurigheid van de door sterbedekkingen afgeleide positiemeting van de maan door de bijdrage van de efemeriden van de planeet aan het foutenbudget van de observatie te verminderen. Ten tweede zou deze strategie ons helpen om de fout in de planetaire efemeriden te testen en mogelijk te karakteriseren, en deze los te koppelen van de onzekerheden in de efemeriden van de manen. Hoewel we dit synergetische experiment onderzoeken in de context van de Juno-missie, kan zo'n unieke combinatie van waarnemingen vanaf de grond en vanuit de ruimte bovendien ook worden geïmplementeerd tijdens de JUICE- en Europa Clipper-missies.

Na de bovengenoemde datasets afzonderlijk te hebben onderzocht, kwantificeren we tenslotte de potentiële synergie tussen de radiometingen van JUICE en Europa Clipper en bestaande astrometrische waarnemingen. De gecombineerde analyse van beide datasets bevestigt dat oude astrometrische metingen, en directe waarnemingen van Io in het bijzonder, de meest veelbelovende mogelijkheden biedt om de robuustheid van de oplossing van de metingen door het radiosysteem te verbeteren. Hetzelfde geldt voor de bepaling van de getijdedissipatie van Io en Jupiter op Io's frequentie. Dit toont duidelijk het belang aan van het benutten van de synergie tussen datasets in een globaal inversiekader om de beste efemeriden voor de Galileïsche manen te verkrijgen en uiteindelijk een robuust beeld te reconstrueren van de huidige toestand van het systeem en de thermische- en baanevolutie.

In het komende decennium zullen de extreem nauwkeurige metingen van JUICE en

Europa Clipper's radiosysteem, versterkt door de gelijkenissen in de onderzoeksdoelen en profielen van de missies, een revolutie bewerkstelligen in de kwaliteit van de efemeridenoplossing voor de Galileïsche satellieten. Om het potentieel van deze unieke dataset volledig te benutten, moeten we echter de consistentie en het realisme van onze dynamische modellen aanzienlijk verbeteren. Dit zal essentieel zijn om de nauwkeurigheidsniveaus te evenaren die voorspeld worden door de in dit proefschrift gepresenteerde analyses, en om te profiteren van veelbelovende bestaande en toekomstige synergieën met andere datasets en datatypes. Het overwinnen van deze uitdagingen heeft de potentie om een robuust en baanbrekend beeld te geven van de huidige dynamica en dissipatie in het Galileïsche systeem. We gaan specifiek in op hoe een verfijnde baanbepaling voor de Galileïsche satellieten zal bijdragen aan een beter begrip van de dynamische geschiedenis van het systeem en de karakterisering van het inwendige van de manen, zowel tegenwoordig als in het verre verleden. We stellen bovendien dat de methoden die we hebben ontwikkeld en de inzichten die we hebben opgedaan in de bepaling van de efemeriden van manen direct relevant zijn voor andere planetenstelsels. De implicaties van het uitgevoerde onderzoek beperken zich niet tot het bezoek van JUICE en Europa Clipper aan de Galileïsche manen, maar breiden zich uit naar de komende verkenning van het Uranische stelsel en de volgende fasen in ons onderzoek van de ijzige satellieten van Jupiter en Saturnus.

1

INTRODUCTION

When Galileo Galilei looked up to the night sky through his homemade telescope back in 1610, he noticed three bright dots next to Jupiter in the sky, and soon spotted a fourth one (Fig. 1.1). Observing them for several consecutive nights revealed the most surprising pattern: unlike other stars, these points appear to move with respect to one another, while always remaining close to Jupiter. This led him to rightfully conclude that he was actually looking at something new: the first natural satellites to be discovered other than our own, bringing another fundamental cornerstone to the heliocentrism revolution. Up to this day and after much more has been discovered about these objects, the four Galilean moons - Io, Europa, Ganymede, and Callisto - have remained some of the most fascinating objects of the Solar System.

Following Galileo's discovery, many more natural satellites have progressively been found orbiting around most planets of the Solar System. The satellite population

Figure 1.1.: Galileo Galilei's telescope observations of Jupiter's moons. Courtesy: University of Michigan Special Collections Library.

of the terrestrial planets is limited to our own moon, and Mars' two asteroid-like satellites. In the outer Solar System, on the other hand, the giants Jupiter, Saturn, Uranus, and Neptune are each surrounded by a myriad of natural satellites. These planets respectively host 95, 146, 27, and 14 confirmed moons (as recognised by the International Astronomical Union, IAU), with more awaiting to be discovered. These outer Solar System satellites form a very diverse population of extremely complex - and captivating - bodies. Jupiter's innermost Galilean moon, Io, is for instance the most volcanically active world in the Solar System, while the subsurface ocean on its neighbour Europa would contain more liquid water than there is on Earth. Further away from the Sun, the Saturnian moons also present some unique features: the climate of the system's largest satellite, Titan, hosts ethane and methane cycles (Lunine and Atreya, 2008). The tiny moon Enceladus, on the other hand, shows signs of intense geological activity which, combined with the confirmed presence of a global subsurface ocean below its icy crust (Iess et al., 2014b; McKinnon, 2015; Thomas et al., 2016), makes this icy world one of the most promising candidates for habitability in the Solar System. In this picture of widely diverse worlds, one specific finding has captivated the space scientific community more than any other: the evidence, either confirmed or tentative, of the presence of subsurface oceans of liquid water lying hidden below the crust of some of these moons (Europa, Ganymede, Callisto, Titan, Enceladus, Mimas, Triton, e.g., Nimmo and Pappalardo, 2016) has revolutionised our conception of habitability in the Solar System.

This is at the core of the strong interest in gas giants' icy satellites, and plays a central role in the lasting interest in the Galilean moons in particular. In an unprecedented effort to further characterise these moons and their internal oceans, the coming decade will see two dedicated missions targeting the Galilean system: ESA's JUpiter ICy moons Explorer (JUICE) and NASA's Europa Clipper (Section 1.3.3). This unique opportunity in the history of space exploration further focusses the attention of the scientific community on the Galilean moons, as it makes preparatory studies essential to maximise the science return of both missions, optimise observation planning and acquisition, and streamline future analyses. This dissertation sets itself in this context, specifically investigating the reconstruction of an unprecedentedly accurate solution for the Galilean moons' orbital dynamics in the wake of the JUICE and Europa Clipper missions. The invaluable scientific implications of such an improved solution, reaching far beyond a better characterisation of the Galilean satellites' orbits, will be explored in the following section.

1.1. The moons' dynamics as key to their interiors and evolution

Since Galileo's exceptional discovery, much has changed regarding the accuracy of our measurement techniques and the diversity of our observation strategies for the Galilean moons. In 1973, Pioneer 10 performing the first flyby of Jupiter ever was the turning point that changed the Jovian system from a distant object of study for Earth astronomers to a prime mission target. Following Pioneer 10, the

Jovian system has also been visited by Pioneer 11, Voyager 1 & 2, Galileo, Ulysses, Cassini, New Horizons, and Juno (Section 1.3). The major advancements and much further knowledge of planetary systems that each of these missions brought have, however, not demeaned the relevance of Galileo's approach: to this day, studying and precisely reconstructing natural satellites' orbits is still key to understanding these distant objects. Improving our knowledge of the moons' dynamics implies refining the moons' so-called ephemerides, which are tabulated solutions reconstructing the motion of natural objects as a function of time. Accurate ephemerides not only allow us to plan and design spacecraft missions (e.g., Jacobson et al., 2000; Jacobson, 2004; Jacobson and French, 2004), but the moons' dynamics also contain crucial information about the moons' present-day interiors and bear witness of their formation and evolution processes (e.g., Lainey et al., 2009, 2012, 2020, 2024).

The system's long-term evolution is driven by tidal dissipation mechanisms, which are shaped by the moons' orbits. Due to the mutual gravitational attraction between the central planet and each satellite, they both raise tides on each other, with an intensity that strongly depends on the distance separating them. While the most well known manifestations of such effects are Earth's ocean tides raised by our own moon, tides are not limited to liquid layers and also induce solid body deformations, which affect the satellites' orbits and rotations. Rocky and icy satellites indeed do not deform instantaneously under the gravitational pull exerted by the central planet, and their visco-elastic deformation dissipates part of the energy through internal friction. This causes the moons' orbits to migrate closer or further from the planet, and slowly synchronises the moons' orbital and rotation rhythms. Tidal dissipation therefore governs the long-term orbital migration rate of the satellites, but it also plays a key role in the evolution of their interiors: it indeed influences the heating rate that they experience, thus modifying their internal structure and properties. This in turn affects the moons' dissipative response to gravitational forcing, and eventually their orbital evolution. This strong coupling between the moons' dynamics and interiors implies that their current orbits and rotations contain signatures of the system's long-term history (e.g., Lainey et al., 2009, 2020, 2024). Improving the moons' ephemerides therefore provides a natural way to extract this information. For the Galilean icy satellites, this is essential to investigate how subsurface oceans could have formed and subsisted until present days, tidal heating representing a key external energy source to sustain liquid water on cold, distant moons (e.g., Nimmo and Pappalardo, 2016).

Since Galileo's own orbit-based revolutionary observations, much has been revealed about natural satellites from their orbits and rotations, due to the complex and intricate feedback between their dynamics and interiors described above. In particular, analyses of the moons' rotations brought part of the evidence for some of the moons' subsurface oceans, as is the case for e.g., Mimas (Tajeddine et al., 2014; Lainey et al., 2024) and Enceladus (Thomas et al., 2016). The orbits of the Galilean moons have, moreover, revealed a strong dissipation in Io and Jupiter. This causes Io to migrate inwards, unlike Europa and Ganymede, such that these three moons are therefore slowly moving out of the Laplace resonance (Lainey et al., 2009). In the Saturnian system, the moons' current orbits led to even more ground-breaking results: their present-day migration rates are consistent with a highly non-linear, frequency-dependent dissipation in Saturn (Lainey et al., 2020).

These results are in good agreement with a resonance locking scenario (different from the crossing or capture in an orbital resonance), in which the dissipation inside Saturn is enhanced at specific frequencies dependent on the planet's interior structure (Fuller et al., 2016). This concept, unlike classical linear evolution models, predicts that the moons' orbits would evolve on timescales linked to the planet interior evolution, thus implying a much faster migration rate. Energy dissipation in the convective envelopes of gas giants was moreover proposed as an alternative explanation for the fast orbital migration of the Saturnian satellites in Terquem (2023). Current constraints on these orbital expansion rates are entirely derived from the moons' orbits (see Section 3.4 for more detail), and actually suggest different scenarios for the formation of Saturn's rings (Wisdom et al., 2022), as well as an alternative explanation for Iapetus' current orbit (Polycarpe et al., 2018), coherent with the capture of Hyperion in a mean-motion resonance with Titan (Colombo et al., 1974). A faster migration of Saturn's moon could also explain the progressive tilting of Saturn's orbit up to its current obliquity (Saillenfest et al., 2021a,b). The characterisation of Saturn's dissipation from the dynamics of its moons has thus upended much of our knowledge and understanding of planetary systems' evolution processes. While a resonance locking mechanism has not yet been evidenced in the Jovian system, it has been postulated that Callisto could also be caught in such a resonance locking configuration (e.g., Downey et al., 2020; Lari et al., 2023).

The JUICE and Europa Clipper missions will directly contribute to answering this question, as part of a much broader effort to further constraining the long-term evolution of the Galilean moons. Radio science measurements from both spacecraft are indeed expected to significantly improve our ephemerides solutions for the Galilean satellites (Section 1.3.3), with far-reaching scientific implications. A better determination of the moons' tidal dissipation parameters will bring invaluable insights into the long-term thermal-orbital evolution of the entire system (e.g., Lainey et al., 2009, 2020), but also into the satellites' current interior structure and properties (e.g., Vance et al., 2018; De Marchi et al., 2022). This will provide much more definitive evidence of an internal ocean on Ganymede and Callisto (Section 1.2), and help understanding the origin and history of these oceans.

In this perspective, and as a continuation of previous efforts to characterise natural satellites from their orbital motion, this dissertation specifically investigates how the JUICE and Europa Clipper missions can improve the Galilean moons' ephemerides. This implies developing new methods and strategies to achieve the most accurate and statistically realistic solutions for the moons' dynamics, thus maximising what can eventually be inferred regarding the satellites' interiors and thermal-orbital history.

1.2. THE GALILEAN MOONS

Before investigating the future contribution of the JUICE and Europa Clipper missions to the moons' ephemerides solution, we first give a detailed look at the uniqueness and complexity of the Galilean system (Fig. 1.2), whose main characteristics are summarised in Table 1.1. We specifically focus on our current knowledge and remaining open questions regarding the present and past states of the moons' interiors and orbits. By drawing up such an overview, this section therefore underlines the fundamental scientific implications of a better determination of the Galilean satellites' dynamics, both for the entire system and for each moon individually.

1.2.1. A UNIQUE SYSTEM

Unlike the Saturnian system which is dominated by Titan, the Galilean moons - Jupiter's four largest satellites - are comparably large and massive. Their mutual gravitational interactions therefore have a noticeable influence on their respective dynamics. Moreover, the orbits of the three innermost Galilean moons Io, Europa, and Ganymede are placed in a very peculiar configuration: Io performs four orbital revolutions in the time Europa and Ganymede respectively take to complete two and one orbit(s) (Fig. 1.3). This 1:2:4 mean motion resonance (MMR), commonly referred to as the Laplace resonance, shapes the long-term thermal-orbital evolution of the entire Galilean system. It indeed acts as an eccentricity forcer for Io and Europa, preventing their orbit from getting circularised and keeping a strong tidal dissipation active for these moons (e.g., Lari, 2018). Because of the Laplace resonance, and the consequent transfer of energy from Io to Europa and Ganymede, the strong tidal dissipation between Io and Jupiter dominates the evolution of the entire system. The strong tidal heating that it induces is responsible for Io's active volcanism (Section 1.2.2) and non-negligibly contribute to the survival of Europa's subsurface ocean (Section 1.2.3).

The Laplace resonance is postulated to remain stable for another 10^5 years (Musotto et al., 2002), and is likely to capture Callisto as well in the future (Lari et al., 2020; Celletti et al., 2022). However, while crucial to unravel the long-term evolution of the system, the origin and history of the Laplace resonance are still

Figure 1.2.: The Galilean satellites, ordered by increasing distance to Jupiter - from left to right: Io, Europa, Ganymede, and Callisto. Courtesy: NASA/JPL/DLR.

Table 1.1.: Main properties of the four Galilean satellites: Io, Europa, Ganymede, and Callisto. The orbital period, radius, and bulk density values are taken from NSSDCA (NASA Space Science Data Coordinated Archive). The normalised moments of inertia come from Anderson et al. (2001b) (Io), Gomez Casajus et al. (2021) (Europa), Gomez Casajus et al. (2022) (Ganymede), and Anderson et al. (2001a) (Callisto). Are also reported presupposed interior structure inferred from gravity measurements, as investigated in Anderson et al. (2001b, 1998, 1996, 2001a) for Io, Europa, Ganymede, and Callisto, respectively.

	Io	**Europa**	**Ganymede**	**Callisto**
Type of moon	rocky	icy	icy	icy
Sub-surface ocean?	no	yes	yes	?
Orbital period [days]	1.77	3.55	7.16	16.7
Radius [km]	1821.5	1560.8	2631.2	2410.3
Bulk density [kg/m^{-3}]	3530	3010	1940	1830
MoI factor [-]	0.37685	0.3547	0.3156	0.3549
Differentiated?	yes	yes	yes	not fully
Interior structure	metallic core	metallic core		
	rocky mantle	rocky mantle		(mixed) icy-rocky interior
	crust	water-ice shell		(water?)-ice shell

debated. While the MMR has been postulated to be primordial (Greenberg, 1987; Peale and Lee, 2002), it could also result from a later capture (Yoder, 1979; Henrard, 1983). These different scenarios predict very different tidal heating rate and history for the Galilean moons' interiors, with critical implications for the formation and evolution of the moons' internal oceans. Periods of enhanced eccentricity, either as the Laplace resonance evolves (if the resonance is primordial) or prior to the formation of the current configuration, may indeed have induced strong tidal heating inside the moons, and thus partial ice melting and ocean growth (Ojakangas and Stevenson, 1986; Hussmann and Spohn, 2004; Bland et al., 2009; Běhounková et al., 2021). Such high-eccentricity episodes have furthermore been suggested as a possible explanation for Ganymede's mix of young and old terrains, shown in Fig. 1.2 (see Section 1.2.4 for more detail). Constraining the long-term orbital evolution of the system, of which the moons' current orbits bear witness, is therefore critical to understanding the history of the moons' surfaces and interiors.

Better understanding the Galilean satellites' dynamics, as well as their origin and thermal-orbital evolution, has implications extending far beyond the limit of the Jovian system. With four large satellites and extremely diverse bodies, the latter can indeed be seen as a miniature version of our own Solar System, and studying its history thus provides invaluable insights into that of our own Solar System, but also of exo-planetary systems. Last but not least, the (putative) presence of subsurface oceans of liquid water on Europa, Ganymede, and Callisto elevated these moons as leading candidates for potential habitats in the Solar System. An improved characterisation of the evolution of these satellites' orbits and interiors is therefore critical to understanding how sub-surface oceans have formed and evolved to their present-day states, an essential step in our investigation of habitability conditions.

1.2.2. Io

Io is the innermost Galilean moon, and is very different from the other three. Its eccentric orbit (maintained by the Laplace resonance) and its proximity with Jupiter induce a strong tidal forcing on this moon. As a result, its solid tides can reach up to a hundred meters, and intense heating due to tidal dissipation makes Io a volcanic world, with hundreds of active volcanoes covering its surface (e.g., Lopes et al., 2023). Tidal effects also cause Io to (currently) migrate inwards (Lainey et al., 2009), slowly driving the satellites out of resonance.

Constraining Io's ephemeris is therefore crucial, as the dissipation between Jupiter and Io drives the evolution of the Laplace resonance and thus the thermal-orbital evolution of the entire Galilean system. However, Io's highly radiative environment makes it a very challenging mission target, and direct measurements from a spacecraft are scarce (with the exception of the two Io flybys recently performed as part of Juno's extended mission phase). No flyby around Io is for instance planned for either JUICE or Europa Clipper (see Section 1.3.3 for more detail). In addition to insights derived from telescope images (e.g., Veeder et al., 2012), current constraints on Io's internal dissipation therefore come from ground-based astrometry measurements (Lainey et al., 2009). However, disentangling the similar signatures of Jupiter and Io's dissipations in Io's orbit (see Section 2.3.4) is extremely difficult in the absence of direct measurements of Io's tidal deformation, leading to extremely strong correlations (i.e., linear dependency between the two parameters impeding their unambiguous determination).

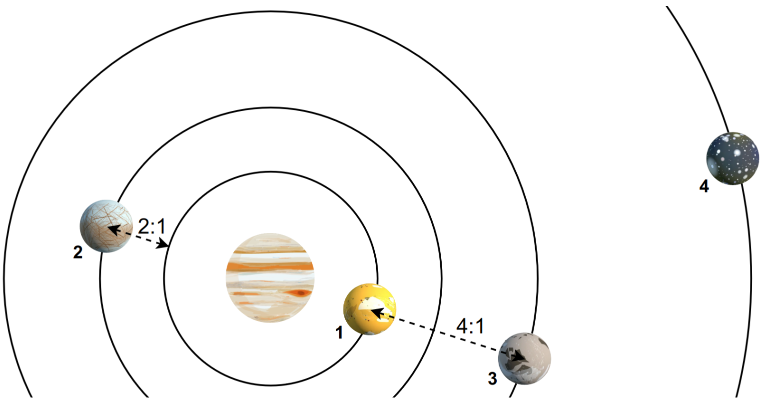

Figure 1.3.: The orbital configuration of the Galilean system (orbits are to scale, the natural bodies' sizes are not), with 1: Io, 2:Europa, 3:Ganymede, and 4:Callisto. The three innermost Galilean moons - Io, Europa, and Ganymede - are caught in a 4:2:1 MMR. Courtesy for the design of Jupiter and its moons: ESA.

Moreover, our poor knowledge of the moon's interior is another limiting factor to a better characterisation of its tidal response. Io's normalised moment of inertia estimated from the Galileo mission's gravity measurements indicates a differentiated interior in agreement with a three-layer model consisting of a metallic core, rocky mantle, and crust (see Table 1.1). The characteristics of Io's mantle, and its thermal state in particular, are however still disputed. The presence of a global magma ocean inside Io has been suggested based on Galileo's magnetic measurements (Khurana et al., 2011), but alternative models and explanations have also been provided (Roth et al., 2017). Io's interior therefore remains poorly determined, with models as different as a fully solid, partially melted mantle, or global magma ocean still being disputed (see Steinke 2021 for a detailed overview). This implies that our knowledge of Io's visco-elastic properties is currently ill-constrained. Overall, the poor characterisation of the dissipation inside Io and Jupiter prevents robustly mapping the estimation results to long-term evolution, which is critical to obtaining a complete and fully consistent picture of the Galilean system's dynamics.

1.2.3. EUROPA

The next Galilean satellite is the icy moon Europa, which the Galileo mission identified as one of the most promising candidates for exo-terrestrial habitability. Galileo's magnetic field measurements indeed brought evidence of the presence of a liquid water ocean below Europa's icy shell and above its silicate mantle (Khurana et al., 1998; Kivelson et al., 2000). In addition to liquid water, Europa seems to possess two other key ingredients to the development of life: carbon-based molecules and energy.

Regarding the latter, tidal heating represents a key external source of energy to help sustain the presence of an internal ocean of liquid water on Europa (Sotin et al., 2009; Nimmo and Pappalardo, 2016). The amount of dissipation occurring within this moon can, however, not yet be quantified: it is indeed weaker than for Io, despite Europa's larger eccentricity, due to its larger distance to Jupiter. Consequently, the smaller signal in the moon's dynamics could not be extracted from astrometry as done for Io (Lainey et al., 2009). The combination of JUICE and Europa Clipper radio science measurements are expected to remedy this, making a crucial step towards a more detailed characterisation of Europa's heat budget, critical to investigate the origin and evolution of its subsurface ocean (Section 1.3.3).

Another important crucial ingredient for habitability is time: Europa would need to be in stable thermal-orbital state for long enough to give life the opportunity to develop, as it did on Earth. Whether Europa fulfils this later condition is nonetheless still debated. As mentioned in Section 1.2.1, different evolution scenarios co-exist to explain the history of the Galilean system and how it led to its present configuration. Europa's young surface features and very few craters, in agreement with the presence of an internal ocean (Greenberg et al., 1998; Pappalardo et al., 1999), are themselves a key part of the puzzle formed by the system's history. They are indeed indicative of a strong tidal dissipation and of recent resurfacing processes. In particular, the diversity of Europa's surface features may bear witness of recent variations of the moon's ice thickness, suggesting changes in Europa's internal ocean deeply linked to the evolution of the Laplace resonance (Hussmann and Spohn, 2004).

The coupling between the moon's interior and orbital evolution is actually an essential aspect of its habitability potential: Běhounková et al. (2021) indeed showed that intense tidal heating during high-eccentricity periods, correlated to the evolution of the Laplace resonance, could trigger the partial melting of Europa's rocky mantle. This has the potential to enhance seafloor volcanic activity, strengthening ocean-mantle interactions and enriching the ocean chemistry, with critical implications for astrobiology. While stability is, as discussed above, a necessary ingredient to the emergence of life, some activity can still be beneficial as means to power such interactions between Europa's ocean and its deep interior. The above hypothesis of a magmatic seafloor activity supporting Europa's habitability has however been challenged by the use of a different mantle models (Green et al., 2024). A better determination of the moons' current dissipation and orbital migration rates, achieved through improved ephemerides solutions, will allow us to put tighter constraints on the system's long-term evolution, and thus to assess the likelihood of different thermal-orbital scenarios for the evolution of the moons' and of their internal oceans.

1.2.4. GANYMEDE

The third Galilean moon, Ganymede, is the largest moon of the Solar System, with a radius about 0.4 times that of the Earth. It is also the only natural satellite to generate its own magnetic field (Kivelson et al., 1996). This causes complex interactions with the Jovian environment, as Ganymede's magnetic field interacts with Jupiter's (Kivelson, 2004; Van Hoolst et al., 2024, and references therein). Ganymede is also thought to host a subsurface ocean although that detection, based on Galileo's magnetic field measurements combined with aurora observations (Kivelson et al., 2002; Saur et al., 2015), is less firm than for Europa. If the presence of such an ocean is confirmed, it might however contain more liquid water than our own planet does. It is interesting to note that the currently presupposed interior structure of Ganymede is similar to Europa's, being that of a differentiated body with a metallic core, rocky mantle, and water-ice shell. The liquid water layer would, however, be trapped between a high-pressure ice layer below and a low-pressure ice outer shell on top, rather than in direct contact with the rocky mantle as is thought to be the case for Europa (see Section 1.2.3). This, combined with the absence of present activity on Ganymede's surface, suggests a limited ocean chemistry compared to Europa's, and thus a lesser astrobiology potential.

Ganymede is nevertheless a very complex and interesting body, which occupies a special, intermediate place among the Galilean moons: its mix of old and young surface features (Fig. 1.2) indeed gives us access to much earlier stages of the Galilean system's history than what can be achieved by studying Io or Europa, while presenting traces of a past internal activity which are absent on Callisto. Ganymede's surface is indicative of a much more ancient resurfacing (Greenberg, 2010) and could be remnants of a period of intense tidal heating, and thus of ocean thickening, due to the excitation of Ganymede's eccentricity by Laplace-like resonances prior to the formation of the present configuration (Showman et al., 1997; Bland et al., 2009).

Explaining the presence of liquid water on Ganymede implies different contribution ratios between the various energy sources, compared to the Europa case. For such a large satellite, radiogenic heating indeed plays a much more dominant role in the moon's heat budget (Bland et al., 2009). Furthermore, Ganymede is further away from Jupiter compared to Io and Europa, and thus currently experiences milder tidal heating. However, as mentioned above, the pumping of Ganymede's eccentricity could have strengthened the tidal heating rate experienced by this moon in the past. The detailed characterisation of Ganymede's hydrosphere by the JUICE mission during its orbital phase will shed light on these questions (Van Hoolst et al., 2024).

1.2.5. CALLISTO

The furthest of the Galilean satellites is also the only one presently not caught in the Laplace resonance, although its eventual capture has been postulated (Lari et al., 2020; Celletti et al., 2022). Callisto presents a much older, heavily cratered surface compared to Ganymede's, showing no sign of recent geological activity. Evidence of an internal ocean below this seemingly dead surface, still based on Galileo's magnetometer measurements (Khurana et al., 1998), is also much weaker than it is for Europa or Ganymede. The survival of this presupposed ocean is an important question, given that Callisto is too far away from Jupiter to experience significant tidal heating (e.g., Nimmo and Pappalardo, 2016), especially since tidal dissipation is not enhanced by the Laplace resonance unlike for the three other Galilean moons.

The existing estimation of Callisto's moment of inertia indicates a less differentiated body than Ganymede (Anderson et al., 2001a, see Table 1.1)[1]. These differences between the moons' differentiation levels possibly originate from different accretion rates during their formation in the circumplanetary disk (e.g., Canup and Ward, 2009). They could, however, also result from different thermal evolution paths, deeply linked to the history of the Laplace resonance. As Callisto is not caught in the MMR, it is nevertheless unlikely that it experienced the same periods of intense tidal heating due to eccentricity pumping as Ganymede might have (Showman et al., 1997; Bland et al., 2009).

The orbital evolution of Callisto remains key to our understanding of the system's history: the fact that this moon has not yet been captured in the Laplace resonance is an important constraint for different evolution scenarios, both for the Galilean system and for the MMR itself. This is for instance a decisive factor when assessing the likelihood of an active resonance locking mechanism for Callisto (Section 1.1). A faster orbital migration for Callisto, although not impossible, appears challenging to reconcile with the current orbital configuration of the Galilean system (Lari et al., 2023). The determination of Callisto's tidal migration rate from JUICE radio science will allow us to firmly confirm or exclude this possible evolution scenario.

[1]This estimate should however be considered carefully, as it is poorly constrained due to Galileo's five flybys all being nearly equatorial.

1.3. The exploration of the Galilean moons

The upcoming JUICE and Europa Clipper missions will follow in the steps of centuries of Galilean moons exploration, both ground- and space-based.

1.3.1. Ground observations

To this day, most of the observational constraints on the Galilean moons' dynamics come from ground-based astrometry. Both the available data sets and resulting ephemerides solutions will be discussed in detail in Chapter 3. To nonetheless give a brief introductory overview, current ephemerides rely on observations starting back at the end of the 19$^{\text{th}}$ century, following the invention of the photographic plate. Accurate photometric measurements of mutual events (i.e., eclipses and occultations of one moon by another), on the other hand, started to be recorded in 1973 and have been performed every 6 years ever since, whenever Jupiter crosses the ecliptic and creates opportunities for this specific type of events.

More recently, novel observation techniques and strategies in astrometry have been explored for moons' ephemerides applications. The improvement of our stellar catalogues, most notably thanks to the Gaia mission (Brown et al., 2018, 2021), has radically enhanced the potential of stellar occultation observations (i.e., occuring when a moon passing in front of a bright enough star, see Section 3.3.1). Our very precise knowledge of the star position now allows us to reconstruct the moon's position at the time of the event with an accuracy of a few kilometres only (Morgado et al., 2019a, 2022). Such an accuracy level is more than one order of magnitude better than what can be achieved with classical techniques (see details in Section 3.3.1), revolutionising ground-based astrometry for moon position determination.

While yielding exceptionally accurate measurements, stellar occultations are rare events, which unfortunately limits their contribution to the ephemerides. Just as recent efforts were made to develop more accurate observation techniques, new measurement strategies were also explored to exploit more frequent events. In this perspective, it was suggested to include the observations of so called mutual approximations in ephemerides solutions (Morgado et al., 2016, 2019b). Mutual approximations can be seen as pseudo mutual events where the distance between two targets in the sky reaches a minimum, instead of a perfect alignment as is the case for a typical eclipse or occultation event. As such, they are much more frequent than mutual events, but achieve comparable accuracy levels. Both stellar occultations and mutual approximations thus show very complementary advantages, boosting the potential of astrometry for natural satellites' ephemerides applications.

1.3.2. The age of planetary missions

The first flyby of Jupiter by Pioneer 10 marked the beginning of a new era where in-situ measurements and observations in the Jovian system become possible, a turning point immortalised by the first spacecraft-based images of the Galilean moons ever taken (Fig. 1.4a). Following Pioneer 10's footsteps, numerous missions have visited the Jovian system. Pioneer 11 performed the second Jovian flyby shortly after his predecessor (in 1973 and 1974, respectively). Jupiter was later shortly visited

1

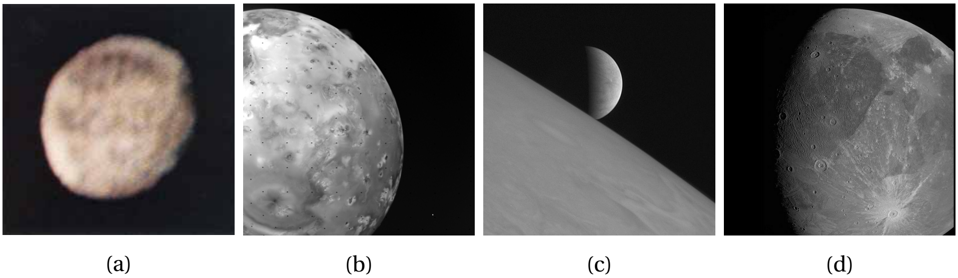

Figure 1.4.: From left to right: picture of Ganymede taken by Pioneer 10; Io as seen by Voyager; Europa rising observed by the New Horizons spacecraft; Ganymede during one of Juno's flybys (Courtesy: NASA).

by several spacecraft on their way to the more distant regions of the outer Solar System, offering multiple opportunities to take more pictures and measurements of the planet and its moons. The Voyager 1 and 2 missions for instance collected many images of the Galilean satellites during their Jupiter encounters, leading to a better characterisation of the moons' surfaces (Smith et al., 1979b,a). Among other major findings, these observations led to the discovery of active volcanism on Io (Fig. 1.4b), and evidence of complex (past) surface activity on Europa and Ganymede. The Cassini and New Horizons spacecraft also passed through the Jovian system in late 2000 and 2007 on their way to Pluto and Saturn, respectively, the former even spending about 6 months studying Jupiter and its moons in conjunction with the Galileo mission (e.g., Hansen et al., 2004; Throop et al., 2004; Vasavada and Showman, 2005).

Unlike the above-mentioned missions who did not linger in the Jovian system, the Galileo mission was specifically dedicated to studying Jupiter and its moons and, in 1995, became the first spacecraft to ever enter orbit around an outer planet. To this day, most of our knowledge about the Galilean satellites follows from Galileo's measurements, collected during the spacecraft's multiple flybys (7, 11, 8, and 8 flybys at Io, Europa, Ganymede, and Callisto, respectively). The main scientific outcomes of the mission, already mentioned in Section 1.2, include evidences for internal oceans on Europa, Ganymede, and possibly Callisto, a deeper characterisation of Io's volcanism following Voyager's discovery, as well as a detailed picture of magnetic interactions in the Jovian system, including the detection of Ganymede's own dynamo. The probable presence of liquid water beneath the icy crust of Europa, and possibly Ganymede and Callisto, radically affected our definition of habitability within and beyond the boundaries of the Solar System, and identified these moons as prime targets for decades of planetary exploration to follow.

Finally, the Juno spacecraft entered orbit around Jupiter in 2016 and is now in its extended mission phase, foreseen to last until 2025. The focus of the Juno mission is primarily on the central planet itself, but the remarkable insights it provided also pave the way for the next exploration steps: a better characterisation of the Jovian environment directly benefits follow-up missions, such as the moons' explorers JUICE and Europa Clipper (Section 1.3.3). Some of Juno's main scientific achievements include a much more detailed picture of Jupiter's magnetosphere (e.g., Connerney et al., 2022; Moore et al., 2018, 2019) and atmosphere (Bolton et al., 2017; Kaspi et al., 2018; Li et al., 2020). Nonetheless, the improved determination of the planet's gravity field (Iess et al., 2018; Durante et al., 2020; Idini and Stevenson, 2021), including the detection of unexpected time variations, will benefit JUICE and Europa Clipper's radio science investigations of the moons' orbits and interiors the most. Jupiter's gravitational attraction indeed influences both the spacecraft and moons' dynamics. By providing a refined gravity model, the Juno mission limits the impact of Jupiter's gravity coefficients uncertainties on the quality of the moons' solution.

In addition to its main Jupiter investigations, the Juno spacecraft also performed two flybys around Ganymede at the end of its nominal mission, improving our knowledge of the moon's magnetic field (Weber et al., 2022), but also gravity, geology, surface features and composition, etc. (Hansen et al., 2022). As part of Juno's extended missions, a flyby of Europa also occurred in 2022, followed by two flybys around Io in late 2023 and early 2024. Given the rarity of direct in-situ measurements of Io, these two flybys are expected to be extremely valuable for future solutions of the Galilean system's dynamics.

1.3.3. THE JUICE AND EUROPA CLIPPER MISSIONS ERA

Following the growing interest in Jupiter's icy moons and in their potential as possible exo-terrestrial habitats, two missions will target Jupiter's Galilean moons in the coming decade. ESA's JUpiter ICy moons Explorer (JUICE) is now on its way to the Jovian system. It will be joined by NASA's Europa Clipper spacecraft, to be launched in 2024 and arriving at Jupiter in 2030, one year before JUICE.

Both missions, although focussing on different moons, have similar objectives: by studying mostly Europa for Europa Clipper, Ganymede and Callisto for JUICE, the two spacecraft will reconstruct an unprecedentedly detailed picture of the Galilean satellites, investigating their habitability potential and shedding light on the origin and evolution of the Galilean system, providing invaluable insights into planetary systems formation in general. In particular, Europa Clipper's more than 50 flybys at Europa and JUICE's orbital phase around Ganymede will allow for an extremely thorough characterisation of the two moons' hydrospheres.

The two missions are highly synergistic. On one hand, JUICE's unique mission design, including the first orbital phase around a natural satellite (except our own) combined with a flyby tour, will provide valuable insights into Callisto's dynamics and interiors (21 flybys planned around that moon), before entering orbit around Ganymede. With only two dedicated JUICE flybys, information on Europa will be limited, but Europa Clipper will take care of this missing piece of the puzzle. The complementarity between the two missions' Jovian tours is illustrated in Fig. 1.5, which also highlights the overlapping of their timelines. Given the strongly coupled dynamics of the Galilean satellites, this inter-mission synergy represents a unique opportunity to reconstruct an extremely accurate, yet statistically balanced, solution for the moons' ephemerides, with critical implications for our understanding of their interiors and evolution (see Section 1.1). While this dissertation primarily

1

focusses on the JUICE mission, it is therefore necessary to consider both missions concurrently, which has become customary in ephemerides-dedicated simulations over the course of this project (Magnanini et al., 2024; Fayolle et al., 2023b, 2024).

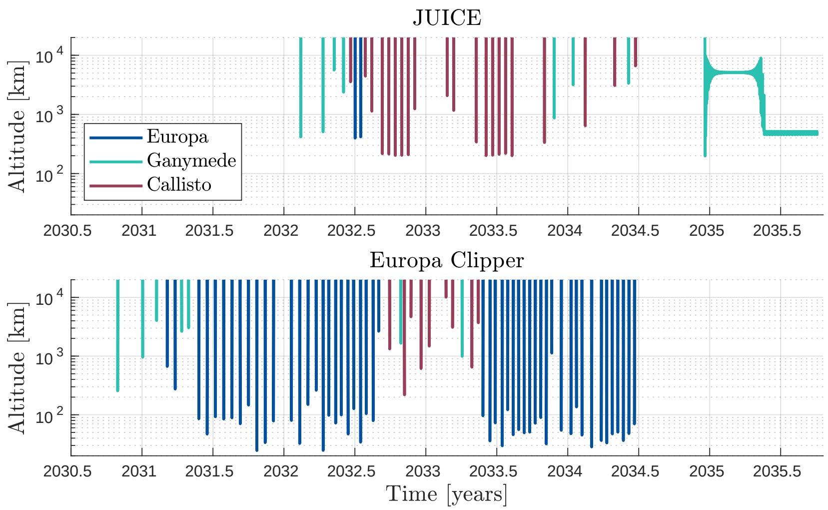

Figure 1.5.: Timeline and altitude of the JUICE and Europa Clipper flybys around Europa, Ganymede, and Callisto, according to the latest mission trajectories[2][3].

In the JUICE-Europa Clipper framework, moons' ephemerides improvement will mainly be achieved through radio science tracking of the spacecraft during their close encounters with the satellites. These measurements indeed contain indirect signatures of the moons' dynamics captured in the spacecraft's own orbits (see discussion in Section 1.4). For JUICE, the contribution of the 3GM (Gravity & Geophysics of Jupiter and Galilean Moons, Iess et al., 2024) dedicated radio science instrument to ephemerides will be supported by PRIDE (Planetary Radio Interferometry and Doppler Experiment, Gurvits et al. 2023). JUICE-PRIDE will provide phase-referenced VLBI (Very Long Baseline Interferometry) measurements of the spacecraft position (Duev et al., 2012, 2016), alongside *ah hoc* Doppler observables (Bocanegra-Bahamón et al., 2018). Unlike JUICE, Europa Clipper will unfortunately not be equipped with dual-frequency X/Ka-band tracking capabilities, but will carry an X-band coherent transponder. Radio science will not only contribute to a better determination of the moons' dynamics, but also constrain their gravity fields, rotations, and tidal deformations, which all contain signatures of the satellites' interiors. This dissertation, which focusses on improving the ephemerides specifically, hence yielding a refined characterisation of tidal dissipation

[2]JUICE trajectory: juice_mat_crema_5_0_20220826_20351005_v01 `https://www.cosmos.esa.int/web/spice/spice-for-juice`

[3]Europa Clipper trajectory: 21F31_MEGA_L241010_A300411_LP01_V4_postLaunch_scpse `https://naif.jpl.nasa.gov/pub/naif/EUROPACLIPPER/kernels/spk/`

in the system (Section 1.1), contributes to the broader radio science objective of reconstructing an unprecedentedly detailed and accurate picture of the system's past and present thermal-orbital state.

Radio science tracking will moreover not be the only means to characterise the moons' dynamics and interiors (see JUICE's instrument set in Fig. 1.6). Space-based optical data from the science and navigation cameras (for JUICE: JANUS and NavCam, respectively; for Europa Clipper: EIS - Europa Imaging System) could also contribute to the ephemerides. Measurements by JUICE's altimeter GALA (GAnymede Laser Altimeter, Hussmann et al., 2024) could furthermore slightly improve JUICE's orbit determination (Villamil et al., 2021). However, GALA's main contribution will mostly concern the determination of the moons' topography and interiors (Hussmann et al., 2019), constraining the latter from measurements of the moons' rotations and tidal responses. JUICE's radar (RIME, Bruzzone et al., 2024) and magnetometer (J-MAG, Dougherty et al., 2024) will also provide invaluable insights into the satellites' interiors. Similar instruments onboard the Europa Clipper spacecraft will tackle comparable scientific investigations. Relevant inter-instrument synergies will be revisited in Chapter 10 when discussing the scientific implications of an improved ephemerides determination.

1.4. SCIENTIFIC RATIONALE AND RESEARCH OBJECTIVES

Current ephemerides for natural satellites are primarily based on astrometric observations, either Earth- or space-based (Lainey et al., 2004a, 2007, 2009, 2012,

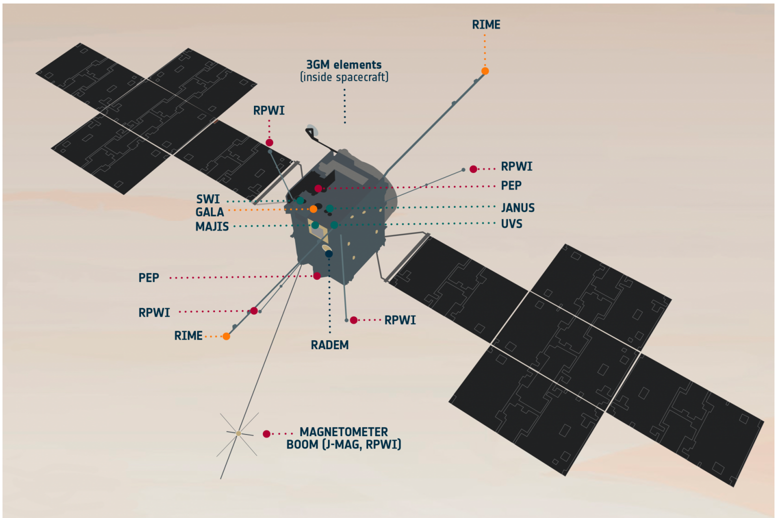

Figure 1.6.: JUICE's instrument set, including the 3GM radio science package, altimeter GALA, radar RIME, magnetometer J-MAJ, science camera JANUS. Courtesy: ESA.

2017, 2020, see more detail in dedicated Section 3.4). The upcoming, almost simultaneous arrival of two spacecraft in the Jovian system in the 2030s, and the exceptional accuracy of their radio science measurements, will, however, prompt a radical paradigm shift in moons' ephemerides determination. Including JUICE and Europa Clipper radio science indeed has the potential to significantly improve the quality of the moons' state solutions, but this requires to develop and investigate the required tools, methodologies, and observation strategies to ensure that the solution fully benefits from these missions. This is essential to obtain the best characterisation of the system's dynamics to date, bringing crucial insights in the origin and history of the Galilean moons. It therefore directly contributes to fulfilling both JUICE and Europa Clipper's scientific objectives: constraining the evolutionary path that led to the present system is key to our understanding of planetary systems formation and habitability.

1.4.1. The Galilean moons' ephemerides - current challenges

Including JUICE and Europa Clipper radio science in the Galilean moons' ephemerides solution poses a number of challenges. The first of them is deeply linked to the indirect nature of the measurements. Radio science observables (see Section 3.3.2) are indeed only directly sensitive to the spacecraft's dynamics. The latter nonetheless contain indirect signatures of the moons' orbits via the gravitational attraction exerted on the spacecraft, especially during close encounters. Reconstructing a global and consistent solution for the moons' dynamics from radio science therefore requires solving for both the spacecraft and moons' orbits. This can be achieved with two different strategies, which will be discussed in more detail in Section 3.4.1. A brief introduction is however necessary to understand the rationale for part of the work presented in this dissertation (Section 1.4). The moons' and spacecraft's states are typically estimated separately, using a so-called decoupled approach (Antreasian et al., 2008; Rosenblatt et al., 2008; Durante et al., 2019). An alternative approach, in which we concurrently solve for both the spacecraft and natural satellites' dynamics, has however also been applied to similar problems (Jacobson, 2014, 2022). The analytical framework required for such a coupled estimation is nonetheless not available in the literature, complicating the interpretation of existing analyses. The respective performances of the coupled and decoupled strategies have moreover not been compared yet, a step which would nonetheless be crucial in light of past difficulties encountered when trying to adopt a coupled approach (Durante et al., 2019; Zannoni et al., 2020; Jacobson, 2022).

In addition to the methodology aspects discussed above, achieving an extremely accurate, yet fully consistent, solution for the dynamics of the Galilean satellites and associated parameters requires combining diverse observation types in a single solution. The complex and strongly coupled dynamics of the Galilean system (e.g., Lainey et al., 2006) indeed severely complicate the reconstruction of a statistically coherent dynamical solution. Because of the unique configuration created by the Laplace resonance, constraining our knowledge of Io, Europa, and Ganymede would ideally require a balanced data set able to yield a stable estimation of their dynamics. Due to the short time span of the missions ($\sim$ 5 years) and their strong focus on Europa and Ganymede (see Section 1.3.3), solely relying on JUICE and Europa Clipper radio science cannot yield a stable, statistically coherent solution (e.g., Dirkx et al., 2017). In a complex dynamical system such as the one formed by the Galilean moons, it is therefore critical to exploit existing or novel synergies between different data types, and to investigate the potential of innovative observation strategies for ephemerides generation purposes. This includes recent astrometry techniques such as stellar occultations and mutual approximations (see Section 1.3), but also unique observation opportunities created by the presence of one or more spacecraft in the Jovian system. Identifying such possibilities and quantifying their contribution to the quality of the moons' ephemerides solutions is the second research avenue explored in this dissertation.

Prior to this dissertation, JUICE and Europa Clipper radio science simulation analyses primarily investigated the determination of the moons' gravity fields, rotations, and tides (Cappuccio et al., 2020a), a preparation effort that continued throughout the course of this work (Di Benedetto et al., 2021; De Marchi et al., 2021, 2022; Cappuccio et al., 2022). Oftentimes, radio science analyses for past missions also focussed on the determination of physical parameters. The above-mentioned, specific challenges associated with the coherent estimation of the moons' dynamics from tracking measurements of an in-system spacecraft therefore typically remain unnoticed or were circumvented (Durante et al., 2019; Zannoni et al., 2020). The use of radio science data in existing ephemerides solutions is moreover somewhat under-documented, with some specificities of the underlying estimation methodology remaining untransparent. In the context of the JUICE and Europa Clipper missions, rare ephemerides-dedicated studies limited themselves to a single, sometimes simplified, state estimation method and/or data set (Dirkx et al., 2017). This dissertation will push back these existing limitations, both in terms of methodology and inter-data set synergies, as will be further detailed in the following.

1.4.2. Research questions

The main objective of this dissertation is to pave the way for future global inversion analyses of radio science and astrometry, key to improving natural satellites' ephemerides and eventually furthering our understanding of planetary systems' evolution. In the context of the upcoming JUICE and Europa Clipper missions, and in light of their promises and challenges discussed above, what this goal entails is twofold. It requires investigating different state estimation strategies to best exploit the information on the moons' dynamics encoded in spacecraft tracking measurements, as well as exploring the potential of other types of observations to most efficiently complement the JUICE-Europa Clipper radio science data set. Such an approach does not only aim at improving the ephemerides accuracy, but also how realistic the statistical assessment of the solution's uncertainties is. Given the complexity of solving for the strongly coupled dynamics of the Galilean system, combining all available data types in an optimal way has the potential to provide the most complete picture to date of the present-day dynamics of the Galilean satellites, thus opening a windows on the long-term history of the system. In this perspective, this dissertation answers the following research question:

1

What are the best observation and inversion strategies to improve the determination of the Galilean moons' ephemerides after the JUICE and Europa Clipper missions?

Answering the above will first require us to draw up a detailed overview of the main dynamical modelling aspects driving the orbital and rotational motion of the Galilean satellites, which will be the focus of Chapter 2. Special attention will be paid to tidal models, because of their crucial influence on the evolution of the moons' orbits and interiors. Chapter 3 will continue by presenting the underlying inversion principle behind the determination of moons' ephemerides, along with a description of the available data sets and existing solutions.

After having laid out the necessary background theory and models, as well as the current state-of-art for natural satellites' ephemerides, we start by comparing different state estimation techniques when solving for the dynamics of different bodies (spacecraft, moons, central planet) from radio science. In Chapter 4, we propose a detailed inversion framework to concurrently estimate all relevant states and dynamical parameters of interest from a single, or combined, set of observations, currently critically missing in the literature. For the JUICE test case, we compare the performance of this coupled approach with the more commonly-used, decoupled estimation approach separately solving for the spacecraft's orbit and natural bodies' dynamics. Chapter 4 thus answers the following questions:

1. *How do coupled and decoupled estimation strategies compare when reconstructing natural satellites' orbits from spacecraft measurements?*

2. *What are the main challenges of the reconstruction of a coupled, global solution for the Galilean satellites' dynamics from JUICE-only data?*

Relying on the coupled estimation method developed in Chapter 4, we then analyse novel observation techniques and strategies to further improve the determination of the Galilean moons' dynamics. Chapter 5 starts by considering VLBI tracking capabilities, and more specifically JUICE-PRIDE, as a powerful means to constrain the ephemerides of the Galilean satellites. Building on the work by Dirkx et al. (2017), we assess the contribution of nominal VLBI tracking measurements of the JUICE spacecraft, paying special attention to the out-of-plane component of the moons' positions (i.e., in the direction perpendicular to the moons' orbital plane), which is typically poorly constrained by classical radio science observables (see Section 3.3.2). Moreover, we provide the first study of simultaneous, multi-spacecraft VLBI tracking of both JUICE and Europa Clipper, which can yield exceptionally accurate measurements of their relative angular position. We quantify the potential of these unique measurements, made possible by the remarkable synergy between the two missions. Taking one step further, Chapter 5 also proposes different ways to exploit PRIDE-JUICE measurements for validation purposes, an essential step to eventually reconstruct a fully consistent solution for the dynamics of the Galilean satellites. This PRIDE analysis thus answers the research questions:

3. *Which improvement and validation opportunities can PRIDE VLBI measurements bring to the joint JUICE-Europa Clipper ephemerides solution?*

4. *Which opportunities will the JUICE and Europa Clipper missions offer to perform multi-spacecraft VLBI measurements, and how will such data contribute to the solution?*

As discussed above, and despite the revolutionary solution improvement expected from JUICE and Europa Clipper radio science, ground-based astrometry - on which current ephemerides are based (see Chapter 3) - is expected to still significantly contribute to the estimation. The following chapters investigate this potential, specifically focussing on stellar occultations and mutual approximations as very promising, yet under-explored, measurement strategies (Section 1.3.1). In this perspective, Chapter 6 develops the missing framework required to include mutual approximations in ephemerides solutions. By performing a detailed analysis of this new methodology and comparing it with an existing, approximate approach, we answer the following:

5. *How should mutual approximation observations between two moons be used in the estimation to reconstruct the moons' dynamics?*

Instead of focussing on new types of observations not yet widely applied in ephemerides solutions, Chapter 7 proposes a synergistic combination of well-established techniques. As the accuracy of astrometric measurements of the moons' positions improves, the uncertainty in the ephemeris of the central planet starts playing a bigger role. For stellar occcultations, reaching kilometre level accuracies, this error source can even dominate the error budget of the observations (Morgado et al., 2022). However, it can be mitigated by extracting information on the local position of the planet from VLBI tracking of an in-situ spacecraft, allowing the ephemerides solution to fully benefit from the exceptional accuracy of stellar occultation measurements. Chapter 7 describes this novel, combined measurement strategy in detail, and assesses its potential for the Jovian system based on promising Juno test cases. This eventually addresses the following research question:

6. *How can spacecraft tracking contribute to further reducing the error budget of the most accurate ground-based astrometry observations?*

After having separately investigated the performance of different inversion methodologies and the contribution of various data sets, we finally combine simulated JUICE-Europa Clipper radio science with astrometric observations, using the coupled state estimation approach laid out in Chapter 4. Chapter 8 presents the underlying methodology of this global inversion, addressing how to merge very diverse data sets in a single estimation, and quantifies the contribution of each type of astrometric observations to the radio science solution. This chapter therefore covers the two questions:

7. *How would adding existing astrometry data improve the JUICE-Europa Clipper radio science solution?*

8. *Which existing astrometric observations will be most beneficial to combine with JUICE and Europa Clipper radio science data sets?*

This global inversion analysis represents the final cornerstone of this work. It indeed provides the required methodology to combine diverse measurements in a single estimation, which will be critical for JUICE and Europa Clipper ephemerides analyses, and highlights which data sets are expected to be the most valuable.

Chapter 9 then brings together the conclusions of the separate analyses gathered in this dissertation to answer the above research questions. Overall, this work provides a broad overview of various estimation and observation techniques to improve the Galilean moons' ephemerides, in the context of the upcoming JUICE and Europa Clipper missions. Their extremely accurate radio science measurements and unique mission configurations will push the existing dynamical models and solutions to their limit. This will trigger new challenges, which are also compiled and examined in Chapter 9, alongside possible mitigation avenues.

The exceptional ephemerides accuracy attainable when such difficulties are resolved will open unprecedented opportunities to further our understanding of planetary systems dynamics and evolution. As a final step, Chapter 10 therefore considers the scientific implications of such a refined determination of the Galilean moons' dynamics. The perspectives that this work uncovers for our understanding and characterisation of other planetary moon systems, in light of future exploration prospects, are discussed in the last pages of this dissertation.

2

DYNAMICS OF NATURAL SATELLITES

The determination of natural satellites' ephemerides requires the accurate modelling of their translational dynamics and rotations including, critically, the incorporation of tidal effects. In this chapter, we present and discuss the underlying models, assumptions, as well as possible sources of modelling inconsistencies. As underlined in Section 1.1, the long-term evolution of the moons' translational and rotational dynamics is driven by tidal dissipation mechanisms. A detailed discussion of the chosen tidal models and of their implementation is therefore essential. Given that this dissertation focusses on ephemerides determination, this chapter also considers the different models and related parameters from an estimation perspective, and examines specific difficulties arising in this context.

2.1. TRANSLATIONAL DYNAMICS

The dynamics of a natural satellite around its central planet are governed by its equations of motion. Among the various accelerations acting on the satellite, the gravitational interactions, including tidal effects, are the ones dominating the satellite's dynamics. In the following, we provide a general formulation for the equations of motion (Section 2.1.1), before discussing the modelling of the gravitational potentials and resulting accelerations (Section 2.1.2). Tidal effects, on the other hand, will be discussed in more detail in a dedicated section (Section 2.3).

2.1.1. EQUATIONS OF MOTION

We choose to express the equations of motion describing the dynamics of a natural satellite in a planetocentric reference frame (i.e., centred at Jupiter for the Galilean satellites, with fixed axes). In the following, the central body is always denoted by the index 0. We will start by examining the acceleration exerted on an extended satellite i due its mutual gravitational interaction with another extended body j in an inertial frame, before moving to a non-inertial planetocentric frame, and finally providing a complete formulation for the satellite's equations of motion.

MUTUAL GRAVITATIONAL INTERACTION IN AN INERTIAL FRAME

Adopting a similar formalism as in e.g., Lainey et al. (2004b), the acceleration of an extended body i due to its gravitational interaction with another extended body j can be decomposed as

$$\ddot{\mathbf{r}}_{ji}^{(j\rightarrow i)} = \ddot{\mathbf{r}}_{ji}^{(\bar{j}\rightarrow\bar{i})} + \ddot{\mathbf{r}}_{ji}^{(\hat{j}\rightarrow\bar{i})} + \ddot{\mathbf{r}}_{ji}^{(\bar{j}\rightarrow\hat{i})} + \ddot{\mathbf{r}}_{ji}^{(\hat{j}\rightarrow\hat{i})}, \tag{2.1}$$

where $\mathbf{r}_{ji}$ and $\ddot{\mathbf{r}}_{ji}$ respectively correspond to the relative position and acceleration vectors of body i with respect to body j. The symbols $\bar{k}$ and $\hat{k}$ refer to the respective contributions of the point-mass and extended gravitational potentials of a body k. The first and second terms thus describe the effect of the point mass and extended body j on point mass i, while the third term accounts for the effect of body i's extended potential on point mass j. Using Newton's third law, the latter can be rewritten as

$$\ddot{\mathbf{r}}_{ji}^{(\bar{j}\rightarrow\hat{i})} = -\frac{m_i}{m_j}\ddot{\mathbf{r}}_{ij}^{(\hat{i}\rightarrow\bar{j})}. \tag{2.2}$$

Finally, the figure-figure interactions (Dirkx et al., 2019a) represented by the term $\ddot{\mathbf{r}}_{\hat{i}\hat{j}}$ in Eq. 2.1, which describe the mutual effects of the extended gravitational potentials of i and j on one another, can be safely neglected for our applications (Lainey et al., 2004b; Dirkx et al., 2016). Eq. 2.1 thus becomes

$$\ddot{\mathbf{r}}_{ji}^{(j\rightarrow i)} = \ddot{\mathbf{r}}_{ji}^{(\bar{j}\rightarrow\bar{i})} + \ddot{\mathbf{r}}_{ji}^{(\hat{j}\rightarrow\bar{i})} - \frac{m_i}{m_j}\ddot{\mathbf{r}}_{ij}^{(\hat{i}\rightarrow\bar{j})}. \tag{2.3}$$

CENTRAL BODY GRAVITATIONAL ACCELERATION

The acceleration of body i due to its gravitational interaction with central body 0, expressed with respect to the non-inertial reference frame centred at body 0, is noted $\ddot{\mathbf{r}}_{i}^{(0\rightarrow i)}$ and defined as

$$\ddot{\mathbf{r}}_{i}^{(0\rightarrow i)} = \ddot{\mathbf{r}}_{0i}^{(0\rightarrow i)} - \ddot{\mathbf{r}}_{i0}^{(i\rightarrow 0)}, \tag{2.4}$$

where $\ddot{\mathbf{r}}_{0i}^{(0\rightarrow i)}$ and $\ddot{\mathbf{r}}_{i0}^{(i\rightarrow 0)}$ are respectively the inertial acceleration of body i caused by the central body 0, and vice versa. Substituting Eq. 2.3 in the above with the appropriate indices leads to

$$\ddot{\mathbf{r}}_{i}^{(0\rightarrow i)} = \ddot{\mathbf{r}}_{0i}^{(\bar{0}\rightarrow\bar{i})} - \ddot{\mathbf{r}}_{i0}^{(\bar{i}\rightarrow\bar{0})} + \left(\frac{m_i+m_0}{m_i}\right)\ddot{\mathbf{r}}_{0i}^{(\hat{0}\rightarrow\bar{i})} - \left(\frac{m_i+m_0}{m_0}\right)\ddot{\mathbf{r}}_{i0}^{(\hat{i}\rightarrow\bar{0})}. \tag{2.5}$$

THIRD BODY PERTURBATIONS

Similarly, the acceleration of body i with respect to the reference frame origin fixed at body 0 due to the mutual gravitational interactions between i and a third body j should also account for the acceleration of the central body 0 due to j. This third body perturbation can therefore be expressed as

$$\ddot{\mathbf{r}}_{i}^{(j\rightarrow i)} = \ddot{\mathbf{r}}_{ji}^{(j\rightarrow i)} - \ddot{\mathbf{r}}_{j0}^{(j\rightarrow 0)}, \tag{2.6}$$

where the two terms can both be obtained from Eq. 2.3.

COMPLETE FORMULATION FOR THE EQUATIONS OF MOTION

For a system with N satellites orbiting around a central planet (index 0), the total acceleration exerted on a moon i can therefore be expressed as follows (in the planetocentric reference frame):

$$\ddot{\mathbf{r}}_i = \ddot{\mathbf{r}}_i^{(0\to i)} + \sum_{k=0,k\neq i}^{N} \ddot{\mathbf{r}}_i^{(k\to i)} + \mathbf{a}_{\mathrm{T}} + \mathbf{a}_{\mathrm{R}}, \tag{2.7}$$

where Eqs. 2.3, 2.5, and 2.6 can be used to compute the above. Other third body perturbations, such as the ones exerted by other planets of the Solar System (typically modelled as point masses), can be included in a similar manner as the accelerations due to other satellites. Additionally, relativistic and tidal accelerations, respectively denoted $\mathbf{a}_{\mathrm{T}}$ and $\mathbf{a}_{\mathrm{R}}$, are also included. The exact formulation of the tidal acceleration will be discussed in detail in Section 2.3, the choice of tidal model having a significant influence on the effects of tides on the moons' dynamics. Relativistic corrections, which account for space-time curvature when computing gravitational accelerations (both for central and third-body gravitational accelerations) will not be discussed further (more detail can be found in e.g., Combrinck, 2012). Unlike tides, which play a crucial role in the intricate feedback between the moons' orbits and rotations, and are therefore key to the consistent modelling of inter-moon dynamics, relativistic perturbations are of lesser importance for this dissertation work. They indeed do not significantly influence the dynamical evolution of the system, and the accuracy of the adopted models is therefore less critical.

2.1.2. GRAVITY FIELD MODELLING

The gravity field of an extended body k is typically modelled by a spherical harmonics expansion of its gravitational potential:

$$U_k(r,\phi,\lambda) = \frac{Gm_k}{r}\sum_{n=0}^{\infty}\left(\frac{R_k}{r}\right)^n \sum_{m=0}^{\infty}\left[\bar{C}^k_{nm}\cos(m\lambda) + \bar{S}^k_{nm}\sin(m\lambda)\right]\bar{P}_{nm}(\sin\phi). \tag{2.8}$$

m_k is the total mass of body k and R_k represents its equatorial radius. The radial distance, r, latitude, ϕ, and longitude, λ, are the spherical coordinates of the point at which the potential is evaluated, in the reference frame fixed to body k. $\bar{C}^k_{nm}$ and $\bar{S}^k_{nm}$ are body k's normalised cosine and sine spherical harmonics coefficients of degree n and order m, respectively, and $\bar{P}_{nm}$ designates the normalised associated Legendre polynomial.

SPHERICAL HARMONICS GRAVITY COEFFICIENTS

The normalised spherical harmonics coefficients can be obtained from the unnormalised coefficients C^k_{nm} and S^k_{nm} as follows:

$$\begin{pmatrix}\bar{C}^k_{nm}\\ \bar{S}^k_{nm}\end{pmatrix} = \sqrt{\frac{(n+m)!}{(2-\delta_{0m})(2n+1)(n-m)!}}\begin{pmatrix}C^k_{nm}\\ S^k_{nm}\end{pmatrix}, \tag{2.9}$$

where δ_{0m} is the Kronecker delta. These coefficients are directly related to the internal density distribution of body k by (e.g., Lambeck, 1988):

$$\begin{pmatrix} \bar{C}^k_{nm} \\ \bar{S}^k_{nm} \end{pmatrix} = \frac{1}{m_k(2n+1)} \int_{V_k} \rho_k(r,\phi,\lambda) \left(\frac{r}{R_k}\right)^n \bar{P}_{nm}(\sin\phi) \begin{pmatrix} \cos m\lambda \\ \sin m\lambda \end{pmatrix} dV, \tag{2.10}$$

where $\rho_k(r,\phi,\lambda)$ describes the internal density of body k at these coordinates.

The monopole (i.e., $n=0$) describes the potential of a point mass body, while the degree one coefficients represent a possible offset between the body's centre of mass and the origin of the body-fixed reference frame. Since the latter is typically chosen to coincide with the centre of mass, however, these coefficients are usually equal to zero. Regarding the degree two coefficients, $\bar{C}_{21}$ and $\bar{S}_{21}$ are equal to zero if the principal axis of inertia and the body's rotation axis are aligned. On the contrary, non-zero (possibly time-varying) $\bar{C}_{21}$ and $\bar{S}_{21}$ values would describe how the rotation pole deviates from the body-fixed z-axis. Similarly, a non-zero $\bar{S}_{22}$ coefficient would indicate a misalignment between the body's x- and y axes and the equatorial moments of inertia.

For typical dynamical studies of natural satellites (typically caught in synchronous rotation, see Section 2.2.2), the body-fixed reference frame is generally defined such that the satellite's axes (almost) align with its principal axes of inertia. In particular, small deviations between the satellite's polar axis and its principal axis of inertia are commonly neglected, and $\bar{C}_{21}$, and $\bar{S}_{21}$ are set to zero. It must however be noted that we chose not to assume $\bar{S}_{22}=0$ in our model, unlike $\bar{C}_{21}$ and $\bar{S}_{21}$. A small non-zero $\bar{S}_{22}$ value is indeed easily generated by a slight mismodelling of the satellite's rotation around its spin axis. Such a small $\bar{S}_{22}$ will furthermore have a very similar on the moon's orbit as satellite tides, as will be shown in Section 2.4.2. For our purposes, it is therefore critical to include the contribution of a hypothetical non-zero $\bar{S}_{22}$.

From Eq. 2.10, it also follows that the contribution of the body's deep interior to the coefficients $\bar{C}_{nm}, \bar{S}_{nm}$ decreases with n. Out of all coefficients, those of degree two are thus the most affected by the body's deep interior. They can contain valuable information on the internal density distribution, and directly relate to the body's principal moments of inertia (see Section 2.2.1). Higher degree coefficients, on the other hand, are mostly affected by the body's outer layers (e.g., icy shell for icy satellites like Europa, Ganymede, or Callisto).

DEGREE TWO POTENTIAL

The potential expansion is often truncated at degree and order two which, assuming $\bar{C}^k_{10} = \bar{C}^k_{11} = \bar{S}^k_{11} = \bar{C}^k_{21} = \bar{S}^k_{21} = 0$, leads to the following simplified expression:

$$\begin{aligned} U_k(r,\phi,\lambda) = \frac{Gm_k}{r} + \frac{Gm_k R_k^2}{r^3} \Bigg[& \frac{\bar{C}^k_{20}}{2} \left(3\sin^2\phi - 1\right) \\ & +3\left(\bar{C}^k_{22}\cos(2\lambda) + \bar{S}^k_{22}\sin(2\lambda)\right)\cos^2\phi \Bigg]. \end{aligned} \tag{2.11}$$

Assuming that the body-fixed latitude ϕ at which the potential is evaluated is equal to 0 (i.e., zero inclination and obliquity, and a perfect alignment of the body's equatorial and orbital planes), the above can be further simplified into

$$U_k(r,\phi,\lambda) = \frac{Gm_k}{r} + \frac{Gm_k R_k^2}{r^3}\left[-\frac{\bar{C}_{20}^k}{2} + 3\left(\bar{C}_{22}^k\cos(2\lambda) + \bar{S}_{22}^k\sin(2\lambda)\right)\right]. \tag{2.12}$$

RESULTING GRAVITATIONAL ACCELERATION

The potential given by Eq. 2.8 is expressed in the reference frame fixed to body k, and the resulting acceleration sensed by a point mass body j due to the extended gravitational potential of body k (including the point mass contribution) in the inertial frame is thus given by

$$\ddot{\mathbf{r}}_{kj}^{(k\to\bar{j})} = -\mathbf{R}_k \nabla_k U_k(r_j,\phi_j,\lambda_j), \tag{2.13}$$

where the gradient is calculated in the body-fixed frame. $\mathbf{R}_k$ is the rotation matrix describing the rotation from the reference frame fixed to body k to the inertial reference frame in which the acceleration $\ddot{\mathbf{r}}_{kj}$ is expressed. Circling back to the gradient expression given by Eq. 2.8, the above acceleration accounts for both body k's point mass and extended body contributions (first two right-hand side terms in Eq. 2.3). All other relevant terms in Eqs. 2.3, 2.5, and 2.6 can be similarly obtained from the gravitational potential gradient of the relevant perturbing body.

If we only consider the gravitational potential up to degree and order two as given by Eq. 2.12, the acceleration becomes (here kept in the body-fixed frame):

$$\begin{aligned}\ddot{\mathbf{r}}_{kj}^{(k\to j)} = -\frac{3}{2}\frac{Gm_k}{R_k^2}\left(\frac{R_k}{r_{kj}}\right)^4 \Bigg(&\left[\bar{C}_{20}^k + 6\left(\bar{C}_{22}^k\cos(2\lambda_j) + \bar{S}_{22}^k\sin(2\lambda_j)\right)\right]\hat{\boldsymbol{r}} \\ &+4\left[\bar{C}_{22}^k\sin(2\lambda_j) - \bar{S}_{22}^k\cos(2\lambda_j)\right]\hat{\boldsymbol{t}}\Bigg),\end{aligned} \tag{2.14}$$

with $\hat{\boldsymbol{r}}$ and $\hat{\boldsymbol{t}}$ the unit vectors corresponding to the radial and tangential directions (in the body-fixed frame).

2.2. ROTATIONAL DYNAMICS

The presence of the rotation matrix $\mathbf{R}_k$ and body j's longitude (λ_j) and latitude (ϕ_j) in Eq. 2.13 highlights the critical importance of the rotational dynamics in the modelling of gravitational interactions. As will be shown in Section 2.3, the consistent implementation of tides and rotation is also critical to properly model the moons' orbital evolution caused by tidal dissipation and correctly interpret estimation results. This section introduces the rotation models used for natural satellites, starting with the general Euler equations (Section 2.2.1) before discussing the analytical formulation commonly used to model a synchronous rotational rate, in which most natural satellites are caught (Section 2.2.2).

2

2.2.1. EULER EQUATIONS

The rotation of a non-deformable solid body is defined by the Euler equation:

$$\frac{d(\mathbf{I}\boldsymbol{\omega})}{dt} + \boldsymbol{\omega} \times (\mathbf{I}\boldsymbol{\omega}) = \sum_i \boldsymbol{\Gamma}_i, \tag{2.15}$$

where $\mathbf{I}$ is the inertia tensor of the rigid body, $\boldsymbol{\omega}$ is the rotation vector and the right-hand side represents the sum of all torques exerted on the body. Two important coupling aspects, however, complicate the above. First, the torques $\boldsymbol{\Gamma}_i$ might depend on the inertia tensor. Second, the inertia tensor $\mathbf{I}$ varies with time under the combined effects of tides and rotation, which both cause the body to deform. Properly accounting for the intricate feedback between the body's deformation and rotation would require replacing the above simplified formulation (only valid for a non-deformable body) by the Laplace tidal equations (see e.g., Mathis and Le Poncin-Lafitte, 2009) leading to a dramatically more complex model formulation, as will be further discussed at the end of this section.

INERTIA TENSOR

The inertia tensor of a given body depends on its internal density distribution as follows (e.g., Dehant and Mathews, 2015):

$$\mathbf{I} = \int_V \rho(\mathbf{r}) \left[(\mathbf{r}\cdot\mathbf{r})\mathbf{1}_{3\times 3} - \mathbf{r}\cdot\mathbf{r}^{\mathrm{T}}\right] dV. \tag{2.16}$$

Similarities with Eq. 2.10 highlight the relation between the inertia tensor components and the degree 2 spherical harmonics gravity coefficients. After integrating Eq. 2.16, the inertia tensor can indeed be written as (Lambeck, 1988)

$$\mathbf{I} = \begin{pmatrix} I_{xx} & I_{xy} & I_{xz} \\ I_{yx} & I_{yy} & I_{yz} \\ I_{zx} & I_{zy} & I_{zz} \end{pmatrix} = mR^2 \begin{pmatrix} \frac{C_{20}}{3} - 2C_{22} & -2S_{22} & -C_{21} \\ -2S_{22} & \frac{C_{20}}{3} + 2C_{22} & -S_{21} \\ -C_{21} & -S_{21} & -2\frac{C_{20}}{3} \end{pmatrix} + I_m \mathbf{1}_{3\times 3} \tag{2.17}$$

with I_m the mean moment of inertia, defined as the mean value of the diagonal elements of $\mathbf{I}$. The principal moments of inertia I_{xx}, I_{yy}, and I_{zz} (also respectively denoted A, B, and C) are given by the diagonal elements of $\mathbf{I}$ (with $A \leq B \leq C$, and $A = B$ for axisymmetric bodies), and are directly related to the body's internal density distribution. The mean moment of inertia, I_m, can be expressed as

$$I_m = \frac{A+B+C}{3}. \tag{2.18}$$

Combining Eqs. 2.9, 2.17, and 2.18, the gravity field coefficients C_{20} and C_{22} can finally be linked to the principal moments of inertia:

$$C_{20} = \frac{A+B-2C}{2mR^2}, \tag{2.19}$$

$$C_{22} = \frac{B-A}{4mR^2}. \tag{2.20}$$

DYNAMICAL VS. KINEMATIC ROTATIONAL MODELS

The most consistent way to account for the natural satellite's rotation in our dynamical model would be to concurrently integrate the body's deformation, rotation, and translational dynamics. This approach, although ensuring the full consistency of the satellite's rotational and translational dynamics, increases the model's complexity by expanding the set of equations to be integrated, which should then also include the Laplace tidal equations (e.g., Mathis and Le Poncin-Lafitte, 2009). In addition to being computationally intensive, it raises several other challenges. First, the determination of a proper initial state for the satellite's rotation, whose proper modes should be properly dampened, is critical but not trivial to obtain (Rambaux et al., 2012; Martinez and Dirkx, 2024). Second, for icy satellites, the decoupling of their core and icy shell in the presence of a liquid ocean further complicates the modelling of these different internal layers.

Despite its appealing ability to provide a fully consistent link between the moon's interior (inertia tensor $\boldsymbol{I}$, Eq. 2.17) and rotation ($\boldsymbol{\omega}$), such a coupled model solving for the Laplace tidal equations alongside the moon's translational and rotational equations of motion is therefore not deemed worth the implementation and computational load in typical icy satellites' dynamic studies. Simpler, kinematic models, which do not require propagating the satellite's rotation but instead rely on analytical approximations, are usually preferred and will be discussed in Section 2.2.2. Such modelling approaches circumvent initialisation issues for the rotational state, and facilitate the estimation of relevant parameters by defining a clear parametrisation for the moon's rotation. For icy moons, however, accounting for the core/shell decoupling would still require to extend typical parametrisations (see details in Section 2.2.2 and discussion in Section 10.1.2).

GRAVITATIONAL TORQUE

The main torque driving the rotational dynamics of a natural satellite i is the one exerted by the central planet 0 on the moon's extended shape. The gravitational torque caused by a point mass planet on an aspherical satellite is given by (e.g., Rambaux et al., 2012)

$$\boldsymbol{\Gamma}_i^{(0)} = -m_0 \mathbf{r}_i \times \nabla U_i(-\mathbf{r}_i), \tag{2.21}$$

with $\mathbf{r}_i$ the position vector of satellite i with respect to the central planet, and U_i the gravitational potential of i (Eq. 2.8). Truncating the potential expansion to degree two and assuming zero inclination and obliquity (Eq. 2.14) yields the following:

$$\boldsymbol{\Gamma}_i^{(0)} = -\frac{6Gm_0m_i}{R_i}\left(\frac{R_i}{r_i}\right)^3\left(\bar{C}_{22}^i\sin(2\lambda) - \bar{S}_{22}^i\cos(2\lambda)\right)\hat{\boldsymbol{h}}, \tag{2.22}$$

with $\hat{\boldsymbol{h}}$ the unit vector aligned with the orbit normal.

While the gravitational torque defined by Eq. 2.22 is the dominant one, it must be noted that Eq. 2.15 should also account for other torques, such as the ones caused by the extended perturbing body, as well as effects of the perturbing torque on a fully extended body (i.e., beyond degree two expansion), and third-body perturbations (Efroimsky and Williams, 2009).

2.2.2. SYNCHRONOUS ROTATION MODEL

The time evolution of a natural satellite's rotation governed by Eq. 2.15 leads to different possible equilibria, referred to as Cassini's states (Peale, 1969). When locked in a Cassini state, the orbital normal and the rotational pole of a moon precess at the same rate, around the same axis. While such an equilibrium implies a (small) non-zero zero obliquity (e.g., Baland et al., 2016), we will still neglect any obliquity effects for the Galilean satellites (theoretical estimates are indeed very small, Baland et al., 2012; Chen et al., 2014), and assume that their orbital and spin axes are perfectly aligned, with no precession.

Furthermore, the rotational dynamics of a natural satellite are typically approximated by a once-per-orbit rotation around its spin axis. If the orbit is perfectly circular, this is equivalent to assuming that the body's principal axis of minimum inertia is always pointing towards the central planet (i.e., the body-fixed longitude of the planet is zero). However, non-zero eccentricity and/or inclination prevent the moon's rotation from being exactly synchronous. The satellite's response - driven by its internal structure and properties - to the central torque acting on its dynamical figure and to third body forcings, causes its rotation to further deviate from a fully synchronous state.

These variations are typically modelled as librations (i.e., different components of a frequency decomposition of a body's perturbed rotation). We can distinguish between longitudinal and latitudinal librations. The former represent deviations between the pointing direction of the body's long axis (x-axis) and the direction to the central planet (thus contained within the equatorial plane when the obliquity is zero). Latitudinal librations, on the other hand, describe oscillations of the rotational pole around the satellite's y-axis. For most natural satellites, latitudinal librations (caused by non-zero inclination and/or obliquity, and out-of-plane torques) are small and their effects on the moon's orbit are limited. In the following, we will therefore focus on longitudinal librations, which can be further decomposed into *optical* and *physical* librations. The former are geometric effects of the orbit's eccentricity, while physical librations arise as a response to forcing torques, and depend on the satellite's internal structure and properties. The total longitudinal libration, defined as the angle between the pointing of the empty focus and the direction to the central planet, can thus be defined as

$$\lambda = \phi + \gamma, \tag{2.23}$$

with ϕ and γ the optical and physical librations, respectively. It should be noted that the total libration angle λ is the body-fixed longitude of the central planet.

OPTICAL LIBRATION

Focusing on the effect of a non-zero eccentricity on the pointing of the satellite's long-axis and assuming a perfectly synchronous rotation[1], the satellite's rotation

[1] identical rotational and orbital periods, i.e., $\omega = n$ with ω and n the moon's rotation rate and orbital mean motion, respectively

angle δ is related to the mean anomaly M (see Fig. 2.1):

$$\delta = M - \gamma = nt - \gamma. \tag{2.24}$$

In the absence of physical librations (i.e., $\gamma = 0$), the above is oftentimes described as the satellite's principal axis of inertia always pointing towards the orbit's empty focus. This, however, results from an approximation in eccentricity which, as will be demonstrated in Section 2.3.4, may significantly affect the effects of satellite tides on the moon's own orbit.

Denoting with β the angle between the orbit's long axis and the direction to the satellite as seen from the empty focus, the cosine rule gives (see Fig. 2.2)

$$\cos\beta = \frac{\frac{1}{e}\left(1-\frac{r}{a}\right)+e}{\left(1-\frac{r}{a}\right)+1}, \tag{2.25}$$

with a, e, and r the semi-major axis, eccentricity, and distance of the satellite to the central planet, respectively. Using the following expansion for $1 - r/a$ as a function of the mean anomaly (e.g., Murray and Dermott, 2000)

$$1 - \frac{r}{a} = e\cos M - \frac{1}{2}e^2(1-\cos 2M) - \frac{3}{8}e^3(\cos M - \cos 3M) + O(e^4), \tag{2.26}$$

one obtains

$$\cos\beta = \frac{\cos M + \frac{1}{2}e(1+\cos 2M) - \frac{3}{8}e^2(\cos M - \cos 3M)}{1 + e\cos M - \frac{1}{2}e^2(1-\cos 2M) - \frac{3}{8}e^3(\cos M - \cos 3M)} + O(e^4). \tag{2.27}$$

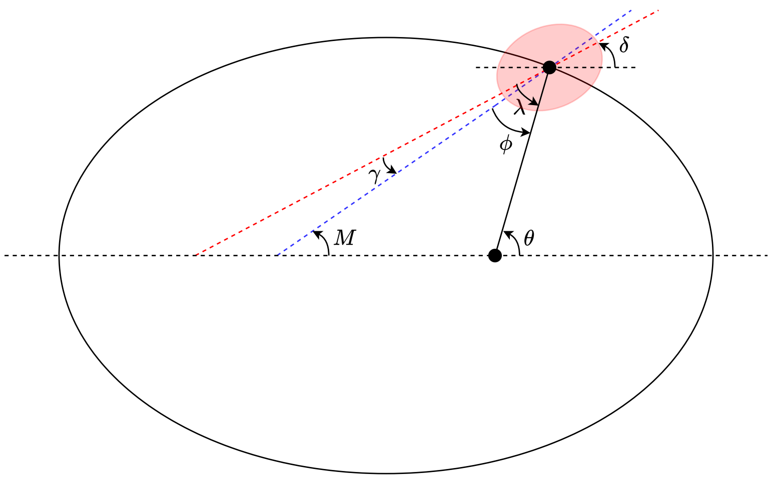

Figure 2.1.: Schematic representation of the pointing direction of the satellite's long axis with and without physical librations (in red and blue, respectively), with respect to the direction to the central planet. δ represents the satellite's rotation angle, while γ and ϕ respectively describe the physical and optical librations. θ and M are the true and mean anomalies, respectively.

2

Performing a Taylor series expansion of the above for very small eccentricities, with a truncation at $O(e^3)$, eventually yields (e.g., Murray and Dermott, 2000)

$$\cos\beta = \cos M - \frac{1}{8}e^2(\cos M - \cos 3M) + O(e^3). \tag{2.28}$$

This shows that the satellite's long-axis does not exactly point to the empty focus, and that this approximation, although widely used, is only valid up to $O(e^2)$.

From Eq. 2.24, the optical libration angle, defined between the satellite-to-planet axis and the satellite's long axis pointing direction, can be expressed as (Fig. 2.1):

$$\phi = M - \theta = -2e\sin M + O(e^3) \tag{2.29}$$

where θ denotes the satellite's true anomaly. Conic expansions are commonly used to express the optical libration as a function of the eccentric anomaly E instead of M, providing us with a straightforward way to compute ϕ from the satellite's cartesian state:

$$\phi = M - \theta = -2e\sin E + O(e^2), \tag{2.30}$$

$$e\sin E = \frac{\mathbf{r}\cdot\mathbf{v}}{|\mathbf{r}\times\mathbf{v}|}. \tag{2.31}$$

While offering a very convenient implementation, such a truncation in eccentricity has severe implications for the consistency of our models and, in particular, significantly affects the moons' orbital migration caused by tides, as will be discussed in detail in Section 2.4.1.

PHYSICAL LIBRATIONS

Physical librations can be divided between free and forced librations, the former typically being dampened over planetary system evolution timescales. Forced

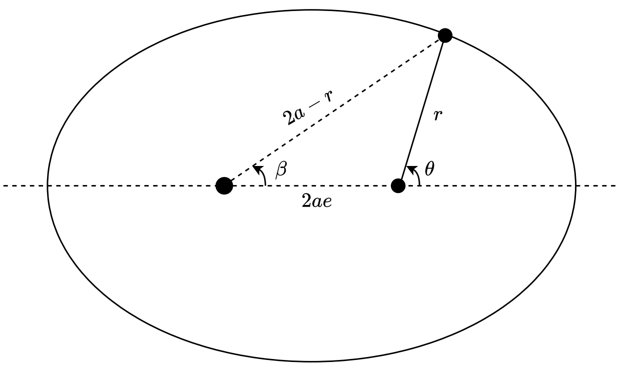

Figure 2.2.: Definition of the empty focus angle β for a satellite at a distance r from the central planet, on a elliptic orbit of semi-major axis a and eccentricity e.

librations, on the other hand, are caused by external torques acting on the rotating body. Assuming an ideal Keplerian orbit, the frequencies of the forced librations induced by the central planet would be multiples of the orbital period. In practice, orbital perturbations and third body torques also introduce librations at different frequencies. Nevertheless, the physical libration spectrum is dominated by the satellite's orbital frequency, and we will therefore restrict our physical libration model to this single component.

The once-per-orbit libration can be obtained from the linearised equations for the synchronous rotation of a natural satellite (e.g., Murray and Dermott, 2000; Williams et al., 2001; Rambaux et al., 2010):

$$\ddot{\gamma} + 3n^2 \frac{B-A}{C}\gamma = 3n^2 \frac{B-A}{C}(\theta - M) \tag{2.32}$$

$$= 6n^2 \frac{B-A}{C} e \sin M, \tag{2.33}$$

with the right-hand side term describing the forcing at the orbital frequency. Defining the satellite's resonant frequency as

$$\omega_0 = n\sqrt{\frac{3(B-A)}{C}}, \tag{2.34}$$

the libration angle then becomes (e.g., Van Hoolst et al., 2008; Rambaux et al., 2010)

$$\begin{aligned} \gamma &= \mathscr{A} \sin M, \\ \mathscr{A} &= 2e\frac{\omega_0^2}{\omega_0^2 - n^2} \approx 6e\frac{B-A}{C}. \end{aligned} \tag{2.35}$$

While this libration amplitude holds for a completely rigid body, Van Hoolst et al. (2013) provide a revised form of the above equation accounting for the influence of tidal deformation. In both cases, the amplitude of the once-per-orbit physical libration is directly related to the satellite's moments of inertia and orbital eccentricity.

TOTAL LIBRATION

Using the expressions derived in Eq. 2.29 and 2.35 for the optical and physical librations, respectively, the total libration angle given by Eq. 2.23 can thus be re-written as (Lainey et al., 2019)

$$\lambda = -2e \sin M + \mathscr{A} \sin M = \mathscr{B} e \sin M, \tag{2.36}$$

with the total amplitude $\mathscr{B} = -2 + \mathscr{A}/e$. This formulation is useful for estimation purposes, allowing us to determine a single, combined libration amplitude at the orbital period frequency. The same approximation as in Eq. 2.30 is then often used to express the total libration angle as a function of the eccentric anomaly:

$$\lambda = \mathscr{B} e \sin E + O(e^2). \tag{2.37}$$

2

2.3. TIDES

The equations of motion provided in Section 2.1 describe the effect of the gravitational interactions between two extended bodies on their dynamics. However, these models assume fully rigid bodies, and therefore neglect tidal effects (i.e., the deformation of the bodies' shape, rotation, and gravity caused by their anelastic response to mutual gravitational forcing). As evidenced in Section 1.1, however, tides drive the long-term evolution of natural satellites' orbits and interiors, and are therefore critical to include in ephemerides analyses (as will be shown in Section 3.4.2). In the following, we define the tidal potential (Section 2.3.1) and derive the governing equations for the effects of tides on both the moons' rotations (Section 2.3.3) and orbits (Section 2.3.4). These derivations are not presented as a unified whole in literature, making it difficult to trace underlying assumptions and resulting inconsistencies between different formulations and/or implementations. The complete overview provided in the following sections allows us to connect and further existing insights regarding the modelling of tidal effects for natural satellites' dynamics. The respective advantages of different modelling approaches, including implementation challenges, will finally be examined in Section 2.4.1, and considered through the prism of ephemerides determination in Section 2.4.2.

The derivations presented in this section make use of a number of conic motion expressions. For the sake of conciseness, they are provided together in Appendix A for reference.

2.3.1. TIDAL POTENTIAL

The gravitational pull of a body j (here treated as a point mass) generates a so-called tidal bulge on body i, responsible for its deformation. The tide-inducing potential at any point on body i's surface caused by j is given by

$$V_i^{(j)}(\mathbf{r}^\star) = \frac{Gm_j}{R_i}\sum_{n=2}^{\infty}\left(\frac{R_i}{r_{ij}}\right)^{n+1} P_n(\hat{\mathbf{r}}^\star\cdot\hat{\boldsymbol{r}}_{ij}), \tag{2.38}$$

where $\mathbf{r}^\star$ is the position of the point at which the potential is evaluated, and $\boldsymbol{r}_{ij}$ is the position of the tidal-inducing body j with respect to body i (see Fig. 2.3).

The deformation of body i's gravity field caused by the tidal bulge described by Eq. 2.38 in turn raises the following gravitational potential:

$$U_i^{(j)}(\mathbf{r}) = \frac{Gm_j}{R_i}\sum_{n=2}^{\infty} k_n^i\left(\frac{R_i}{r}\right)^{n+1}\left(\frac{R_i}{r_{ij}}\right)^{n+1} P_n\left(\hat{\mathbf{r}}\cdot\hat{\mathbf{r}}_{ij}\right), \tag{2.39}$$

with $\mathbf{r}$ defining the position at which the potential is calculated with respect to body i. The gravity field variations caused by tides, and the resulting tidal bulge potential that they raise are driven by the tidal Love numbers k_{nm}^i, which describe the body's visco-elastic response to tidal forcing (n and m respectively denoting the degree and order of the Love number). These are frequency-dependent complex numbers whose imaginary part defines the phase lag of the tidal response, which will be further

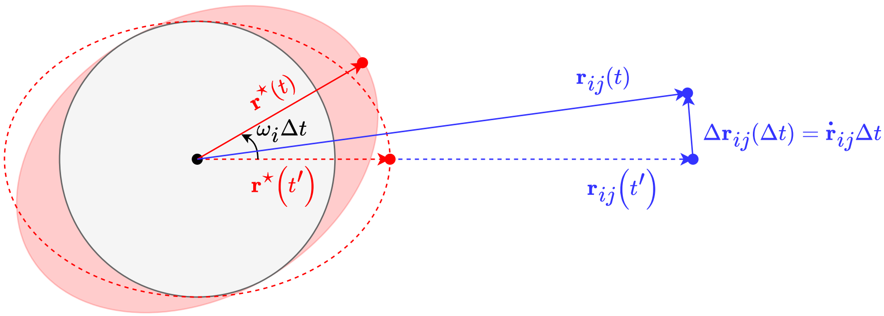

Figure 2.3.: Schematic representation of the tidal deformation (solid red ellipsoid) of body i (left) at time t due to the tidal potential (dashed red ellipsoid) raised by point mass body j (right) at time t'. The rotation of body i and orbital motion of body j during the time lag $\Delta t = t - t'$ are also represented.

discussed below. As done in Eq. 2.39, we typically only consider a unique Love number $k_i^{(n)}$ for each degree n, neglecting the (very) small dependency to the order m caused by the body's asphericity (Rovira-Navarro et al., 2023). It is interesting to note that similar Love numbers h_{nm} and l_{nm} are used to describe body i's shape deformation due to tides (i.e., its radial and lateral surface displacement under the effects of tides, see e.g., Petit et al. 2010).

The second degree Love number k_2 has (by far) the largest effect on the tidal potential, as can be deduced from Eq. 2.39. It is therefore the easiest tidal Love component to extract from radio science measurements: our own moon is the only natural satellite for which statistically significant estimates of degree 3 Love numbers are currently available (Konopliv et al., 2013; Lemoine et al., 2013). While it is unlikely that JUICE's GCO will make it possible to estimate Ganymede's k_3, the determination of its second degree Love number should be sensitive enough to detect possible order- or frequency-dependent variations (De Marchi et al., 2022), or lateral heterogeneities (Rovira-Navarro et al., 2023) (see discussion in Section 10.1). The tidal potential given by Eq. 2.39 is therefore often reduced to its degree two component, leading to the following simplified expression:

$$U_i^{(j)}(\mathbf{r}) = \frac{G m_j k_2^i}{2R_i}\left(\frac{R_i}{r}\right)^3\left(\frac{R_i}{r_{ij}}\right)^3\left(3\left(\hat{\mathbf{r}}\cdot\hat{\mathbf{r}}_{ij}\right)^2 - 1\right). \tag{2.40}$$

Due to a body's visco-elastic response to tidal stresses, there is a lag between the perturbing potential and the body's response. This is represented as a quality factor

2

Q, directly related to k_2's imaginary part, $\Im(k_2)$:

$$Q = \frac{|k_2|}{\Im(k_2)}. \tag{2.41}$$

Q is frequency-dependent, and depends on the body's rheology (e.g., Efroimsky and Lainey, 2007; Efroimsky and Makarov, 2014). A rigorous description of this frequency dependency is given by the expanded Love functions $k_2(\omega_{lmpq})$ and $Q(\omega_{lmpq})$ (e.g., Efroimsky and Makarov, 2014), which provide the real and imaginary part of the k_2 Love number as a function of the Fourier modes ω_{lmpq} ($lmpq$ referring to the four indices defining the Fourier modes in the Kaula expansion, see Kaula 1966). The tidal forcing for both planet- and satellite-raised tides is dominated by a single leading frequency, driven by the rotation period of the tide-raising body and by the moon's orbital period (as will be further discussed below). Nevertheless, a complete and consistent modelling of the tidal response would ideally require extracting a body's tidal parameters from an appropriate rheology model (from which the above Love numbers can be defined), accounting for all possible forcing frequencies, at the expense of a severe increase in model complexity. This justifies the success of simplified models for typical spacecraft orbit reconstruction and/or ephemerides determination.

The most widely-used approximations are the constant phase lag (CPL) and constant time lag (CTL) models, both offering different representations of the lag between the raising of the tidal potential and the point at which its influence is evaluated (i.e., between $\hat{r}$ and $\hat{r}_{ij}$ in Eq. 2.40). Both models, however, rely on important and much disputed assumptions (Efroimsky and Makarov, 2013; Makarov and Efroimsky, 2013). The CPL model, in particular, assumes a constant angular phase lag, which does not hold for eccentric orbits (Efroimsky and Makarov, 2013). Both the CPL and CTL models moreover overlook the frequency-dependent nature of the response of a body's interior to tidal forcing. Such an assumption is unacceptable for long-term evolution analyses: tidal dissipation causes the orbit of a natural satellite to either shrink or expand (see Section 2.3.4), affecting the frequency of the tidal forcing and thus the effective Q value, which in turn defines the amount of tidal energy dissipated in the system (e.g., Efroimsky and Lainey, 2007; Efroimsky and Williams, 2009; Renaud et al., 2021).

For shorter timescales, such as the ones considered for typical ephemerides studies, the frequency-dependency of the tidal dissipation occurring inside a body (planet or satellite) is nonetheless of lesser significance. Combined with the simplicity of its formulation, this makes the CTL model extremely attractive for our purposes. We can moreover introduce a different *constant* time lag for each excited tidal frequency. This implies that the response of e.g., Jupiter to the tidal forcing of each Galilean moon, each of them exciting a different frequency, is modelled by a different time lag. This approach still does not model a body's tidal dissipation as coherently as what could be achieved by incorporating an adequate rheology model in our simulations. However, it circumvents the inherent limitations of the CTL model, without dramatically increasing the complexity of our dynamical model.

In the CTL model, the time lag of the dissipation occurring in body i due to tides raised by body j is related to the tidal quality factor $Q_i^{(j)}$ by the following (e.g., Lainey et al., 2007),

$$\Delta t_i^{(j)} = \frac{T_i^{(j)} \arcsin\left(1/Q_i^{(j)}\right)}{2\pi}, \tag{2.42}$$

2

where $Q_i^{(j)}$ denotes the tidal quality factor of body i at the forcing frequency of the tides raised by j, while $T_i^{(j)}$ refers to the period of this tidal forcing. For tides raised by the satellite i on the planet 0, this period depends on the satellite's orbital period and on the planet's rotational period defined as $T_i^{\mathrm{orb}} = 2\pi/n_i$ and $T_0^{\mathrm{rot}} = 2\pi/\omega_0$, respectively, with n_i the mean motion of satellite i and ω_0 the planet's rotational rate:

$$T_0^{(i)} = \frac{T_i^{\mathrm{orb}}\, T_0^{\mathrm{rot}}}{2|T_0^{\mathrm{rot}} - T_i^{\mathrm{orb}}|} = \frac{2\pi}{2\,|\omega_0 - n_i|}. \tag{2.43}$$

For the tides raised once per orbit by the planet on a fully synchronous satellite, on the other hand, the tidal forcing period is

$$T_i^{(0)} = \frac{2\pi}{n_i}. \tag{2.44}$$

2.3.2. FORCE FORMULATION

Starting with the tides raised by the satellite i on the central planet 0, the force acting on the satellite i due the planet's tidal bulge is given by (in the body-fixed frame)

$$\boldsymbol{F}_i^{(0)} = -m_i \nabla U_0^{(i)}(\boldsymbol{r}_i). \tag{2.45}$$

In the following, the tidal potential raised at time t follows from the forcing experienced at time t', due to the time lag Δt of the tidal deformation, with $t = t' + \Delta t$. For the sake of conciseness, the superscript $'$ generally indicates that the quantity under consideration is evaluated at time t'. Replacing the potential $U_0^{(i)}(\boldsymbol{r}_i)$ by the expression provided in Eq. 2.40 yields

$$\boldsymbol{F}_i^{(0)} = -\frac{G m_i^2 k_2^0}{2R_0} \nabla \left(\left(\frac{R_0}{r_i'}\right)^3 \left(\frac{R_0}{r_i}\right)^3 \left(3\left(\hat{\mathbf{r}}_i' \cdot \hat{\mathbf{r}}_i\right)^2 - 1\right)\right), \tag{2.46}$$

where k_2^i denotes the real part of the complex Love number of degree 2 (here and in the rest of this chapter).

Computing the gradient of this potential in the body-fixed frame finally gives

$$\boldsymbol{F}_i^{(0)} = -\frac{3 G m_i^2 k_2^0}{2R_0^2} \left(\frac{R_0}{r_i'}\right)^3 \left(\frac{R_0}{r_i}\right)^4 \left(\left[1 - 5\left(\hat{\boldsymbol{r}}_i' \cdot \hat{\boldsymbol{r}}_i\right)^2\right] \hat{\boldsymbol{r}}_i + 2\left(\hat{\boldsymbol{r}}_i' \cdot \hat{\boldsymbol{r}}_i\right) \hat{\boldsymbol{r}}_i'\right). \tag{2.47}$$

Similarly, due to Newton's third law, the satellite's tidal bulge affects its own orbit, with a force of the same magnitude and opposite direction as the one it exerts on the central planet:

$$\boldsymbol{F}_i^{(i)} = -\frac{3Gm_0^2 k_2^i}{2R_i^2}\left(\frac{R_i}{r_i'}\right)^3\left(\frac{R_i}{r_i}\right)^4\left(\left[1-5\left(\hat{\boldsymbol{r}}_i'\cdot\hat{\boldsymbol{r}}_i\right)^2\right]\hat{\boldsymbol{r}}_i+2\left(\hat{\boldsymbol{r}}_i'\cdot\hat{\boldsymbol{r}}_i\right)\hat{\boldsymbol{r}}_i'\right). \tag{2.48}$$

Remarkably, comparing Eq. 2.47 and 2.48 shows that the tidal force exerted on the satellite has the same form irrespective of whether we consider tides raised by the central planet or by the satellite itself.

Taking the force due to the tides raised on the satellite as an example (Eq. 2.48) and following Mignard (1980), $\boldsymbol{r}_i'$ can be related to the tidal time lag $\Delta t_i^{(0)}$ and the satellite's velocity in the body-fixed frame, $\dot{\boldsymbol{r}}_i$, using a first order approximation:

$$\boldsymbol{r}_i' = \boldsymbol{r}_i - \Delta t_i^{(0)}\left(\dot{\boldsymbol{r}}_i - \boldsymbol{\omega}_i\times\boldsymbol{r}_i\right) + O\left(\left(\Delta t_i^{(0)}\right)^2\right), \tag{2.49}$$

with $\boldsymbol{\omega}_i$ the rotation vector of the satellite i. The inverse of the distance r_i' can furthermore be expanded as follows

$$\left(\frac{1}{r_i'}\right)^3 = \left(1+3\Delta t_i^{(0)}\frac{\boldsymbol{r}_i\cdot\dot{\boldsymbol{r}}_i}{r_i^2}\right)\left(\frac{1}{r_i}\right)^3 + \left(\Delta t_i^{(0)}\right)^2. \tag{2.50}$$

The above expansion and the first order approximation for $\boldsymbol{r}_i'$ given by Eq. 2.49 can then be substituted in Eq. 2.48. After extensive simplifications and a truncation at $O\left(\left(\Delta t_i^{(0)}\right)^2\right)$, the expression for the tidal force eventually becomes (e.g., Lainey et al., 2007; Lari, 2018)

$$\boldsymbol{F}_i^{(i)} = -\frac{3Gm_0^2 k_2^i R_i^5}{r_i^8}\left(\mathbf{r}_i + \Delta t_i^{(0)}\left(2\frac{\mathbf{r}_i\cdot\dot{\mathbf{r}}_i}{r_i^2}\mathbf{r}_i + \left(\dot{\mathbf{r}}_i + \mathbf{r}_i\times\boldsymbol{\omega}_i\right)\right)\right). \tag{2.51}$$

An almost identical expression can similarly be obtained for the tides raised on the central planet:

$$\boldsymbol{F}_i^{(0)} = -\frac{3Gm_i^2 k_2^0 R_0^5}{r_i^8}\left(\mathbf{r}_i + \Delta t_0^{(i)}\left(2\frac{\mathbf{r}_i\cdot\dot{\mathbf{r}}_i}{r_i^2}\mathbf{r}_i + \left(\dot{\mathbf{r}}_i + \mathbf{r}_i\times\boldsymbol{\omega}_0\right)\right)\right). \tag{2.52}$$

An alternative formulation can be obtained by decomposing the velocity vector $\dot{\mathbf{r}}_i$ into its radial and tangential components, assuming that the satellite's rotation pole is aligned with the normal to the orbital plane (e.g., Hut, 1981):

$$\boldsymbol{F}_i^{(i)} = -\frac{3Gm_0^2 k_2^i R_i^5}{r_i^7}\left(\left(1+3\Delta t_i^{(0)}\frac{\hat{\mathbf{r}}_i\cdot\dot{\mathbf{r}}_i}{r_i}\right)\hat{\mathbf{r}}_i + \Delta t_i^{(i)}\left(\dot{\theta}_i-\omega_i\right)\hat{\mathbf{t}}_\mathbf{i}\right), \tag{2.53}$$

where ω_i is the rotation rate of the satellite, and $\dot{\theta}_i$ its angular velocity. The advantage of this formulation is twofold. First, it makes the dependency on the difference between the orbital velocity and rotational rate explicit, which becomes convenient when examining the effects of tides on the moon's orbit (see Section 2.3.4). Second, it decomposes the tidal force into radial and tangential components, which are commonly referred to as radial and librational tides, respectively.

A widely-used formulation trick exploits the fact that the averaged amount of energy dissipated by librational tides over one orbit is equal to 4/3 that dissipated by radial tides (Murray and Dermott, 2000). This allows us to re-write Eq. 2.53 as

$$\boldsymbol{F}_i^{(i)} = -\frac{7Gm_0^2k_2^iR_i^5}{r_i^7}\left(1+3\Delta t_i^{(0)}\frac{\hat{\mathbf{r}}_i\cdot\dot{\mathbf{r}}_i}{r_i}\right)\hat{\mathbf{r}}_i. \tag{2.54}$$

This circumvents the need to explicitly include the moon's rotation in the tidal force. The extreme sensitivity of the satellite tide effects to the rotational dynamics modelling (see Section 2.3.4) therefore makes the above formulation extremely attractive. In the rest of this dissertation, we therefore apply Eq. 2.54 to model satellite tides, while the complete force formulation (Eq. 2.53) is used for planet tides. In light of its importance for our work, the underlying assumption of this simplified model (i.e., librational tides dissipating 4/3 of the energy dissipated by radial tides) and its applicability will be demonstrated and discussed in Section 2.3.4.

2.3.3. EFFECTS OF TIDES ON THE MOONS' ROTATIONS

The tidal bulge raised by the central planet on a satellite generates a torque, which can be computed as follows (using Eq. 2.53):

$$\boldsymbol{\Gamma}_i^{(i)} = \mathbf{r}_i \times \mathbf{F}_i^{(i)} \tag{2.55}$$

$$= -3Gm_0^2k_2^i\Delta t_i^{(0)}\frac{R_i^5}{r_i^6}(\dot{\theta}_i-\omega_i)\hat{\mathbf{h}}_i. \tag{2.56}$$

Substituting Eq. A.1 and A.6 in the above, and computing the average tidal torque over one orbit, one obtains:

$$\left|\boldsymbol{\Gamma}_i^{(i)}\right| = -\frac{3Gm_0^2k_2^i\Delta t_i^{(0)}R_i^5}{2\pi a^6(1-e^2)^6} \cdot\left[\frac{n}{(1-e^2)^{\frac{3}{2}}}\int_0^{2\pi}(1+e\cos\theta)^8\frac{dM}{d\theta}d\theta-\omega_i\int_0^{2\pi}(1+e\cos\theta)^6\frac{dM}{d\theta}d\theta\right]\hat{\boldsymbol{h}}, \tag{2.57}$$

where all orbit-related quantities by default refer to the satellite (subscripts are omitted for the sake of conciseness). Using the relation between the true and mean anomalies (Eq. A.7) leads to

$$\left|\boldsymbol{\Gamma}_i^{(i)}\right| = -\frac{3Gm_0^2k_2^i\Delta t_i^{(0)}R_i^5}{2\pi a^6(1-e^2)^{\frac{9}{2}}} \cdot\left[\frac{n}{(1-e^2)^{\frac{3}{2}}}\int_0^{2\pi}(1+e\cos\theta)^6 d\theta-\omega_i\int_0^{2\pi}(1+e\cos\theta)^4 d\theta\right]\hat{\boldsymbol{h}}, \tag{2.58}$$

2

which after integrating and re-arranging gives

$$\left|\boldsymbol{\Gamma}_i^{(i)}\right| = -3Gm_0^2 k_2^i \Delta t_i^{(0)} \frac{R^5}{a^6}\left[n\left(1+\frac{27}{2}e^2\right) - \omega_i\left(1+\frac{15}{2}e^2\right)\right]\hat{\boldsymbol{h}} + O(e^4). \tag{2.59}$$

Assuming a circular orbit, this would eventually lead to a fully synchronous rotational state, with $\omega_i = n$, and the satellite's long axis always pointing towards the central planet. Because of the orbit's eccentricity, however, the averaged tidal torque can only be equal to zero if the satellite's rotation is slightly faster than its orbital motion (see Fig. 2.4), as follows (Levrard, 2008; Wisdom, 2008):

$$\omega_i = n\left(1+6e^2\right). \tag{2.60}$$

It must be noted that the exact value of the equilibrium rotation rate is contingent upon the adopted tidal dissipation model. A similar, but slightly different relation is also often given in literature and actually corresponds to the CPL model (Rambaux and Castillo-Rogez, 2013):

$$\omega_i = n\left(1+\frac{19}{2}e^2\right). \tag{2.61}$$

Eq. 2.60 defines a pseudo-synchronous rotation (i.e., slightly faster than the satellite's orbital motion), which would yield a zero averaged torque over one orbit, for the case of a non zero eccentricity. Despite this rotational rate appearing to describe an equilibrium state, this result is in contradiction with what is observed in the Solar System (full synchronicity, i.e., $\omega = n$). It moreover appears inconsistent with realistic rheology models for terrestrial bodies and natural satellites, which predict this equilibrium to be unstable (Makarov and Efroimsky, 2013). Most natural satellites are indeed found in fully synchronous rotations, even if their orbits are slightly eccentric. Their capture in spin-orbit resonance can be explained by the effect of the torque exerted by the central planet on the asymmetrical shape of the satellite (Eq. 2.22), counterbalancing the tidal torque given by Eq. 2.59. Taking into account both the torques caused by the body's aspherical shape (Eq. 2.22, for now keeping $\bar{S}_{22} = 0$) and tides (Eq. 2.59), the evolution of the satellite's rotation is described by the following expression of the Euler equation (Eq. 2.15):

$$\frac{d(\mathbf{I}_i\boldsymbol{\omega}_i)}{dt} + \boldsymbol{\omega}_i \times (\mathbf{I}_i\boldsymbol{\omega}_i) = -\frac{6Gm_0 m_i}{R_i}\left(\frac{R_i}{r_i}\right)^3\left(\bar{C}_{22}^i \sin(2\lambda)\right)\hat{\boldsymbol{h}} + \boldsymbol{\Gamma}_i^{(i)}. \tag{2.62}$$

The above can be further simplified by substituting $\boldsymbol{\omega}_i = \omega_i\hat{\boldsymbol{h}}$, leading to (after projection to the orbit normal)

$$C\dot{\omega}_i = -\frac{6Gm_0^2}{R_i}\left(\frac{R_i}{r_i}\right)^3 \bar{C}_{22}^i \sin(2\lambda) + \Gamma_i^{(i)}, \tag{2.63}$$

with $\Gamma_i^{(i)}$ the tidal torque projected onto the orbital normal $\hat{\boldsymbol{h}}$[2] and C the largest principal moment of inertia. Note that substituting Eqs. 2.20,2.24, and 2.29 in

[2]This out-of-plane component exactly describes the tidal torque when assuming zero inclination and obliquity.

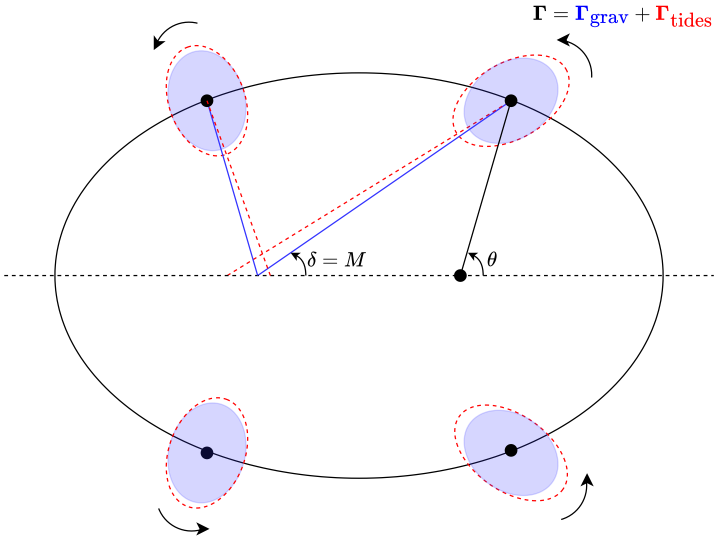

Figure 2.4.: Schematic representation of the pointing direction of the satellite's elongated shape (in blue) and tidal bulge (in red) over one orbit. While the average gravitational torque is zero for an axially symmetric body in synchronous rotation, the dissipation time lag prevents the tidal torque from exactly cancelling out.

the above, one can recover the linearised equation for the physical libration of a synchronous satellite given by Eq. 2.32.

The capture in a fully synchronous rotational state occurs if the maximum torque caused by the body's aspherical shape is larger than the averaged counter-balancing tidal torque (Goldreich and Peale, 1966; Rambaux and Castillo-Rogez, 2013). It is moreover important to keep in mind that while the central planet's longitude is equal (or close) to zero in the satellite-fixed rotating frame for a fully synchronous satellite, we are here considering the case when the satellite is not (yet) caught in spin-orbit resonance. The spin-orbit resonance capture condition can thus be described by the following condition:

$$6Gm_0 m_i \frac{R_i^2}{r_i^3} \bar{C}_{22}^i > \left|\Gamma_i^{(i)}\right|. \tag{2.64}$$

From Eq. 2.59 and neglecting the terms in e^2, the averaged tidal torque can be further simplified:

$$\left|\Gamma_i^{(i)}\right| = -3Gm_0^2 k_2^i \Delta t_i^{(0)} \frac{R^5}{a^6} (n - \omega_i), \tag{2.65}$$

The tidal time lag $\Delta t_i^{(0)}$ is here related to the period defined in Eq. 2.43 (and not Eq. 2.44 as would be the case for an already fully synchronous satellite). After substituting Eq. 2.42 and 2.43 to replace $\Delta t_i^{(0)}$, and expressing $\bar{C}_{22}^i$ as a function of the principal moments of inertia A and B (Eq. 2.20), one obtains

$$\frac{3}{2}Gm_0\left(\frac{1}{r}\right)^3(B-A) > \frac{3}{2}Gm_0^2\frac{k_2^i}{Q_i^{(0)}}\frac{R^5}{a^6}\frac{\omega_i - n}{|\omega_i - n|}. \tag{2.66}$$

Considering that the moon's initial rotational rate (before damping) is typically faster than the synchronous rate and assuming a small eccentricity eventually yields the following spin-orbit resonance condition (e.g., Rambaux and Castillo-Rogez, 2013):

$$\frac{B-A}{C} > \frac{1}{C}\frac{k_2^i}{Q_i^{(0)}}\frac{R_i^5 n^2}{G}. \tag{2.67}$$

This condition is fulfilled by most natural satellites (e.g., Goldreich and Peale, 1966; Rambaux and Castillo-Rogez, 2013), including the Galilean moons, which are indeed known to be locked in spin-orbit resonance.

Circling back to Eq. 2.59, it follows that the tidal torque does not exactly average out over one orbital period. The effect of the residual torque obtained over one orbit should therefore be accounted for in Section 2.3.4, when quantifying the influence of satellite tides on the moon's own dynamics. Moreover, the discrepancy observed between Eqs. 2.60 and 2.61, for two different tidal models, brings another evidence of the critical coupling between the moon's tides and rotation. This further strengthens the need for a complete analysis of their combined effects on the moons' dynamics, as will be examined in the following.

2.3.4. EFFECTS OF TIDES ON THE MOONS' ORBITS

As shown in Section 2.3.2, both the tides raised in the central planet and in the satellite exert an acceleration on the latter, and therefore influence the evolution of the moon's orbit. Their orbital effects can be decomposed into the contributions of the radial and librational tides, respectively. The former is caused by the tidal deformation at periapsis being stronger than the one experienced at apoapsis. Librational tides, on the other hand, are related to the variation of orbital velocity along the orbit (i.e., acceleration at periapsis, deceleration at apoapsis), and to the effect of the tidal torque. Because of the time lag in dissipation, the averaged effect of the tidal torque indeed does not exactly average out over one orbit for a fully synchronous satellite (see Section 2.3.3). Fig. 2.3 illustrates that the direction of the torque induced by the tidal bulge on body i depends on whether the tide-raising body j is on a sub- or super-stationary orbit (i.e, if its orbital period is smaller or larger than the rotational period of body i). For the super-stationary case, the tidal bulge always points ahead of body j (see Fig. 2.3.2), therefore exerting a positive acceleration on body i. The opposite is true if the tide-raising body lies below the stationary orbit.

In the following, we precisely examine the effects of both satellite and planet tides on the evolution of the satellite's orbital characteristics. It must be noted that we continue to neglect obliquity tides. The limited latitudinal variations of the tidal bulge's orientation caused by a small, non-zero obliquity would anyway have little impact on the evolution of the satellite's semi-major axis and eccentricity - driven by eccentricity tides - on which this section focuses. We do not investigate the small effect of obliquity tides on the Galilean moons' inclinations, but the interested reader is referred to the extensive analytical analysis by Boué and Efroimsky (2019).

LINEAR APPROXIMATIONS FOR THE SEMI-MAJOR AXIS AND ECCENTRICITY EVOLUTION

Linear approximations are available for the secular variations that both planet and satellite tides induce in the satellite's semi-major axis a_i and eccentricity e_i (Goldreich and Soter, 1966). Specifically, the effects of the tidal bulge raised by the satellite i on the planet 0 can be modelled as (e.g., Peale et al., 1979; Malhotra, 1991; Lari, 2018)

$$\frac{da_i^{(0)}}{dt} = 3\frac{m_i}{m_0}\frac{k_2^0}{Q_0^{(i)}}\left(\frac{R_0}{a_i}\right)^5 n_i a_i, \tag{2.68}$$

$$\frac{de_i^{(0)}}{dt} = \frac{57}{8}\frac{m_i}{m_0}\frac{k_2^0}{Q_0^{(i)}}\left(\frac{R_0}{a_i}\right)^5 n_i e_i. \tag{2.69}$$

The variation of the semi-major axis is positive: the satellite i typically lies beyond the stationary orbit (for all major moons of both Jupiter and Saturn), and planet tides therefore cause the satellite's orbit to expand.

For satellite tides, however, two different expressions for the secular evolution of the semi-major axis can be found in the literature. While the following formulation is the most commonly used (e.g., Goldreich and Soter, 1966; Lainey et al., 2009; Lari, 2018):

$$\frac{da_i^{(i)}}{dt} = -21\frac{m_0}{m_i}\frac{k_2^i}{Q_i^{(0)}}\left(\frac{R_i}{a_i}\right)^5 n_i a_i e_i^2, \tag{2.70}$$

another result is obtained in e.g., Emelyanov (2018); Boué and Efroimsky (2019):

$$\frac{da_i^{(i)}}{dt} = -57\frac{m_0}{m_i}\frac{k_2^i}{Q_i^{(0)}}\left(\frac{R_i}{a_i}\right)^5 n_i a_i e^2. \tag{2.71}$$

The evolution of the eccentricity under satellite tides, on the other hand, is consistent and given by the following expression:

$$\frac{de_i^{(i)}}{dt} = -\frac{21}{2}\frac{m_0}{m_i}\frac{k_2^i}{Q_i^{(0)}}\left(\frac{R_i}{a_i}\right)^5 n_i e_i. \tag{2.72}$$

While the existing discrepancy in the $da_i^{(i)}/dt$ formulations is not yet perfectly understood (Emelyanov, 2018), it is of critical importance when modelling the moon's orbital evolution due to tides, or extracting tidal dissipation parameters from the moon's orbital migration rate.

In the following, we therefore investigate the origin of the apparent inconsistency between Eqs. 2.70 and 2.71. In light of the absence of disagreement for the planet tides case, we specifically focus on the semi-major axis and eccentricity variations caused by the tides that the satellite raises on its own orbit. To this end, we quantify the total energy dissipated due to tides over one orbit, treating the radial and librational tides separately. Special attention will be paid to the influence of the moon's rotation, including physical librations, often overlooked in the literature. In the following derivations, we take an energy-based approach (similar to the one adopted in e.g., Hut, 1981), but identical results can be found using Gauss' planetary equations (see Appendix B.1).

RADIAL TIDES CONTRIBUTION

The radial component of the complete tidal force given by Eq. 2.53 is

$$F_r = -3Gm_0^2 k_2 \frac{R^5}{r^7}\left(1 + 3\frac{\dot{r}}{r}\Delta t\right). \tag{2.73}$$

For the sake of conciseness, the notations in the above expression and in the rest of this section have been simplified: by default, the absence of subscript and/or superscript refers to satellite-related properties, while $\boldsymbol{r}$ represents the position vector of satellite i with respect to the central planet 0. Δt denotes the time lag associated with tides raised by the planet 0 on satellite i (i.e., $\Delta t_i^{(0)}$).

From Eq. 2.73, the orbital energy dissipated by the radial tidal force over one orbit can be computed as follows:

$$(\Delta E_{\text{orb}})_r = \int_0^{2\pi} F_r \frac{dr}{d\theta} d\theta, \tag{2.74}$$

which after substituting $dr/d\theta$ by Eq. A.3 leads to

$$(\Delta E_{\text{orb}})_r = -9Gm_0^2 k_2 \Delta t R^5 ae(1-e^2)\int_0^{2\pi} \frac{\dot{r}}{r^8}\frac{\sin\theta}{(1+e\cos\theta)^2} d\theta. \tag{2.75}$$

We then replace $\dot{r}$ in the above using Eq. A.5:

$$(\Delta E_{\text{orb}})_r = -\frac{9Gm_0^2 k_2 \Delta t R^5}{a^6(1-e^2)^{\frac{15}{2}}} ne^2 \int_0^{2\pi} \sin^2\theta\,(1+e\cos\theta)^6\, d\theta. \tag{2.76}$$

After integration, the total orbital energy dissipated is

$$(\Delta E_{\text{orb}})_r = -9\pi Gm_0^2 k_2 \Delta t \frac{R^5}{a^6} ne^2 + O(e^4). \tag{2.77}$$

Considering the averaged energy dissipation over one orbital period, one finally obtains the following dissipate rate:

$$\left|\frac{dE_{\text{orb}}}{dt}\right|_r = -\frac{9}{2} Gm_0^2 k_2 \Delta t \frac{R^5}{a^6} n^2 e^2 + O(e^4). \tag{2.78}$$

Making use of the definition of the orbital energy (Eq. A.9) and its time derivative (Eq. A.10), one can deduce the time evolution of the satellite's semi-major axis caused by the radial component of its own tidal perturbing potential:

$$\left.\frac{da}{dt}\right|_r = -9\frac{m_0}{m_i}k_2\Delta t\frac{R^5}{a^4}n^2e^2 + O(e^4). \tag{2.79}$$

Conservation of the angular momentum finally allows us to derive an expression for de/dt based on da/dt (Eq. A.13):

$$\left.\frac{de}{dt}\right|_r = -\frac{9}{2}\frac{m_0}{m_i}k_2\Delta t\frac{R^5}{a^5}n^2e + O(e^3). \tag{2.80}$$

LIBRATIONAL TIDES CONTRIBUTION

Now considering the tangential component of the tidal force given by Eq. 2.53

$$F_t = 3Gm_0^2k_2\Delta t\frac{R^5}{r^7}\left(\omega - \dot{\theta}\right), \tag{2.81}$$

the resulting change of orbital energy over one period is given by

$$(\Delta E_{\mathrm{orb}})_t = \int_0^{2\pi} rF_t d\theta \tag{2.82}$$

$$= 3Gm_0^2k_2\Delta tR^5\int_0^{2\pi}\frac{\omega-\dot{\theta}}{r^6}d\theta. \tag{2.83}$$

Expressing r and $\dot{\theta}$ as a function of θ using Eq. A.1 and A.6, respectively, yields

$$(\Delta E_{\mathrm{orb}})_t = -\frac{3Gm_0^2k_2\Delta tR^5}{a^6(1-e^2)^{\frac{15}{2}}}n \cdot\left[\int_0^{2\pi}(1+e\cos\theta)^8d\theta - \frac{\omega}{n}(1-e^2)^{\frac{3}{2}}\int_0^{2\pi}(1+e\cos\theta)^6d\theta\right]. \tag{2.84}$$

After integration, we obtain

$$(\Delta E_{\mathrm{orb}})_t = -6\pi Gm_0^2k_2\Delta t\frac{R^5}{a^6}n\left[\left(1+14e^2\right) - \frac{\omega}{n}\left(1+6e^2\right)\right] + O(e^4). \tag{2.85}$$

Averaging the energy dissipated over one orbital period then gives the following orbital energy dissipation rate:

$$\left.\frac{dE_{\mathrm{orb}}}{dt}\right|_t = -3Gm_0^2k_2\Delta t\frac{R^5}{a^6}n^2\left[1+14e^2 - \frac{\omega}{n}\left(1+6e^2\right)\right] + O(e^4). \tag{2.86}$$

To avoid making any assumption regarding the satellite's rotation rate ω yet, in light of the results in Section 2.3.3, we choose to express it as:

$$\omega = n(1+\alpha e^2), \tag{2.87}$$

with $\alpha = 0$ for fully synchronous rotation and $\alpha = 6$ for pseudo-synchronous rotation (i.e., average torque = 0 over one orbit assuming an axially symmetric body under the CTL model, see Section 2.3.3). Eq. 2.86 then becomes

$$\left|\frac{dE_{\text{orb}}}{dt}\right|_t = -3\,(8-\alpha)\,Gm_0^2 k_2 \Delta t \frac{R^5}{a^6} n^2 e^2 + O(e^4). \tag{2.88}$$

Using the relation between the semi-major axis and orbital energy again (Eq. A.9), the evolution of the satellite's semi-major axis due to the tangential component of the tidal force is

$$\left|\frac{da}{dt}\right|_{\text{t}} = -6\,(8-\alpha)\,\frac{m_0}{m_i} k_2 \Delta t \frac{R^5}{a^4} n^2 e^2 + O(e^4). \tag{2.89}$$

We now compute the change of orbital momentum over one orbital period due to the torque generated by the tidal force's tangential component:

$$(\Delta h)_t = \int_0^{2\pi} r F_t \frac{d\theta}{\dot\theta}, \tag{2.90}$$

$$= \frac{Gm_0^2 k_2 \Delta t R^5}{a^6 (1-e^2)^6} \int_0^{2\pi} (1+e\cos\theta)^6 \left(\frac{\omega}{\dot\theta} - 1\right) d\theta, \tag{2.91}$$

which after expressing $\dot\theta$ as a function of θ (Eq. A.6) becomes

$$(\Delta h)_t = -\frac{3Gm_0^2 k_2 \Delta t R^5}{a^6(1-e^2)^6} \cdot \left[\int_0^{2\pi} (1+e\cos\theta)^6 d\theta - \frac{\omega}{n}(1-e^2)^{\frac{3}{2}} \int_0^{2\pi} (1+e\cos\theta)^4 d\theta\right]. \tag{2.92}$$

After integration and replacing ω by Eq. 2.87, we obtain

$$(\Delta h)_t = -6\pi\,(6-\alpha)\,Gm_0^2 k_2 \Delta t \frac{R^5}{a^6} e^2 + O(e^4). \tag{2.93}$$

Averaging over one orbital period finally provides the angular momentum rate:

$$\left|\frac{dh}{dt}\right|_t = -3\,(6-\alpha)\,Gm_0^2 k_2 \Delta t \frac{R^5}{a^6} n e^2 + O(e^4). \tag{2.94}$$

From the angular momentum definition, Eq. A.12 provides a relation between the time variations in semi-major axis, eccentricity, and angular momentum. Substituting Eq. 2.89 and 2.94 in Eq. A.12 gives the following damping eccentricity rate:

$$\left|\frac{de}{dt}\right|_t = \frac{m_0}{m_i} k_2 \Delta t \left(\frac{R}{a}\right)^5 n^2 e\,[-3(8-\alpha) + 3(6-\alpha)] + O(e^3) \tag{2.95}$$

$$= -6\frac{m_0}{m_i} k_2 \Delta t \left(\frac{R}{a}\right)^5 n^2 e + O(e^3). \tag{2.96}$$

COMBINED EFFECTS OF RADIAL AND LIBRATIONAL SATELLITE TIDES

The total rate describing the semi-major axis evolution caused by satellite tides is directly given by the sum of the radial and librational tidal effects (Eq. 2.79 and 2.89, respectively):

$$\frac{da}{dt} = \left|\frac{da}{dt}\right|_r + \left|\frac{da}{dt}\right|_t \tag{2.97}$$

$$= -(57-6\alpha)\frac{m_0}{m_i}k_2\Delta t\frac{R^5}{a^4}n^2e^2 + O(e^4), \tag{2.98}$$

and the total eccentricity damping rate is similarly obtained from Eq. 2.80 and 2.96:

$$\frac{de}{dt} = \left|\frac{de}{dt}\right|_r + \left|\frac{de}{dt}\right|_t \tag{2.99}$$

$$= -\frac{21}{2}\frac{m_0}{m_i}k_2\Delta t\left(\frac{R}{a}\right)^5 n^2e + O(e^3). \tag{2.100}$$

Crucially, Eq. 2.98 highlights that the secular variation of the semi-major axis induced by satellite tides is extremely sensitive to the moon's rotation, described by Eq. 2.87. The eccentricity damping rate, on the other hand, is independent of α and thus insensitive to the adopted rotation model. This strongly suggests that the discrepancy observed between different da/dt formulations in the literature might be rotation-related, as will be shown in the next section.

It is also insightful to compute the total amount of dissipated energy by satellite tides, and to compare the respective contribution of the radial and librational tides. The total energy dissipated by the radial component of the tidal force over one orbit corresponds to the change of orbital energy given by Eq. 2.77 (no change in rotational energy in the absence of an effective torque):

$$(\Delta E)_r = (\Delta E_{\rm orb})_r = -9\pi G m_0^2 k_2\Delta t\frac{R^5}{a^6}ne^2 + O(e^4). \tag{2.101}$$

The energy dissipated by librational tides, on the other hand, is the sum of the changes in orbital and rotational energy:

$$(\Delta E)_t = (\Delta E_{\rm orb})_t + (\Delta E_{\rm rot})_t \tag{2.102}$$

The orbital energy contribution is given by Eq. 2.85 which, once combined with Eq. 2.87, can be re-written as:

$$(\Delta E_{\rm orb})_t = -6\pi(8-\alpha)G m_0^2 k_2\Delta t\frac{R^5}{a^6}ne^2 + O(e^4), \tag{2.103}$$

while the rotational energy dissipated over one orbit can be derived from Eq. 2.93 as follows:

$$(\Delta E_{\rm rot})_t = -\omega(\Delta h)_t \tag{2.104}$$

$$= -6\pi(6-\alpha)G m_0^2 k_2\Delta t\frac{R^5}{a^6}ne^2 + O(e^4). \tag{2.105}$$

2

The total energy dissipated by librational tides thus becomes

$$(\Delta E)_t = -12\pi G m^2 k_2 (\Delta t) \frac{R^5}{a^9} n e^2 + O(e^4). \tag{2.106}$$

Combining Eq. 2.101 and 2.106, the total amount of energy dissipated by satellite tides over one orbit is

$$(\Delta E)_{\text{total}} = -21\pi G m^2 k_2 (\Delta t) \frac{R^5}{a^9} e^2 + O(e^4). \tag{2.107}$$

This result is remarkable in that it is independent of α, and therefore holds irrespective of any assumption regarding pseudo or full synchronous rotation for the satellite (see discussion in Section 2.3.3). The dissipated energy is the same in both cases but, depending on the rotation model, is divided differently between orbital and rotational energy. A perhaps even more important conclusion can be drawn from Eq. 2.101 and 2.106: the energy dissipated by librational tides relates to the contribution of radial tides as

$$(\Delta E)_t = \frac{4}{3} (\Delta E)_r . \tag{2.108}$$

This result was already introduced in Section 2.3.2 to reformulate the complete tidal force into an simpler formulation (Eq. 2.54), circumventing the need to explicitly incorporate librational tides, and thus avoiding rotation-related considerations. We here demonstrate that the validity of the above does not depend on the value of α, making this alternative tidal model extremely attractive, as will be discussed in more detail in Section 2.4.1.

Circling back to the discrepancy in semi-major axis evolution

Recalling the expression we derived for the evolution of the semi-major axis due to satellite tides (Eq. 2.98) and substituting the time lag Δt by Eq. 2.42, we obtain

$$\frac{d a_i^{(i)}}{dt} = -(57 - 6\alpha) \frac{m_0}{m_i} \frac{k_2^i}{Q_i^{(0)}} \frac{R^5}{a_i^4} e_i^2 + O(e^4). \tag{2.109}$$

Assuming a perfectly synchronous satellite ($\alpha = 0$), the above is actually consistent with Eq. 2.71. The more commonly used expression for $da_i^{(i)}/dt$ given by Eq. 2.70, however, matches with the pseudo-synchronous model (Eq. 2.60, i.e., $\alpha = 6$). This result directly follows from most studies considering that the tidal torque perfectly averages out over one orbital period (or, equivalently, that the angular momentum remains constant), which is however not exactly the case for fully synchronous satellites (Eq. 2.59). Although the averaged value of this torque is small, its cumulative effect on the orbit, neglected in Eq. 2.70, is of the same order of magnitude as the radial tides effects, and explains the discrepancy currently observed in literature (e.g., Goldreich and Soter, 1966; Emelyanov, 2018; Boué and Efroimsky, 2019).

As discussed in Section 2.3.3, considering an averaged tidal torque equal to zero is equivalent to assuming a pseudo-synchronous rotation, which is inconsistent with the present rotational state of natural satellites population. However, this non-zero tidal torque can be compensated by a small shift in the pointing direction of the satellite's long axis (e.g., Yoder and Peale, 1981; Rambaux and Castillo-Rogez, 2013). This corresponds to a non-zero $\bar{S}_{22}$ value (Section 2.1.2), which affects the satellite's orbit in a very similar way as tidal dissipation (see Section 2.4.2. Looking at Eq. 2.22, a non-zero $\bar{S}_{22}$ coefficient indeed induces a non-cancelling, counter-balancing torque (see complete derivation in Appendix B.3):

$$\boldsymbol{\Gamma}_i^{(S_{22})} = 6Gm_0m_i\frac{R_i^2}{a_i^3}S_{22}\left[1-\left(\mathscr{B}+\frac{3}{2}\right)e^2\right], \tag{2.110}$$

with $\mathscr{B}$ the total libration amplitude (Eq. 2.23).

To conclude, Eq. 2.71 accurately models the effect of satellite tides on the semi-major axis evolution. However, the *effective* semi-major axis drift would be the one obtained the zero tidal torque assumption (Eq. 2.70), since the contributions of the small residual tidal torque (Eq. 2.59) and of the counter-balancing $\bar{S}_{22}$ torque 2.110 cancel out. This again highlights the sensitivity of the tidally driven evolution of the satellite's orbital elements to the moon's rotation model (see detailed discussion in Section 2.4.1).

INFLUENCE OF PHYSICAL LIBRATIONS

Recalling the definition of the satellite's rotation angle in the presence of physical librations (Eq. 2.24)

$$\delta = nt - \gamma, \tag{2.111}$$

the rotation rate $\omega = \dot{\delta}$ becomes

$$\omega = n - \dot{\gamma}. \tag{2.112}$$

Substituting the expression for the satellite's physical libration (Eq. 2.35) finally yields

$$\omega = n - \frac{\mathscr{A}}{e}ne\cos M. \tag{2.113}$$

Taking the time derivative of Eq. 2.29:

$$2ne\cos M = \dot{\theta} - n + O(e^3), \tag{2.114}$$

the rotation rate of the satellite becomes

$$\omega = n + \frac{\mathscr{A}}{2e}\left(n-\dot{\theta}\right), \tag{2.115}$$

and the tidal force for a fully synchronous satellite can eventually be re-written as

$$\boldsymbol{F}_i^{(i)} = -\frac{3Gm_0^2k_2^iR_i^5}{r_i^7}\left(\left(1+3\Delta t_i^{(0)}\frac{\hat{\mathbf{r}}_i\cdot\dot{\mathbf{r}}_i}{r_i}\right)\hat{\mathbf{r}}_i - \Delta t_i^{(i)}\left(1+\frac{\mathscr{A}}{2e}\right)\left(n_i-\dot{\theta}_i\right)\right), \tag{2.116}$$

where only the librational tides component is affected by the presence of the once-per-orbit physical libration.

From this modified tidal force formulation, one can derive the physical libration's contribution to the amount of energy dissipated due to tides (the details of the derivation can be found in Appendix B.2). This extra dissipated energy can be expressed as a factor of the total energy dissipated in the absence of physical libration (Eq. 2.117):

$$(\Delta E)_\gamma = \left(\frac{4}{7}\frac{\mathscr{A}}{e} + \frac{\mathscr{A}^2}{7e^2}\right)(\Delta E)_{\gamma=0}\,. \tag{2.117}$$

This implies that the physical libration also affects the expressions for the evolution of the semi-major axis and eccentricity caused by satellite tides. Following the same derivation approach as for the no physical libration case (see Appendix B.2 for details), Eqs. 2.98 and 2.100 eventually become

$$\left|\frac{da}{dt}\right|_\gamma = \left(-57 - 24\frac{\mathscr{A}}{e}\right)\frac{m_0}{m_i}\frac{k_2}{Q}\frac{R^5}{a^4}ne^2, \tag{2.118}$$

$$\left|\frac{de}{dt}\right|_\gamma = -\left(\frac{21}{2} + \frac{9\mathscr{A}}{4e}\right)\frac{m_0}{m_i}\frac{k_2}{\Delta t}\frac{R^5}{a^5}ne. \tag{2.119}$$

This demonstrates that the physical libration enhances the effects of satellite tides and is therefore critical to include in our models, as will be further discussed in Section 2.4.2. It is moreover interesting to note that the above is in remarkable agreement with the expression given in Efroimsky (2018), obtained using a much more general formalism applicable to any linear rheology, which brings additional confidence into the consistency of the modelling approach adopted in this chapter.

NEW INSIGHTS ON SATELLITE TIDES MODELLING

The analytical developments presented above, once combined together, give a complete picture of satellite tide effects on the moons' dynamics. This includes a number of relations and insights not typically presented or fully appreciated in literature. In light of existing inconsistencies (see Eqs. 2.70 and 2.71), and of the critical importance of extracting reliable dissipation estimates from the moons' orbits (see Section 1.1), it is actually crucial to shed light on the various assumptions behind classical model formulations, and to question their applicability.

The models overview outlined in previous sections clearly highlights the very intricate feedback between the moon's rotation and the effect of satellite tides on its own orbit. The pseudo-synchronous rotations described by Eqs. 2.60 and 2.61 not only depend on the assumed tidal model, but also follow from assuming that the satellite tidal torque averages out over one orbital orbit. However, this is in disagreement with the rotational states of most Solar System's moons (including the Galilean satellites), which are caught in fully synchronous rotations ($\omega = n$). Realising that neither Eqs. 2.60 or 2.61 hold, it automatically follows from Eq. 2.59 that the averaged tidal torque is non-zero. In Eq. 2.109, we actually demonstrated that neglecting the influence of this tidal torque is precisely what causes the discrepancy between the different semi-major axis rates given by Eqs. 2.70 and 2.71 (zero and non-zero tidal torques, respectively). This is, however, not the only influential factor to be considered. In practice, the pointing of the moon's long-axis will be slightly shifted (i.e., not exactly pointing to the central planet at pericentre) to generate the necessary torque to counter-balance the one caused by satellite tides (Eq. 2.110). Eq. 2.70 therefore describes the *effective* impact of satellite tides on the moon's semi-major axis, when accounting for the fact that the effect of the tidal torque, while not zero, is balanced by that of a small $\bar{S}_{22}$ offset.

Our derivations evidenced the extreme sensitivity of the satellite's librational tides to the moon's rotation. However, we proved that the result obtained by Murray and Dermott (2000), quantifying the contribution of librational tides as 4/3 of that of radial tides, equally holds for pseudo- or fully-synchronous rotations. This is an important finding, particularly promising for a rotation modelling-proof implementation (see Section 2.4.1). Finally, we evaluated the contribution of the main once-per-orbit physical libration to the total energy dissipated due to tides (Eq. 2.117). Re-deriving this result, first provided in Efroimsky (2018) in a more general framework, validates the consistency of our models and derivation approach. It furthermore allows us to quantify, for the first time, the effect of physical libration on the evolution of the satellite's semi-major axis and eccentricity (Eqs. 2.118 and 2.119). Implications for the robust estimation of tidal dissipation from its signature in the moon's dynamics will again be examined in Section 2.4.2.

2.3.5. ALTERNATIVE TIDAL MODELS

As introduced in Section 2.3.1, the tides raised on a body affect its shape, internal density distribution, and thus its gravity field. Instead of the force formulation given in Section 2.3.2, typically used for moons' ephemerides applications, in which the tidal potential (Eq. 2.40) is evaluated directly (Eq. 2.45), the effects of tides on the dynamics can therefore also be modelled directly via the time variations they induce on a body's gravity field. Similar to the static gravity field of a rigid body (Eq. 2.8), the gravitational potential raised by the tidal bulge (Eq. 2.39) can also be expanded into a spherical harmonics expansion. The resulting time-varying coefficients can be added as small variations of the static gravity coefficients. For the tides raised by body k on body j, these gravity field variations are defined as (e.g., Petit et al., 2010)

$$\Delta\bar{C}^j_{nm} - i\Delta\bar{S}^j_{nm} = \frac{k^j_{nm}}{2n+1}\frac{m_k}{m_j}\left(\frac{R_P}{r_{jk}}\right)^{n+1}\bar{P}_{nm}(\sin\phi_j)e^{-im\lambda_j}, \tag{2.120}$$

with ϕ_j and λ_j the body-fixed latitude and longitude of the perturbing body j, and r_{jk} the distance between j and k.

The above directly allows us to model the effects of both planet and satellite tides on the moon's own orbit, as well as on the spacecraft's dynamics via the tidal variations of the moon's gravity field. This explains why this modelling approach is traditionally preferred in gravity field-focussed studies (e.g., Cappuccio et al., 2020a; Magnanini et al., 2024). Eq. 2.120 nonetheless directly depends on the central planet's satellite-fixed latitude Φ_j and longitude λ_j. This reveals the same sensitivity to the consistency of the rotation and tidal models as the complete force formulation (Eq. 2.53, see Section 2.3.4). This model thus suffers from the same caveat when investigating the effect of the tides raised by a satellite on its own orbit, and is therefore not perfectly suited for our ephemerides-focussed applications.

2.4. IMPLEMENTATION CONSIDERATIONS

We demonstrated in Section 2.3.4 how the effects of satellite tides on its own orbit, and especially on its orbital expansion rate, are sensitive to the modelling of the moon's rotation. In the following, we discuss what this entails for the applicability of the different tidal models presented in Section 2.3 when specifically focussing on moons' ephemerides.

2.4.1. MODELLING CONSISTENCY

As shown in Section 2.3, a small difference in the modelling of the moon's rotation of the order e^2 (see Eq. 2.87 and subsequent derivations depending on α) still strongly affects the secular evolution of its semi-major axis under the effects of satellite tides (Eq. 2.98). Although this mismatch is very small for natural satellites given their typically low eccentricity, it yields conflicting linear approximations for the satellite's semi-major axis rate (e.g., Emelyanov, 2018). For ephemerides-related studies, focussed on the accurate reconstruction of the moons' dynamics and orbital evolution, such inconsistencies should therefore be avoided, as they may impact the tidal dissipation estimates. It is however important to note that this only holds for satellite tides: the effects of the tides raised on the central planet, on the other hand, do not strongly depend on the moon's rotation model (see Section 2.3.2).

IMPLICATIONS FOR CLASSICAL ROTATION MODELLING

The synchronous rotation model with superimposed librations introduced in Section 2.2.2 is typically applied when modelling the moons' dynamics. However, common implementations of said model heavily rely on expansions truncated at $O(e^2)$. First, as shown in Eq. 2.23, the total libration angle is usually expressed as a function of the eccentric anomaly instead of the mean anomaly, taking advantage of the following conic expansion

$$e \sin M = e \sin E + O(e^2) = \frac{\mathbf{r} \cdot \mathbf{v}}{\mathbf{r} \times \mathbf{v}} + O(e^2). \tag{2.121}$$

This trick offers a very elegant implementation solution: it avoids the need to determine the satellite's pointing direction at each instant of the propagation, which can instead directly be retrieved from its cartesian state. Despite its appeal, the expansion truncation at $O(e^2)$ on which this formulation relies nonetheless directly conflicts with the model consistency requirements discussed above. A second, alternative approach consists in defining the moon's orientation by determining the direction to the empty focus. As shown in Section 2.2.2, however, the satellite's long-axis does not exactly point towards the empty focus, and this simplification again results from a $O(e^2)$ approximation (see Eq. 2.28).

In addition to these eccentricity truncation issues, determining the orientation of the satellite's long-axis at each instant furthermore raises another challenge. If computed from the *instantaneous* state (whether in cartesian or Keplerian elements), the moon's rotation will follow all short-period osculations of the orbit (e.g., Dirkx et al., 2016; Lainey et al., 2019). This behaviour is, however, not physical: inertia in the satellite's rotation indeed prevents it from instantaneously matching short-lived orbital variations (i.e., well below the proper mode, Rambaux et al., 2012; Martinez and Dirkx, 2024), which typically average out over time. Several approaches are possible to try bypassing this complication, such as computing an *averaged* position for the empty focus (Dirkx et al., 2016) or using geometric elements in place of regular Keplerian ones (Lainey et al., 2019). Leaving aside the increase in computational load and model complexity required by the averaged empty focus strategy, the applicability of both methods anyway strongly depends on how perturbed the orbit is. This issue is nevertheless of critical importance given the extreme sensitivity of the satellite tides to the perfect consistency of our orbital and rotational models.

Which model for satellite tides on the moons' orbits?

The complications mentioned above regarding the implementation of the satellite's orientation pose important consistency issues for all satellite tide models relying on an explicit formulation of the moon's rotation. In the complete tidal force formulation (Eq. 2.53), the term proportional to $\Delta t(\dot{\theta}-\omega)\hat{\boldsymbol{t}}$ introduces this dependency to the satellite's rotation rate, still present in the resulting secular evolution of the semi-major axis (Eq. 2.98). Similarly, modelling tidal effects as time variations of the gravity field also directly involves the moon's rotation rate, via the body-fixed longitude λ of the tide-raising body (Eq. 2.120). Neither of these rotation-sensitive models is therefore perfectly suited to model the effects of tides on the satellite's orbit, as long as the inconsistencies between the tidal and rotational models are not resolved. This could be achieved with a fully coupled model, in which both the satellite's translational and rotational dynamics are concurrently integrated together with its rheology-dependent tidal deformations (Section 2.2.1), following a similar approach as in Boué et al. (2016). However, the overhead in model complexity and computational load that such an approach would imply (especially for multi-layered interiors of icy satellites) has so far prevented its implementation for natural satellites' ephemerides determination purposes.

The methodology presented in Section 2.3.2, however, offers a promising alternative to the explicit incorporation of the rotational tides in the tidal force. Accounting for the contribution of the moon's rotation (i.e., librational tides) as 4/3 of the tidal energy dissipated due to radial tides indeed circumvents this modelling consistency issue. In Section 2.3.4, we moreover demonstrated that this approximation is valid irrespective of the exact rotational model adopted for the moon, as long as its rotation rate can be expressed in the form given by Eq. 2.87. This above holds whether one assumes a pseudo or fully synchronous rotation, and ensures that the satellite tides induce the correct secular evolution of the moon's semi-major axis (see Section 2.3.4). In addition to guaranteeing the consistency of our tidal model,

2

this formulation moreover offers an easier implementation by removing the need to determine the exact pointing direction of the moon's long axis.

This approach is widely applied in present ephemerides analyses (e.g., Lainey et al., 2007, 2009, 2012, 2019, 2020), as it ensures that the proper dissipation value can be extracted from the moon's orbit. In the rest of this dissertation, we therefore systematically make use of the *implicit* modelling of the librational tides, using the force formulation provided in Eq. 2.54 for satellite tides (see Chapters 4, 5, and 8). This choice was motivated by our focus on natural satellites' ephemerides, as it represents the most robust and reliable strategy to model the effect of satellite tides on the moon's own orbit in a fully consistent manner. Nonetheless, while perfectly suited for the moons' dynamics, this approach does not model the tidal effects sensed by a orbiting spacecraft due to the tide-induced variations of a satellite's gravity field. It would require modelling said gravity variations (e.g., following the methodology outlined in Section 2.3.5), again raising possible inconsistencies between the modelling of tides for the moons and for the spacecraft (see Chapters 5 and 8, and extended discussion in Section 9.1.2).

2.4.2. Estimation challenges

As discussed in Section 1.1, improving the ephemeris solution of a given natural satellite is particularly critical to refine our estimate of its present orbital migration. This expansion rate is, as demonstrated in Section 2.3.4, directly related to the amount of energy dissipated due to tides, both in the central planet and in the satellite itself. A better characterisation of tidal dissipation in the system is thus essential to our understanding of both its long-term orbital evolution, and of the current thermal state of the moons' interiors (e.g., Lainey et al., 2009, 2012). For the above reasons, our ability to extract tidal dissipation parameters from the moons' present-day dynamics is of key importance.

These parameters are mostly retrieved from the linear variation that tidal dissipation induces on the moon's semi-major axis (Eq. 2.98). However, other effects - either enhancing the effect of tides or affecting the moon's orbit in a similar way - might affect the estimation if not properly accounted for. In particular, special attention should be paid to the modelling of librations and of a potential non-zero $\bar{S}_{22}$ coefficient (see Section 2.3.4).

Once-per-orbit physical libration

Eq. 2.117 shows that the main once-per-orbit physical libration (Eq. 2.35) enhances the effects of the satellite's librational tides (Efroimsky, 2018). Depending on the ratio between the libration amplitude $\mathscr{A}$ and eccentricity e[3], the physical libration can account for a significant fraction of the observed effects of satellite tides on the moon's orbit. It is therefore essential to include this once-per-orbit libration in our models, as the estimation would otherwise provide an overestimated, *effective* value for the satellite's k_2/Q. The approximations for the secular evolution of the moon's

[3] about 0.2 for Io, assuming a libration amplitude of $9 \cdot 10^{-4}$ rad (Van Hoolst et al., 2020).

semi-major axis and eccentricity can moreover be adapted accordingly to account for these effects (Eq. 2.118 and 2.119, respectively).

It should however be noted that, while the physical libration γ strengthens the effects of tidal dissipation in the satellite, it is not the only way in which it influences the moon's dynamics. Keeping in mind that this libration affects the satellite-fixed longitude λ of the central planet, it therefore has an impact on the effect of the satellite's gravitational potential on its own orbit. In particular, considering the acceleration exerted by the degree two potential (Eq. 2.14), it becomes apparent that the main effect of the physical libration will be very similar to the one caused by the $\bar{C}_{20}$ and $\bar{C}_{22}$ coefficients. This entails that the libration signature will not be too strongly correlated to that of tidal dissipation. It should therefore be possible to extract the amplitude $\mathscr{A}$ from the spacecraft and/or moons' dynamics (see more detailed discussion on the estimation of the moons' librations in Section 10.1.2) and correct the estimated value of $k2/Q$ accordingly (using Eq. 2.118). Provided that the physical libration is properly accounted for in our models, it should thus not impede the proper estimation of tidal dissipation parameters.

NON-ZERO $\bar{S}_{22}$ COEFFICIENT

The problem posed by the influence of a non-zero $\bar{S}_{22}$ value is, however, of a different nature. Looking at Eq. 2.14, the only radial effect of $\bar{S}_{22}$ is the one induced by the (small) optical and physical librations, causing the satellite-fixed longitude of the central planet to slightly depart from zero. These effects nonetheless almost exactly cancel over one orbital period. The acceleration due to $\bar{S}_{22}$ mostly acts in the tangential direction, similar to the tidal acceleration (Eq. 2.53). While the $\bar{S}_{22}$ is typically very small (see Section 2.1.2), any small departure from an exact zero value causes a similar drift in semi-major axis and eccentricity as induced by satellite tides (see Appendix B.3). Complete derivations for the effect of a non zero $\bar{S}_{22}$ value on the satellite's semi-major axis and eccentricity are provided in Appendix B.3.

Simultaneously extracting tidal dissipation parameters and a non-zero $\bar{S}_{22}$ from the moon's orbit is therefore extremely challenging, their very comparable signatures being difficult to disentangle. One possible approach would be to force the $\bar{S}_{22}$ value to be exactly zero in our models. This, however, might not be a physically realistic assumption: a small non-zero $\bar{S}_{22}$ is indeed expected to counter-balance the tidal torque over one orbit (see discussion in Section 2.3.4). An alternative is to estimate a parameter accounting for the combined effect of tides and $\bar{S}_{22}$. This strategy is actually equivalent to considering the *effective* semi-major axis and eccentricity evolution for an averaged tidal torque equal to zero (see Section 2.3.4).

These considerations again pertain to the consistent modelling of tides, gravity, and rotation to accurately model their combined effects on the satellite's dynamics. The specific $\bar{S}_{22}$ issue discussed above was of limited importance for work performed in this dissertation, which mostly focussed on simulations: the dynamical environment can indeed be made perfectly consistent with the *reality* described by (simulated) observations. However, it will be a critical aspect to consider in the future, when proceeding to real data analyses of JUICE and Europa Clipper (see discussions in Chapter 9). Investigating whether the static $\bar{S}_{22}$ value can be estimated from its effect on the spacecraft's dynamics, as a possible avenue for isolating it from the tidal dissipation signature, will be particularly interesting.

3

MOONS EPHEMERIDES - AN OVERVIEW

Since the discovery of the Galilean moons in the 17th century, refining the ephemerides of natural satellites has been a powerful means to understand the physical effects affecting celestial dynamics, prepare for dedicated in-situ spacecraft missions (e.g., Galileo, Cassini, JUICE, Europa Clipper), and even characterise the satellites' present orbital evolution and thermal state (Lainey et al., 2009, 2012, 2020, and discussion in Section 1.1).

This chapter presents an overview of the fitting process involved in the determination of natural satellites' ephemerides, as well as a top-level description of the different observations used to this end. In particular, we distinguish between astrometry observations, on which current solutions mostly rely, and radio science tracking measurements from in-situ spacecraft. For the latter, we introduce the different strategies currently applied to incorporate radio science data in the inversion, anticipating the comparative methodology analysis conducted in Chapter 4. We choose to give this chapter a strong focus on the Galilean system as the main object of study of the work presented in this dissertation. Nonetheless, the fitting methods, observation types and properties, and general considerations to be presented in the following are not-system dependent, and equally relevant for the ephemerides of other natural satellites.

3.1. HISTORICAL BACKGROUND FOR THE GALILEAN SYSTEM

Despite numerous observations following Galileo Galilei's over the 17th and 18th centuries, the first dynamical models for the Galilean system had to wait until the end of the 18th century, when different theories were then successively proposed by Bailly, Lagrange, and Laplace. The latter introduced the famous 1:2:4 MMR between Io, Europa, and Ganymede, now well-known as the Laplace resonance (Section 1.2.1). Following these very preliminary models, the first complete analytical theory of the Galilean moons' dynamics was proposed by Sampson (1921), later expanded and revisited in Lieske's work exploiting the computational power brought by modern-day computers (e.g., Lieske, 1977). Lieske's first Galilean ephemerides (labelled as E1) were successively updated to prepare for the Voyager and Galileo missions (E2 and E4 versions, respectively, Lieske 1980), and upgraded post-missions (into E3 and E5, respectively) (Lieske, 1998).

Lieske's extensive and remarkable work nevertheless still relied on analytical formulations which soon could not be reconciled with the increasing accuracy of the observations. The next ground-breaking advancement came in the form of numerical solutions, which were first published in the Galileo mission era (e.g., Murrow and Jacobson, 1988; Jacobson et al., 2000). The simple model originally used to generate these solutions (planet-satellites gravitational interactions, excluding tides) was progressively upgraded by Lainey et al. (2004b) and subsequent publications from the same author. The parallel improvement of our dynamical models and quality of the observations (both ground- and space-based) has led to the continuous refinement of the natural satellites' ephemerides, both for the Galilean moons and other moon systems (e.g., Lainey et al., 2004a, 2007, 2009, 2012, 2017, 2020; Jacobson, 2010, 2014, 2022). At the dawn of the JUICE and Europa Clipper missions, the boundaries of current solutions for the Galilean satellites are about to get pushed back to unprecedented accuracy levels, challenging once again the quality of our present dynamical models (see later discussions in Chapters 4 and 5). To investigate possible improvement avenues for the natural satellites' ephemerides, and in particular for the Galilean moons in the JUICE-Europa Clipper context, it is essential to first review the present-day solutions and already-available data sets.

3.2. Fitting a dynamical model to observations

The determination of ephemerides solutions, whether for natural satellites or other celestial bodies, requires fitting a dynamical model to a set of available observations by adjusting a number of parameters (referred to as estimated parameters). The principle is identical to spacecraft orbit determination (see e.g., Gill and Montenbruck, 2013; Milani and Gronchi, 2010), but involves different dynamics and observations, and poses different challenges. In the following, we briefly describe the estimation process (Section 3.2.1), before discussing data weighting aspects in Section 3.2.2.

3.2.1. Inversion principle

The ephemerides fitting process typically involves the estimation of an initial state for all moons under consideration, denoted $\boldsymbol{y}_0$ and defined at a reference epoch t_0, as well as related physical parameters, $\boldsymbol{p}$.

Least-squares fit

To estimate these parameters from a given observation set, the most commonly used inversion method is a linearised least-squares approach, which maps the effect of a (small) variation in the parameter vector, $\Delta\boldsymbol{q}$ ($\boldsymbol{q}$ combines both initial state and physical parameters) into the resulting observation values. Minimising the observation residuals (in a weighted least squares sense) is done in an iterative manner, by computing an update in the estimated parameter values at each iteration i (e.g., Gill and Montenbruck, 2013):

$$\Delta \boldsymbol{q}_i = \left(\boldsymbol{H}_i^T \boldsymbol{W} \boldsymbol{H}_i\right)^{-1} \boldsymbol{H}_i^T \boldsymbol{W} \Delta \boldsymbol{h}_i, \tag{3.1}$$

where $\boldsymbol{H}_i$ and $\boldsymbol{W}$ respectively refer to the observation partial (computed at iteration i) and weight matrices, the latter being further discussed in Section 3.2.2. $\Delta \boldsymbol{h}_i$ are the observation residuals to be minimised through the successive least-squares iterations. They are defined as the differences between the real observations used in the least-squares fit, $\boldsymbol{h}_{\text{obs}}$, and those computed with our models from the parameter values $\boldsymbol{q}_i$ at iteration i:

$$\Delta \boldsymbol{h}_i = \boldsymbol{h}_i\left(\boldsymbol{q}_i\right) - \boldsymbol{h}_{\text{obs}}. \tag{3.2}$$

It should be noted that Eq. 3.1 directly involves the so-called covariance matrix of the estimated parameters, $\boldsymbol{P}$, defined as follows:

$$\boldsymbol{P} = \left(\boldsymbol{H}^T \boldsymbol{W} \boldsymbol{H}\right)^{-1}. \tag{3.3}$$

$\boldsymbol{P}$ provides a *statistical* description of the quality of the estimated solution, based on the expected precision of the observations (via $\boldsymbol{W}$, see more detail in Section 3.2.2) and on the sensitivity of said observations to the estimated parameters (via $\boldsymbol{H}$, see Eq. 3.7). In particular, the diagonal elements of $\boldsymbol{P}$ give the variance of each estimated parameter, while the off-diagonal elements are the covariances of each combination of two parameters (and thus provide the parameters' correlations):

$$\boldsymbol{P} = \begin{pmatrix} \sigma_{q_1}^2 & \rho_{12}\sigma_{q_1}\sigma_{q_2} & \cdots & \rho_{1n}\sigma_{q_1}\sigma_{q_n} \\ \rho_{12}\sigma_{q_2}\sigma_{q_1} & \sigma_{q_2}^2 & \cdots & \rho_{2n}\sigma_{q_2}\sigma_{q_n} \\ \cdots & \cdots & \cdots & \cdots \\ \rho_{1n}\sigma_{q_n}\sigma_{q_1} & \rho_{2n}\sigma_{q_2}\sigma_{q_n} & \cdots & \sigma_{q_n}^2 \end{pmatrix}, \tag{3.4}$$

where σ_{q_i} and ρ_{ij} respectively represent the formal error (i.e., standard deviation) of parameter q_i and its correlation with parameter q_j. The realism of the estimation quality's description given by $\boldsymbol{P}$ depends on the quality of both our dynamical and observational models. Provided that these models are perfect, the formal uncertainties and correlations are representative of the *true* estimation errors that the iterative least-squares process (Eq. 3.1) eventually converges to (i.e., differences between the parameters' *true* and estimated values). It is essential to keep in mind that, in the absence of additional data sets that could be used to validate the solution[1], the formal errors are our unique means to assess the quality of our parameter estimates. We indeed do not know the parameters' true values, and the realism of the covariance matrix is therefore of critical importance. More detailed discussions on possible modelling issues causing the formal and true errors to

[1]see extended discussion in Chapter 5 on the essential role of such independent data sets for JUICE-Europa Clipper radio science ephemerides determination.

deviate can be found in Chapters 4, 5, and 8, when considering the limitations of the covariance description for our ephemerides analyses.

It must be noted that Eqs. 3.1 and 3.3 correspond to the basic formulation of a weighted linearised least-squares inversion, and do not account for the possible consideration of a priori knowledge or consider parameters. The former constrains the covariance of certain parameters based on existing estimates (i.e., based on prior measurements and/or analyses). This is done by incorporating the so-called a priori covariance matrix, $\boldsymbol{P}_0$, modifying the covariance matrix as follows (e.g., Gill and Montenbruck, 2013)[2]:

3

$$\boldsymbol{P} = \left(\boldsymbol{P}_0^{-1} + \boldsymbol{H}_i^T \boldsymbol{W} \boldsymbol{H}_i\right)^{-1}. \tag{3.5}$$

The so-called *consider parameters*, on the other hand, designate parameters which are not directly estimated, but whose uncertainties should still be accounted for in the fitting process, as they might affect the determination of other parameters. When including such consider parameters, the covariance definition becomes (Gill and Montenbruck, 2013)[3]:

$$\boldsymbol{P}_c = \boldsymbol{P} + \left(\boldsymbol{P}\boldsymbol{H}^\mathrm{T}\boldsymbol{W}\right)\left(\boldsymbol{H}_c\boldsymbol{P}_c\boldsymbol{H}_c^\mathrm{T}\right)\left(\boldsymbol{P}\boldsymbol{H}^\mathrm{T}\boldsymbol{W}\right)^\mathrm{T}, \tag{3.6}$$

where $\boldsymbol{P}$ is the covariance matrix given by Eq. 3.3 (or Eq. 3.5 if a priori information is included). $\boldsymbol{H}_c$ and $\boldsymbol{P}_c$ respectively denote the observation partials with respect to the consider parameters, and the covariance matrix of these parameters. $\boldsymbol{P}_0$ and $\boldsymbol{P}_c$ are built identically to $\boldsymbol{P}$ (Eq. 3.3): diagonal elements are the a priori or consider parameters' variances, respectively, while off-diagonal elements contain the corresponding covariances. Both the a priori and consider covariances will be discussed in more detail when applied to our analyses in Chapters 4 and 5.

OBSERVATION PARTIALS

In Eq. 3.1, the observation partials matrix, $\boldsymbol{H}_i$, relates the observation vector $\boldsymbol{h}$ to the current parameter values $\boldsymbol{q}_i$, as follows:

$$\boldsymbol{H}_i = \frac{\partial \boldsymbol{h}}{\partial \boldsymbol{q}_i}. \tag{3.7}$$

At this point, it is useful to introduce a distinction between dynamical and observational parameters, denoted by $\boldsymbol{p}_{\mathrm{dyn}}$ and $\boldsymbol{p}_{\mathrm{obs}}$, respectively, and both concatenated in the physical parameter vector $\boldsymbol{p}$. The full parameter vector $\boldsymbol{q}$ can thus be decomposed as

$$\boldsymbol{q} = \left[\boldsymbol{y}_0\ ;\ \boldsymbol{p}_{\mathrm{dyn}}\ ;\ \boldsymbol{p}_{\mathrm{obs}}\right]^\mathrm{T}, \tag{3.8}$$

with the parameters $\boldsymbol{p}_{\mathrm{obs}}$ directly affecting the observation values, and not the dynamics of the natural satellites (e.g., observation biases). For each single

[2] The corresponding modified formulation for the least-squares equation (Eq. 3.1) can also be found in Gill and Montenbruck (2013) and is not reported here for the sake of brevity.

[3] see footnote 2

observation h contained in the vector $\boldsymbol{h}$ and acquired at time t, its first order sensitivity to a variation in the estimated parameters can therefore be expanded as follows:

$$\frac{\partial h(t)}{\partial \boldsymbol{q}_i} = \left[\frac{\partial h(t)}{\partial \boldsymbol{y}(t)} \frac{\partial \boldsymbol{y}(t)}{\partial \boldsymbol{y}_{0,i}} \; ; \; \frac{\partial h(t)}{\partial \boldsymbol{y}(t)} \frac{\partial \boldsymbol{y}(t)}{\partial \boldsymbol{p}_{\mathrm{dyn},i}} \; ; \; \frac{\partial h(t)}{\partial \boldsymbol{p}_{\mathrm{obs},i}} \right]. \tag{3.9}$$

Both terms highlighted in green in the right-hand side of Eq. 3.9 directly follow from the adopted dynamical model, which after integration give the state vector $\boldsymbol{y}$ at any time t as a function of the initial state and dynamical model parameters:

$$\boldsymbol{y}(t) = \mathscr{F}(\boldsymbol{y}_0, \boldsymbol{p}_{\mathrm{dyn}}, t). \tag{3.10}$$

For the moons, the dynamical function $\mathscr{F}$ is given by the equations of motion provided in Section 2.1.1, relying on the dynamical models presented over the entire Chapter 2. On the other hand, the terms in blue in Eq. 3.9 are related to the observation models (i.e., how a given observable relates to the actual state of the body under consideration):

$$h(t) = \mathscr{H}\left(\boldsymbol{y}(t), \boldsymbol{p}_{\mathrm{obs}}\right). \tag{3.11}$$

These observation models will be presented in Section 3.3, when introducing the relevant astrometric and radio science observations used in moons' ephemerides.

3.2.2. DATA WEIGHTING

The matrix $\boldsymbol{W}$, introduced in Eq. 3.1, is used to apply different weights to each observation. These weight values are supposed to provide a statistical description of the random errors affecting the observations: the inverse of $\boldsymbol{W}$ can actually be defined as the observations covariance matrix, as opposed to the parameters' covariance defined in Eq. 3.3. It must be noted that only random errors are accounted for, while systematic ones are handled in a different way. The latter do not affect the precision of the measurements, but their accuracy. They can therefore be directly incorporated as biases to the observation models (Eq. 3.11), offering the possibility to estimate them along with other parameters.

Before diving into the construction of the weight matrix, we will first examine its role in the fitting process and its influence on the estimation solution.

A CRITICAL ROLE IN THE WEIGHTED LEAST-SQUARES SOLUTION

Natural satellites' ephemerides are based on many diverse observation techniques and data sets, all affected by different error sources and exhibiting wildly different precision levels (see more detail in Section 3.3). To obtain a statistically balanced solution, it is therefore essential to adjust the different observations' respective contribution to the least-squares solution based on their supposed quality. As mentioned in Section 3.2.1, in an ideal scenario where all observational and dynamical models (Eqs. 3.10 and 3.11, respectively) are perfect, a balanced solution would be characterised by:

1. formal uncertainties adequately describing the true estimation errors;
2. observation residuals $\Delta \boldsymbol{h}$ (after the least-squares fit has converged) matching the *true* statistical properties of the observations (mean, standard deviation, etc.).

Putting aside the impact of possible mismodelling issues (see Section 3.2.1 and more detail in Chapters 4, 5, and 8), failing to design an appropriate weight matrix would greatly affect the consistency of the estimation solution described by the two above conditions. First, applying either over- or underestimated weights to certain observations would respectively give them too much or too little importance in the fit. In case of under-weighting, very precise measurements might show large residuals. On the other hand, the solution may get pulled towards poor quality data points if over-weighted. Second, the formal errors and correlations - directly dependent on the observations' weights (Eq. 3.3) - would not offer a realistic representation of the quality of the estimation solution. Adopting a suitable weighting strategy is thus not only critical to obtain a balanced estimation, but also to ensure that the solution can be interpreted in a statistically meaningful way.

BUILDING THE WEIGHT MATRIX

Assuming N perfectly *independent* observations, with random errors adequately described by white noise, $\boldsymbol{W}$ is often expressed as a block diagonal matrix:

$$\boldsymbol{W} = \begin{pmatrix} \boldsymbol{P}^{-1}_{\text{obs},1} & \mathbf{0}_{n_1 \times n_2} & \dots & \mathbf{0}_{n_1 \times n_i} & \dots & \mathbf{0}_{n_1 \times n_N} \\ \mathbf{0}_{n_2 \times n_1} & \boldsymbol{P}^{-1}_{\text{obs},2} & \dots & \mathbf{0}_{n_2 \times n_i} & \dots & \mathbf{0}_{n_2 \times n_N} \\ \dots & \dots & \dots & \dots & \dots & \dots \\ \mathbf{0}_{n_N \times n_1} & \mathbf{0}_{n_N \times n_2} & \dots & \mathbf{0}_{n_N \times n_i} & \dots & \boldsymbol{P}^{-1}_{\text{obs},N} \end{pmatrix}, \tag{3.12}$$

with $\boldsymbol{P}_{\text{obs,i}}$ the covariance of a single observation i of size n_i[4]. $\boldsymbol{P}_{\text{obs,i}}$ is defined identically as the estimated parameters covariance in Eq. 3.3: the diagonal elements are the variances of the observation's components, while off-diagonal elements account for possible intra-observation correlations. What is typically referred to as the observation's weight in the literature is the inverse of its variance: $w_i = 1/\sigma_i^2$.

Here and in the following, it is critical to keep in mind the distinction between inter-observation correlations (i.e., in-between two measurements), and intra-observation correlations (i.e., in-between the different components of a single observation, in case the observable size if larger than one). Eq. 3.12 assumes that all observations are perfectly independent from one another: all off block diagonal elements being set to zero reflects the absence of inter-observation correlations. This block diagonal weight matrix can, however, account for possible intra-observation correlations. The latter can for instance arise between the two components of an object's angular position measurement in the sky (see astrometric observations in Section 3.3.1), or between the three components of a spacecraft's measured position (see normal points concept in Section 3.4.1).

[4]The size of single observation is possibly larger than one if it contains several components/coordinates, as for e.g., angular measurements, see Section 3.3.1

Defining a realistic covariance matrix, $\boldsymbol{P}_{\text{obs,i}}$ for each observation i is in practice very challenging. Even when indications are provided by e.g., the observer or calibration tests, we indeed do not exactly know how precise a given observation is. Starting from the pre-supposed accuracy $\sigma_{k,0}$ of a given observation subset k, the weight σ_k used in the inversion can be refined iteratively to be consistent with either the RMS (root mean squares) or standard deviation of the residuals obtained for this particular observation set k (e.g., Jacobson et al., 2000; Lainey et al., 2007, 2019).

Furthermore, assuming zero inter-observation correlations does not systematically hold for all observation subsets, especially if the measurement cadence is high. Similar observations acquired over a very short period of time can indeed not be considered as independent, due to time-correlations in both the information content and the errors affecting the measurements. The first issue is for instance encountered in the Cassini space astrometry data set, in which several observations are sometimes acquired within 10 minutes (very high observation cadence for astrometry standards), with some overlap in their information content (Lainey et al., 2019). Correlations between subsequent radio science measurements, on the other hand, mostly originate from their error sources[5]. In particular, the media propagation delays affecting the radio science observables (see Section 3.3.2) depend on the electron density in both the interplanetary plasma and the Earth's atmosphere. Depending on 1) the electron content temporal and spatial variability, and 2) the measurements' cadence, part of the noise may be common over subsequent observations (Kuchynka et al., 2014). In practice, the dual-frequency (X/Ka-band) radio-link will, however, greatly mitigate this issue for the JUICE spacecraft, by strongly reducing the dispersive noise caused by media propagation (e.g., Mariotti and Tortora, 2013).

To circumvent the observation correlation issues mentioned above, a common strategy is de-weigh the observations by a factor $\sqrt{N}$ (N being the number of observations), essentially providing an averaged data point at the accuracy level initially expected for the whole subset of observations (see e.g., Lainey et al., 2019, for an example in space-based astrometry). These averaged observations are sometimes referred to as normal points (e.g., Abbot et al., 1973; Pitjeva, 2009) and are commonly used when processing space-based observations (either astrometry or radio science), typically characterised by large data volumes collected over short periods of time.

3.3. OBSERVATIONS

This section provides an overview of the various observations which can and have been used in natural satellites' ephemerides determination. We start with the astrometric data, on which ephemerides solutions have historically mostly relied. We then describe radio science measurements with a strong focus on those expected from JUICE and Europa Clipper. For both the astrometry and radio science data sets, we will present the different types of observations and their corresponding

[5]Unlike in the natural satellites astrometry case, the rapidly changing dynamics of an interplanetary spacecraft and the very high radio science accuracy limit the risk of information content overlap between subsequent measurements.

3

observables, and provide an indication of their typical accuracy. To ensure consistency in our formulations, we first need to introduce some common notations and definitions, including the light-time effect which equally affects astrometry and radio science measurements.

LIGHT-TIME DEFINITION

Here and in the rest of this section, the subscript and/or superscript t refers to the signal transmission (one-way radio science, see Section 3.3.2) or light emission (astrometry), while r designates its reception. The light-time equation is used to (iteratively) determine the time interval, ρ, elapsed between the transmission/emission at time t_t and the reception at time t_r:

$$\rho = t_r - t_t = \frac{|\boldsymbol{r}_r(t_r) - \boldsymbol{r}_t(t_t)|}{c} + \sum_i \delta t_i, \tag{3.13}$$

where $\boldsymbol{r}_r(t_r)$ and $\boldsymbol{r}_t(t_t)$ represent the receiver and transmitter/emitter position vectors at time t_r and t_t, respectively, in an inertial frame. The light-time corrections δt_i account for medium propagation delays and relativistic effects, as well as, for radiometric measurements, instrumental delays. For the sake of conciseness, we further simplify the notations by defining

$$\boldsymbol{r}_t^r = \boldsymbol{r}_r(t_r) - \boldsymbol{r}_t(t_t) \tag{3.14}$$

as the relative position of the receiver at reception time t_r with respect to the transmitter/emitter at time t_t.

3.3.1. ASTROMETRY

As mentioned in Section 1.3.1 and to be further discussed in Section 3.4, astrometry is the main contributor to present-day ephemerides for natural satellites, including the Galilean moons. Before investigating the ephemerides improvement achievable with JUICE and Europa Clipper radio science, which is a core goal of this dissertation, it is therefore crucial to first consider the diversity and quality of the existing astrometry data set. This is also essential to explore possible radio science – astrometry synergies, as will be done in Chapters 7 and 8. We purposely limit the scope of the following section to a top-level overview of the different types of astrometric measurements, and of their accuracy levels. Specific details on how such observations are used in our analyses can nonetheless be found in Chapter 8, which presents these data sets in light of their potential synergies with JUICE and Europa Clipper radio science.

OBSERVATION TYPES AND ERROR SOURCES

The main types of astrometric observations traditionally used in present-day natural satellites' ephemerides were already briefly introduced in Section 1.3.1. Adopting the same classification as the one used in Chapter 8, we distinguish between the following categories: classical astrometry, mutual phenomena, mutual approximations, space-based astrometry, and stellar occultations. Radar measurements, which are technically not defined as 'astrometric' observations, are also considered. The first two observation types refer to 'old' techniques which formed the bulk of the data available for natural satellites ephemerides (e.g., Lainey et al., 2004a) before the advent of planetary missions and the recent development of new observation methods (e.g., stellar occultations and mutual approximations).

Classical astrometry

Classical astrometry provides either *absolute* or *relative* measurements of the satellites' positions, most commonly from photographic plates or CCD imaging. The progressive improvement of the available stellar catalogues, recently spectacularly boosted by the Gaia mission (Brown et al., 2018, 2021), gradually brought the observation accuracy from a few hundreds mas (milli-arcseconds) to the 100 mas level.

Absolute position measurements typically use the target's right ascension, α, and declination, δ, as observables (i.e., the target's longitude and latitude on the celestial sphere):

$$h_{\alpha,\delta} = \begin{pmatrix} \alpha_t\left(\boldsymbol{r}_t^r\right) \\ \delta_t\left(\boldsymbol{r}_t^r\right) \end{pmatrix}. \tag{3.15}$$

Relative position measurements, on the other hand, express the position coordinates of a target t with respect to another object used as reference, and designated by the subscript 0 in the following. Such relative coordinates can be expressed in multiple ways. Common relative position observables are the differential right ascension and declination coordinates, defined as the difference between the target's and the reference's absolute right ascensions and declinations:

$$h_{\Delta\alpha,\Delta\delta} = \begin{pmatrix} \Delta\alpha_0^t \\ \Delta\delta_0^t \end{pmatrix} = \begin{pmatrix} \alpha_t\left(\boldsymbol{r}_t^r\right) - \alpha_0\left(\boldsymbol{r}_0^r\right) \\ \delta_t\left(\boldsymbol{r}_t^r\right) - \delta_0\left(\boldsymbol{r}_0^r\right) \end{pmatrix}. \tag{3.16}$$

Another common relative position representation is given by the tangential coordinates X and Y, obtained by a gnomonic projection of the differential right ascension and declination onto the celestial sphere. To second order, they are defined as (Lainey, 2002)

$$h_{X,Y} = \begin{pmatrix} X_0^t \\ Y_0^t \end{pmatrix} = \begin{pmatrix} \Delta\alpha_0^t\ \cos\delta_0 - \Delta\alpha_0^t\ \Delta\delta_0^t\ \sin\delta_0 \\ \Delta\delta_0^t + \frac{1}{2}\left(\Delta\alpha_0^t\right)^2 \sin\delta_0\ \cos\delta_0 \end{pmatrix}. \tag{3.17}$$

These coordinates are sometimes expressed in an alternative way, using the separation s (i.e., apparent distance of the target to the reference point/object) and position angle p, measured with respect to the celestial North direction.

Mutual phenomena

Mutual phenomena (or mutual events) designate eclipses or occultations of a natural satellite by another, as observed from Earth. These observations therefore require a particular geometry, only attained when the central planet crosses the ecliptic (every six years for the Jovian system, Section 1.3.1). Unfortunately, this geometry constraint

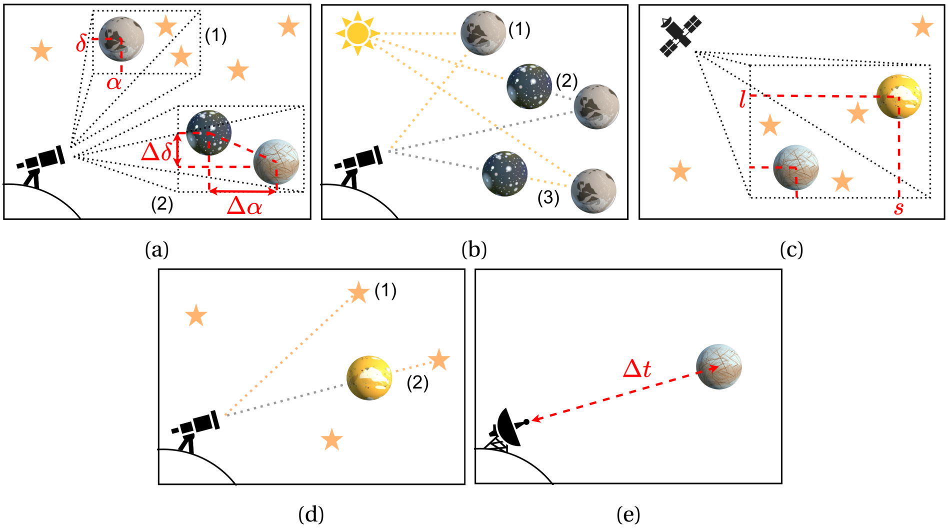

Figure 3.1.: Schematic representation of different types of astrometric observations used for ephemerides purposes. a: classical astrometry (1: absolute, 2: relative), b: mutual events (1: no event, 2: eclipse, 3: occultation), c: space-based astrometry, d: stellar occultation (1: no occultation, 2: occultation), e: radar. Explanations for the different observables can be found in the text.

severely limits the number of these observations, which can provide more accurate position measurements than what classical astrometry typically achieves (Arlot and Emelyanov, 2019).

Due to the nature of the measurements, the observation of a mutual event, unlike classical astrometry, can only constrain the *relative* position of the two moons involved in the phenomenon. What is primarily measured is the light-curve of the occulted or eclipsed satellite, with the received photometric flux reaching a minimum at the moment of the occultation/eclipse. The timing of the event, which can be extracted from the light-curve, represents the prime observable of a mutual event. However, in the absence of a complete analytical framework to include timing observables in the state estimation (i.e., missing formulation for the observation partials - in orange - in Eq. 3.9), directly exploiting this quantity is challenging (see the discussion on mutual approximations below, and the subsequent analysis in Chapter 6). Nonetheless, knowing the geometry required for the mutual event to occur, one can instead derive information about the relative position of the two satellites at the (measured) time of the occultation/eclipse. Mutual events are therefore typically reported using differential right ascension and declination (Eq. 3.16) or tangential coordinates (Eq. 3.17) as observables.

For eclipse observations, it must moreover be noted that the light-time computation given by Eq. 3.13 needs to be slightly modified (Noyelles et al., 2003; Lainey et al., 2004a): the light-time from the eclipsing satellite should indeed use as reference the moment where the eclipsed satellite enters the penumbra, such that

$$\rho_{\text{eclipsing}} = \rho_{\text{eclipsed}} - \Delta t_{\text{eclipsing}-\text{eclipsed}}, \tag{3.18}$$

where $\Delta t_{\text{eclipsing}-\text{eclipsed}}$ represents the time that light takes to travel from the eclipsing satellite to the eclipsed one.

Mutual approximations

This recently proposed observation concept (Morgado et al., 2016) was already briefly introduced in Section 1.3.1. By considering pseudo mutual events (i.e., close encounter of two satellites in the sky rather than the perfect alignment required by eclipses and occultations), such a technique achieves similar accuracy levels as mutual events, without being bounded by such strict geometry requirements.

However, the most appropriate observable to incorporate such observations in the ephemerides fitting process remains ambiguous (Emelyanov, 2017; Morgado et al., 2019b). The time at which the apparent distance between two satellites reaches a minimum, referred to as central instant t_c, should theoretically be the primary observable. Nonetheless, the present absence in literature of an analytical formulation for the central instant observation partials (orange terms in Eq. 3.9) has so far motivated the use of either numerical partials or simplified alternative observations (Emelyanov, 2017). This gap is actually addressed in Chapter 6, which proposes an analytical framework to directly use central instants in the moons' state estimation and compares the respective performances of the different observable options.

Space-based astrometry

In the planetary missions era, space-based astrometry (i.e., images of natural satellites taken from a spacecraft camera) started playing a key role in ephemerides solutions (e.g., Lieske, 1998; Jacobson et al., 2000; Lainey et al., 2017, 2019). Differences with respect to ground-based astrometry are multiple: the geometry of space-based observations is indeed different from the one that can be achieved from Earth, and the ratio between the data volume and timespan of the data set is typically much larger than for ground-based astrometry (see discussion on related data weighting aspects in Section 3.2.2). The much smaller distance separating the target from the receiver moreover implies that a given angular separation error translates into a significantly lower *effective* position uncertainty. However, other error sources specific to space-based observations still limit the accuracy of space imaging measurements (see discussion at the end of this section).

In classical astrometry, the observed object typically appears as a single point on the photographic plate or CCD image. For space astrometry, on the other hand, the (much) smaller target-observer distance implies that the target is usually observed as an extended object whose position cannot simply be extracted as that of a single bright point on the image. It first requires determining the position of the photometric centre through a limb fitting process accounting for the object's extended shape. The resulting position measurements for the target's estimated centre are then given in pixel coordinates, namely s and l (for sample and line coordinates, respectively). Converting them to absolute positions requires accounting for the camera's properties, the position of the target with respect to the spacecraft, and the position of the spacecraft itself.

Radar

Although very different in nature, and not proper *astrometric* observations per se, radar ranging measurements have also been included in recent ephemerides. These measurements rely on the reflection of a circularly polarised signal (transmitted by a ground-based radar facility) on the surface of the targeted object (here a natural satellite), and the subsequent reception of the reflected signal by the same radar telescope on Earth. By measuring the round-trip light time, one can infer the distance separating the target from the receiver:

$$r_r^t = \frac{c\,(t_t - t_r)}{2}. \tag{3.19}$$

The accuracy of the light time measurement directly translates into a ranging error, which for the Galilean satellites could achieve levels only surpassed by stellar occultations (typically around a few tens of kilometres, Brozović et al. 2020a). Given how distant the natural satellites of the outer Solar System are, Earth-based radar measurements are however only achievable with extremely powerful radar telescopes. With the recent loss of the Arecibo facility, the potential of this ranging technique therefore suffered a severe setback.

Stellar occultations

The observation principle of a stellar occultation is identical to its mutual event equivalent, but occurs between a star and a moon, rather than between two moons. More precisely, the occultation of a sufficiently bright star by a moving satellite is recorded and, knowing the position of the star, translated into an *absolute* angular position measurement (typically using absolute right ascension and declination observables, Eq. 3.15). This is an important distinction with respect to mutual events, which provide a *relative* position constraint: in the latter case, the position of the reference object is another moon, whose position is typically also to be refined in the ephemerides fitting process. Just as for mutual events, it should moroever be noted that stellar occultations are photometric observations, based on the recording of the light curve of the occulted star. The primary observable should therefore again be the timing of the occultation, nevertheless converted into a position measurement for the same reasons as those mentioned for mutual events (see previous discussion).

As already mentioned in Section 1.3.1, Gaia's recent improvements of the stellar catalogues have brought the accuracy attainable with stellar occultations down to the few kilometres level, an unprecedented achievement for ground-based astrometry (Morgado et al., 2019a, 2022). This makes these observations extremely appealing for natural satellites' ephemerides, and opens promising synergy opportunities with radio science, which this dissertation starts investigating in Chapter 7. It is finally interesting to note that these observations should not be reduced to position measurements only: the recording of an occultation by several observers also allows for a better determination of both the photometric centre position and the shape of the occulting satellite (Morgado et al., 2022). A major drawback of this observation technique, however, is the rarity of such events: for the Galilean satellites, only a few stellar occultations occurred since 2016 (Morgado et al., 2022).

Error sources

After accounting for the light time delay given by Eq. 3.13, astrometric observations should still be corrected for aberration, refraction, and phase effects. Aberration here refers to the influence of the non-zero velocity of the observer (typically on Earth) on the light-time calculation. This is corrected by replacing $\boldsymbol{r}_r(t_r)$ by $\boldsymbol{r}_r(t_r-\rho)$ in the calculation of the light-time, ρ, in Eq. 3.13 which then becomes

$$\rho = \frac{\left|\boldsymbol{r}_r(t_r-\rho)-\boldsymbol{r}_t(t_r-\rho)\right|}{c}+\sum_i \delta t_i. \tag{3.20}$$

In addition to the above, corrections should be applied for the refraction of light in the atmosphere (e.g., Stone, 1996), as well as for the effect of the solar phase angle on the measured disk-integrated photometry. The latter can cause an offset between the photocentric centre and the centre of figure (e.g., Lindegren, 1977; Emelyanov, 2021), and is therefore particularly relevant for mutual event, mutual approximation, and stellar occultation observations.

After correcting for the above-mentioned phenomena, the remaining errors in astrometric observations most commonly originate from (e.g., Desmars et al., 2009)

- error in the recording of the observation time,
- errors or omissions in the phase, aberration, and refraction corrections,
- stellar catalogue errors (if applicable),
- offset between the centre of mass and the photometric centre or the centre of figure,
- instrumental errors.

For space-based astrometry or highly accurate ground astrometry (e.g., stellar occultations), topography and shape model errors can also play a significant role in the quality of the measurement. For space astrometry specifically, spacecraft orbit determination and limb fitting errors should moreover be accounted for.

Available observations of the Galilean satellites

Following Galileo Galilei's discovery, the determination of the Galilean satellites' dynamics have benefited from the continuous collection of new observations and from the parallel improvement of our measurement techniques. An overview of the astrometric (and radar) observations available for the Galilean moons which are used in present ephemerides solutions has already been compiled as part of the work presented in Chapter 8 (Section 8.2 specifically), and will therefore not be described in detail. The interested reader is also referred to the detailed review on the history of Galilean satellites' observations in Arlot (2019).

Summarising, the current data sets include:

- Earth-based classical astrometry from 1891 to present day (see e.g., Lieske, 1998; Jacobson et al., 2000; Lainey, 2002, for more detailed descriptions of these observations),
- mutual events, which have been consistently observed and reported every six years since the 1973 campaign (see Arlot, 2019, for a review),
- Arecibo radar observations (1999-2016, Brozović et al. 2020a),
- stellar occultations (Morgado et al., 2022),
- space astrometry from the Voyager and Galileo spacecraft.

These data sets and their typical accuracies are summarised in Table 3.1, while Fig. 3.2 illustrates the temporal distribution of these observations (also including their accuracies). It clearly highlights the much larger observation volume available since the 1970s, boosted by the advent of the mutual event campaigns and of space astrometry (the Voyager and Cassini mission timelines can actually be identified in Fig. 3.2 from their accurate measurements). More detailed insights (not reported here for the sake of brevity) can be gained from Figs. 8.1 and 8.2 and the corresponding discussion in Chapter 8, which distinguish between the different types of astrometric observations. Most of these observations (except space astrometry) are moreover publicly available in the NSDC (Natural Satellites Data Center) database[6].

3.3.2. Radio science

In the following, we provide the observation models for different radio science observables, and discuss the error sources which affect such measurements. Although radio science data acquired during past missions to the Jovian system will be briefly mentioned for the sake of completeness, we here specifically focus on the observables relevant for JUICE and Europa Clipper, since other radio science data sets were not considered in this dissertation (see discussion on relevant radio science data sets for Galilean moons' ephemerides at the end of this section). For a more complete overview of other possible radiometric measurement types and/or configurations, the interested reader is referred to Moyer (2005). We moreover restrict ourselves to measurements collected in a radio science context, and not for navigation purposes (see e.g., Hener et al. 2024 for a good overview of the differences). In particular, both JUICE and Europa Clipper radio science will use Doppler and ranging data. Phase-referencing VLBI measurements of JUICE's position will also be provided by PRIDE. Examining the contribution of these future radio science data sets to the Galilean moons' ephemerides solutions will be the core of Chapters 4 and 5.

[6]NSDC database for Galilean satellites observations: `http://nsdb.imcce.fr/obspos/bjupogae.htm`

Table 3.1.: Astrometry and radio science data sets considered in this dissertation to determine the Galilean moons' ephemerides. The timespans of the different data sets are provided, along with an indication of their typical accuracy (given for the target object i.e., the moons for astrometry and radar measurements, and the spacecraft for radio-science). The radio science data refer to future measurements.

	Data type	**Data set(s)**	**Timespan**	**Typical accuracy**
Astrometry	Classical astrometry	photographic plates and CCD imaging	1891 - present	several hundreds of kms
	Mutual events	observations every 6 years	1973 - 2021	a few hundreds of kms
	Space-based astrometry	Voyager imaging Galileo imaging	1978 - 1979 1994 - 1997	a few kms to a few tens of kms
	Stellar ocultations		2016 - present	a few kms
Radar	Range	Arecibo observations	1999 - 2016	around 10 - 20 kms
Radio science[a]	Doppler	JUICE Europa Clipper	2032 - 2035 2030 - 2034	12 μm/s 12 μm/s
	Range	JUICE Europa Clipper	2032 - 2035 2030 - 2034	< 0.2 m 1 m
	VLBI[b]	PRIDE JUICE	2032 - 2035	0.3 - 1.0 nrad[c]

[a] We here provide the accuracy levels expected for future JUICE and Europa Clipper radio science measurements.
[b] This refers to phase-referencing VLBI.
[c] See PRIDE VLBI error budget designed in Chapter 5.

3

3

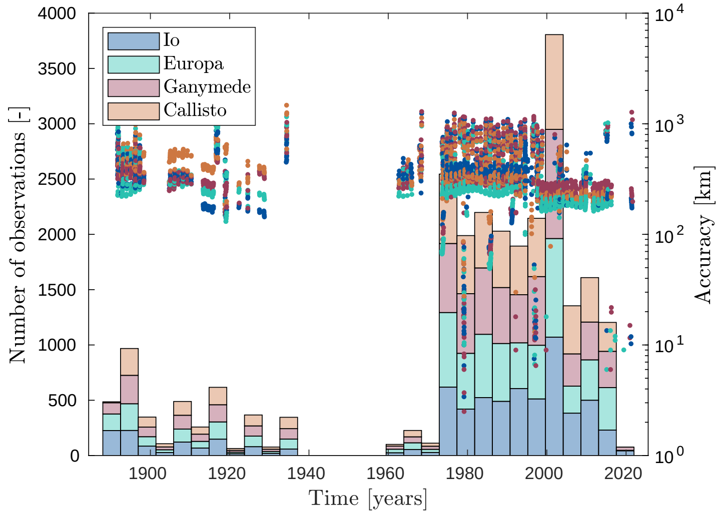

Figure 3.2.: Distribution of the available astrometric observations over time (same data set as in Chapter 8, see references therein), plotted as a histogram on the left axis, along with their accuracies (shown with dots, and plotted on the right axis), for all types of astrometric observations combined (including radar). The colours indicate which moon is observed.

Observation types and error sources

Both JUICE and Europa Clipper will rely on two-way tracking to generate range and Doppler measurements. This implies that the signal sent by a transmitter on Earth will be received and re-transmitted by the spacecraft, and eventually received by the same ground station which initially transmitted the signal (see Fig. 3.3). In the following, the indices 1 and 2 respectively designate the uplink (station-spacecraft) and downlink (spacecraft-station) legs.

Ranging measurements

Starting with range observables, they provide a measure of the distance between the target (i.e., spacecraft) and the receiver (i.e., ground-station on Earth), in the line-of-sight direction. A two-way range observable can be defined as

$$h_{\text{range}}(t) = c\left(t_{r_2} - t_{t_1}\right), \tag{3.21}$$

where t_{t_1} and t_{r_2} respectively designate the signal initial transmission and final reception times. t denotes the epoch used as reference for the measurement, which can be set to either the reception time t_{r_2} or transmission time t_{t_1} (see Fig. 3.3).

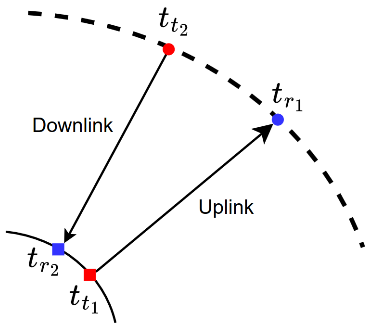

Figure 3.3.: Schematic representation of a two-way link tracking configuration. The square and circle-shaped markers respectively represent the spacecraft and ground station's positions. The red and blue colours indicate whether we consider the signal's transmission or reception, respectively.

The above can moreover be related to the light-time equation (Eq. 3.13) as:

$$\begin{aligned} h_{\text{range}} &= c\left(\rho_2 + \rho_1 + t_{t_2} - t_{r_1}\right) \\ &= r_{t_2}^{r_2} + r_{t_1}^{r_1} + c\left(t_{t_2} - t_{r_1}\right) + c\sum_i \delta t_{1,i} + c\sum_i \delta t_{2,i}. \end{aligned} \tag{3.22}$$

$t_{t_2} - t_{r_1}$ represents the signal re-transmission delay by the spacecraft, while $\delta t_{1,i}$ and $\delta t_{2,i}$ are the light-time corrections applied over the uplink and downlink legs, respectively.

Doppler measurements

Typical Doppler measurements, on the other hand, provide the integrated Doppler shift over a certain time interval Δt. This is essentially equivalent to integrating the observed range rate, as follows:

$$h_{\text{doppler}}(t) = \frac{1}{\Delta t}\left(h_{\text{range}}\left(t + \frac{\Delta t}{2}\right) - h_{\text{range}}\left(t - \frac{\Delta t}{2}\right)\right), \tag{3.23}$$

where the light-time effects are encompassed in the range observation formulation (Eq. 3.22). Such a Doppler measurement is obtained by comparing the frequencies of the transmitted and received signals. The total phase change over the integration time Δt is then measured with a cycle counter (see Thornton and Border 2005 for more detail), eventually providing the integrated range-rate described by Eq. 3.23.

VLBI measurements

Different VLBI techniques can be used to measure the angular position of a transmitting spacecraft. The well-known Delta-DOR technique makes use of multi-tone carrier signal modulation to this end (Curkendall and Border, 2013). On the other hand, phase-referencing VLBI correlates the signal simultaneously received at multiple ground stations while using a nearby background radio source as phase calibrator phase. PRIDE, the radio-astronomy experiment part of the JUICE mission (see Section 1.3.3) will provide VLBI measurements of the spacecraft using the latter, and we will therefore focus on phase-referencing VLBI in the following. More detail on the differences between the two VLB techniques mentioned above and on their respective performance for spacecraft tracking can be found in Gurvits et al. (2023).

Phase-referencing VLBI observables are the target's (i.e., spacecraft) right ascension and declination. Unlike the range and Doppler observables described above, phase-referencing VLBI involves an atypical tracking configuration. The transmitter is here the spacecraft, but the signal is received by multiple telescopes on Earth, a necessary condition to the phase-referencing technique (see e.g., Bocanegra Bahamon, 2019). The measurement is eventually expressed with respect to the geocentre, and the observable can be written as

$$h_{\text{vlbi}} = \begin{pmatrix} \alpha\left(\boldsymbol{r}_t^{\text{geo}}\right) \\ \delta\left(\boldsymbol{r}_t^{\text{geo}}\right) \end{pmatrix}, \tag{3.24}$$

which only differs from the equivalent classical astrometry observable (Eq. 3.15) because α and δ are here expressed with respect to the geocentre, and not to the position of a single receiver.

Error sources

The errors affecting the above-mentioned radio science measurements result from the combination of the following effects (e.g., Asmar et al., 2005; Iess et al., 2014a):

- media propagation delays (interplanetary plasma, troposphere, ionosphere),
- instrumental noise (including thermal noise, mechanical noise, frequency instability of the transponder or clock, etc.),
- uncertainties and biases in Earth orientation parameters and ground station locations,
- numerical noise.

The influence of numerical noise is particularly relevant for the averaged Doppler observables (Eq. 3.23), as it increases for small integration times Δt. This is, however, a practical error caused by round-off errors due to finite number representation, and can therefore be mitigated with adequate software implementations (Zannoni and Tortora, 2013). For phase-referencing VLBI specifically, errors in the ICRF position of the radio-source used as phase calibrator also play an important role (e.g., Pradel et al., 2006, see Chapter 5). A detailed error budget is beyond the scope of this section, and specific values describing the expected quality of JUICE and Europa Clipper radio science measurements will later be provided in Chapters 4, 5, and 8. It is however insightful to provide some rough orders of magnitude (reported in Table 3.1), for comparison with astrometric observations.

EXISTING AND FUTURE RADIO SCIENCE FROM GALILEAN SYSTEM MISSIONS

The complete radio science data set available (or soon to be) for the Galilean system comes from the following past, current, and upcoming missions:

- Ulysses[7]: Doppler, range, VLBI;
- Galileo: Doppler, VLBI;
- Juno (flybys of Galilean moons): Doppler;
- JUICE: Doppler, range, VLBI;
- Europa Clipper: Doppler, maybe range.

The Ulysses and Galileo radio science data sets have been included in past JPL solutions (e.g., Jacobson et al., 2000). Radiometric measurements acquired during Juno's recent flybys around the Galilean satellites (extended mission phase, started in 2021), on the other hand, have already been processed in gravity field analyses (Gomez Casajus et al., 2022), but not yet incorporated in any published natural satellites' ephemerides.

The ephemerides estimations conducted as part of this dissertation do not consider these first three data sets. They rather focus on evaluating the future contribution of the JUICE and Europa Clipper radio science (Chapters 4 and 5), also in light of potential synergies with the existing astrometry data sets (Chapters 6 and 8). The contribution of the Ulysses and Galileo data sets is anyway expected to be limited due to their poor measurement quality, as suggested by an independent preliminary analysis (A. Magnanini, private communication, see more detail in Section 8.5). Details on the expected tracking configuration, quantity, and quality for JUICE and Europa Clipper radio science observables considered in our analyses are specified whenever relevant in Chapters 4, 5, and 8, and therefore not repeated here.

3.4. CURRENT EPHEMERIDES: METHODS & SOLUTIONS

In the following, we discuss the state-of-the-art in natural satellites' ephemerides, both in terms of inversion methodology and quality of the existing solutions. In particular, we elaborate upon the different strategies applicable when incorporating radio science in the estimation, as touched upon in Section 1.4.1 and to be further analysed in Chapter 4. We also briefly describe the latest ephemerides available for the Galilean moons, before investigating future improvement strategies in the rest of this dissertation.

3.4.1. COMBINING ASTROMETRY AND RADIO SCIENCE

The most immediate difficulty when estimating the moons' dynamics from spacecraft tracking data, as mentioned in Section 1.4.1, originates from the indirect nature of the constraints that such measurements provide: the information on the moons' positions is extracted from the spacecraft's motion under the moons' gravitational attraction, which requires solving for both the spacecraft and the moons' dynamics.

When exploiting radio science tracking of a spacecraft for planetary or natural satellites' ephemerides determination, the dynamics of the spacecraft and of the

[7] only two flybys around Jupiter

natural bodies are typically not estimated concurrently. The spacecraft orbit is instead solved for independently in an arc-wise manner, alongside a (usually small) local correction to the ephemeris of the natural body under consideration (e.g., Durante et al., 2019; Di Ruscio, 2021; Fienga et al., 2021b). Rather than directly incorporating the spacecraft tracking observables, this correction to the natural body's state, referred to as a normal point[8], can be added as a substitute input to the ephemerides determination.

While these normal points are often reduced to their range component (Fienga et al., 2021a; Di Ruscio, 2021), a complete state correction observable can be obtained for body k, at the reference epoch t_i (corresponding to the arc over which both the spacecraft's state and the natural body's state correction are estimated):

$$\boldsymbol{h} = \Delta \boldsymbol{y}_k(t_i). \tag{3.25}$$

The weight assigned to this observable when included in the global ephemerides estimation directly follows from the statistical error describing the quality of the arc-wise solution:

$$\boldsymbol{\sigma}_{\boldsymbol{h}} = \boldsymbol{\sigma}(\boldsymbol{y}_k(t_i)). \tag{3.26}$$

Reconciling these independent, local state estimates (or corrections) in a global, coherent solution of the moons' dynamics is then attempted in a subsequent step, where the influence of the spacecraft's orbit is no longer directly accounted for.

An alternative approach, which will be described in much more detail in Chapter 4, consists in concurrently solving for the spacecraft's local states and the moons' orbits in a single estimation step. As discussed in Section 1.4.1, such an estimation strategy has already been applied (e.g., Jacobson, 2014, 2022; Lainey et al., 2020), including for the ephemerides of the Galilean satellites (Jacobson et al., 2000). All details of the adopted methodology (including the exact model formulation, but also critical data merging and weighting aspects) were however not made available. In particular, and circling back to the fitting process described in Section 3.2.1, using a coupled approach implies that the initial state vector $\boldsymbol{y}_0$ needs to be somehow expanded to also include the arc-wise spacecraft's states. The exact formulation of this estimation model has however not been reported in literature. It will be provided in Chapter 4 and later slightly extended in Appendix 5.8.

The advantages and disadvantages of the coupled and decoupled strategies will be discussed in Chapter 4, which provides the first detailed comparison of their respective performance and merits, focussing on their future application to JUICE and Europa Clipper radio science inversions.

3.4.2. Latest Galilean moons' ephemerides

The two main providers of ephemerides solutions for natural satellites are JPL (Jet Propulsion Laboratory) and IMCCE (Institute of Celestial Mechanics and

[8] This is similar to the normal point concept introduced in Section 3.2.2, but here referring to a post-fit product rather pre-fit observations.

Computation of Ephemerides). Focussing on the Jovian system, the most recent solution (at the time of writing) made available by the former is labelled jup380, while their latest official release remains the previous version (jup365)[9]. On the other hand, the newest ephemerides delivered by IMCCE, obtained with the NOE software (see Chapter 8), is NOE-5-2023[10]. The JPL and IMCCE solutions are respectively being used to plan the operations of the Europa Clipper and JUICE missions.

ORBITAL SOLUTIONS

Both the JPL and IMCCE solutions rely on very similar astrometric data sets (see Section 3.3.1): Earth-based astrometry and radar observations, Voyager and Galileo imaging data, HST (Hubble Space Telescope) observations and Gaia data for the IMCCE ephemerides. The JPL inversion, on the other hand, also includes radio science measurements from past missions, among which those acquired by the Galileo spacecraft. While the exact radio science data sets used in jup365 or jup380 are not specified, radiometric measurements from the Ulysses mission were also considered in previous JPL solutions, such as the one reported in Jacobson et al. (2000). The JPL ephemerides typically rely on a global, coupled inversion of astrometry and radio science (see previous discussion in Section 3.4.1). Due to the lack of details provided on the exact methodology, data sets selection, and data processing, it is nonetheless difficult to evaluate the contribution of the radio science data in the JPL ephemerides with respect to the astrometry-only IMCCE solution.

Fig. 3.4 shows the differences in the Galilean moons' positions obtained when comparing jup380 and NOE-5-2023 over the period 2015-2030. For Io, Europa, and Ganymede, differences remain, on average, constrained within 10-15 km (with Europa's tangential position locally exhibiting larger discrepancies). This seems to be consistent with the accuracy levels expected for these latest ephemerides solutions (V. Lainey, personal communication, 2023). Callisto's tangential position, however, shows rather large differences (about 40 km on average). Considering the quality of the existing astrometry and upcoming radio science data sets (Table 3.1) in light of the present solutions' accuracy (indicated by Fig. 3.4) clearly highlights why JUICE and Europa Clipper measurements are expected to bring a significant ephemerides improvement. Precisely quantifying the quality of the attainable solution, while accounting for the complications related to the use of spacecraft-derived constraints (Section 3.4.1), is the focus of Chapters 4, 5, and 8.

It is also worth mentioning that discrepancies in the underlying dynamical models used to fit the observations can explain some of the differences observed between the JPL and IMCCE solutions. In particular, tidal dissipation was not modelled in the latest release version from JPL (jup365), leading to much larger differences with respect to the IMCCE ephemerides than those reported in Fig. 3.4. This has however been corrected in the more recent jup380 solution (see discussion below).

[9]Both JPL solutions are available at https://ssd.jpl.nasa.gov/ftp/eph/satellites/bsp/
[10]IMCCE solution available at https://ftp.imcce.fr/pub/ephem/satel/NOE/JUPITER/2023/

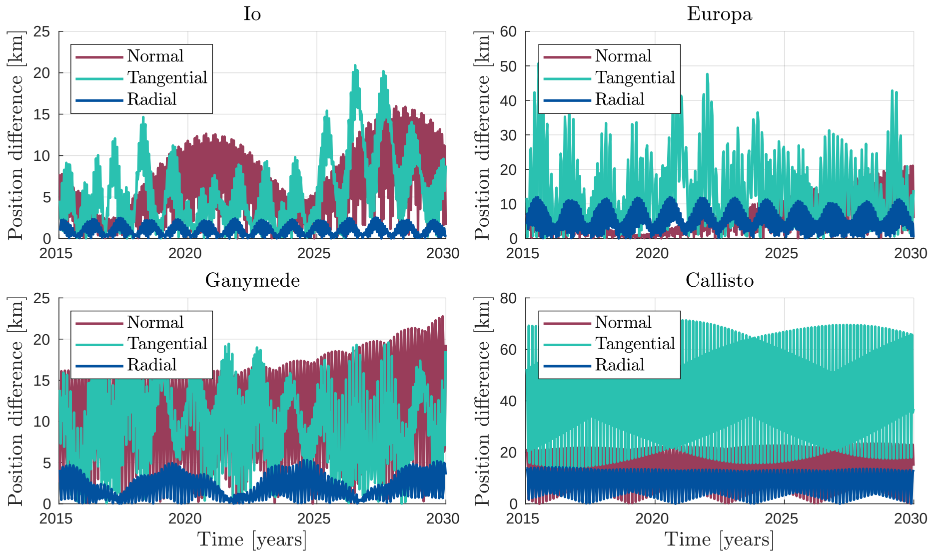

Figure 3.4.: Differences in position for the four Galilean satellites between the jup380 and NOE-5-2023 ephemerides (JPL and IMCCE solutions, respectively). The position differences are expressed in the RTN (radial, tangential, normal) reference frame.

Tidal dissipation estimation[11]

Estimating the drift in the Galilean satellites' mean motion caused by tides, already mentioned by De Sitter (1931), was first attempted while still relying on simplified, analytical representations of the moons' dynamics in Lieske (1987); Aksnes and Franklin (2001). This, however, led to very small and inconsistent estimates. Dissipation estimation prospects changed radically when Lainey and Tobie (2005) added tidal effects to their numerical model, originally developed in Lainey et al. (2004b,a). Using the tidal force formulation presented in Section 2.3.2, relevant tidal parameters can indeed be extracted from the signatures of both planet and satellite tides in the moon's dynamics.

It is particularly interesting to note that the differences between the release (jup365) and latest (jup380) versions of the JPL ephemerides for the Galilean satellites evidence the significant influence of tidal dissipation on the moons' orbits. Dissipation (both in Jupiter and in Io) was indeed only added in the latter solution. Fig. 3.5 displays the differences between the two ephemerides for Io: the quadratic drift in tangential position due to the secular mean motion shift induced by tides is

[11] The focus of this section is again purposely kept on the Galilean system. For a more general overview of the present-day estimates of tidal dissipation parameters in the Solar System, the interested reader is referred to Lainey (2016) and, for the Saturnian system specifically, to the updated results provided in Lainey et al. (2020) (see also Jacobson 2022 for an alternative study of dissipation in the Saturnian system).

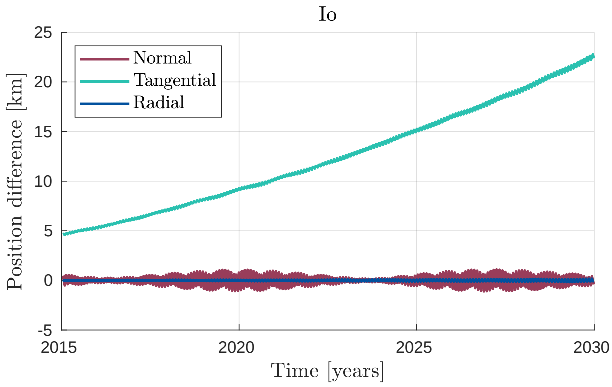

Figure 3.5.: Differences in position for Io between the jup365 and jup380 ephemerides (tidal dissipation was not accounted for in the former, but added in the latter). The position differences are expressed in the RTN (radial, tangential, normal) reference frame.

distinctly observable. This clearly demonstrates that such effects are large enough to be detectable from the available observations.

Fitting existing astrometric observations to the above-mentioned tidal force model allowed Lainey et al. (2009) to obtain the present best estimates of dissipation in Io and in Jupiter at Io's frequency:

$$(k_2/Q)^j = (1.102 \pm 0.203) \times 10^{-5} \tag{3.27}$$

$$(k_2/Q)^i = 0.015 \pm 0.003. \tag{3.28}$$

This strong dissipation seems consistent with the intense heating experienced by Io's surface, and has important implications regarding the moon's thermal state and the evolution of the Laplace resonance (Lainey et al., 2009, and Sections 1.1 and 10.1 of this dissertation). Refining the above estimates is therefore at the core of the rationale for improving current ephemerides by exploiting JUICE and Europa Clipper's future contributions (see the global inversion analysis presented in Chapter 8, and extended discussion in Section 10.1).

4

Decoupled and coupled moons' ephemerides estimation strategies

M. S. Fayolle, D. Dirkx, V. Lainey, L. I. Gurvits, P. N. A. M. Visser

When reconstructing natural satellites' ephemerides from space missions' tracking data, the dynamics of the spacecraft and natural bodies are often solved for separately, in a decoupled manner. Alternatively, the ephemeris generation and spacecraft orbit determination can be performed concurrently. This method directly maps the available data set to the estimated parameters' covariances while fully accounting for all dynamical couplings. It thus provides a statistically consistent solution to the estimation problem, whereas this is not directly ensured with the decoupled strategy. For the Galilean moons in particular, the JUICE mission provides a unique, although challenging, opportunity for ephemerides improvement. For such a dynamically coupled problem, choosing between the two state estimation strategies will be influential. This paper quantifies the Galilean moons' state uncertainties attainable when applying a coupled estimation strategy to simulated JUICE data, and discusses the challenges that remain to be addressed to achieve such a coupled solution from real observations. We first provide a detailed, explicit formulation for the coupled approach, which was still missing in the literature although already used in past studies. We then assessed the relative performances of the two ephemerides generation

An earlier version of this chapter is published in Planetary and Space Science (Fayolle et al., 2022): Fayolle, M., Dirkx, D., Lainey, V., Gurvits, L. I., & Visser, P. N. A. M. (2022). Decoupled and coupled moons' ephemerides estimation strategies application to the JUICE mission. Planetary and Space Science, 219, 105531.

techniques for the JUICE test case. To this end, we used both decoupled and coupled models on simulated JUICE radiometric data. We compared the resulting covariances for the Galilean moons' states, and showed that the decoupled approach yields slightly lower formal errors for the moons' tangential positions. However, the coupled model can reduce the state uncertainties by more than one order of magnitude in the radial direction (i.e., towards the central body). It also proved more sensitive to the dynamical coupling between Io, Europa and Ganymede, allowing the state solutions for the first two moons to fully benefit from JUICE orbital phase around Ganymede. On the other hand, we showed that the choice of state estimation methods does not strongly affect the moons' gravity field determination. Many issues still remain to be solved before a concurrent estimation strategy can be successfully applied, especially to reconstruct the moons' dynamics over long timescales. Nonetheless, our analysis highlights promising ephemerides improvements and thus motivates future efforts to reach a coupled state solution for the Galilean moons.

4.1. Introduction

The upcoming JUICE mission[1] (JUpiter ICy moons Explorer) will focus on the three Galilean moons Europa, Ganymede, and Callisto. The JUICE spacecraft is expected to arrive in the Jovian system in 2031, with a launch planned in 2023. It will first execute a series of flybys (2, 7, and 21 flybys at Europa, Ganymede, and Callisto, respectively), from 2032 to 2034. JUICE will then initiate its orbital phase around Ganymede, with an eccentricity ranging from 0.6 to 0 (GEO and GCO500 phases: Ganymede Elliptic Orbit and Ganymede Circular Orbit, respectively, both at an altitude of 5000 km). In May 2035, after a second elliptical phase, the spacecraft will eventually enter its final circular orbit at 500 km altitude (denoted GCO500), for a nominal period of 4 months. This mission profile, displayed in Fig. 4.1 and adopted in the rest of this paper, was obtained from the version 5.0 of the CReMA (Consolidated Report on the Mission Analysis)[2].

The JUICE spacecraft will carry one dedicated radio science instrument (3GM: Gravity and Geophysics of Jupiter and the Galilean Moons, e.g., Di Benedetto et al., 2021), which will provide highly accurate range and Doppler measurements (see Section 4.3.3). These 3GM observations will be complemented by PRIDE (Planetary Radio Interferometry and Doppler Experiment, e.g., Gurvits et al., 2013). The latter does not require any additional onboard instrument and uses tracking or 3GM radiometric signals to derive angular position measurements of the spacecraft with respect to the ICRF (International Celestial Reference Frame), as well as supplementary Doppler observables (e.g., Duev et al., 2012; Bocanegra-Bahamón et al., 2018; Molera Calvés et al., 2021). The radiometric data to be acquired by both 3GM and PRIDE are expected to contribute to a more accurate determination of the Galilean moons' states (Dirkx et al., 2016, 2017; Lari and Milani, 2019; Cappuccio et al., 2020a). Improved ephemerides are crucial to better understand the long-term thermal-orbital evolution of these moons, which is strongly driven by

[1] https://sci.esa.int/web/juice

[2] https://www.cosmos.esa.int/web/spice/spice-for-juice

tidal dissipation in both Jupiter and the satellites themselves (Peale, 1999; Hussmann and Spohn, 2004; Greenberg, 2010; Hay et al., 2020, see Section 1.1). The moons' ephemerides provide a natural way to extract the current rates of tidal dissipation, through the observed migration rates of the satellites (e.g., Lainey and Tobie, 2005; Lainey et al., 2009). Furthermore, a better characterisation of tidal dissipation mechanisms can provide tighter constraints on the moons' interiors, which is critical to investigate sub-surface ocean's properties (or confirm the existence of a putative ocean for Callisto, e.g., Lunine, 2017).

For natural satellites' ephemerides, the estimations of the spacecraft's and moons' dynamics are typically not performed in a coupled manner (e.g., Rosenblatt et al., 2008; Durante et al., 2019). Instead, when ephemerides are to be determined from flybys, the spacecraft trajectory with respect to the central body (i.e., body at which the flyby is performed) is determined from the available tracking data, along with the central body's state at the flyby epoch. The per-flyby state solutions for the natural body define the so-called *normal points* (see Section 3.4.1), which are then used in a second global estimation to reconstruct the long-term dynamics of this body (e.g., Durante et al., 2019).

If needed, a unified model may also be used, in which the spacecraft dynamics are determined in a multi-arc fashion, and the natural bodies' dynamics in a single-arc fashion, during a single inversion. Such an approach, used for instance by Dirkx et al. (2019b); Lari and Milani (2019), has the advantage of automatically incorporating all dynamical couplings, as well as the full sensitivity to physical

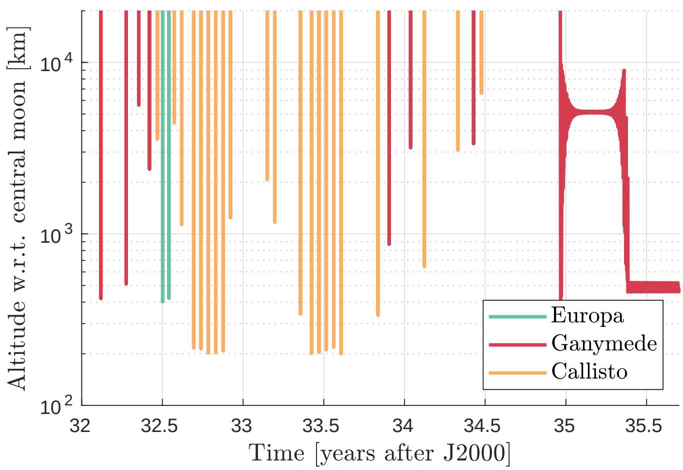

Figure 4.1.: Altitude of the JUICE spacecraft with respect to the Galilean moons during the flyby and orbital phases, based on CReMA 5.0. The vertical lines directly provide the closest-approach distances for the flyby series, while the orbit of JUICE around Ganymede is clearly identifiable, starting slightly before 2035.

parameters of both types of dynamics. The decoupled strategy, on the other hand, reconstructs the moons' dynamics from the normal points, which only capture the moons' kinematics (and not dynamics) at each flyby. However, while desirable, a coupled solution for the spacecraft's and moons' states is not always achievable in practice (e.g., Durante et al., 2019). It indeed requires the moons' dynamical models (with respect to the planet) to be consistent over both short and long timescales, to the accuracy level of the spacecraft's dynamics (with respect to the moon). Here, short and long timescales respectively refer to typical flyby duration (i.e., a few hours) and entire mission timeline (i.e., several years, so still short with respect to system evolution's timescale).

For the JUICE mission, we will be presented with a unique situation: the mission profile indeed involves a combination of flybys around multiple satellites and an extended orbit phase around Ganymede, which was never before performed in a planetary mission. Additionally, three of the four Galilean moons are in resonance, making the estimation of the different moons' dynamics strongly coupled, with the added complication that JUICE will provide a strong imbalance in data for these three moons. As a result, the estimation of ephemerides from JUICE-only data is (close to be) an ill-posed mathematical problem (Dirkx et al., 2017). Due to the complexity and novelty of the mission profile, and to the strong dynamical couplings that are involved, the concurrent single- and multi-arc estimation strategy appears particularly well-suited for the JUICE test case. In this paper, we compare the simulated state estimation solutions obtained with both the decoupled and coupled approaches, to quantify the impact of the adopted estimation strategy.

We limit ourselves to a covariance analysis, complemented by a deterministic simulation performed as verification. As already highlighted, the practical applicability of the coupled method to the JUICE mission is however not guaranteed, as bringing the dynamical models fidelity down to the required accuracy level will be really challenging. By definition, these issues cannot be addressed by a covariance analysis, as the resulting formal uncertainties do not account for inaccuracies in the dynamical models used for the moons and the JUICE spacecraft, or in the models representing the observations' errors. Our paper thus assesses which uncertainty levels could be obtained with a coupled estimation, provided that our dynamical models are accurate enough for a viable solution to be achieved. The formal uncertainties we obtain therefore quantify the coupled strategy's requirements in terms of dynamical modelling accuracy. Besides comparison purposes, precisely evaluating the performance of the decoupled method is thus also crucial in case obtaining a global coupled solution for the Galilean moons remains beyond (current) modelling capabilities. It must be noted that modelling issues, while not directly addressed by our covariance analysis, remain nonetheless deeply relevant for this study and will therefore be extensively discussed (see Sections 4.2.4 and 4.5.2). More generally, the limitations and scope of our formal analysis will be further detailed in Section 4.2.4.

The details of the coupled model, as well as the issues associated with its implementation and application, are not found in the literature, despite its application in a number of past studies (e.g., Dirkx et al., 2019b; Lari and Milani, 2019; Magnanini, 2021). Therefore, we choose to provide a detailed exposition of our coupled method in Section 4.2, completed by a shorter description of the decoupled approach. The models used to either propagate the moons' and spacecraft's dynamics or simulate JUICE radio science measurements are then described in Section 4.3. Section 4.4 presents the results of our comparative analysis of the coupled and decoupled estimation strategies, first for the flyby phase only, and then for the entire JUICE mission. Finally, Section 4.5 discusses in more detail the strengths and challenges of both estimation methods, before our conclusions are summarised in Section 4.6.

4.2. ESTIMATION FRAMEWORK

This section describes the whole estimation process, for both the coupled and decoupled approaches introduced in Section 4.1. The complete formulation for the coupled single- and multi-arc state estimation model, still missing in the literature, is provided in Section 4.2.2. For the sake of completeness, our implementation of the decoupled strategy for the JUICE case is given in Section 4.2.3. This section thus directly highlights the main differences between the two estimation strategies.

All methods described in the following were implemented in our TU Delft Astrodynamics Toolbox (Tudat) software[3], and are therefore freely available.

4.2.1. COVARIANCE ANALYSIS

We first briefly review the propagation of the variational equations and describe how covariance matrices are generated and propagated in our simulations, as typically implemented in any estimation process, either single- and/or multi-arc.

VARIATIONAL EQUATIONS FORMULATION

The variational equations describe how the dynamics of the system are influenced by the parameters to be estimated. In the following, we adopt the nomenclature of Gill and Montenbruck (2013). The state vector is denoted as $\mathbf{y}$ and is propagated numerically from the initial time t_0 using

$$\dot{\mathbf{y}}(t) = \mathbf{f}(\mathbf{y}, \mathbf{p}, t), \tag{4.1}$$

where $\mathbf{p}$ is a vector of parameters influencing the system's dynamics or the observations, and $\mathbf{f}$ represents the dynamical model (described in Section 4.3). Unless otherwise indicated, all states are expressed in a reference frame with inertial orientation (e.g., J2000). We stress that, in a general formulation, the states $\mathbf{y}$ need not be translational states, but may be any type of dynamics, of any number of bodies (see Mazarico et al. (2017); Dirkx et al. (2019a) for an example of coupled translational-rotational dynamics estimation of multiple bodies).

[3]Documentation: `https://tudat-space.readthedocs.io`
Full source code: `https://github.com/tudat-team/tudat-bundle`

The state transition matrix $\mathbf{\Phi}(t,t_0)$ and sensitivity matrix $\mathbf{S}(t)$ are defined as

$$\mathbf{\Phi}(t,t_0) = \frac{\partial \mathbf{y}(t)}{\partial \mathbf{y}(t_0)}, \tag{4.2}$$

$$\mathbf{S}(t) = \frac{\partial \mathbf{y}(t)}{\partial \mathbf{p}}. \tag{4.3}$$

The differential equations used to solve for $\mathbf{\Phi}$ and $\mathbf{S}$ are termed the variational equations, and are given by

$$\frac{d\mathbf{\Phi}(t,t_0)}{dt} = \frac{\partial \mathbf{f}(\mathbf{y},\mathbf{p},t)}{\partial \mathbf{y}(t)}\mathbf{\Phi}(t,t_0), \tag{4.4}$$

$$\frac{d\mathbf{S}(t)}{dt} = \frac{\partial \mathbf{f}(\mathbf{y},\mathbf{p},t)}{\partial \mathbf{y}(t)}\mathbf{S}(t) + \frac{\partial \mathbf{f}(\mathbf{y},\mathbf{p},t)}{\partial \mathbf{p}}, \tag{4.5}$$

4

with the following initial conditions:

$$\mathbf{\Phi}(t_0,t_0) = \mathbf{1}_{n\times n}, \tag{4.6}$$

$$\mathbf{S}(t_0) = \mathbf{0}_{n\times n_p}, \tag{4.7}$$

where n and n_p represent the sizes of the state vector $\mathbf{y}$ and parameter vector $\mathbf{p}$, respectively. The single-arc and multi-arc formulations are essentially identical, with the sole difference that the multi-arc solution is obtained by subsequent, independent, integrations of Eqs. (4.1), (4.4) and (4.5).

A variant of the multi-arc method, referred to as the constrained multi-arc approach, uses the fact that the arc-wise state estimates obtained for a given body should be consistent to further constrain the estimation solution (Alessi et al., 2012; Serra et al., 2018). In our analysis, we however chose to limit ourselves to the unconstrained multi-arc estimation. During the first part of the mission, the flybys are indeed temporarily distant, such that propagating information from previous arcs would not efficiently constrain the JUICE spacecraft's state. When arcs are contiguous (i.e., orbital phase around Ganymede), the high quality of the estimation solution anyway undermines the use of multi-arc constraints.

PROPAGATED COVARIANCE

Let $\mathbf{h}(T,\mathbf{q})$ denote the set of all modelled observations generated up to a time T. The design matrix $\mathbf{H}(T,\mathbf{q})$ associated with these observations is then formed by computing

$$\mathbf{H}(T,\mathbf{q}) = \frac{\partial \mathbf{h}(T,\mathbf{q})}{\partial \mathbf{q}}, \tag{4.8}$$

with $\mathbf{q}$ a vector containing the estimated parameters (e.g., Gill and Montenbruck, 2013; Milani and Gronchi, 2010). It usually includes initial states parameters, represented by the vector $\mathbf{y}_0$, and a subset of the parameters $\mathbf{p}$ influencing the dynamical or observational models. To simplify the notations, the vector of estimated parameters $\mathbf{q}$ will be divided as $\mathbf{q} = [\mathbf{y}_0; \mathbf{p}]$ in the following. It should however be noted that the exact definition of $\mathbf{q}$ depends on the estimation model, and that $\mathbf{y}_0$ and $\mathbf{p}$ might not directly incorporate all initial states, dynamical and observational models. More details on how $\mathbf{y}_0$ and $\mathbf{p}$ are precisely defined for both the coupled and decoupled models will be provided in Sections 4.2.2, 4.2.3 and 4.3.3.

The covariance matrix of $\mathbf{q}$ obtained using data up to time T is denoted $\mathbf{P}_{\mathbf{qq}}(T)$ and is given by

$$\mathbf{P}_{\mathbf{qq}}(T) = \left(\mathbf{P}_{\mathbf{qq},0}^{-1} + \left(\mathbf{H}^T(T)\mathbf{W}(T)\mathbf{H}(T)\right)\right)^{-1}, \tag{4.9}$$

where $\mathbf{P}_{\mathbf{qq},0}$ is the a priori covariance matrix of the parameters $\mathbf{q}$ (see Section 4.2.3 for a priori knowledge in our JUICE test case). The matrix $\mathbf{W}(T)$ contains the weights associated with all observations up to time T. In most cases, it is set as a diagonal matrix with $W_{ii} = \sigma_{h,i}^{-2}$, implicitly assuming the measurement uncertainties to be uncorrelated. This is however not the case in every estimation step of the decoupled model, as will be discussed in Sections 4.2.3 and 4.2.3. $\sigma_{h,i}$ denotes the uncertainty of observation i. The covariance $\mathbf{P}_{\mathbf{qq}}(T)$ can be used to compute the covariance of the state $\mathbf{y}$ at any later time t. We refer to this propagated covariance as $\mathbf{P}_{\mathbf{yy}}(t,T)$ and define it as

$$\mathbf{P}_{\mathbf{yy}}(t,T) = [\mathbf{\Phi}(t,t_0);\mathbf{S}(t)]\mathbf{P}_{\mathbf{qq}}(T)[\mathbf{\Phi}(t,t_0);\mathbf{S}(t)]^T, \tag{4.10}$$

where Φ and $\mathbf{S}$ are the state transition and sensitivity matrices obtained through Eqs. 4.4, 4.5, 4.6 and 4.7. For the covariances in Eqs. (4.9) and (4.10), the formal errors are obtained from the square root of the diagonal elements of $\mathbf{P}_{\mathbf{qq}}$ and $\mathbf{P}_{\mathbf{yy}}$, respectively.

4.2.2. COUPLED SINGLE- AND MULTI-ARC ESTIMATION

This section describes the extension of the variational equations introduced in Section 4.2.1 to the concurrent estimation of single- and multi-arc states. The formulation specifics are detailed in Section 4.2.2 for the JUICE case.

GENERAL PRINCIPLE

The coupled strategy relies on the concurrent estimation of the spacecraft orbit and natural bodies' ephemerides, as well as of all parameters influencing the dynamics and/or observations (vector $\mathbf{q}$ in Section 4.2.1). The natural bodies' dynamics, on the other hand, are reconstructed over a single arc. More precisely, the spacecraft orbit is solved for in an arc-wise manner (along with any observations- or spacecraft-related parameters, e.g., biases, accelerometer calibrations factors). Such a coupled model allows us to directly and robustly link observation strategies, data quality, mission profile, etc. to the final formal uncertainties in natural bodies' ephemerides and dynamical parameters (tidal dissipation, gravity field coefficients). Fig. 4.2 provides a schematic visualisation of this coupled approach, taking the JUICE flyby phase as an example. A preliminary framework for a concurrent single- and multi-arc estimation was briefly described by Dirkx et al. (2019b). A similar method was also used by Lari and Milani (2019) to study the onset of chaos in the dynamics of the JUICE spacecraft. The following sections provide the detailed and complete formulation for such a coupled estimation procedure for single- and multi-arc dynamics.

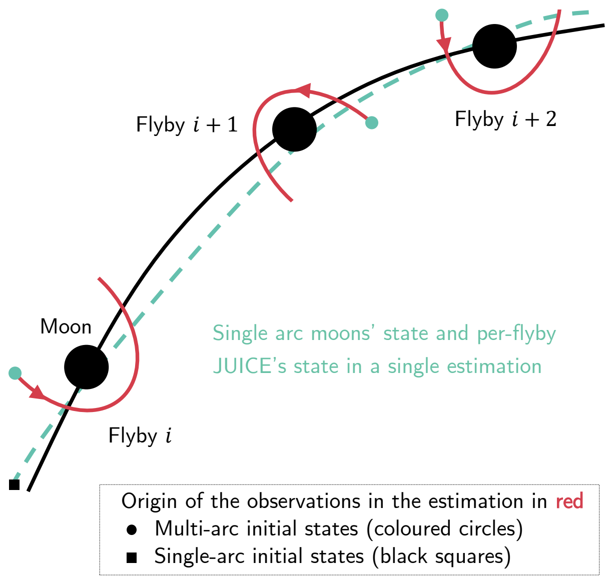

Figure 4.2.: Schematic representation of the coupled spacecraft and moons state estimation model, illustrated for a series of JUICE flybys around a single moon. The solid lines represent the actual trajectories of either the spacecraft or the central moon, while the dashed lines depict the reconstructed moons' dynamics after the estimation process is complete.

COUPLED VARIATIONAL EQUATIONS

We denote the single-arc state vector $\mathbf{y}_S(t)$, of size n_s and associated with the initial time t_0. The multi-arc state, on the other hand, is designated by $\mathbf{y}_M(t)$ and the arc-wise initial time is noted t_i for arc i, with $i = \in [1, N]$ for N arcs. The size of each arc-wise state vector is n_m. The multi-arc state function $\mathbf{y}_M(t)$ is defined as

$$\mathbf{y}_M(t) = \mathbf{y}_{M,i}(t), \tag{4.11}$$

$$t \in [t_i, \tilde{t}_i], \tag{4.12}$$

where $\mathbf{y}_{M,i}(t)$ refers to the state at time t during arc i, and $\tilde{t}_i$ denotes the end time of arc i. It should be noted that the multi-arcs need not be contiguous, and gaps may exist in the arc-wise solutions to Eq. (4.1). Eq. (4.11) is therefore only defined if an arc i exists that satisfies Eq. (4.12) at the time t.

The full state function is given as a combination of the single- and multi-arc states at time t, as follows:

$$\mathbf{y}(t) = \begin{pmatrix} \mathbf{y}_S(t) \\ \mathbf{y}_M(t) \end{pmatrix}. \tag{4.13}$$

For our estimation, we require a linearised model for the change in $\mathbf{y}(t)$ induced by a variation in the parameters $\mathbf{p}$ and in the full vector of initial states $\mathbf{y}_0$, to compute

S and Φ, respectively. We define the full initial state as:

$$\mathbf{y}_0 = \begin{pmatrix} \mathbf{y}_S(t_0) \\ \mathbf{y}_{M,1}(t_1) \\ \vdots \\ \mathbf{y}_{M,N}(t_N) \end{pmatrix}. \tag{4.14}$$

Looking at Eqs. (4.13) and (4.14), the size of the full initial state vector, $\mathbf{y}_0$, is different from that of the state function $\mathbf{y}(t)$, as the former combines all single-arc and multi-arc initial states, while $\mathbf{y}(t)$ only includes the single-arc states and the multi-arc state of the current arc. We note that $\mathbf{p}$ may affect the single- or multi-arc dynamics solutions, or both. The only limitation imposed on the dynamics (Eq. 4.1) is that the differential equation for $\mathbf{y}_S(t)$ must be independent of $\mathbf{y}_M(t)$. The opposite is not true, $\mathbf{y}_M(t)$ being allowed to (and in our case does) depend on $\mathbf{y}_S(t)$. These assumptions only hold if the masses of the multi-arc bodies are negligible with respect to the single-arc bodies'. This is typically the case as the spacecraft's dynamics are generally propagated in a multi-arc manner, while the bodies included in the single-arc solution are often natural bodies (see Section 4.2.2).

4

We use $\mathbf{\Phi}_{SS}(t,t_0)$ and $\mathbf{\Phi}_{MM,i}(t,t_i)$ to refer to the single- and multi-arc state transition matrices, respectively. Similarly, the single- and multi-arc sensitivity matrices are denoted as $\mathbf{S}_S(t)$ and $\mathbf{S}_{M,i}(t)$. We note that, for the multi-arc case, the parameter vector $\mathbf{p}$ can include local parameters that influence the dynamics of a single arc i only, as well as global parameters affecting all arcs. The state transition matrix is defined as the derivative of the current state $\mathbf{y}(t)$ (Eq. 4.13) with respect to both the single-arc initial state $\mathbf{y}_S(t_0)$ at time t_0, and the arc-wise initial states $\mathbf{y}_{M,i}$, at the beginning t_i of each arc. The full state transition matrix, noted $\mathbf{\Phi}(t;t_0,t_i)$, and sensitivity matrix $\mathbf{S}(t)$ can thus be written as

$$\begin{aligned} \mathbf{\Phi}(t;t_0,t_i) &= \frac{\partial \mathbf{y}(t)}{\partial \mathbf{y}_0} \\ &= \begin{pmatrix} \mathbf{\Phi}_{SS}(t,t_0) & \mathbf{0}_{n_s,n_m(i-1)} & \mathbf{0}_{n_s,n_m} & \mathbf{0}_{n_s,n_m(N-i)} \\ \mathbf{\Phi}_{MS,i}(t,t_i) & \mathbf{0}_{n_m,n_m(i-1)} & \mathbf{\Phi}_{MM}(t,t_i) & \mathbf{0}_{n_m,n_m(N-i)} \end{pmatrix}, \end{aligned} \tag{4.15}$$

$$\mathbf{S}(t) = \frac{\partial \mathbf{y}(t)}{\partial \mathbf{p}} = \begin{pmatrix} \mathbf{S}_S(t) \\ \mathbf{S}_{M,i}(t) \end{pmatrix}, \tag{4.16}$$

where we introduced the coupling term

$$\mathbf{\Phi}_{MS,i}(t,t_i) = \frac{\partial \mathbf{y}_{M,i}(t)}{\partial \mathbf{y}_S(t_0)} \tag{4.17}$$

into the state transition matrix. The zero entries in the first row of Eq. (4.15) directly result from the dynamics of $\mathbf{y}_S(t)$ being independent of $\mathbf{y}_M(t)$. For clarification purposes, the dimensions of these zero blocks are specified as subscripts.

To obtain the numerical solution to the coupled variational equations, we first propagate the single-arc dynamics and variational equations, to obtain $\mathbf{y}_S$, $\mathbf{\Phi}_{SS}$ and $\mathbf{S}_S$. For the multi-arc formulation, the differential equations for $\mathbf{\Phi}_{\boldsymbol{MM}}$ are unchanged compared to the classical (decoupled) approach. However, to compute the full state transition and sensitivity matrices, we need a formulation for the coupling term $\mathbf{\Phi}_{MS,i}$ which incorporates the influence of single-arc dynamics on the multi-arc dynamics, as follows:

$$\frac{d\mathbf{\Phi}_{MS,i}(t,t_i)}{dt} = \frac{\partial \dot{\mathbf{y}}_{M,i}(t)}{\partial \mathbf{y}_S(t)}\mathbf{\Phi}_{SS}(t,t_0) + \frac{\partial \dot{\mathbf{y}}_{M,i}(t)}{\partial \mathbf{y}_{M,i}(t)}\mathbf{\Phi}_{MS,i}(t,t_i). \tag{4.18}$$

Similarly, we require a formulation for $\boldsymbol{S}_{MS,i}$, given by

$$\frac{d\mathbf{S}_{M,i}(t)}{dt} = \frac{\partial \dot{\mathbf{y}}_{M,i}(t)}{\partial \mathbf{y}_S(t)}\mathbf{S}_S(t) + \frac{\partial \dot{\mathbf{y}}_{M,i}(t)}{\partial \mathbf{y}_{M,i}(t)}\mathbf{S}_{M,i}(t) + \frac{\partial \dot{\mathbf{y}}_{M,i}(t)}{\partial \mathbf{p}}. \tag{4.19}$$

4

This completes the required formulation for the differential equations governing the evolution of Eqs. (4.15) and (4.16). From the single-arc propagation, we retrieve $\mathbf{y}_S$, $\mathbf{\Phi}_{SS}$ and $\mathbf{S}_S$, appearing in Eqs (4.18) and (4.19), and use as a given when solving the multi-arc dynamics and variational equations.

The advantage of this approach, with two separate integrations to fully populate the coupled $\mathbf{\Phi}$ and $\mathbf{S}$ matrices, is that different numerical settings may be used for the single- and multi-arc segment. In particular, for the case of coupled natural body and spacecraft dynamics estimation, one will typically require a much smaller time-step for propagating the spacecraft than for the natural bodies (as well as possibly a different integrator).

FORMULATION FOR THE JUICE MISSION

In Section 4.2.2 we presented our general framework for propagating coupled single- and multi-arc variational equations. We now discuss specific details of the formulation for the JUICE mission. Our single-arc state vector is defined in a planetocentric reference frame as

$$\mathbf{y}_S(t) = \begin{pmatrix} \mathbf{x}_1^{(0)}(t) \\ \mathbf{x}_2^{(0)}(t) \\ \mathbf{x}_3^{(0)}(t) \\ \mathbf{x}_4^{(0)}(t) \end{pmatrix}, \tag{4.20}$$

where the index 0 refers to Jupiter, and indices 1,2,3,4 correspond to Io, Europa, Ganymede and Callisto, respectively, following the formalism adopted in Dirkx et al. (2016).

Only the spacecraft's dynamics are solved for in arc-wise manner, such that the multi-arc state vector for arc i can simply be written as

$$\mathbf{y}_{M,i}(t) = \mathbf{x}_{\text{sc},i}^{(j_i)}(t). \tag{4.21}$$

We use 'sc' to denote properties relating to the JUICE spacecraft, while j_i designates the index j of the central body during arc i. The reference frame origin is selected as the moon where a flyby is performed during the flyby phase (Europa, Ganymede or Callisto), and as Ganymede during the orbital phase.

Solving the coupled variational equations provides solutions for the derivatives $\frac{\partial \mathbf{x}_{\text{sc},i}^{(j_i)}}{\partial *}$, which describe changes in the moon-centred state of the JUICE spacecraft. However, to evaluate our design matrix $\mathbf{H}$ (see Eq. 4.8), we need to account for the variations in the *observed* position of the spacecraft, often expressed in an inertial frame (e.g., Solar System Barycentre). As a result, the dynamics of the moons influence the observed position of the spacecraft in two distinct manners:

- the dynamical contribution, through the bottom-left block of Eq. (4.15),
- the kinematic or *indirect* contribution, through the variations in the moons' states with respect to the reference frame used for the observed spacecraft's motion.

This methodology automatically allows the incorporation of parameters that directly influence both the spacecraft's and moon's dynamics. Principally, this concerns the moons' spherical harmonic coefficients. Consistently propagating $\mathbf{S}(t)$ for the full system ensures that the covariance of the moons' initial states is robustly propagated to later epochs (see Section 4.2.1).

4

4.2.3. Decoupled single- and multi-arc estimation

To complement the description of the coupled estimation method in Section 4.2.2, the decoupled strategy is now discussed. As this approach does not differ from textbook formulations (e.g., Gill and Montenbruck, 2013; Milani and Gronchi, 2010), less details are provided and we directly address the JUICE case specifically. For our comparative analysis, it is however crucial to make both the decoupled and coupled formulations explicit, to highlight their main differences.

General principle

The decoupled estimation is performed in two separate steps, as shown in Fig. 4.3. The spacecraft's and natural bodies' dynamics are first solved for concurrently, as in the coupled case, but in a multi-arc manner. Only the dynamical coupling between the spacecraft and the central body is thus accounted for in this estimation step (while all dynamical couplings are included to propagate the moons' states, see Section 4.3.2). Since the natural bodies' states are independently estimated for each arc, the adopted dynamical model need not be consistent over long timescales.

This first estimation step therefore provides arc-wise estimated states for the central bodies. These so-called *normal points* are then used as observables in a second step, which aims at reconstructing the natural bodies' dynamics on a more global scale. More precisely, a normal point is defined as the central moon's cartesian state components (vector of size 6) and associated covariances (6-by-6 matrices), determined with respect to Jupiter at the time of closest approach. The covariances $\mathbf{P_{qq}}$ for the arc-wise initial states, resulting from the first estimation step, determine the weights $\mathbf{W}$ (see Eq. 4.9) assigned to each normal point in the second step. The matrix $\mathbf{W}$ is thus not exactly diagonal in this particular case (see Section 4.2.1). It instead shows non-zeros, diagonally-centred, 6-by-6 blocks containing the 6-by-6

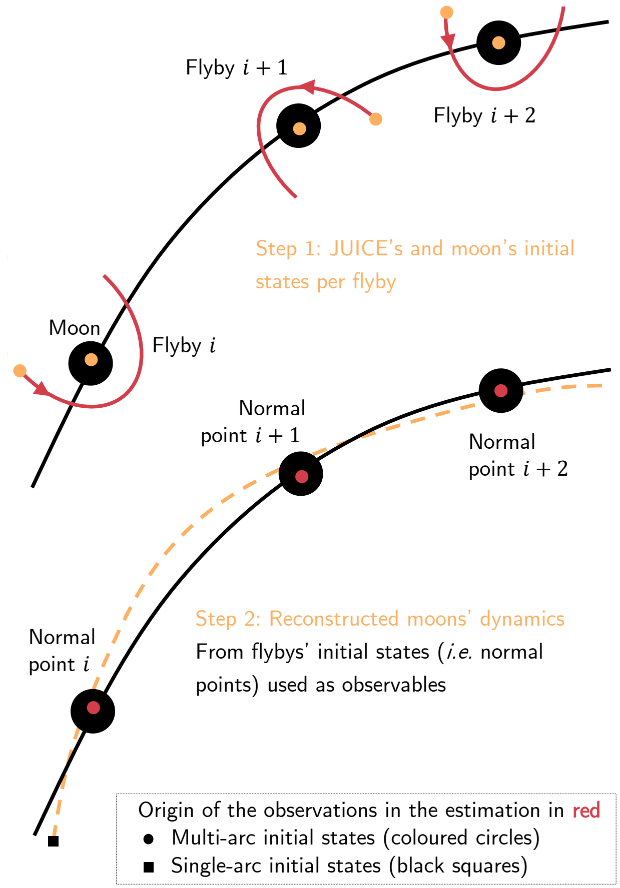

Figure 4.3.: Schematic representations of the decoupled spacecraft and moons state estimations, illustrated for a series of JUICE flybys around a single moon. The solid lines represent the actual trajectories of either the spacecraft or the central moon, while the dashed lines depict the reconstructed moons' dynamics after the estimation process is complete.

normal points' covariances. The entire two-step decoupled estimation process is depicted in Fig. 4.3, using JUICE flybys as an example.

While the coupled model estimates all parameters concurrently, different sets of estimated parameters are defined for the two steps of the decoupled method. An obvious example are the spacecraft's states, which are determined in a multi-arc manner in the first step but are absent from the second step, when reconstructing the global solution for the moons (see Fig. 4.3). As previously mentioned, it must be noted that the first step of the decoupled model only estimates the state of the central moon j when determining the normal point for a flyby around that moon.

The state uncertainties of the other moons are not accounted for, and our decoupled estimation strategy might thus yield slightly too optimistic formal errors for the arc-wise state of moon j. However, as a verification, we ran an additional analysis for the JUICE test case including the other moons' states as consider parameters in the normal points determination process. As an indication, we provide the results obtained for two of the JUICE flybys in Appendix 4.7. This verification showed that these uncertainties have a negligible impact on the normal points solution when using tracking arcs of 8 hours only around each flyby (see Section 4.3.3). This assumption should however be revisited if longer tracking arcs were to be considered for the JUICE flybys, as the influence of the state uncertainties for the non-central moons is then expected to increase. A more complete discussion on the estimated parameters for our JUICE analysis is provided in Section 4.3.3 (see Table 4.3).

DECOUPLED VARIATIONAL EQUATIONS FOR THE JUICE MISSION

As described in Section 4.2.3, the spacecraft's and moon's dynamics are first reconstructed in a multi-arc fashion. For each arc i, the initial translational state to be estimated is thus defined as

$$\mathbf{y}_{M,i}(t_i) = \begin{pmatrix} \mathbf{x}^{(0)}_{j_i,i}(t_i) \\ \mathbf{x}^{(j_i)}_{\mathrm{sc},i}(t_i) \end{pmatrix}, \tag{4.22}$$

where j_i again refers to the index of the central moon for arc i.

In practice, all arcs sharing the same central moon are combined, to allow some dynamical parameters to be estimated globally alongside the arc-wise states (e.g., gravity field coefficients of the central moon). For each moon j, the full initial state is thus built by concatenating the corresponding multi-arc states, as follows:

$$\mathbf{y}_j = \begin{pmatrix} \mathbf{x}^{(0)}_j(t_1) \\ \mathbf{x}^{(j)}_{\mathrm{sc},1}(t_1) \\ \mathbf{x}^{(0)}_j(t_2) \\ \dots \\ \mathbf{x}^{(j)}_{sc,N_j}(t_{N_j}) \end{pmatrix}, \tag{4.23}$$

with N_j the number of arcs with moon j as central body.

The arc-wise state transition matrix $\Phi_i(t, t_i)$ can be derived from Eq. (4.22) as

$$\mathbf{\Phi}_i(t, t_i) = \frac{\partial \mathbf{y}_{M,i}(t)}{\partial \mathbf{y}_{M,i}(t_i)}, t \in [t_i, \tilde{t}_i] \tag{4.24}$$

$$= \begin{pmatrix} \mathbf{\Phi}_{j_i}(t; t_i) & \mathbf{0}_{6,6} \\ \mathbf{\Phi}_{\mathrm{sc},j_i}(t, t_i) & \mathbf{\Phi}_{\mathrm{sc}}(t, t_i) \end{pmatrix}. \tag{4.25}$$

Eq. (4.25) shows some similarities with Eq. (4.15), but also clearly highlights major differences between the coupled and decoupled formulations. In particular, $\mathbf{\Phi}_{\text{sc},j_i}(t, t_i)$ also represents a coupling term, but expressed in a multi-arc fashion and with respect to the central moon j_i only:

$$\mathbf{\Phi}_{\text{sc},j_i}(t;t_i) = \frac{\partial \mathbf{y}_{\text{sc}}(t)}{\partial \mathbf{y}_{j_i}(t_i)}, \tag{4.26}$$

as opposed to Eq. (4.17). The variational equations provided above apply to the first, arc-wise estimation step of the decoupled strategy (see Section 4.2.3). The second phase, in which a single-arc estimation is performed to reconstruct the long-term dynamics of the Galilean moons, follows the regular single-arc approach. The associated variational equations are therefore not detailed in this paper.

4

A PRIORI KNOWLEDGE STRATEGY

As shown in Eq. 4.9, prior knowledge is accounted for in the estimation by means of the a priori covariance matrix $\mathbf{P}_{\mathbf{qq},0}$. Appropriate a priori values for all estimated parameters, referred to as *default* a priori covariances, are further discussed in Section 4.3.3 and are combined in a diagonal matrix $\mathbf{P}_0$ (shortened notation for $\mathbf{P}_{\mathbf{qq},0}$).

For the decoupled case in particular, the moons' arc-wise state solutions first determined at the beginning of each flyby strongly depend on these a priori constraints (see results in Section 4.4.1). Using the same *default* a priori values for all arc-wise moon states, derived from the existing ephemerides solutions, would be a rather conservative approach. It indeed neglects the iterative improvement achievable by progressively including more flybys in the estimation. Even if the observations processed by the estimation remain the same, some additional information is incorporated in the multi-arc model to improve the solution, namely that the arc-wise state solutions for a given moon j are not completely independent from one another. They indeed belong to a single body's trajectory and should thus be dynamically consistent. Such an update strategy for the a priori contraints on the moons' states can be compared to the multi-arc constrained approach for the spacecraft's orbit determination (e.g., Alessi et al., 2012), but applied to the moons' arc-wise states instead of the spacecraft's. It must be noted that using this a priori update strategy introduces some correlations between the arc-wise state components of moon j (i.e., between the different normal points determined for this moon). The off-diagonal blocks of the weight matrix $\mathbf{W}$ are therefore not filled with zeros anymore.

Focusing on the N_j arcs with moon j as central body, more realistic a priori covariances can be derived for arc k by propagating the covariance obtained for arc $k-1$ up to the beginning of arc k. This propagated covariance is denoted as $\mathbf{P}_0^{k\rightarrow k+1}$ in the following. Some state components may nonetheless be poorly constrained by the previous arc's estimation, thus yielding unrealistically large a priori errors in certain directions. The a priori matrix $\mathbf{P}_0^k$ for arc k is thus built as a combination of the default and propagated a priori covariance matrices, as follows:

$$\begin{aligned}\left(\mathbf{P}_0^k\right)^{-1} &= (\mathbf{P}_0)^{-1} + \left(\mathbf{P}_0^{k-1\rightarrow k}\right)^{-1} \\ &= (\boldsymbol{P}_0)^{-1} + \left(\boldsymbol{\Phi}_j(t_{k-1}, t_k)\mathbf{P}_0^{k-1}\Phi_j(t_{k-1}, t_k)^T\right)^{-1},\end{aligned} \tag{4.27}$$

where $\boldsymbol{\Phi}_j(t_{k-1}, t_k)$ is the state transition matrix for moon j, computed from the start of arc $k-1$ to the beginning of the current arc k. This propagation scheme is initialised with the *default* a priori matrix (so $\mathbf{P}_0^{0\rightarrow 1} = \mathbf{0}$, i.e., matrix filled with zeros).

Iterating on the a priori knowledge for the moons' arc-wise states requires to run the first step of the decoupled estimation multiple times, gradually increasing the number of arcs being processed. The final outcome of the multi-arc estimation (i.e., normal points and global parameters' estimates, see Section 4.2.3) is reached when all N_j arcs associated with moon j are included. This process is schematically summarised in Fig. 4.4.

It must be stressed that, in the strategy described above, we only propagate the covariances between moon j's own state components from arc $k-1$ to the beginning of arc k. We thus neglect the influence that uncertainties in other moons' states could have on the propagated a priori covariance for moon j. Discarding the contribution of the other moons is consistent with the philosophy of the decoupled estimation, in which only the central moon's state is determined for each arc. It should however be noted that the a priori used for the normal points might therefore be slightly too optimistic.

The impact of the a priori information on the parameters solution, and especially the effect of the above updating strategy for the arc-wise states, will be further investigated and discussed in Section 4.4.1. For each estimated parameter, the contribution of the a priori information to the solution $c_{\mathbf{q}}$ can be evaluated as follows (e.g., Floberghagen, 2001):

$$c_{\mathbf{q}} = \mathbf{I} - \mathbf{P}\ \mathbf{P}_0^{-1}, \tag{4.28}$$

where $\mathbf{I}$ is to the identify matrix, while $\mathbf{P}$ and $\mathbf{P}_0^{-1}$ refer to the final and a priori covariance matrices, respectively ($\mathbf{P}_{\mathbf{qq}}$ and $\mathbf{P}_{\mathbf{qq},0}^{-1}$ in Eq. 4.9). A $c_{\mathbf{q}}$ equal to 1 indicates that the parameter's estimation relies entirely on the observations, while a value of 0 means that it is based on a priori information.

4.2.4. SCOPE OF THE COMPARATIVE ANALYSIS

As mentioned in Section 4.1, we limit ourselves to a covariance analysis in this study. We compare the performances of the decoupled and coupled models by analysing the formal errors and correlations obtained in both cases. It is important to stress that the coupled model, by concurrently accounting for all dynamical couplings and sensitivities, directly maps the simulated observations to the estimated parameters' covariances. Assuming that the fidelity of both our dynamical and measurement error models is sufficient, the resulting formal errors and correlations are therefore considered to provide a good statistical representation of the estimation solution, while this is not directly true for the decoupled method. Our study characterises how much the solution obtained by decoupling the spacecraft's and moons' state estimation departs from the covariances given by the coupled approach, regarded as statistically consistent.

For any estimation, true errors obtained from real data after completing the iterative least-squares estimation are however larger than the formal errors provided by a covariance analysis. Differences between true and formal errors originate from non-white measurement noise, as well as inaccuracies in the models used for the spacecraft's and planetary system's dynamics. For the JUICE mission data analysis, this situation may even be more severe than for any previous natural satellite's ephemeris determination, due to the much better data quality and subsequent higher requirements on dynamical modelling.

In practice, both the decoupled and coupled methods are limited by the dynamical model fidelity, so that the true errors would be larger than formal ones in the two

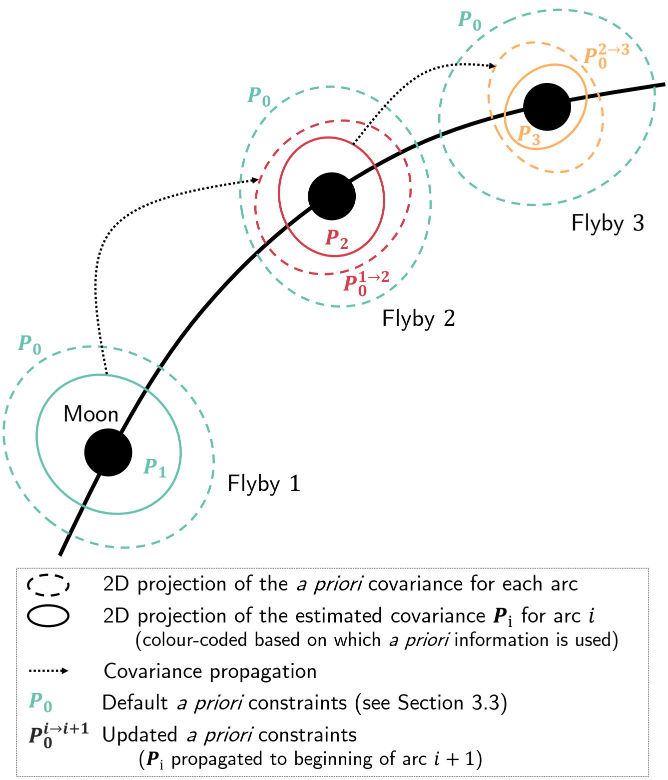

Figure 4.4.: Schematic representation of the iterative strategy for the a priori covariances applied to the first step of the decoupled method (i.e., normal points determination). The solid covariance ellipses are colour-coded to indicate which a priori values are used, with the *default* a priori $\mathbf{P}_0$ represented in green.

cases. The goal of this study is to determine at which point and to what extent the coupled estimation would be beneficial for ephemerides determination, as well as to quantify the dynamical model requirements to achieve this (see Section 4.1). Dynamical mismodelling would nonetheless influence the decoupled and coupled solutions differently, and represent a major challenge for the applicability of the coupled model in particular. These modelling issues will therefore be discussed in more detail in Section 4.5.

4.3. Dynamical and Observation Models

In the following section, we discuss the settings and models used for our simulated covariance analysis for Galilean satellites' ephemerides from JUICE tracking data. The spacecraft's and moons' dynamical models are summarised in Sections 4.3.1 and 4.3.2, respectively, while the estimation and observations settings are described in Section 4.3.3.

4.3.1. Spacecraft Dynamics

When propagating the dynamics of the spacecraft during arc i, the following accelerations were taken into account:

- spherical harmonic acceleration of the central moon j_i, expanded up to degree l_j and order m_j (with $l_1/m_1 = 2/2$, $l_2/m_2 = 4/4$, $l_3/m_3 = 12/12$, $l_4/m_4 = 6/6$). Higher degrees might be accessible from JUICE data, especially for Ganymede, but were purposely not included in our analysis, which primarily focuses on ephemerides determination.

- point-mass acceleration of moon k, for each $k \in \{1,2,3,4\}$, with $k \neq j_i$

- spherical harmonic acceleration of Jupiter, expanded up to degree $l_0 = 8$ and order 0 (zonal terms only),

- point-mass accelerations exerted by Saturn and the Sun,

- cannonball radiation pressure acceleration due to the Sun's radiation,

- arc-wise constant empirical acceleration in the RTN frame (radial, tangential, normal), representing errors in the accelerometer calibration.

We adopted the same models for the environment (gravity fields, ephemerides, etc.) as Dirkx et al. (2016), with a number of exceptions: we used the Jupiter gravity field from Iess et al. (2018), and CReMA 5.0 for the JUICE orbit[4], released by ESA in the form of Spice kernels (Acton Jr, 1996).

[4] https://www.cosmos.esa.int/web/spice/spice-for-juice

4.3.2. Moon Dynamics

When propagating the dynamics of the Galilean moons, we used similar models as Lainey et al. (2004a); Dirkx et al. (2016), taking into account

- the mutual spherical harmonic acceleration between Jupiter and each moon j, with the gravity field of Jupiter expanded up to degree 8 and order 0, and that of the moons to degree and order 2,
- the mutual spherical harmonic accelerations between all moons j and k, with the fields of the bodies expanded up to degree and order 2,
- the point-mass accelerations due to Saturn and the Sun,
- the acceleration exerted on each moon j due to tidal dissipation in Jupiter forced by moon j,
- the acceleration on each moon j due to both planet and satellite tides, using the tidal force formulation defined in e.g., Lainey et al. (2007); Lari (2018).

4

4.3.3. Estimation Settings

As the tracking configurations differ between the flyby and orbital phases of the JUICE mission, different estimation settings were used. An 8-hour tracking arc was defined for each flyby, centred at the time of closest approach. For the orbital phase, we simulated 8 hours of tracking per day. In practice, the JUICE spacecraft will be tracked from three stations of the European Space Tracking network (ESTRACK), the main one being Malargue, which is as of yet the only one enabling both X- and Ka-band tracking. However, we assumed that the other two will also be able to handle Ka-band tracking by the time the JUICE spacecraft arrives in the Jovian system. We thus considered 8 hours per day of almost continuous tracking, except during occultations or for elevations lower than 15 deg (as in e.g., Di Benedetto et al., 2021; Magnanini, 2021).

Tracking arcs of two days, separated by three days without tracking, were used as the nominal tracking configuration for the orbital phase. Nonetheless, the sensitivity of the estimation solution to these tracking settings was investigated by considering one day- and one week-arcs (results are presented in Section 4.4.2). The three days interval between two tracking arcs was merely used to reduce the computational load of our simulations. We verified that adding some buffer between tracking arcs did not affect the resulting formal uncertainties and, most importantly, the way the coupled solution compares to the decoupled one.

For each arc, we simulated both Doppler and range observables which are measurements, in the line of sight direction, of the spacecraft's position and velocity with respect to a ground station, respectively. Doppler observables were modelled with a noise level of 15 μm/s at an integration time of 60 s, while range observables have a noise level of 20 cm. This is quite precise but should actually be a conservative value, given the 1 cm range accuracy achieved by the BepiColombo mission (e.g., Genova et al., 2021). For selected passes, as was done by Dirkx et al.

(2017), we also simulated VLBI observables (lateral position of the target spacecraft) following methodology described by Pogrebenko et al. (2004) and Duev et al. (2016), with a noise level of 0.5 nrad. Doppler data were generated as unbiased, while we included arc-wise biases for both the range and VLBI observables. It should be noted that range and Doppler data are obtained in a topocentric frame, while VLBI observations are measured in the ICRF. For both the flyby and orbital phase, observations are subject to constraints on ground station visibility (e.g., occultation, Sun angle).

When presenting and discussing our results in the rest of this paper, the estimated states will generally be expressed in the RTN frame: the x-axis points from the central body towards the spacecraft or moon, the z-axis is aligned with the normal to the orbital plane and the y-axis completes the reference frame. In the following, they are referred to as the radial, tangential and normal directions, respectively.

In our simulations, we estimated the following set of parameters:

- arc-wise JUICE initial states $\mathbf{x}_{\text{sc}}^{(j_i)}(t_i)$ $(i = 1...N)$, with a priori uncertainty of 5 km and 0.5 m/s on position and velocity components, respectively;
- global or arc-wise Galilean moons' initial states $\mathbf{x}_j^{(0)}(t_0/t_i)$ $(j = 1..4)$. The a priori uncertainty in position was set to 15 km in the three RTN directions. For the velocity components, we used the differences between the latest IMCCE and JPL ephemerides (NOE-5-2021[5] and JUP365[6], respectively) as a conservative a priori. These a apriori values are provided in Table 4.1;
- gravitational parameters of Galilean moons μ_j $(j = 1..4)$, using the a priori uncertainties provided in Schubert et al. (2004) and reported in Table 4.2;
- gravity field coefficients of Galilean moons $C_{lm}^{(j)}$, $\mathbf{S}_{lm}^{(j)}$, up to degree and order 2, 4, 12 (6 when considering the flyby phase only) and 6, for Io, Europa, Ganymede and Callisto respectively. As a priori constraints, we used the formal uncertainties by Schubert et al. (2004) for $\bar{C}_{20}$ and $\bar{C}_{22}$, which are given in Table 4.2. We applied Kaula's rule with $K = 10^{-5}$ for the remaining gravity field coefficients ($\sigma = K/l^2$, Kaula, 1966);
- arc-wise accelerometer bias calibration factors $\mathbf{c}_i$, with the a priori constraint set to 10^{-7} m·s^{-2} (10 times larger than in Cappuccio et al., 2020a);
- arc-wise biases for range observables, with an a priori uncertainty fixed to 0.25 m;
- arc-wise biases for VLBI observables. We set the bias constraint at 0.5 nrad in both right ascension and declination (Charlot et al., 2020).

Table 4.3 specifies whether a parameter is to be estimated globally or in an arc-wise manner. It highlights important differences between the two estimation methods, but also between the two steps of the decoupled approach. It must be

[5]https://ftp.imcce.fr/pub/ephem/satel/NOE/JUPITER/
[6]https://ssd.jpl.nasa.gov/sats/ephem/

Table 4.1.: A priori constraints for the Galilean moons' velocity components. These a priori values are computed as the differences between the NOE-5-2021 and JUP365 ephemerides, averaged over the JUICE mission timeline.

	Radial [m/s]	**Tangential** [m/s]	**Normal** [m/s]
Io	0.98	0.14	0.72
Europa	0.35	0.10	0.74
Ganymede	0.21	0.08	0.32
Callisto	0.16	0.07	0.10

Table 4.2.: A priori constraints for gravitational parameters, normalised $\bar{C}_{20}$ and $\bar{C}_{22}$ coefficients for the four Galilean moons. The values are retrieved from Schubert et al. (2004).

	$\boldsymbol{\mu}$ [km/s^2]	$\bar{\mathbf{C}}_{\mathbf{20}}$ [-]	$\bar{\mathbf{C}}_{\mathbf{22}}$ [-]
Io	0.02	$2.7 \cdot 10^{-6}$	$0.8 \cdot 10^{-6}$
Europa	0.02	$8.2 \cdot 10^{-6}$	$2.5 \cdot 10^{-6}$
Ganymede	0.03	$2.9 \cdot 10^{-6}$	$0.87 \cdot 10^{-6}$
Callisto	0.01	$0.8 \cdot 10^{-6}$	$0.3 \cdot 10^{-6}$

stressed that the moons' gravity field coefficients are only included in the second step of the decoupled approach to account for the influence of uncertainties in the moons' gravity fields on the propagated state solutions (see Eq. 4.10). This is merely a way to avoid obtaining too optimistic formal errors because part of the uncertainties sources would be omitted. The a priori values for these coefficients are directly taken from the formal errors obtained after the first estimation step, and the gravity field solutions are actually not improved further by the second step, compared to these a prioris.

As shown by Dirkx et al. (2016, 2017), the influence of Jupiter's state and gravity field uncertainties on the estimation results was considered negligible in the post-Juno era (Durante et al., 2020), and these parameters were therefore not determined in our simulations. Tidal dissipation parameters were also excluded from the list of parameters to estimate in this preliminary study, keeping the focus of our analysis primarily on state estimation methods and on the resulting solutions for both the spacecraft and the moons.

4.4. RESULTS

This section presents the results of our comparative covariance analyses, performed with both the coupled and decoupled estimation models (Sections 4.2.2 and 4.2.3). We first only considered the flyby phase, before including the orbital phase. The results obtained in the two configurations are presented in Sections 4.4.1 and 4.4.2, respectively.

It should first be highlighted that the estimation problem is very close to being

Table 4.3.: Detailed description of the estimated parameters sets, for both the coupled and decoupled estimation approaches. As mentioned in Section 4.2.3, the parameters change between the first and second steps of the decoupled method. NI stands for ‘not included’.

	Coupled	**Decoupled**	
		1st step	2nd step
JUICE’s states	arc-wise	arc-wise	NI
Moons’ states	global	arc-wise	global
Moons’ gravity coef.	global	global	global
Accelerometer biases	arc-wise	arc-wise	NI
Range biases	arc-wise	arc-wise	NI
VLBI biases	arc-wise	arc-wise	NI

ill-posed, with extremely high condition number for the normal equations (Eq. 4.9). The exact values of the formal errors provided in the coming section should thus be treated cautiously. However, it must be noted that, as a verification, we also performed a deterministic least-squares estimation for the coupled case, to bring confidence in the formal uncertainties level (see Appendix 4.8). It proves that our implementation of the lesser documented coupled model is correct, and that the obtained formal errors would be representative of the true errors under the assumptions of a covariance analysis (perfect dynamical and observational models, to be further discussed in Section 4.5). Our results therefore remain insightful, especially since we focus on comparing two estimation strategies (and not on absolute error values).

Given the near ill-posedness of the Galilean moons’ state estimation problem, it is worth stressing that the condition number is higher when using the decoupled method, which is an important disadvantage of this approach. When reconstructing the moons’ long-term dynamics from the normal points, extremely high correlations between the position and velocity components in the radial and tangential directions even made the estimation problem non-invertible at first. Eventually, only the normal points’ positions were therefore added as observables in the second step of the decoupled method (Section 4.2.3), to partially eliminate these correlations. In most other analyses, the normal points also include the central moon’s position only (e.g., Durante et al., 2019; Di Ruscio et al., 2020; Di Ruscio, 2021).

4.4.1. FLYBYS PHASE ONLY

This section presents the covariance analysis results obtained from observations simulated over the JUICE flyby phase only. We first discuss and compare the resulting formal errors in Galilean moons’ states (Section 4.4.1), and in gravity field coefficients (Section 4.4.1). The sensitivity of the estimation solutions to the a priori covariances for the moons’ initial states is then investigated in Section 4.4.1.

STATE ESTIMATION

Focusing on the first step of the decoupled estimation strategy, the uncertainties of the normal points generated for each flyby are displayed in Fig. 4.5. For each moon, the reduction in the normal points' uncertainties as the number of flybys increases is clear. This is a direct consequence of updating the a priori knowledge for the moons' states, ensuring that each arc benefits from the previous ones (Section 4.2.3). Fig. 4.5 shows that the position of the central moon is much better determined in the radial and tangential directions than it is in the normal direction (i.e., out-of-plane). Interestingly, the errors in radial and tangential positions are of similar orders of magnitude, especially for Callisto. This is due to high correlations between the tangential and radial state components. As an indication, Fig. 4.6 shows the absolute correlations obtained when generating the normal points for the first flybys at Europa, Ganymede and Callisto. Callisto's first normal point is much less correlated than Europa's and Ganymede's. Looking at Fig. 4.5, it appears that this does not indicate a good normal point determination, but, on the contrary, is due to the fact that the first, relatively high altitude flyby performed at Callisto (see

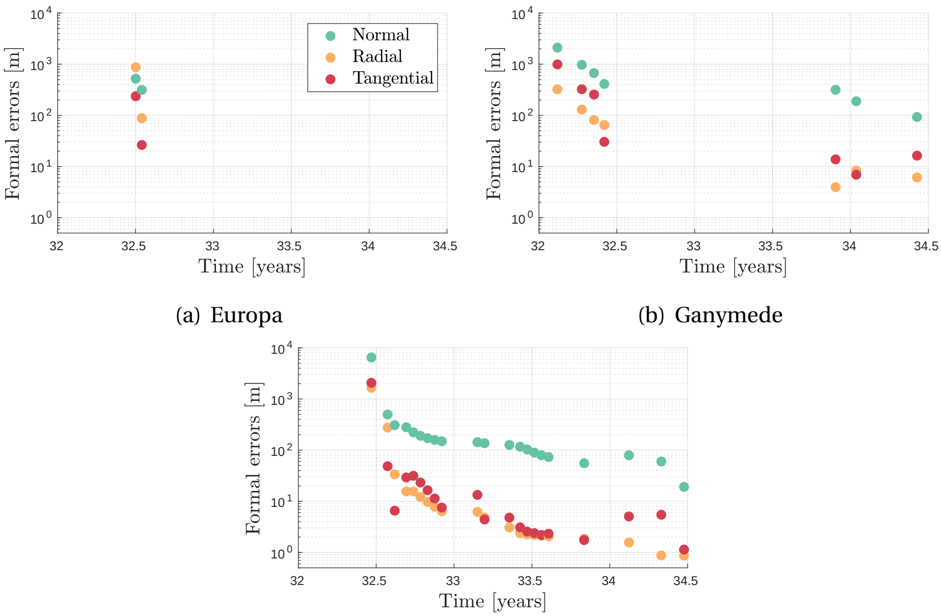

(a) Europa

(b) Ganymede

(c) Callisto

Figure 4.5.: Formal errors in position obtained after the first step of the decoupled estimation for each normal point (i.e., each flyby represented in Fig. 4.1), for the three Galilean moons targeted by the JUICE spacecraft. They correspond to the 1σ uncertainties as provided by the covariance analysis, and are here expressed in the RTN frame.

Fig. 4.1) does not allow the estimation to significantly improve the normal point determination compared to a priori values. The estimated state components for this normal point remain rather uncorrelated (since the *default* a priori covariances assume no correlation between parameters), but the associated formal uncertainties are quite large. The other flybys performed around Callisto, supported by the adopted a priori update strategy (see Section 4.2.3), progressively improve the quality of the normal points determination (see Fig. 4.5), but also yield much higher normal points' correlations, which then become comparable to ones displayed for Europa and Ganymede in Fig. 4.6.

The global solutions for the Galilean moons' dynamics, either reconstructed from the normal points shown in Fig. 4.5 in the decoupled case, or directly outputted by the coupled model, are displayed in Fig. 4.7. The 1σ uncertainties in the moons' states, estimated at the beginning of the flyby phase from all flybys' data, were propagated through the 2030-2038 time period following the methodology presented in Section 4.2.1. The local uncertainty reductions in the propagated solutions clearly indicate when the flybys are performed.

Comparing both solutions in Fig. 4.7, the coupled method leads to lower formal errors in the moons' radial positions (one or two orders of magnitude lower than in the decoupled case). On the other hand, the uncertainties in the moons' tangential positions are comparable between the two estimation strategies, and can even be locally slightly lower with the decoupled approach. These results follow from the similar formal error levels in the normal points' radial and tangential positions (see Fig. 4.5), which translates into uncertainties of comparable orders of magnitude in both directions when reconstructing the global ephemerides solution. On the contrary, the coupled approach is able to more efficiently decorrelate the moon's radial and along-track motion.

Finally, differences between the coupled and decoupled solutions are not so significant in the normal direction and seem more arbitrary: the decoupled method performs slightly better for Io and Ganymede, while the converse is true for Europa

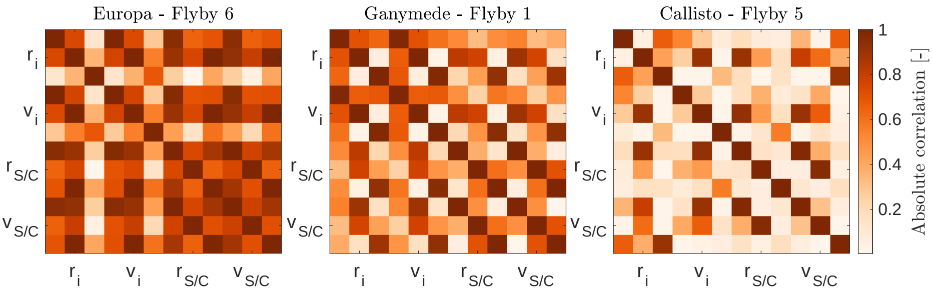

Figure 4.6.: Absolute correlations obtained when generating the first normal point of each moon (so for each first flyby at Europa, Ganymede, and Callisto, respectively). The correlations are computed between the central moon's and spacecraft's state components, both expressed in the RTN frame.

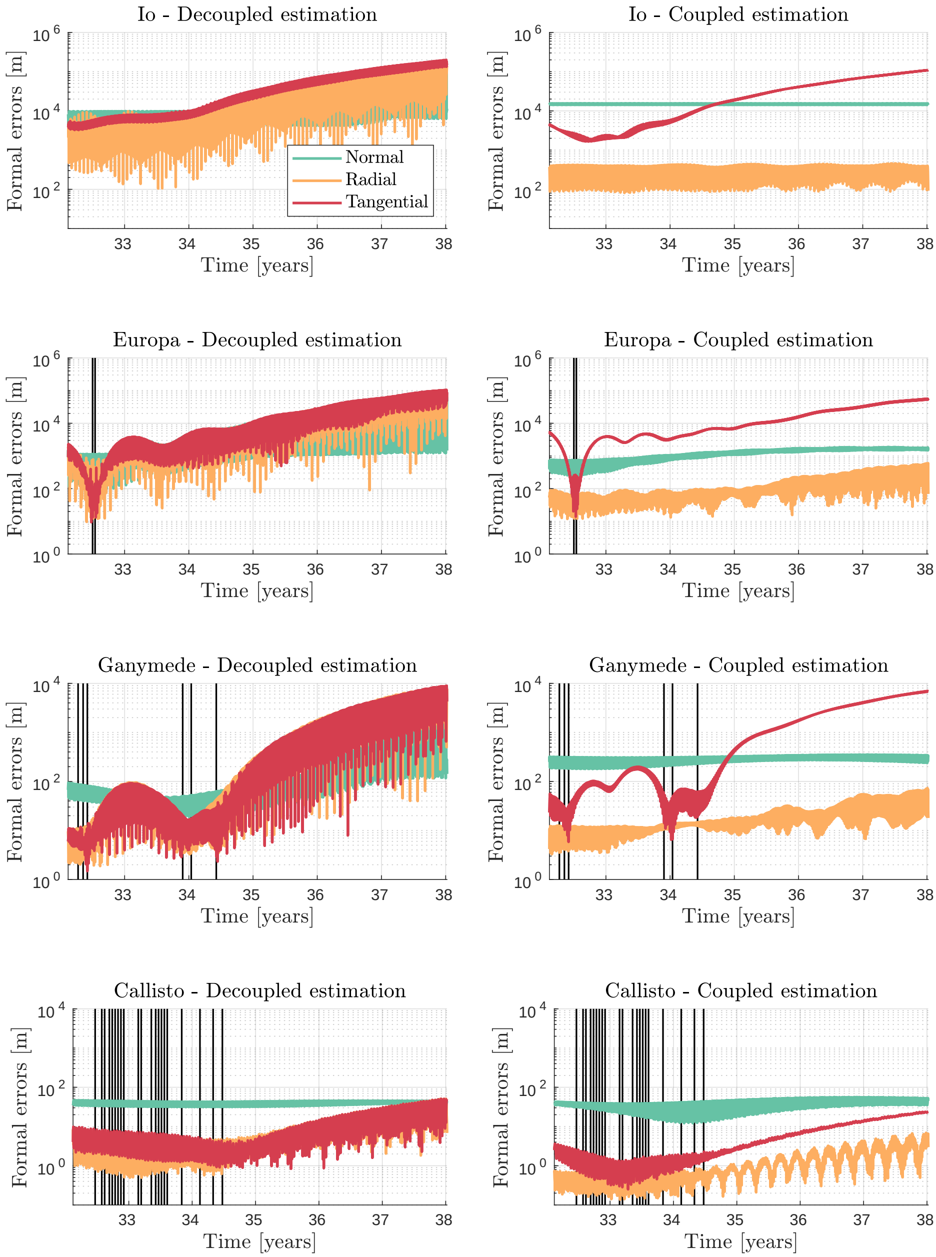

Figure 4.7.: Propagated formal errors in position for the four Galilean moons, obtained with both the decoupled and coupled methods (left and right sides, respectively). These estimated solutions are based on radiometric data simulated for the JUICE flyby phase only. The black vertical lines indicate when the JUICE flybys occur, for each moon (see Fig. 4.1).

and Callisto. The main difference between the two estimation approaches originates from the decoupled strategy only accounting for the dynamical coupling between the moons in the second step, when trying to reconstruct the moons' dynamics using the kinematic information contained in the normal points. The coupled model, on the other hand, includes all dynamical effects at once. As the strong dynamical coupling between the moons mostly manifests itself in the moons' orbital plane, the results obtained in the normal (i.e., out-of-plane) direction are less sensitive to the choice of estimation method.

While tidal dissipation parameters were intentionally excluded from our comparative state estimation analysis, preliminary insights can still be extrapolated from the expected ephemerides quality. Especially, an accurate determination of the moons' along-track positions is crucial to investigate tidal dissipation effects, through the secular change in mean motion that they induce. While the decoupled estimation led to slightly lower formal errors for the tangential positions of the moons (see Fig. 4.7), we should keep in mind that the uncertainties obtained with the coupled model are thought to be more statistically representative, as mentioned in Section 4.2.4. It should therefore be highlighted that the determination of the moons' states in the tangential direction might be too optimistic in the decoupled case, possibly translating into lower formal errors for the tidal parameters. The coupled strategy, on the other hand, may prove beneficial to achieve realistic errors when trying to estimate Jupiter's dissipation at the forcing frequencies of the moons. This would be particularly important to further investigate whether Callisto is caught in a tidal resonance lock (Fuller et al., 2016; Lainey et al., 2020). It is however essential to stress that, with both models, achieving this tangential uncertainty level will be most challenging, and the results may well be limited by dynamical model error, as further discussed in Section 4.5.2.

GRAVITY FIELD ESTIMATION

The formal errors for the moons' gravity field coefficients obtained with the decoupled and coupled approaches are provided in Fig. 4.8, superimposed with their a priori values (Section 4.3.3). The limited number of flybys at Europa (2) and Ganymede (7) does not allow the estimation to significantly improve the gravity field solution with respect to the a priori knowledge. This is true for both the coupled and decoupled models, and neither of them seems to perform systematically and distinctly better for these two moons: for the rare coefficients for which an improvement is noticed compared to the a priori constraints, the formal errors are sometimes lower with one method, sometimes with the other.

Results are different in Callisto's case: the 21 flybys, performed at lower altitudes and condensed over a short period of time (Fig. 4.1), help to determine the gravity field well beyond a priori values. It is interesting to note that our formal uncertainties for Callisto's gravity field are comparable with those obtained in Di Benedetto et al. (2021). As shown in Fig. 4.8, the gravity field uncertainties given by the decoupled solution are slightly larger than those achieved with the coupled model. For some of Callisto's flybys, the decoupled method indeed performs poorly in decorrelating the moon's and spacecraft's arc-wise states, which degrades the gravity field estimation.

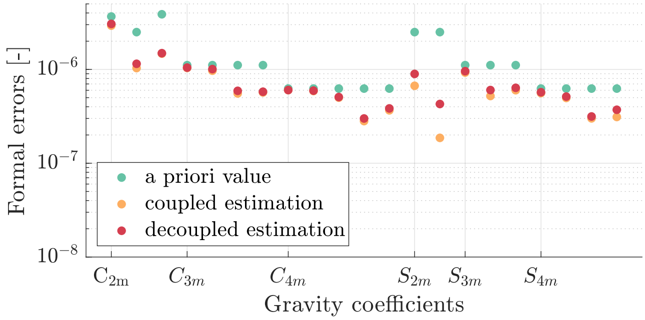

(a) Europa

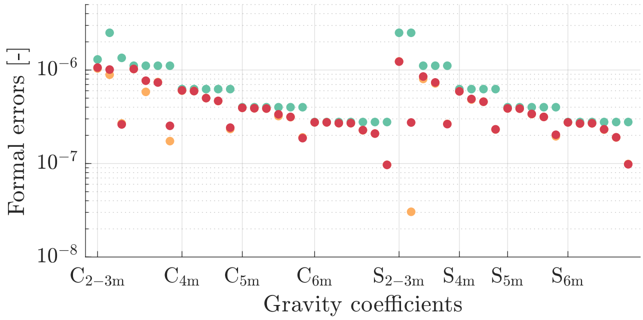

(b) Ganymede

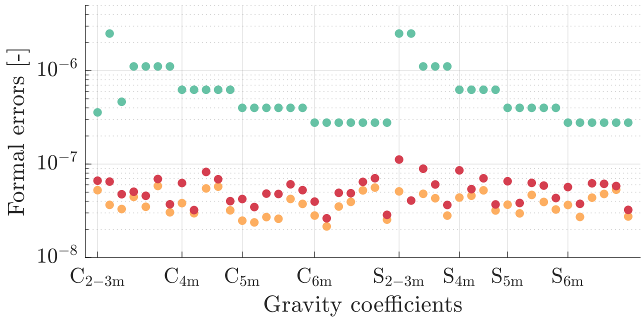

(c) Callisto

Figure 4.8.: Formal errors in gravity field coefficients for the three Galilean moons targeted by JUICE flybys. The coupled and decoupled solutions are compared with respect to a priori values (see Section 4.3.3). The cosine C_{im} and sine S_{im} coefficients (x-axis) are grouped by degree and plotted by increasing order m. The label C/S_{im} indicates where the coefficients of degree i start, and the order m of these coefficients progressively increases until the start of the next group of coefficients (degree $i+1$).

We must nonetheless stress that these differences remain small, the formal errors obtained with the two estimation strategies still being of comparable orders of magnitude.

The decoupled model was actually used in several gravity field estimation studies, mainly to avoid the challenges arising from the reconstruction of dynamically consistent ephemerides over long timescales, as the dynamical model fidelity could not be brought to the required level (e.g., Durante et al., 2019). Our results verified that the decoupled errors for the moons' gravity coefficients are also not too optimistic compared to the coupled solution. This analysis thus confirmed that opting for the normal points strategy for the JUICE flyby phase would not notably affect the gravity fields solution. This is particularly relevant for Callisto, while Ganymede's and Europa's gravity field determination will also significantly benefit from JUICE's orbital phase and the Europa Clipper mission, respectively.

SENSITIVITY TO A PRIORI KNOWLEDGE

The decoupled solution was found to strongly depend on the a priori constraint applied to the moons' states before each flyby. As an experiment, we discarded the update strategy presented in Section 4.2.3 and applied the same *default* a priori covariances to all arcs. The normal points approach then led to rather different results, reported in Table 4.4. All position uncertainties get significantly larger when the state knowledge is not conveyed from one arc to the next. Results are the worst for the moons' radial and tangential positions, with errors increased by more than one order of magnitude. Updating the a priori information after each flyby is thus critical if realistic uncertainties are to be achieved with a decoupled approach. In particular, it progressively helps to decorrelate the central moon's and spacecraft's arc-wise dynamics.

When computing the observations' contribution to the solution using Eq. 4.28, the average $c_{\mathbf{q}}$ value for the moons' positions drops from $c_{\mathbf{q}}$ >0.98 when using updated a priori covariances to ≈ 0.40 with the default ones (except for the first flyby of each moon for which no updated a priori is available and $c_{\mathbf{q}}$ thus remains close to 1). This confirms that the a priori information then becomes predominant and significantly helps the solution. On the contrary, the coupled solution is not noticeably affected by the adopted a priori values for the moons' states ($c_{\mathbf{q}} \approx 1$), and thus appears significantly more robust. It also relies on a more straightforward, update-free strategy as it only uses the *default* a priori values (see Section 4.3.3).

It must be noted that the a priori knowledge for the moons' states, while driving the quality of the decoupled state estimation, has no notable impact on the gravity field solution, irrespective of the selected estimation method. This again shows that the main drawbacks of the normal points strategy do not significantly influence the estimated gravity fields. It confirms that the decoupled method is a good alternative when focusing on gravity field determination, in agreement with conclusions drawn in Section 4.4.1.

Table 4.4.: Formal errors in position for the Galilean moons in the RTN frame, achieved with the decoupled estimation method for different a priori state knowledge. The a priori covariances are either updated from one normal point to the next, as described in Section 4.2.3, or kept fixed to their default values for all normal points. The errors were averaged over one year, starting from the first flyby.

Moons		**A priori values**		**Ratio**
(nb flybys)		updated [1]	constant [2]	[1]/[2]
	R	3.36 km	35.9 km	0.09
Io	T	5.36 km	63.6 km	0.08
(0)	N	7.15 km	20.3 km	0.4
	R	0.845 km	11.5 km	0.07
Europa	T	1.02 km	14.2 km	0.07
(2)	N	0.854 km	9.68 km	0.09
	R	26.5 m	594 m	0.04
Ganymede	T	26.5 m	570 m	0.05
(7)	N	57.2 m	535 m	0.1
	R	3.48 m	36.1 m	0.1
Callisto	T	4.00 m	43.9 m	0.09
(21)	N	39.6 m	118 m	0.3

4.4.2. FLYBY AND ORBITAL PHASES COMBINED

We extended the tracking data set to include the orbital phase at Ganymede in addition to the flybys, again performing the estimation with both the decoupled and coupled methods. Sections 4.4.2 and 4.4.2 present the results for the states and gravity field estimates, respectively, obtained in the so-called nominal tracking configuration for the orbital phase (see Section 4.3.3). The influence of the tracking settings is further analysed in Section 4.4.2.

STATE ESTIMATION

To apply the decoupled estimation to the orbital phase, we generated one normal point per tracking arc and determined the central moon's arc-wise state and the associated covariances at the centre of the arc. The propagated uncertainties in the Galilean moons' states are shown in Fig. 4.9, for both the decoupled and coupled solutions. Callisto's state being almost only constrained by the flyby phase, the formal errors for this moon are similar to those discussed in Section 4.4.1, when excluding the orbital phase, and are therefore not discussed in the following (see Figs. 4.7 and 4.9).

It should be stressed that Ganymede's formal errors fall below 1 m during JUICE orbit, in both the decoupled and coupled cases (Fig. 4.9). However, current dynamical models are likely far from being accurate enough to represent sub-meter level effects. Therefore, achieving the presented level of errors in reality will require these models to be rigorously adapted and validated. The implications of these modelling limitations, which differ for the coupled and decoupled solutions, will be

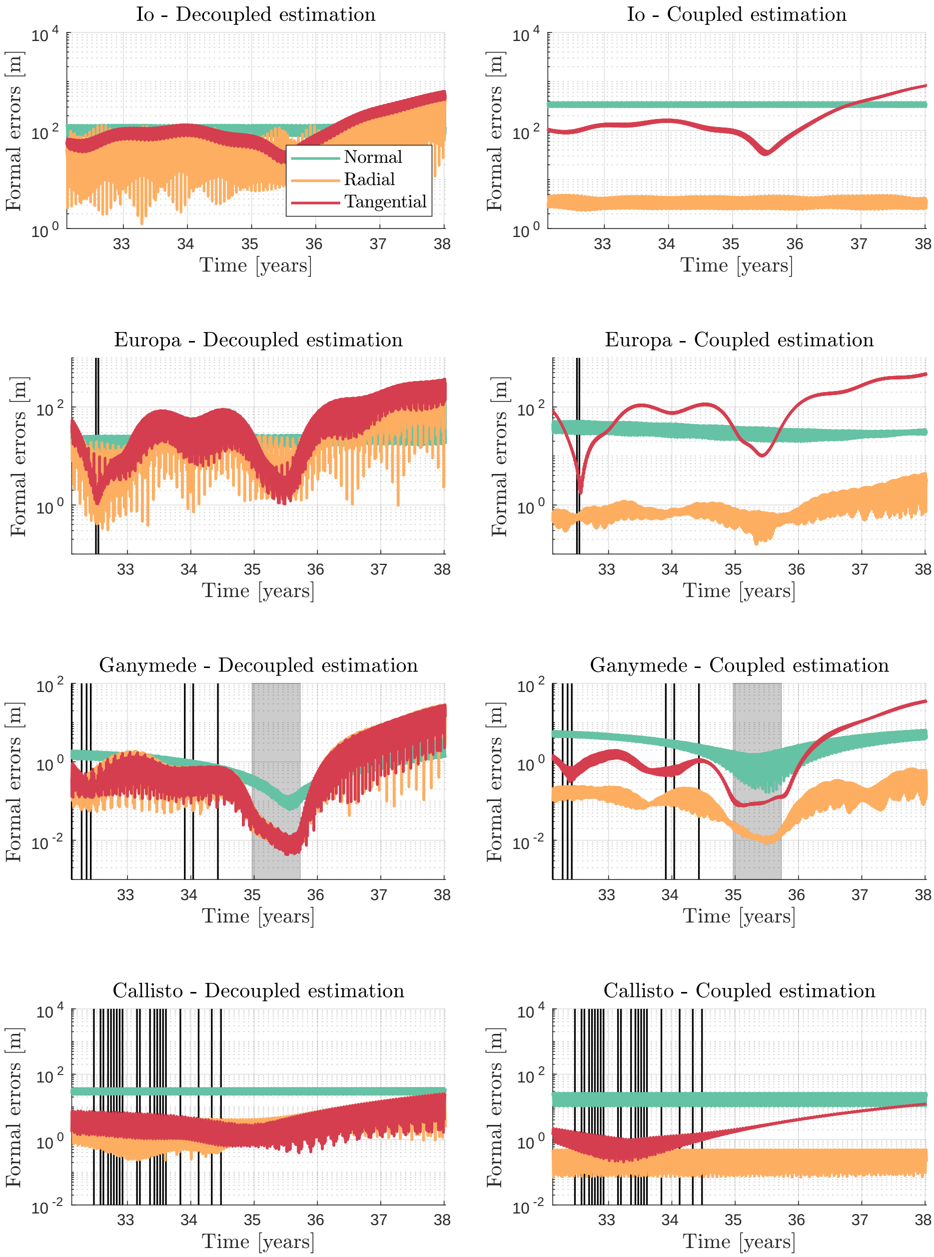

Figure 4.9.: Propagated formal errors in position for the four Galilean moons, obtained with the decoupled and coupled methods (left and right sides, respectively). Tracking data were simulated over both the flybys and orbital phase. The black vertical lines indicate when the JUICE flybys occur, for each moon, and the shaped grey area represents the orbital phase around Ganymede (see Fig. 4.1).

further discussed in Section 4.5.

Comparing Figs. 4.7 and 4.9 directly highlights the ephemerides improvement provided by the orbital phase. For both the coupled and decoupled solutions, the decrease in Ganymede's position uncertainties during JUICE orbit is clear. These results also clearly illustrate the strong dynamical coupling between the three innermost Galilean moons: the errors reduction for Io and Europa with respect to Fig. 4.4.1 is indeed achieved by collecting more observations close to Ganymede.

Fig. 4.9 also confirms the flybys-based conclusions discussed in Section 4.4.1. In particular, the coupled estimation still provides a noticeable improvement in the radial direction, while errors in the moons' tangential positions are overall lower with the decoupled method. It is however interesting to note that these trends are accentuated for some moons, and attenuated for others. For Ganymede, the tangential position uncertainties are noticeably lower with the decoupled model during the orbital phase, and the error reduction in the radial direction achieved by the coupled solution remains limited. The opposite is observed for Io and Europa: the coupled solution's radial position uncertainties are on average one to two orders of magnitude lower than in the decoupled case, while the errors level remains comparable in the tangential direction.

This is caused by differences in how each method captures the strong dynamical coupling between Io, Europa, and Ganymede. In the decoupled approach, the radiometric data collected during JUICE orbit are used to generate normal points solely at Ganymede. At first, these observations thus exclusively improve our knowledge of Ganymede's local states. The coupling between the three moons is only introduced in the second step of the decoupled estimation (Section 4.2.2), and Io's and Europa's solutions therefore benefit from the orbital phase in an indirect way, through very accurate normal points generated at Ganymede. On the contrary, the coupled model directly uses all data to estimate the four moons' states concurrently, and provides the most statistically accurate mapping of data uncertainty covariance to parameter covariance (see Section 4.2.4). In the coupled case, the solution improvement provided by the orbital phase is thus more evenly spread between the three innermost moons.

GRAVITY FIELD ESTIMATION

The results and conclusions regarding the moons' estimated gravity fields are similar to those discussed in Section 4.4.1. For Europa's and Callisto's estimated gravity coefficients, there is actually no noticeable difference with respect to the flybys phase's results, which was expected since the orbital phase at Ganymede does not constrain other moons' gravity fields. The solution for Ganymede is however significantly improved by the orbital phase, as shown in Fig. 4.10. It should be noted that these results rely on a simplified estimation setup, and that gravity field studies based on 3GM data from JUICE's orbital phase estimate Ganymede's gravity along with the moon's rotational parameters, Love numbers, etc. (e.g., Cappuccio et al., 2020a). Nonetheless, the order of magnitude of the formal uncertainties reported in Fig. 4.10 are in agreement with those obtained in dedicated 3GM studies (Cappuccio et al., 2020a; De Marchi et al., 2021).

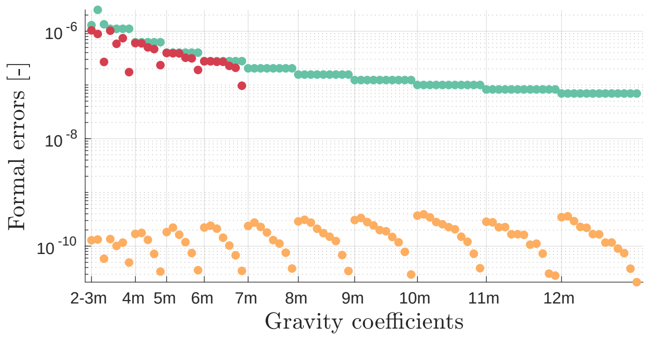

(a) Ganymede - Cosine coefficients

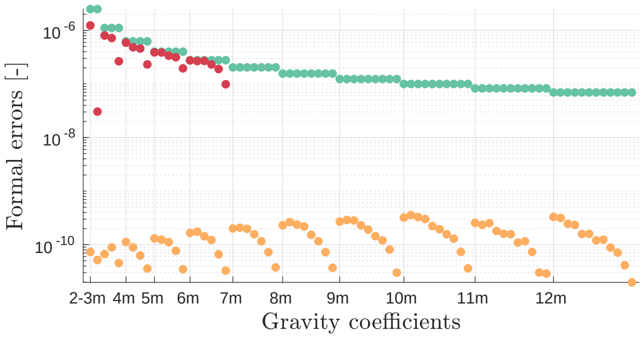

(b) Ganymede - Sine coefficients

Figure 4.10.: Formal errors in Ganymede's gravity field coefficients. The coupled solution obtained when including the tracking data collected over both the flyby and orbital phases is compared with the flyby-only solution (up to degree and order 6 only, see Section 4.3.3). The cosine C_{lm} and sine S_{lm} coefficients (x-axis) are grouped by degree and plotted by increasing order m, with the cosine coefficients first, followed by the sine terms.

In our simulations, limited differences between the coupled and decoupled cases could still be detected from the flybys-based results, at least for Callisto whose gravity coefficients could be estimated beyond their a priori values (see Fig. 4.8). However, such discrepancies between the two models are not observed anymore (for any moon) once the orbital phase is included, which is why Fig. 4.10 only displays the coupled solution. Compared to the flybys, JUICE's orbital phase generates large amount of data, continuously collected over a longer period of time (as opposed to discrete arcs at each flyby). The contribution of the orbital phase thus completely dominates the gravity field solution (see Fig. 4.10). The longer tracking arcs (i.e., 2 days, with 8 hours of tracking per day, instead of 8 hours only for the flybys) and the much larger numbers of observations allow both methods to properly decorrelate the spacecraft's and moon's dynamics, which explains why nearly identical uncertainties are obtained for Ganymede's gravity field in each case. This confirms conclusions drawn in Section 4.4.1, according to which the adopted state estimation strategy does not significantly influence the gravity field solutions.

SENSITIVITY TO TRACKING SETTINGS

We re-ran our simulations with varying arc duration for the orbital phase, to investigate the sensitivity of each estimation method to the tracking configuration. As mentioned in Section 4.3.3, three test cases were considered with arcs of one day, two days (nominal) and one week, respectively. When shortening the tracking arcs from two days to one, the errors grow larger for both the decoupled and coupled solutions. The opposite is true when increasing the arc duration to a full week, as longer arcs allow a better decoupling of JUICE's and Ganymede's dynamics. As expected, this effect is the smallest for Callisto's uncertainties.

Importantly, the relative evolution of the decoupled and coupled solutions as the arc duration varies provides valuable insights into the fundamental differences between the two state estimation approaches. Fig. 4.11 shows ratios in formal errors resulting from different arc durations. Except for Io's and Ganymede's normal positions, the improvement provided by longer arcs is systematically weaker in the decoupled case.

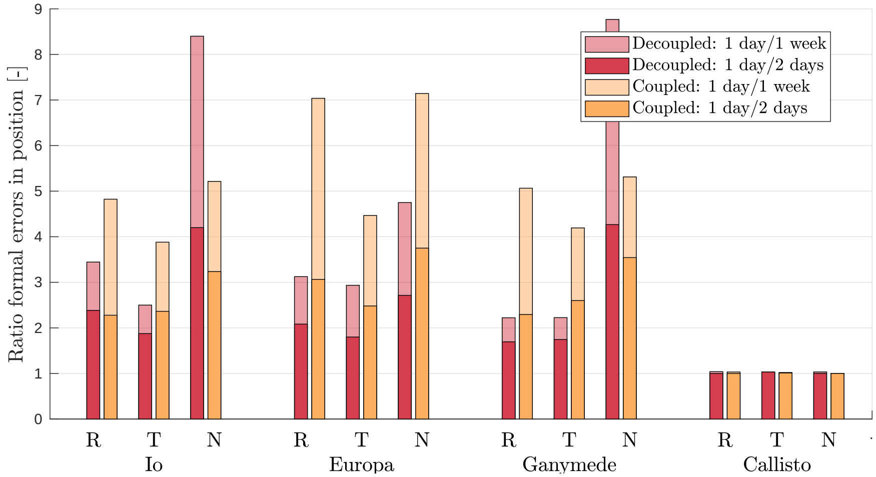

Figure 4.11.: Ratios of the formal errors in position for different arc durations over JUICE's orbital phase (in the RTN frame). The results obtained with both the coupled and decoupled methods are displayed for the four moons (with no noticeable differences for Callisto). For each method and each moon, we provide the ratio of the formal uncertainties obtained with 1 day-arcs over 2-days arcs, and 1 day-arcs over 1 week-arcs.

This is caused by decoupling the spacecraft's and moons' state estimations. As already mentioned, lengthening the tracking arcs generally helps to decorrelate the spacecraft's motion from the central moon's, but does not necessarily reduce the correlations between the moon's own state components. This still results in lower state uncertainties for the normal points. However, it does not automatically reduce the correlations level in the second step of the decoupled estimation, the spacecraft's states being excluded anyway (see Section 4.3.3, Table 4.3). In the decoupled case, the reduction in the moons' state uncertainties thus remains limited by the normal points' high correlations, especially in the radial and tangential directions. On the contrary, the correlations between the spacecraft's and moon's states are directly included in the coupled model, since their dynamics are concurrently estimated. The coupled solution therefore fully benefits from longer tracking arcs, explaining why a more significant improvement is achieved for the radial and tangential positions than what the decoupled model allows.

4.5. DISCUSSION: MAIN STRENGTHS AND CHALLENGES OF BOTH METHODS

This paper assesses the relative performance of two state estimation strategies, applied to the JUICE test case. To put the obtained formal errors and correlations into context, we discuss practical considerations related to data analysis in the following, and how they affect the coupled and decoupled models in different ways. Data processing challenges are detailed in Section 4.5.1, while model-related issues will be addressed in Section 4.5.2. As a possible mitigation strategy, we finally suggest a possible alternative state estimation approach in Section 4.5.3.

4.5.1. DATA PROCESSING CONSIDERATIONS

One of the major differences between the coupled and decoupled techniques lies in the way the available data are processed. The decoupled method can theoretically treat each mission, and each mission phase, independently and generate as many normal points as required by the mission design. These normal points can later be combined with those determined from other missions and/or with different observation sets (e.g., optical, astrometric data). For the coupled solution, however, all data need to be processed at once.

For the Galilean moons test case in particular, reaching a global solution would ideally require to include spacecraft data from various missions, as well as Earth-based optical astrometric observations. More precisely, JUICE's imbalanced data set, with its strong focus on Ganymede, would be efficiently complemented by the Europa Clipper and Juno missions, with over 40 flybys[7] at Europa planned for the former (e.g., Verma and Margot, 2018; Young et al., 2019), and an orbital phase at Jupiter lasting since 2016 for the latter, combined with a few crucial flybys at Io during the extended mission phase. In addition to radiometric data, spacecraft-based optical observations captured with navigation cameras can also be useful to help

[7] at the time of writing

constraining the ephemeris solution. These can be direct imaging of other moons (e.g., JANUS data for JUICE, Dirkx et al. 2017), as well as eclipses and Sun or stellar occultations observed from the spacecraft (Andreoli and Zannoni, 2018).

Additionally, Earth-based photo- and astrometric observations of the Galilean moons have been collected over centuries. They include absolute and differential astrometry, already performed since the 17th century (e.g., data starting from late 19th century used in Lainey et al., 2009), as well as eclipses and occultations (e.g., Arlot and Emelyanov, 2019). More recently, mutual approximations were identified as interesting observables (Morgado et al., 2019a; Fayolle et al., 2021) and the first stellar occultation by the moon Europa was observed in 2017, with a remarkable accuracy of 0.80 mas (i.e., 2.55 km at Jupiter's distance) (Morgado et al., 2019b). Interestingly, the GAIA catalogue will facilitate the observations of such occultations in the future.

Merging all above-mentioned data sets and processing them in a single step does not only make the coupled estimation process slower, but also substantially increases its complexity. It first implies to carefully weigh all different observations to obtain a statistically balanced and realistic solution. The JUICE radiometric data, which led to formal state uncertainties below the meter level for the Galilean moons (see Fig. 4.9), would indeed need to be properly combined with Earth-based optical astrometric data whose current accuracy remains larger than 1km (even stellar occultations). Furthermore, optical astrometric and radiometric tracking data are typically processed by different estimation tools, while the coupled estimation model would require a single software able to handle and process all observation types concurrently, which imposes significant practical constraints (many different observation types required, with, for each of them, suitable error and dynamical models, etc.).

Moreover, Earth-based observations are collected over longer periods of time compared to the spacecraft data, which are condensed over the planetary missions' timeline. This requires dynamical models to be consistent over both short and long timescales, and represents a major challenge for the reconstruction of a coupled solution, which will be further discussed below.

4.5.2. Modelling-related considerations

For the JUICE mission specifically, our covariance analysis indicates that Ganymede's formal state uncertainties get lower than the meter level during the orbital phase (see Fig. 4.9). For such position errors to be meaningful, major modelling efforts would however be essential. Model-related issues are therefore expected to occur when real JUICE data become available, but their influence on the estimation can unfortunately not be easily quantified in a simulation analysis. Dirkx et al. (2016) analysed which effects would likely be detectable from a long-term (several years) signature in the dynamics. However, they did not address the observability and relevance of short-term periodic variations. Such potentially mismodelled dynamical effects (both long- and short-term) are however crucial to discuss here, as they would have different impacts on the coupled and decoupled solutions.

Among possible sources of inaccuracies, the models currently used for the dissipation occurring inside the moons rely on simplified analytical formulations (Lainey et al., 2009; Lari, 2018). These approximations circumvent the need for perfectly consistent rotational and translational models, still unavailable for natural satellites, but are based on time-averaging assumptions. The dissipation inside the moons however directly influences the orbital evolution of the moons themselves and plays a key role in the long-term dynamical history of the Jovian system, such that its accurate modelling is crucial.

Additionally, due to the coupling between the moons' translational and rotational motions, issues can also originate from mismodelled librations. Ganymede's libration will likely be observable in the dynamics of JUICE itself during the orbital phase (Cappuccio et al., 2020a). The coupled model thus presents an interesting oppurtunity, since the libration's signature on the spacecraft and moon dynamics is different but would need to be fitted concurrently, possibly yielding a better constrained solution. On the other hand, modelling inconsistencies in Ganymede's librational motion would more critically degrade the residuals of the coupled solution.

For JUICE specifically, properly modelling the moons' rotations would furthermore require to reconcile what the different instruments are sensitive to. JANUS and GALA (navigation camera and altimeter, respectively) will observe the rotational motion of the moon's surface shell, which might be decoupled from the full body inertial rotation sensed by the radiometric data. Additionally, temporal variations in the central planet's gravity field are also not yet perfectly understood, and are suspected to be responsible for small, unmodelled time-dependent accelerations detected at periapsis in Juno (Durante et al., 2020) and Cassini data (Iess et al., 2019). It should nonetheless be stressed that an imperfect dynamical model can still achieve the required accuracy if properly parametrised (e.g., if time-dependent librational and gravitational variations are adequately adjusted), provided the relevant free parameters are incorporated in the estimation, and sufficiently decorrelate from the other parameters.

The fundamental differences between the coupled and decoupled approaches (see Figs. 4.2–4.3) significantly influence how the above-mentioned modelling issues might affect the estimation solutions. Compared to the coupled case, the decoupled approach indeed estimates more state parameters, determined more locally (Table 4.3), which directly increases the ability of this model to absorb dynamical modelling inaccuracies. Additionally, the long-term moons' dynamics are only reconstructed in the second step of the decoupled estimation, and they are adjusted to the normal points (i.e., arc-wise covariances of the moons' states). For the JUICE flyby phase for example, the decoupled model is thus fitting formal state uncertainties generally ranging from tens up to hundreds of meters (the last flybys at Callisto getting closer to the meter level for the radial and tangential positions). The coupled approach, on the other hand, is directly adjusting the parameters to the radiometric data, with expected accuracies of 20 cm and 15 μm/s for the range and range-rate of JUICE with respect to the Earth (Section 4.3.3). It is therefore significantly easier to obtain flat residuals with the decoupled estimation strategy (i.e., zero-mean residuals, noise within expected observation errors), as observables with accuracies up to $10^1 - 10^2$ m bring sufficient flexibility to (at least partially) absorb dynamical modelling inaccuracies.

The fact that the coupled method estimates the moons' dynamics in a single arc also drastically reduces its ability to absorb such model errors. It indeed implies that the estimation model cannot compensate for modelling inaccuracies by a local moon's state variation without affecting other arcs, and possibly conflicting with their own observational constraints. Furthermore, the decoupled estimation leaves out the arc-wise spacecraft states when determining the moons' long-term dynamics (see Section 4.2.3). The coupled model, on the contrary, imposes perfect consistency between the spacecraft's and moons' state estimation solutions, which further reduces its degrees of freedom.

In practice, the above entails that the concurrent estimation of the spacecraft's and moons' states would need accurate and consistent dynamical models over both short and long timescales. The current modelling fidelity has for example not yet allowed a coupled solution to be achieved from Cassini and Juno data (e.g., Durante et al., 2019). Furthermore, even if a global solution can still be reconstructed for the natural bodies' dynamics, modelling errors are expected to manifest themselves in high, incompressible residuals, due to the coupled strategy's lack of flexibility. On the contrary, in the decoupled case, modelling issues are more likely to be absorbed in the final estimated states and to thus remain unnoticed. Reflecting back on the normal points obtained for JUICE, with errors largely below one meter, more realistic uncertainties in agreement with the available dynamical models would significantly raise this error level. It would therefore degrade the quality of the decoupled estimation, but not prevent obtaining of a viable solution. On the other hand, the (large) post-fit residuals obtained with the coupled estimation can be indicative of the magnitude of the dynamical modelling inaccuracies, and help to interpret the decoupled solution's true uncertainty.

4.5.3. Possible alternative strategy

Despite the promising results obtained with the coupled model, Sections 4.5.1 and 4.5.2 highlighted crucial challenges that would need to be addressed before a reliable and statistically consistent coupled solution can be reconstructed for the Galilean moons' dynamics. Hybrid approaches, halfway between fully coupled and decoupled strategies, could therefore prove promising. In such hybrid scenarios, the coupled model can be applied more locally, rather than on the entire time period of interest. For the JUICE test case, a coupled solution might typically be attainable over the GEO/GCO5000 and/or GCO500 phases. Some flybys could also be processed concurrently (e.g., the two flybys at Europa). It would also be possible to reconstruct a coupled solution over the entire JUICE mission, but to combine it with other mission/data sets in a separate step, to mitigate the data merging issues highlighted in Section 4.5.1.

This would efficiently mitigate the effects of long-term modelling inconsistencies and thus make a coupled solution achievable *locally*. Such *local* coupled solutions can then be treated as normal points or a priori information for other analyses, and combined with those generated for different missions or with optical astrometric data, as discussed in Section 4.5.1. This would also eliminate the need to process astrometric and radiometric data in a single estimation tool as in the fully coupled strategy (see Section 4.5.1), by splitting the data analysis steps. This hybrid approach could represent an interesting alternative: it would potentially allow the estimation solution to benefit from a higher sensitivity to the system's full dynamical coupling, while still guaranteeing that a viable solution can be achieved.

4.6. CONCLUSIONS

We provided the complete formulation for a coupled, concurrent state estimation of the spacecraft and natural bodies from planetary missions' data. Such a coupled model has already been used in past studies (i.e., Dirkx et al., 2019b; Lari and Milani, 2019), but, to the best of our knowledge, was not explicitly described in the literature. We then performed a detailed covariance analysis comparing the decoupled and coupled estimation strategies for the upcoming JUICE mission. The realism of the formal errors given by the coupled model was verified by running a deterministic simulation and comparing the least-squares estimation errors with the formal uncertainties.

The JUICE mission will make us face both unique opportunities and challenges due to the unusual mission profile and unprecedented accuracy of the radiometric data, used to reconstruct the strongly coupled dynamics of the Galilean moons. Our study primarily assessed how a coupled solution, if attainable, would affect the accuracy of the Galilean moons' ephemerides. The results of the decoupled estimation approach, on the other hand, indicate the uncertainty level that would be achievable in case the coupled model failed to reconstruct a viable solution for the moons' dynamics (see discussion in Section 4.5). It must be stressed that we do not anticipate the conclusions of our study to depend on the CReMA (i.e., trajectory) version used for the JUICE spacecraft. While the absolute uncertainty levels for the estimated parameters might vary, the comparison between the two state estimation methods is expected to yield similar results.

We first showed that selecting appropriate a priori values for the moons' states is critical for the decoupled solution. The state solution improvement must be accounted for by updating the a priori covariance from one normal point to the next. Discarding the information gained in previous arcs indeed leads to poorly constrained normal points (limited to kilometer level accuracy). This eventually drives the decoupled solution to be one or two orders of magnitude less accurate than the coupled one, for all moons and in all directions (e.g., tens of meters against ~ 500 m for Ganymede's position uncertainties with and without a priori update, respectively, see Table 4.4).

Furthermore, the flybys-based results already highlighted notable differences between the coupled and decoupled state solutions. The coupled method achieves lower radial position uncertainties ($\sim 10^2$ m for Io and Europa, $\sim 10^1$ m for Ganymede, $\sim 10^0$ m for Callisto), which are one or two orders of magnitude smaller than in the decoupled case. In the tangential direction, the formal errors given by the decoupled approach are however slightly lower: ~ 10 m against ~ 30 m, keeping

Ganymede's initial position uncertainties as an example. As discussed in Section 4.2.4, the coupled model is nonetheless considered to provide a statistically accurate representation of the estimation problem, which might imply that the tangential position uncertainties obtained with the decoupled model are slightly optimistic.

Our results also proved that JUICE orbital phase is crucial for the quality of the ephemerides of the four Galilean moons. Assuming a perfect dynamical model, Ganymede's position uncertainties would even reach submetric levels during the orbit. Interestingly, it seems that Io's and Europa's solutions benefit more from the orbital phase when adopting a coupled approach (Europa's radial position also determined with an accuracy better than one meter, see Fig. 4.4.2), while the improvement appears stronger for Ganymede in the decoupled case. Including the orbital phase in our simulations actually enhances the differences between the two estimation strategies, and indicates that the dynamical coupling between the Galilean moons is better captured by the coupled model.

Concerning dynamical parameters, the adopted state estimation method is not so influential for the gravity field coefficients' estimates. This indicates that the normal points strategy is perfectly adapted for gravity field determination from JUICE radiometric data (e.g., Magnanini, 2021), and generally for most local parameters studies as well. Rotational and tidal dissipation parameters, on the other hand, were omitted from our simulated estimations. Future studies should include these parameters and try determining the dissipation in Jupiter at the moons' frequency (Lainey et al., 2009, 2020). It would then be crucial to investigate whether the decoupled model can achieve realistic uncertainties despite a slightly optimistic estimation of the moons' along-track motion.

As a preliminary step towards an improved solution for the Galilean moons' ephemerides, we limited ourselves to an analysis based on simulated data only. As extensively discussed in Section 4.5, many issues are however expected to arise when real JUICE radiometric data become available and are fed to the estimation process, as happened with Cassini and Juno data (Durante et al., 2019, 2020). For the JUICE test case, the coupled estimation model nonetheless appears to yield promising improvements with respect to the decoupled strategy: it overall reconstructs a more balanced solution for the three Galilean moons in resonance, with significantly reduced uncertainties in the moons' radial positions. Despite the challenging issues that may emerge, this motivates future efforts to achieve a coupled state estimation for the Galilean moons.

4.7. Appendix A: Influence of the non-central moons' states as consider parameters on the normal points determination

This appendix presents a subset of the results verifying how the normal point generated for a flyby's central moon is affected by uncertainties in the other moons' states. As mentioned in Section 4.2.3, the first step of the decoupled model only estimates the arc-wise state solution for the central moon and neglects the possible contribution of these uncertainties. As a verification, we quantified the influence of this simplification by adding the non-central moons' states as consider parameters for each normal point determination.

We only show the results obtained for two specific flybys. One is the first flyby of JUICE's flyby tour, which is performed around Ganymede. Since the uncertainties in the other moons' states are then still limited to their a priori knowledge, we could expect their influence on Ganymede's estimated state solution to be significant. The 12th flyby at Callisto was also selected as a particularly interesting one: the uncertainties of Callisto's normal points are indeed noticeably reduced from this flyby onward (formal errors smaller than 10 m in the radial and tangential directions, see Fig. 4.5), while Ganymede's and Europa's states are still poorly determined and could therefore affect Callisto's solution.

The results for the two above-described flybys are provided in Tables 4.5 and 4.6. They showed that including the other moons' states as consider parameters does not noticeably affect the formal errors obtained for the central moon's normal point. This confirms the validity of our simplified approach and allow us to keep excluding the non-central moons' states from the first step of the decoupled estimation. It must be noted that while this appendix only presents only two flybys in detail, this analysis was conducted for all JUICE flybys, with identical conclusions.

4

4.8. Appendix B: Deterministic simulation as a verification

While we limited ourselves to covariance analyses in our comparative study (see Section 4.2.4), we also performed a complete least-squares estimation as a verification of the coupled model, which we will refer to as a *deterministic* simulation in the following. Our goal is to check whether the formal uncertainties discussed in our paper are consistent with the parameters values that would be estimated from non-ideal observations (i.e., including biases and noises) using an iterative least-squares inversion. This is especially important given the high condition number

Table 4.5.: Normal point determination for the 1st flyby at Ganymede, with and without including the other moons' states as consider parameters in the estimation. The formal errors in Ganymede's arc-wise state are provided in inertial coordinates.

Formal errors in Ganymede's state		**Other moons' states** Excluded	Consider parameters	**Relative difference** [%]
Position	x	989 m	991 m	0.18
	y	147 m	151 m	2.8
	z	2.12 km	2.21 km	~0
Velocity	v_x	0.0645 m/s	0.0645 m/s	~0
	v_y	0.0104 m/s	0.0104 m/s	~0
	v_z	0.145 m/s	0.145 m/s	~0

Table 4.6.: Normal point determination for the 12th flyby at Callisto, with and without including the other moons' states as consider parameters in the estimation. The formal errors in Callisto's arc-wise state are provided in inertial coordinates.

Formal errors in Callisto's state		**Other moons' states** Excluded	Consider parameters	**Relative difference [%]**
Position	x	1.69 m	1.70 m	1.4
	y	6.63 m	6.63 m	~0
	z	126 m	126 m	~ 0
Velocity	v_x	$2.71 \cdot 10^{-5}$ m/s	$2.71 \cdot 10^{-5}$ m/s	~0
	v_y	$4.59 \cdot 10^{-5}$ m/s	$4.59 \cdot 10^{-5}$ m/s	~0
	v_z	$1.53 \cdot 10^{-3}$ m/s	$1.53 \cdot 10^{-3}$ m/s	~0

4

encountered when inverting the normal equations (see Sections 4.4.1 and 4.4.2).

4.8.1. SCOPE OF THE VERIFICATION

The deterministic simulations presented in this appendix remain within the scope of some major assumptions of the covariance analysis: in our simulated environment, this verification indeed still relies on *perfect* dynamical and observational models. The additional simulations presented in the following thus do not hinder or replace the discussion in Section 4.5.2 on dynamical modelling fidelity and its possible effect on the coupled and decoupled solutions. Deviations between the true errors and the statistical behaviour predicted by formal uncertainties mostly originate from observational and dynamical modelling inaccuracies. Therefore, this analysis is not meant as a validation and cannot investigate how representative *formal* errors are of the *true* errors that would be obtained from real data. It could be possible to purposely introduce perturbations in our dynamical models. However, simulating such errors such that their effects are representative of the limitations of our current models is not straightforward. It would require a dedicated, extensive analysis of our current dynamical and observational models, as discussed in Section 4.5, and was therefore deemed beyond the scope of this comparative state estimation study.

Nonetheless, running a deterministic simulation still allows us to check that the *formal* uncertainties are consistent with the *true* errors resulting from the iterative least-square estimation, presuming that the assumptions of the covariance analysis hold. Such a verification ensures that our implementation of the estimation model is correct and demonstrates that our formal uncertainties are reliable in a covariance analysis context.

We only conducted such a deterministic simulation for the coupled model. It is indeed currently less widely applied and less documented than the decoupled estimation method, and such a verification thus becomes relevant. The coupled model being an extension of the classical formulations used by the decoupled estimation, the added value of performing a separate deterministic verification for the decoupled model appears limited. Additionally, implementing and running the entire least-squares estimation with the decoupled model would be more demanding, since it relies on two consecutive estimation steps (Fig. 4.3) and in practice also requires multiple sequential estimations to determine all normal points, due to the chosen a priori update strategy (see Section 4.2.3).

4.8.2. APPROACH AND SETTINGS

When performing an iterative weighted least-squares inversion, the variation in parameters values $\Delta\mathbf{q}_i$, at each iteration i, is given by (e.g., Gill and Montenbruck, 2013)

$$\Delta\mathbf{q}_i = \left(\mathbf{P}_{\mathbf{qq},0}^{-1} + \mathbf{H}_i^T\mathbf{W}_i\mathbf{H}_i\right)^{-1}\left(\mathbf{H}_i^T\mathbf{W}_i\Delta\mathbf{z}_i + \mathbf{P}_{\mathbf{qq},0}^{-1}\Delta\mathbf{q}_{0,i}\right),$$

where $\Delta\mathbf{z}_i$ is the vector containing the observations residuals at iteration i, and $\Delta\mathbf{q}_{0,i}$ is the difference between the current parameters estimates and their a priori values. The rest of the notation follows that of Eq. 4.9.

In our simulations, *true* errors are directly defined as the difference between the *true* parameters values (i.e., values assumed in our simulated environment) and their estimated values. To keep our simulation as realistic as possible, the observations are modelled with the bias and noise levels given in Section 4.3.3: noise levels of 20 cm, 15 μm/s and 0.5 nrad for range, Doppler and VLBI observations, respectively, with biases of 1 m for range measurements and 0.5 nrad for VLBI data. We also applied small initial perturbations to the a priori values of the estimated parameters, to mimic imperfect knowledge of the *true* parameters values. The way the initial parameters' offsets were defined is detailed below:

- moons' initial states: initial perturbation $\Delta\mathbf{q}_0$ calculated such that, once propagated over the duration of the JUICE mission, the difference between the perturbed and unperturbed moons' trajectories would be of the order of magnitude of the current ephemerides' accuracy (see Section 4.3.3). This led to initial offsets of 100 m in position and 5 mm/s in velocity.

- JUICE's arc-wise states: offset of 100 m in position and 0.01 m/s in velocity (in all inertial directions);

- other parameters (gravitational parameters, gravity coefficients, accelerometer calibration biases, range and VLBI observation biases): perturbation set to 5% of their *true* values.

Some differences should be noted with respect to the nominal estimation settings used for our covariance analyses (Section 4.3.3). Io's initial state was removed from the list of estimated parameters, due to the absence of Io's flyby, resulting in a lack of observations at this moon. The least-squares inversion could indeed not converge when trying to estimate its state alongside with those of the other Galilean moons. This already provides valuable insights about the challenges one will face when conducting real data analysis (as further discussed in Section 4.5). It should be noted that this convergence issue is only caused by JUICE's imbalanced data set, and that many more difficulties are to be expected when dynamical and observational models will be confronted with real data (see discussion in Section 4.5). It is also important to highlight that this was only observed when perturbing the a priori values of the estimated parameters. When no initial perturbation is applied, the least-squares estimation could converge while solving for Io's state along with the other moons'. All true errors were then found to be smaller than 3σ, σ designating the corresponding formal errors.

Furthermore, the elevation and occultation checks normally performed to verify the viability of an observation were switched off, thus assuming constant link during the tracking arcs. One specific tracking arc did not have enough viable observations for the estimation problem to converge otherwise. While this issue could have also been fixed with tighter a priori constraints, we adopted a simpler approach. We must stress that removing the visibility requirements, thus adding a few observations, does not lessen the relevance of our verification analysis, since it focuses first and foremost on the consistency between true and formal uncertainties provided by the coupled model, and not on absolute error values.

We conducted this iterative least-squares inversion for the flyby phase case only. This was mostly motivated by the high computational load required by such deterministic runs. We do expect similar results and conclusions when including the orbital phase at Ganymede.

4.8.3. RESULTS

After 5 iterations, the least-squares inversion reached convergence, and the final observations residuals are provided in Fig. 4.12. As expected, the residuals follow a Gaussian distribution with almost zero mean, and a standard deviation close to the observations noise level (Section 4.3.3). This can most clearly be observed for the Doppler residuals, due to the larger number of observations available compared to range and VLBI data.

The histogram of the ratios between true and formal errors is displayed in Fig. 4.13, and all ratio values are between 0 and 9. Precisely quantifying which true to formal errors ratio should be expected is far from straightforward, as it is both data- and parameter-dependent. While true errors 2 to 3 times larger than formal errors can be typically expected for planetary ephemerides (Jones et al., 2015, 2020, for Saturn's ephemeris derived from VLBA observations), larger true to formal errors ratios have been found for dynamical parameters estimated from spacecraft tracking data (gravity fields, rotational parameters, etc.) (e.g., Konopliv et al., 2011; Mazarico et al., 2015). These results were however all based on real observations, such that inaccurate dynamical or observations error models significantly contributed to the true/formal errors discrepancy.

In our simulations, however, our models are still deemed perfect, and true errors should be comparable to formal uncertainties if the estimation is able to converge towards the correct parameters values. In other JUICE simulation studies, true errors were indeed found to be similar or even slightly lower than formal ones for Callisto's gravity field in Di Benedetto et al. (2021), although it is unclear if the parameters values were initially perturbed, and by how much. In Lari and Milani (2018), similar

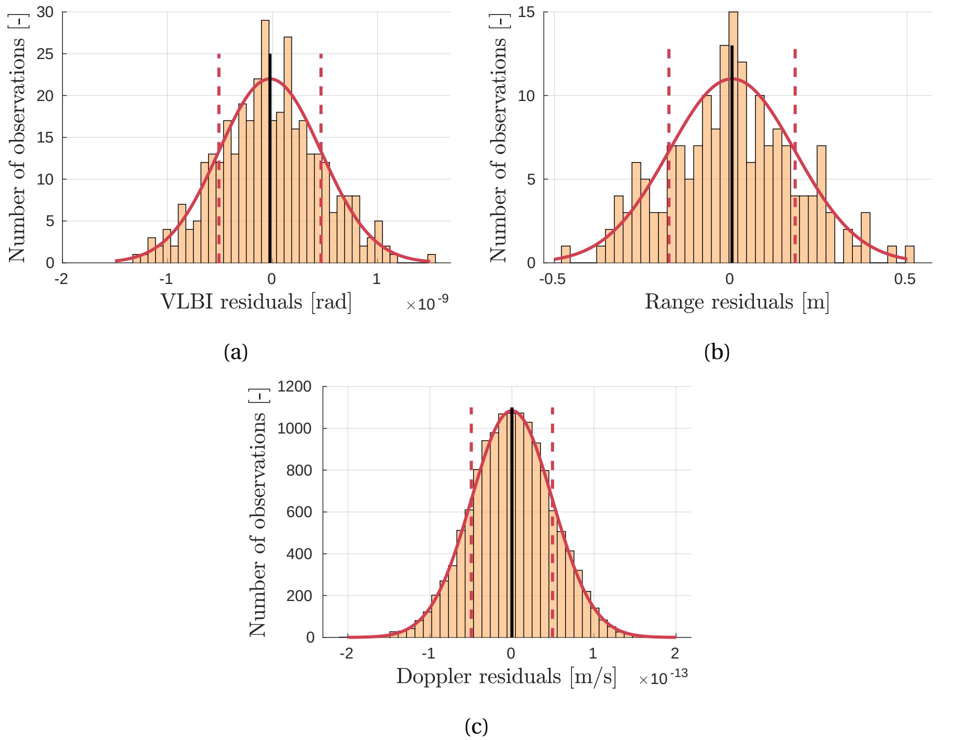

Figure 4.12.: Observations residuals after the weighted least-squares estimation reached convergence (from left to right: VLBI, range, and Doppler residuals). The black vertical lines indicate the mean of the residuals for each observation type, while the dashed vertical lines represent the standard deviation around the mean value.

results were obtained, but true errors were averaged over 10 experiments with different initial parameters perturbations (smaller than those we applied).

In our simulation, for most parameters (97% of the 432 estimated parameters), the true error is smaller than 3σ (i.e., true to formal errors ratio smaller than 3). A significant fraction (62%) of the true errors are actually smaller than 1σ. These results confirm that, for the vast majority of estimated parameters, the coupled estimation model is able to properly converge towards the *true* parameter value, and that errors can be expected to be in agreement with 3σ uncertainties. All parameters exhibiting a true to formal errors ratio larger than 3 were actually found to be Europa-related properties (gravity field coefficients, initial position along the x-axis, etc.). Due to the limited amount of observations collected at Europa (only two flybys, see Fig. 4.1), these parameters are either highly correlated (second degree and order gravity field coefficients with Europa's state), or cannot be estimated beyond their a priori constraints ($c_{\mathbf{q}}$ close to 1 for Europa's other gravity coefficients, implying a

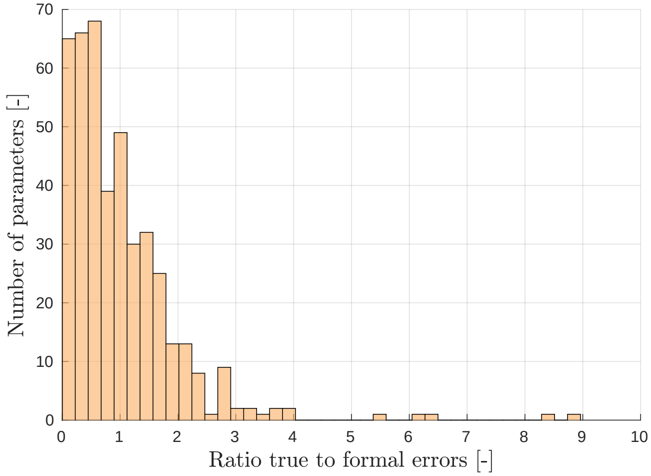

Figure 4.13.: Distribution of the ratio between true and formal errors for all estimated parameters. A value smaller than 1 indicates that the true estimation error is lower than the associated formal uncertainty. 432 parameters were estimated in total.

so-called *biased* estimation). This might at least partially explain why unexpectedly large true to formal errors ratios were obtained for these parameters.

Overall, this deterministic simulation succeeded in verifying that the 3σ uncertainties provided by the coupled estimation are good indicators of the expectable estimation errors. This increased confidence in our covariance analyses. The effect of inaccuracies in dynamical or observational modelling was however not investigated (see discussion in Section 4.5). Interestingly, and despite still relying on ideal models, this simulation nonetheless highlighted issues arising when trying to complete the least-squares estimation, due to the high condition number resulting from the lack of observations at Io and Europa.

5

Contribution of PRIDE VLBI products to ephemerides

M. S. Fayolle, D. Dirkx, G. Cimo, L. I. Gurvits, V. Lainey, P. N. A. M. Visser

In the coming decade, JUICE and Europa Clipper radio science will yield the most accurate estimation to date of the Galilean moons' physical parameters and ephemerides. JUICE's PRIDE (Planetary Radio Interferometry and Doppler Experiment) will help achieve such a solution by providing VLBI (Very Long Baseline Interferometry) observations of the spacecraft's lateral position, complementing nominal radio science measurements. In this paper, we quantify how PRIDE VLBI can contribute to the moons' ephemerides determination, in terms of attainable solution improvement and validation opportunities. To this end, we simulated VLBI data for JUICE, but also investigated the possibility to perform simultaneous tracking of JUICE and Europa Clipper, thus ultimately generating both single- and dual-spacecraft VLBI. We considered various tracking and data quality scenarios for both VLBI types, and compared the formal uncertainties provided by covariance analyses with and without VLBI. These analyses were performed for both global and local (i.e., per-flyby) estimations of the moons' states, as eventually achieving a global solution first requires proceeding arc-per-arc. We showed that both single- and multi-spacecraft VLBI measurements only bring limited improvement to the global state estimation, but significantly contribute to the moons' normal points (i.e., local states at flyby times), most notably in the out-of-plane direction. Finally, we designed a validation plan exploiting PRIDE VLBI to progressively validate the classical radio science solution,

This chapter is under revision for publication in Icarus (Fayolle et al., 2024): Fayolle, M. S., Dirkx, D., G. Cimo, L. I. Gurvits, Lainey, V., & Visser, P. N. A. M. Contribution of PRIDE VLBI products to the joint JUICE-Europa Clipper moons' ephemerides solution.

whose robustness and statistical realism is sensitive to modelling inconsistencies. PRIDE will indeed be invaluable to overcome possible dynamical modelling challenges, and eventually achieve the uncertainty levels promised by JUICE-Europa Clipper analyses.

5.1. INTRODUCTION

In the 2030s, both ESA's JUpiter ICY moons Explorer (JUICE) and NASA's Europa Clipper spacecraft will study Jupiter's Galilean satellites (Grasset et al., 2013; Witasse et al., 2024; Pappalardo et al., 2021). They will perform a series of flybys around these moons, with a strong focus on Callisto (JUICE) and Europa (Europa Clipper), followed by an 8-month orbital phase around Ganymede for JUICE. The strong interest in the Galilean system was strengthened from the Galileo mission, with the detection, either tentative or confirmed, of subsurface oceans of liquid water below the icy crust of the three outermost satellites (Europa, Ganymede, and Callisto) (Khurana et al., 1998; Kivelson et al., 2000, 2002). Both JUICE and Europa Clipper missions are specifically designed to confirm the findings of the Galileo mission, and provide the most detailed characterisation to date of the moons' hydrospheres (Petricca et al., 2023; Roberts et al., 2023).

5

As part of their scientific objectives, data from JUICE and Europa Clipper will further constrain the formation and long-term evolution of the Galilean system, a critical step to understand how the moons' internal oceans could have formed and survived until present-day. Our understanding of the system's thermal-orbital evolution indeed remains incomplete, with fundamental questions still open regarding the history of the Laplace resonance (Yoder, 1979; Greenberg, 1987) and the possibility of a rapid migration of Callisto's orbit if caught in a resonance-locking mechanism (Lari et al., 2023). Answering those will require a better understanding of tidal dissipation mechanisms, which govern the moons' orbital migration (e.g., Lainey et al., 2009, 2020) and heats up their interiors (Nimmo and Pappalardo, 2016). The Galilean system can moreover be seen as a miniature version of the Solar System. Understanding its formation and history will therefore bring invaluable insights into planetary systems evolution in general (e.g., Deienno et al., 2014; Heller et al., 2015).

The moons' current orbits result from these long-term evolution processes, and therefore bear witness of the satellites' orbital and interior history. Improving our ephemerides solutions for the Galilean satellites is thus a natural way to gain insights into the system's thermal-orbital evolution. In planetary space missions such as JUICE and Europa Clipper, this is primarily achieved by extracting the dynamical signatures of the Galilean satellites from the radiometric tracking measurements of the spacecraft during their close encounters with the moons (flybys or orbital phase).

For this purpose, JUICE will benefit from a dedicated radio science instrument 3GM (Gravity & Geophysics of Jupiter and Galilean Moons, Iess et al. 2024), while Europa Clipper will rely on the spacecraft's nominal tracking and communication radio capabilities (Mazarico et al., 2023). The potential of classical radio science observables from both JUICE and Europa Clipper has already been demonstrated for ephemerides determination applications (Magnanini, 2021; Magnanini et al., 2024; Fayolle et al., 2022). These measurements are nonetheless limited by the observation geometry: range and Doppler data mostly constrain the spacecraft's motion (position and velocity, respectively) in the line-of-sight direction.

To alleviate this limitation, JUICE will take advantage of an additional support experiment: the Planetary Radio Interferometry and Doppler Experiment (PRIDE), which has already been successfully used for, among others, the Huygens Probe, Venus Express, and Mars Express missions (Pogrebenko et al., 2004; Bocanegra-Bahamón et al., 2018; Duev et al., 2016). PRIDE provides phase-referenced VLBI (Very Long Baseline Interferometry) measurements of the spacecraft's position. This is achieved by simultaneously detecting the signal transmitted by JUICE with several ground-based radio telescopes, while nodding between the target (i.e., spacecraft) and a nearby stable background radio source used as a phase calibrator. This allows PRIDE to accurately reconstruct the lateral position of the spacecraft in the ICRF (International Celestial Reference Frame), providing the missing information on JUICE's position components orthogonal to the line-of-sight. Because of the strong geometrical complementarity with the range and Doppler measurements, PRIDE VLBI data are expected to significantly help constraining the Galilean moons' dynamics. A more detailed discussion on the main differences and advantages of the PRIDE phase-referencing technique with respect to classical Delta-DOR VLBI can be found in Gurvits et al. (2023).

The contribution of JUICE-PRIDE to the ephemerides solution has already been investigated by Dirkx et al. (2017). As expected, VLBI measurements were found to mostly improve the estimation of the out-of-plane position of Jupiter and its moons. However, this previous analysis, performed with an earlier version of the JUICE trajectory, focussed on a JUICE-only radio science solution. In addition, the methodology underlying this study, while sufficient for a preliminary analysis, did not properly capture the dynamical interactions between the spacecraft, moons and Jupiter in its uncertainty quantification. Since this first study, the expected simultaneous presence of the JUICE and Europa Clipper spacecraft in the Jovian system has radically changed the picture, the synergy between their Jovian tours greatly benefiting the ephemerides estimation. Thanks to this unique dual-mission configuration, joint JUICE-Europa Clipper analyses indeed achieve significantly more accurate and stable solutions than previous single-mission studies (Magnanini et al., 2024).

Investigating the potential of PRIDE as a powerful validation experiment, and as an additional data set to obtain a robust and stable solution, then becomes critical. The extremely low uncertainty levels predicted to be achievable by existing simulations (e.g., Fayolle et al., 2022; Magnanini et al., 2024) will indeed be extremely difficult to achieve in practice. Previous attempts to reconstruct a consistent, global solution for the motion of natural satellites from a series of radio science flybys, in the context of the Cassini mission, have proven extremely sensitive to dynamical modelling issues, sometimes preventing or complicating the obtention of a reliable coupled solution (Durante et al., 2019; Zannoni et al., 2020; Jacobson, 2022).

The extremely accurate radio science data from JUICE and Europa Clipper will impose an even more stringent requirement on the consistency of our dynamical models. Similar issues as for the Cassini case are therefore expected to arise (e.g., Dirkx et al., 2017; Fayolle et al., 2022). Overcoming these modelling challenges requires proceeding gradually, by first performing local state estimations to gradually reconstruct a coherent, global solution for the moons' ephemerides. PRIDE will be instrumental in achieving this, by providing completely independent VLBI measurements of the spacecraft position. These will be extremely valuable to validate the solutions based on range and Doppler data, as well as to detect and identify potential modelling issues.

Furthermore, the presence of two in-system spacecraft opens novel, unique opportunities to perform simultaneous VLBI tracking of both JUICE and Europa Clipper. This tracking configuration, referred to as multi-spacecraft VLBI in the following, will provide extremely accurate measurements of the relative angular position between the two spacecraft. These can translate into constraints on the relative position of the Galilean moons with respect to one another, as most of JUICE's flybys occur around Ganymede and Callisto, while Europa Clipper focusses on Europa. These unique observations therefore have the potential to greatly help constraining the strongly coupled dynamics of the Galilean system.

In light of the above, this paper analyses the contribution of various PRIDE VLBI products to the moons' ephemerides determination from JUICE and Europa Clipper radio science. We specifically quantify how much VLBI measurements can improve the solution obtained from Doppler and range data, both for local and global estimations of the moons' orbits. To this end, we pay particular attention to the error budgets of our VLBI observables, using more detailed and realistic random and systematic noises than in (Dirkx et al., 2017). We moreover identify promising opportunities to perform multi-spacecraft tracking and assess the contribution of the resulting observables to the ephemerides solution. Finally, several validation strategies enabled by the PRIDE VLBI technique are explored. We discuss their potential, and investigate their upcoming role in the progressive reconstruction of a statistically consistent solution for the Galilean moons' ephemerides from JUICE and Europa Clipper data.

We first describe our simulated VLBI observables in Section 5.2, before presenting the details of our joint JUICE-Europa Clipper estimation setup in Section 5.3. The underlying numerical model used for the estimation is extended from Fayolle et al. (2022). Sections 5.4 and 5.5 then present the results obtained when adding single- and multi-spacecraft VLBI measurements, respectively, to the joint JUICE-Europa Clipper ephemerides solution. Finally, Section 5.6 discusses the various validation opportunities offered by the PRIDE VLBI technique and Section 5.7 provides the main conclusions of our analyses.

5.2. VLBI OBSERVABLES

Our analyses will rely on simulated VLBI observables to quantify the expected PRIDE contribution to the ephemerides solution for the Galilean moons. In this perspective, this section presents our simulated VLBI measurements, starting with describing the adopted error budget and the search process for the VLBI phase calibrators in Sections 5.2.1 and 5.2.2, respectively. We then discuss the conditions and opportunities to perform multi-spacecraft VLBI tracking between the JUICE and Europa Clipper spacecraft in Section 5.2.3.

5.2.1. Error budget for phase-referencing VLBI

To make our simulations as realistic as possible, the noise budget assigned to VLBI simulated data was designed based on past measurements. The main error sources are media propagation delays (interplanetary plasma, troposphere, and ionosphere), instrumental signal delays, clock offsets and instabilities, signal-to-noise ratio (SNR) of the spacecraft's signal and calibrator's broadband emission, as well as uncertainties in ground stations' coordinates, and Earth's orientation parameters (Pradel et al., 2006). Moreover, the quality of past VLBI data is often assessed by analysing post-fit residuals, which are however not only sensitive to the accuracy of the VLBI measurements but also affected by the quality of the orbit determination solution and by the position uncertainty of the calibrator in the ICRF.

Phase-referencing VLBI was conducted with both the Venus Express (VEX) and Mars Express (MEX) spacecraft as observing targets. For the former, the analysis of pre-fit residuals between the VLBI data points and the a priori trajectory of the spacecraft revealed a large discrepancy between right ascension and declination (Duev et al., 2012). The low declination of the MEX spacecraft (ranging from −11 deg to −13 deg), combined with a relatively large separation (2.5 deg) with respect to the phase calibrator, resulted in the poor cancellation of tropospheric and ionospheric effects, mostly translating in a large declination error. The MEX VLBI measurements, on the other hand, show smaller pre-fit residuals: the median values of the rms residuals are 0.03 mas and 0.06 mas[1] in right ascension and declination, respectively, with a 2-min integration time (Duev et al., 2016).

Furthermore, Jones et al. (2020) provide an overview of the VLBI measurements of the Cassini spacecraft over the entire mission duration (2004-2017). After removing outliers due to poor a priori orbit determination solution for Cassini and/or large separation between the spacecraft and calibrator (larger than 7 deg), the rms residuals are 0.24 mas and 0.36 mas in right ascension and declination, respectively. The orbit determination error and the uncertainty in the calibrators' ICRF positions can however account for half of these residuals. Both error sources are not inherently related to the VLBI measurement accuracy, and they will be accounted for independently in our simulations. We thus consider a VLBI measurement quality of 0.6 nrad ($\sim$ 0.12 mas) and 0.9 nrad ($\sim$ 0.18 mas) for Cassini's VLBI data in right ascension and declination, respectively.

VLBI astrometry of the Juno spacecraft during the early phase of the mission has also been published, yielding rms (post-fit) residuals of 0.4 mas and 0.6 mas in right ascension and declination, respectively (Jones et al., 2019; Park et al., 2021). These residuals are larger than for Cassini, due to the poorer quality of Juno's a priori orbit solution available at the beginning of the mission, as well as large calibrator

[1] 1 mas = 4.84 nrad

5

Table 5.1.: Error budget from past VLBI measurements, and selected noise levels for our simulations. Some numbers are struck out to indicate that they are deemed not representative of the typical VLBI accuracy.

Data	**$1\sigma(\alpha)$ [mas]**	**$1\sigma(\delta)$ [mas]**	**Comment**
Pre-fit residuals for VEX Duev et al. (2012)	0.09	~~0.25~~	Unfavourable target's declination (between -11 and -13 deg)
Pre-fit residuals for MEX Duev et al. (2016)	0.03	0.06	
Post-fit residuals for Cassini Jones et al. (2020)	0.12	0.18	After removing calibrator's and spacecraft's position uncertainty (~50% of the residuals' rms)
Simulation-based errors Pradel et al. (2006)	[0.03 ; 0.045]	[0.05 ; 0.13]	Total tropospheric effect

Selected noise	**$1\sigma(\alpha)$**	**$1\sigma(\delta)$**
Poor VLBI case	0.12 mas ≈ 0.6 nrad	0.18 mas ≈ 0.9 nrad
Good VLBI case	0.04 mas ≈ 0.2 nrad	0.06 mas ≈ 0.3 nrad
Ka-band case	0.02 mas ≈ 0.1 nrad	0.03 mas ≈ 0.15 nrad

5

position errors for some epochs (Jones et al., 2019). The few published Juno VLBI measurements were thus not considered representative of the accuracy typically expected from VLBI phase-referencing tracking.

Based on these existing measurements, and excluding the pessimistic errors in declination obtained with VEX, we selected two different Gaussian random noise budgets for our simulated VLBI observables (see Table 5.1):

- Poor VLBI noise case: $\sigma(\alpha) = 0.12$ mas and $\sigma(\delta) = 0.18$ mas, based on Cassini VLBI post-fit residuals after removing the estimated contribution of the calibrators' positions ;

- Good VLBI noise case: $\sigma(\alpha) = 0.04$ mas[2] and $\sigma(\delta) = 0.06$ mas, consistent with MEX VLBI measurements and with the minimum tropospheric effect errors.

The above only encompasses random error sources, and does not account for the systematic bias induced by an error in the calibrator's ICRF position, which will be addressed in Section 5.2.2.

These error levels are consistent with the simulation-based analysis of VLBI systematic errors in Pradel et al. (2006). They indeed identified wet tropospheric effects as the dominant error source, apart from the uncertainty in the calibrator's position, which in our case is treated as a separate bias (see Section 5.2.2). The error due to the total tropospheric effect was found comprised between 0.03 and 0.045 mas in right ascension, and between 0.05 and 0.13 mas in declination. These values give an indication of the minimum noise level that can be expected for VLBI measurements, and are in line with our good VLBI case. Moreover, the existing VLBI measurements on which we based our error budget did not benefit from dual-frequency calibration techniques to cancel ionospheric effects, nor from water vapor radiometers for wet tropospheric delay calibration. The quality of these data points can thus be considered rather conservative with respect to the highest accuracy achievable with the phase-referencing VLBI technique (Jones et al., 2020).

It should also be noted that the random errors in VLBI observables cannot be perfectly represented by purely uncorrelated white noise. In practice, some uncertainty sources (e.g., atmospheric delays) are time-dependent, limiting how frequently *independent* (i.e., uncorrelated) VLBI data points can be obtained. In the following, we will therefore consider different VLBI measurement cadences to account for this and avoid overestimating the data volume and information content of the VLBI data set (see Section 5.3.2).

The two VLBI noise budgets mentioned above rely on past X-band VLBI measurements and thus indirectly assume tracking at similar frequencies. However, JUICE is also equipped with Ka-band tracking capabilities. While no existing VLBI data at such frequencies can be exploited to derive realistic noise budgets, a factor two to four improvement can be theoretically expected between X- and Ka-band measurements. We thus considered an additional case, referred to as Ka-band case (see Table 5.1), with VLBI noise level set to half their X-band values in the best case

[2] The error in right ascension was set to 0.04 mas instead of 0.03 mas to keep the same ratio between the good and poor VLBI noises in both right ascension and declination.

scenario. The actual feasibility of Ka-band VLBI tracking will eventually depend on the availability of both suitable calibrators at these frequencies (see Section 5.2.2), and VLBI arrays with sufficient number of Ka-band-capable telescopes.

5.2.2. PHASE-REFERENCING VLBI CALIBRATORS

The phase-referencing VLBI technique used by PRIDE requires nodding between the target (spacecraft) and a nearby radio source, used as calibrator, to yield very accurate measurements of the target's lateral position in the ICRF. For each of our simulated VLBI data points (see Section 5.3.2), we therefore first verified that a suitable phase calibrator is available, which implies fulfilling the following conditions.

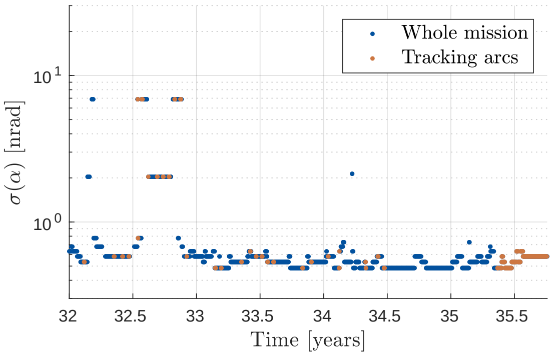

(a) Uncertainties in right ascension.

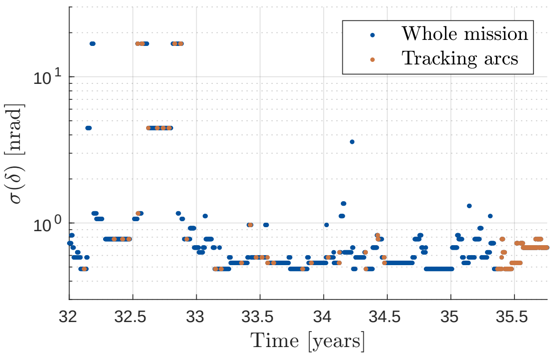

(b) Uncertainties in declination.

Figure 5.1.: Uncertainties in the ICRF positions of the phase calibrators identified over the course of the JUICE mission, using the latest JUICE trajectory (see Section 5.3.1). The blue dots represent all calibrators (at all epochs), while we highlighted in orange the epochs corresponding to an active tracking session during the flyby and orbital phases, when VLBI measurements are actually possible.

First, the radio source must have a sufficiently high total flux density at X- and Ka-bands (e.g., at least ~30 mJy as was the case for MEX observations in 2013, Duev et al., 2016). Furthermore, the source must be compact (i.e., bright) enough for a major part of the total flux density coming from a compact, mas-scale morphology. Additionally, the angular separation between the calibrator and the spacecraft should typically be smaller than 2 deg to obtain accurate phase-calibrated measurements.

Moreover, as mentioned in Section 5.2.1, an error in the calibrator's ICRF position would introduce a systematic bias in the spacecraft's angular position derived from the VLBI observation. For each calibrator identified over JUICE's Jovian tour, we therefore extract its position uncertainty from the Radio Fundamental Catalog (rfc2023b[3]), as shown in Fig. 5.1, to be applied as a systematic bias. The influence of such biases, which vary over the mission duration as different calibrators are used, is thus directly accounted for in our estimations (see Section 5.3.4). From Fig. 5.1, the averaged uncertainty values are 0.8 nrad and 1.3 nrad in right ascension and declination, respectively. However, the calibrators' position accuracy is significantly worse between mid-2032 and 2033, due to the absence of better calibrators within 2 deg of the spacecraft. This period unfortunately overlaps with eight of JUICE's flybys, including its two flybys at Europa, and will be further discussed in our results (Section 5.4).

A similar calibrator search was conducted in Ka-band, but the limited number of catalogued radio source at these frequencies yielded poor results (no suitable Ka-band calibrator during the flyby phase). Our results for the Ka-band case should therefore be treated carefully, as they depend on the hypothetical presence of a nearby appropriate calibrator. In the following, we arbitrarily used X-band calibrators for our Ka-band analyses. If the added-value of Ka-band VLBI is demonstrated, future observation campaigns to densify the Ka-band radio source background should be conducted before JUICE reaches the Jovian system.

5.2.3. Multi-spacecraft in-beam measurements

As mentioned in Section 5.1, the simultaneous presence of JUICE and Europa Clipper in the Jovian system will make it possible to perform concurrent VLBI tracking of the two spacecraft. Such multi-spacecraft VLBI measurements have already been acquired for various Mars missions: between the Phoenix spacecraft and the Martian orbiters MRO (Mars Reconnaissance Orbiter) and Odyssey (Fomalont et al., 2010), and between MEX (Mars Express), TGO (Trace Gas Orbiter), and MRO (Molera Calvés et al., 2021).

Performing multi-spacecraft VLBI tracking requires the two spacecraft (here JUICE and Europa Clipper) to be concurrently transmitting, with a suitable calibrator within 2 deg of the targets, as for single-spacecraft VLBI. Moreover, for in-beam tracking to be feasible, the angular separation between the two target spacecraft should be smaller than the beam size of a typical single-dish telescope involved in the observation (~3 arcmin for a 30-m-class radio telescope observing at X-band). In addition to these feasibility requirements, some additional conditions should also

[3] http://astrogeo.org/rfc/

5

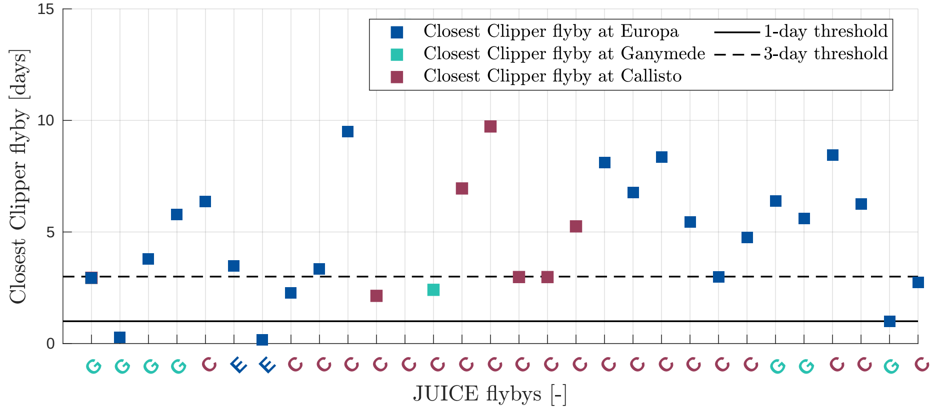

Figure 5.2.: Timespan between each JUICE flyby and the temporarily nearest Europa Clipper flyby, using the latest mission trajectories (see Section 5.3.1), to identify multi-spacecraft tracking opportunities. The colours indicate around which moon each flyby is performed, and the horizontal plain and dashed lines represent a time interval limit of one and three days, respectively.

be fulfilled for the multi-spacecraft VLBI measurements to significantly contribute to the moons' ephemerides estimation. The most promising opportunities indeed occur when the two spacecraft are both temporally close to an encounter (*i.e* flyby) with a moon, such that the spacecraft's motions still contain signatures of the moons' dynamics. When looking for multi-spacecraft VLBI tracking opportunities, we therefore focus on combinations of two flybys, one by JUICE and one by Europa Clipper, less than three days apart. This also ensures that the (potentially relatively large) pre-encounter and clean-up manoeuvres planned three days before and after each flyby (ESOC, 2019; Young et al., 2019), respectively, are excluded from the tracking arcs and do not affect the estimation.

Based on these requirements, Fig. 5.2 highlights possible multi-spacecraft VLBI opportunities. In total, 11 flyby combinations meet the maximum time interval requirement of three days, as summarised in Table 5.2. Seven of them involve flybys performed around two different moons (referred to as multi-moon flyby combinations). The remaining five, on the other hand, are flybys performed at the same moon (single-moon flyby combinations), including a flyby of Europa by both spacecraft with less than four hours in-between. The potential of such tracking configurations, due to their unique geometry, to validate the radio science solution(s) or detect dynamical modelling issues will be discussed and exploited in Section 5.6.

Multi-spacecraft VLBI tracking will yield very accurate measurements of the relative position of the two spacecraft in the ICRF. However, a distinction should be made between in-beam and telescope nodding phase referencing. If the two spacecraft are close enough (less than 3 arcminutes), their signals can be simultaneously tracked

Table 5.2.: Combinations of JUICE and Europa Clipper flybys allowing for multi-spacecraft VLBI tracking.

	JUICE flyby at	Clipper flyby at	Time interval [h]	In-beam possible
1	Ganymede	Europa	70.7	no
2	Ganymede	Europa	6.5	yes
3	Europa	Europa	3.7	yes
4	Callisto	Europa	54.3	yes
5	Callisto	Callisto	51.3	yes
6	Callisto	Ganymede	57.8	partially
7	Callisto	Callisto	71.5	no
8	Callisto	Callisto	71.5	no
9	Callisto	Europa	71.4	partially
10	Ganymede	Europa	23.9	no
11	Callisto	Europa	65.6	partially

within the primary beam of the radio telescope. In such in-beam configuration, many systematic errors affecting the quality of the measurement cancel out (Majid and Bagri, 2007; Fomalont et al., 2010). Based on previous in-beam experiments, an accuracy of 0.1 nrad could then be expected for the relative angular position measurement (Fomalont et al., 2010). To be conservative, we also considered a poor accuracy case. Given the very small angular separation between the two targets and the cancellation of many measurement errors (Majid and Bagri, 2007), we used the good single-spacecraft VLBI case (see Section 5.2.1) for the poor in-beam VLBI error.

For nodding multi-spacecraft measurements (when the two spacecraft are too far apart for in-beam tracking), the noise budget is slightly worse as the error cancellation is not as effective. For our good noise case, we used the same error levels for single-spacecraft VLBI (see Section 5.2.1). However, for the poor noise case, we set our multi-spacecraft VLBI errors halfway between single-spacecraft VLBI's best and worst cases, the latter being too pessimistic for multi-spacecraft tracking. For single-spacecraft VLBI, large errors are indeed only obtained for large angular separations, or with phase calibrators whose ICRF positions are poorly constrained, neither of these two conditions being relevant in a multi-spacecraft tracking configuration. Table 5.3 summarises these different noise levels for multi-spacecraft VLBI.

Table 5.3.: Selected error levels for simulated multi-spacecraft VLBI measurements.

Selected noise	$1\sigma(\alpha)$ [nrad]		$1\sigma(\delta)$ [nrad]	
	in-beam	nodding	in-beam	nodding
Poor case	0.2	0.4	0.3	0.6
Good case	0.1	0.2	0.1	0.3

5

5.3. ESTIMATION SETUP FOR JOINT JUICE - EUROPA CLIPPER SOLUTIONS

This section describes the estimation setup for our JUICE-Europa Clipper radio science simulations, starting with the models used to propagate the dynamics of both the moons and spacecraft in Section 5.3.1. Sections 5.3.2 and 5.3.3 then present the simulated observables and state estimation strategies applied in our analyses, respectively, before Section 5.3.4 lists the various parameters to be estimated.

5.3.1. DYNAMICAL MODELS

Following the recommendations formulated in Dirkx et al. (2016) and the models used in Fayolle et al. (2023b), the dynamics of the Galilean satellites were propagated in a jovocentric frame using the following set of accelerations:

- mutual spherical harmonics acceleration between Jupiter and each moon, considering all zonal coefficients for Jupiter up to degree 10, and expanding the moons' gravity fields up to degree and order 2;
- mutual spherical harmonics acceleration between the four Galilean moons, including interactions between terms up to degree and order 2;
- point mass gravity from the Sun and Saturn;
- relativistic acceleration corrections;
- tidal effect on the orbit of moon k due to the tides raised on Jupiter by moon k (see discussion below);
- tidal effect on the orbit of moon k due to the tides raised by Jupiter.

The moons' gravity field coefficients were taken from Schubert et al. (2004), while Jupiter's gravity field was based on the current state-of-the-art model at mid-Juno mission (Iess et al., 2018; Durante et al., 2020). We used the latest IAU model for Jupiter's rotation (Archinal et al., 2018), and the moons' rotations were assumed to be synchronous, with their long axis pointing towards the empty focus of their orbit (e.g., Lari, 2018).

We chose to directly model the effects of tides on the moons' orbits, following the formulation proposed in e.g., Lari (2018); Lainey et al. (2019), instead of introducing time-variation of the satellites' gravity fields due to tidal deformation. The motivation for this modelling choice is twofold. First, it circumvents the need for (near)-perfect consistency between our tidal and rotational models to accurately reproduce the effects of tides on the moons' dynamics (e.g., Dirkx et al., 2016). More importantly, this allows us to focus on the signature of the tidal effects present in the moons' orbits specifically, and not in the gravity field variations sensed by the spacecraft (analysed in Magnanini et al., 2024). This allows us to investigate how PRIDE VLBI measurements might help estimate tidal dissipation parameters via an improved determination of the moons' ephemerides.

Our estimation setup also requires propagating Jupiter's dynamics (heliocentric frame), for which the following accelerations set was considered:

- mutual spherical harmonics acceleration between Jupiter and the Sun, expanding both gravity fields up to degree and order 2;
- point mass gravity from all planets in the Solar System and from the four Galilean satellites;
- relativistic acceleration corrections.

Finally, the orbits of the JUICE and Europa Clipper spacecraft were propagated with respect to the central moon of each flyby and/or orbital phase, using the latest available trajectories as references[4][5]. The following set of accelerations was considered:

- spherical harmonics gravitational acceleration from Jupiter (zonal coefficients up to J_{10});
- spherical harmonics gravitational acceleration from the central moon up to degree and order 13 (Europa), 15 (Ganymede), and 9 (Callisto) (see Section 5.3.4);
- point mass gravity from the other (non-central) Galilean moons, the Sun, and Saturn;
- solar radiation pressure from the Sun;
- arc-wise empirical accelerations, constant in the RTN (radial, tangential, normal) frame (nominal values set to zero), modelling possible accelerometer calibration errors.

Regarding the latter, one set of empirical accelerations was considered for each flyby and for each daily arc during JUICE's GCO (Ganymede Circular Orbit) phase. Longer arcs were however considered in-between flybys for multi-spacecraft tracking (Section 5.2.3), during which daily empirical accelerations were added to modelled expected perturbations of the spacecraft's dynamics.

5.3.2. SIMULATED RADIO SCIENCE OBSERVATIONS

For our covariance analyses, we first simulated classical radio science measurements (Doppler and range) for both JUICE and Europa Clipper. For the sake of clarity, the range and Doppler-only solution, with no VLBI included, will be referred to as the baseline solution in the rest of this paper.

For JUICE, we assumed a X/Ka-band link and three tracking arcs of 6h each per flyby, one centred around the closest approach and the other two planned 12h before and after the flyby, following the configuration used in Cappuccio et al. (2022). In addition, the GCO was divided in day-long arcs, with 8h of tracking per

[4] JUICE trajectory: juice_mat_crema_5_0_20220826_20351005_v01 https://www.cosmos.esa.int/web/spice/spice-for-juice

[5] Europa Clipper trajectory: 21F31_MEGA_L241010_A300411_LP01_V4_postLaunch_scpse https://naif.jpl.nasa.gov/pub/naif/EUROPACLIPPER/kernels/spk/

5

day. For each of these tracking arcs, Doppler and range data were simulated with a noise level of 12 μm/s (60s of integration time) and 20 cm, respectively. Although in agreement with similar JUICE simulation analyses (e.g., Cappuccio et al., 2022), this range noise budget is very conservative based on BepiColombo's sub-centimeter ranging accuracy (Cappuccio et al., 2020b; Genova et al., 2021).

For Europa Clipper, only Doppler measurements were simulated. We assumed a noise level of 0.1 mm/s during the 4h-long tracking arcs centred at each closest approach, due to the unavailability of the high gain antenna (HGA) (Mazarico et al., 2023). We also considered more accurate Doppler data with a noise of 0.05 mm/s, to be acquired during the navigation passes (HGA available). These additional passes are, on average, scheduled 20h before and after each flyby (Magnanini et al., 2024).

We then also simulated single- and multi-spacecraft PRIDE VLBI observations. Since our analyses focus on the contribution of such measurements, we considered different data acquisition and noise level scenarios, varying the following settings:

- VLBI random noise, using the different error budgets defined in Section 5.2.1;
- measurement cadences (i.e., how often can an *independent* VLBI data point be generated, Section 5.2.1) of 1 h, 20 min, 5 min, and 2 min;
- frequency of the VLBI tracking sessions during JUICE's GCO (from weekly to monthly).

We also tested different tracking scenarios for multi-spacecraft VLBI, essentially distinguishing between two types of configuration (see Fig. 5.3):

1. *mid-arc tracking*: single tracking arc centred in-between the JUICE and Europa Clipper flybys involved in the flyby combination of interest;
2. *arc bounds tracking*: for each flyby combination, two tracking arcs occurring respectively just after the first close encounter and just before the second one.

While we varied the duration of the multi-spacecraft tracking arcs, we always ensured that the total tracking duration is identical between the two above cases (i.e., using halved arcs for the arc bounds tracking case). Regarding the quality of the simulated multi-spacecraft VLBI observables, we adopted the two different noise budgets presented in Table 5.3. Finally, navigation Doppler data were also simulated during the longer arcs required for multi-spacecraft tracking, with a noise level of 80 μm/s at an integration time of 1h (ESOC, 2019). These Doppler observables were merely included to constrain the empirical accelerations added over these longer arcs (see Section 5.3.1).

5.3.3. ESTIMATION STRATEGY

To quantify the relative improvement of the estimation solution achievable with PRIDE VLBI, we performed multiple covariance analyses, in different scenarios. The covariance matrix **P** of the estimated parameters is given by the following (Gill and Montenbruck, 2013):

$$\mathbf{P} = \left(\mathbf{H}^{\mathrm{T}}\mathbf{W}\mathbf{H} + \mathbf{P}_0^{-1}\right)^{-1}, \tag{5.1}$$

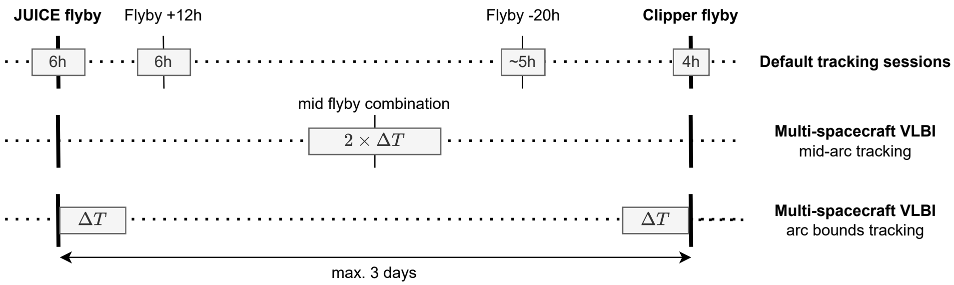

Figure 5.3.: Multi-spacecraft VLBI tracking configurations, illustrated for a flyby combination where the JUICE flyby occurs before the Europa Clipper one. The grey boxes represent the radio science tracking sessions, with their durations indicated inside. ΔT denotes the (varying) duration of the multi-spacecraft tracking arc (see Section 5.5).

where $\mathbf{W}$ designates the observations weight matrix and $\mathbf{H}$ is the observations partial matrix with respect to the estimated parameters. $\mathbf{P}_0$, on the other hand, contains the a priori covariances of the estimated parameters, accounting for our knowledge of these parameters prior to the estimation. As will be highlighted in Section 5.3.4, some of our estimations also include consider parameters (i.e., parameters that are not directly estimated, but whose uncertainties are accounted for in the estimation). The statistical representation of the estimation accuracy is then provided by the so-called consider covariance analysis $\mathbf{P}_c$, defined as:

$$\mathbf{P}_c = \mathbf{P} + \left(\mathbf{P}\mathbf{H}^{\mathrm{T}}\mathbf{W}\right)\left(\mathbf{H}_c\mathbf{C}\mathbf{H}_c^{\mathrm{T}}\right)\left(\mathbf{P}\mathbf{H}^{\mathrm{T}}\mathbf{W}\right)^{\mathrm{T}}. \tag{5.2}$$

$\mathbf{P}$, $\mathbf{H}$, and $\mathbf{W}$ refer to the same matrices as in Eq. 5.1, and $\mathbf{H}_c$ and $\mathbf{C}$ respectively designate the observation partials with respect to the consider parameters and the covariance matrix describing our knowledge of these parameters. The formal uncertainties of the estimated parameters are given by the square root of the diagonal elements of $\mathbf{P}$ and $\mathbf{P}_c$. Finally, these formal errors can be propagated to any epoch t, the propagated covariance being obtained as follows:

$$\mathbf{P}(t) = \left[\Phi(t,t_0);\mathbf{S}(t)\right]\mathbf{P}\left[\Phi(t,t_0);\mathbf{S}(t)\right], \tag{5.3}$$

where $\Phi(t,t_0)$ and $\mathbf{S}(t)$ are the state transition and sensitivity matrices, respectively. Eq. 5.3 can also be applied to propagate the consider covariance $\mathbf{P}_c$ instead of $\mathbf{P}$.

Covariance analyses, while perfectly adapted for our purposes, inherently rely on a number of simplifying assumptions. In particular, our dynamical models should be able to perfectly represent reality, which is particularly difficult to achieve for the non-conservative accelerations acting on the spacecraft. The resulting formal uncertainties therefore provide a too optimistic statistical representation of the true estimation errors. While we take this into consideration in our discussion, it does not impact the relevance of our approach, since we focus on the *relative* contribution of PRIDE VLBI with respect to a baseline solution.

However, as discussed in Section 5.1, modelling inconsistencies do not only yield discrepancies between true and formal errors, but might also prevent obtaining a consistent, stable solution. Overcoming these issues will require an iterative process, starting with reconstructing the spacecraft and flyby moons' orbits locally using the so-called normal points (i.e., arc-wise state solutions for the flybys' central moons, determined at the closest approach). These local estimates of the moons' states would then be reconciled into a global solution in a subsequent step. The main challenges of a direct global estimation of the moons' dynamics will be further discussed in Section 5.6, along with possible mitigation strategies. Because of these foreseen difficulties, we nonetheless chose not to solely focus on a global ephemerides solution, but to also consider the determination of the moons' normal points (i.e., per-flyby solutions) as an intermediate estimation step. In our analyses, we therefore apply both strategies, which are described in more detail in Fayolle et al. (2022):

- Local estimation, determining the central moon's normal point for each flyby and each tracking arc during the orbital phase for JUICE. These normal points are estimated perfectly independently from one another (unlike in Fayolle et al., 2022);

- Global estimation, reconstructing a single solution for the moons' orbits over the timelines of the JUICE and Europa Clipper missions. This model has been extended with respect to Fayolle et al. (2022) to also account for the concurrent estimation of the central planet's state (see 5.3.4). More details on the extended formulation can be found in Appendix 5.8.

5

In Sections 5.4 and 5.5, we thus assess the contribution of PRIDE VLBI data to both types of solution. We also specifically discuss how VLBI could help going from arc-wise state solutions to a single, fully consistent picture of the system's dynamics over the entire missions' timeline (see Section 5.6).

5.3.4. ESTIMATED PARAMETERS

The parameters estimated from the simulated radio science observables described in Section 5.3.2 are reported in Table 5.4. We distinguish between the global and local state estimation setups introduced in Section 5.3.3, and specify if each parameter is estimated globally or locally (e.g., per arc). The arc and pass definitions refer to those defined in Section 5.3.2. Finally, regarding the moons' gravity field spherical harmonics expansion, we extended it up to the point where expanding it further no longer affects the state estimation results.

The main addition of our baseline setup compared to most radio science solutions lies in estimating Jupiter's state along with the Galilean moons' orbits. While unnecessary for gravity field analyses, this becomes relevant for moons' ephemerides determination. Existing JUICE and/or Europa Clipper simulations indeed predict extremely low formal uncertainties, reaching sub-metre levels for Ganymede's radial position during JUICE orbital phase (e.g., Fayolle et al., 2022; Magnanini et al., 2024).

Table 5.4.: Estimated and consider parameters included in both our global and local state estimations (see Section 5.3.3). All parameters are by default estimated, except for those reported in italic which are either estimated or included as consider parameters.

Parameters	Global estimation	Local estimation	A priori constraint
Jupiter parameters			
Initial state	global	not included	1 km (position) ; 0.1 m/s (velocity)
Gravitational parameter μ_0	global	global	from Juno, Durante et al. (2020)
Zonal gravity coef. up to degree 10	global	global	from Juno, Durante et al. (2020)
Rotation rate and pole orientation	global	global	from Juno, Durante et al. (2020)
Inverse tidal quality factor at each moon's frequency	global	not included	none
Moons parameters			
Initial states	global	per arc	15 km (position) ; 1.0 m/s (velocity)
Gravitational parameters μ_i	global	global	Schubert et al. (2004)
Gravity coef. up to degree and order 2 (Io), 13 (Europa), 15 (Ganymede), and 9 (Callisto).	global	global	Schubert et al. (2004) for C_{20} and C_{22} Kaula's rule[6] for other coefficients
Inverse tidal quality factor for each moon	global	not included	none
Spacecraft parameters			
JUICE and Europa Clipper's states	per arc	per arc	5 km (position) ; 0.5 m/s (velocity)
Empirical accelerations	per arc	per arc	$5 \cdot 10^{-8}$ m/s^2
Range biases (for JUICE)	per pass	per pass	1.2 m (Cappuccio et al., 2022)
Single-spacecraft VLBI biases	per pass	per pass	calibrator's position uncertainty
Multi-spacecraft VLBI biases	per pass	per pass	0.1 nrad (good) ; 0.25 nrad (poor)

5

When facing such accuracy levels, the influence of Jupiter's position error can no longer be neglected and needs to be accounted for in our analyses.

It should be noted that, in the absence of real data, no unique estimation setup is currently predetermined for JUICE and Europa Clipper radio science estimations. For this reason, we kept a certain flexibility in our setup. We adopted the configuration in which both range and VLBI biases are estimated as nominal. However, we kept alternative options, such as including observation biases as consider parameters, for additional analyses meant to investigate the sensitivity of our solutions to the estimation setup choice (see Sections 5.4 and 5.5). Although estimating observation biases will not necessarily pose a particular challenge, we used these parameters as a proxy to simulate a potential deterioration of the simulation-based solution, possibly too optimistic, when moving to real data analysis. Range biases were selected because of their influence on the determination of the absolute position of the Jovian system, moons, and spacecraft, which directly affects the contribution of PRIDE VLBI measurements. Including biases as consider parameters also allows us to account for the fact that an arc-wise constant value might not be able to adequately model the systematic error in the measurements. Nonetheless, unless otherwise indicated, the results presented in the rest of this paper are obtained with the nominal setup (i.e., estimating all biases).

5

5.4. Results: single-spacecraft VLBI

This section presents our results regarding the contribution of single-spacecraft PRIDE VLBI measurements of the JUICE spacecraft to the moons' state estimation. We first describe the baseline radio science solution in Section 5.4.1, before presenting the improvement achieved with VLBI for the global and normal points solutions in Sections 5.4.2 and 5.4.3, respectively. The latter addresses the VLBI contribution to the local, intermediate estimation results for the moons' states, which will be essential to eventually achieve the global ephemerides solution discussed in Section 5.4.2. It is therefore critical to quantify the improvement provided by VLBI with both approaches (see more detailed discussion in Section 5.6).

5.4.1. Baseline solution without VLBI

Before quantifying the improvement provided by VLBI, the baseline radio science solution for the moons' ephemerides, based on JUICE-Europa Clipper range and Doppler (classical) data, must first be briefly discussed. As our analyses focus on PRIDE VLBI specifically, we limit ourselves to a top-level description of the formal uncertainty levels that can be expected from JUICE and Europa Clipper *classical* radio science measurements. More detailed results and discussions can nonetheless be found in dedicated studies, including more complete analyses of the Jovian system's tidal parameters considering the full effects of tidal dissipation both on the moons' and spacecraft's orbits (Cappuccio et al., 2020a, 2022; De Marchi et al., 2021, 2022; Magnanini et al., 2024; Mazarico et al., 2023).

[6] Kaula's rule: $\sigma = K/l^2$, $K = 10^{-5}$, l=degree

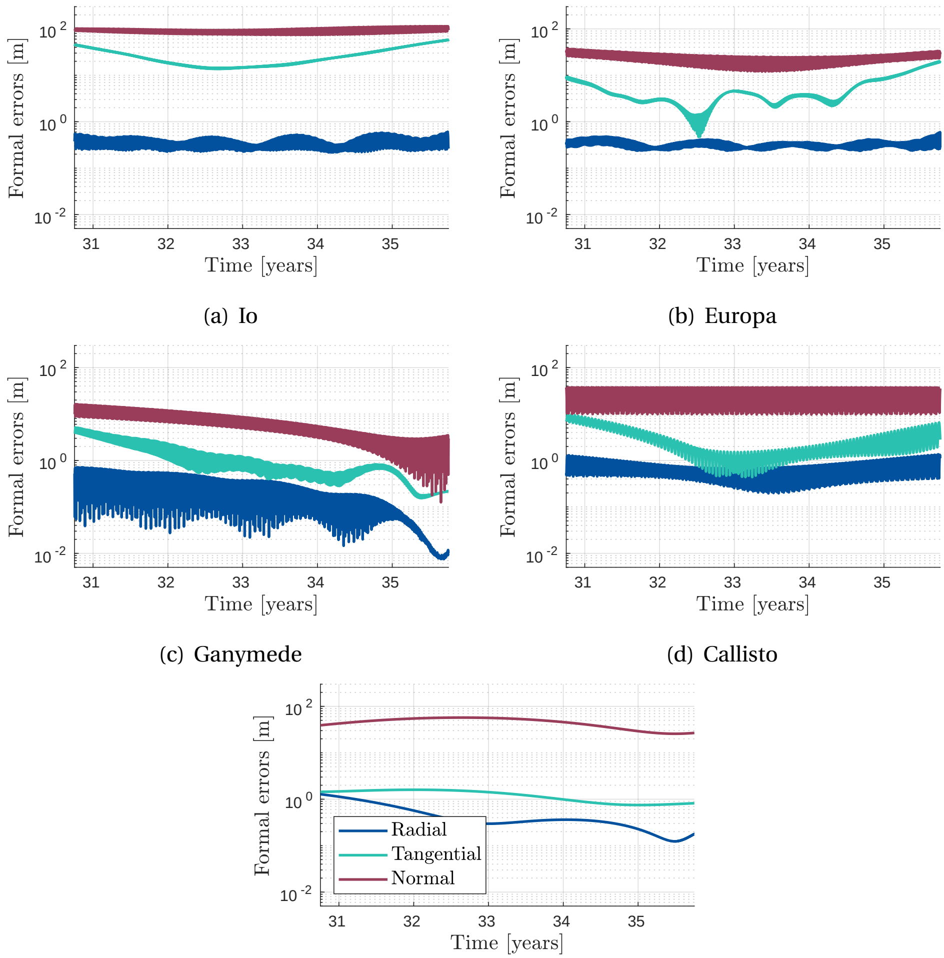

(a) Io (b) Europa (c) Ganymede (d) Callisto (e) Jupiter

Figure 5.4.: Baseline formal errors as a function of time for Jupiter and the Galilean moons' positions, estimated from JUICE's and Europa Clipper's range and Doppler simulated data. For the sake of conciseness, the calendar years are shown without preceeding digits "20".

The formal position uncertainties of our baseline solutions are shown in Fig. 5.4, for both Jupiter and its Galilean satellites. Jupiter's position errors are at the sub-metre level in the radial direction, around 1-2 m for the along-track component and a few tens of metres in the out-of-plane direction. While seemingly small, these errors are not negligible compared to the moons' position uncertainties, confirming the need to account for the Jovian ephemeris error in our estimations (Section 5.3.4). In the moons' solutions, the flybys and orbital phase also yield very low propagated errors. The signature of the Europa Clipper flybys at Europa, and of JUICE orbital phase around Ganymede, are particularly visible. As expected, the in-plane position components show very low uncertainty levels, on average at the metre level for the radial direction and slightly larger (tens of metres) for the tangential position. These directions are well constrained by Doppler and range data, and the improvement achievable with VLBI is therefore expected to be limited. This, however, does not hold for the normal direction, with larger formal uncertainties at around a hundred metres. Good quality VLBI data (good noise case, see Section 5.2.1) are expected to provide measurements of JUICE's lateral position with an accuracy of about 120-200 m. Considering that multiple VLBI data points will be acquired and that the VLBI geometry is mostly sensitive to the normal direction, this suggests that PRIDE could improve the moons' out-of-plane positions.

The results presented in Fig. 5.4 were obtained with the nominal estimation setup. Nonetheless, a baseline covariance analysis was also conducted with range biases as consider parameters, which increased the position errors by a factor five to eight, depending on the moon and direction, compared to Fig. 5.4. For our analyses, the degradation of the baseline solution's accuracy in the out-of-plane direction, where PRIDE VLBI is expected to provide the largest improvement, is particularly relevant. For our purposes, we nonetheless adopted as *nominal* the setup yielding a more optimistic baseline solution, to avoid overestimating the contribution of PRIDE VLBI observables.

5.4.2. VLBI contribution to the global solution

After simulating VLBI measurements of the JUICE spacecraft as described in Section 5.3.2, we added these observables to the radio science estimation. In the following, we describe their contribution to the *global* state solution for the Galilean satellites for different tracking and data quality configurations. The results are summarised in Table 5.5.

We first discuss the GCO phase, during which performing VLBI tracking yields no noticeable improvement. In the best case scenario, the improvement reaches $\sim 8\%$ for certain state parameters, but remain around 1-2 % for most moons' position components. These uncertainty reductions, already negligible, are moreover only achieved in a very optimistic configuration, assuming frequent VLBI tracking sessions (i.e., every week), very dense VLBI outputs (one independent measurement every 2 min) and exceptional data quality (Ka-band noise budget). Consequently, performing VLBI tracking GCO is not worth the negligible improvement it brings to the solution, and we did not consider such tracking options in the rest of our analyses.

Now focussing on VLBI tracking simulated during the flyby phase, Table 5.5 shows the contribution of such observables to the global ephemerides solution for both Jupiter and its moons. The results are expressed as the relative improvement in the propagated position uncertainties with respect to the baseline solution (Fig. 5.4), averaged over the missions' timelines. It must be noted that the error reductions are nearly constant over time, and are therefore adequately represented by the average improvement values provided in Table 5.5. Overall, the sensitivity of the PRIDE VLBI contribution to the adopted tracking settings behaves as expected,

Table 5.5.: Improvement in **averaged** formal position uncertainties (percentage) with respect to the solution obtained with no VLBI, for various VLBI tracking and acquisition scenarios (but VLBI tracking during the flyby phase only). The position errors are computed in the RTN frame, and only improvements larger than 5% are reported.

Cadence VLBI	Noise budget	Jupiter			Io			Europa			Ganymede			Callisto		
		R	T	N	R	T	N	R	T	N	R	T	N	R	T	N
1 h	poor	-	-	-	-	-	-	-	-	-	-	-	-	-	-	-
1 h	good	-	-	7.0	-	-	-	-	-	-	-	-	-	-	-	-
1 h	Ka-band	-	-	7.6	-	-	-	-	-	-	-	-	-	-	-	-
20 min	poor	-	-	7.4	-	-	-	-	-	-	-	-	-	-	-	5.0
20 min	good	-	-	11.5	-	-	-	-	-	-	-	-	-	5.1	10.1	17.1
20 min	Ka-band	-	7.8	17.5	-	-	-	-	-	-	-	-	-	8.8	18.5	33.8
5 min	poor	-	-	10.1	-	-	-	-	-	-	-	-	-	-	7.2	11.8
5 min	good	-	8.4	18.5	-	-	-	-	-	-	-	-	-	9.2	19.7	36.7
5 min	Ka-band	8.7	12.9	31.4	-	-	-	-	-	6.8	-	-	7.5	15.5	28.7	55.2
2 min	poor	-	-	12.4	-	-	-	-	-	-	-	-	-	5.2	11.7	20.7
2 min	good	7.0	10.9	26.6	-	-	-	-	-	5.1	-	-	5.6	13.6	26.1	50.1
2 min	Ka-band	12.5	15.2	40.9	-	-	-	-	-	11.9	-	6.8	12.5	20.1	33.4	65.1

the improvement becoming stronger with increasing measurement cadence and more accurate observations. In particular, more frequent VLBI data points could notably improve the PRIDE VLBI contribution. However, it is yet unclear if such a high measurement cadence is realistically achievable (due to inter-measurements correlations, see Section 5.2.1). Assessing this will require detailed analyses of the statistical properties of real JUICE VLBI data once available. For our preparatory analyses, we consider a VLBI cadence of one data point every 20 minutes as a reasonable scenario.

As suspected, the improvement is the strongest in the normal direction, for Jupiter and Callisto in particular. The limited number of JUICE flybys (or absence thereof) around Europa and Io implies that only few VLBI data points are strongly sensitive to the dynamics of these two moons, explaining the poor VLBI contribution. For Ganymede, the GCO phase yields an extremely accurate baseline solution, which effectively prevents VLBI tracking from notably improving the solution beyond what Doppler and ranging data can already achieve. Furthermore, even for Jupiter and Callisto, adding JUICE VLBI data only brings limited improvement. Their out-of-plane position errors get reduced by about 11.5% and 17.1%, assuming that accurate (good noise case) VLBI measurements can be acquired every 20 minutes. The determination of Callisto's in-plane position, mainly in the along-track direction, also slightly improves upon adding VLBI measurements. This is an indirect effect of a better determination of Jupiter's tangential (and radial) position achieved with VLBI. However, the very weak signal of Callisto's dissipation on its own orbit, mostly noticeable in the along-track direction, will still remain far from detectable in JUICE tracking data, even with VLBI. On the other hand, the observed improvement for Jupiter's dissipation at Callisto's frequency is too limited to noticeably affect our ability to determine whether Callisto is caught in a resonance lock (see Section 5.1).

The above results, which already show very limited VLBI contribution, are furthermore sensitive to the choice of baseline setup and solution. If VLBI biases are not estimated and must be included as consider parameters, adding VLBI measurements actually degrades the moons' state solutions. Remarkably, this still holds when range biases are also treated as consider parameters, i.e., with a more pessimistic baseline solution, which theoretically would leave more improvement margin for PRIDE VLBI. In a consider covariance analysis, the formal errors are automatically raised, by an amount that depends on both the consider parameters covariance and the weights assigned to the observations sensitive to said parameters (see Eq. 5.2). For VLBI biases, the very high accuracy of the VLBI observables yields large weights, such that the consider biases significantly affect the covariance results. This highlights the importance of the VLBI calibrators and, more specifically, of their position uncertainty in the ICRF. This could motivate future observation campaigns to identify more suitable or better characterised radio sources, as will be further discussed in the next section.

5.4.3. Contribution to local state solutions

As mentioned in Section 5.3.3, the reconstruction of a global, coherent solution for the Galilean system's dynamics from real data will require proceeding step-by-step,

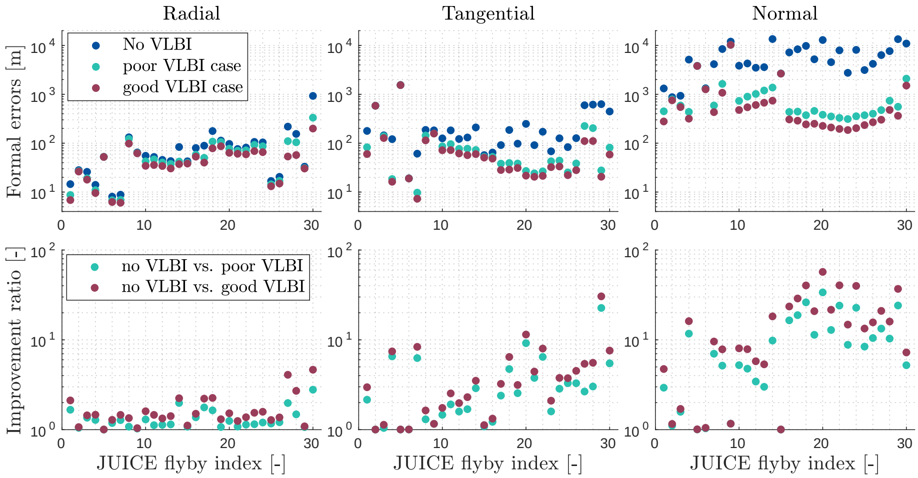

Figure 5.5.: Formal uncertainties for the normal points generated for each of JUICE's 30 flybys, with and without including VLBI measurements (top panels). The bottom panels show the ratio between the baseline errors (without VLBI) and the uncertainties obtained with VLBI.

starting with arc-wise state estimations for both the spacecraft and the moons. The results in Section 5.4.2 indicate that PRIDE VLBI data will have a very limited influence on the quality of the final ephemerides. In this section, we however assess how much PRIDE VLBI will contribute to the process of achieving such a global solution, by quantifying the improvement of the moons' normal points achievable with VLBI data (see more detailed discussion in Section 5.6). The moons' local state uncertainties are actually significantly larger than those achieved with a global estimation. Each flyby is indeed processed independently, without constraining the local solutions for a given moon to form a consistent, single trajectory (Fayolle et al., 2022). The VLBI contribution to the moons' normal points is therefore stronger than for the global estimation, for which the extreme accuracy of the baseline solution limits the margin for further improvement (see Section 5.4.2).

Fig. 5.5 shows the position formal errors obtained for each normal point (per-flyby solution, see Section 5.3.3), with and without VLBI, as well as the improvement ratio between the two solutions. As observed in the global estimation results (Section 5.4.2), VLBI tracking mostly reduces the flyby moon's position in the out-of-plane direction. The VLBI contribution to the flyby moon's normal position only appears negligible for a few flybys, namely flybys 2, 3, 5, 6, 9, and 15. They actually correspond to situations where VLBI measurements cannot be simulated, either because no calibrator is available (see Fig. 5.1) or because the tracking visibility conditions are not met. For the rest of the JUICE flybys, however, VLBI data significantly reduce the normal point uncertainties in the out-of-plane direction, with an averaged improvement ratio of about 10 and 20 for the poor and good

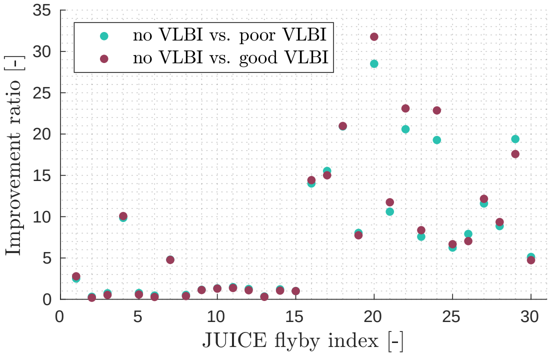

(a) VLBI biases based on original calibrators (see Fig. 5.1).

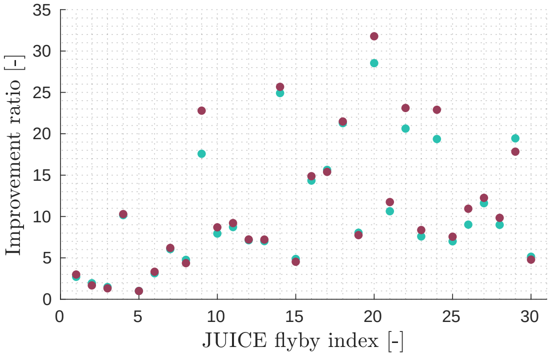

(b) Refined VLBI biases based on artificial, better characterised calibrators.

Figure 5.6.: Improvement ratio of the flyby moon's normal position uncertainty enabled by VLBI tracking, when estimating range biases but including VLBI biases as consider parameters, for different sets of phase calibrators.

VLBI error budgets, respectively. VLBI tracking can also help refine the flyby moon's along-track position, depending on the flyby geometry and accuracy of the baseline solution. Unlike for the moons, the improvement in the spacecraft's local state at each flyby's closest approach is however very limited, reaching at most 30% with the best VLBI noise budget and in the normal direction only.

Focussing on the PRIDE contribution to the moons' state solutions, the good VLBI noise case automatically yields lower uncertainties than the more pessimistic error budget. Nonetheless, the latter can still provide a significant improvement with respect to the baseline solution (see Fig. 5.5, especially for the normal direction). This demonstrates the potential of PRIDE VLBI data as a powerful means to refine our local estimation of the moons' states, irrespective of the measurements accuracy. Section 5.6 will further explore the key role that these more accurate normal points can play in helping us reconstruct a consistent global solution for the moons' dynamics.

Similarly as for the global estimation case (Section 5.4.2), we investigated the sensitivity of our normal point results with respect to the choice of estimation setup. To this end, we re-conducted our analysis while assuming that VLBI biases cannot be estimated and must be accounted for as consider parameters. As expected, this weakens the contribution of PRIDE VLBI to the local flyby moon's states. Fig. 5.6a shows the improvement ratio of the flyby moon's normal position uncertainty achieved with VLBI in such an estimation setup (as in Fig. 5.5, the other two directions show much more limited improvement). In addition to the few above-mentioned flybys with unfavourable VLBI tracking conditions, flybys 8 to 14 now also show negligible improvement. These flybys overlap with the period of the JUICE Jovian tour when the identified phase calibrators are characterised by abnormally poorly constrained ICRF positions (referred to as poor calibrators in the following). Such calibrators yield large systematic VLBI errors for flybys 8 to 15 (Fig. 5.1), which strongly affect the estimation if they cannot be better determined.

We therefore assessed how better-suited calibrators (which could be found with a dedicated campaign, e.g., Duev et al. 2016) would improve the determination of the corresponding normal points. To this end, we substituted the poor calibrators with an artificial one, with a more typical position uncertainty. The latter was set to the average value computed among all suitable calibrators identified over JUICE flyby phase (i.e., all calibrators with a position error lower than 2 nrad in Fig. 5.1). Fig. 5.6b shows how this indeed further improves the solution achieved with VLBI data for flybys 8-15. This further demonstrates the importance of using adequate, and sufficiently characterised radio source as phase calibrators, to avoid introducing systematic errors in our estimation and to maximise the added-value of VLBI tracking.

5

5.5. RESULTS: MULTI-SPACECRAFT IN-BEAM VLBI

This section presents the solution improvement achievable by performing multi-spacecraft VLBI tracking of the JUICE and Europa Clipper spacecraft. Using the 11 flyby combinations identified in Section 5.2.3, we simulated these unique observables and included them in our state estimation. Sections 5.5.1 and 5.5.2 respectively discuss the contribution of multi-spacecraft VLBI to the global ephemerides solution and normal points estimation. We used the same baseline solution as presented in Section 5.4.1.

5.5.1. VLBI CONTRIBUTION TO THE GLOBAL SOLUTION

Table 5.6 presents the relative improvement of the moons' global state solutions achieved with multi-spacecraft tracking VLBI, for the different tracking configurations defined in Section 5.3.2. As with single-spacecraft VLBI, we only provide the average improvement, given that PRIDE VLBI contribution to the propagated errors is almost constant over the missions' duration. As expected, longer tracking arcs and more accurate measurements strengthen the contribution of the multi-spacecraft VLBI

Table 5.6.: Improvement in **averaged** formal position uncertainties (percentage) with respect to the solution obtained with no VLBI, for various multi-spacecraft VLBI tracking scenarios (see Section 5.3.2 and Fig. 5.3). The position errors are computed in the RTN frame, and only improvements larger than 5% are reported.

Tracking arc		**Noise budget**	**Jupiter**			**Io**			**Europa**			**Ganymede**			**Callisto**		
			R	T	N	R	T	N	R	T	N	R	T	N	R	T	N
2×4h	arc bounds	poor	7.8	5.9	41.2	-	-	-	6.9	-	18.8	-	5.1	-	7.4	7.1	7.0
2×4h	mid-arc	poor	9.2	6.0	39.6	10.0	7.3	7.9	7.1	6.3	17.9	6.2	6.4	7.1	8.1	7.2	6.5
2×8h	arc bounds	poor	9.9	7.5	44.1	8.6	7.8	8.4	8.9	7.6	22.5	6.6	7.1	9.4	9.4	9.3	9.8
2×8h	mid-arc	poor	10.7	7.2	42.1	12.8	10.6	13.5	9.3	10.1	26.0	7.4	8.3	11.1	9.4	9.4	9.5
2×12h	arc bounds	poor	10.1	6.9	45.1	11.4	11.5	8.9	10.7	10.0	27.9	7.2	8.5	11.4	9.6	10.4	11.2
2×12h	mid-arc	poor	12.3	8.0	43.7	12.2	12.4	8.1	10.7	10.9	32.5	8.3	9.7	15.1	10.1	10.8	11.4
2×24h	arc bounds	poor	14.0	10.5	50.7	14.6	14.6	10.9	13.3	12.2	34.2	10.2	11.0	15.6	13.2	16.2	20.6
2×24h	mid-arc	poor	16.5	10.0	48.6	13.9	14.8	9.7	13.8	11.7	44.4	12.5	13.2	24.3	13.4	15.6	17.9
Full tracking		**poor**	**18.7**	**11.9**	**51.2**	**16.1**	**16.6**	**12.2**	**16.3**	**13.6**	**47.4**	**15.0**	**15.4**	**28.4**	**15.7**	**18.0**	**21.5**
2×4h	arc bounds	good	13.6	10.3	55.7	6.0	7.9	-	10.3	6.3	31.5	7.9	8.9	10.6	11.2	10.1	9.7
2×4h	mid-arc	good	16.0	10.6	56.1	12.3	10.8	10.1	10.0	8.6	30.5	10.3	10.4	13.4	13.8	13.1	13.2
2×8h	arc bounds	good	16.1	13.4	58.0	12.4	12.3	10.9	12.3	10.5	35.9	10.1	10.9	14.2	13.5	15.1	18.8
2×8h	mid-arc	good	18.8	13.6	58.9	15.2	14.5	15.4	12.9	12.7	40.3	12.7	13.2	19.5	15.2	16.1	18.4
2×12h	arc bounds	good	18.3	16.3	60.4	14.9	15.6	11.8	15.3	12.8	42.8	11.9	12.8	20.4	16.1	18.4	24.3
2×12h	mid-arc	good	20.7	13.9	60.5	14.8	16.2	11.3	14.2	12.6	46.7	14.6	15.3	25.3	16.4	18.8	22.0
2×24h	arc bounds	good	23.8	18.8	65.9	17.7	18.8	13.7	18.4	15.1	50.4	16.9	16.6	28.3	20.0	26.2	37.2
2×24h	mid-arc	good	26.3	18.4	65.3	17.1	19.0	13.8	18.6	14.7	56.6	21.3	19.8	38.2	20.2	25.3	34.0
Full tracking		**good**	**28.5**	**20.1**	**67.6**	**19.2**	**21.1**	**15.2**	**21.3**	**16.4**	**59.1**	**24.5**	**22.4**	**41.5**	**21.8**	**27.4**	**37.5**

5

observables to the solution. In the following, we adopt tracking arcs of 2×8 hours as the nominal configuration. Longer tracking arcs are deemed too optimistic regarding the additional tracking resources that would be required both onboard the spacecraft and on ground. The full tracking configuration covering the entire time gap separating the JUICE and Europa Clipper flybys thus depicts an optimal, yet practically unrealistic tracking scenario, but is merely intended to quantify the strongest improvement possibly achievable.

On average, for identical tracking durations, it first appears more beneficial to acquire multi-spacecraft VLBI measurements in the mid-arc tracking scenario. However, the nominal transmitting sessions are centred around the flybys (Section 5.3.2, Fig. 5.3). For combinations with a rather long time gap between the two flybys (> 1 day), mid-arc tracking might thus require planning a full additional tracking session in-between the two flybys, for both spacecraft, with the necessary resource allocations that this implies. The arc bounds tracking strategy, on the other hand, will exploit the fact that each spacecraft is already transmitting close to its flyby. This approach effectively limits the additional tracking resources with respect to the mid-arc option. Comparing the results of the 2×8 h arc bounds and 2×4 h mid-arc tracking cases in Table 5.6, which require comparable extra resources, we recommend adopting the arc bounds strategy when planning future multi-spacecraft VLBI tracking.

Overall, the contribution of multi-spacecraft VLBI measurements to the moons' global states is stronger than for single-spacecraft VLBI (see Section 5.4.2). This also holds when comparing the results obtained with poor multi-spacecraft and good single-spacecraft VLBI, despite them sharing comparable noise budgets (Tables 5.1 and 5.3). The improvement is particularly strong for Jupiter and Europa. For Europa, the reason for this significant improvement is twofold. First, Europa is involved in 7 out of the 11 flyby combinations during which multi-spacecraft VLBI tracking is performed (Table 5.2). Second, most of these Europa flybys are Europa Clipper flybys, and Europa Clipper's coarser radio science solution leaves more margin for improvement compared to JUICE's. The contribution to Jupiter's state estimation, on the other hand, is an indirect effect of the measurement geometry: by constraining the relative positions of the two spacecraft close to some of their flybys, multi-spacecraft VLBI constrains the moons' relative dynamics in their orbit around Jupiter, which greatly helps refine Jupiter's position.

Unlike in the single-spacecraft VLBI case, our baseline setup, by estimating both range and VLBI biases, yields a rather conservative quantification of the multi-spacecraft VLBI contribution. Systematic VLBI errors are indeed small (Section 5.2.3) and therefore do not strongly affect the solution. However, the improvement attainable with VLBI only gets larger when using a slightly more pessimistic baseline solution such as the one obtained when range biases are not estimated (see Appendix 5.9). The above strengthens the robustness of our findings, hinting that multi-spacecraft VLBI measurements might improve the moons' ephemerides solution further than suggested by Table 5.6, depending on the quality of the baseline solution.

It must moreover be noted that the time elapsed in-between the two flybys is shorter than one day for 3 combinations out of 11 in Table 5.2. For these combinations, multi-spacecraft tracking could be performed without extending the nominal tracking sessions (Section 5.3.2). Interestingly, the solution improvement achievable with these three combinations is not negligible, as shown in Table 5.9 in Appendix 5.10. In the good VLBI noise case, Jupiter and Callisto's normal position errors still get reduced by about 53% and 27%, respectively, against 58% and 36% with all 11 flyby combinations. This result demonstrates that non-negligible improvement could still be achieved with multi-spacecraft VLBI without necessarily requiring extra resources.

Finally, we investigated the role played by the navigation Doppler data simulated during the multi-spacecraft VLBI tracking arcs (see Section 5.3.2). However, they only contributed to estimating the extra empirical accelerations added to our setup to account for the perturbations (e.g., manoeuvres) influencing the spacecraft's orbits over longer arcs. No improvement of the moons' orbit solutions was indeed noticed when adding Doppler navigation data only. The uncertainty reductions reported in Table 5.6 can therefore be confidently attributed to multi-spacecraft VLBI.

5

5.5.2. VLBI CONTRIBUTION TO LOCAL STATE SOLUTIONS

Multi-spacecraft VLBI measurements were also included in the normal points determination, to assess the contribution of such observables to the moons' arc-wise solutions. Fig. 5.7 shows the improvement achieved for the two moons involved in each flyby combination. While the contribution of multi-spacecraft VLBI is again

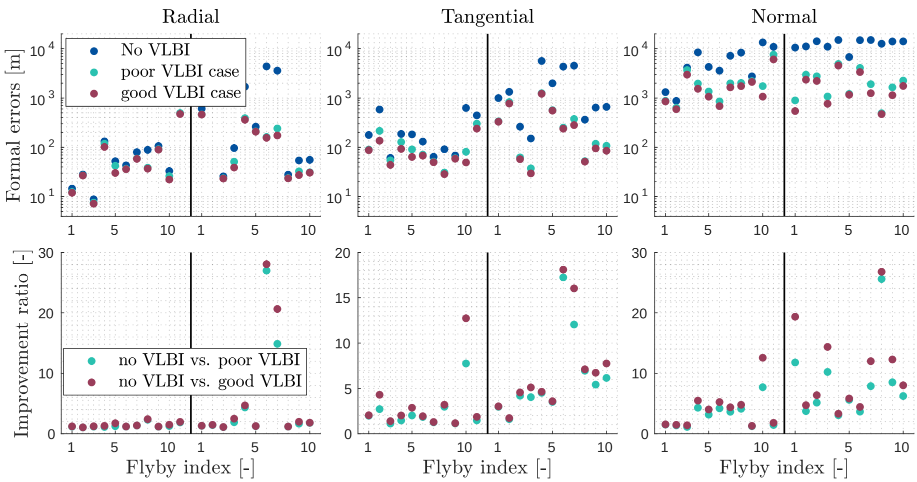

Figure 5.7.: Formal uncertainties for the normal points generated for each of the 11 flyby combinations in Table 5.2, with and without including multi-spacecraft VLBI measurements (top panels). The bottom panels show the ratio between the baseline errors (without VLBI) and the uncertainties obtained with VLBI.

Table 5.7.: Improvement ratio for the flyby moons' position uncertainties (percentage), when adding different VLBI data sets with respect to the baseline estimation (without VLBI). The values reported in this table are averaged over the 11 flyby combinations during which multi-spacecraft tracking is possible (Table 5.2).

	Noise budget	**VLBI data set**	**Improvement ratio**		
			R	T	N
JUICE flybys	poor VLBI	single-spacecraft VLBI	1.4	4.3	8.9
		multi-spacecraft VLBI	1.4	2.3	11.3
		both VLBI	1.7	8.4	17.6
JUICE flybys	good VLBI	single-spacecraft VLBI	1.8	5.8	13.4
		multi-spacecraft VLBI	1.5	3.2	4.0
		both VLBI	2.3	8.4	17.6
Europa Clipper flybys	poor VLBI	single-spaeccraft VLBI	-	-	-
		multi-spacecraft VLBI	5.3	6.2	8.3
		both VLBI	5.4	8.2	17.3
Europa Clipper flybys	good VLBI	single-spacecraft VLBI	-	-	-
		multi-spacecraft VLBI	6.0	7.1	10.7
		both VLBI	6.2	9.5	23.6

the largest for the moons' normal positions, the improvement in this direction is lower than with single-spacecraft VLBI (see Figs. 5.5 and 5.7). On the contrary, however, the reduction of the in-plane position uncertainties is slightly stronger with multi-spacecraft VLBI. On average, the moons' radial and along-track local positions indeed get reduced by more than a factor three and four, respectively, even with the poor VLBI error budget.

This can be explained by the difference in the nature of the observables: while single-spacecraft VLBI provides a direct measure of JUICE's lateral position in the ICRF, multi-spacecraft observations are only sensitive to JUICE and Europa Clipper relative position. They therefore indirectly constrain the relative motion of the flybys' moons, instead of their absolute positions. Consequently, depending on the geometry of the flyby combination, the signature of the moons' out-of-plane positions in the multi-spacecraft VLBI observables is not systematically as strong as it would be for single-spacecraft VLBI. On the other hand, multi-spacecraft tracking might provide slightly tighter constraints on the moons' in-plane motion. This strong dependency on the tracking geometry also explains the variability of the multi-spacecraft VLBI contribution from one flyby combination to another (see Fig. 5.7).

Interestingly, the improvement is much stronger for the central moons of Europa Clipper's flybys than for JUICE's. This logically follows from Europa Clipper's baseline state estimation being less accurate, due to the lower quality of Europa Clipper's tracking (see Section 5.3.2). The uncertainties of the moon's normal points however become comparable between JUICE and Europa Clipper's flybys once multi-spacecraft VLBI is included. Starting from a coarser solution, the relative

5

improvement is thus stronger for the Europa Clipper estimation.

Finally, it should be mentioned that the improvement provided by multi-spacecraft VLBI is not limited to the flyby moons' state solutions, but also extends to the spacecraft orbit determination. On average, multi-spacecraft tracking can lower the spacecraft's position uncertainties at closest approach by about a factor 5, 2.5, and 50 in the radial, tangential, and normal directions, respectively, regardless of the choice of VLBI noise budget. While not the primary focus of our analyses, smaller uncertainty ellipses for the spacecraft's local states might greatly help disentangling mismodelling effects affecting either the spacecraft's or the moons' dynamics, as will be further discussed in Section 5.6.

Overall, the general trends highlighted in Fig. 5.7 for a specific case (8h-long arcs, arc bounds tracking) do not strongly depend on the tracking configuration considered. All tracking setups reported in Table 5.6 for the global estimation were also tested for the normal points determination. Interestingly, unlike what was observed in Section 5.4, simulating multi-spacecraft VLBI tracking close to both flybys, and not in the middle of the arc, yields better results. This can be expected when reconstructing local state solutions at flyby time: the moon's dynamical signature is stronger in tracking measurements acquired immediately before or after the close encounter.

Finally, we also quantified the combined improvement attainable when both single- and multi-spacecraft VLBI observables are included in the estimation. The improvement ratio of the flyby moons' position components with single-spacecraft VLBI only, multi-spacecraft VLBI only, and both types of VLBI are reported in Table 5.7. Adding all VLBI measurements does significantly reduce the normal points' uncertainties for the flyby moons, in all three directions. Given that PRIDE is a JUICE experiment, no single-spacecraft VLBI tracking was considered for the Europa Clipper spacecraft. Remarkably, however, the solution for Europa Clipper's flyby moons notably improves when adding JUICE's nominal tracking measurements to the estimation. This is an indirect effect of the better state solution achieved for JUICE's flyby which, via the constraints provided by the multi-spacecraft tracking measurements, also constrain Europa Clipper's flyby solution. In addition to these quantitative improvements, the synergy between single- and multi-spacecraft VLBI reaches its full potential when exploited to validate the baseline radio science solution(s), as will be explored in Section 5.6.

5.6. PRIDE VLBI as a powerful validation means

While our results indicate that PRIDE VLBI may not significantly contribute to the moons' global state estimation (Sections 5.4.2 and 5.5.1), it can greatly reduce *local* state estimation uncertainties and play a key role in helping us eventually achieve a global solution. As discussed in Section 5.3.3, when reconstructing the dynamics of natural satellites from spacecraft tracking, mismodelling of the spacecraft or moons' dynamics might impede the direct reconstruction of a global solution for the moons' orbits. A global state estimation for the moons indeed requires the spacecraft and moons' dynamical models to be consistent over both short and long timescales (typical flyby duration, i.e., a few hours, vs. entire mission). In particular, combining all available flybys at a given moon in a single solution increases the observation timespan, such that additional perturbations and possibly mismodelled effects become relevant. As mentioned in Section 5.1, such modelling issues led to solution instabilities and eventually prevented the reconstruction of a global ephemeris for Titan and Dione from Cassini flybys' radio science data (Durante et al., 2019; Zannoni et al., 2020).

For JUICE and Europa Clipper radio science analyses, this modelling consistency requirement is even made more severe by the very good accuracy levels for the moons' ephemerides predicted by simulations (Fayolle et al., 2022; Magnanini et al., 2024). For these formal uncertainties to be physically meaningful, our dynamical models should be consistent to the same (sub-meter) level. For the spacecraft's dynamics, this makes the coherent modelling of all spacecraft perturbations essential (manoeuvres, solar radiation pressure, accelerometer errors, etc.). Based on past Cassini data analyses, issues related to specific aspects of the moons' dynamical models will also arise. In particular, the modelling of (frequent-dependent) tidal dissipation in the central planet and the moons, as well as variations of the central planet's gravity field and rotation, are expected to be critical (Durante et al., 2019; Zannoni et al., 2020).

Traditionally, the moons' orbits are first solved for in an arc-wise manner, using the normal points approach mentioned in Section 5.3.3. This strategy is perfectly adapted to gravity field studies (Durante et al., 2019) and moreover circumvents the above-mentioned modelling challenges. It indeed relaxes the modelling requirements by letting the moon's *local* state solution absorb part of the models' inaccuracies (see Fayolle et al., 2022, for a more detailed discussion). When reconstructing the moons' dynamics using a decoupled approach, these normal points (i.e., arc-wise state estimates and their corresponding formal uncertainties) are then used as observables to reconstruct a global solution (see more detail in Fayolle et al., 2022). Generating per-flyby, *local* state solutions for the moons will therefore be an indispensable first step when determining the Galilean moons' ephemerides from JUICE-Europa Clipper radio science. These local state estimations will be the groundwork for gradually progressing towards a global, coupled inversion of the spacecraft and moons' dynamics over the entire mission(s) duration.

By providing an additional set of independent measurements of the spacecraft's lateral position in the ICRF, PRIDE VLBI not only yields an improved local estimation, but can also help us moving from the normal points determination to the reconstruction of a single, consistent solution for the moons' orbits. In the following, we propose an iterative PRIDE-based validation strategy, showing how VLBI data can improve and/or validate the estimation solutions at various stages of this process. Section 5.6.1 first discusses how the refined normal points obtained with VLBI (Sections 5.4.3 and 5.5.2) can be used to detect possible inconsistencies in our models and investigate their possible causes. Capitalising on these local analyses, Section 5.6.2 then presents several validation steps exploiting PRIDE VLBI to facilitate the estimation of a global, coupled solution for the moons' dynamics.

5.6.1. APPLICATION TO THE LOCAL STATE ESTIMATIONS

As shown by our results presented in Sections 5.4.3 and 5.5.2, adding VLBI measurements to the estimation can significantly lower the state uncertainties associated with the moons' normal points. In addition to this promising quantitative improvement, verifying the statistical consistency of the arc-wise state solutions obtained with and without VLBI (Fig. 5.8) can bring valuable insights into the consistency of our models, which might later affect our ability to achieve a global solution.

Detecting inconsistencies between the normal points with and without VLBI would suggest either dynamical mismodelling issues or larger-than-expected systematic VLBI errors. The latter is nonetheless rather unlikely, considering that we will have a good estimate of the expected error budget of our VLBI measurements. Moreover, we should be able to identify such observation errors by analysing our post-fit residuals. In particular, they should manifest themselves as non-flat, incompressible residuals for VLBI observations specifically, not observable for Doppler and/or range measurements. Finally, it must be noted that large systematic errors in the VLBI measurements would most likely be caused by the use of poor calibrators, which can clearly identified (see Fig. 5.1). For the flybys that would show inconsistencies between the normal points with and without VLBI, a detailed characterisation campaign of the radio source used as calibrator can be performed a posteriori (see e.g., Duev et al., 2012). This would yield a better phase calibration, and will allow us to eliminate unexpectedly large systematic biases from our measurements.

After addressing VLBI measurement-related issues, remaining inconsistencies between the refined and nominal normal points (i.e., without and with VLBI, respectively, as illustrated by the right-hand side of Fig. 5.9) can be safely attributed

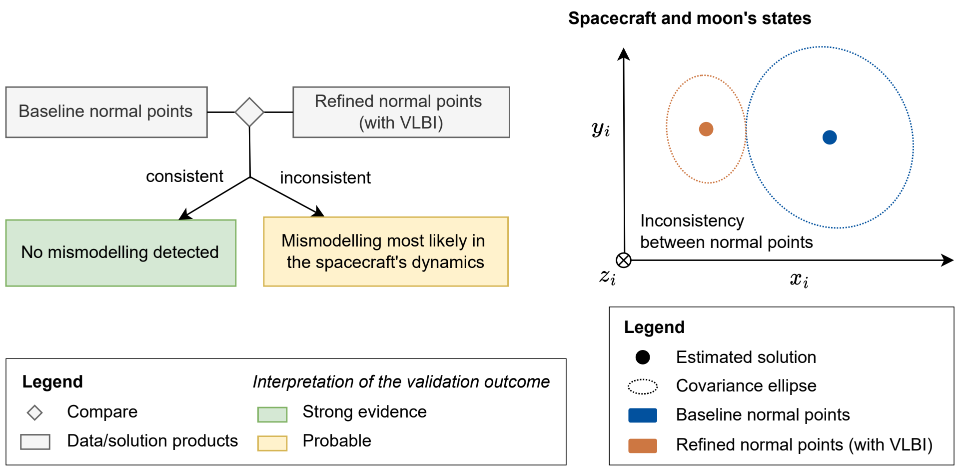

Figure 5.8.: Validation of the statistical consistency between the moons' normal points reconstructed with and without VLBI measurements.

to dynamical modelling issues. Given that the reconstruction of the flybys' normal points does not force the moons' local states to form a single, consistent trajectory, modelling inconsistencies are, at this stage, more likely to originate from the spacecraft's dynamics.

5.6.2. Application to the global state estimation

Following the careful analyses of our local solutions described in Section 5.6.1, the next step is to perform a global, coupled estimation of the moons' dynamics. While such an estimation strategy is expected to yield the most statistically consistent state solution (Fayolle et al., 2022), successfully achieving the above will require proceeding gradually. Provided that instabilities caused by modelling inconsistencies do not prevent us from obtaining such a global solution, modelling errors are still expected to translate into large, non-flat residuals and/or large true-to-formal errors. A fully statistically consistent and robust ephemerides solution for the Galilean moons from classical radio science measurements thus cannot be achieved directly, but can only be attained through an iterative process. This will imply, in particular, detecting and overcoming various inconsistencies and inaccuracies in our models affecting the quality and realism of the solution. In the following, we explore how PRIDE VLBI can facilitate this process, by identifying, isolating, and whenever possible mitigating potential modelling inconsistencies. In the subsequent discussion, we designate by *preliminary* global solution an intermediate global estimation result (without VLBI), obtained when working towards a final, fully consistent solution. This solution corresponds to the nominal estimation setup described in Section 5.3.4.

VLBI as independent measurements

An important first validation step to assess the statistical realism of the *preliminary* global solution is to verify that said solution is compatible with the VLBI measurements of the spacecraft's angular position. As illustrated in Fig. 5.9, the pre-fit VLBI (i.e., *raw* measurements, as in not included in the estimation) should fall within the error ellipse defined by the preliminary global solution's covariance. As the VLBI data are not yet included in the estimation, they are only affected by the measurement error, and not by potential dynamical mismodelling. A discrepancy between the VLBI measurements and the preliminary global solution would thus indicate either an unquantified systematic bias in the VLBI data (see Section 5.6.1), or issues in the global estimation (e.g., large true-to-formal errors ratio).

Relatively large true-to-formal error ratios can be expected when reconstructing natural satellites' ephemerides from radio science, compared to astrometry-based solutions. The observational constraints on the moons' dynamics, derived from spacecraft tracking measurements, are indeed indirect in nature. Estimations of physical parameters from tracking data are thus affected by modelling inacccuracies in the spacecraft's dynamics, and therefore typically show larger true-to-formal error ratios. Based on previous radio science estimations of e.g., natural bodies' gravity fields and rotations, ratios of about 10 can be expected (e.g., Milani et al., 2001; Konopliv et al., 2011; Mazarico et al., 2015). Last but not least, as previously

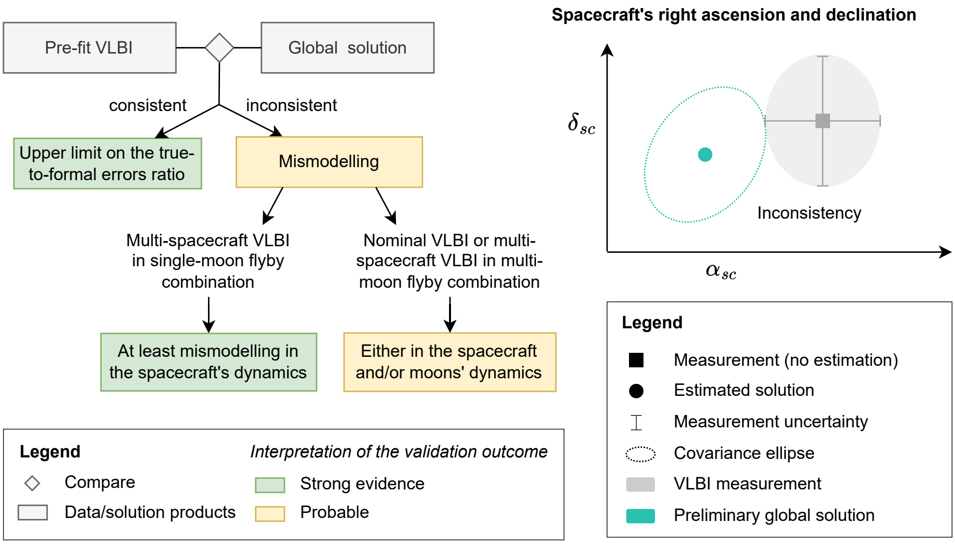

Figure 5.9.: Comparison between a preliminary global solution (without VLBI) and the pre-fit VLBI measurements to detect or quantify possible inconsistencies in the estimation.

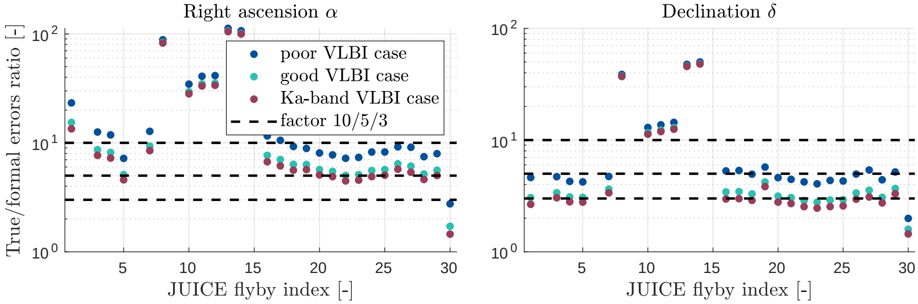

Figure 5.10.: Detection threshold for possible inconsistencies between the global solution (without VLBI) and the single-spacecraft pre-fit VLBI measurements, expressed as the minimum true-to-formal error ratio required for such discrepancies to be detectable.

mentioned, determining the moons' orbits from radio science imposes to consistently model the dynamics of both the spacecraft and moons, a requirement even more stringent for JUICE and Europa Clipper analyses due to the expected low formal uncertainties (Fayolle et al., 2022). In our analyses, we thus considered three, five, and ten as a realistic range of true-to-formal errors ratios. Any detection threshold comparable to or lower than these ratios indicates that VLBI tracking might be realistically sensitive to possible inconsistencies in the preliminary global solution,

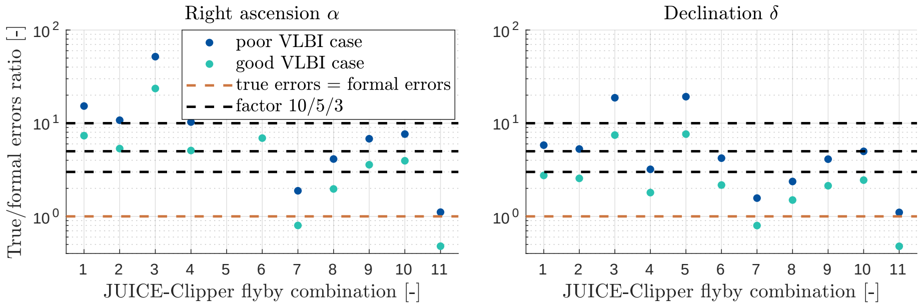

Figure 5.11.: Detection threshold for possible inconsistencies between the global solution (without VLBI) and the multi-spacecraft pre-fit VLBI measurements, expressed as the minimum true-to-formal error ratio required for such discrepancies to be detectable.

or at least provide an upper limit on the true errors for the moons' states.

To quantify the probability that VLBI data can detect discrepancies between true and formal errors, we projected the error ellipse of the spacecraft's position given by the preliminary global solution onto the plane-of-the-sky, to be compared with the expected VLBI measurement uncertainty. As illustrated in Fig. 5.9, we could then determine the minimum true estimation errors in JUICE's right ascension and declination for the global solution **not to overlap** with the VLBI measurement. In practice, a discrepancy can be detected if the estimated solution, within the confidence region statistically described by its formal uncertainties, is not consistent with the VLBI measurement, even when accounting for the uncertainty of the latter. This imposes a limit on the *minimum* true estimation error required for the VLBI observable to detect a possible inconsistency, referred to as the discrepancy detection threshold in the following.

We computed this threshold for each flyby, both for single- and multi-spacecraft VLBI tracking (Figs. 5.10 and 5.11, respectively). For the former, we compare the uncertainty in JUICE's right ascension and declination predicted by the global estimation (without VLBI) with the expected VLBI accuracy. The use of multi-spacecraft VLBI for validation is nearly identical, except that we focus on the *relative* lateral position of JUICE and Europa Clipper with respect to each other. Figs. 5.10 and 5.11 show, for each flyby or flyby combination, the ratio between the true and formal errors in the spacecraft's right ascension and declination corresponding to the discrepancy detection threshold defined above. A threshold value equivalent to a realistic true-to-formal errors ratio for our analyses (see discussion above) indicates that VLBI measurements can be meaningfully used to investigate possible inconsistencies in the estimation.

Fig. 5.10 shows that single-spacecraft VLBI tracking could meaningfully contribute to validating the preliminary global solution for most flybys. Assuming the worst VLBI error budget and a true-to-formal errors ratio equal to ten, PRIDE VLBI could detect inconsistencies in JUICE's right ascension for 14 out of 30 flybys. For JUICE's declination, the discrepancy detection threshold is lower, and an estimation error only five times larger than the formal uncertainty would be detectable for half of the flybys. Improving the VLBI precision would lower this threshold further: in the good error budget case, VLBI data would be sensitive to any true-to-formal error ratio larger than three in declination for flybys 20 to 30. Interestingly, the detection level is rather consistent between the different flybys, with the exception of flybys 8-15 with poor VLBI calibrators (see Fig. 5.1 and discussion in Section 5.4).

Fig. 5.11 highlights similar validation opportunities for multi-spacecraft VLBI tracking, for the 11 possible flyby combinations identified in Section 5.2.3. As in the single-spacecraft VLBI case, inconsistencies in declination will be easier to detect: a true-to-formal error ratio of three should be detectable for 9 out of 11 combinations, in the good VLBI error case. The slightly larger variability of the detection threshold compared to Fig. 5.10 can be explained by the relative nature of multi-spacecraft VLBI tracking: how the accuracy of such measurements compares to the preliminary solution depends on the relative geometry of JUICE and Europa Clipper, and on whether part of the preliminary solution's uncertainties cancel out when computing the error ellipse for the two spacecraft's relative right ascension and declination.

Overall, our results show that pre-fit VLBI will be able to detect inconsistencies in the preliminary global solution for a number of flybys and/or flyby combinations, provided that the true errors are large enough with respect to the formal uncertainties. Alternatively, detecting no discrepancy would demonstrate the realism of the estimation solution, and allow us to put an upper limit on the true-to-formal error ratio.

In most cases, the validation step described above will however not be sufficient to precisely identify the source of the potential inconsistencies, if detected. A notable exception, highlighted in Fig. 5.9, arises for multi-spacecraft VLBI acquired during a single-moon flyby combination (flyby combinations 3, 5, 7, and 8, see Table 5.2). In such a tracking configuration, the VLBI data points are almost insensitive to the moon's state estimation, except for the possible slight change in the moon's position error during the time elapsed between the JUICE and Europa Clipper flybys. This effect, however, is deemed small, especially for flybys combination 3 in which only three hours separate the two flybys around Europa. The outcome of our first validation step for these single-moon flyby combinations will therefore primarily depend on the consistency of the spacecraft's orbit solution. As such, they will represent a unique opportunity to isolate modelling issues affecting the spacecraft's dynamics.

Comparing local and global solutions

Finally, the state solution provided by the global estimation at the time of a flyby i should be statistically compatible with the corresponding normal point. As shown in Sections 5.4.3 and 5.5.2, VLBI tracking, either in single or multi-spacecraft configuration, can significantly reduce the uncertainty ellipses of the moons' normal points. This enhances the potential of this local vs. global state estimation comparison, by facilitating the detection of possible inconsistencies. The refined arc-wise solutions, with reduced uncertainties, indeed become sensitive to much

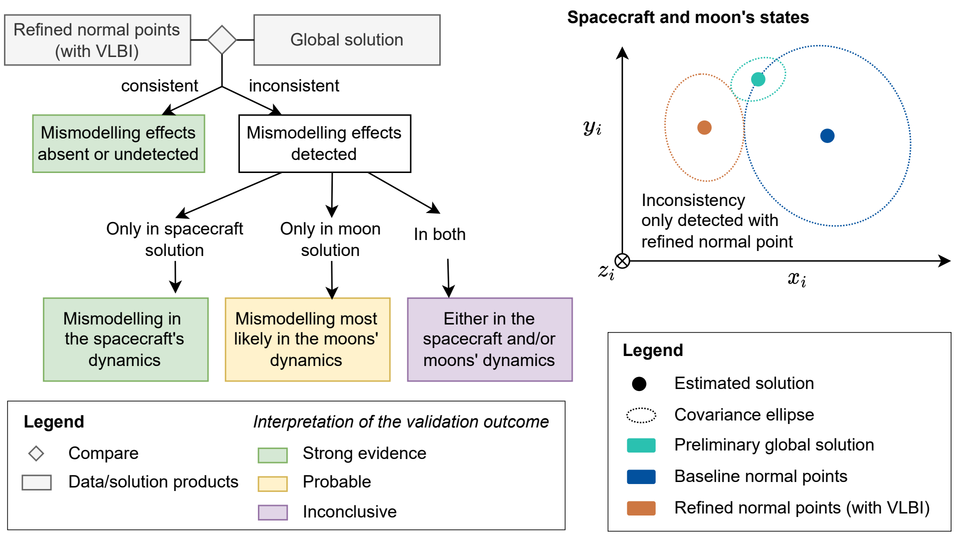

Figure 5.12.: Validation strategy exploiting the moons' refined normal points obtained with VLBI to detect possible inconsistency in a global preliminary solution.

smaller discrepancies (see Fig. 5.12).

As in the previous validation steps, the main challenge is to identify the source of the observed discrepancies. Our ability to do so will strongly depend on the state parameters concerned by the said inconsistencies (see Fig. 5.12). The arc-wise state solutions for the spacecraft and the moons can be analysed separately to try disentangling different mismodelled effects. If inconsistencies are only detected in the spacecraft's state solution, they are more likely to originate from mismodelling of the spacecraft dynamics, while the opposite is true for the moons' solution. However, no firm conclusion can be drawn if the discrepancies concern both the spacecraft and moons' solutions.

Critically, the outcomes of this validation step must be considered in light of previous results. As described in Section 5.6.1, we should be able to eventually discriminate between VLBI systematic errors and dynamical mismodelling effects. Furthermore, combining the different tests described above (Figs. 5.9 and 5.12) will help further isolate modelling issues specifically affecting the spacecraft or moons' dynamics. We will moreover be able to confirm our conclusions by exploiting the unique potential of multi-spacecraft VLBI in the four single-moon flyby combinations identified in Table 5.2, as such measurements will be robust against errors in the moons' state solutions.

5.7. CONCLUSION

Building on the previous work by Dirkx et al. (2017), we investigated the contribution of PRIDE VLBI to the Galilean moons' ephemerides solution, in the context of the JUICE and Europa Clipper missions. We considered both a global and local state estimation, the latter representing a necessary intermediate step to eventually achieve a coherent solution for the moons' dynamics over the entire missions' timeline. We simulated *single-spacecraft* VLBI measurements of the JUICE spacecraft, but also explored the possibility to perform simultaneous VLBI tracking of JUICE and Europa Clipper (multi-spacecraft VLBI). We quantified the contribution of both types of VLBI data to the moons' global and local state estimations, under various tracking and data quality scenarios.

Overall, both single- and multi-spacecraft VLBI measurements do not significantly improve the *global* ephemerides solution for the Galilean moons, the contribution of the latter nonetheless being stronger. For realistic tracking configurations, the improvement provided by single- and multi-spacecraft VLBI can reach up to 17% (for Callisto) and 36% (for Europa), respectively, assuming good VLBI data quality. The attainable improvement is severely limited by the very accurate baseline solution already achieved with range and Doppler data.

It must be noted that our single-spacecraft VLBI results proved rather sensitive to systematic errors in the VLBI measurements. For each tracking pass, the position error of the selected phase calibrator can thus have a significant influence, as highlighted in Fig. 5.6. This could, however, be mitigated in various ways. Our results indeed motivate future campaigns to densify the phase reference calibrators currently identified within the required patch of the sky, or to refine our knowledge of the ICRF position of known calibrators. In particular, we identified a specific period, overlapping with 8 out of 30 JUICE flybys, during which finding better calibrators would be critical to performing high-quality PRIDE observations (see Section 5.2.2). The lack of suitable calibrators in Ka-band also calls for dedicated reference source densification campaigns. Alternatively, one could exploit the fact that some tracking arcs rely on the same calibrator, as extracting a common bias over several arcs will be easier. It might moreover be possible to reduce VLBI errors by using multiple visible phase calibrators during a single pass. However, properly assessing both the feasibility and actual potential of such a strategy would require dedicated further analyses.

The possible contribution of PRIDE VLBI is moreover not limited to a quantitative improvement of the state estimation. For each flyby, the local estimation of the central moon's state (i.e., normal point) represents an essential step before a global, fully consistent solution can be reconstructed from all flybys combined. The contribution of PRIDE VLBI to the flyby moons' normal points is much stronger than for the global ephemerides solution. This is most noticeable in the out-of-plane direction where poor-quality single- and multi-spacecraft VLBI data respectively reduce the position uncertainty by a factor 10 and 6 on average. This highlights the crucial role that PRIDE VLBI can play in the progression towards a global solution for the moons' dynamics.

VLBI also offers multiple opportunities to validate and improve the statistical realism of the baseline solution derived from classical radio science observables. To exploit this potential, we have designed a PRIDE VLBI-based validation plan, which exploits two features of the VLBI data set. First, PRIDE provides *independent* measurements, which the baseline solution can be compared against. Second, the ability of VLBI data to reduce the moons' local state uncertainties will facilitate the detection of possible inconsistencies in the estimation. In particular, the careful analysis of the observation residuals and state estimation solutions in different configurations will help disentangle inconsistency sources, from observation errors to various dynamical modelling discrepancies. The unique geometry of multi-spacecraft tracking VLBI data acquired when both JUICE and Europa Clipper are performing a flyby around the same moon will be particularly valuable to isolate specific mismodelling issues.

PRIDE VLBI will therefore greatly contribute to overcoming dynamical modelling issues in the estimation, gradually working towards the very low uncertainty levels predicted by simulations for the moons' ephemerides and the Jovian system's tidal dissipation parameters (e.g., Fayolle et al., 2023b; Magnanini et al., 2024). As such, PRIDE will play an indirect, yet crucial, role in the reconstruction of an unprecedentedly accurate and fully consistent solution for the Galilean moons' dynamics, essential to further our understanding of the Galilean system's long-term evolution.

5

5.8. CONCURRENT STATE ESTIMATION OF A CENTRAL PLANET AND ITS SATELLITE(S) FROM SEVERAL ORBITING SPACECRAFT

As mentioned in Section 5.3.3, our global estimation setup follows the coupled model described in Fayolle et al. (2022). We recall that the states of the moons are then determined globally, while the spacecraft's dynamics are solved for in an arc-wise manner. In this appendix, we expand the mathematical formulation provided in Fayolle et al. (2022) to include the central planet (here Jupiter) in the estimation and to account for several spacecraft (here JUICE and Europa Clipper).

In this more complete configuration, additional implementation subtleties arise when handling the various central body dependencies. The different bodies and spacecraft's states are indeed typically expressed and estimated with respect to their central body, which might be included in the propagation. The full state vector is defined as

$$\mathbf{y}(t) = \begin{pmatrix} \mathbf{y}_P(t) \\ \mathbf{y}_M(t) \\ \mathbf{y}_{S_1}(t) \\ \vdots \\ \mathbf{y}_{S_N}(t) \end{pmatrix}. \tag{5.4}$$

$\mathbf{y}_P(t)$ refers to the central planet's state. $\mathbf{y}_M(t)$ is the moons' state vector with respect to the central planet, of size $6 \times n$ with n the number of moons. Finally, $\mathbf{y}_{S_i}(t)$

represents the state of the i^{th} spacecraft with respect to its arc-wise central moon $m_{i,j}$. N is the number of spacecraft involved in the estimation (equal to 2 in our analyses).

The full initial state vector to be estimated can thus be written as follows:

$$\mathbf{y}_0 = \begin{pmatrix} \mathbf{y}_P(t_0) \\ \mathbf{y}_M(t_0) \\ \mathbf{y}_{S_1}(\mathbf{t}_{S_1}) \\ \vdots \\ \mathbf{y}_{S_N}(\mathbf{t}_{S_N}) \end{pmatrix} \tag{5.5}$$

where $\mathbf{t}_{S_i}$ contains the arc-wise reference epochs for spacecraft S_i. The spacecraft's states being estimated in an arc-wise manner, their initial state vector can be further expanded:

$$\mathbf{y}_{S_i}(\mathbf{t}_{S_i}) = \begin{pmatrix} \mathbf{y}_{S_i,1}(t_{S_i,1}) \\ \vdots \\ \mathbf{y}_{S_i,a_1}(t_{S_i,a_i}) \end{pmatrix}, \tag{5.6}$$

5

with a_i the number of arcs over which spacecraft S_i is propagated, and $t_{S_i,j}$ the reference epoch of arc j.

However, the equations of motion and variational equations are generally propagated in a single reference frame. States expressed in this global propagation reference frame will be designed by the superscript $\star$ in the following. In contrast to Eq. 5.4, the *propagated* state can be defined as

$$\mathbf{y}^\star(t) = \begin{pmatrix} \mathbf{y}_P^\star(t) \\ \mathbf{y}_M^\star(t) \\ \mathbf{y}_{S_1}^\star(t) \\ \vdots \\ \mathbf{y}_{S_N}^\star(t) \end{pmatrix}. \tag{5.7}$$

The propagated and estimated states can be related using the following:

$$\mathbf{y}_P(t) = \mathbf{y}_P^\star(t) \tag{5.8}$$

$$\mathbf{y}_M(t) = \mathbf{y}_M^\star(t) + \mathbf{y}_P^\star(t) \tag{5.9}$$

$$\mathbf{y}_{S_i}(t) = \mathbf{y}_{S_i}^\star(t) + \mathbf{y}_{m_{i,j}}^\star(t), \text{with } t \in \left[t_{S_i,j}; \tilde{t}_{S_i,j}\right] \tag{5.10}$$

with $m_{i,j}$ the central moon of spacecraft S_i during arc j. $t_{S_i,j}$ and $\tilde{t}_{S_i,j}$ respectively represent the start and end times of arc j for spacecraft S_i.

In our analyses, the covariance matrix $\mathbf{P}$ describes the uncertainties and correlations of the state parameters with respect to their respective central bodies, according to Eq. 5.4. To compute $\mathbf{P}$ using Eq. 5.1, the observation matrix $\mathbf{H}$ must first be computed to obtain the covariance matrix:

$$\mathbf{H}(\mathbf{q}) = \frac{\partial \mathbf{h}(\mathbf{q})}{\partial \mathbf{q}}, \tag{5.11}$$

with $\mathbf{h}$ the observations vector and $\mathbf{q}$ the parameters vector, which can be written as $\mathbf{q} = [\mathbf{y}_0, \mathbf{p}]^T$. $\mathbf{y}_0$ is the initial state given by Eq. 5.5, and $\mathbf{p}$ contains the non-state parameters. Focusing on the estimation of the initial state, we can then write, for a single observation:

$$\frac{\partial h(\mathbf{q})}{\partial \mathbf{y}_0} = \frac{\partial h(\mathbf{q})}{\partial \mathbf{y}_0^\star}\frac{\partial \mathbf{y}_0^\star}{\partial \mathbf{y}_0}, \tag{5.12}$$

$$= \frac{\partial h(\mathbf{q})}{\partial \mathbf{y}^\star(t)}\mathbf{\Phi}^\star(t, t_0, \mathbf{t}_{S_1}, \ldots, \mathbf{t}_{S_N})\frac{\partial \mathbf{y}_0^\star}{\partial \mathbf{y}_0}. \tag{5.13}$$

$\frac{\partial h(\mathbf{q})}{\partial \mathbf{y}^\star(t)}$ and $\Phi^\star(t, t_0, \mathbf{t}_{S_1}, \ldots, \mathbf{t}_{S_N})$ can be computed after propagating the variational equations with respect to the global propagation reference frame, while $\frac{\partial \mathbf{y}_0^\star}{\partial \mathbf{y}_0}$ can be derived from Eq. 5.10. It must be noted that $\Phi^\star(t, t_0, \mathbf{t}_{S_1}, \ldots, \mathbf{t}_{S_N})$ is equivalent to the state transition matrix $\Phi(t, t_0)$ in Eq. 5.3. A less detailed notation was indeed adopted in the core part of the paper for the sake of conciseness.

Finally, the propagated covariance is given by

$$\mathbf{P}(t) = \left(\frac{\partial \mathbf{y}(t)}{\partial \mathbf{y}_0}\right)\mathbf{P}\left(\frac{\partial \mathbf{y}(t)}{\partial \mathbf{y}_0}\right)^T. \tag{5.14}$$

The partials in Eq. 5.14 must again be re-written with respect to the *propagated*, and not *estimated*, state:

$$\frac{\partial \mathbf{y}(t)}{\partial \mathbf{y}_0} = \frac{\partial \mathbf{y}(t)}{\partial \mathbf{y}^\star(t)}\frac{\partial \mathbf{y}^\star(t)}{\partial \mathbf{y}_0^\star}\frac{\partial \mathbf{y}_0^\star}{\partial \mathbf{y}_0} \tag{5.15}$$

$$= \frac{\partial \mathbf{y}(t)}{\partial \mathbf{y}^\star(t)}\mathbf{\Phi}^\star(t, t_0)\frac{\partial \mathbf{y}_0^\star}{\partial \mathbf{y}_0}. \tag{5.16}$$

Again, $\frac{\partial \mathbf{y}(t)}{\partial \mathbf{y}^\star(t)}$ and $\frac{\partial \mathbf{y}_0^\star}{\partial \mathbf{y}_0}$ can be extracted from Eq. 5.10.

This small model extension completes the coupled estimation formulation provided in Fayolle et al. (2022). The main addition is the possibility to include the central planet's state in the estimation, which allows us to account for the Jovian ephemeris uncertainty in our analyses (Section 5.3.4). The proposed implementation can however be applied to any planetary system and is versatile enough to accommodate any number of moons or spacecraft.

5.9. MULTI-SPACECRAFT VLBI CONTRIBUTION TO THE GLOBAL SOLUTION WITH DIFFERENT ESTIMATION SETUPS

As discussed in Section 5.5.1, our choice of baseline estimation setup - estimating both range and VLBI biases - leads to a conservative estimate of the global solution improvement attainable with multi-spacecraft VLBI. For the sake of completeness,

Table 5.8.: Improvement in **averaged** formal position uncertainties (percentage) with respect to the solution obtained with no VLBI, for various multi-spacecraft VLBI tracking scenarios. The position errors are computed in the RTN frame, and only improvements larger than 5% are reported. We chose this low threshold value for this table to better support our discussion on the influence of the tracking configuration).

Tracking arc	Noise budget	Jupiter R	Jupiter T	Jupiter N	Io R	Io T	Io N	Europa R	Europa T	Europa N	Ganymede R	Ganymede T	Ganymede N	Callisto R	Callisto T	Callisto N
Range and VLBI biases estimated																
2×8h arc bounds	poor	9.9	7.5	44.1	8.6	7.8	8.4	8.9	7.6	22.5	6.6	7.1	9.4	9.4	9.3	9.8
16h mid-arc	poor	10.7	7.2	42.1	12.8	10.6	13.5	9.3	10.1	26.0	7.4	8.3	11.1	9.4	9.4	9.5
Full tracking	poor	18.7	11.9	51.2	16.1	16.6	12.2	16.3	13.6	47.4	15.0	15.4	28.4	15.7	18.0	21.5
2×8h arc bounds	good	16.1	13.4	58.0	12.4	12.3	10.9	12.3	10.5	35.9	10.1	10.9	14.2	13.5	15.1	18.8
16h mid-arc	good	18.8	13.6	58.9	15.2	14.5	15.4	12.9	12.7	40.3	12.7	13.2	19.5	15.2	16.1	18.4
Full tracking	good	28.5	20.1	67.6	19.2	21.1	15.2	21.3	16.4	59.1	24.5	22.4	41.5	21.8	27.4	37.5
Range and VLBI biases considered																
2×8h arc bounds	poor	16.9	16.1	55.8	8.0	7.0	17.0	-	11.2	34.2	10.2	13.5	11.4	23.0	23.4	23.0
16h mid-arc	poor	22.3	19.5	59.5	-	7.6	19.7	-	11.2	36.1	14.0	15.8	13.7	25.6	26.2	25.1
Full tracking	poor	38.5	31.8	71.7	12.3	13.9	20.5	12.3	17.5	54.7	27.7	26.8	35.1	37.1	40.4	43.4
2×8h arc bounds	good	24.4	23.9	63.2	10.9	11.2	21.5	-	14.8	46.4	15.7	18.4	19.2	28.6	29.4	30.2
16h mid-arc	good	30.4	27.2	67.3	7.0	11.8	23.0	-	14.6	49.5	20.6	21.2	21.9	31.3	32.4	32.9
Full tracking	good	47.8	38.5	79.6	17.6	19.1	26.6	20.0	21.7	68.6	34.5	32.4	51.2	42.5	47.4	52.8

Table 5.9.: Improvement in **averaged** formal position uncertainties (percentage) with respect to the baseline solution. The results are obtained in the arc bounds tracking configuration (tracking arcs of 8h), exploiting different subsets of the flyby combinations in Table 5.2. Only improvements larger than 5% are reported.

Time limit in-between flybys	Noise budget	Jupiter R	Jupiter T	Jupiter N	Io R	Io T	Io N	Europa R	Europa T	Europa N	Ganymede R	Ganymede T	Ganymede N	Callisto R	Callisto T	Callisto N
3 days (Table 5.6)	poor	9.9	7.5	44.1	8.6	7.8	8.4	8.9	7.6	22.5	6.6	7.1	9.4	9.4	9.3	9.8
1 day	poor	5.9	-	35.4	-	-	7.0	-	4.8	13.4	-	-	-	5.4	-	-
3 days (Table 5.6)	good	16.1	13.4	58.0	12.4	12.3	10.9	12.3	10.5	35.9	10.1	10.9	14.2	13.5	15.1	18.8
1 day	good	11.3	8.0	52.9	5.0	7.0	8.8	7.1	7.1	26.8	6.2	7.3	9.2	8.4	5.9	-

we ran the same analysis while including range and VLBI biases as consider parameters. The results are reported in Table 5.8 for a limited number of tracking configurations, and indeed show larger improvements than with the baseline setup. Only Io and Europa's in-plane position uncertainties slightly degrade when adding range and VLBI biases as consider parameters instead of estimating them. This can be explained by the fact that Europa's solution, and thus indirectly Io's, strongly rely on Europa Clipper radio science (i.e., Doppler only, Section 5.3.2). The baseline solution for these components is thus less sensitive to range biases, and only the VLBI contribution is notably affected by the change of estimation setup. However, for the rest of the state parameters, the VLBI improvement strengthens when the observation biases are not estimated, due to the deterioration of the baseline solution. Overall, as mentioned in Section 5.5.1, our results indicate that a stronger contribution could possibly be expected from multi-spacecraft VLBI measurements, depending on the accuracy of the baseline solution.

5.10. MULTI-SPACECRAFT VLBI CONTRIBUTION TO THE GLOBAL SOLUTION FOR DIFFERENT SETS OF FLYBY COMBINATIONS

11 flyby combinations were identified as representing promising opportunities to perform multi-spacecraft VLBI tracking (Section 5.2.3, Table 5.2). An upper threshold of three days between each JUICE flyby and the closest Europa Clipper flyby was applied. However, as discussed in Section 5.5.1, such an elapsed time in-between the two flybys would require extending the nominal tracking sessions and thus be more resource-demanding. Interestingly, the JUICE and Europa Clipper flybys are planned less than one day apart for three combinations (Table 5.2), such that multi-spacecraft VLBI could be acquired at minimal expense, without extending the nominal tracking arcs. Table 5.9 compares the solution improvement achieved when simulating multi-spacecraft VLBI either during all 11 combinations, or just during the above-mentioned three combinations with close flybys. The results are discussed in Section 5.5.1.

6

MUTUAL APPROXIMATIONS FOR EPHEMERIDES DETERMINATION

M. S. FAYOLLE, D. DIRKX, P. N. A. M. VISSER, V. LAINEY

The apparent close encounters of two satellites in the plane of the sky, called mutual approximations, have been suggested as a different type of astrometric observation to refine the moons' ephemerides. The main observables are then the central instants of the close encounters, which have the advantage of being free of any scaling and orientation errors. However, no analytical formulation is available yet for the observation partials of these central instants, leaving numerical approaches or alternative observables (i.e., derivatives of the apparent distance instead of central instants) as options. Filling that gap, this paper develops an analytical method to include central instants as direct observables in the ephemerides estimation and assesses the quality of the resulting solution. To this end, the apparent relative position between the two satellites is approximated by a second-order polynomial near the close encounter. This eventually leads to an expression for mutual approximations' central instants as a function of the apparent relative position, velocity, and acceleration between the two satellites. The resulting analytical expressions for the central instant partials were validated numerically. In addition, we ran a covariance analysis to compare the estimated solutions obtained with the two types of observables (central instants versus alternative observables), using the Galilean moons of Jupiter as a test case. Our analysis shows that alternative observables are almost equivalent to central instants in most cases. Accurate individual weighting of each alternative observable, accounting for the mutual approximation's characteristics (which are automatically

An earlier version of this chapter is published in Astronomy & Astrophysics (Fayolle et al., 2021): Fayolle, M., Dirkx, D., Visser, P. N. A. M., & Lainey, V. (2021). Analytical framework for mutual approximations-Derivation and application to Jovian satellites. Astronomy & Astrophysics, 652, A93.

included in the central instants' definition), is however crucial to obtain consistent solutions between the two observable types. Using central instants still yields a small improvement of 10-20% of the formal errors in the radial and normal directions (RSW frame), compared to the alternative observables' solution. This improvement increases when mutual approximations with low impact parameters and large impact velocities are included in the estimation. Choosing between the two observables thus requires careful assessment, taking into account the characteristics of the available observations. Using central instants over alternative observables ensures that the state estimation fully benefits from the information encoded in mutual approximations, which might be necessary depending on the application of the ephemeris solution.

6.1. Introduction

Natural satellites are among the most fascinating objects in our Solar System. In particular, leading candidates for extraterrestrial habitats are found among Jovian and Saturnian satellites. Knowing more about the past history of these moons is key to understanding whether they offer life-favourable conditions now and, therefore, to analysing the conditions for habitability in our Solar System and beyond (Marion et al., 2003; Parkinson et al., 2008; Lunine, 2017). However, the moons' origin and evolution still remain poorly understood, while they are crucial to investigate the existence and stability of these putative habitats (e.g., Crida and Charnoz, 2012; Ćuk et al., 2016; Fuller et al., 2016).

6

Measuring and fitting the current motion of natural satellites provides valuable insights into their dynamical history. In particular, it helps to understand tidal dissipation mechanisms, which play a crucial role in planetary systems' orbital evolution (Lainey et al., 2009, 2012, 2020; Fuller et al., 2016). More generally, determining natural satellites' dynamics indirectly gives hints about planetary formation processes (e.g., Heller et al., 2015; Samuel et al., 2019).

As our interest in natural satellites grows, more dedicated missions are being proposed to explore them (JUICE, Europa Clipper, IVO, MMX, etc.). Precise knowledge of the moons' current states then also becomes crucial to optimise the orbital design of such missions, for instance to propose efficient orbital insertions and flybys (Murrow and Jacobson, 1988; Raofi et al., 2000; Lynam and Longuski, 2012). Due to inaccuracies in the predicted state of the targeted body, corrective manoeuvres are indeed required before and after flybys (or, similarly, orbital insertions) and can be significantly reduced by improved ephemerides.

Determining the orbits of natural satellites is typically achieved with observations of their absolute positions in the sky or of their relative motion with respect to one another. Spacecraft-based observations (either radiometric tracking or optical data) can also be used, but they are much sparser because they are only collected during planetary missions. Extremely precise measurements are moreover necessary to be sensitive to very weak dynamical effects, such as tidal forces, which drive the orbital evolution of planetary systems. Unfortunately, the precision of Earth-based classical astrometric observations is limited, typically ranging from 50 to 150 milliarcseconds (mas) (e.g., Stone, 2001; Kiseleva et al., 2008; Robert et al., 2017).

A lot of effort has thus been dedicated to develop more precise types of observations. For example, relative measurements of the positions of two satellites in the sky plane have been shown to be more accurate, with a precision down to 30 mas (Peng et al., 2012). Relative astrometric observations can indeed benefit from the so-called precision premium: the precision is significantly improved when apparent distances get smaller than 85 mas. In such a situation, instrumental and astronomical error sources tend to have a similar effect on the measurement of each of the two satellites' position, and thus eventually cancel out (Morrison and Gilmore, 1994; Peng et al., 2008).

Alternatively, the relative position of two satellites can also be precisely measured by observing mutual events - occultations or eclipses (e.g., Emelyanov, 2009; Emelyanov et al., 2011; Dias-Oliveira et al., 2013; Arlot et al., 2014). During mutual events, one satellite masks the other, resulting in a drop of the flux received by the observer. Those mutual phenomena can provide measurements of satellites' relative positions with a precision of about 10 mas (Emelyanov, 2009; Dias-Oliveira et al., 2013). However, they can only be witnessed during the equinox of the central planet, which occurs every 6 years for Jupiter and 15 years for Saturn. This significantly limits the number of available observations.

To overcome the limitations of the above-mentioned observations, a very promising alternative technique called mutual approximation was recently proposed by Morgado et al. (2016), though initially suggested in Arlot et al. (1982). This method determines the so-called central instant at which a close encounter occurs in the sky plane (i.e., the apparent distance between two satellites reaches a minimum, see Fig. 6.1). The precision of mutual approximations was found to be comparable to that of mutual events (Morgado et al., 2016, 2019b).

Central instants are free of any orientation and scaling errors in the instrumental frame: they do not depend on the absolute value of the apparent distance itself, nor on the relative orientation of the two satellites (Emelyanov, 2017). This eliminates two major error sources present in classical astrometric observations. Properly recording the observational time at the ground station becomes crucial, but this can be easily achieved with GPS receivers or dedicated software. Most importantly, mutual approximations occur very regularly, and thus offer a very promising alternative to eclipses and occultations (Morgado et al., 2016, 2019b).

To estimate ephemerides using mutual approximations, the observation partials for central instants are required. They link a small variation of the parameters to be estimated (natural satellites' states in our case) to a change in the observable. However, the central instants' complex definition and their relation to the satellites' states makes deriving these equations difficult. Other astronomic observables only depend on the apparent (relative) position of the observed body which is an indirect function of its inertial position, after projection on the plane of the sky. Mutual approximations, on the other hand, are also determined by the apparent relative velocity and acceleration of the two satellites. As a consequence, such observations are affected by the satellites' inertial relative dynamics, and not only by their position.

Emelyanov (2017) and Morgado et al. (2019b) therefore assumed that variational equations could not be solved analytically when using central instants, as analytical partials were not yet available (or easily derivable) for such observables. Those central instants partials could be computed numerically, but this process is highly computationally demanding (Emelyanov, 2017) and can also be error prone. Consequently, it was suggested to use a modified observable and fit the derivative of the apparent distance instead of the central instant itself (Emelyanov, 2017; Morgado et al., 2019b). This modified observable can be expressed as a simple function of the relative position and velocity of the two satellites (see Section 6.2.5). Moreover, the apparent distance derivative is by definition equal to zero at closest encounter, which significantly simplifies the equations.

This indirect method is currently the recommended approach to obtain the mutual approximations' observation partials (Emelyanov, 2017; Morgado et al., 2019b). Fundamentally, defining the central instant t_c directly or stating that the derivative of the apparent distance should be equal to zero at t_c both express the fact that the point of closest approach is reached at this instant. However, the information both observable types convey to the state estimation is not necessarily identical and it has not yet been proven that fitting the derivative of the apparent distance is equivalent to fitting the central instants. Actually, using numerical partials for central instants led to convergence issues in Emelyanov (2017), while none were encountered with alternative observables. This would indicate that the two observables are not completely interchangeable.

6

To extend the current framework available for the mutual approximation technique,

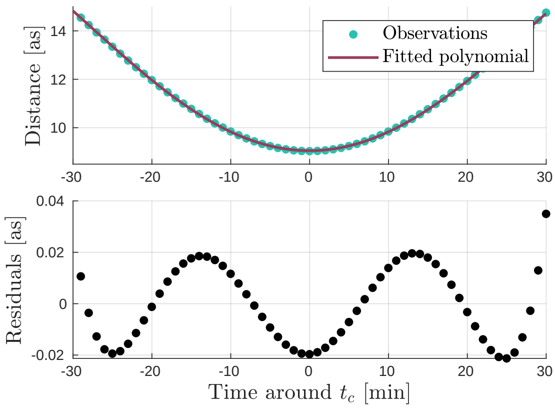

Figure 6.1.: Observation of a mutual approximation (i.e., close encounter between two natural satellites). The apparent distance between the two satellites (blue dots in the top panel) is frequently measured and a polynomial is used to fit these observations and estimate the central instant of the close encounter (typically fourth-order polynomial, displayed in purple). The residuals between the apparent distances measurements and the fitted polynomial are shown in black (bottom panel).

this paper develops an analytical formulation for the observation partials of the central instants. To achieve this, the relative motion of the two satellites in the plane of the sky is approximated by a polynomial function around the close encounter. The polynomial coefficients are defined from the relative position, velocity, and acceleration of the two satellites, as seen from the observer. It thus becomes possible to derive analytical expressions for the change in central instant induced by a variation in either the two satellites' or the observer's states. We successfully performed the state estimation with mutual approximations' suggested alternative observables (derivatives of the apparent distance) and with central instants separately, using our analytical observation partials for the latter. This comparison aims at quantifying the influence of the observable choice on the estimated solution. We show that it is essential to adopt an appropriate weighting strategy when using alternative observables to achieve consistent results between the two observable types, but that central instants can nonetheless yield a 10-20% reduction in formal errors.

We develop the analytical framework for mutual approximations' central instants in Section 6.2, while the details of the observables simulation and state estimation are provided in Section 6.3. The results of our comparative analysis are discussed in Section 6.4, first using a simple test case limited to mutual approximations between Io and Europa, before extending it to the four Galilean moons. The main concluding points are summarised in Section 6.5. All the numerical simulations presented in this paper were conducted using the Tudat toolkit developed by the Astrodynamics & Space Missions department of Delft University of Technology (see Appendix C in Dirkx et al., 2019a).

6.2. USING MUTUAL APPROXIMATIONS IN THE ESTIMATION

In this section, we first provide a formal definition to describe the observation of a mutual approximation between two satellites in Section 6.2.1. We develop an analytical formulation for the central instants and their observation partials in Section 6.2.2 and Section 6.2.3, respectively. The light-time effect contribution to those partials is discussed in Section 6.2.4. Finally, the alternative mutual approximations' observable (i.e., derivative of the apparent distance, as introduced in Section 6.1) is presented in more detail in Section 6.2.5.

6.2.1. MUTUAL APPROXIMATION DEFINITION

A mutual approximation involves an observer (denoted by the subscript O in the following), which is most commonly a ground station, and two natural satellites, between which a close encounter is observed (subscripts $S1$ and $S2$, respectively). Because light has a finite speed, the time at which the mutual approximation is observed (observation time t_O) differs from the time at which the light eventually received by the observer got reflected by each of the satellites (t_{S1} and t_{S2} for satellites 1 and 2, respectively).

The relative range vectors between the satellites and the observer can thus be defined as follows (see Fig. 6.2):

$$\boldsymbol{r}_O^{S_1} = \boldsymbol{r}_{S1}(t_{S1}) - \boldsymbol{r}_O(t_O), \tag{6.1}$$

$$\boldsymbol{r}_O^{S_2} = \boldsymbol{r}_{S2}(t_{S2}) - \boldsymbol{r}_O(t_O). \tag{6.2}$$

The relative velocity and acceleration of the two satellites can then be expressed as

$$\dot{\boldsymbol{r}}_O^{S_i} = \frac{d\boldsymbol{r}_O^{S_i}}{dt} = \frac{d\boldsymbol{r}_{Si}}{dt}(t_{Si}) - \frac{d\boldsymbol{r}_O}{dt}(t_O), \tag{6.3}$$

$$\ddot{\boldsymbol{r}}_O^{S_i} = \frac{d^2\boldsymbol{r}_O^{S_i}}{dt^2} = \frac{d^2\boldsymbol{r}_{Si}}{dt^2}(t_{Si}) - \frac{d^2\boldsymbol{r}_O}{dt^2}(t_O); i \in \{1,2\}. \tag{6.4}$$

As mentioned in Section 6.1, a mutual approximation is defined as a point of closest encounter of two satellites in the field of view of an observer (see Fig. 6.1). This corresponds to the moment at which the apparent distance between the two moons reaches a minimum. The apparent distance as seen by an observer is

$$d = \sqrt{X^2 + Y^2}, \tag{6.5}$$

where X and Y are the coordinates of the relative position between the satellites, in the instrumental frame of the observer.

6

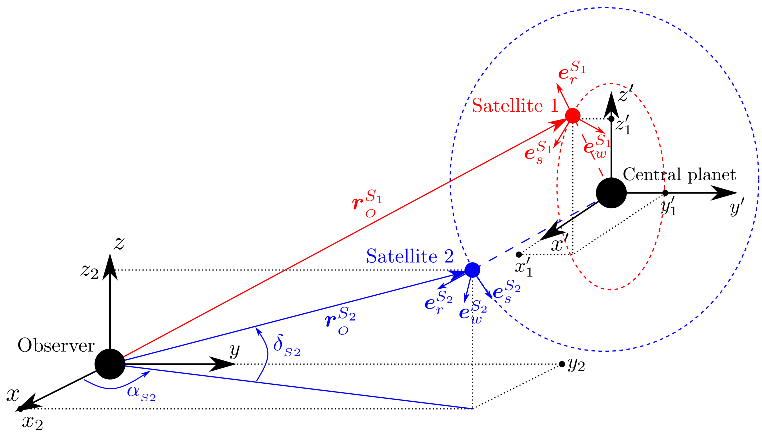

Figure 6.2.: Schematic representation of the different coordinate systems and positions. The first satellite and all associated notations are depicted in red, while blue is used for the second satellite. $\boldsymbol{r}_O^{S_i}$ denotes the relative position vector between satellite i and the observer, and $[x_i, y_i, z_i]$ correspond to the observer-centred cartesian coordinates of satellite i. α_{Si} and δ_{Si} refer to the right ascension and declination of satellite i, as seen by the observer. $[x'_i, y'_i, z'_i]$ are the satellites' central body-centred cartesian coordinates. $[\boldsymbol{e}_r^{S_i}, \boldsymbol{e}_s^{S_i}, \boldsymbol{e}_w^{S_i}]$ defines the RSW reference frame associated with satellite i. The vectors $\boldsymbol{e}_r^{S_i}$, $\boldsymbol{e}_s^{S_i}$, and $\boldsymbol{e}_w^{S_i}$ correspond to the radial, normal, and axial directions, respectively.

The apparent relative position coordinates X and Y are defined as

$$X = (\alpha_{S2} - \alpha_{S1}) \cos\left(\frac{\delta_{S1} + \delta_{S2}}{2}\right), \tag{6.6}$$

$$Y = \delta_{S2} - \delta_{S1}. \tag{6.7}$$

X and Y thus depend on the right ascensions α_{Si} and declinations δ_{Si} of the two satellites, which are functions of the inertial relative range vectors with respect to the observer:

$$\alpha_{S_i}\left(\boldsymbol{r}_O^{S_i}\right) = 2\arctan\left(\frac{y_i}{\sqrt{x_i^2 + y_i^2} + x_i}\right), \tag{6.8}$$

$$\delta_{S_i}\left(\boldsymbol{r}_O^{S_i}\right) = \frac{\pi}{2} - \arccos\left(\frac{z_i}{\sqrt{x_i^2 + y_i^2 + z_i^2}}\right), \tag{6.9}$$

where $[x_i, y_i, z_i]$ correspond to the components of the relative range vectors $\boldsymbol{r}_O^{S_i}$ (see Fig. 6.2). X and Y are thus time-dependent, as they are indirectly defined by the time-varying relative range vectors between each of the two satellites and the observer. In the rest of this paper, r_i denotes the norm of these relative range vectors and $r_{i_{xy}}$ the norm of the reduced vector $[x_i, y_i, 0]$. δ_m refers to the average declination, such that $\delta_m = \left(\delta_{T_1} + \delta_{T_2}\right)/2$. The differences in right ascension and declination are noted $\Delta\alpha = \alpha_{T2} - \alpha_{T1}$ and $\Delta\delta = \delta_{T2} - \delta_{T1}$.

By definition, the central instant t_c of a mutual approximation (recorded by the observer) fulfills the following condition:

$$\frac{d}{dt}\left(\sqrt{X(t_c)^2 + Y(t_c)^2}\right) = 0. \tag{6.10}$$

The apparent distance at t_c is referred to as the impact parameter of the mutual approximation and denoted d_c.

6.2.2. ANALYTICAL EXPRESSIONS FOR CENTRAL INSTANTS

The central instant t_c is typically determined by fitting a fourth order polynomial to the apparent distance history between two satellites (see Fig. 6.1). The roots of the derivative of the fitted polynomial provide the estimated central instant of the close encounter. For simulated mutual approximations, the procedure can be iterated to improve the precision of the predicted central instants by re-centring the polynomial fit on the current estimate of the point of closest approach.

A fourth order polynomial is needed to reproduce the relative motion of the two satellites over the typical duration of a close encounter (i.e., 60 minutes). However, when focusing on only a fraction of this event, a fourth order polynomial is not necessary. For instance, a second order polynomial provides a fit over the interval $[t_c - 15\text{min}; t_c \ \ +15\text{min}]$ which is as good as the one provided by a fourth order polynomial over the whole event, as shown in Appendix 6.6.

6

To derive observation partials, we quantify the effect of very small changes in position and velocity of the two satellites. We are thus investigating only slight variations of the central instant t_c, and can limit our analysis to short time intervals centred on the current estimate of t_c. Consequently, for our analysis, it is safe to approximate the apparent relative motion of the two satellites by a second order polynomial only.

Around the point of closest approach, the relative position coordinates X and Y can thus be expressed as a function of three polynomial coefficients each:

$$X(t-t_c) = a_0 + a_1(t-t_c) + a_2(t-t_c)^2, \tag{6.11}$$

$$Y(t-t_c) = b_0 + b_1(t-t_c) + b_2(t-t_c)^2. \tag{6.12}$$

These polynomial coefficients are directly given by the apparent relative position, velocity, and acceleration coordinates at central instant t_c. Introducing the relative time $t' = t - t_c$ as well as simplified notations ($X_c = X(t_c)$, $\dot{X}_c = \dot{X}(t_c)$, etc.), Eqs. 6.11 and 6.12 can be rewritten as follows:

$$X(t') = X_c + \dot{X}_c t' + \frac{\ddot{X}_c}{2} t'^2, \tag{6.13}$$

$$Y(t') = Y_c + \dot{Y}_c t' + \frac{\ddot{Y}_c}{2} t'^2. \tag{6.14}$$

6

The relative velocity coordinates are then approximated by a first order polynomial when close enough to the central instant:

$$\dot{X}(t') = \dot{X}_c + \ddot{X}_c t', \tag{6.15}$$

$$\dot{Y}(t') = \dot{Y}_c + \ddot{Y}_c t'. \tag{6.16}$$

Higher-order terms could be included in Eqs. 6.13-6.16. However, as discussed above, a second-order polynomial is well-suited to reproduce the apparent relative motion of the two satellites around the point of closest encounter. Higher-order terms can thus be safely neglected, as shown by the verification of our analytical partials for central instants (see Appendix 6.9).

As already mentioned in Section 6.2.1, the derivative of the apparent distance is equal to zero at central instant t_c. Therefore, the dot product between the relative position and velocity vectors must be equal to zero, leading to the following condition:

$$\begin{aligned}&\left(X_c + \dot{X}_c t' + \frac{\ddot{X}_c}{2} t'^2\right)\left(\dot{X}_c + \ddot{X}_c t'\right)\\ &+\left(Y_c + \dot{Y}_c t' + \frac{\ddot{Y}_c}{2} t'^2\right)\left(\dot{Y}_c + \ddot{Y}_c t'\right) = 0.\end{aligned} \tag{6.17}$$

The above equation can be rewritten as a third-order polynomial expression in t':

$$\begin{aligned}&\left(\ddot{X}_c^2 + \ddot{Y}_c^2\right) t'^3 + 3\left(\dot{X}_c \ddot{X}_c + \dot{Y}_c \ddot{Y}_c\right) t'^2\\ &+ 2\left(\dot{X}_c^2 + \dot{Y}_c^2 + X_c \ddot{X}_c + Y_c \ddot{Y}_c\right) t' + 2\left(X_c \dot{X}_c + Y_c \dot{Y}_c\right) = 0.\end{aligned} \tag{6.18}$$

Solving for t' is equivalent to finding the roots of this cubic polynomial, which can be done analytically with Cardano's formula (e.g., Weisstein, 2002b). In case the cubic polynomial has three real roots, the closest to the current t_c estimate should be selected, the other two falling outside the nominal duration of the close encounter event in most cases. An analytical expression can thus be derived for t', as a function of the apparent position, velocity, and acceleration components at t_c:

$$t' = f\left(X_c, Y_c, \dot{X}_c, \dot{Y}_c, \ddot{X}_c, \ddot{Y}_c\right). \tag{6.19}$$

Formulations for $\dot{X}$ and $\dot{Y}$ are derived from expressions for X and Y (Eqs. 6.6 and 6.7), as follows:

$$\begin{aligned} \dot{X} &= \Delta\dot{\alpha}\cos(\delta_m) - \Delta\alpha\sin(\delta_m)\,\dot{\delta}_m, && (6.20)\\ \dot{Y} &= \Delta\dot{\delta}. && (6.21)\end{aligned}$$

$\dot{\alpha}$ and $\dot{\delta}$ can be computed from Eqs. 6.8 and 6.9 as a function of the inertial relative position and velocity:

$$\begin{aligned} \dot{\alpha}_{S_i} &= \frac{x_i\dot{y}_i - y_i\dot{x}_i}{r_{i_{xy}}^2}, && (6.22)\\ \dot{\delta}_{S_i} &= \frac{-z_i\left(x_i\dot{x}_i + y_i\dot{y}_i\right) + r_{i_{xy}}^2\dot{z}_i}{r_i^2 r_{i_{xy}}}; i \in 1,2. && (6.23)\end{aligned}$$

Finally, the apparent relative acceleration components $\ddot{X}$ and $\ddot{Y}$ are required and can be similarly derived:

$$\begin{aligned} \ddot{X} &= \Delta\ddot{\alpha}\cos(\delta_m) - 2\dot{\delta}_m\Delta\dot{\alpha}\sin(\delta_m) - \Delta\alpha\left(\dot{\delta}_m^2\cos(\delta_m) + \ddot{\delta}_m\sin(\delta_m)\right) && (6.24)\\ \ddot{Y} &= \Delta\ddot{\delta}, && (6.25)\end{aligned}$$

where the second time derivatives of α and δ also depend on the inertial relative acceleration:

$$\ddot{\alpha}_{S_i} = \frac{-2\left(x_i\dot{y}_i - y_i\dot{x}_i\right)\left(x_i\dot{x}_i + y_i\dot{y}_i\right)}{r_{i_{xy}}^4} + \frac{\left(x_i\ddot{y}_i - y_i\ddot{x}_i\right)}{r_{i_{xy}}^2}, \tag{6.26}$$

$$\begin{aligned}\ddot{\delta}_{S_i} = \frac{1}{r_i^2 r_{i_{xy}}}\Bigg[&-z_i\left(x_i\ddot{x}_i + y_i\ddot{y}_i\right) + r_{i_{xy}}^2\ddot{z}_i - z_i\frac{\left(x_i\dot{y}_i - y_i\dot{x}_i\right)^2}{r_{i_{xy}}^2}\\ &+\frac{2\left(\boldsymbol{r}_O^{S_i}\cdot\dot{\boldsymbol{r}}_O^{S_i}\right)}{r_i^2}\left(z_i(x_i\dot{x}_i + y_i\dot{y}_i) - \dot{z}_i r_{i_{xy}}^2\right)\Bigg]; i \in \{1,2\}.\end{aligned} \tag{6.27}$$

Inserting Eqs. 6.8-6.9, 6.22-6.23, and 6.26-6.27 into Eqs. 6.6-6.7, 6.20-6.21, and 6.24-6.25 gives a direct analytical expression for t', and therefore for the central instant t_c, via Eq. 6.19.

6

6.2.3. PARTIALS WITH RESPECT TO THE NATURAL SATELLITES' STATES

To estimate ephemerides using central instants as observables, the partials of t_c with respect to the states of the two natural satellites are required. Recalling the analytical expression obtained for t' (Eq. 6.19) and noting $\boldsymbol{q}$ the vector of parameters, the central instants partials are

$$\frac{\partial t'}{\partial \boldsymbol{q}} = \frac{\partial f\left(X_c, Y_c, \dot{X}_c, \dot{Y}_c, \ddot{X}_c, \ddot{Y}_c\right)}{\partial \boldsymbol{q}} \tag{6.28}$$

$$= \frac{\partial f}{\partial [X_c, Y_c]} \frac{\partial [X_c, Y_c]}{\partial \boldsymbol{q}} + \frac{\partial f}{\partial [\dot{X}_c, \dot{Y}_c]} \frac{\partial [\dot{X}_c, \dot{Y}_c]}{\partial \boldsymbol{q}} + \frac{\partial f}{\partial [\ddot{X}_c, \ddot{Y}_c]} \frac{\partial [\ddot{X}_c, \ddot{Y}_c]}{\partial \boldsymbol{q}}. \tag{6.29}$$

The partials of the relative apparent position, velocity, and acceleration can be decomposed as a function of the partials of α_{s_i}, δ_{s_i}, $\dot{\alpha}_{s_i}$, $\dot{\delta}_{s_i}$, $\ddot{\alpha}_{s_i}$, and $\ddot{\delta}_{s_i}$, as follows:

$$\frac{\partial [X, Y]}{\partial \boldsymbol{q}} = \frac{\partial [X, Y]}{\partial [\alpha, \delta]_{s_i}} \frac{\partial [\alpha, \delta]_{s_i}}{\partial \boldsymbol{q}}; i \in \{1, 2\}, \tag{6.30}$$

$$\frac{\partial [\dot{X}, \dot{Y}]}{\partial \boldsymbol{q}} = \frac{\partial [\dot{X}, \dot{Y}]}{\partial [\alpha, \delta]_{s_i}} \frac{\partial [\alpha, \delta]_{s_i}}{\partial \boldsymbol{q}} + \frac{\partial [\dot{X}, \dot{Y}]}{\partial [\dot{\alpha}, \dot{\delta}]_{s_i}} \frac{\partial [\dot{\alpha}, \dot{\delta}]_{s_i}}{\partial \boldsymbol{q}}, \tag{6.31}$$

$$\frac{\partial \left[\ddot{X}, \ddot{Y}\right]}{\partial \boldsymbol{q}} = \frac{\partial [\ddot{X}, \ddot{Y}]}{\partial [\alpha, \delta]_{s_i}} \frac{\partial [\alpha, \delta]_{s_i}}{\partial \boldsymbol{q}} + \frac{\partial [\ddot{X}, \ddot{Y}]}{\partial [\dot{\alpha}, \dot{\delta}]_{s_i}} \frac{\partial [\dot{\alpha}, \dot{\delta}]_{s_i}}{\partial \boldsymbol{q}} + \frac{\partial [\ddot{X}, \ddot{Y}]}{\partial [\ddot{\alpha}, \ddot{\delta}]_{s_i}} \frac{\partial [\ddot{\alpha}, \ddot{\delta}]_{s_i}}{\partial \boldsymbol{q}}. \tag{6.32}$$

From the definition of the apparent position (X, Y), velocity $(\dot{X}, \dot{Y})$, and accelerations $(\ddot{X}, \ddot{Y})$ in Eqs. 6.6-6.7, 6.20-6.21, and 6.24-6.25, their partials with respect to the satellites' states can be easily derived (the proof is left as an exercise to the reader). Finally, the partials of α, δ, $\dot{\alpha}$, $\dot{\delta}$, $\ddot{\alpha}$, and $\ddot{\delta}$ also need to be computed with respect to the position and velocity vectors of the two satellites.

To quantify the influence of the uncertainties in the observer's state on the estimated solution, partials with respect to $\boldsymbol{r}_O$ and $\dot{\boldsymbol{r}}_O$ might also be required. All derivations are provided in Appendix 6.7. Our analytical formulation for the partials of the central instants with respect to both the satellites' and observer's states were validated numerically. The results of this verification are reported in Appendix 6.9.

6.2.4. LIGHT-TIME EFFECTS

In Section 6.2.3, the contribution of the light-time effects was not yet included in the observation partials and we therefore assumed that both t_O and t_{Si} were fixed. Corrections required to account for the finite speed of light are now discussed. When computing light-time effects, we typically fix either the time at the observed body (here t_{Si}) or the time at the observer (t_O). The other one is determined via an iterative scheme to ensure that the difference between the two times matches the light-time calculated from the observer and observed bodies' states (Moyer, 2005). For mutual approximations, the reception time should always be fixed. Fixing the two transmission times would indeed lead to two different inconsistent reception times for a unique observation. The light-time equations are expressed as follows (Moyer, 2005):

$$t_{Si} - t_O = \frac{\left|\boldsymbol{r}_{Si}(t_{Si}) - \boldsymbol{r}_O(t_O)\right|}{c}; i \in \{1,2\}, \tag{6.33}$$

where c refers to the speed of light and the observation time t_O is a fixed unique value.

The partials of the light-time with respect to a vector of parameters $\boldsymbol{q}$ can then be derived from Eq. 6.33:

$$\frac{\partial t_{Si}}{\partial \boldsymbol{q}} = \frac{1}{c}\frac{\boldsymbol{r}_O^{S_i}}{r_O^{Si}}\left(\frac{\partial \boldsymbol{r}_{Si}}{\partial \boldsymbol{q}}(t_{Si}) - \frac{\partial \boldsymbol{r}_O}{\partial \boldsymbol{q}}(t_O) + \dot{\boldsymbol{r}}_{Si}(t_{Si})\frac{\partial t_{S1}}{\partial \boldsymbol{q}}\right). \tag{6.34}$$

Solving for the partials of t_{Si} with respect to $\boldsymbol{q}$, we finally obtain (Moyer, 2005)

$$\frac{\partial t_{Si}}{\partial \boldsymbol{q}} = \frac{1}{c}\frac{\boldsymbol{r}_O^{Si}}{r_O^{Si} - \boldsymbol{r}_O^{Si}\cdot\frac{\dot{\boldsymbol{r}}_{Si}}{c}}\left(\frac{\partial \boldsymbol{r}_{Si}}{\partial \boldsymbol{q}}(t_{Si}) - \frac{\partial \boldsymbol{r}_O}{\partial \boldsymbol{q}}(t_O)\right). \tag{6.35}$$

The time t_{Si} thus depends on both the natural satellite's and observer's states. As already mentioned, right ascension and declination partials with respect to the vector of parameters $\boldsymbol{q}$ were provided for fixed t_O and t_{Si} in Section 6.2.3. When accounting for the light-time effect, the complete formulation for those partials becomes

$$\frac{\partial\,[\alpha,\delta]_{S_i}}{\partial \boldsymbol{q}} = \left.\frac{\partial\,[\alpha,\delta]_{S_i}}{\partial \boldsymbol{q}}\right|_{t_{Si}} + \left[\dot{\alpha},\dot{\delta}\right]_{S_i}\frac{\partial t_{Si}}{\partial \boldsymbol{q}};\; i \in \{1,2\}. \tag{6.36}$$

The same applies to the partials of $\dot{\alpha}$, $\dot{\delta}$, $\ddot{\alpha}$, and $\ddot{\delta}$, and leads to the following expressions:

$$\frac{\partial[\dot{\alpha},\dot{\delta}]_{S_i}}{\partial \boldsymbol{q}} = \left.\frac{\partial[\dot{\alpha},\dot{\delta}]_{S_i}}{\partial \boldsymbol{q}}\right|_{t_{Si}} + [\ddot{\alpha},\ddot{\delta}]_{S_i}\frac{\partial t_{Si}}{\partial \boldsymbol{q}}, \tag{6.37}$$

$$\frac{\partial[\ddot{\alpha},\ddot{\delta}]_{S_i}}{\partial \boldsymbol{q}} = \left.\frac{\partial[\ddot{\alpha},\ddot{\delta}]_{S_i}}{\partial \boldsymbol{q}}\right|_{t_{Si}} + [\dddot{\alpha},\dddot{\delta}]_{S_i}\frac{\partial t_{Si}}{\partial \boldsymbol{q}};\; i \in \{1,2\}. \tag{6.38}$$

According to Eq. 6.38, the complete partials for $\ddot{\alpha}_{S_i}$ and $\ddot{\delta}_{S_i}$ require one to compute $\dddot{\alpha}_{S_i}$ and $\dddot{\delta}_{S_i}$ (see Eq. 6.38), and thus the time derivative of the relative acceleration of each satellite with respect to the observer. This would significantly increase both the implementation and computational efforts, while the $\ddot{\alpha}_{S_i}$ and $\ddot{\delta}_{S_i}$ partials only marginally contribute to the central instant partials (at most of the order of 0.001% for the case of the Galilean satellites, see Appendix 6.10, Table 6.7). As a consequence, neglecting the light-time effects when computing the partials for $\ddot{\alpha}_{S_i}$ and $\ddot{\delta}_{S_i}$ was considered a fair simplifying assumption, which was applied in the rest of this analysis.

6

6.2.5. ALTERNATIVE OBSERVABLES

As already mentioned in Section 6.1, the alternative observable recommended by Morgado et al. (2019b) correspond to the derivative of the apparent distance, defined as

$$h = \frac{d}{dt}\left(\sqrt{X^2+Y^2}\right) = \frac{X\dot{X}+Y\dot{Y}}{\sqrt{X^2+Y^2}}. \tag{6.39}$$

If X and Y and their time derivatives $\dot{X}$ and $\dot{Y}$ were computed at the exact central instant t_c of the close encounter, the observable h would by definition be equal to zero. This is however not the case. This observable thus indirectly evaluates the difference between the current estimate of t_c and its true value by quantifying how much the derivative of the apparent distance departs from zero.

In contrast to central instants which also depend on the satellites' relative accelerations, alternative observables are thus only a function of their relative position and velocity. The partials of such an observable with respect to a vector of parameters $\boldsymbol{q}$ are much easier to derive than for central instants and are given by Morgado et al. (2019b):

$$\frac{\partial h}{\partial \boldsymbol{q}} = \frac{1}{\sqrt{X^2+Y^2}}\left(X\frac{\partial \dot{X}}{\partial \boldsymbol{q}} + \dot{X}\frac{\partial X}{\partial \boldsymbol{q}} + Y\frac{\partial \dot{Y}}{\partial \boldsymbol{q}} + \dot{Y}\frac{\partial Y}{\partial \boldsymbol{q}}\right) - \frac{X\dot{X}+Y\dot{Y}}{\left(X^2+Y^2\right)^{3/2}}\left(X\frac{\partial X}{\partial \boldsymbol{q}} + Y\frac{\partial Y}{\partial \boldsymbol{q}}\right). \tag{6.40}$$

The results of the comparison between the two types of observables are discussed in Section 6.4.

6.3. OBSERVATIONS SIMULATION AND EPHEMERIDES ESTIMATION

We first describe how mutual approximations are simulated in Section 6.3.1, before introducing the covariance analysis used to compare the two observable types in Section 6.3.2. The strategy applied to weigh the mutual approximations' observables is then discussed in Section 6.3.3. Finally, Section 6.3.4 defines an additional figure of merit to analyse the estimation solution.

6.3.1. MUTUAL APPROXIMATIONS SIMULATION

We used simulated mutual approximations in our analysis. As a preliminary test case, we first propagated the trajectories of Io and Europa only, and detected close encounters between these two moons (results discussed in Sections 6.4.1 to 6.4.4). A more complete simulation including all Galilean moons was also conducted to verify the findings of the former simple test case (Section 6.4.5).

The orbits of the Galilean moons were propagated using a simplified dynamical model. For each of the moons, we considered only the point-mass gravitational accelerations exerted by Jupiter and the three other satellites. A more detailed dynamical model (e.g., Dirkx et al., 2016; Lainey et al., 2004a) would yield more accurate propagated orbits for the Galilean moons, and thus affect the predicted mutual approximations. However, we focus on comparing two types of mutual approximations' observables. High-accuracy dynamical modelling is therefore not critical for this study, as long as the same set of simulated observations is used for both observable types.

Mutual approximations were simulated for the period 2020-2029. To limit the number of observations, we only considered mutual approximations with an impact parameter lower than 30 arcseconds (as), in agreement with Morgado et al. (2019b). We selected three of the ground stations involved in the 2016-2018 observational campaign reported in Morgado et al. (2019b), designated by FOZ, OHP, and OPD (their coordinates are reported in Table 6.1). To ensure the feasibility of the observation, daytime events were discarded. In addition, the lower limit on the distance between the mutual approximation and the limb of Jupiter was set to 10 as. Only mutual approximations observable from the three ground stations under an elevation angle larger than 30 degrees were included.

When achievable under the aforementioned conditions, a single event can be observed by several ground stations. Those multiple observations of one mutual approximation were assumed to have uncorrelated noise and thus they were added as independent observations to the state estimation. This implies that such simultaneous observations improve the estimation solution by increasing the size of the observational data set, as formal errors are expected to scale down with $\sqrt{n}$ (n being the total number of observations). Finally, weather conditions were taken into account to obtain a realistic set of observations. Due to bad weather conditions, about 35% of the predicted mutual approximations could not be observed during the 2016-2018 campaign (Morgado et al., 2019b). We took a conservative approach to simulate these bad weather conditions and discarded 50% of the viable observations, selected arbitrarily using a uniform distribution.

The distribution per year of the remaining simulated mutual approximations is shown in Fig. 6.3. Fig. 6.3a displays the fraction of simulated events per ground station, while Fig. 6.3b focuses on the number of mutual approximations for each combination of two Galilean moons. It is interesting to note that no mutual approximation respecting the conditions mentioned in the previous paragraphs could be found in 2020, and that some years are more favourable to such events due to the time evolution of the Earth - Jovian system relative geometry.

6.3.2. Covariance analysis

To compare state estimations obtained with the two types of mutual approximation observables, we limited ourselves to a covariance analysis. Despite its limitations (Gaussian observation noise, dynamical and observational models assumed perfect), such an analysis is well-adapted for comparison purposes. Formal errors are known to be too optimistic compared to true errors, but we only focus on comparing two sets of estimation errors and not on absolute error values. Since mutual approximations are almost exclusively sensitive to the relative dynamics between the two satellites while both their absolute states are estimated, realistic errors are anyway difficult to achieve without including other observations.

In our simulations, the estimated parameters were the initial states of the

Table 6.1.: Ground stations' geodetic coordinates. The three ground stations reported in this table are the ones from which the observations of the mutual approximations are simulated. The table is adapted from Morgado et al. (2019b).

Alias Site Location	Longitude [E]	Latitude [N]	Altitude [m]
FOZ Foz do Iguacu PR-Brazil	- 54°35'37.0"	- 25°26'05.0"	184
OHP Haute-Provence France	05°42'56.5"	43°55'54.7"	633
OPD Itajuba MG-Brazil	- 45°34'57.5" W	- 22°32'07.8"	1864

moons involved in the mutual approximations. In most of our analysis, only the Jupiter-centred initial states of Io and Europa are estimated (Sections 6.4.1 to 6.4.4), while we also solved for the initial states of Ganymede and Callisto in the more complete case used for verification (see Section 6.4.5). For the moons' initial position components, a priori covariance of 100 km was considered, while it was set to 100 m/s for their initial velocity. These a priori values are large, but were only included to slightly constrain the estimation, thus avoiding an ill-posed problem and making the comparison between the estimation solutions obtained with the two observable types possible.

6.3.3. DATA WEIGHTS

Observation weights are usually applied to account for the quality of the data. For our comparative analysis, it is essential to ensure that the data weights are consistent between the two types of observables. We used an error of 3.5 s for the central instants t_c (average error obtained over the 104 observed mutual approximations of the 2016-2018 campaign reported in Morgado et al., 2019b).

To derive appropriate weights for the alternative observables, the shape of the simulated mutual approximation must be taken into account. By definition, the derivative of the apparent distance (i.e., alternative observable) is always equal to zero at $t = t_c$. However, an error of 3.5 seconds in the determination of the central instant would shift this value away from zero. The exact value of the resulting alternative observable error directly depends on the specific geometry of each mutual approximation. The alternative observable error was thus individually computed for

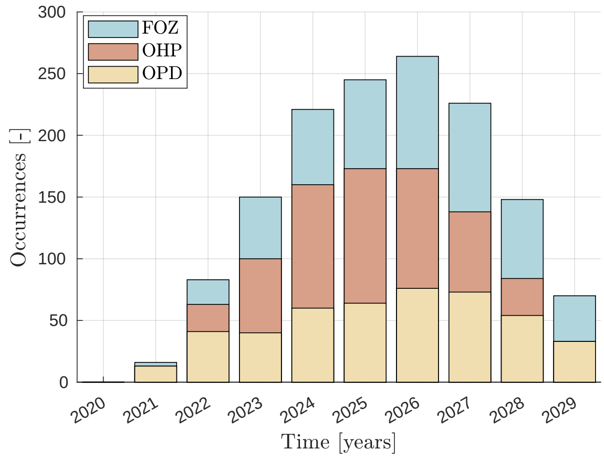

(a)

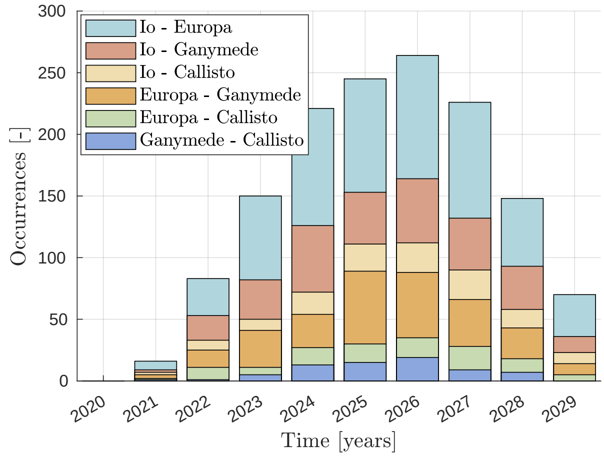

(b)

Figure 6.3.: Distribution of the simulated mutual approximations per year, depending on the ground station (panel a) and on the two moons involved (panel b). Mutual approximations which have been discarded to mimic the effect of bad weather conditions are not included in this distribution.

each observation, as follows:

$$\sigma_{\text{alt.}} = \frac{\left|\dot{d}(t_c - \sigma_{t_c})\right| + \left|\dot{d}(t_c + \sigma_{t_c})\right|}{2}, \tag{6.41}$$

where σ_{t_c} is set to its averaged value (σ_{t_c} = 3.5 s) and $\dot{d}$ is the derivative of the apparent distance (given by Eq. 6.39).

Consistent weights between the two observables are not only needed to perform a meaningful comparison. When using alternative observables, weighting can be an indirect way to account for the satellites' relative dynamics during the close encounter. Indeed, a non-zero value for the derivative of the apparent distance at t_c only quantifies how much the observed central instant departs from the current point of closest approach. However, it does not provide any information about the current apparent distance minimum. For a given non-zero value of the apparent distance derivative, the difference between the observed and current central instants entirely depends on the satellites' apparent relative dynamics, which drive the geometry of the observed encounter.

This effect is, by definition, inherently captured by central instants, for which applying an appropriate constant weight value is thus suitable. For alternative observables, on the other hand, individual weights accounting for each mutual approximation's dynamics, as given in Eq. 6.41, are crucial. This is necessary to translate an error in the estimated central instant to an error in the derivative of the apparent distance. The importance of applying this weighting strategy to obtain consistent estimation solutions with the two different observable types is demonstrated in Section 6.4.4. Furthermore, we computed the appropriate alternative observables' weights for the past mutual approximations observed during the 2016-2018 campaign and reported in Morgado et al. (2019b). These weights are provided in Appendix 6.11 and should be used when including the 2016-2018 mutual approximations in the state estimation.

6.3.4. Contribution of each observation to the solution

To perform a detailed comparison of the two observable types, the mutual approximations' contributions to the solution were used as an additional figure of merit to complement the covariance analysis. In this study, each observation's contribution to the solution is defined as the root-mean-square (RMS) of the weighted observation partial with respect to the parameters of interest's vector $\boldsymbol{q}$. For example, the contribution c of an observation h to Io's Jupiter-centred initial position vector is expressed as:

$$c_{(\boldsymbol{r}_{\mathrm{Io}})}(h) = \sqrt{\left(\frac{\partial h}{\partial x_{\mathrm{Io}}(t_0)}\right)^2 + \left(\frac{\partial h}{\partial y_{\mathrm{Io}}(t_0)}\right)^2 + \left(\frac{\partial h}{\partial z_{\mathrm{Io}}(t_0)}\right)^2}, \tag{6.42}$$

where t_0 is the initial epoch at which Io's state is estimated. The contribution $c_{(\boldsymbol{q})}(h)$ to the vector of parameters $\boldsymbol{q}$ is then normalised as follows (the bar indicates normalisation):

$$\bar{c}_{(\boldsymbol{q})}(h) = \frac{\log\left(c_{(\boldsymbol{q})}(h)\right) - \log\left(\min(\boldsymbol{c}_{(\boldsymbol{q})})\right)}{\log\left(\max\left(\boldsymbol{c}_{(\boldsymbol{q})}\right)\right) - \log\left(\min \boldsymbol{c}_{(\boldsymbol{q})})\right)}, \tag{6.43}$$

where $\boldsymbol{c}_{(\boldsymbol{q})}$ is the vector containing the contributions of the entire set of mutual approximations with respect to $\boldsymbol{q}$ (for one type of observable).

6.4. RESULTS

We present here the results of the comparison between the ephemeris estimation determination solutions obtained using either central instants or alternative observables. The comparison is first conducted for a simple test case with Io and Europa only, to analyse how each mutual approximation contributes to the ephemerides solution and how this affects the relative performance of the two types of observables. Results of this first analysis are presented in Sections 6.4.1 to 6.4.4. A more complete test case also including Ganymede and Callisto is used to verify those findings (Section 6.4.5).

6.4.1. COMPARISON OVER THE 2020-2029 OBSERVATIONAL PERIOD

We first only simulated mutual approximations between the two innermost Galilean moons, for the period 2020–2029, and estimated Io's and Europa's initial states from those simulated observations. The evolution of the formal errors with time is displayed in Fig. 6.4, as more mutual approximations are included in the estimation. The differences in formal errors between the two types of observables do not exceed 20% at the end of our simulation, after ten years of observations. Alternative observables and central instants lead to comparable formal errors evolutions. At first order, this proves that the two types of mutual approximations' observables are largely equivalent, at least when enough observations are added to the state estimation. It validates the recommendations formulated in Morgado et al. (2019b), but seems to contradict the results on numerical partials in Emelyanov (2017).

Nonetheless, using central instants still results in slightly lower formal errors for each component of both Io's and Europa's initial position. The formal error improvement is stronger in the radial and normal directions (about 20% for both Io and Europa at the end of simulation) and less significant in the axial direction (only 10-12%). As mentioned in Section 6.2.5, the observation partials developed for the central instants account for variations in the apparent relative acceleration between the two satellites, while this is not the case for alternative observables. The additional information captured by central instants thus principally lies within the orbital plane of the Galilean moons, within which the inter-moons accelerations primarily act. On the other hand, the central instants are not significantly more sensitive than alternative observables to state variations in the axial direction.

Interestingly, the difference in formal errors between the two types of observables is not constant over time, as clearly highlighted by Fig. 6.4. It can be as low as a few percents (e.g., Io's normal position in year 2021) or as high as 35% (e.g., Io's normal position during the first half of year 2027). This is related to the mutual approximations' heterogeneous contribution to the solution: it varies from one observation to another, but also between the two observable types. The cause of this heterogeneity is further discussed in Section 6.4.2.

First, as expected, the contribution of each mutual approximation depends on the time at which it occurs. Observations collected further in time (with respect to the initial epoch t_0 at which the states are estimated) indeed contribute more to the initial state solution. This directly results from the fact that later observations provide tighter constraints to the initial state due to the orbit propagation: the effect of a

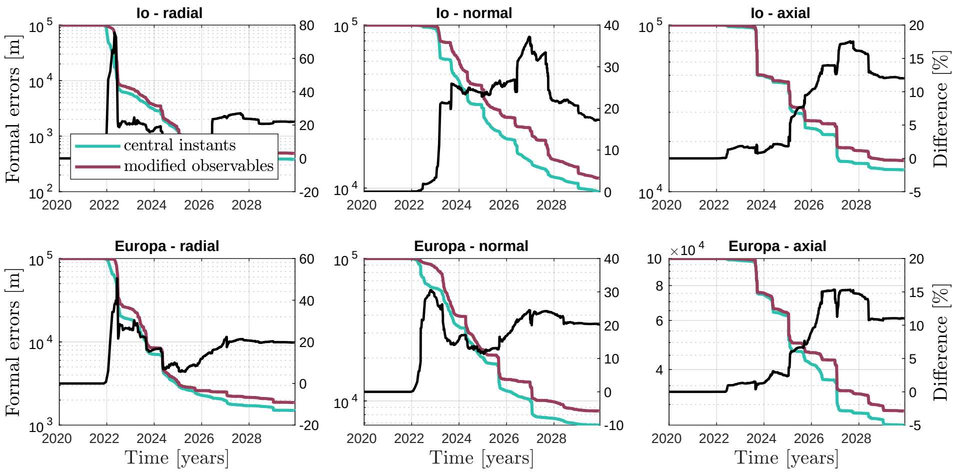

Figure 6.4.: Time evolution of the formal errors in Io's and Europa's initial RSW coordinates (radial, normal, and axial directions, see Fig. 6.2), as more observations are progressively included in the state estimation. The blue and purple lines respectively display the central instants and modified observables cases (left y-axis). The black line (right y-axis) represents the relative difference (in percentage) between the two solutions as a function of time. The formal errors are equal to their a priori values (i.e., 100 km, see Section 6.3.2) until the inclusion of the first mutual approximation (towards the end of 2021) and no difference between the two observables' solutions is thus observed beforehand.

slight variation in the initial state of Io and Europa on their trajectories grows with time. However, this time trend similarly affects both observable types and thus it has no noticeable influence on the solution improvement provided by central instants.

Nonetheless, the observable type choice also has an effect on some mutual approximations' contribution to the estimated solution. Fig. 6.5 displays the normalised contribution ratio of central instants over alternative observables, as defined in Section 6.3.4, for each mutual approximation. Some mutual approximations, mostly concentrated in the 2026-2027 period, contribute significantly less to both Io's and Europa's estimated positions when alternative observables are used instead of central instants. As expected, these observations coincide with an increase of the difference in formal errors between the two observables. The coming sections investigate why this discrepancy between the two observable types only concerns some mutual approximations and specific observational periods.

6.4.2. Influence of the mutual approximations' characteristics

To better characterise the difference between the two observable types, we further analyse the relative contribution of each observation and the effect of the mutual

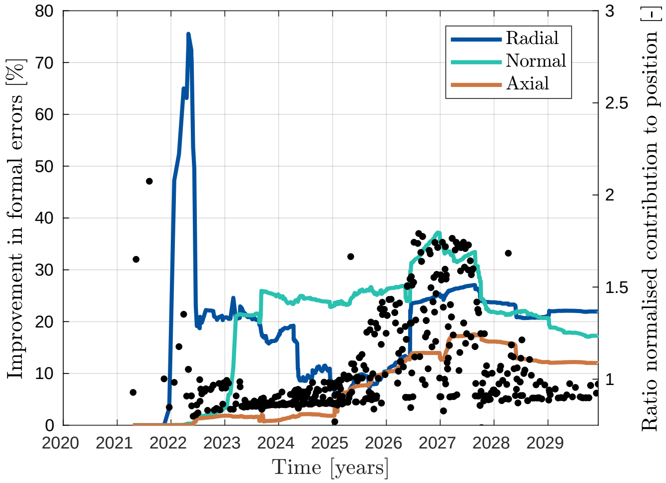

(a)

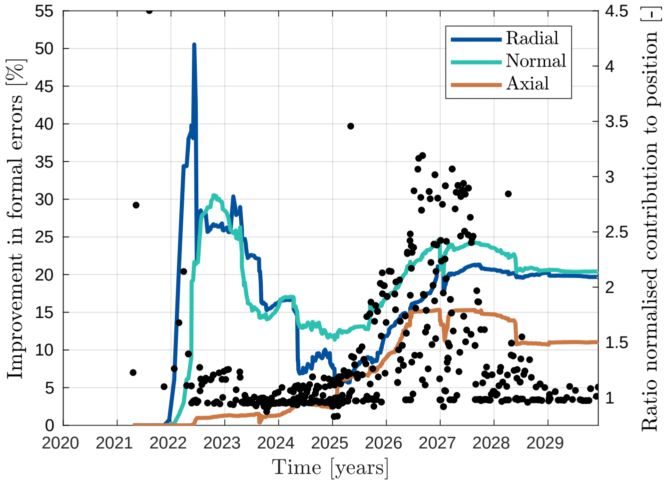

(b)

Figure 6.5.: Reduction in formal errors obtained by using central instants instead of alternative observables, as more observations are added to the solution. This is displayed on the left axis, for the three RSW position components (panel a: Io, panel b: Europa). On the right axis (black dots), the ratio between the normalised contributions of central instants over their corresponding alternative observables is plotted, for each mutual approximation (normalised contributions are computed as in Eq. 6.43).

approximation's characteristics. Section 6.4.2 discusses the influence of the impact parameter and velocity on each mutual approximation's contribution to the solution, for both central instants and alternative observables. The link between those characteristics and the observation geometry is explored in Section 6.4.2.

Influence of impact parameter and velocity on each mutual approximation's contribution

Focusing on the central instants case first, Fig. 6.6a shows that each mutual approximation's contribution to the estimated positions (averaged between Io and Europa) strongly depends on the impact parameter and velocity. Highest contributions are systematically obtained with both low impact parameter and velocity (up to about 7 as and 1 mas/s, respectively). Mutual approximations with either low impact parameter and high impact velocity, or high impact parameter but low impact velocity also contribute significantly to the ephemerides solution.

Using alternative observables instead of central instants alters the way some mutual approximations contribute to the estimated solution, as hinted in Section 6.4.1. Fig. 6.6b displays the ratio between central instants' and alternative observables' contributions to the estimated initial positions (contributions were again averaged between Io and Europa). Mutual approximations characterised by low impact parameter and high impact velocity contribute significantly less to the solution when switching to alternative observables. More precisely, most mutual approximations with impact parameters lower than 5 as and impact velocities larger than 4 mas/s contribute about 2 times more to the estimated solution when using central instants instead of alternative observables.

This analysis proves that the differences between the two observable types for some mutual approximations is amplified by specific impact characteristics. Furthermore, mutual approximations identified as unfavourable for alternative observables (low impact parameters with large impact velocities) are not evenly distributed over the 2020-2029 observational period, but rather concentrated in the 2026-2027 interval. As expected, it corresponds to the period during which the differences in formal errors between the two observables increase (Section 6.4.1, see Fig. 6.5).

It is interesting to note that mutual approximations characterised by extremely low impact parameters are also unfavourable from an observational perspective, and not only from an estimation point of view. If the two satellites eventually become so close that a (partial) occultation occurs, the observer cannot distinguish between their images anymore, introducing a gap in the apparent distance measurements near the point of closest approach and thus leading to a larger error in the estimated central instant (Morgado et al., 2019b).

Link to the observation geometry

Interestingly, most of the mutual approximations simulated over the 2026-2027 period are characterised by low impact parameters (lower than 5 as), while it is not the case outside of this time interval. This is clearly shown in Fig. 6.8, where impact parameters are displayed in black.

The apparent relative motion of the two moons is driven by two parameters: their inertial relative motion in the Jovian system and the observation geometry. Fig. 6.7 focuses on the former and shows the absolute distance between Io and Europa for

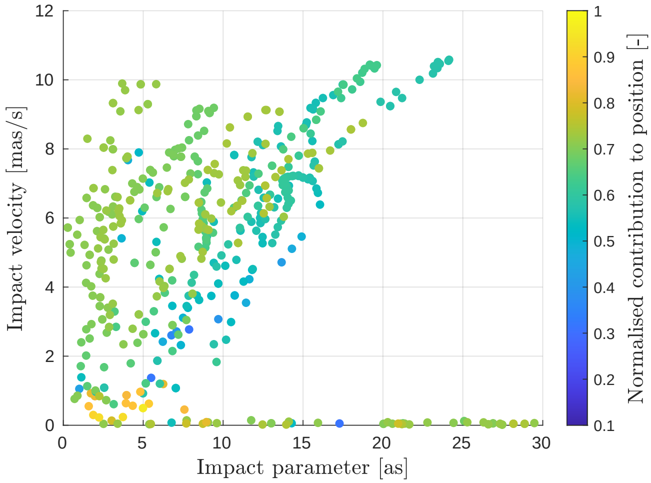

(a)

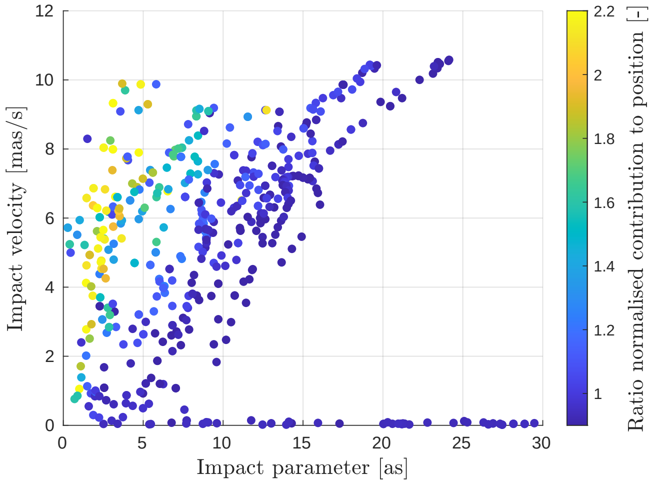

(b)

Figure 6.6.: Observations' contributions to the estimated initial positions' solution (in colours), as a function of each mutual approximation's characteristics (impact parameters and impact velocities, reported on the x- and y-axes, respectively). Panel a: normalised contribution (Eq. 6.43) of each mutual approximation to the solution (averaged between Io and Europa), when using central instants. Panel b: ratio between the normalised contributions of central instants over their corresponding alternative observables.

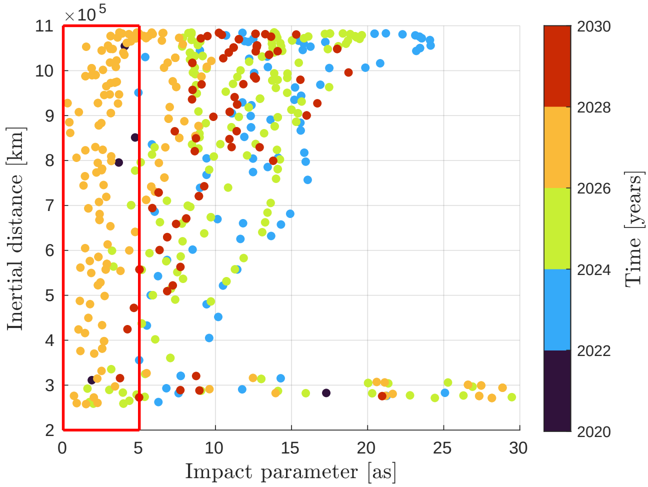

Figure 6.7.: Effect of the inertial geometry on the mutual approximations' impact characteristics. Both the impact parameter and the inertial distance between Io and Europa (as opposed to apparent distance as seen from the ground stations) are displayed, for each mutual approximation. The colours represent the time of the observation.

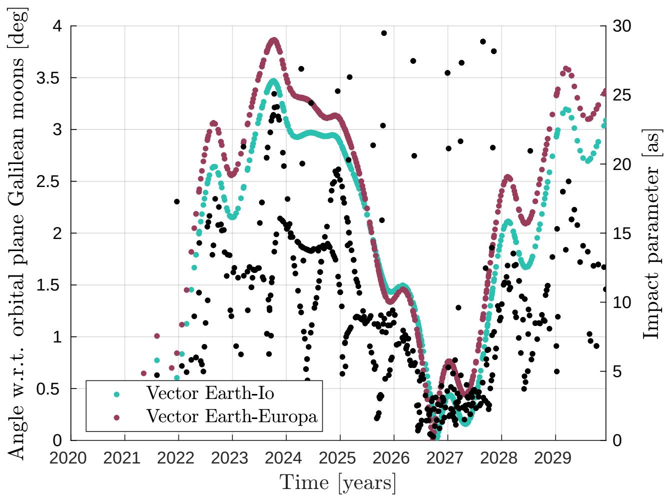

Figure 6.8.: Effect of the observation geometry on the mutual approximations' impact parameters. The angle between the orbital plane of the Galilean moons and the observation vectors (Earth-Io in blue and Earth-Europa in purple) is plotted for each mutual approximation. The corresponding impact parameters (in as) are represented by black dots.

each mutual approximation, as a function of the corresponding impact parameter. The time at which each mutual approximation occurs is displayed in colours. When excluding the 2026-2027 interval (orange dots), the impact parameters take a wide range of values (up to the limit of 30 as). The lowest impact parameters usually coincide with low inertial distances between Io and Europa, typically below $3.5 \cdot 10^5$ km (see the fraction of Fig. 6.7 highlighted in red). It should be noted that the reverse is not true: low inertial distances do not automatically lead to low impact parameters.

However, during the 2026-2027 period, mutual approximations with low impact parameters are systematically achieved, even for large inertial distances between Io and Europa. This difference between the inertial and apparent relative motions is caused by the evolution of the observation geometry. Fig. 6.8 displays the angle between the orbital plane of the Galilean moons and the two observation vectors (Earth-Io and Earth-Europa), for each mutual approximation. The 2026-2027 period coincides with an almost perfect alignment between the satellite-observer vectors and the moons' orbital plane, resulting in overall lower apparent distances during Io-Europa close encounters. Those low impact parameters then regularly happen to be combined with large impact velocities. This is why mutual approximations with both aforementioned characteristics, for which the differences between the two observable types are the largest (see Section 6.4.2), mostly occurred during years 2026 and 2027.

Such an observational period is thus not a special isolated case, but rather a periodic effect of the Earth - Jovian system geometry. Therefore, mutual approximations less favourable to alternative observables are expected to occur repeatedly, about every 6 years, and coincide with the so-called 'mutual events season' during which eclipses and occultations occur. Implications of this effect of the observation geometry concerning the selection of the appropriate mutual approximations' observable type are discussed in Section 6.4.3.

It must be stressed that the selected weighting strategy for alternative observables (Section 6.3.3) accounts for the mutual approximation's characteristics, and thus indirectly for the close encounter's geometry. The aforementioned impact of the observation geometry on the equivalence between the two observable types and more precisely on the benefit of using central instants over alternative observables is therefore already attenuated by our careful weighting of the latter. Section 6.4.4 investigates the consequences of this geometry effect when not taken into consideration in the observation weights.

OBSERVATIONAL PERIOD REDUCED TO 2026-2027

To quantify the impact of using a limited observation set when it unfortunately corresponds to the observational period less favourable to alternative observables, we ran additional simulations including only 2026-2027 mutual approximations in the state estimation. Table 6.2 compares the improvement in formal errors provided by central instants over alternative observables with either complete (2020-2029) or partial (2026-2027) observation sets.

As expected, the differences in formal errors between the two observables increase when only considering 2026-2027 observations, except for Europa's axial position component. The improvement provided by central instants is multiplied by factors ranging from 1.5 to 3 for most position and velocity components. Compared to results obtained with the complete observation set, formal errors' improvements in the axial direction become more significant. They are even comparable to those achieved in the radial direction for both Io's and Europa's velocity.

Although alternative observables and central instants were proven to lead to very comparable solutions in nominal configurations, the influence of the available set of observations must thus not be neglected. If the number of mutual approximations is limited, or the period over which they were observed too short, it is recommended to investigate the characteristics of the available mutual approximations before selecting an observable type. The improvement provided by using central instants is indeed amplified when exclusively including mutual approximations observed under unfavourable observation angles (2026-2027 period in our case).

6.4.3. IMPLICATIONS

If enough observations are available, the improvement achieved by using central instants instead of alternative observables is limited to about 20% for our Io-Europa test case. However, such improvement might still be relevant when concurrently estimating other dynamical parameters along with natural bodies' ephemerides. Accurate determination of the tidal dissipation, in particular, is required to gain

Table 6.2.: Improvements in the final errors obtained with central instants, using two different observations sets. The improvement in formal errors obtained with central instants is computed with respect to formal errors resulting from alternative observables, in two different cases. First, all mutual approximations simulated over the whole 2020-2029 period are included (referred to as case [1] in the table). Second, only mutual approximations occurring during the 2026-2027 period are selected (referred to as [2]).

Parameters		Improvement formal errors 2020-2029 [1]	2026-2027 [2]	Ratio [2]/[1]
Position Io	radial	21.9 %	45.2 %	2.1
	normal	17.4 %	26.7 %	1.5
	axial	12.0 %	29.5 %	2.5
Velocity Io	radial	17.3 %	26.5 %	1.5
	normal	22.3 %	46.3 %	2.1
	axial	2.9 %	25.1 %	8.6
Position Europa	radial	19.7 %	59.8 %	3.0
	normal	20.4 %	27.8 %	1.4
	axial	11.0 %	2.5 %	0.2
Velocity Europa	radial	22.1 %	29.3 %	1.3
	normal	19.7 %	59.7 %	3.0
	axial	4.2 %	33.6 %	7.8

insights into the orbital evolution of planetary systems.

Recent estimations from astrometric data indeed showed that Saturn's tidal quality factor Q can vary by several orders of magnitude from one moon's forcing frequency to another (Lainey et al., 2020). These results are highly inconsistent with current evolution models, thus highlighting the need for accurate frequency-dependent estimation of tidal parameters (Fuller et al., 2016). This is for instance not yet done for Jupiter, whose tidal quality factor is currently only determined at Io's frequency (Lainey et al., 2009). A 20% improvement in the formal errors of the natural satellites' initial states might be critical for such applications. As many perturbing dynamical effects can be absorbed by a variation in the initial state, any improvement in the state estimation can indeed help to detect and estimate such small tidal effects.

Furthermore, a 20% improvement in the predicted position and/or velocity of the targeted body is not negligible for orbital design applications. It can indeed affect the corrective manoeuvres required before and after a flyby or an orbital insertion, allowing for a more efficient design and thus reducing the ΔV budget. The impact of the mutual approximations' observables choice then depends on the timing of the manoeuvre. Fig. 6.9 displays the improvement in propagated errors in radial, normal, and axial direction for both Io's and Europa's positions. The 20% difference in the formal errors of the initial states can increase once propagated, at least in the radial and normal directions. Depending on the time at which the manoeuvre is planned, the improvement in the accuracy of the predicted targeted body's state might thus be higher than 20% if central instants are used. Looking at Fig. 6.9a, differences can reach up to 35% for Io's radial and normal position components while they increase up to almost 40% for Europa (see Fig. 6.9b).

For Europa, the largest differences in propagated errors clearly correspond to the 2026-2027 period and thus coincide with the least favourable observation geometry for alternative observables (see discussion in Section 6.4.2). This effect is however barely noticeable in Fig. 6.9a, for Io's case. Yet, it should be pointed that when a very sensitive manoeuvre is planned during such a particular observational period, the impact of the observable choice on the quality of the estimated solution might not be negligible.

All aforementioned points are direct consequences of the imperfect equivalence between the two types of observables, which might be accentuated when fewer observations are available. In practice, however, this would be balanced by other observations combined with mutual approximations in the state estimation. Building on Section 6.4.2, it is nonetheless worth highlighting that the number and distribution of the observations should be carefully considered when selecting an appropriate observable for the processing of mutual approximations data.

The fact that the alternative observables' unfavourable observational period corresponds to the mutual events season might also be an interesting finding for the processing of the mutual events themselves. Indeed, if the timings at which eclipses and occultations occur were to be directly used as observables (as it is the case with mutual approximations' central instants), the effect of the observation geometry would first need to be carefully investigated.

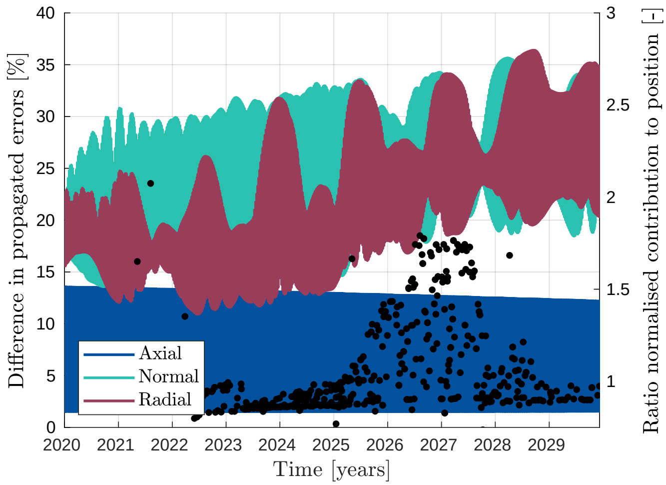

(a)

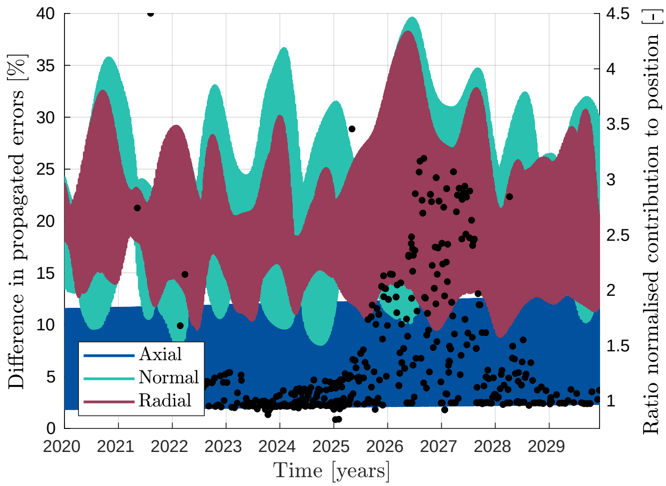

(b)

Figure 6.9.: Propagated formal errors in position components over the observational period (panel a: Io, panel b: Europa). The errors in position are expressed in the RSW frame (Fig. 6.2) and are obtained from the propagated covariance matrix and estimated initial states. The black dots (right axis) display the ratio between the normalised contributions of central instants over their corresponding alternative observables, for each mutual approximation.

6.4.4. INFLUENCE OF THE WEIGHTING SCHEME

When enough mutual approximations are available, the quality of the match between the two observable types' solutions actually strongly depends on the accurate weighting of each mutual approximation. As highlighted in Section 6.3.3, individual weights have to be computed for alternative observables. Using a single averaged value for alternative observables' weights yields a much larger discrepancy with respect to the central instants solution over the full simulation, as reported in Table 6.3. Compared to formal errors obtained with alternative observables, those achieved with central instants are then reduced by a factor 1.5 to 2.7 for the initial position components, and up to a factor 4 for the velocity components.

These results clearly prove that the equivalence between the two observable types is conditioned by the appropriate weighting of alternative observables. As mentioned in Section 6.3.3, it is crucial to carefully compute suitable observation weights to ensure that the alternative observables indirectly take into account the geometry of the close encounter in the plane of the sky.

Emelyanov (2017) already conducted a comparative analysis between the two types of observables, although the central instant partials were computed numerically. Interestingly, a convergence issue was encountered with alternative observables, while none was reported for central instants. This indicates that the two observables types were not perfectly equivalent in this case, which might be due to the weighting

Table 6.3.: Comparison of the final formal errors obtained with the two types of observables, when applying constant weight values. The final errors in the moons' positions are expressed in Jovicentric cartesian coordinates. The central instants solution uses a constant weight $\sigma_{t_c} = 3.5$ s (see Section 6.3.3). For the alternative observables, we use the average of the individual weights defined by Eq. 6.41: $\sigma_{\text{alt.}} = 8.87 \times 10^{-3}$ mas/s.

Parameters	Formal errors with Central instants [1]	Formal errors with Alternative observables [2]	Ratio [2]/[1]
x'_{Io}	7.01 km	11.2 km	1.6
y'_{Io}	10.4 km	17.6 km	1.7
z'_{Io}	14.5 km	37.3 km	2.6
$\dot{x}'_{\text{Io}}$	0.372 m/s	1.30 m/s	3.5
$\dot{y}'_{\text{Io}}$	0.373 m/s	0.904 m/s	2.4
$\dot{z}'_{\text{Io}}$	0.562 m/s	1.86 m/s	3.3
x'_{Europa}	2.31 km	6.24 km	2.7
y'_{Europa}	13.6 km	20.5 km	1.5
z'_{Europa}	26.3 km	49.1 km	1.9
$\dot{x}'_{\text{Europa}}$	0.191 m/s	0.535 m/s	2.8
$\dot{y}'_{\text{Europa}}$	0.222 m/s	0.851 m/s	3.8
$\dot{z}'_{\text{Europa}}$	0.454 m/s	1.75 m/s	3.9

issue we just highlighted.

6.4.5. Verification case: Four Galilean moons

As verification, we simulated mutual approximations between the four Galilean moons of Jupiter. Ganymede's and Callisto's initial states were then estimated in addition to Io's and Europa's. The resulting formal errors in the four moons' initial states are provided in Table 6.4. Even if not displayed here, the time evolution of the errors in Io's and Europa's initial states show a behaviour comparable to what was observed in the first test case limited to Io and Europa only (see Fig. 6.4). The final formal errors are however a bit lower in the four moons' case.

Similarly to the Io-Europa test case, using central instants over alternative observables mostly improves errors in the radial and normal directions, but only has a marginal effect on the axial errors. For Europa's axial position, the estimation is even 2% better with alternative observables. As shown in Table 6.4, differences in formal errors between the two types of observables are significantly lower for Callisto than for the three other moons. These differences are only of a few percents, while they reach about 10% for Io's, Europa's, and Ganymede's initial positions.

Again, the contribution of each mutual approximation to the estimated ephemerides solution also reflects the higher sensitivity of central instants to the complex dynamics at play in the Jovian system. Fig. 6.10 shows the contribution of every observation to the initial position of Io (dark blue), Europa (light blue),

Table 6.4.: Comparison of the formal errors in the initial positions of the four Galilean moons. The formal errors in position are expressed in the RSW frame (see Fig. 6.2) and are provided for the two types of observables. The last column displays the relative difference between the two. All predicted mutual approximations over the period 2020-2029 were included in the state estimation.

Moon	Position component	Formal errors [km] Central instants	Formal errors [km] Alternative observables	Relative difference [%]
Io	Radial	0.222	0.242	8.2
	Normal	6.60	7.30	9.6
	Axial	4.49	4.57	1.7
Europa	Radial	0.908	1.02	10.7
	Normal	5.27	5.90	10.7
	Axial	10.3	10.1	2.2
Ganymede	Radial	1.22	1.37	11.3
	Normal	5.99	6.39	6.2
	Axial	17.9	18.1	1.1
Callisto	Radial	1.55	1.56	0.7
	Normal	8.64	8.93	3.2
	Axial	25.5	26.0	1.6

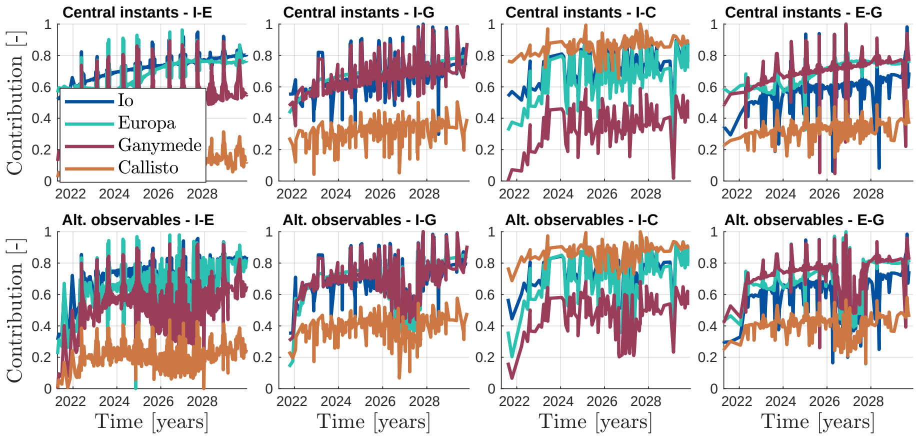

Figure 6.10.: Normalised contribution of mutual approximations between Io and Europa (I-E, left plots), Io and Ganymede (I-G, centre-left plots), Io and Callisto (I-C, centre-right plots), Europa and Ganymede (E-G, right plots) to the initial position of Io (dark blue), Europa (light blue), Ganymede (purple), and Callisto (orange). Results for Europa-Callisto and Ganymede-Callisto mutual approximations are not presented here, but do not show any trend that is not already highlighted by the contributions of the other observations.

Ganymede (purple), and Callisto (orange). As expected, all mutual approximations contribute to estimating the initial states of Io, Europa, and Ganymede because of the Laplace resonance between these three moons. On the other hand, only mutual approximations directly involving Callisto significantly help determine its initial state.

In Fig. 6.10, clear periodic patterns can be identified in the central instants case, at least when enough observations are available, such as for Io-Europa, Io-Ganymede, and Europa-Ganymede mutual approximations. While still present, those patterns are however less pronounced for the alternative observables case. They are directly related to the relative motion of the satellites in the Jovian system (inertial motion, as opposed to apparent). This again indicates that part of the information encoded in mutual approximations is not fully captured by alternative observables.

As already highlighted by the Io-Europa case (Section 6.4.1), central instants are indeed more sensitive to the apparent relative acceleration between the two satellites. Central instants' partials directly account for any acceleration variation induced by a small change in initial states, while alternative observables do not. This may also explain why differences between the two observables are lower for Callisto. As it is the most remote moon with respect to Jupiter, the distance between Callisto and each of the three other moons is larger than the distances between Io, Europa, and Ganymede, resulting in smaller inter-moon accelerations. Furthermore, because of the Laplace resonance between the three innermost Galilean satellites, accelerations exerted by one of these three moons on the other two strongly influence their dynamics. These two combined effects might strengthen the advantage of central instants over alternative observables for Io, Europa, and Ganymede, compared to Callisto.

Overall, all findings obtained in the first simple Io-Europa test case are confirmed by this second analysis extended to the four Galilean moons. The two types of observables lead to almost equivalent solutions if the alternative observables are properly weighted (see Section 6.3.3), despite a 10% reduction of the formal errors in both radial and normal directions when using central instants. The effect of the observation geometry is also similar to the Io-Europa case: low impact parameter, large impact velocity mutual approximations simulated in 2026-2027 are unfavourable to alternative observables.

6.5. CONCLUSION & DISCUSSION

We developed an analytical formulation for the observation partials of the mutual approximations' central instants. This allows those central instants to be directly used as observables to estimate the ephemerides of natural satellites. Our analytical method relies on a second-order polynomial to approximate the relative motion of two satellites around their point of closest approach. From this polynomial function, we derived an expression for the central instant as a function of the apparent relative position, velocity, and acceleration of the two satellites.

Higher-order terms could theoretically be included in our formulation. Using a third-order polynomial to reproduce the apparent relative motion of the two moons (Eqs. 6.11-6.12) would lead to a fourth-order polynomial for the central instant (Eq. 6.18). The roots of such a polynomial could still be computed analytically, but at the cost of a dramatic increase in complexity. However, a second-order polynomial has been proven sufficient to capture the apparent relative dynamics of the two satellites around their closest encounter and to yield highly accurate analytical partials for central instants.

Numerically computing partials for central instants, on the other hand, is extremely computationally demanding (Emelyanov, 2017). It requires to independently propagate small variations in each of the estimated parameters (at least 6 initial state components for each of the two moons involved). Afterwards, the new central instants must be determined, which is a time-consuming process in itself. Should central instants be used, our analytical approach is thus significantly faster than the numerical computation of the observation partials.

We conducted a comparative covariance analysis using either only central instants, or only mutual approximation's alternative observables to estimate the Galilean moons' ephemerides. When using the entire set of viable mutual approximations over the period 2020-2029, the difference in formal errors does not exceed 20% between the two types of observables. The central instants achieve the best ephemerides solution because alternative observables do not account for some of the dynamical effects affecting the close encounter (e.g., apparent relative acceleration between the two satellites). In contrast, these effects are directly captured by central instants, which is beneficial for the resulting estimated solution.

Overall, we still prove alternative observables to be almost equivalent to central instants, but only under specific conditions. First, when using alternative observables, the shape of the observed close encounter must indirectly be accounted for in the calculation of the observation weights, while it is automatically included in the central instant case. Individual and accurate weighting of each event, based on the apparent relative dynamics of the satellites, is then crucial to obtain a consistent solution. It is indeed necessary to convert any error in the estimated central instant to an error in the derivative of the apparent distance. We show that when using a single averaged value to weigh all mutual approximations, the formal errors in initial states obtained with central instants were 1.5 to 4 times lower than with alternative observables in our test case. As discussed in Section 6.4.4, an inappropriate weighting scheme could thus possibly explain previous indications of a non-equivalence between the two observable types (Emelyanov, 2017). When using alternative observables, we therefore recommend to adopt the weighting strategy described in Section 6.3.3, and more precisely to compute the weights with Eq. 6.41. In Appendix 6.11, we provide the appropriate alternative observables' weights for the 2016-2018 mutual approximations reported in Morgado et al. (2019b). These weight values should be applied for these observations to be properly included in the state estimation.

Furthermore, all mutual approximations do not homogeneously contribute to the ephemerides solution. The satellites' dynamics are overall better constrained by mutual approximations with a low impact parameter (typically below 7 as) and low relative velocity (1 mas/s), for both observable types. However, some characteristics in particular are unfavourable to alternative observables: mutual approximations with low impact parameters but large impact velocities contribute significantly more to the estimated solution when using central instants (factor 2 to 3). Preferring central instants is thus particularly advantageous for these specific mutual approximations, which are not isolated events but periodically represent most of the observations for one or two years (see discussion in Section 6.4.2).

Choosing between the two types of observables when estimating ephemerides from mutual approximations therefore requires critical evaluation. If many mutual approximations are available to estimate the moons' ephemerides, one can safely use alternative observables without substantially degrading the solution. However, this does not systematically hold for a small set of observations, especially if they are all collected during the alternative observables' unfavourable observation period. The formal error reduction provided by our method then strongly depends on the mutual approximations' characteristics.

The relevance of selecting central instants over alternative observables eventually depends on the application of the ephemerides solution. As detailed in Section 6.4.3, a 10-20% improvement in the formal errors of the satellites' state might be significant when concurrently estimating tidal parameters. It may also be non-negligible for mission design applications. Improved ephemerides are indeed crucial to design efficient flybys or orbital insertions requiring only limited corrective manoeuvres. The timing of the manoeuvres must then be taken into consideration to select a suitable observable, especially if they coincide with observation geometries less

6

favourable to alternative observables.

As mentioned in Section 6.4.3, a comparable analysis could be conducted for mutual events. We expect to obtain consistent results with respect to the mutual approximations' case, given the similarities between the two types of observation. However, all mutual events occur during the alternative observables' unfavourable observational period. It is thus important to confirm the influence of the observation geometry on the differences between central instants' and alternative observables' state estimation solutions. This could be an interesting result, in case the timings of eclipses and occultations are directly used as observables, as for mutual approximations.

6.6. APPENDIX A: FITTING A POLYNOMIAL TO A CLOSE ENCOUNTER'S APPARENT DISTANCE HISTORY

As described in Section 6.1, the apparent distance history during a close encounter between the two satellites is typically fitted with a fourth order polynomial (e.g., Morgado et al., 2016). This allows to estimate the mutual approximation's central instant, as well as other properties such as the impact parameter. In this appendix, we discuss the influence of the order of the fitting polynomial. The maximum absolute values of the residuals between the fitted polynomial and the true apparent distance history are reported in Table 6.5 (for the first mutual approximations predicted between Io and Europa, starting from 01/01/2020). For clarity, the apparent distance observations, fitted polynomial, and resulting residuals are displayed in Fig. 6.11 for the first mutual approximation.

When switching from a fourth order to a second order polynomial to reproduce the apparent distance history over the whole duration of the close encounter (i.e., 60 minutes), the residuals increase by almost a factor 10. However, if we only focus on a small fraction of the event (here only 30 minutes centred on the central instant), a second order polynomial achieves similar residuals as a fourth order polynomial applied to the full close encounter duration. This proves that a second order polynomial is well-suited when focusing on short time intervals centred on t_c. This is the case when deriving observation partials for central instants, as we then only consider slight changes in t_c, induced by small variations of the estimated parameters.

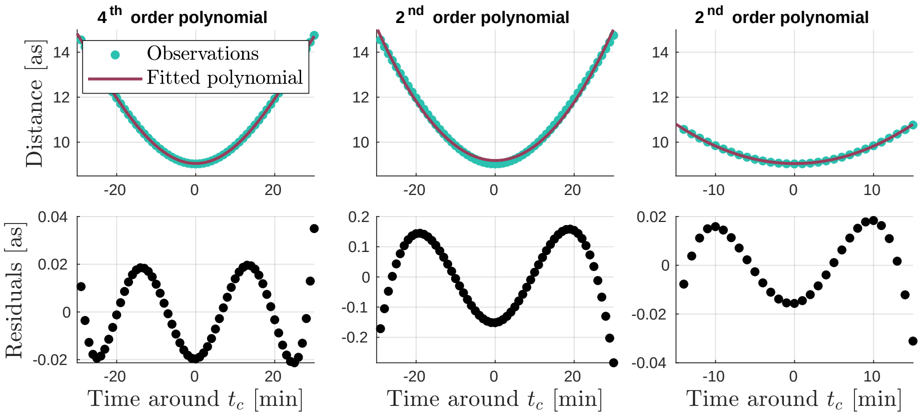

Figure 6.11.: Apparent distance measurements during a mutual approximation (blue dots on top panels). The polynomial used to fit these observations is typically a fourth order one (left panel). A second order polynomial was also tested, for the whole duration of the event (middle panels) and over a reduced time interval (30 minutes) centred on the central instant t_c. For each of the three case, the residuals between the fitted polynomial and the true apparent distance history are displayed in the bottom panels.

Table 6.5.: Maximum absolute values for the residuals between the apparent distance history and the fitted polynomial. The residuals are compared between three configurations: fourth order and second order polynomials used over the whole duration of the close encounter (i.e., 60 minutes: $[t_c - 30\text{min}; t_c + 30\text{min}]$) and second order polynomial over a reduced interval centred on the central instant (only 30 minutes: $[t_c - 15\text{min}; t_c + 15\text{min}]$). Results are reported for 5 mutual approximations.

Mutual approx.	Max. absolute residual value [as]		
	$[t_c - 30\text{min}; t_c + 30\text{min}]$		$[t_c - 15\text{min}; t_c + 15\text{min}]$
	4^{th} order	2^{nd} order	2^{nd} order
1	$3.50 \cdot 10^{-2}$	$2.84 \cdot 10^{-1}$	$3.11 \cdot 10^{-2}$
2	$3.13 \cdot 10^{-2}$	$2.45 \cdot 10^{-1}$	$2.97 \cdot 10^{-2}$
3	$3.55 \cdot 10^{-2}$	$2.67 \cdot 10^{-1}$	$3.28 \cdot 10^{-2}$
4	$3.84 \cdot 10^{-2}$	$2.99 \cdot 10^{-1}$	$3.40 \cdot 10^{-2}$
5	$3.78 \cdot 10^{-2}$	$2.79 \cdot 10^{-1}$	$3.32 \cdot 10^{-2}$

6.7. APPENDIX B: POSITION AND VELOCITY PARTIALS OF α_{Si}, δ_{Si}, $\dot{\alpha}_{Si}$, $\dot{\delta}_{Si}$, $\ddot{\alpha}_{Si}$ AND $\ddot{\delta}_{Si}$

6.7.1. α_{Si} AND δ_{Si} PARTIALS

First, we derive the partials of the right ascension α_{Si} and declination δ_{Si} with respect to the two satellites' and observer's positions, as follows:

$$\left.\frac{\partial \alpha_{Si}}{\partial \boldsymbol{r}_{Si}}\right|_{t_{Si}} = -\left.\frac{\partial \alpha_{Si}}{\partial \boldsymbol{r}_{O}}\right|_{t_{Si}} = \frac{1}{r_{i_{xy}}^2}\begin{pmatrix} -y_i \\ x_i \\ 0 \end{pmatrix}, \tag{6.44}$$

$$\left.\frac{\partial \delta_{Si}}{\partial \boldsymbol{r}_{Si}}\right|_{t_{Si}} = -\left.\frac{\partial \delta_{Si}}{\partial \boldsymbol{r}_{O}}\right|_{t_{Si}} = \frac{1}{r_i^2 r_{i_{xy}}}\begin{pmatrix} -x_i z_i \\ -y_i z_i \\ r_{i_{xy}}^2 \end{pmatrix}, \tag{6.45}$$

$$\left.\frac{\partial\,[\alpha,\delta]_{Si}}{\partial \boldsymbol{r}_{Sj}}\right|_{t_{Si}} = \begin{pmatrix} 0 \\ 0 \\ 0 \end{pmatrix}; i \neq j. \tag{6.46}$$

The partials of α_{Si} and δ_{Si} with respect to the velocity vectors are by definition equal to zero:

$$\left.\frac{\partial\,[\alpha,\delta]_{Si}}{\partial \dot{\boldsymbol{r}}_{Si}}\right|_{t_{Si}} = \left.\frac{\partial\,[\alpha,\delta]_{Si}}{\partial \dot{\boldsymbol{r}}_{O}}\right|_{t_{Si}} = \left.\frac{\partial\,[\alpha,\delta]_{Si}}{\partial \dot{\boldsymbol{r}}_{Sj}}\right|_{t_{Si}} = \begin{pmatrix} 0 \\ 0 \\ 0 \end{pmatrix}; i \neq j. \tag{6.47}$$

6.7.2. $\dot{\alpha}_{Si}$ AND $\dot{\delta}_{Si}$ PARTIALS

The partials of $\dot{\alpha}_{Si}$ and $\dot{\delta}_{Si}$ with respect to the position vectors of the two satellites and the observer are

$$\left.\frac{\partial \dot{\alpha}_{Si}}{\partial \boldsymbol{r}_{Si}}\right|_{t_{Si}} = \frac{1}{r_{i_{xy}}^4}\begin{pmatrix} \dot{y}_i\left(y_i^2 - x_i^2\right) + 2x_i y_i \dot{x}_i \\ \dot{x}_i\left(y_i^2 - x_i^2\right) - 2x_i y_i \dot{y}_i \\ 0 \end{pmatrix}, \tag{6.48}$$

$$\left.\frac{\partial \dot{\delta}_{Si}}{\partial \boldsymbol{r}_{Si}}\right|_{t_{Si}} = \frac{-1}{r_i^2 r_{i_{xy}}}\begin{pmatrix} z_i \dot{x}_i - x_i \dot{z}_i \\ z_i \dot{y}_i - y_i \dot{z}_i \\ x_i \dot{x}_i + y_i \dot{y}_i \end{pmatrix} - \frac{2\dot{z}_i r_{i_{xy}}}{r_i^4}\begin{pmatrix} x_i \\ y_i \\ z_i \end{pmatrix} + \frac{z_i\left(x_i \dot{x}_i + y_i \dot{y}_i\right)}{r_i^4 r_{i_{xy}}}\left[\frac{z_i^2}{r_{i_{xy}}^2}\begin{pmatrix} x_i \\ y_i \\ 0 \end{pmatrix} + \begin{pmatrix} 3x_i \\ 3y_i \\ z_i \end{pmatrix}\right], \tag{6.49}$$

$$\left.\frac{\partial[\dot{\alpha},\dot{\delta}]_{Si}}{\partial \boldsymbol{r}_{O}}\right|_{t_{Si}} = -\left.\frac{\partial[\dot{\alpha},\dot{\delta}]_{Si}}{\partial \boldsymbol{r}_{Si}}\right|_{t_{Si}}, \tag{6.50}$$

$$\left.\frac{\partial[\dot{\alpha},\dot{\delta}]_{Si}}{\partial \boldsymbol{r}_{Sj}}\right|_{t_{Si}} = \begin{pmatrix} 0 \\ 0 \\ 0 \end{pmatrix}; i \neq j. \tag{6.51}$$

We also compute partials of $\dot{\alpha}_{Si}$ and $\dot{\delta}_{Si}$ with respect to the two satellites' and the observer's velocity vectors:

$$\left.\frac{\partial \dot{\alpha}_{Si}}{\partial \dot{\boldsymbol{r}}_{Si}}\right|_{t_{Si}} = -\left.\frac{\partial \dot{\alpha}_{Si}}{\partial \dot{\boldsymbol{r}}_{O}}\right|_{t_{Si}} = \frac{1}{r_{i_{xy}}^2}\begin{pmatrix} -y_i \\ x_i \\ 0 \end{pmatrix}, \tag{6.52}$$

$$\left.\frac{\partial \dot{\delta}_{Si}}{\partial \dot{\boldsymbol{r}}_{Si}}\right|_{t_{Si}} = -\left.\frac{\partial \dot{\delta}_{Si}}{\partial \dot{\boldsymbol{r}}_{O}}\right|_{t_{Si}} = \frac{1}{r_i^2 r_{i_{xy}}}\begin{pmatrix} -x_i z_i \\ -y_i z_i \\ r_{i_{xy}}^2 \end{pmatrix}, \tag{6.53}$$

$$\left.\frac{\partial \left[\dot{\alpha}, \dot{\delta}\right]_{Si}}{\partial \dot{\boldsymbol{r}}_{Sj}}\right|_{t_{Si}} = \begin{pmatrix} 0 \\ 0 \\ 0 \end{pmatrix}; i \neq j. \tag{6.54}$$

6.7.3. $\ddot{\alpha}_{Si}$ AND $\ddot{\delta}_{Si}$ PARTIALS

The partials of $\ddot{\alpha}_{Si}$ and $\ddot{\delta}_{Si}$ with respect to position vectors lead to more complex expressions. We therefore split those partials into two terms. The first one, denoted as $g_{\ddot{\alpha}_{Si}}$ or $g_{\ddot{\delta}_{Si}}$, correspond to the contribution of the acceleration partials (more details about how to compute them are provided in Appendix 6.8). The rest of the partial expression is included in the other term ($g'_{\ddot{\alpha}_{Si}}$ or $g'_{\ddot{\delta}_{Si}}$).

We thus obtain the following formulation for the partial of $\ddot{\alpha}_{Si}$ with respect to the position of satellite i:

$$\left.\frac{\partial \ddot{\alpha}_{Si}}{\partial \boldsymbol{r}_{Si}}\right|_{t_{Si}} = g_{\ddot{\alpha}_{Si}} + g'_{\ddot{\alpha}_{Si}}, \text{ with} \tag{6.55}$$

$$g_{\ddot{\alpha}_{Si}} = \begin{pmatrix} x_i \frac{\partial \ddot{y}_i}{\partial x_{Si}} - y_i \frac{\partial \ddot{x}_i}{\partial x_{Si}} \\ x_i \frac{\partial \ddot{y}_i}{\partial y_{Si}} - y_i \frac{\partial \ddot{x}_i}{\partial y_{Si}} \\ x_i \frac{\partial \ddot{y}_i}{\partial z_{Si}} - y_i \frac{\partial \ddot{x}_i}{\partial z_{Si}} \end{pmatrix}, \tag{6.56}$$

$$g'_{\ddot{\alpha}_{Si}} = \begin{pmatrix} \ddot{y}_i \\ \ddot{x}_i \\ 0 \end{pmatrix} + \frac{2}{r_{i_{xy}}^2}\begin{pmatrix} -2x_i \dot{x}_i \dot{y}_i - y\dot{y}_i^2 + y\dot{x}_i^2 \\ 2y_i \dot{x}_i \dot{y}_i + x\dot{x}_i^2 - x\dot{y}_i^2 \\ 0 \end{pmatrix} + \frac{4\left(x_i \dot{y}_i - y_i \dot{x}_i\right)\left(x_i \dot{x}_i + y_i \dot{y}_i\right)}{r_{i_{xy}}^4}\begin{pmatrix} x \\ y \\ 0 \end{pmatrix}. \tag{6.57}$$

The partials of $\ddot{\alpha}_{Si}$ with respect to the position vectors of the observer and of the other satellite j are

$$\left.\frac{\partial \ddot{\alpha}_{Si}}{\partial \boldsymbol{r}_{O}}\right|_{t_{Si}} = \begin{pmatrix} x_i \frac{\partial \ddot{y}_i}{\partial x_O} - y_i \frac{\partial \ddot{x}_i}{\partial x_O} \\ x_i \frac{\partial \ddot{y}_i}{\partial y_O} - y_i \frac{\partial \ddot{x}_i}{\partial y_O} \\ x_i \frac{\partial \ddot{y}_i}{\partial z_O} - y_i \frac{\partial \ddot{x}_i}{\partial z_O} \end{pmatrix} - g'_{\ddot{\alpha}_{Si}}, \tag{6.58}$$

6

$$\left.\frac{\partial \ddot{\alpha}_{Si}}{\partial \boldsymbol{r}_{Sj}}\right|_{t_{Si}} = \begin{pmatrix} x_i \dfrac{\partial \ddot{y}_i}{\partial x_{Sj}} - y_i \dfrac{\partial \ddot{x}_i}{\partial x_{Sj}} \\ x_i \dfrac{\partial \ddot{y}_i}{\partial y_{Sj}} - y_i \dfrac{\partial \ddot{x}_i}{\partial y_{Sj}} \\ x_i \dfrac{\partial \ddot{y}_i}{\partial z_{Sj}} - y_i \dfrac{\partial \ddot{x}_i}{\partial z_{Sj}} \end{pmatrix}; i \neq j. \tag{6.59}$$

Similarly, the position partials of $\ddot{\delta}_{Si}$ are written as follows:

$$\left.\frac{\partial \ddot{\delta}_{Si}}{\partial \boldsymbol{r}_{Si}}\right|_{t_{Si}} = g_{\ddot{\delta}_{Si}} + g'_{\ddot{\delta}_{Si}}, \text{ with} \tag{6.60}$$

$$g_{\ddot{\delta}_{Si}} = \frac{-z_i}{r_i^2 r_{i_{xy}}} \begin{pmatrix} x_i \dfrac{\partial \ddot{x}_i}{\partial x_{Si}} + y_i \dfrac{\partial \ddot{y}_i}{\partial x_{Si}} \\ x_i \dfrac{\partial \ddot{x}_i}{\partial y_{Si}} + y_i \dfrac{\partial \ddot{y}_i}{\partial y_{Si}} \\ x_i \dfrac{\partial \ddot{x}_i}{\partial z_{Si}} + y_i \dfrac{\partial \ddot{y}_i}{\partial z_{Si}} \end{pmatrix} + \frac{r_{i_{xy}}}{r_i^2} \begin{pmatrix} \dfrac{\partial \ddot{z}_i}{\partial x_{Si}} \\ \dfrac{\partial \ddot{z}_i}{\partial y_{Si}} \\ \dfrac{\partial \ddot{z}_i}{\partial z_{Si}} \end{pmatrix}, \tag{6.61}$$

$$\begin{aligned} g'_{\ddot{\delta}_{Si}} = {} & \frac{1}{r_i^2 r_{i_{xy}}} \begin{pmatrix} -z_i \ddot{x}_i + 2x_i \ddot{z}_i \\ -z_i \ddot{y}_i + 2y_i \ddot{z}_i \\ -x_i \ddot{x}_i - y_i \ddot{y}_i \end{pmatrix} - \frac{\ddot{\delta}_{Si}}{r_i^2 r_{i_{xy}}^2} \begin{pmatrix} x_i (r_{i_{xy}}^2 - z_i^2) \\ y_i (r_{i_{xy}}^2 - z_i^2) \\ 2z_i r_{i_{xy}}^2 \end{pmatrix} \\ & -4\left(z_i \left(x_i \dot{x}_i + y_i \dot{y}_i\right) - \dot{z}_i r_{i_{xy}}^2\right)\left(\boldsymbol{r}_O^{S_i} \cdot \dot{\boldsymbol{r}}_O^{S_i}\right) \boldsymbol{r}_O^{S_i} - \frac{x_i \dot{y}_i - y_i \dot{x}_i}{r_i^2 r_{i_{xy}}^5} \begin{pmatrix} 2z_i \left(y_i^2 \dot{y}_i + x_i y_i \dot{x}_i\right) \\ 2z_i \left(x_i^2 \dot{x}_i + 2y_i^2 \dot{x}_i - x_i y_i \dot{y}_i\right) \\ -r_{i_{xy}}^2 \left(x_i \dot{y}_i - y_i \dot{x}_i\right) \end{pmatrix} \\ & + \frac{2}{r_i^2} \begin{pmatrix} -2x_i \dot{z}_i \left(y_i \dot{y}_i + z_i \dot{z}_i\right) + \dot{x}_i \dot{z}_i \left(-3x_i^2 - y_i^2 + z_i^2\right) \\ -2y_i \dot{z}_i \left(x_i \dot{x}_i + z_i \dot{z}_i\right) + \dot{y}_i \dot{z}_i \left(-x_i^2 - 3y_i^2 + z_i^2\right) \\ -r_{i_{xy}}^2 \dot{z}_i^2 \end{pmatrix} + \frac{2\left(x \dot{x}_i + y_i \dot{y}_i\right)}{r_i^2} \begin{pmatrix} 2z_i \dot{x}_i \\ 2z_i \dot{y}_i \\ 2z_i \dot{z}_i + x_i \dot{x}_i + y_i \dot{y}_i \end{pmatrix}, \end{aligned} \tag{6.62}$$

$$\left.\frac{\partial \ddot{\delta}_{Si}}{\partial \boldsymbol{r}_{O}}\right|_{t_{Si}} = \frac{-z_i}{r_i^2 r_{i_{xy}}} \begin{pmatrix} x_i \dfrac{\partial \ddot{x}_i}{\partial x_{O}} + y_i \dfrac{\partial \ddot{y}_i}{\partial x_{O}} \\ x_i \dfrac{\partial \ddot{x}_i}{\partial y_{O}} + y_i \dfrac{\partial \ddot{y}_i}{\partial y_{O}} \\ x_i \dfrac{\partial \ddot{x}_i}{\partial z_{O}} + y_i \dfrac{\partial \ddot{y}_i}{\partial z_{O}} \end{pmatrix} + \frac{r_{i_{xy}}}{r_i^2} \begin{pmatrix} \dfrac{\partial \ddot{z}_i}{\partial x_{O}} \\ \dfrac{\partial \ddot{z}_i}{\partial y_{O}} \\ \dfrac{\partial \ddot{z}_i}{\partial z_{O}} \end{pmatrix} - g'_{\ddot{\delta}_{Si}}, \tag{6.63}$$

$$\left.\frac{\partial \ddot{\delta}_{Si}}{\partial \boldsymbol{r}_{Sj}}\right|_{t_{Si}} = \frac{-z_i}{r_i^2 r_{i_{xy}}} \begin{pmatrix} x_i \dfrac{\partial \ddot{x}_i}{\partial x_{Sj}} + y_i \dfrac{\partial \ddot{y}_i}{\partial x_{Sj}} \\ x_i \dfrac{\partial \ddot{x}_i}{\partial y_{Sj}} + y_i \dfrac{\partial \ddot{y}_i}{\partial y_{Sj}} \\ x_i \dfrac{\partial \ddot{x}_i}{\partial z_{Sj}} + y_i \dfrac{\partial \ddot{y}_i}{\partial z_{Sj}} \end{pmatrix} + \frac{r_{i_{xy}}}{r_i^2} \begin{pmatrix} \dfrac{\partial \ddot{z}_i}{\partial x_{S_j}} \\ \dfrac{\partial \ddot{z}_i}{\partial y_{S_j}} \\ \dfrac{\partial \ddot{z}_i}{\partial z_{S_j}} \end{pmatrix}; i \neq j. \tag{6.64}$$

Finally, the velocity partials also have to be derived for $\ddot{\alpha}_{Si}$ and $\ddot{\delta}_{Si}$. We again split the partials expressions into two terms, designated by $k_{\ddot{\alpha}_{Si}}$ and $k'_{\ddot{\alpha}_{Si}}$ (or $k_{\ddot{\delta}_{Si}}$ and $k'_{\ddot{\delta}_{Si}}$). Again $k_{\ddot{\alpha}_{Si}}$ corresponds to the contribution of the acceleration partials.

Starting with the partials of $\ddot{\alpha}_{Si}$ with respect to the satellites' and observer's velocity vectors, we obtain the following expressions:

$$\left.\frac{\partial \ddot{\alpha}_{Si}}{\partial \dot{\boldsymbol{r}}_{Si}}\right|_{t_{Si}} = k_{\ddot{\alpha}_{Si}} + k'_{\ddot{\alpha}_{Si}}, \text{ with} \tag{6.65}$$

$$k_{\ddot{\alpha}_{Si}} = \frac{1}{r_{i_{xy}}^2}\begin{pmatrix} x_i \frac{\partial \ddot{y}_i}{\partial \dot{x}_{Si}} - y_i \frac{\partial \ddot{x}_i}{\partial \dot{x}_{Si}} \\ x_i \frac{\partial \ddot{y}_i}{\partial \dot{y}_{Si}} - y_i \frac{\partial \ddot{x}_i}{\partial \dot{y}_{Si}} \\ x_i \frac{\partial \ddot{y}_i}{\partial \dot{z}_{Si}} - y_i \frac{\partial \ddot{x}_i}{\partial \dot{z}_{Si}} \end{pmatrix}, \tag{6.66}$$

$$k'_{\ddot{\alpha}_{Si}} = \frac{2}{r_{i_{xy}}^4}\begin{pmatrix} (y_i^2 - x_i^2)\dot{y}_i + 2x_i y_i \dot{x}_i \\ (y_i^2 - x_i^2)\dot{x}_i - 2x_i y_i \dot{y}_i \\ 0 \end{pmatrix}, \tag{6.67}$$

$$\left.\frac{\partial \ddot{\alpha}_{Si}}{\partial \dot{\boldsymbol{r}}_{O}}\right|_{t_{Si}} = \frac{1}{r_{i_{xy}}^2}\begin{pmatrix} x_i \frac{\partial \ddot{y}_i}{\partial \dot{x}_{O}} - y_i \frac{\partial \ddot{x}_i}{\partial \dot{x}_{O}} \\ x_i \frac{\partial \ddot{y}_i}{\partial \dot{y}_{O}} - y_i \frac{\partial \ddot{x}_i}{\partial \dot{y}_{O}} \\ x_i \frac{\partial \ddot{y}_i}{\partial \dot{z}_{O}} - y_i \frac{\partial \ddot{x}_i}{\partial \dot{z}_{O}} \end{pmatrix} - k'_{\ddot{\alpha}_{Si}}, \tag{6.68}$$

$$\left.\frac{\partial \ddot{\alpha}_{Si}}{\partial \dot{\boldsymbol{r}}_{Sj}}\right|_{t_{Si}} = \frac{1}{r_{i_{xy}}^2}\begin{pmatrix} x_i \frac{\partial \ddot{y}_i}{\partial \dot{x}_{Sj}} - y_i \frac{\partial \ddot{x}_i}{\partial \dot{x}_{Sj}} \\ x_i \frac{\partial \ddot{y}_i}{\partial \dot{y}_{Sj}} - y_i \frac{\partial \ddot{x}_i}{\partial \dot{y}_{Sj}} \\ x_i \frac{\partial \ddot{y}_i}{\partial \dot{z}_{Sj}} - y_i \frac{\partial \ddot{x}_i}{\partial \dot{z}_{Sj}} \end{pmatrix}; i \neq j. \tag{6.69}$$

Lastly, we obtain the following formulations for the partials of $\ddot{\delta}_{Si}$ with respect to the satellites' and observer's velocity vectors:

$$\left.\frac{\partial \ddot{\delta}_{Si}}{\partial \dot{\boldsymbol{r}}_{Si}}\right|_{t_{Si}} = k_{\ddot{\delta}_{Si}} + k'_{\ddot{\delta}_{Si}}, \text{ with} \tag{6.70}$$

$$k_{\ddot{\delta}_{Si}} = \frac{-z_i}{r_i^2 r_{i_{xy}}}\begin{pmatrix} x_i \frac{\partial \ddot{x}_i}{\partial \dot{x}_{Si}} + y_i \frac{\partial \ddot{y}_i}{\partial \dot{x}_{Si}} \\ x_i \frac{\partial \ddot{x}_i}{\partial \dot{y}_{Si}} + y_i \frac{\partial \ddot{y}_i}{\partial \dot{y}_{Si}} \\ x_i \frac{\partial \ddot{x}_i}{\partial \dot{z}_{Si}} + y_i \frac{\partial \ddot{y}_i}{\partial \dot{z}_{Si}} \end{pmatrix} + \frac{r_{i_{xy}}}{r_i^2}\begin{pmatrix} \frac{\partial \ddot{z}_i}{\partial \dot{x}_{Si}} \\ \frac{\partial \ddot{z}_i}{\partial \dot{y}_{Si}} \\ \frac{\partial \ddot{z}_i}{\partial \dot{z}_{Si}} \end{pmatrix}, \tag{6.71}$$

$$k'_{\ddot{\delta}_{Si}} = \frac{2z_i\left(y_i\dot{x}_i - x_i\dot{y}_i\right)}{r_{i_{xy}}^2}\begin{pmatrix} -y_i \\ x_i \\ 0 \end{pmatrix} + \frac{2}{r_i^2}\begin{pmatrix} -x_i\dot{z}_i\left(r_{i_{xy}}^2 - z_i^2\right) + 2x_i z_i\left(x_i\dot{x}_i + y_i\dot{y}_i\right) \\ -y_i\dot{z}_i\left(r_{i_{xy}}^2 - z_i^2\right) + 2y_i z_i\left(x_i\dot{x}_i + y_i\dot{y}_i\right) \\ -\left(r_{i_{xy}}^2 - z_i^2\right)\left(x_i\dot{x}_i + y_i\dot{y}_i\right) - 2z_i\dot{z}_i r_{i_{xy}}^2 \end{pmatrix}, \tag{6.72}$$

$$\left.\frac{\partial \ddot{\delta}_{Si}}{\partial \dot{\boldsymbol{r}}_O}\right|_{t_{Si}} = \frac{-z_i}{r_i^2 r_{i_{xy}}} \begin{pmatrix} x_i \dfrac{\partial \ddot{x}_i}{\partial \dot{x}_O} + y_i \dfrac{\partial \ddot{y}_i}{\partial \dot{x}_O} \\ x_i \dfrac{\partial \ddot{x}_i}{\partial \dot{y}_O} + y_i \dfrac{\partial \ddot{y}_i}{\partial \dot{y}_O} \\ x_i \dfrac{\partial \ddot{x}_i}{\partial \dot{z}_O} + y_i \dfrac{\partial \ddot{y}_i}{\partial \dot{z}_O} \end{pmatrix} + \frac{r_{i_{xy}}}{r_i^2} \begin{pmatrix} \dfrac{\partial \ddot{z}_i}{\partial \dot{x}_O} \\ \dfrac{\partial \ddot{z}_i}{\partial \dot{y}_O} \\ \dfrac{\partial \ddot{z}_i}{\partial \dot{z}_O} \end{pmatrix} - k'_{\ddot{\delta}_{Si}}, \tag{6.73}$$

$$\left.\frac{\partial \ddot{\delta}_{Si}}{\partial \dot{\boldsymbol{r}}_{Sj}}\right|_{t_{Si}} = \frac{-z_i}{r_i^2 r_{i_{xy}}} \begin{pmatrix} x_i \dfrac{\partial \ddot{x}_i}{\partial \dot{x}_{Sj}} + y_i \dfrac{\partial \ddot{y}_i}{\partial \dot{x}_{Sj}} \\ x_i \dfrac{\partial \ddot{x}_i}{\partial \dot{y}_{Sj}} + y_i \dfrac{\partial \ddot{y}_i}{\partial \dot{y}_{Sj}} \\ x_i \dfrac{\partial \ddot{x}_i}{\partial \dot{z}_{Sj}} + y_i \dfrac{\partial \ddot{y}_i}{\partial \dot{z}_{Sj}} \end{pmatrix} + \frac{r_{i_{xy}}}{r_i^2} \begin{pmatrix} \dfrac{\partial \ddot{z}_i}{\partial \dot{x}_{Sj}} \\ \dfrac{\partial \ddot{z}_i}{\partial \dot{y}_{Sj}} \\ \dfrac{\partial \ddot{z}_i}{\partial \dot{z}_{Sj}} \end{pmatrix} ; i \neq j. \tag{6.74}$$

6.8. APPENDIX C: ACCELERATION PARTIALS

As shown in Appendix 6.7, computing $\ddot{\alpha}_{S_i}$ and $\ddot{\delta}_{S_i}$ partials requires first computing the partials of those relative acceleration, starting from Eq. 6.4:

$$\frac{\partial \ddot{\boldsymbol{r}}_O^{S_i}}{\partial \boldsymbol{q}} = \frac{\partial \ddot{\boldsymbol{r}}_{Si}(t_{Si})}{\partial \boldsymbol{q}} - \frac{\partial \ddot{\boldsymbol{r}}_O(t_O)}{\partial \boldsymbol{q}}; \ i \in \{1,2\}. \tag{6.75}$$

The vector of parameters $\boldsymbol{q}$ can either refer to one of the satellites state $\boldsymbol{s}_{Si}(t_{Si})$ or to the observer state $\boldsymbol{s}_O(t_O)$. We first consider the partials with respect to the observer state, given by

$$\frac{\partial \ddot{\boldsymbol{r}}_O^{S_i}}{\partial \boldsymbol{s}_O(t_O)} = \frac{\partial \ddot{\boldsymbol{r}}_{Si}(t_{Si})}{\partial \boldsymbol{s}_O(t_O)} - \frac{\partial \ddot{\boldsymbol{r}}_O(t_O)}{\partial \boldsymbol{s}_O(t_O)}; \ i \in \{1,2\}. \tag{6.76}$$

The acceleration $\ddot{\boldsymbol{r}}_{Si}(t_{Si})$ of the satellite i at time t_{Si} depends on the observer state $\boldsymbol{s}_O$ at $t = t_{Si}$, assuming the observer's body indeed exerts an acceleration on satellite i (although such acceleration is usually negligible, see simplifying assumptions discussed at the end of this appendix). Eq. 6.76 must thus be rewritten as

$$\begin{aligned} \frac{\partial \ddot{\boldsymbol{r}}_O^{S_i}}{\partial \boldsymbol{s}_O(t_O)} &= \frac{\partial \ddot{\boldsymbol{r}}_{Si}(t_{Si})}{\partial \boldsymbol{s}_O(t_{Si})} \frac{\boldsymbol{s}_O(t_{Si})}{\boldsymbol{s}_O(t_O)} - \frac{\partial \ddot{\boldsymbol{r}}_O(t_O)}{\partial \boldsymbol{s}_O(t_O)} \\ &= \frac{\partial \ddot{\boldsymbol{r}}_{Si}(t_{Si})}{\partial \boldsymbol{s}_O(t_{Si})} \boldsymbol{\Phi}_O(t_O, t_{Si}) - \frac{\partial \ddot{\boldsymbol{r}}_O(t_O)}{\partial \boldsymbol{s}_O(t_O)}; \ i \in \{1,2\}. \end{aligned} \tag{6.77}$$

Similarly, acceleration partials with respect to the two satellites' states are expressed as follows:

$$\frac{\partial \ddot{\boldsymbol{r}}_O^{S_i}}{\partial \boldsymbol{s}_{Si}(t_{Si})} = \frac{\partial \ddot{\boldsymbol{r}}_{Si}(t_{Si})}{\partial \boldsymbol{s}_{Si}(t_{Si})} - \frac{\partial \ddot{\boldsymbol{r}}_O(t_O)}{\partial \boldsymbol{s}_{Si}(t_O)} \boldsymbol{\Phi}_{Si}(t_{Si}, t_O), \tag{6.78}$$

$$\frac{\partial \ddot{\boldsymbol{r}}_O^{S_i}}{\partial \boldsymbol{s}_{Sj}(t_{Sj})} = \frac{\partial \ddot{\boldsymbol{r}}_{Si}(t_{Si})}{\partial \boldsymbol{s}_{Sj}(t_{Si})} \boldsymbol{\Phi}_{Sj}(t_{Sj}, t_{Si}) - \frac{\partial \ddot{\boldsymbol{r}}_O(t_O)}{\partial \boldsymbol{s}_{Sj}(t_O)} \boldsymbol{\Phi}_{Sj}(t_{Sj}, t_O); \ \{i,j\} \in \{1,2\}, j \neq i. \tag{6.79}$$

According to Eqs. 6.77-6.79, four state transition matrices need to be computed. However, a few remarks must be considered, in light of the computational effort this would require. For mutual approximations between the Galilean moons observed from the Earth, the satellite-observer distance is comparable between the two satellites. The difference between the two times t_{S_1} and t_{S_2} is thus very small, and the state transition matrices $\mathbf{\Phi}_{Si}(t_{Si}, t_{Sj})$ (with $\{i, j\} \in \{1, 2\}$ and $j \neq i$) are consequently close to unit matrices. The difference between each time t_{Si} and the observation time t_O is larger. However, looking at Eqs. 6.77-6.79, the state transition matrices $\mathbf{\Phi}_O(t_O, t_{Si})$ and $\mathbf{\Phi}_{Si}(t_{Si}, t_O)$ are always multiplied by partials of the observer's body acceleration with respect to one of the satellite's state, or the other way around. Considering the large satellites - observer distances, these accelerations partials can actually be neglected.

Overall, for mutual approximations between Galilean moons, the state transition matrices appearing in Eqs. 6.77-6.79 can be either approximated by unit matrices, or the entire acceleration partial term they contribute to can be neglected. This significantly simplifies the implementation and reduces the computational effort. Acceleration partials are anyway only required to compute the partials of $\ddot{\alpha}_{S_i}$ and $\ddot{\delta}_{S_i}$, which represent a marginal contribution of the total central instant partials (see Section 6.2.4). Simplifying assumptions to compute those acceleration partials can therefore be made safely.

6.9. APPENDIX D: VERIFICATION OF THE ANALYTICAL PARTIALS

The central instants partials derived in Section 6.2.3 were validated numerically, by comparing the analytically estimated change in central instant with the actual change obtained when applying a small variation to the estimated parameters. Partials were expressed with respect to $\boldsymbol{r}_{S_1}(t_{S_1})$, $\boldsymbol{r}_{S_2}(t_{S_2})$ and $\boldsymbol{r}_O(t_O)$ (for the first satellite's, second satellite's and observer's states, respectively). Analytical approximations of the changes in central instants were derived from the observation partials with respect to the initial state of interest, multiplied with the appropriate state transition matrix, as follows:

$$\Delta t_c = \frac{\partial t_c}{\partial \boldsymbol{r}_{S_1}(t_{S_1})} \mathbf{\Phi}\left(t_{S_1}, t_0\right) \Delta \boldsymbol{r}_{S_1}(t_0), \tag{6.80}$$

$$\Delta t_c = \frac{\partial t_c}{\partial \boldsymbol{r}_{S_2}(t_{S_2})} \mathbf{\Phi}\left(t_{S_2}, t_0\right) \Delta \boldsymbol{r}_{S_2}(t_0), \tag{6.81}$$

$$\Delta t_c = \frac{\partial t_c}{\partial \boldsymbol{r}_O(t_O)} \mathbf{\Phi}\left(t_O, t_0\right) \Delta \boldsymbol{r}_O(t_0). \tag{6.82}$$

The results of the numerical verification are reported in Table 6.6. The extremely low differences found between the analytical and numerical changes in central instant prove the validity of our analytical partials.

Table 6.6.: Comparison between analytical and numerical solutions for the changes in central instants, after applying a small variation (0.001%) in the initial states of Io, Europa and the Earth. Analytical approximations of the changes are derived from the central instants partials provided in Section 6.2.3. Results are here only reported for the 20 first mutual approximations detected in 2020 (although verification was conducted over 200 observations).

Mutual approx.	Change in t_c analytical [s]	Change in t_c numerical [s]	Relative error [-]
1	2.17458	2.17455	$7.84 \cdot 10^{-6}$
2	36.7842	36.7824	$4.85 \cdot 10^{-5}$
3	73.9007	73.8972	$4.76 \cdot 10^{-5}$
4	94.9994	94.9951	$4.56 \cdot 10^{-5}$
5	111.043	111.038	$4.74 \cdot 10^{-5}$
6	132.098	132.092	$4.55 \cdot 10^{-5}$
7	169.169	169.161	$4.55 \cdot 10^{-5}$
8	203.983	203.974	$4.58 \cdot 10^{-5}$
9	206.006	206.198	$9.30 \cdot 10^{-4}$
10	241.156	241.145	$4.53 \cdot 10^{-5}$
11	261.643	261.631	$4.35 \cdot 10^{-5}$
12	278.322	278.309	$4.51 \cdot 10^{-5}$
13	298.557	298.544	$4.21 \cdot 10^{-5}$
14	335.416	335.403	$4.04 \cdot 10^{-5}$
15	371.133	371.117	$4.27 \cdot 10^{-5}$
16	372.219	372.205	$3.84 \cdot 10^{-5}$
17	408.219	408.202	$4.23 \cdot 10^{-5}$
18	445.273	445.254	$4.21 \cdot 10^{-5}$
19	464.009	463.996	$2.82 \cdot 10^{-5}$
20	482.288	482.267	$4.21 \cdot 10^{-5}$

6

6.10. Appendix E: Contribution of the $\ddot{\alpha}_{Si}$ and $\ddot{\delta}_{Si}$ partials to the central instant partials

Table 6.7 gives the relative contributions of the $\ddot{\alpha}_{Si}$ and $\ddot{\delta}_{Si}$ partials to the total central instant partials. They are reported for the first five Io-Europa mutual approximations in 2020 and are shown to be negligible.

6.11. Appendix F: Alternative observables' weights for past mutual approximations (2016-2018 observational campaign)

We computed the alternative observables' weights for the mutual approximations observed during the 2016-2018 campaign, which are provided in Morgado et al.

Table 6.7.: Relative contributions of the $\ddot{\alpha}_{Si}$ and $\ddot{\delta}_{Si}$ partials to the total central instants partials. The partials are computed with respect to the first satellite's state $\boldsymbol{s}_{S1}$, second satellite's state $\boldsymbol{s}_{S2}$, and observer's state $\boldsymbol{s}_{O}$, all expressed in cartesian coordinates. Results are only reported for 5 mutual approximations (five first Io-Europa mutual approximations from 01/01/2020).

Mutual approx.	Relative contribution to the t_c partials [%]					
	w.r.t. first satellite's state $\boldsymbol{s}_{S1} = [\boldsymbol{r}_{S1}\ \dot{\boldsymbol{r}}_{S1}]^T$					
	x_{S1}	y_{S1}	z_{S1}	$\dot{x}_{S1}$	$\dot{y}_{S1}$	$\dot{z}_{S1}$
1	$6.8\cdot10^{-7}$	$1.3\cdot10^{-4}$	$3.2\cdot10^{-4}$	$1.1\cdot10^{-5}$	$9.1\cdot10^{-8}$	$9.3\cdot10^{-8}$
2	$5.4\cdot10^{-6}$	$2.8\cdot10^{-4}$	$1.0\cdot10^{-3}$	$1.3\cdot10^{-4}$	$1.0\cdot10^{-6}$	$6.4\cdot10^{-7}$
3	$4.9\cdot10^{-6}$	$2.2\cdot10^{-4}$	$8.0\cdot10^{-4}$	$1.1\cdot10^{-4}$	$8.8\cdot10^{-7}$	$3.9\cdot10^{-7}$
4	$1.2\cdot10^{-6}$	$9.8\cdot10^{-5}$	$2.9\cdot10^{-4}$	$1.3\cdot10^{-5}$	$1.4\cdot10^{-8}$	$4.7\cdot10^{-8}$
5	$3.0\cdot10^{-6}$	$1.2\cdot10^{-5}$	$4.4\cdot10^{-4}$	$6.5\cdot10^{-5}$	$5.1\cdot10^{-7}$	$1.0\cdot10^{-7}$
	w.r.t. second satellite's state $\boldsymbol{s}_{S2} = [\boldsymbol{r}_{S2}\ \dot{\boldsymbol{r}}_{S2}]^T$					
	x_{S2}	y_{S2}	z_{S2}	$\dot{x}_{S2}$	$\dot{y}_{S2}$	$\dot{z}_{S2}$
1	$2.5\cdot10^{-7}$	$3.3\cdot10^{-5}$	$7.9\cdot10^{-5}$	$2.2\cdot10^{-5}$	$8.7\cdot10^{-8}$	$1.2\cdot10^{-9}$
2	$7.1\cdot10^{-7}$	$7.1\cdot10^{-5}$	$2.6\cdot10^{-4}$	$7.8\cdot10^{-5}$	$2.7\cdot10^{-7}$	$1.6\cdot10^{-7}$
3	$6.5\cdot10^{-7}$	$5.5\cdot10^{-5}$	$2.0\cdot10^{-4}$	$6.4\cdot10^{-5}$	$1.4\cdot10^{-7}$	$4.7\cdot10^{-8}$
4	$3.5\cdot10^{-7}$	$2.6\cdot10^{-5}$	$7.2\cdot10^{-5}$	$2.6\cdot10^{-5}$	$1.0\cdot10^{-8}$	$2.2\cdot10^{-7}$
5	$4.1\cdot10^{-7}$	$3.1\cdot10^{-5}$	$1.1\cdot10^{-4}$	$3.7\cdot10^{-5}$	$3.4\cdot10^{-9}$	$1.7\cdot10^{-7}$
	w.r.t. observer's state $\boldsymbol{s}_{O} = [\boldsymbol{r}_{O}\ \dot{\boldsymbol{r}}_{O}]^T$					
	x_{O}	y_{O}	z_{O}	$\dot{x}_{O}$	$\dot{y}_{O}$	$\dot{z}_{O}$
1	$1.7\cdot10^{-6}$	$5.3\cdot10^{-5}$	$1.7\cdot10^{-4}$	$8.6\cdot10^{-3}$	$3.5\cdot10^{-6}$	$8.3\cdot10^{-5}$
2	$1.0\cdot10^{-5}$	$9.0\cdot10^{-5}$	$6.1\cdot10^{-4}$	$4.4\cdot10^{-2}$	$9.2\cdot10^{-4}$	$5.5\cdot10^{-4}$
3	$8.7\cdot10^{-6}$	$7.2\cdot10^{-5}$	$4.6\cdot10^{-4}$	$3.7\cdot10^{-2}$	$9.0\cdot10^{-4}$	$4.8\cdot10^{-4}$
4	$2.8\cdot10^{-6}$	$4.3\cdot10^{-5}$	$1.5\cdot10^{-4}$	$9.6\cdot10^{-3}$	$2.4\cdot10^{-5}$	$1.5\cdot10^{-4}$
5	$5.1\cdot10^{-6}$	$4.1\cdot10^{-5}$	$2.5\cdot10^{-4}$	$2.2\cdot10^{-2}$	$6.0\cdot10^{-4}$	$2.9\cdot10^{-4}$

(2019b). Tables 6.8-6.11 contain the weight values obtained with Eq. 6.41, following the weighting strategy described in Section 6.3.3. We have shown this approach to be crucial to obtain consistent estimation solutions between central instants and alternative observable in Section 6.4.4.

For consistency purposes, the errors in central instant $\sigma(t_c)$ given in Morgado et al. (2019b) were translated into errors in the alternative observable $\sigma_{\text{alt.}}$ using the same ephemerides as the ones used in Morgado et al. (2019b) (i.e., JUP310 with DE435 from JPL). Tables 6.8 and 6.9 focus on mutual approximations observed in 2016, while Tables 6.10 and 6.11 are dedicated to the years 2017 and 2018, respectively. The coordinates of the six different ground stations can be found in Morgado et al. (2019b). We recommend to use the computed weight values $\sigma_{\text{alt.}}$ when including the 2016-2018 observations in the state estimation with alternative observables.

Table 6.8.: Appropriate weights for alternative observables (in mas/s), for the mutual approximations observed in 2016 (Morgado et al., 2019b). The letters I, E, G, and C respectively designate Io, Europa, Ganymede, and Callisto. This table is adapted from Morgado et al. (2019b).

Date	Event	Station	t_c (UTC)	$\sigma(t_c)$ [s]	$\sigma_{alt.}$ [mas/s]
2016-02-03	E-G	OPD	04:48:01.1	4.2	$1.357 \cdot 10^{-2}$
2016-02-08	I-E	FOZ	06:29:38.4	0.6	$2.428 \cdot 10^{-3}$
2016-02-15	I-E	FOZ	08:39:28.5	1.1	$3.769 \cdot 10^{-3}$
2016-02-24	I-G	OPD	01:53:25.5	1.1	$3.508 \cdot 10^{-3}$
		FEG	01:53:27.3	4.0	$1.276 \cdot 10^{-2}$
2016-02-25	I-E	GOA	23:55:58.2	2.4	$7.070 \cdot 10^{-3}$
2016-03-04	I-E	GOA	02:09:59.3	2.3	$4.095 \cdot 10^{-3}$
2016-04-02	I-E	FOZ	05:45:57.1	2.2	$3.206 \cdot 10^{-3}$
		OPD	05:46:03.2	2.5	$3.643 \cdot 10^{-3}$
		FEG	05:45:59.1	3.8	$5.538 \cdot 10^{-3}$
2016-04-02	I-C	OPD	23:24:20.4	1.2	$1.846 \cdot 10^{-3}$
		FOZ	23:24:22.4	1.4	$2.153 \cdot 10^{-3}$
		FEG	23:24:22.3	3.5	$5.383 \cdot 10^{-3}$
2016-04-12	I-C	OPD	04:35:29.7	8.9	$1.631 \cdot 10^{-2}$
		FOZ	04:35:31.1	1.1	$2.016 \cdot 10^{-3}$
		FEG	04:35:29.1	2.5	$4.581 \cdot 10^{-3}$
2016-04-12	I-E	FOZ	04:45:49.0	10.1	$1.167 \cdot 10^{-3}$
2016-04-12	E-C	FOZ	05:01:34.6	1.9	$3.337 \cdot 10^{-3}$
		FEG	05:01:36.1	4.2	$7.376 \cdot 10^{-3}$
2016-04-12	I-E	OPD	21:17:16.2	0.8	$1.653 \cdot 10^{-3}$
2016-04-19	I-E	OPD	23:35:15.3	1.0	$2.456 \cdot 10^{-3}$
		FOZ	23:35:14.2	2.1	$5.158 \cdot 10^{-3}$
		GOA	23:35:13.3	2.2	$5.404 \cdot 10^{-3}$
		UTF	23:35:15.2	3.2	$7.860 \cdot 10^{-3}$
		OHP	23:35:13.9	1.5	$3.686 \cdot 10^{-3}$
2016-04-20	E-C	OHP	20:15:57.8	1.8	$2.474 \cdot 10^{-3}$
2016-04-24	I-G	OPD	22:35:12.0	0.5	$2.609 \cdot 10^{-3}$
		UTF	22:35:13.1	2.6	$1.357 \cdot 10^{-2}$
2016-04-29	I-G	OPD	00:32:28.1	2.4	$1.023 \cdot 10^{-2}$
		UTF	00:32:28.6	4.2	$1.790 \cdot 10^{-2}$
2016-05-02	I-G	OPD	01:08:50.3	1.5	$7.411 \cdot 10^{-3}$
		FOZ	01:08:50.7	2.3	$1.136 \cdot 10^{-2}$
		FEG	01:08:49.1	1.8	$8.893 \cdot 10^{-3}$
		UTF	01:08:51.1	4.5	$2.223 \cdot 10^{-2}$

Table 6.9.: See Table 6.8.

Date	Event	Station	t_c (UTC)	$\sigma(t_c)$ [s]	$\sigma_{\text{alt.}}$ [mas/s]
2016-05-03	E-G	OPD	01:04:55.4	1.3	$2.391 \cdot 10^{-3}$
		UTF	01:04:55.5	1.9	$3.494 \cdot 10^{-3}$
2016-05-06	E-C	OPD	00:59:06.8	6.5	$7.955 \cdot 10^{-3}$
2016-05-19	E-G	FOZ	22:52:31.9	1.0	$3.485 \cdot 10^{-3}$
2016-05-27	E-G	FEG	02:00:21.8	5.5	$1.853 \cdot 10^{-2}$
2016-06-17	I-E	OPD	00:48:02.9	1.3	$1.059 \cdot 10^{-2}$
		FEG	00:48:07.0	4.8	$3.910 \cdot 10^{-2}$
2016-06-28	I-G	OPD	23:58:57.1	1.4	$3.857 \cdot 10^{-3}$
		FEG	23:58:59.0	1.1	$3.031 \cdot 10^{-3}$
2016-06-28	I-E	OPD	22:36:02.2	0.5	$2.567 \cdot 10^{-3}$
		FEG	22:36:02.9	1.2	$6.160 \cdot 10^{-3}$
2016-07-08	E-G	OPD	21:51:35.5	0.6	$1.445 \cdot 10^{-3}$
		FEG	21:51:32.6	3.3	$7.946 \cdot 10^{-3}$

Table 6.10.: Same as Table 6.8 for mutual approximations in 2017.

Date	Event	Station	t_c (UTC)	$\sigma(t_c)$ [s]	$\sigma_{\text{alt.}}$ [mas/s]
2017-02-07	I-E	FOZ	04:36:54.1	1.0	$3.525 \cdot 10^{-3}$
2017-02-26	I-E	FOZ	04:32:43.5	1.3	$4.368 \cdot 10^{-3}$
2017-02-27	I-G	FOZ	03:36:51.3	1.1	$1.609 \cdot 10^{-3}$
2017-03-07	I-G	FOZ	03:00:44.4	32.9	$2.126 \cdot 10^{-3}$
2017-03-14	I-G	FOZ	07:19:33.8	1.1	$6.109 \cdot 10^{-4}$
2017-04-04	I-E	OHP	20:43:34.4	0.7	$3.227 \cdot 10^{-3}$
2017-04-06	I-E	FEG	03:46:43.1	2.2	$6.249 \cdot 10^{-3}$
2017-04-08	E-G	FOZ	01:52:40.5	1.0	$1.924 \cdot 10^{-3}$
2017-04-13	I-E	FOZ	05:49:28.3	1.0	$2.712 \cdot 10^{-3}$
2017-05-06	I-G	GOA	02:16:30.2	1.7	$4.460 \cdot 10^{-3}$
2017-05-08	I-E	FOZ	01:11:26.5	1.0	$2.124 \cdot 10^{-3}$
2017-05-13	I-G	FOZ	04:47:32.1	1.0	$2.418 \cdot 10^{-3}$
2017-05-15	I-E	FEG	03:23:43.1	1.7	$3.237 \cdot 10^{-3}$
2017-05-31	E-G	FEG	22:30:36.2	27.9	$9.891 \cdot 10^{-4}$
2017-06-08	I-E	FEG	23:48:57.1	7.5	$6.752 \cdot 10^{-3}$
		GOA	23:48:58.1	1.8	$1.621 \cdot 10^{-3}$
2017-06-23	I-E	FOZ	23:17:09.0	1.1	$8.644 \cdot 10^{-4}$
		GOA	23:17:07.7	1.9	$1.493 \cdot 10^{-3}$
2017-07-06	E-G	FOZ	22:58:42.6	1.4	$8.937 \cdot 10^{-4}$
		FEG	22:58:41.1	19.4	$1.238 \cdot 10^{-2}$
2017-07-25	I-E	FOZ	22:40:24.8	1.2	$2.166 \cdot 10^{-3}$
		FEG	22:40:21.3	3.3	$5.957 \cdot 10^{-3}$
2017-08-02	G-C	FEG	23:38:20.0	7.7	$4.172 \cdot 10^{-3}$
2017-08-10	E-C	FOZ	23:41:23.6	48.2	$1.680 \cdot 10^{-3}$
2017-08-24	I-G	FEG	22:35:37.6	6.6	$3.915 \cdot 10^{-3}$

Table 6.11.: Same as Table 6.8 for mutual approximations in 2018.

Date	Event	Station	t_c (UTC)	$\sigma(t_c)$ [s]	$\sigma_{\text{alt.}}$ [mas/s]
2018-03-05	I-E	FOZ	05:10:29.7	0.6	$1.378 \cdot 10^{-3}$
2018-03-11	I-G	OPD	05:40:46.7	1.8	$6.834 \cdot 10^{-4}$
		FOZ	05:40:47.0	2.0	$7.594 \cdot 10^{-4}$
2018-03-12	I-E	OPD	07:20:57.6	0.5	$1.236 \cdot 10^{-3}$
		FOZ	07:20:58.8	1.4	$3.461 \cdot 10^{-3}$
2018-03-17	I-E	FOZ	03:15:03.2	0.8	$2.898 \cdot 10^{-3}$
2018-03-24	I-E	FOZ	05:18:47.9	0.7	$2.527 \cdot 10^{-3}$
2018-04-06	I-E	OPD	02:40:32.0	1.2	$3.641 \cdot 10^{-3}$
		FOZ	02:40:31.4	1.0	$3.034 \cdot 10^{-3}$
2018-06-11	E-G	FEG	23:03:46.0	1.8	$2.885 \cdot 10^{-3}$
		GOA	23:03:45.1	1.2	$1.923 \cdot 10^{-3}$
2018-06-19	E-G	FOZ	01:55:19.9	1.1	$1.785 \cdot 10^{-3}$
2018-06-22	I-G	FEG	02:17:09.5	7.2	$1.005 \cdot 10^{-3}$
		OPD	02:17:12.6	4.5	$6.282 \cdot 10^{-4}$
		FOZ	02:17:12.5	5.6	$7.818 \cdot 10^{-4}$
		GOA	02:17:09.9	6.5	$9.074 \cdot 10^{-4}$
2018-06-23	I-E	FOZ	00:40:47.4	1.1	$4.486 \cdot 10^{-3}$
2018-07-07	I-G	OPD	00:30:56.8	1.1	$1.829 \cdot 10^{-3}$
		FEG	00:30:57.0	2.2	$3.658 \cdot 10^{-3}$
2018-07-11	E-C	OPD	22:48:02.8	1.4	$1.010 \cdot 10^{-3}$
2018-07-12	I-E	FEG	01:07:36.3	2.5	$5.285 \cdot 10^{-3}$
		OPD	01:07:37.4	1.0	$2.114 \cdot 10^{-3}$
2018-07-13	E-G	OPD	02:01:30.9	1.1	$9.424 \cdot 10^{-4}$
		FEG	02:01:29.9	5.4	$4.626 \cdot 10^{-3}$
2018-07-19	I-C	OPD	01:52:08.6	1.9	$1.502 \cdot 10^{-3}$
		FOZ	01:52:09.3	2.1	$1.661 \cdot 10^{-3}$
2018-08-07	E-G	OPD	23:15:18.8	1.3	$2.118 \cdot 10^{-3}$
2018-08-12	I-E	OPD	23:54:58.4	1.1	$1.186 \cdot 10^{-3}$
		FOZ	23:54:58.5	1.2	$1.294 \cdot 10^{-3}$

7

Synergies between spacecraft VLBI tracking and stellar occultations

M. S. Fayolle, V. Lainey, D. Dirkx, L. I. Gurvits, G. Cimo, S. B. Bolton

Stellar occultations currently provide the most accurate ground-based measurements of the positions of natural satellites (down to a few kilometres for the Galilean moons). However, when using these observations in the calculation of satellite ephemerides, the uncertainty in the planetary ephemerides dominates the error budget of the occultation. We quantify the local refinement in the central planet's position achievable by performing Very Long Baseline Interferometry (VLBI) tracking of an in-system spacecraft temporally close to an occultation. This demonstrates the potential of using VLBI to enhance the science return of stellar occultations for satellite ephemerides. We identified the most promising observation and tracking opportunities offered by the Juno spacecraft around Jupiter as perfect test cases, for which we ran simulations of our VLBI experiment. VLBI tracking at Juno's perijove close to a stellar occultation locally (in time) reduces the uncertainty in Jupiter's angular position in the sky to 250-400 m. This represents up to an order of magnitude improvement with respect to current solutions and is lower than the stellar occultation error, thus allowing the moon ephemeris solution to fully benefit from the observation. Our simulations showed that the proposed tracking and observation experiment can

An earlier version of this chapter is published in Astronomy & Astrophysics (Fayolle et al., 2023a): Fayolle, M., Lainey, V., Dirkx, D., Gurvits, L. I., Cimo, G., & Bolton, S. J. (2023). Spacecraft VLBI tracking to enhance stellar occultations astrometry of planetary satellites. Astronomy & Astrophysics, 676, L6.

efficiently use synergies between ground- and space-based observations to enhance the science return on both ends. The reduced error budget for stellar occultations indeed helps to improve the moons' ephemerides, which in turn benefit planetary missions and their science products, such as the recently launched JUICE and upcoming Europa Clipper missions.

7.1. INTRODUCTION

In addition to classical astrometry, various ground-based observation techniques have been developed and intensively used to study the orbital motion of natural satellites (e.g., Arlot and Emelyanov, 2019, and references therein). Observations of stellar occultations, which occur when a moon passes in front a star, have proven particularly promising (Morgado et al., 2019a, 2022). Thanks to the Gaia star catalogues, with sub-mas (milliarcsecond) precision for the star positions (Gaia et al., 2018; Brown et al., 2021), stellar occultations provide the most accurate ground-based measurements to date for natural satellite positions (accuracy of the order of 1 mas, i.e., a few km for the Galilean satellites, Morgado et al., 2022).

These observations constrain the moons' positions in the plane of the sky, typically in the International Celestial Reference Frame (ICRF). However, improving satellite ephemerides requires information on the moons' relative positions with respect to the central planet, rather than their absolute positions in the ICRF. To use stellar occultations in satellite ephemeris generation, the uncertainty in the planet's position thus directly increases the effective error budget of the stellar occultations.

For recent occultations by the Galilean satellites, discrepancies between observed and predicted events (the latter being ephemerides-based) are still significant and

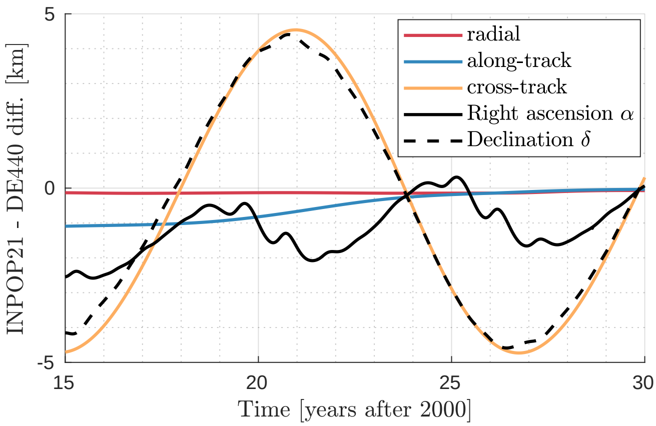

Figure 7.1.: Difference between INPOP21 and DE440 planetary ephemerides for Jupiter in radial, along-track (tangential), and cross-track (out-of-plane) directions. Deviations in right ascension α and declination δ are also provided.

vary depending on which planetary ephemerides are considered, as reported in Morgado et al. (2022). Non-negligible differences indeed remain between different Jovian ephemerides, indicating possible errors or discrepancies. This is illustrated in Fig. 7.1 for the most recent solutions: INPOP21 (Fienga et al., 2021b) and DE440 (Park et al., 2021). The deviations are small for the in-plane components, especially in the radial direction, which significantly benefited from Juno tracking data (e.g., Fienga et al., 2021a). The discrepancy is larger, however, in the out-of-plane direction, with a long-term periodic effect building up to 4.5 km. In right ascension and declination, differences can amount up to 2 km and 5 km, respectively, which is comparable to a typical stellar occultation accuracy.

A possible means to mitigate this error source is to combine spacecraft VLBI tracking with stellar occultation observations. To demonstrate the added value of such an experiment, we quantify the local refinement in Jupiter's position provided by phase-referencing VLBI observations of an orbiting spacecraft in the close vicinity of stellar occultations. Phase-referenced VLBI tracking relies on a nearby radio source (within a few degrees of the spacecraft) to perform phase calibration and obtain accurate measurements of a spacecraft's position in the ICRF (e.g., Jones et al., 2010; Duev et al., 2012, 2016). If the spacecraft orbits close to Jupiter, this also provides valuable constraints on Jupiter's position in the ICRF. It is worth mentioning that we focus on Jupiter's angular position ($\alpha_{\text{Jup}}, \delta_{\text{Jupiter}}$) in the sky, which directly affects the stellar occultation error budget (Section 7.2.1), and do not intend to improve Jupiter's global fit. We exploit the presence of the Juno spacecraft in the Jovian system (Bolton et al., 2017) and use two experiment opportunities that it offers, in 2023 and 2024, as test cases for our study.

To quantify the improvement in the effective stellar occultation error budget provided by the VLBI data, we can use the INPOP21-DE440 deviations (Fig. 7.1) as a conservative lower limit for the current uncertainty in Jupiter's position. Our two test occultations of interest, in 2023 and 2024, coincide with Jupiter's crossing the ecliptic. It thus also corresponds to a local minimum for the INPOP21-DE440 difference, mostly originating from a small discrepancy in Jupiter's orbit orientation. Consequently, the periodic behaviour observed in Fig. 7.1 illustrates the discrepancies between the two fits, but is likely not indicative of the exact evolution of the ephemeris error in time. This would imply that the uncertainty in Jupiter's out-of-plane position at time t can in practice be expected to take any value up to ~4.5 km. We thus chose the averaged difference between INPOP21 and DE440 as a better metric for Jupiter's position error.

The principle of the experiment is described in Section 7.2, where upcoming tracking and observation opportunities are also identified, to be used as test cases. Section 7.2 presents the simulations performed for two stellar occultations, to demonstrate the local improvement in Jupiter's right ascension and declination accuracy, and the resulting improvement in stellar occultation quality for satellite ephemerides. The results and conclusions are discussed in Sections 7.3 and 7.4, respectively.

7.2. EXPERIMENT PRINCIPLE AND SIMULATIONS

7.2.1. EXPERIMENT AND NEXT OPPORTUNITIES

Fig. 7.2 summarises the configuration of the proposed experiment. A stellar occultation by Callisto is used as an example and would nominally measure the moon's position (α, δ) in the ICRF to an accuracy of a few kilometres (green ellipse). Reconstructing the moon's orbit around Jupiter requires accounting for Jupiter's own position error (assuming the two errors are uncorrelated) as

$$\sigma^2\left(\boldsymbol{r}_{\text{Callisto/Jup}}\right) = \sigma^2\left(\boldsymbol{r}_{\text{Callisto}}\right) + \sigma^2\left(\boldsymbol{r}_{\text{Jup}}\right), \tag{7.1}$$

where $\boldsymbol{r}_{\text{Callisto/Jup}}$ denotes Callisto's position with respect to Jupiter, while $\boldsymbol{r}_{\text{Callisto}}$ is the moon's position with respect to the Solar System barycentre (SSB), as provided by the stellar occultation. However, Jupiter's ephemeris error is similar to or possibly larger than the occultation uncertainty (red ellipse in Fig. 7.2). VLBI tracking of Juno during the perijove(s) closest to the occultation would help refine Jupiter's barycentric position, as was already done in the past by Jones et al. (2019, 2021).

Since each of Juno's orbits lasts about 40 days, the occultation might occur a few weeks away from the closest perijove. We therefore propose to track the spacecraft during the two perijoves surrounding the stellar occultation. This would constrain

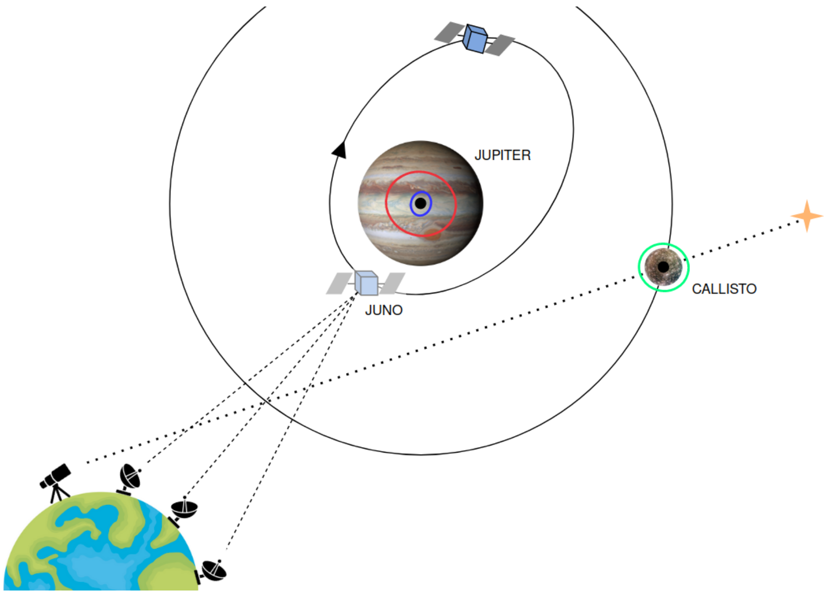

Figure 7.2.: Illustration of the proposed experiment (not to scale). The occultation yields a very accurate measurement of Callisto's position in the ICRF (small green ellipse centred at Callisto). Tracking the Juno spacecraft at the perijove(s) closest to the occultation would reduce Jupiter's initial position uncertainty (red ellipse) to the smaller blue ellipse.

Jupiter's position both before and after the observation, thus ensuring a reduced uncertainty at occultation time.

Two promising occultations will occur in the near future, one by Ganymede on 23 October 2023 (star magnitude $G = 11.3$) and one by Callisto on 15 January 2024 ($G = 8.8$). Table 7.1 provides the dates and times of the Juno perijoves preceding and following these two occultations. For each of these perijoves we identified suitable phase calibrators within two degrees of the Juno spacecraft. The sources taken into consideration for this work are listed in Table 7.2. We also ran a coverage analysis for Juno tracking from three major VLBI telescope networks: the European VLBI Network[1] (EVN), the Very Long Baseline Array[2] (VLBA), and the Long Baseline Array[3] (LBA). None of the networks can alone ensure tracking during the four perijoves of interest. In particular, EVN cannot cover the perijoves surrounding Ganymede's 2023 occultation, while VLBA and LBA each miss one perijove of Callisto's 2024 occultation.

7.2.2. Simulation set-up

The aim of our analysis is to quantify the local (in time) uncertainty reduction in Jupiter's right ascension and declination at the time of the occultation(s) using VLBI. As illustrated in Fig. 7.3, this was achieved in two steps. First, we determined the error associated with Juno's orbit (Fig. 7.3, left), referred to as Juno state estimation. Second, we used Juno's estimated orbit uncertainty to construct VLBI observables re-centred at Jupiter with realistic errors. We could subsequently estimate Jupiter's state at the time of the occultation from these VLBI data points (Fig. 7.3, right) referred to as Jupiter state estimation.

It should be noted that this study relied on simulated observations and was limited to covariance analyses. This approach is well adapted to quantify the contribution of VLBI measurements to Jupiter's local position, even if the real data analysis will

7

[1]https://www.evlbi.org/
[2]https://public.nrao.edu/telescopes/vlba/
[3]https://www.atnf.csiro.au/vlbi/overview/index.html

Table 7.1.: Predicted occultations by the Galilean satellites and corresponding Juno perijoves. Stellar occultations were predicted for the years 2023 and 2024 only. For each VLBI network, the coverage percentage indicates the fraction of the 6h arc during which more than three stations (per network) can track Juno's radio signal (minimum elevation of 10 deg).

Occultations		**Juno perijoves**		**VLBI networks coverage**		
Date	Occulting moon	Date	Time [UTC]	EVN	VLBA	LBA
23-10-2023	**Ganymede**	15-10-2023	10:52:58	0 %	100 %	55 %
		22-11-2023	12:16:47	0 %	45 %	100 %
15-01-2024	**Callisto**	30-12-2023	12:36:20	42.8 %	0 %	100 %
		03-02-2024	21:47:30	80 %	100 %	0 %

Table 7.2.: Selected phase calibrators for each of the four perijoves.

Juno perijoves	Name calibrator	Separation with target [deg]	Position uncertainty $\sigma(\alpha)$ [nrad]	$\sigma(\delta)$ [nrad]	Total flux density [Jy]
15-10-2023	J0244+1320	1.10	0.5	1.0	0.207
22-11-2023	J0225+1134	1.37	0.7	0.8	0.313
30-12-2023	J0211+1051	1.40	0.5	0.8	0.516
03-02-2024	J0225+1134	1.81	0.7	0.8	0.313

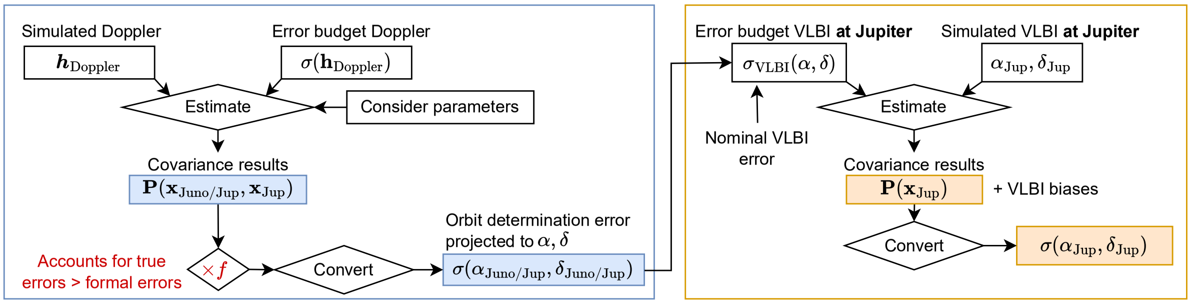

Figure 7.3.: Workflow used to quantify the reduction in Jupiter's position uncertainty (in the plane of the sky) achievable with the proposed VLBI experiment.

7

later require a full fit. All results, from both Juno's and Jupiter state estimations, are therefore based on formal uncertainties derived from covariance matrices.

Starting with Juno state estimation, we simulated Doppler measurements during the perijoves preceding and following each of the two occultation opportunities (Section 7.2.1). Doppler data were generated every 60s over 6h tracking arcs, with a noise of 0.05 mm/s in agreement with the residuals from Juno radio science experiment (Iess et al., 2018).

For the purpose of our analysis, which focused on a local rather than global fit improvement for Jupiter, we only needed to consider two perijoves for each occultation. As a consequence, we chose not to estimate all dynamical parameters usually determined from Juno data. Only Juno's and Jupiter's states were estimated at perijove time t_{PJ}, the latter ensuring that the Jovian ephemeris uncertainty was included in Juno's orbit error. Similarly, we also added a number of consider parameters to account for their influence on the estimation (e.g., Gill and Montenbruck, 2013):

- Jupiter's spherical harmonics gravity coefficients up to degree and order 2, and zonal coefficients up to degree 10;
- Jupiter's pole orientation and rotation rate;
- Empirical accelerations on Juno, required to fit Doppler data. We assumed constant components in the radial, tangential, and normal (RTN) directions, estimated every 10 min during a two-hour window around perijove time, as described in Durante et al. (2020).

The uncertainty values for all the consider parameters were taken from the estimation results at mid-Juno mission (Iess et al., 2018; Durante et al., 2020) and are reported in Table 7.4.

Doppler data alone cannot notably improve Jupiter's state uncertainties beyond their a priori constraints. The main objective of this first estimation step, however, is to obtain the covariance describing Juno's orbit uncertainty $\mathbf{P}(\mathbf{x}_{\mathrm{Juno/Jup}})(t_{\mathrm{PJ}})$, which can be extracted from the full covariance matrix and directly used to re-centre VLBI observables to Jupiter's centre of mass (Fig. 7.3), using the same methodology as in Dirkx et al. (2017). The total uncertainty $\sigma_{\mathrm{VLBI}}(\alpha,\delta)$ for these observables needs to account for the nominal error budget for VLBI observations $\sigma_{\star}(\alpha,\delta)$, and for Juno's orbit error

$$\sigma^2_{\mathrm{VLBI}}(\alpha,\delta)(t) = \sigma^2_{\star}(\alpha,\delta) + \sigma^2(\alpha_{\mathrm{Juno/Jup}},\delta_{\mathrm{Juno/Jup}})(t), \tag{7.2}$$

where $\sigma(\alpha_{\mathrm{Juno/Jup}},\delta_{\mathrm{Juno/Jup}})(t)$ is the projection of the propagated covariance $\mathbf{P}(\mathbf{x}_{\mathrm{Juno/Jup}})(t)$ to right ascension and declination. The noise value of a single VLBI observation $\sigma_{\star}(\alpha,\delta)$ was conservatively set to 1.0 nrad based on recent phase-referencing VLBI tracking of Cassini and Mars Express spacecraft (Jones et al., 2010, 2019; Duev et al., 2016). Since formal uncertainties are typically known to be too optimistic compared to the true errors (e.g., Dirkx et al., 2017), a factor f was first applied to Juno's state covariance before propagating it from perijove to occultation time. We used both $f = 1$ and $f = 5$, but our nominal results, unless otherwise indicated, correspond to the latter conservative case to ensure that Juno's orbit error is not underestimated.

Independent VLBI observables re-centred to Jupiter were simulated every 20 minutes, using the error model in Eq. 7.2. A systematic bias was also added to these observations, corresponding to the uncertainty in the phase calibrator's position in the ICRF (Table 7.2). These biases were included as consider parameters. As such, they cannot be reduced in the estimation process, which ensures that this uncertainty source is conservatively accounted for in our results. Four additional tracking configurations were considered: tracking by the EVN, VLBA, and LBA networks individually, as well as a perfect coverage case where all three are involved. From the VLBI data, we estimated Jupiter's state at occultation time. The resulting uncertainties in Jupiter's right ascension and declination $\sigma(\alpha_{\text{Jup}}, \delta_{\text{Jup}})$ correspond to the blue error ellipse in Fig. 7.2 and are discussed in the following section.

7.3. EXPECTED CONTRIBUTION

From the simulated Doppler measurements, we first estimated Juno's state with respect to Jupiter at perijove time. We obtained formal uncertainties in right ascension and declination $\sigma(\alpha_{\text{Juno/Jup}}, \delta_{\text{Juno/Jup}})$ between 50 and 120 m (perijove-dependent). Those uncertainties and their correlations were then propagated over the entire arc, as shown in Fig. 7.4 for the 15 October 2023 perijove. Jupiter-centred VLBI measurements could then be constructed at any time t from the instantaneous orbit determination error.

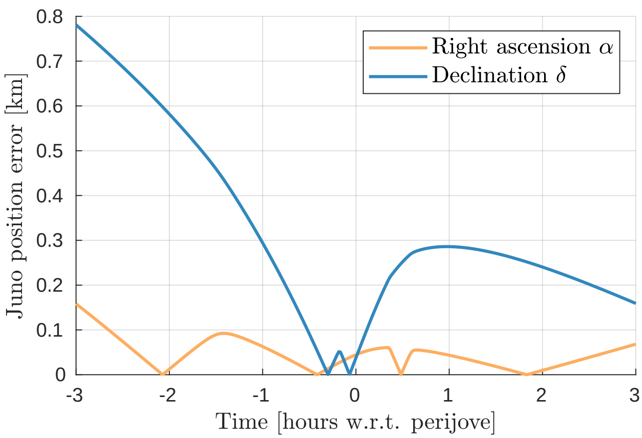

Figure 7.4.: Propagated errors in Juno's right ascension and declination for the 15 October 2023 perijove, preceding Ganymede's occultation. The results correspond to the $f = 1$ case (i.e., no scaling of Juno's determination orbit error).

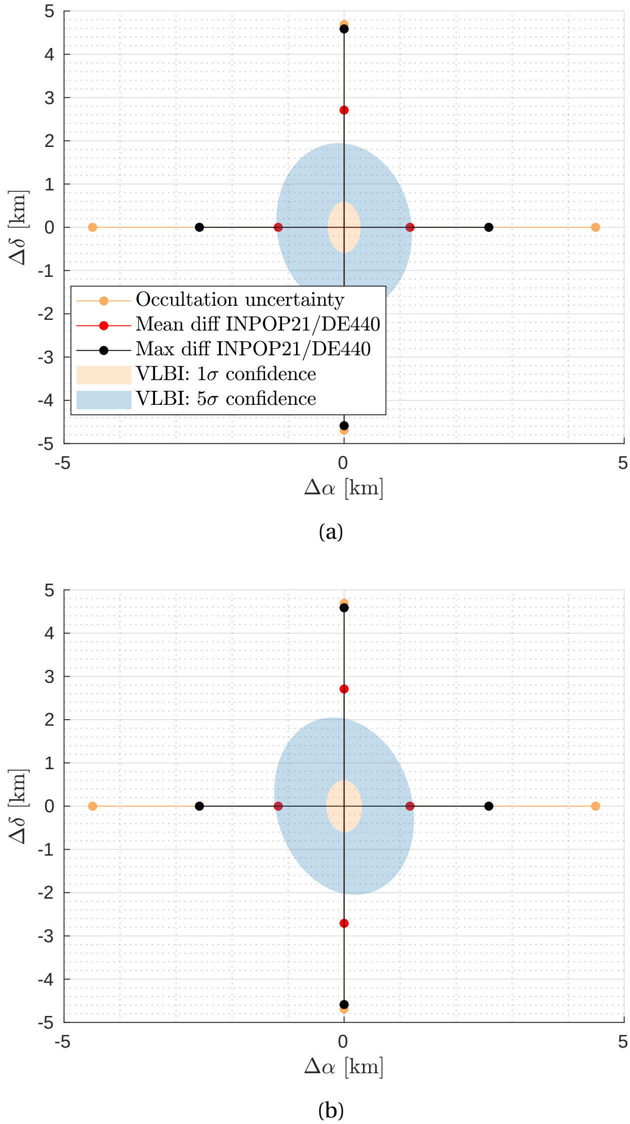

Figure 7.5.: Uncertainties in α_{Jup} and δ_{Jup} at occultation time. Panel a: Occultation by Ganymede on 23 October 2023; Panel b: occultation by Callisto on 15 January 2024. Markers on the x- and y-axes indicate the averaged and maximum deviation between INPOP21 and DE440 (over the period 2015–2030), as well as the typical uncertainty for stellar occultations (based on Morgado et al., 2022). The coloured confidence ellipses represent the 1σ (orange) and 5σ (blue) covariances in Jupiter's position resulting from VLBI tracking.

Table 7.3.: Formal errors in Jupiter's position. The formal uncertainties are provided for different VLBI tracking configurations, and are expressed as uncertainties in right ascension and declination at the occultation time. Results are given for $f = 1$ and $f = 5$, f being the factor applied to Juno's state covariance to re-scale the orbit error.

VLBI network(s)	**23-10-2023 occultation**				**15-01-2024 occultation**			
	$\sigma(\alpha_{\text{Jup}})$ [km]		$\sigma(\delta_{\text{Jup}})$ [km]		$\sigma(\alpha_{\text{Jup}})$ [km]		$\sigma(\delta_{\text{Jup}})$ [km]	
	$f = 1$	$f = 5$	$f = 1$	$f = 5$	$f = 1$	$f = 5$	$f = 1$	$f = 5$
EVN	N.A.	N.A.	N.A.	N.A.	0.32	0.36	0.49	0.80
VLBA	0.28	0.31	0.54	0.63	0.43	0.45	0.81	0.92
LBA	0.30	0.31	0.51	0.58	0.38	0.41	0.73	0.85
All	0.28	0.29	0.51	0.58	0.30	0.32	0.46	0.60

Uncertainties in $\alpha_{\text{Jup}}, \delta_{\text{Jup}}$ estimated from the VLBI observations are displayed in Fig. 7.5. The orange and blue ellipses represent the 1σ and 5σ covariances (in both cases a factor $f = 5$ was first applied to Juno's orbit error). The latter is a very conservative case, again accounting for formal errors possibly being too optimistic. For both occultations, VLBI tracking leads to 1σ errors of 300 m and 600 m, for α_{Jup} and δ_{Jup} respectively (in the worst-case scenario, i.e., $f = 5$). This is well below both the stellar occultations accuracy and the estimated error of the current Jupiter ephemeris, and would thus allow the moons' ephemerides to fully benefit from the exceptional quality of these observations.

The estimated errors in α_{Jup} and δ_{Jup} are respectively about a factor of 4 and a factor of 5 smaller than the average difference between the two ephemerides solutions. With respect to the maximum INPOP21-DE440 deviation, the uncertainty reduction almost reaches a factor of 10. Even when considering the very pessimistic 5σ confidence ellipse, a significant improvement is still attainable for $\sigma(\delta_{\text{Jup}})$.

As mentioned in Section 7.1, the differences between the current ephemerides give a conservative estimate of Jupiter's state uncertainty. The two ephemerides are based on the same observation set (Fienga et al., 2021b; Park et al., 2021) and rely on comparable dynamical models, and may therefore possess common biases. VLBI tracking, on the other hand, provides the absolute measures of Jupiter's position in the sky, with biases at the sub-nrad level. The local improvement in the Jovian ephemeris provided by VLBI may thus be greater than our results indicate.

Finally, the results shown in Fig. 7.5 assumed continuous VLBI tracking during the 6h arcs, which would require different networks to be involved (Table 7.1). Table 7.3 presents the outcome of various tracking scenarios. For Ganymede's occultation on 23 October 2023, only relying on either VLBA or LBA is sufficient to ensure errors comparable to those obtained with the two networks (irrespective of the factor f applied to Juno's orbit error). This does not hold for Callisto's occultation which would benefit from using multiple networks, especially in the $f = 5$ case. To optimise the outcome of the experiment, relying on two or three VLBI networks for each perijove would thus be ideal.

7.4. CONCLUSIONS

To optimise the science return of stellar occultations for satellite ephemerides calculations, VLBI tracking of an in-system spacecraft can be used to locally reduce the uncertainty in the central planet's position, which directly contributes to the occultation error budget. To demonstrate the potential of this VLBI experiment, we performed simulations for two promising observation opportunities with the Juno spacecraft, in 2023 and 2024. For both test cases our results indicate that VLBI tracking will indeed reduce the uncertainty in Jupiter's position to the sub-kilometre level at occultation time (Section 7.3), ensuring that it no longer dominates the stellar occultation error budget.

This also represents a unique opportunity to test our current planetary and satellites ephemerides, which are both involved in the prediction of stellar occultations, and both have estimated errors at a level similar to or higher than the stellar occultations. In practice, offsets between predicted and observed occultations already indicated possible errors and/or discrepancies in the existing solutions (Morgado et al., 2022). Our experiment could help quantify them, possibly identifying their origin and distinguishing between planetary and satellite ephemerides errors.

Finally, this experiment would serve as a preparation for the upcoming JUICE and Europa Clipper missions. First, it would help to improve the Galilean satellites' ephemerides before the missions, which can reduce pre- and post-flyby corrective manoeuvres (Bellerose et al., 2016; Boone et al., 2017; Hener et al., 2024). Moreover, if proven successful, similar experiments could be implemented for any other mission, including JUICE and Europa Clipper. By exploiting synergies between different measurement techniques, which will likely be critical in order to achieve a high-accuracy ephemeris solution from the missions' data (Fayolle et al., 2022), it would capitalise on the presence of one or more in-system spacecraft to also benefit ground-based observations, and therefore enhance the science return of the mission(s). Among other advantages, radio occultation studies could benefit from the VLBI tracking experiments proposed here, the Doppler data being directly useful for such analyses (Bocanegra-Bahamón et al., 2019), while VLBI measurements can refine Jupiter's local state at occultation time.

7.5. APPENDIX A: CONSIDER PARAMETER UNCERTAINTIES

Table 7.4 provides the uncertainties for each of the consider parameters used in Juno state estimation. These uncertainties are based on mid-mission results (Iess et al., 2018; Durante et al., 2020).

Table 7.4.: Uncertainties for the consider parameters. Except for empirical accelerations $\boldsymbol{a}_{\text{emp}}$, all parameters refer to Jupiter.

Parameter	**Consider uncertainty**
μ	8.9×10^{9} [m^{3}s^{-2}]
J_2	1.7×10^{-9} [-]
C_{21}	2.3×10^{-9} [-]
C_{22}	1.1×10^{-9} [-]
S_{21}	1.5×10^{-9} [-]
S_{22}	1.0×10^{-9} [-]
J_3	3.3×10^{-9} [-]
J_4	2.4×10^{-9} [-]
J_5	4.2×10^{-9} [-]
J_6	6.7×10^{-9} [-]
J_7	1.2×10^{-8} [-]
J_8	2.1×10^{-8} [-]
J_9	3.6×10^{-8} [-]
J_{10}	6.5×10^{-8} [-]
α	4.0×10^{-5} [deg]
δ	5.0×10^{-5} [deg]
$\boldsymbol{a}_{\text{emp}}$	2×10^{-8} [ms^{-2}]

7

8

MERGING LONG-TERM ASTROMETRY AND RADIO SCIENCE

M. S. FAYOLLE, A. MAGNANINI, V. LAINEY, D. DIRKX, M. ZANNONI, P. TORTORA

The upcoming JUICE and Europa Clipper missions targeting Jupiter's Galilean satellites will provide radio science tracking measurements of both spacecraft. Such data are expected to significantly help estimating the moons' ephemerides and related dynamical parameters (e.g., tidal dissipation parameters). However, the two missions will yield an imbalanced dataset, with no flybys planned at Io, condensed over less than six years. Current ephemerides' solutions for the Galilean moons, on the other hand, rely on ground-based astrometry collected over more than a century which, while being less accurate, bring very valuable constraints on the long-term dynamics of the system. An improved solution for the Galilean satellites' complex dynamics could however be achieved by exploiting the existing synergies between these different observation sets. To quantify this, we merged simulated radio science data from both JUICE and Europa Clipper spacecraft with existing ground-based astrometric and radar observations, and performed the inversion in different configurations: either adding all available ground observations or individually assessing the contribution of different data subsets. Our discussion specifically focusses on the resulting formal uncertainties in the moons' states, as well as Io's and Jupiter's tidal dissipation parameters. Adding astrometry stabilises the moons' state solution, especially beyond the missions' timelines. It furthermore reduces the uncertainties in $1/Q$ *(inverse of*

An earlier version of this chapter is published in Astronomy & Astrophysics (Fayolle et al., 2023b): Fayolle, M., Magnanini, A., Lainey, V., Dirkx, D., Zannoni, M., & Tortora, P. (2023). Combining astrometry and JUICE–Europa Clipper radio science to improve the ephemerides of the Galilean moons. Astronomy & Astrophysics, 677, A42.

the tidal quality factor) by a factor two to four for Jupiter, and about 30-35% for Io. Among all data types, classical astrometry data prior to 1960 proved particularly beneficial. Overall, we also show that ground observations of Io add the most to the solution, confirming that ground observations can fill the lack of radio science data for this specific moon. We obtained a noticeable solution improvement when making use of the complementarity between all different observation sets. The promising results obtained with simulations thus motivate future efforts to achieve a global solution from actual JUICE and Europa Clipper radio science measurements.

8.1. INTRODUCTION

Due to the Laplace resonance between Io, Europa, and Ganymede, Jupiter's Galilean satellites form a complex dynamical system (e.g., Lainey et al., 2006). Reconstructing the long-term evolution of the Jovian system is thus extremely challenging, but will shed light on the formation and history of both the system itself (Peale, 1999; Greenberg, 2010), our own Solar System (Heller et al., 2015), and exoplanetary systems in general (Horner et al., 2020). In particular, an improved ephemerides' solution for the Galilean moons is expected to provide crucial insights into tidal dissipation mechanisms in the Jovian system, with direct implications for the moons' orbital evolution (Lainey et al., 2009; Greenberg, 2010; Fuller et al., 2016; Hay et al., 2020). This would also lead to a better characterisation of the moons' interior evolution, which would help to constrain the past and present properties of sub-surface oceans on Europa and Ganymede, as well as confirm the existence of such an ocean on Callisto (Spohn and Schubert, 2003; Schubert et al., 2004; Greenberg, 2010; Lunine, 2017).

Current solutions for the Galilean moons' ephemerides (Lainey et al., 2004a, 2009) mostly rely on ground-based astrometry, supplemented by space-based optical observations from Voyager and Galileo (Jacobson et al., 2000; Haw et al., 2000; Smith et al., 1979a). Radio science measurements acquired from the Galileo spacecraft during its moon flybys are included in a number of solutions, but the tracking accuracy was limited (S-band, low gain antenna) and not comparable to that of recent planetary missions (Jacobson et al., 2000; Gomez Casajus et al., 2021). Moreover, these data are not publicly available at present, limiting efforts to incorporate them into ephemeris solutions.

However, in the coming decade, the JUICE (JUpiter ICy moons Explorer) and Europa Clipper missions will both visit the Jovian system and specifically target the Galilean satellites. NASA's Europa Clipper mission will start its flyby tour in 2030 and perform more than 50 flybys of Europa. On the ESA side, the JUICE spacecraft will execute a series of flybys around the Galilean moons from 2032 to 2034 (two, seven, and nine at Europa, Ganymede, and Callisto, respectively). It will then enter an orbital phase of about eight months around Ganymede (first elliptical at an altitude of 5000 km, then circular at 500 km), before the planned mission end in 2035. The exceptional accuracy of the radiometric science data to be generated during the missions (e.g., Cappuccio et al., 2022; Mazarico et al., 2023), enhanced by the complementarity of their tours and concurrent schedules, is expected to bring

8

unique insights into the Galilean satellites' dynamics.

Several simulation studies have analysed the science return from both JUICE's and Europa Clipper's radio science, and indicated that the post-missions formal uncertainties for the moons' state solutions could reach unprecedentedly low levels (Cappuccio et al., 2020a; Magnanini, 2021; Fayolle et al., 2022). However, exploiting the complementarity between the future radio science measurements and existing ground-based observations could yet further improve and stabilise the reconstruction of the Galilean moons' dynamics. For the Saturnian system, the independent determination of Titan's tidal dissipation parameters from ground astrometry and Cassini's radio science already led to very consistent solutions, indicating that Titan's migration rate might have been much faster than expected (Lainey et al., 2020). This suggests the potential of global solutions capitalising on the synergies between diverse data types.

In practice, and for the Galilean moons in particular, astrometry and radio science are indeed very complementary datasets. While ground observations have been collected over more than a century, radio science measurements are by definition concentrated during planetary missions' timelines. Radio science thus provides shorter, but highly accurate data points. Existing ground-based observations are also relatively evenly distributed among the four Galilean satellites. JUICE and Europa Clipper, on the contrary, will provide an imbalanced dataset with a strong focus on Europa, Ganymede, and to a lesser extent Callisto, and no direct flyby performed at Io. The lack of data for Io has especially been identified as an important caveat in previous preparation studies for the two missions (e.g., Dirkx et al., 2017). The dynamics of Io, Europa, and Ganymede are indeed strongly coupled due to the Laplace resonance, such that missing observational constraints for one of these three moons degrades the stability of the inversion and affects the estimation solution.

In this paper, we combine the existing astrometry and radar observations, used to generate the latest Galilean moons' ephemerides (NOE-5-2021[1]), with radio science products from the JUICE and Europa Clipper spacecraft, as simulated in former analyses (Cappuccio et al., 2022; De Marchi et al., 2022; Di Benedetto et al., 2021; Magnanini et al., 2024; Mazarico et al., 2023). We aim to quantify the synergy between the different datasets and its impact on the accuracy level of future ephemerides' solutions for the Galilean satellites. We considered different data subsets among all existing observations, and analyse their respective contribution to the joint solution. In particular, we investigated the improvement separately provided by classical astrometry, mutual phenomena, radar data, stellar occultations, and space-based astrometry. We finally quantified the added-value of potential future observation campaigns prior to JUICE's and Europa Clipper's Jovian tours.

On a more practical perspective, this study also demonstrates the ability to obtain a consistent solution while relying on several software currently tailored for different applications. The reconstruction of the moons' motion from astrometry is performed by NOE, a software developed in IMCCE (Institut de Mecanique Celeste et de Calcul des Ephemerides) used to generate state-of-the-art moons ephemerides for various systems (Lainey et al., 2009; Lainey, 2016; Lainey et al., 2019, 2020). On

[1] https://ftp.imcce.fr/pub/ephem/satel/NOE/JUPITER/2021/

8

the other hand, simulating JUICE and Europa Clipper radio science observables and subsequently solving for both the spacecraft's and moons' dynamics was performed using two dedicated software packages: JPL's orbit determination software MONTE (Mission Analysis, Operations, and Navigation Toolkit Environment, Evans et al., 2018) and Tudat (TU Delft Astrodynamics Toolbox). Various missions' radio science analyses already relied on MONTE (e.g., Iess et al., 2018; Durante et al., 2019; Zannoni et al., 2020), while Tudat, an open-source astrodynamics and estimation software developed at TU Delft, was used in a number of simulated estimation studies (e.g., Dirkx et al., 2017; Villamil et al., 2021; Fayolle et al., 2021).

Both softwares were recently used to simulate the expected state solution for the Galilean moons from JUICE and/or Europa Clipper radio science (Fayolle et al., 2022; Magnanini et al., 2024) with slightly different estimation setups (Section 8.3.3). In the present article, we retain the minor differences in estimation settings between the two tools, as we consider both to be equally representative of the estimation setup that will be used for the missions' data analysis. As will be shown in Section 8.4, these minor differences in setup yield only minor differences in results. Keeping the small differences between MONTE and Tudat setups in our analysis not only provides important validation for the results provided by each tool, but it also provides more confidence in the robustness of the uncertainty results of one specific setup.

All datasets used in our joint estimation are first presented in Section 8.2, starting with astrometry and radar observations before providing more details on the simulated JUICE and Europa Clipper radio science products. Section 8.3 then describes the inversion strategy adopted in this work to combine not only different observation sets, but also different dynamical and propagation models for the spacecraft. The resulting global solution is discussed in Section 8.4, along with detailed analyses of the contribution of different observation types, before conclusions can be drawn in Section 8.5.

8.2. DATASETS

This section describes the different observation sets to be included in the global inversion. The astrometry and radar data are first described in Sections 8.2.1 and 8.2.2, followed by the simulated radio science measurements for both JUICE and Europa Clipper missions in Section 8.2.3. The synergies between the two datasets are finally further discussed in Section 8.2.4.

8.2.1. EXISTING ASTROMETRY

All astrometric and radar observations used in IMCCE's latest ephemerides' solution for the Galilean satellites (NOE-5-2021) are shown in Figs. 8.1–8.2, the black vertical line separating past observations from predicted ones (after 2024). We distinguish between five main types of observations, displayed on separate rows. Astrometric data include both ground-based and space-based (SA) observations. The former encompasses classical astrometry (CA), mutual phenomena (MP), and stellar occultations (SO). Finally, existing radar observations of the Galilean satellites were

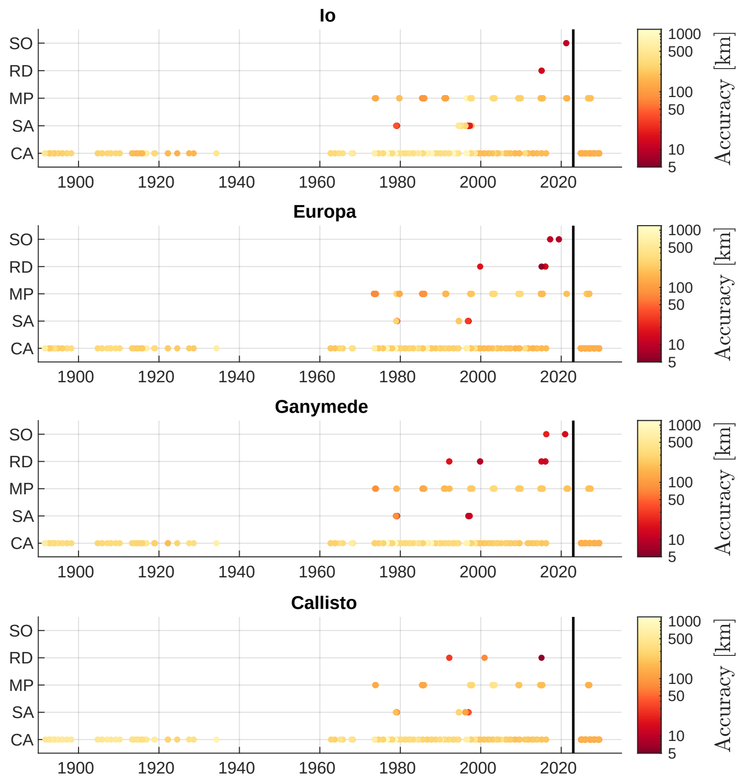

Figure 8.1.: Distribution of the astrometric observations between the five main observation types: CA (classical astrometry), SA (space-based astrometry), MP (mutual phenomena), RD (radar), SO (stellar occultation). The colour indicates the accuracy of each measurement (see also Fig. 8.2). The black vertical line delimits existing data and simulated future ones.

8

also included in our dataset (RD). For the sake of brevity, all above observations are designated as the 'astrometric dataset' in the rest of the paper even though they also include a few radar data.

The weight assigned to each data point in the inversion (see Section 8.3.2), which can be interpreted as a measure of accuracy, is displayed on the vertical axis in Fig. 8.2 and colour-coded in Fig. 8.1. These observation weights are nominally determined through an iterative process ensuring that they are consistent with the root-mean-square (RMS) of the residuals, and a 3σ ruling is applied to exclude outliers. Moreover, if many observations (N) are acquired in a short time span, such that they cannot be considered as independent measurements, they are de-weighted by a factor $\sqrt{N}$. More details on the weighting process, for space-based astrometry in particular, can be found in Lainey et al. (2019).

We include classical astrometry data from 1891 up to 2016. No data were available

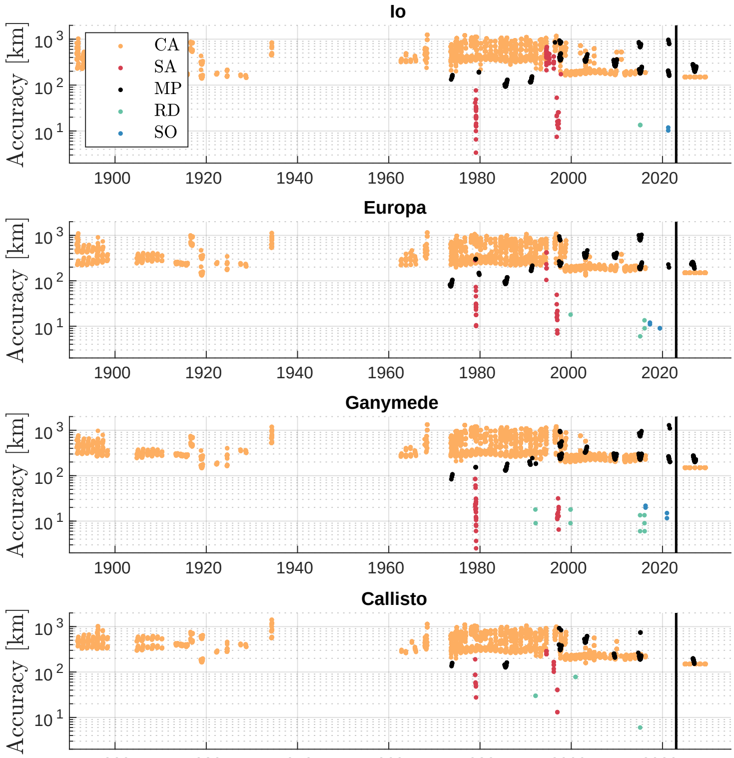

Figure 8.2.: Accuracy of the different ground- and space-based astrometric and radar data, for each of the main observation types (see Fig. 8.1). The accuracy of the space astrometry is expressed with respect to the spacecraft, and not with respect to Earth as for the other observations. The black vertical line delimits existing data and simulated future ones.

8

after 2016, as such observations are rarely performed for the Galilean satellites nowadays, due to the exceptional accuracy achieved with more novel observation techniques (e.g., stellar occultations, see discussion below). Classical astrometry provides either absolute or inter-satellite position measurement in the plane of the sky. As shown in Figs. 8.1–8.2, old astrometry typically shows low accuracy (several hundreds of kilometres). Nonetheless, some old photographic plates have been digitised and re-reduced using recent star catalogues (e.g., Robert et al., 2011), improving the accuracy of the observations. In addition to the data provided in Robert et al. (2011), recently reduced observations were also included in the estimation (not yet publicly available, from V. Robert, private communication).

Mutual phenomena designate occultations and eclipses of one moon by another. Such events require specific observation geometries, with the two moons aligned either with the Sun (eclipses) or with the Earth (occultations). For the Galilean satellites, they occur every six years when the Sun crosses their orbital plane. They have been observed since 1973, the latest mutual campaign to be recorded having taken place in 2021 (e.g., Aksnes and Franklin, 1976; Arlot et al., 2006b, 2014; Emelyanov et al., 2022).

Finally, stellar occultations currently represent the most accurate ground-based observation technique (Morgado et al., 2019a, 2022) for the Galilean satellites. They rely on recording the drop in the photometric flux received by an observer as a moon passes in front of a star. With the help of recent Gaia star catalogues, which provide a very accurate position for the occulted star (Gaia et al., 2018; Brown et al., 2021), the observation of the event allows to determine the moon's position in the ICRF (International Celestial Reference Frame) with an accuracy of a few milliarcseconds, equivalent to a few kilometres at Jupiter's distance. Since the availability of a highly accurate star catalogue is key to the quality of such observations, the first published stellar occultation by a Galilean moon (Europa) only occurred in 2017. Such events moreover require the Galilean satellites to pass in front of a bright enough star (maximum magnitude of 11.5, Morgado et al., 2019a), and are therefore not very frequent. Only five stellar occultations are currently included in our dataset.

It is worth noting that the stellar occultations' uncertainty indicated in Figs. 8.1–8.2 was actually artificially increased by 1.5 mas to account for the error in Jupiter's ephemeris (e.g., Fienga et al., 2021b). This error source could eventually be mitigated using Gaia data, by extracting information about the Jovian system barycentre's position from Gaia's observations of Jupiter's outer satellites. Alternatively, the VLBI tracking experiment proposed in Chapter 7 could also help reducing the contribution of Jupiter's error to the occultation's error budget. This would be critical to achieve the expected few kilometres accuracy for stellar occultations.

In addition to ground-based observations, space-based astrometry was also performed during planetary missions. In particular, both the Galileo and Voyager spacecraft were able to take images of the Galilean moons (e.g., Haw et al., 2000; Smith et al., 1979a). Those observations are interesting because of the different geometry under which they were taken, but they are affected by errors in the spacecraft orbit determination. For Galileo and Voyager, this error was very high compared to modern missions, significantly reducing the quality of the space astrometry data. In Figs. 8.1–8.2, their accuracy is expressed with respect to the spacecraft and not with respect to Earth, and thus cannot be directly compared with that of ground-based astrometric observations.

Regarding ground-based radar observations, only 22 measurements from Arecibo are available (Brozović et al., 2020a). Their number is limited, but they yield highly accurate measurements of the moons' line-of-sight ranges with respect to Earth (accuracy between 10 μs and 250 μs for the time delay measurement, equivalent to 6-80 km). The information provided by radar data actually distinguishes them from astrometric observations, which typically measure position(s) in the plane of the sky.

8.2.2. FUTURE ASTROMETRY FOR THE PERIOD 2024-2029

To complement the existing set of astrometric and radar data described in Section 8.2.1, we also used future astrometric observations for the 2024-2029 period preceding the arrival of the JUICE and Europa Clipper spacecraft in the Jovian system, which were originally simulated for a past study investigating pre-mission ephemerides' solutions (V. Lainey, private communication). Including such synthetic data in our analyses allows us to quantify how much such Earth-based observations could contribute to a post-mission combined solution. Given the unprecedented accuracy level expected for the radio science products of both missions (see Section 8.2.3 for more details), this is a key analysis to justify the need for future observation campaigns and identify which yet missing observations could efficiently complement JUICE's and Europa Clipper's data.

In addition to simulated classical astrometric observations, the upcoming mutual phenomena period, which will occur in 2027, is included. For classical astrometry, we generated around 1000 observations per moon and considered an accuracy of 150 km at Jupiter's distance, in agreement with the most accurate observations recently collected. This is representative of the expected accuracy for future observation campaigns, particularly given the availability of the very accurate Gaia GDR3 catalogue. Regarding mutual phenomena, 535 measurements were simulated (all moons combined), with accuracy levels comparable to recent observations (150-200 km). These synthetic observations are all reported in Figs. 8.1–8.2, on the right-hand side of the black line. As for radar observations, the set of existing data is limited to the 22 measurements acquired since 1992. Given the loss of Arecibo, which dramatically reduces the ground-based radar observation capability, we chose not to include simulated radar data before the beginning of the JUICE and Europa Clipper missions.

8.2.3. Simulated radio science data

The radio science dataset contains simulated range and Doppler measurements for the JUICE and Europa Clipper spacecraft. Both missions will generate such tracking data during flybys at Europa, Ganymede, and Callisto, as well as during Ganymede's orbital phase for JUICE.

8

For JUICE's Jovian tour, we considered a X/Ka-band radio-link and assumed 48 hours of radiometric tracking centred at each flyby's closest approach, from the ESTRACK ground stations (Cappuccio et al., 2022). We applied a noise of 20 cm for ranging measurements, which may be a rather conservative estimate given the recent performance of the BepiColombo radio science instrument (sub-centimetre accuracy, Cappuccio et al., 2020a; Genova et al., 2021), and 12 μm/s for Doppler data (at an integration time of 60 s). The orbital phase around Ganymede was divided into 24 hours-long arcs, with eight hours of tracking per day during which both range and Doppler measurements are generated.

We simulated four hours of tracking at each closest approach for the Europa Clipper spacecraft, assuming a noise level of 0.1 mm/s as the X/Ka-band high-gain antenna (HGA) is then not available due conflict with other instruments (Mazarico et al., 2023). The navigation tracking passes were however also included, in agreement with the current mission operation plan and recommended tracking setup for Europa Clipper simulations (e.g., Magnanini et al., 2024). During these tracking arcs occurring further before or after the closest approach, the HGA can be used and the noise for Doppler data is thus divided by two. The average duration of the navigation tracking passes is five hours and they typically occur 20h before and after the closest approach. Range measurements could also be collected during such arcs, for which we assumed a noise of 1 m.

8.2.4. SYNERGISTIC COMBINATION

Figs. 8.1-8.2 highlight the main characteristics of the astrometry (and radar) dataset. Here, we described where synergies with radio science data will originate from. First, astrometry and radar observations are significantly less accurate than radio science measurements, with accuracies ranging from a few kilometres to several hundreds of kilometres depending on the observation type. However, they cover a much longer time span, starting in the 1890s until 2021, and even extending until the beginning of the JUICE and Europa Clipper missions if simulated data are included. Adding astrometry and radar observations is thus crucial to be sensitive to long-term signals in the moons' dynamics (e.g., dissipation effects). This is particularly important for the Galilean satellites as their dynamics show many long-period effects with different frequencies, which are difficult to distinguish from one another (Lainey et al., 2006). Radio science measurements, on the other hand, are confined to the missions' timelines, for a total period of less than six years. The expected accuracy is however orders of magnitude better than what is achievable from ground-based observations (e.g., Magnanini et al., 2024).

Furthermore, Figs. 8.1–8.2 clearly illustrate that the astrometry dataset is more balanced than the radio science data, with observations more evenly distributed among the four Galilean satellites. JUICE and Europa Clipper, on the other hand, strongly focus on Europa and Ganymede, respectively. While Callisto is still targeted by a total of 30 flybys with both spacecraft, no flyby of Io is planned in the nominal mission scenarios. As already mentioned in Section 8.1, adding existing astrometric and radar observations of this moon is thus particularly critical, since it is in mean-motion resonance with Europa and Ganymede.

Finally, ground-based astrometry and radio science observables characterise the moons' dynamics under different observation geometries and are sensitive to the moons' motion projected in different directions. Astrometry typically measures the (absolute or relative) position of the satellites in the plane of the sky, while radio science's classical measurements, namely ranging and range-rate, probe the spacecraft's position and velocity in the Earth's line-of-sight direction.

While comparing the astrometry and radio science datasets and their synergies, it is also worth noting a few of their major differences which might affect the estimation solution(s). First, astrometry and radio science measurements are affected by different noise sources. In particular, astrometry and radar data are sensitive to the offset between the centre of figure (COF) and centre of mass (COM), measuring the former while trying to solve for the latter. While this was not accounted for in our analysis, combining radio science with astrometry will be an effective way to estimate the COF-COM offset and thus mitigate this error source (see Section 8.5).

Radio science tracking, on the other hand, only indirectly probes the moons' dynamics around Jupiter, by reconstructing the spacecraft's trajectory as it passes in the close (gravitational) proximity of the Galilean satellites. This implies that additional parameters influencing the spacecraft's orbit determination solution need to be solved for concurrently with the moons' dynamics (Fayolle et al., 2022; Magnanini et al., 2024), as listed in Section 8.3.3. In practice, the number of estimated parameters significantly increases when introducing radio science measurements, especially since all spacecraft-related parameters are typically solved for locally, in an arc-wise manner. This can affect the stability of the inversion and the estimation solution.

8.3. INVERSION METHODOLOGY

This section presents the adopted strategy to perform the global inversion of astrometric and radio science data. Section 8.3.1 provides a top-level description of the propagation and estimation setups, before Section 8.3.2 details the merging process to combine astrometry and radio science data in the estimation. Finally, the list of estimated parameters can be found in Section 8.3.3.

8.3.1. PROPAGATION AND ESTIMATION SETUPS

As mentioned in Section 8.1, we rely on three different softwares to obtain a combined solution with astrometry and radio science. The NOE software is used to propagate the moons' dynamics over the entire time span of the astrometric dataset and compute the associated partials (see Fig. 8.3). To this end, the gravity fields of Jupiter and the Galilean satellites are modelled by spherical harmonics expansions, extended up to degree and order two for the moons and including zonal coefficients up to degree ten for Jupiter. The moons' rotation is assumed to be synchronous, with the tidal bulge pointing towards the empty focus of the orbit (Lainey et al., 2019; Lari, 2018). Jupiter's rotation include precession and nutations terms, following the IAU model (Archinal et al., 2018). To propagate the dynamics of the Galilean moons, the following accelerations are considered (Lainey et al., 2004a; Dirkx et al., 2016): mutual spherical harmonics acceleration between Jupiter and each moon i, mutual spherical harmonics acceleration in-between the Galilean moons, tidal dissipation (using the formulation presented in e.g., Lainey et al. 2017; Lari 2018), third-body perturbation from Saturn and the Sun, and general relativity acceleration corrections.

On the radio science side, the equations of motion and variational equations for the spacecraft are solved with both Tudat and MONTE. Both tools propagate the dynamics of the spacecraft, using the latest JUICE[2] and Europa Clipper [3] trajectories as baselines. The gravitational accelerations exerted by the moons on the spacecraft are modelled using spherical harmonics gravity models up to degree and order two for Io, 13 for Europa, 50 for Ganymede, nine for Callisto. Additionally, the spherical harmonics gravitational acceleration from Jupiter (with zonal coefficients up to degree ten), point-mass gravitational accelerations from

[2]JUICE trajectory: juice_mat_crema_5_0_20220826_20351005_v01: https://www.cosmos.esa.int/web/spice/spice-for-juice

[3]Europa Clipper trajectory: 21F31_MEGA_L241010_A300411_LP01_V4_postLaunch_scpse: https://naif.jpl.nasa.gov/pub/naif/EUROPACLIPPER/kernels/spk/

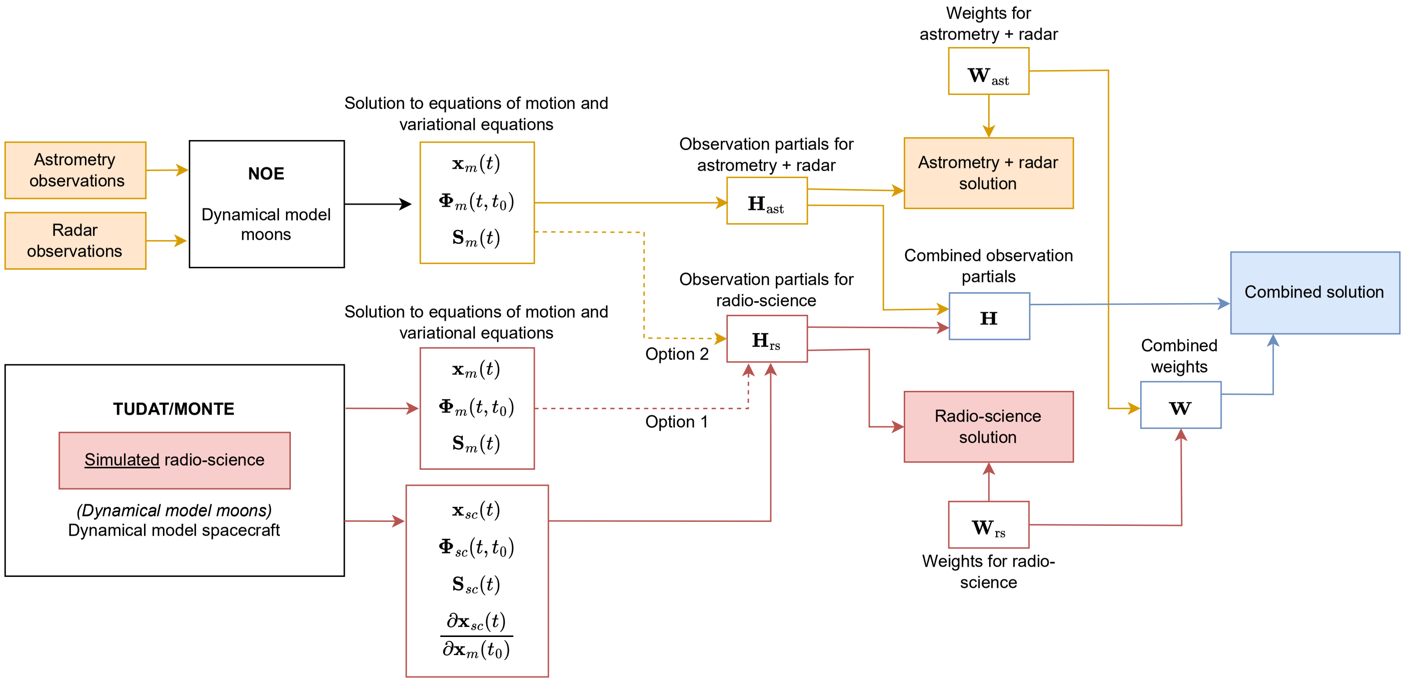

Figure 8.3.: Schematic summary of the global inversion methodology detailed in Sections 8.3.1 and 8.3.2. The main interfaces between the three software (NOE, Tudat, and MONTE), as well as their inputs and outputs are represented. In particular, the two different strategies to include the solutions of the moons' equations of motion and variational equations in the radio science partials (Section 8.3.2) are illustrated by the dotted lines. The mathematical notations correspond to those used in Section 8.3.2.

8

the Sun and Saturn, and the solar radiation pressure acceleration are considered. From the spacecraft's propagated trajectories, both softwares can simulate radio science measurements with expected noise levels (see Section 8.2.3) and provide the corresponding observation partials. NOE and Tudat or MONTE thus each provide part of the required inputs, allowing us to perform a combined estimation (see Fig. 8.3). Section 8.3.2 describes in detail how the astrometric and radio science observations were merged in the inversion process.

For the purpose of our analyses, we chose to primarily rely on covariance results (see details in Section 8.3.2). We indeed focus on quantifying the improvement attainable from a combined solution, which is well described by comparing formal uncertainties. It is however worth specifying that, as discussed in Section 8.2.1, the weights assigned to the existing astrometric observations are based on the RMS of the residuals, and thus on real data analysis.

8.3.2. MERGING ASTROMETRIC AND RADIO SCIENCE PARTIALS

The inversion approach adopted in our analyses follows the coupled estimation strategy described in detail in Fayolle et al. (2022), with limited extensions to allow for the merging of different datasets, as summarised below. The covariance matrix $\boldsymbol{P}$ for the estimated parameters $\boldsymbol{p}$ is given by the following equation (e.g., Gill and Montenbruck, 2013):

$$\boldsymbol{P} = \left(\boldsymbol{H}^{\mathrm{T}}\boldsymbol{W}\boldsymbol{H} + \boldsymbol{P}_0^{-1}\right)^{-1}, \tag{8.1}$$

where $\boldsymbol{H}$ is the observations partial matrix, $\boldsymbol{W}$ is the matrix containing the weights to be applied to each observation and $\boldsymbol{P}_0$ is the a priori covariance matrix of the estimated parameters.

The full observation partial matrix $\boldsymbol{H}$ can be decomposed between the astrometric (denoted as 'ast') and radio science ('rs') data subsets (see Fig. 8.3), as follows:

$$\boldsymbol{H} = \begin{pmatrix} \boldsymbol{H}_{\mathrm{ast}} \\ \boldsymbol{H}_{rs} \end{pmatrix} = \begin{pmatrix} \frac{\partial \boldsymbol{h}_{\mathrm{ast}}}{\partial \boldsymbol{p}} \\ \frac{\partial \boldsymbol{h}_{\mathrm{rs}}}{\partial \boldsymbol{p}}, \end{pmatrix} \tag{8.2}$$

where $\boldsymbol{h}_{\mathrm{ast}}$ and $\boldsymbol{h}_{\mathrm{rs}}$ represent the astrometric and radio science observations, respectively. The parameters vector $\boldsymbol{p}$ can be written as

$$\boldsymbol{p} = \left[\boldsymbol{x}_m(t_0) \quad \boldsymbol{x}_{\mathrm{sc}}(\boldsymbol{t}_i) \quad \boldsymbol{q}_{\mathrm{dyn}} \quad \boldsymbol{q}_{\mathrm{obs}}\right]^{\mathrm{T}}, \tag{8.3}$$

with $\boldsymbol{x}_m(t_0)$ the concatenated initial state vector for the four Galilean moons, and $\boldsymbol{x}_{\mathrm{sc}}(\boldsymbol{t}_i)$ the vector containing all the arc-wise initial states of both the JUICE and Europa Clipper spacecraft. t_0 refers to the global reference epoch, while $\boldsymbol{t}_i$ contains the initial times of each arc. $\boldsymbol{q}_{\mathrm{dyn}}$ and $\boldsymbol{q}_{\mathrm{obs}}$ correspond to the non-state parameters influencing the moons' and spacecraft's dynamics and the observations (e.g., biases), respectively. By definition, the astrometric observations are not sensitive to spacecraft-related parameters, such that only a subset of the parameters vector $\boldsymbol{p}$ is considered in the computation of their partials. In the merging process, zero-filled columns are thus added when relevant.

Using Eq. 8.3 to expand the formulation for astrometric partials, we obtain for a single observation $h_{\text{ast}}(t)$ in $\boldsymbol{H}_{\text{ast}}$ (t being the observation time):

$$\frac{\partial h_{\text{ast}}(t)}{\partial \boldsymbol{p}} = \begin{bmatrix} \frac{\partial h_{\text{ast}}(t)}{\partial \boldsymbol{x}_m(t_0)} & \frac{\partial h_{\text{ast}}(t)}{\partial \boldsymbol{x}_{\text{sc}}(\boldsymbol{t}_i)} & \frac{\partial h_{\text{ast}}(t)}{\partial \boldsymbol{q}_{\text{dyn}}} & \frac{\partial h_{\text{ast}}(t)}{\partial \boldsymbol{q}_{\text{obs}}} \end{bmatrix} \tag{8.4}$$

$$= \begin{bmatrix} \frac{\partial h_{\text{ast}}(t)}{\partial \boldsymbol{x}_m(t)} \begin{pmatrix} \boldsymbol{\Phi}_m(t,t_0) & \mathbf{0} & \boldsymbol{S}_m(t) \end{pmatrix} & \frac{\partial h_{\text{ast}}(t)}{\partial \boldsymbol{q}_{\text{obs}}} \end{bmatrix}, \tag{8.5}$$

where $\boldsymbol{\Phi}_m(t,t_0)$ and $\boldsymbol{S}(t)$ are the state transition and sensitivity matrices for the moons dynamics, defined as:

$$\boldsymbol{\Phi}_m(t,t_0) = \frac{\partial \boldsymbol{x}_m(t)}{\partial \boldsymbol{x}_m(t_0)} \;\; ; \;\; \boldsymbol{S}_m(t) = \frac{\partial \boldsymbol{x}_m(t)}{\partial \boldsymbol{q}_{\text{dyn}}}. \tag{8.6}$$

The astrometric subset of the design matrix $\boldsymbol{H}_{\text{ast}}$ is thus fully derived from the variational equations solution for the moons' dynamics. On the other hand, the spacecraft's states are influenced by the moons' orbital motion, and the radio science partials $\boldsymbol{H}_{\text{rs}}$ therefore depend on both the moons' and spacecraft's states:

$$\frac{\partial h_{\text{rs}}(t)}{\partial \boldsymbol{p}} = \begin{bmatrix} \frac{\partial h_{\text{rs}}(t)}{\partial \boldsymbol{x}_m(t_0)} & \frac{\partial h_{\text{rs}}(t)}{\partial \boldsymbol{x}_{\text{sc}}(\boldsymbol{t}_i)} & \frac{\partial h_{\text{rs}}(t)}{\partial \boldsymbol{q}_{\text{dyn}}} & \frac{\partial h_{\text{rs}}(t)}{\partial \boldsymbol{q}_{\text{obs}}} \end{bmatrix} \tag{8.7}$$

$$= \begin{bmatrix} \frac{\partial h_{\text{rs}}(t)}{\partial \boldsymbol{x}_{\text{sc}}(t)} \begin{pmatrix} \frac{\partial \boldsymbol{x}_{\text{sc}}(t)}{\partial \boldsymbol{x}_m(t_0)} & \boldsymbol{\Phi}_{\text{sc}}(t,\boldsymbol{t}_i) & \boldsymbol{S}_{\text{sc}}(t) \end{pmatrix} & \frac{\partial h_{\text{rs}}(t)}{\partial \boldsymbol{q}_{\text{obs}}} \end{bmatrix}, \tag{8.8}$$

where $\boldsymbol{\Phi}_{\text{sc}}(t,\boldsymbol{t}_i)$ and $\boldsymbol{S}_{\text{sc}}(t)$ represent the state transition and sensitivity matrices for the spacecraft's dynamics. Because of the coupling between the moons' and spacecraft's dynamics, computing $\frac{\partial \boldsymbol{x}_{\text{sc}}(t)}{\partial \boldsymbol{x}_m(t_0)}$ and $\boldsymbol{S}_{\text{sc}}(t)$ in Eq. 8.8 also requires to solve the moons' variational equations (Fayolle et al., 2022).

When computing the observation partials for (simulated) radio science data only with the MONTE or Tudat software, the equations of motion and variational equations for both the moons and the spacecraft are concurrently integrated, to account for the coupling in their dynamics. This implies that both NOE and Tudat or MONTE can provide their own solutions for $\boldsymbol{\Phi}_m(t,t_0)$ and $\boldsymbol{S}_m(t)$, as illustrated in Fig. 8.3. Two different approaches can thus be considered:

8

1. Independently integrating the moons' variational equations with different software;
2. Importing the moons' solution provided by a single software into the other(s).

The first option is straightforward to apply and allows for the direct stacking of the partials matrices $\boldsymbol{H}_{\text{ast}}$ and $\boldsymbol{H}_{\text{rs}}$, each generated with different software (NOE, and Tudat or MONTE, respectively) but using the same reference epoch t_0. However, the solutions to the equations of motion and variational equations for the moons must then be consistent between the two software, which was carefully verified in our case (between NOE and both Tudat or MONTE).

The second option is to directly import NOE's solution for $\boldsymbol{\Phi}_m(t,t_0)$ and $\boldsymbol{S}_m(t)$ into Tudat or MONTE to avoid propagating the moons' dynamics with different software. While this strategy is more demanding implementation-wise, it automatically ensures that the moons' dynamics are fully consistent between the astrometric $\boldsymbol{H}_{\text{ast}}$ and radio science $\boldsymbol{H}_{\text{rs}}$ partials. In practice, we implemented both options and showed that they indeed lead to equivalent results for our JUICE-Europa Clipper case (see results in Section 8.4).

8.3.3. Estimated parameters

From the astrometric and/or radio science datasets, we estimate various parameters characterising the Jovian system and influencing the dynamics of the Galilean satellites. These include the initial states for Io, Europa, Ganymede, and Callisto, estimated at the reference epoch t_0 (set in the middle of the JUICE and Europa Clipper expected timelines), as well as the moons' gravitational parameters μ_i, $i \in [1:4]$ and their gravity field coefficients up to degree and order 13, 50, and 9 for Europa, Ganymede, and Callisto, respectively. Regarding Jupiter, we estimate its gravitational parameter μ_0, zonal coefficients (J_2 to J_6), and pole orientation (right ascension α and declination δ at the reference epoch t_0). Finally, tidal dissipation parameters include the $1/Q$ of Jupiter at a single frequency, and the $1/Q$ of Io at Jupiter's frequency.

Spacecraft-related parameters are also determined when including radio science in the solution. Different subsets of the following set of parameters are estimated in the MONTE and Tudat setups. In addition to the arc-wise initial states of the JUICE and Europa Clipper spacecraft (estimated in both setups), the spacecraft-related parameters include various observation-related parameters: range biases (both setups), antenna phase centre positions (MONTE only), accelerometer calibration factors (Tudat only), solar radiation pressure coefficients (MONTE only).

The above describes a simplified setup compared to detailed simulations studying the achievable radio science solution at the end of the JUICE and/or Europa Clipper missions (Magnanini, 2021; Magnanini et al., 2024; Fayolle et al., 2022). In particular, only Io's and Jupiter's tidal dissipation parameters are estimated, with no frequency-dependency introduced for $1/Q$. However, our study aims at quantifying the relative improvement achieved with global inversion with respect to a radio science or astrometry-only solution. Keeping the setup close to the one currently used for the astrometry-only inversion (e.g., Lainey et al., 2009) facilitates this comparison and the analysis of the estimation results.

Furthermore, as shown by the list of estimated parameters, the nominal setups for the joint JUICE-Europa Clipper estimation in Tudat and MONTE show some small differences. These different setups were independently used in past radio science simulation studies (Magnanini et al., 2024; Fayolle et al., 2022, for MONTE and Tudat setups, respectively). The reason for keeping them as such is twofold. First, both are realistic and representative setups for simulation purposes, since the optimal estimation setup cannot be fixed before real data become available. Second, using perfectly identical setups is challenging due to the lack of certain software capabilities (e.g., antenna phase centre positions not readily available in Tudat) and/or to the significant modifications that it would have required (e.g., including accelerometer calibration factors in the MONTE setup). On the other hand, and especially considering the absence of a unique preconised setup for a joint radio science inversion of JUICE and Europa Clipper, keeping these discrepancies between the two softwares also allows us to verify that our general results are not affected by the details of the covariance analysis setup.

It makes our comparative results more robust by ensuring that the specific settings chosen do not substantially impact the results, and are thus more representative in light of the potential deviations that are expected to arise between simulations and real data solutions. Section 8.4 will thus provide results obtained with both Tudat and MONTE. Simulated analyses of radio science experiments performed with different tools and slightly different setups should result in comparable results if both setups are representative. Experience from past missions shows that differences of a factor two or three are not uncommon (see for instance BepiColombo simulations in e.g., Schettino et al., 2015; Imperi et al., 2018). Moreover, a difference of a comparable order between absolute uncertainties in simulated analyses and real mission data analysis is to be expected.

8.4. Results

This section presents the results of the global inversion, in comparison with the astrometry only or radio science only solutions. We then quantify the individual contribution of various subsets of the astrometry dataset, distinguishing between different types of observations or different targets. A detailed comparison between JUICE-only and Europa Clipper-only is provided in Magnanini et al. (2024).

8.4.1. Combined solution from astrometry and radio science

As discussed in Section 8.1, combining astrometric data with planetary missions' radio science measurements is mostly expected to help reconstructing the long-term orbital motion of the Galilean satellites. We thus focussed our analysis on the resulting uncertainties in the moons' states, as well as tidal dissipation parameters of Io and Jupiter. Three different simulated inversion solutions were generated: first with astrometry or radio science data only, and then using the complete observations set. All inversions were independently performed with both the Tudat and MONTE software, adding the astrometric observation partials and weights retrieved from NOE when relevant.

Software consistency

The solution based on astrometry only was used as a benchmark to compare the inversion results independently provided by our three software. This is to ensure that the computation of the covariance matrix according to Eq. 8.1 is fully consistent between the tools. For astrometric observations, all inputs to Eq. 8.1 are indeed identical, as they are directly provided by the NOE software (Fig. 8.3), with no need to include the JUICE and Europa Clipper spacecraft in the estimation. The three solutions were in agreement and provided the same formal uncertainties for all estimated parameters.

For both the radio science and combined configurations, the two different approaches described in Section 8.3.2 led to similar results (for a given software). For the sake of conciseness, Table 8.1 thus only provides one set of results for each software, which were equivalently obtained with both inversion strategies. Whether the solutions to the equations of motion and variational equations for the Galilean satellites were directly imported from the NOE software or separately recomputed when simulating the spacecraft dynamics did not affect the solution, demonstrating the consistency of the different software. In the rest of our analyses, the two approaches were thus considered equivalent. All Tudat results were obtained with both methods, while the second strategy was preferred in the MONTE setup (i.e., the moons' dynamical and variational equations were integrated with MONTE independently from NOE, for implementation reasons).

INFLUENCE ON THE MOONS' STATE ESTIMATION

This section discusses the results of the global inversion for the Galilean satellites state estimation, analysing correlations (Fig. 8.4) as well as formal uncertainties (Fig. 8.5, 8.6, and 8.7). First looking at the impact on the correlations between state parameters, Fig. 8.4 shows the relative change ϵ in absolute decorrelation when adding astrometry, with respect to the radio science only case, defined as follows:

$$\epsilon = \frac{\left(1-|c_{ij}^{\text{all}}|\right)-\left(1-|c_{ij}^{\text{rs}}|\right)}{1-|c_{ij}^{\text{rs}}|}, \tag{8.9}$$

where $1-|c_{ij}^{\text{rs}}|$ and $1-|c_{ij}^{\text{all}}|$ are the decorrelation between parameters i and j in the radio science only and combined (radio science and astrometry) cases, respectively. Focusing on decorrelations (1 − correlations) rather than correlations allows to scale changes as a function of the distance to full correlation: a decrease in correlation between two parameters indeed has a stronger influence on the inversion if the two parameters were originally fully correlated than if they were already rather decorrelated.

8

Fig. 8.4 shows that including astrometry in the solution decreases the correlations for most state parameters (shown as decorrelation increase in Fig. 8.4). This is not only observed between state components of the same moon, but also between different moons. For fewer parameters, the correlations actually increase, which can be caused by the heterogeneous effect of adding more data (i.e., more information) on the uncertainties of different estimated parameters. If the additional observations help to reduce the uncertainty in parameter i, its correlation with parameter j whose uncertainty remains unchanged might increase. Nonetheless, adding astrometry overall reduces the strong correlations between the states of Io, Europa, and Ganymede caused by the Laplace resonance. This improvement originates from adding observations over a longer time span, as well as direct measurements of Io's position which are critically missing in the JUICE and Europa Clipper radio science dataset.

Similar observations can be made from the state uncertainties obtained for the Galilean moons. During the period of the two missions, only Io's solution

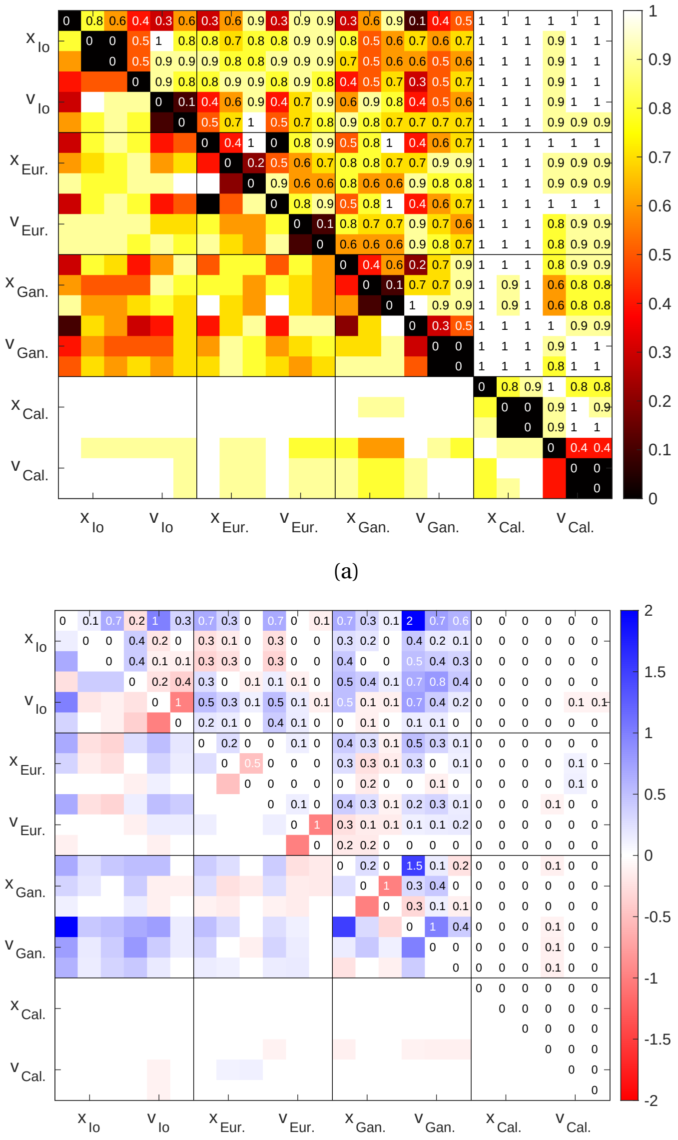

(a)

(b)

Figure 8.4.: Effect of combining radio science and astrometry on the decorrelations between the moons' initial states (in jovocentric coordinates). Panel a: decorrelations for the radio science-only solution. Darker colours indicate lower decorrelations, thus stronger correlations. Panel b: relative differences in decorrelations between the combined and radio science-only solutions (see Eq. 8.9). Blue and red indicate an increase and a decrease in decorrelation, respectively.

benefits from adding astrometry data to the estimation (Fig. 8.5), while the other moons' states could not be improved in this time interval beyond the radio science solution. This is expected given the unprecedentedly low uncertainties predicted by simulations for JUICE and/or Europa Clipper (Fayolle et al., 2022; Magnanini et al., 2024). For a joint solution relying on both missions, the position uncertainties for Europa, Ganymede, and Callisto achieve sub-meter accuracy in the radial direction, while they do not exceed a few tens of meters in the tangential and normal directions. However, when using radio science data only, Io's state solution is solely based on indirect constraints originating from the well-determined dynamics of the other two moons in resonance. Including astrometry thus has a stronger effect for this moon: it reduces the averaged uncertainty in the radial and tangential positions by about a factor two (Fig. 8.5).

While radio science measurements alone already provide an extremely accurate solution for the Galilean moons' states during the JUICE and Europa Clipper missions, the formal uncertainties start to dramatically increase once propagated beyond the missions' timeline, especially in the radial and tangential directions. The solution is particularly unstable for the three moons in resonance whose dynamics are mutually affected by their state uncertainties. This is illustrated in Fig. 8.6a, using Europa as an example (results for the other moons can be found in Appendix 8.6). The propagated uncertainties show a similar increase with time for both radial and tangential positions, although the errors in the radial direction remain about two orders of magnitude lower than the tangential ones. Uncertainties in the normal direction, on the other hand, do not strongly degrade upon propagation. These differences between in-plane and out-of-plane uncertainty propagation can be explained by the fact that most dynamical perturbations, as well as the Laplace resonance, act within the moons' orbital plane. This causes in-plane position errors to quickly propagate into larger uncertainties, which however do not strongly affect the out-of-plane motion.

Merging the radio science data with astrometry, however, brings observational constraints over a much longer time span and thus significantly helps maintaining low uncertainty levels (Fig. 8.6b). The formal errors in the moons' tangential positions obtained from the complete dataset indeed tend to asymptotically get closer to the astrometry solution when getting further away from the missions period (2030-2035), as the influence of JUICE and Europa Clipper diminishes. Similarly, the radial position error level does not degrade as strongly as in the radio science case. For the moon's normal position errors, which are significantly more stable upon long-term propagation, adding astrometry has a smaller effect.

To analyse the long-term error propagation further, Fig. 8.7 displays the state uncertainty levels for all moons, averaged over the period 1890-2030 (after backward propagation). In particular, the radio science-only solution errors are extremely high for the tangential positions (as in Fig. 8.6), and adding astrometry can reduce them by more than one order of magnitude for Io, Europa, and Ganymede. Callisto is however a notable exception: as the moon is not in resonance, the low uncertainty levels reached during the JUICE and Europa Clipper missions remain relatively stable upon propagation. The combined solution is thus closer to the radio science case,

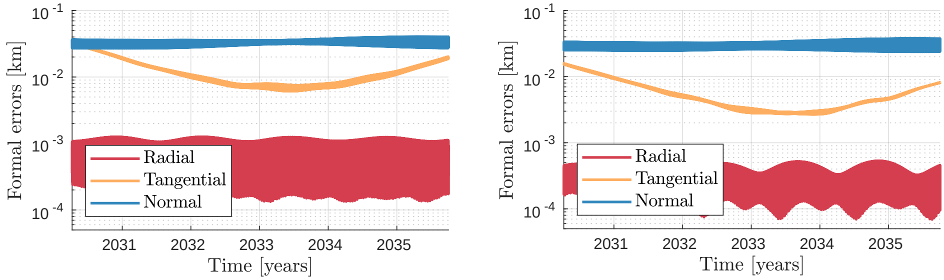

(a) (b)

Figure 8.5.: Evolution of the formal uncertainties in Io's state during the timelines of the JUICE and Europa Clipper missions. Panel a: radio science only solution, panel b: global inversion results (astrometry and radio science combined).

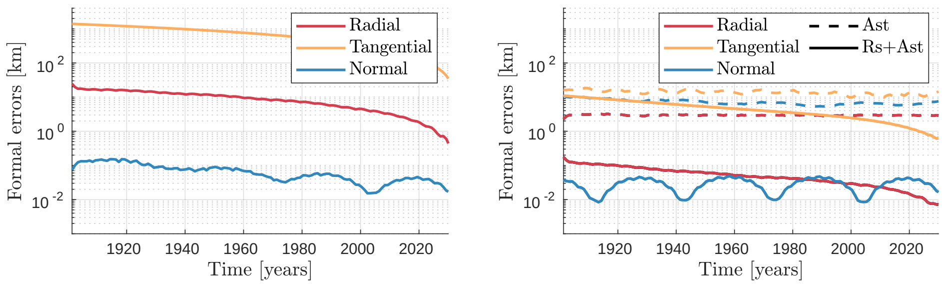

(a) (b)

Figure 8.6.: Propagated formal uncertainties in Europa's position (from 2030 to 1890) for the radio science (Rs), astrometry (Ast) and combined solutions (Rs+Ast), obtained with Tudat and NOE. Panel a: radio science solution, panel b: astrometry-only and combined solutions. The errors are given in the RTN (radial, tangential, normal) directions and the scales are identical on both Fig. 8.6a and 8.6b. To keep both the computational and memory loads manageable, we used a propagation output of one point per year and performed data smoothing over five-year windows to avoid aliasing effects. While this does not allow for local uncertainty analyses, it is nonetheless sufficient to investigate the long-term behaviour of the position errors far from the missions period.

and the astrometry dataset does not provide any significant improvement. It should however be noted that various additional perturbations and uncertainty sources, such as gravitational perturbations by the inner moons and asteroids (see detailed discussion in Section 8.5), would also affect the long-term error propagation and deteriorate the accuracy of Callisto's solution.

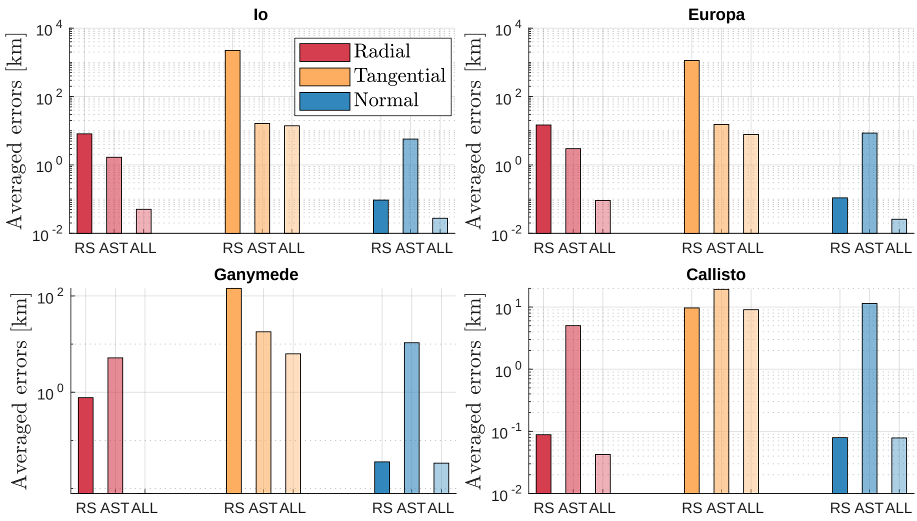

Figure 8.7.: Formal uncertainties in the Galilean moons' satellites, averaged over the period 1890-2030. The results are provided for the radio science (RS), astrometry (AST), and combined (ALL) solutions.

INFLUENCE ON THE TIDAL DISSIPATION PARAMETERS

The formal errors obtained for $1/Q_{\text{Jupiter}}$ and $1/Q_{\text{Io}}$ in the three different configurations are reported in Table 8.1. It should be noted that Tudat and MONTE provide different uncertainties for the radio science solution. While the results are surprisingly very close for $\sigma(1/Q_{\text{Jupiter}})$ in the radio science-only case, this does not reflect the behaviour obtained for other parameters. The error in $1/Q_{\text{Io}}$ obtained with Tudat is indeed three times larger than the one provided by MONTE, and the moons' state uncertainties (not showed in Table 8.1) show similar differences (factor two to three, depending on the considered moon and direction). These discrepancies can be at least partially explained by differences in the tracking and estimation setups used for the joint JUICE-Europa Clipper analysis, as mentioned in Section 8.3.3. Differences between the two software can also contribute to the observed disparity (see Section 8.3.1).

Finally looking at the combined solution, the uncertainties in $1/Q_{\text{Jupiter}}$ are a factor two to four smaller than for the radio science case, depending on the software and estimation setup. We also obtained a consistent 30-35% improvement for $1/Q_{\text{Io}}$ with both MONTE and Tudat. With respect to the current, astrometry-based solution, the combined solution actually represents an order of magnitude improvement. Overall, the attainable uncertainty reduction in both $1/Q_{\text{Jupiter}}$ and $1/Q_{\text{Io}}$ thus seems significant. This improvement could be anticipated from the long-term propagation of the moons' state solutions shown in Fig. 8.8. Combining radio science and astrometry indeed strongly reduces the uncertainty in the along-track direction (by more than one order of magnitude). This is crucial for the determination of the moons' tidal dissipation parameters, as the tidal effects are mostly detectable from the moons' orbits through the secular change in mean motion that they cause. Those results, even if obtained in a simplified, (partially) simulation-based setup, indicate that adding astrometry to JUICE and Europa Clipper data is a promising approach to better constrain tidal dissipation effects in the Jovian system.

It is worth noting that including astrometry in the solution also slightly reduces the (high) correlation between Jupiter's and Io's tidal dissipation parameters. Taking the Tudat setup as an example, the 92% correlation between $1/Q_{\text{Jupiter}}$ and $1/Q_{\text{Io}}$ when relying on radio science solely is brought down to about 87% in the combined case. This still represents a ~60% improvement in the solution departure from full correlations (8% with radio science to 13% with both radio science and astrometry).

8.4.2. CONTRIBUTION OF DIFFERENT ASTROMETRIC OBSERVABLE TYPES

To further analyse which observations most effectively contribute to reducing the uncertainties in $1/Q_{\text{Jupiter}}$ and $1/Q_{\text{Io}}$, we ran simulations including only subsets of the available astrometry data to the simulated radioscience data. We first considered each type of observations independently. In addition to radio science, we thus separately incorporated classical astrometry, space-based astrometry, mutual phenomena, radar data, and stellar occultations. The resulting formal uncertainties are reported in Table 8.2. For each data subset, results are also provided as a percentage of the total improvement in $\sigma(1/Q_{\text{Jupiter}})$ and $\sigma(1/Q_{\text{Io}})$ achieved when adding all astrometric observations to radio science. We chose to show and discuss the individual contribution of different datasets based on the estimation formal errors, for which this distinction is stronger and more directly observable than for the correlations between parameters.

When looking at the individual contribution of each data type in Table 8.2, classical astrometry has the biggest influence on the solution. More precisely, it seems that old measurements (i.e., acquired before 1960) are the most beneficial, while they only account for 20% of all classical astrometric data, which is consistent with the discussion in Section 8.4.1. As shown in Figs. 8.1–8.2, these observations typically show low accuracy (100s km to 1000 km). Nonetheless, they provide invaluable constraints on the long-term dynamics of the Galilean satellites and thus play a

8

Table 8.1.: Formal uncertainties in $1/Q$ of Io and Jupiter.

	$1/Q_{\text{Jupiter}}$ [-]	$1/Q_{\text{Io}}$ [-]
Astrometry		
	$2.5 \cdot 10^{-6}$	$1.7 \cdot 10^{-2}$
Radio science		
MONTE	$1.3 \cdot 10^{-6}$	$1.0 \cdot 10^{-3}$
Tudat	$1.5 \cdot 10^{-6}$	$3.0 \cdot 10^{-3}$
Combined		
MONTE	$3.0 \cdot 10^{-7}$	$7.0 \cdot 10^{-4}$
Tudat	$7.3 \cdot 10^{-7}$	$1.9 \cdot 10^{-3}$

Table 8.2.: Formal uncertainties in $1/Q$ of Io and Jupiter. The formal uncertainties are obtained from radio science simulated data combined with various subsets of the astrometric observations (N_{ast} being the number of observations contained in each subset). The relative contributions of each data subsets are also provided. They are expressed as fractions of the total improvement achieved by adding all astrometric observations to the radio science only solution.

Dataset radio science +	N_{ast} [-]	1σ [-]		**Contribution astrometry**	
		$\mathbf{1/Q_{Jupiter}}$	$\mathbf{1/Q_{Io}}$	$\mathbf{1/Q_{Jupiter}}$	$\mathbf{1/Q_{Io}}$
no astrometry	0	$1.5 \cdot 10^{-6}$	$3.0 \cdot 10^{-3}$	-	-
all astrometry	14 454	$7.3 \cdot 10^{-7}$	$1.9 \cdot 10^{-3}$	100%	100%
classical astrometry					
all	12 073	$9.8 \cdot 10^{-7}$	$2.3 \cdot 10^{-3}$	67%	64%
before 1960	2 473	$1.2 \cdot 10^{-6}$	$2.3 \cdot 10^{-3}$	39%	64%
after 1960	9 600	$1.3 \cdot 10^{-6}$	$2.8 \cdot 10^{-3}$	26%	18%
mutual phenomena	2 043	$1.3 \cdot 10^{-6}$	$2.9 \cdot 10^{-3}$	26%	9%
ground-based radar	22	$1.3 \cdot 10^{-6}$	$2.8 \cdot 10^{-3}$	26%	18%
stellar occultation	5	$1.4 \cdot 10^{-6}$	$2.9 \cdot 10^{-3}$	13%	9%
all Io observations	3 814	$9.3 \cdot 10^{-7}$	$2.4 \cdot 10^{-3}$	74%	55%
future astrometry	4 877	$1.5 \cdot 10^{-6}$	$3.0 \cdot 10^{-3}$	-	-

crucial role in the determination of Jupiter's and Io's tidal dissipation parameters.

Comparatively, mutual phenomena provide a smaller improvement. They are however relatively recent observations (performed from 1973 onwards) and, as such, do not provide nearly as strong constraints as classical astrometry on the Galilean satellites' dynamics. For ground-based radar and stellar occultations, only 22 and 5 data points are respectively available. Nevertheless, their contribution to the estimation of $1/Q_{\text{Jupiter}}$ and $1/Q_{\text{Io}}$ is not negligible. While these are also very recent observations (starting in the 1990s and late 2010s for radar and stellar occultations, respectively), both measurement techniques demonstrate exceptional accuracy (see Figs. 8.1–8.2, Brozović et al., 2020a; Morgado et al., 2019a, 2022), which explains why they still provide a meaningful contribution to the solution. While ground-based radar capabilities are strongly reduced by the loss of Arecibo, these results provide strong motivation to continue observing future stellar occultation events.

The space-based astrometry data acquired during the Galileo and Voyager missions were found to not noticeably contribute to the determination of $1/Q_{\text{Jupiter}}$ and $1/Q_{\text{Io}}$, such that the solution including these observations is identical to the radio science only case (thus not reported in Table 8.1). This result follows from the limited accuracy of the Voyager and Galileo data, but it does not reflect the quality and contribution of space-based astrometry in general. For our particular case of the Galilean satellites, the accuracy of the upcoming space astrometry data from the JUICE and Europa Clipper missions is expected to be closer to that of Cassini ISS observations, which have been proven invaluable in ephemerides and tidal dissipation studies for the Saturnian system (Lainey et al., 2017, 2019, 2020).

We then considered only observations of Io, without discriminating between different types of astrometric measurements. As shown in the last row of Table 8.2, this Io-only dataset can already account for about 74% and 55% of the total improvement attainable when adding all astrometric observations to radio science (for $\sigma(1/Q_{\text{Jupiter}})$ and $\sigma(1/Q_{\text{Io}})$, respectively). The significance of this result is strengthened by the fact that Io's data points only represent about 26% of the entire astrometry set. This confirms that ground-based observations of Io most efficiently complement the radio science dataset, and alleviate JUICE and Europa Clipper's lack of direct constraints on Io's dynamics. As discussed in Section 8.2.4, Io's observations are thus a crucial aspect of the strong synergy between the radio science and astrometry.

We also quantified the contribution of potential future astrometric observations, simulated between 2023 and the beginning of JUICE's and Europa Clipper's Jovian tours (see Section 8.2.2). These additional ground-based data could however not help reducing the estimated uncertainties further, for neither Io's and Jupiter's tidal dissipation parameters nor the Galilean moons' states (see Table 8.1). The added value of future astrometric observations, whose accuracy cannot compete with that of radio science measurements, directly suffers from their temporal proximity with the JUICE and Europa Clipper missions. This could be foreseen looking at formal uncertainties predicted for the radio science only solution close to the missions' period: they are indeed comparable or lower than the ~150-200 km accuracy level expected for astrometric data in near-future observational campaigns. While crucial to properly constrain the ephemerides of the Galilean system before the arrival of the two spacecraft, acquiring new ground-based observations is thus not expected to noticeably improve the post-missions reconstruction of the Galilean moons' dynamics.

8.5. DISCUSSION AND CONCLUSIONS

8

We showed that adding decades of astrometry and radar observations to the radio science data expected from the upcoming JUICE and Europa Clipper missions helps estimating Io's and Jupiter's dissipation parameters. Uncertainties in Io's and Jupiter's tidal dissipation parameters are reduced by a factor two to four, depending on the software and simulation settings (see Section 8.4.1) It also stabilises the moons' dynamics solution which, if solely based on radio science tracking of the spacecraft, degrades rapidly outside the missions' time bounds (see Fig. 8.8). Conversely, the radio science data from JUICE and Europa Clipper will reduce the uncertainties in Io's and Jupiter's dissipation parameters by one order of magnitude with respect to the current, astrometry-based solution.

With respect to the rest of the astrometry dataset, Io's observations contribute the most to the joint radio science and astrometry solution. They indeed provide direct information about Io's orbital motion which are otherwise missing in the radio science tracking data, due to the absence of any flyby planned around that moon. Despite showing limited accuracy, old classical astrometry observations also proved very valuable thanks to the unique constraints they impose on the moons' long-term dynamics.

On the other hand, we showed that near-future astrometric data potentially acquired before the spacecraft reach the Jovian system could not noticeably improve the joint estimation. The added-value of such observations is limited when radio science data are included in the estimation, as the latter then dominate the solution close to the JUICE and Europa Clipper missions period. Until such radio science measurements become available in the 2030s, astrometric data to be collected in the coming years are nonetheless still valuable. As has already been investigated in a separate study (V. Lainey, private communication), these observations will indeed help improving the moons' ephemerides' solution available before the missions start, which is a key aspect of the preparation effort. Additionally, more observation campaigns will be required after both missions end, to avoid the moons' state uncertainties rapidly deteriorating over time.

Our results rely on simulated measurements for JUICE's and Europa Clipper's radio science, and on the subsequent formal uncertainties obtained for the different estimated parameters. It is nonetheless worth noting that these formal errors likely indicate too optimistic uncertainty levels. In the particular case of the JUICE and Europa Clipper missions, unique challenges are expected to arise. The unprecedented accuracy of the radio science measurements, combined with JUICE's unique mission profile, indeed predicts meter-level determination of the moons' radial positions (even down to a few centimeters for Ganymede's during JUICE's orbital phase). For such estimation errors to actually be attainable, our dynamical models of both the moons and the spacecraft would need to reach comparable accuracy levels over relevant time scales, as discussed in e.g., Fayolle et al. (2022). The uncertainties in the Galilean moons' states and related dynamical parameters might thus be larger than predicted, which also implies that the improvement provided by astrometry could be stronger in practice.

8

Among the different effects which will require significant model refinement for the JUICE and Europa Clipper data to be exploited to their full potential, tidal dissipation mechanisms are critical to our understanding of the Galilean satellites' interiors and orbital evolution, which are key scientific objectives of both missions. In this analysis, we relied on the constant $1/Q$ assumption, but various approaches exist to incorporate tidal dissipation into the dynamical model (constant time lag, frequency-dependent $1/Q$, resonance locking (Fuller et al., 2016), etc.). However, a fully consistent implementation for both the moons and the central planet, with a coherent modelling of the bodies' deformation response, remains ambiguous (see Chapter 2). A deeper analysis of the different tidal modelling strategies and their influence on the estimation solution will thus be crucial to provide robust results for tidal dissipation parameters (Magnanini et al., 2024).

Additionally, some uncertainty sources in the satellites' dynamical model were neglected and should be analysed in future studies. This includes, among others, the gravitational perturbations by asteroids or by Jupiter's inner moons, whose orbital motions and masses are less accurately determined than those of the Galilean moons. The influence of the COM-COF offset should also be quantified. The possibility to exploit the combination of radio science and astrometry data to estimate this offset and thus mitigate its effect on the solution could also be explored. This would also further motivate the need for future astrometric observations during the JUICE and Europa Clipper missions, to complement the contribution of JUICE's altimeter GALA (mostly limited to the orbital phase around Ganymede).

Possible mismodelling of the spacecraft's dynamics would also indirectly affect the moons' ephemerides' solution. Accurately modelling all perturbations impacting the orbital motions of JUICE and Europa Clipper will thus be critical (e.g., manoeuvres, solar radiation pressure, errors in the High Accuracy Accelerometer (HAA) calibration, etc.). Moreover, in addition to the already mentioned potential inaccuracies in the current Jovian system model, time-variations in Jupiter's gravity field and rotation or inconsistencies in the satellites' rotation models could also affect the spacecraft orbit determination. Finally, for JUICE specifically, errors in the accelerometer calibration are particularly important and should be further analysed.

On the observations side, other datasets could be considered in future studies. In particular, radio science data from the Galileo and Juno missions are not included in our current work. The former is however not expected to significantly improve the solution (A. Magnanini, private communication): the Galileo spacecraft could indeed only rely on an S-band, single frequency link due to the failure of the X-band high gain antenna. The resulting radio science measurements therefore showed relatively low accuracy compared to current missions (Jacobson et al., 2000; Gomez Casajus et al., 2021). On the other hand, the contribution of Juno data to the solution might suffer from its (temporal) proximity with the JUICE and Europa Clipper timelines, with the notable exception of the two flybys around Io planned for early 2024. These flybys are expected to bring invaluable information on Io's ill-constrained dynamics and should thus later be added to the joint solution for the Galilean moons. Finally, Gaia data, by refining the orbits of Jupiter's outer moons (Section 8.2.1), could help quantifying the error in the Jovian ephemeris and mitigating its impact on the moons' solution (see also Chapter 7). This is of particular interest for stellar occultations, as removing the contribution of Jupiter ephemeris would reduce their error budget to a few kilometres only (see Section 8.2.1).

As already mentioned, our current results rely on simulated observations for the radio science side. In practice, many additional difficulties will arise when processing real radio science measurements and merging them with astrometry. Accurate dynamical modelling has already been identified as an important obstacle to a balanced ephemerides' solution for the Galilean satellites from JUICE and Europa Clipper data. Combining old astrometric observations with spacecraft radio science will make this requirement even more stringent by requiring our dynamical models to be consistent over both long- and short timescales. The appropriate weighting of extremely diverse data types and datasets, with different noise properties and accuracies, also represents a major challenge. Finally, quantifying and mitigating the influence of the COM-COF offset will be crucial in future real data analyses.

Nonetheless, our analysis proves successful in generating a combined, global solution by relying on three different tools with distinct focusses and capabilities (moons' ephemerides or spacecraft dynamics, astrometry or radio science data). Our results show that exploiting the synergies between the different datasets can substantially improve the inversion solution, and the estimation of tidal dissipation parameters in particular. This encourages future efforts to work towards such a global solution, to fully exploit the JUICE and Europa Clipper radio science measurements when they become available.

8.6. Appendix A: Propagated formal position uncertainties for the four Galilean satellites

This appendix presents the formal position uncertainties propagated from 2033, in the middle of the JUICE and Europa Clipper science tours, to 1890 when the first astrometric observations included in our analyses were acquired. Fig. 8.8 displays the results for the four Galilean satellites, while only those obtained for Europa are shown in Section 8.4.1.

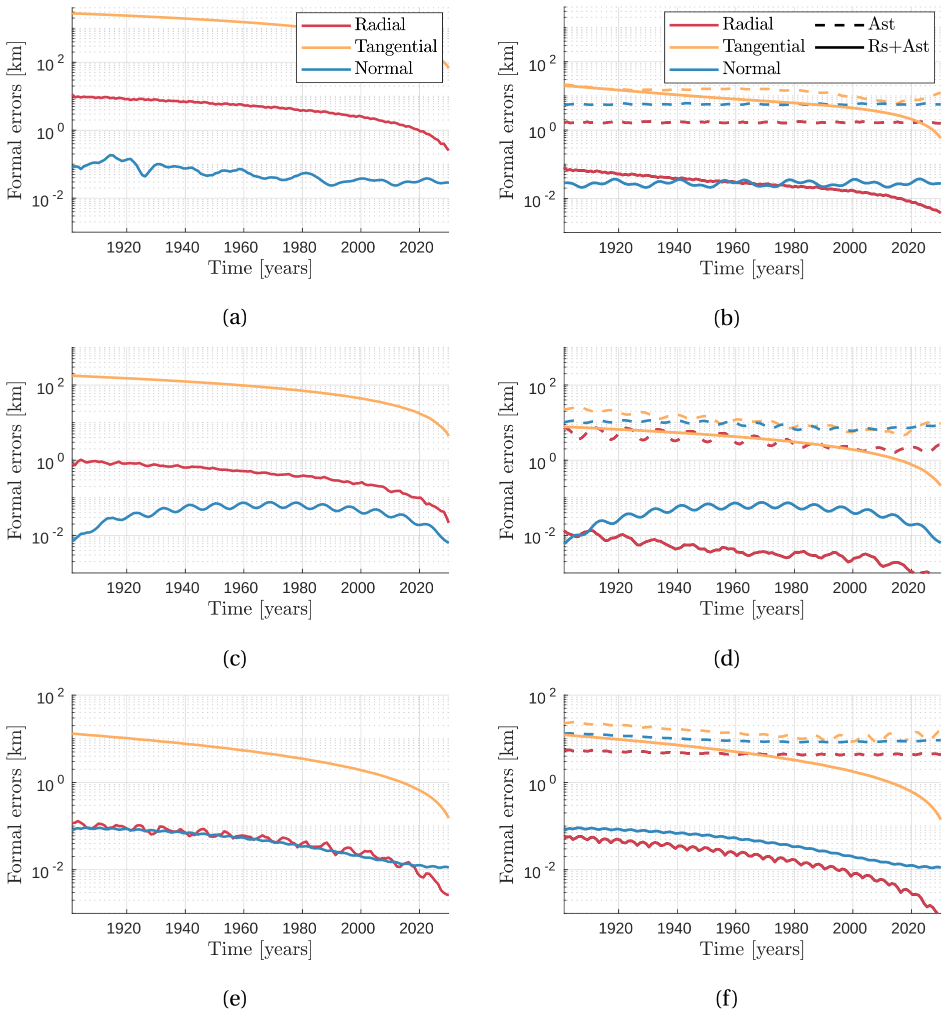

Figure 8.8.: Propagated formal uncertainties in the moons' RTN positions (from 2030 to 1890) for the radio science (Rs), astrometry (Ast) and combined solutions (Rs+Ast), obtained with Tudat and NOE. We used a propagation output of one point per year only and performed data smoothing over five-year windows to avoid aliasing effects (see Fig. 8.6). The top panels present the results obtained for Io (panels a & b), the middle panels correspond to Ganymede (panels c & d), and the bottom ones to Callisto (panels e & f). The left hand side panels (a, c, e) always display the radio science only solutions, while the right hand side panels (b, d, f) show both the astrometry-only and combined solutions.

9

Conclusions and outlook

Chapters 4, 5, 6, 7, and 8 have each addressed one or more of the research questions highlighted in Chapter 1. We now summarise our findings, bringing them together to address our main research objective. The different steps taken in this dissertation have furthermore raised additional questions, and opened new avenues of research. This chapter discusses these perspectives, and the opportunities and challenges that await in the field of natural moons' ephemerides. In Section 9.1, we first specifically focus on the moons' ephemerides improvement attainable with JUICE-Europa Clipper upcoming radio-science measurements. Section 9.2 then compiles our findings regarding the potential of new astrometric observation strategies, before Section 9.3 finally examines the results and perspectives of a combined inversion of astrometry and radio-science data.

9.1. Reconstructing the Galilean moons' orbits from JUICE and Europa Clipper radio science

Chapters 4 and 5 together investigated promising techniques and strategies to estimate natural satellites' dynamics from radio science tracking of one or several in-situ spacecraft, applied to JUICE and Europa Clipper. Combining the results of these chapters provides an overview of the possible approaches, challenges, and mitigation strategies essential to achieve an accurate, but also robust and consistent, ephemerides solution for the Galilean moons.

As highlighted in Section 3.4.1, two different approaches currently co-exist when using radio science for natural satellites' state estimations. Typically, the spacecraft and moons' dynamics are solved for separately (i.e., decoupled strategy). Chapter 4, however, provides the first detailed formulation in literature of an alternative, coupled approach where the spacecraft's local states and the moons' orbits are concurrently estimated in a single step. Given the exceptional moons' ephemerides accuracy achievable from JUICE and Europa Clipper radio science (see below), the uncertainty in Jupiter's position will moreover have a non-negligible effect on the solution. The implementation of the coupled estimation model makes it possible to incorporate this central planet's contribution in a natural and fully consistent manner. This has been presented in Chapter 5 which, combined with Chapter 4, thus gives a complete overview of the underlying estimation methodologies behind the reconstruction of natural satellites' dynamics from spacecraft radio science.

The formal uncertainty levels expected from a joint JUICE-Europa Clipper radio science inversion, assuming a coupled estimation strategy is applied, can be found in Chapter 5[1]. Covariance analyses indicate that the moons' radial positions could theoretically be determined at the meter or sub-meter level and, for Ganymede, can even reach down to a few centimeters during JUICE's orbital phase. The formal errors in the tangential direction, on the other hand, are constrained in the 1–10 m range for Europa, Ganymede, and Callisto, while they remain around a few tens of meters for Io. Finally, the determination of the moons' out-of-plane positions is slightly less accurate (10–100 m). Attaining such formal uncertainty levels will, however, first require overcoming a few critical challenges, as will be discussed in the following.

9.1.1. MAIN RESULTS AND FINDINGS

After introducing both the coupled and decoupled approaches for radio science-based moons' state estimation, Chapter 4 compared their respective performance and limitations for the JUICE case, specifically answering the following research question:

How do coupled and decoupled estimation strategies compare when reconstructing natural satellites' orbits from spacecraft measurements?

The added-value of concurrently estimating the moons' and spacecraft's states is the strongest in the radial direction: formal errors for the moons' radial positions are typically one order of magnitude lower with the coupled model than with the decoupled one (e.g., a few meters vs. a few tens of meters for Io, see Fig. 4.9). Interestingly, this trend is inverted in the along-track direction, for which the decoupled estimation yields lower formal uncertainties. Overall, these results follow from the decoupled estimation yielding comparable uncertainty levels for the radial and along-track position components (unlike in the coupled case where the radial position is much better constrained). This results from the poor decorrelation of these two directions in the arc-wise, local state estimation step. As argued in Chapter 4, the coupled solution, by automatically accounting for all dynamical dependencies, nonetheless provides the most consistent and statistically realistic measure of the achievable uncertainties.

9

This indicates that adopting a decoupled approach might lead to unrealistically low errors for the moons' along-track positions, with a possible effect on the determination of tidal dissipation parameters. Our analyses moreover show that the strong dynamical coupling between Io, Europa, and Ganymede due to the Laplace resonance is only fully captured by the coupled model: the improvement observed in Io and Europa's radial position errors when including the orbital phase (with respect

[1]The analyses presented in Chapter 4 were still limited to a JUICE-only configuration, and the results obtained in Chapter 5 are therefore considered more representative of what will be achieved after the JUICE and Europa Clipper missions

to considering the flyby tour only) is significantly stronger with the coupled model than the decoupled one (see Fig. 4.9). In the JUICE mission case, the uniqueness of the Galilean system's dynamical configuration, combined with the imbalanced focus of the mission tour on Ganymede and Callisto (see Section 1.3), thus makes the coupled estimation approach the most promising estimation strategy.

However, achieving a global, fully consistent solution for the dynamics of the Galilean satellites will be far from straight-forward. Chapter 4 therefore also discussed the major obstacles to overcome before a coupled approach can be successfully applied to the moons' state estimation from JUICE (and Europa Clipper) radio science:

What are the main challenges of the reconstruction of a coupled, global solution for the Galilean satellites' dynamics from JUICE-only data?

The first barrier to the direct application of a coupled estimation model is a data merging issue. As will be elaborated upon in Section 9.3, the key to bringing our ephemerides solution to unprecedented accuracy levels is to fully exploit synergies between various existing and upcoming data sets. By definition, the coupled estimation strategy described in Chapter 4 would however require to process all observations concurrently, in a single estimation step. This first poses a very practical challenge, by requiring the use of a single tool able to consistently handle very diverse data sets, typically processed separately in present natural satellites' ephemerides determination. Data weighting and biases considerations will also bring difficulties of their own (Section 3.2.2). The data properties, volume, and quality indeed strongly differ from one set of observations to another, which will require designing adequate weighing strategies to obtain a statistically balanced solution, as will be further discussed in Section 9.3.2.

Furthermore, modelling inconsistencies, both in the spacecraft and moons' dynamics, also represent a major obstacle to the reconstruction of a consistent ephemerides solution. Such issues for instance arose in past Cassini radio science analysis, already when trying to reconstruct a coherent ephemeris for a single moon (Durante et al., 2019; Zannoni et al., 2020). The strong dynamical coupling between the Galilean moons, however, imposes to consider the entire system to obtain a dynamically consistent solution and rigorously account for the influence of the Laplace resonance. This puts an even more stringent requirement on the quality of our models: they indeed need to be consistent for the entire system and to adequately reproduce the dynamics of both the spacecraft (short timescales) and moons (longer timescales), with an accuracy well below the formal error levels of our simulated state estimations. For the Galilean system, and the JUICE and Europa Clipper missions specifically, the following effects will be particularly critical to model accurately (this will be elaborated upon in Section 9.1.2):

- non-conservative forces acting on the spacecraft,
- central planet's rotation and gravity variations,
- coupling between the moons' tides, rotations, and orbits.

After realising how the above-mentioned challenges might impede the use of a coupled estimation approach and prevent the ephemerides solution from achieving the formal errors predicted by simulations, Chapter 5 investigated how other JUICE radio data could help overcome these difficulties. More specially, we analysed the role of JUICE PRIDE as a supporting experiment in the pursuit of a coherent coupled solution for the system's dynamics. In addition to nominal, single-spacecraft VLBI tracking, we capitalised on the concurrent presence of JUICE and Europa Clipper in the Galilean system to explore unique opportunities for simultaneous VLBI tracking of both spacecraft. Chapter 5 thus addressed the following:

Which improvement and validation opportunities can PRIDE VLBI measurements bring to the joint JUICE - Europa Clipper ephemerides solution?

Which opportunities will the JUICE and Europa Clipper missions offer to perform multi-spacecraft VLBI measurements, and how will such data contribute to the solution?

In addition to single-spacecraft VLBI, we identified 11 combinations of JUICE and Europa Clipper flybys offering promising opportunities for multi-spacecraft VLBI (Table 5.9). We however showed that the contribution of both single- and multi-spacecraft VLBI to a global, coupled state solution for the moons will remain limited, once such a solution can be achieved (see Sections 5.4.2 and 5.5.1).

The improvement achievable with both single- or multi-spacecraft VLBI is nonetheless much stronger when determining *local*, arc-wise solutions for both the spacecraft and moons' states. In light of the challenges to overcome before a global solution can be reconstructed (see discussion above), starting with a decoupled estimation will be a necessary first step. PRIDE VLBI will help obtaining more accurate normal points in the out-of-plane direction, with typical formal errors around several hundreds of meters (see Fig. 5.10). This represents an average uncertainty reduction factor of 10-20 with respect to the classical radio science solution. Depending on the flyby geometry, a noticeable improvement can also be achieved in the along-track direction (up to almost one order of magnitude for a few specific flybys, bringing the local formal error from the 100 m level to a few tens of meters). These local improvements will in turn facilitate progressing towards a coupled estimation, and thus a coherent global solution for the moons' dynamics.

We furthermore investigated the potential of the PRIDE VLBI technique to validate the radio science solution(s). Independent VLBI measurements of the spacecraft's lateral position in the sky can indeed be compared to JUICE' orbit solution reconstructed from range and Doppler data. Any discrepancy would either indicate

1. a systematic bias in the VLBI observables, which we would then be able to recover and validate using background densification campaigns,

2. possible discrepancies between the orbit solution's statistical confidence region and its real accuracy, indicative of dynamical or observation noise modelling issues.

Detecting such discrepancies between raw VLBI measurements and the radio science solution (or, equivalently, the absence thereof) will moreover allow us to put an upper limit on the true-to-formal error ratios (Section 5.6.2), thus providing us with a means to assess *true* estimation errors. More precisely, our results indicate that true errors exceeding three to five times[2] the corresponding formal uncertainties could be detectable with PRIDE VLBI measurements.

Taking one step further, the refined arc-wise solutions attainable once VLBI is included will automatically be sensitive to much smaller discrepancies with respect to a preliminary global solution (see schematic representation in Fig. 5.12). This will also facilitate identifying possible discrepancies. If combined, the validation capabilities of single- and multi-spacecraft VLBI will moreover enhance each other, being sensitive to different mismodelling or error sources. A perfect example is the simultaneous tracking of JUICE and Europa Clipper in a single-moon flyby combination (i.e., both spacecraft each performing a flyby around the same moon): the resulting VLBI measurements are almost independent of any mismodelling in the moon's dynamics, but sensitive to errors in the spacecraft models.

PRIDE VLBI will therefore offer invaluable opportunities to progressively validate the radio science estimation of the Galilean system's dynamics. In particular, it will play a crucial role in overcoming some of the challenges discussed above, which might otherwise prevent us from obtaining a robust and dynamically consistent global solution for the moons' orbits. Ironically, if VLBI eventually helps attain such a solution, the moons' ephemerides will become accurate enough that adding VLBI measurements to the estimation will no longer bring a significant improvement. VLBI will nonetheless be invaluable in bringing the estimation solution to such accuracy levels in the first place, with critical implications for our understanding of the Galilean system's dynamical and thermal history (see Chapter 10).

9.1.2. Outlook

Building on the discussion initiated in the above Section 9.1.1, we further discuss possible intermediate steps and analyses to overcome the various obstacles complicating a coupled estimation of the spacecraft and moons' dynamics.

9

A step-by-step approach towards a global solution

The results of Chapters 4 and 5, together with the discussion in Section 9.1.1, highlight the need to proceed gradually to eventually reconstruct a global solution for the Galilean system's dynamics. To this end, we recommend starting with local, per-flyby estimations of the moons' states before progressing towards a global solution. The thorough analysis of the solution's statistical realism and consistency at each intermediate step will be essential, especially in view of an eventual global inversion of diverse data sets (see Section 9.3). In the Cassini case, the instability of the radio science-only solution (e.g., Jacobson, 2022) significantly obscures the interpretation of the dynamical solution obtained for the Saturnian moons (see Section 10.2.2). For the Galilean satellites, significant efforts must therefore be

[2] depending on the quality of the VLBI measurements

dedicated to validating the JUICE-Europa Clipper radio science estimation as a standalone solution, before a global inversion of various data set can eventually be attempted.

The objective and strategy behind the VLBI-based validation plan proposed in Chapter 5 and discussed in Section 9.1.1 remain applicable to any set of independent observations. In particular, the strong synergies within JUICE and Europa Clipper's instrument sets and the unique simultaneous presence of two spacecraft in the Galilean system offer invaluable validation opportunities which should be exploited to their fullest potential. Besides PRIDE VLBI measurements, other independent data sets can and should be used to this end, as will be discussed in Section 9.2.2.

Investigating dynamical modelling inconsistencies

While our analyses have highlighted the risk for dynamical mismodelling to affect the estimation process, precisely assessing the impact of such modelling issues on the solution is extremely difficult in a simulation framework. It would require introducing some discrepancies in the models used to respectively simulate and estimate the moons' and spacecraft's dynamics. The nature of the problem itself is however such that we do not know how their dynamics differ from what our current models predict. The difficulties encountered in Cassini radio science analyses perfectly illustrate this challenge (Durante et al., 2019; Zannoni et al., 2020): when trying to interpret and correct such inconsistencies, one is faced with our insufficient understanding both of the limitations of the available models, and of the dynamical and physical effects yet to be accounted for. One should nonetheless keep in mind that this is, in practice, an iterative process essential to the progressive improvement of our models. The orbit determination of the Juno spacecraft offers a perfect example: unmodelled physical signatures, which first had to be absorbed in extra empirical accelerations (Durante et al., 2020), eventually led to the refinement of Jupiter's gravity field and rotation models (e.g., Durante et al., 2022). Circling back to the most pressing modelling challenges identified in Section 9.1.1, a few aspects can be elaborated upon.

Non-conservative forces acting on the spacecraft

9

All perturbations acting on the spacecraft (e.g., manoeuvres, effects of exospheric drag, radiation pressure, solar array flexing, propellant sloshing, thermal and antenna emission recoil pressure) must be adequately modelled and/or parametrised. This is particularly critical in a coupled estimation, when simultaneously solving for the spacecraft and moons' dynamics, as any mismodelled effect might spill in the moons' solution. The JUICE's High Accuracy Accelerometer (HAA) will play a crucial role in characterising such non-conservative perturbations. Accounting for the accelerometer measurements in the orbit determination process (as investigated for the BepiColombo mission, De Filippis et al., 2024), as well as for the influence of HAA calibration errors (Cappuccio et al., 2020b), will therefore be essential.

A promising approach to investigate the latter is to exploit the available spectral characterisation of the HAA performance (Cappuccio et al., 2020b) to model the accelerometer errors in the form of unexpected and unparametrised perturbations. Including such perturbations in JUICE's dynamical model, and investigating their influence on the state estimation, would be an important first step to start analysing the impact of mismodelled effects. It would be particularly interesting to quantify how such modelling errors, restricted to the spacecraft's dynamics, may eventually affect the moons' ephemerides solution due to the indirect nature of the radio science measurements and to the coupling of the spacecraft and moons' dynamics (especially during JUICE orbital phase). The HAA power spectrum given in Cappuccio et al. (2020b) shows that the accelerometer is primarily designed to operate within the $5 \cdot 10^{-6} - 5 \cdot 10^{-1}$ Hz frequency range. The orbital motion of the Galilean satellites are, however, mostly driven by frequencies either at the extreme lower end of this range (Io's orbital frequency is $6.5 \cdot 10^{-6}$ Hz), or significantly lower (see e.g., Lainey et al., 2006). Although a detailed analysis is required, this already indicates that mismodelled effects susceptible to eventually affect the moons' ephemerides determination might unfortunately not be properly captured by the accelerometer.

It must be noted that these modelling issues will also be (partially) mitigated by the parallel developments of refined models for the non-gravitational accelerations affecting the spacecraft dynamics. Recent advances have for instance been made in the context of the BepiColombo mission (di Stefano et al., 2023), which uses the same accelerometer as JUICE (Italian Spring Accelerometer, Iafolla et al., 2010). Such modelling development efforts focus on effects whose magnitudes are too small to be properly captured by the accelerometer, but which can still noticeably degrade the quality of the orbit determination solution (e.g., solar radiation, thermal recoil pressure, antenna emission recoil pressure). The resulting upgraded models will directly benefit future JUICE and Europa Clipper analyses, which will in turn prompt further modelling improvements.

Central planet's rotation and gravity variations

The central planet's pole motion and potential time- and longitude-dependent variations of its gravity field (respectively linked to Jupiter's normal modes and wind dynamics), if non-modelled, might also affect our ability to reconstruct a coherent solution for the moons' dynamics (e.g., Zannoni et al., 2020). For the Jovian system, these effects will nonetheless be better constrained at the time of the JUICE and Europa Clipper missions thanks to Juno's insights. The time variations of Jupiter's gravity field identifiable in Juno gravity field measurements can for instance be exploited to refine our model of Jupiter's gravity field beyond the classical approach of a static field and tidal variations (Iess et al., 2019; Durante et al., 2020, 2022). The same holds for Jupiter's rotational pole orientation, recently estimated from Juno radio science data (Lari et al., 2024).

Coupling between the moons' tides, rotations, and orbits

Regarding the modelling of the natural satellites' dynamics, one of the top priorities should be to investigate the influence of possible inconsistencies between the rotational and tidal models (or in the parametrisation of these models). The results in Section 2.3.4 clearly demonstrate how intricate the combined feedback of tides and rotation on the moon's orbit is, and how a slight mismodelling of the satellite's rotation can affect its tidally-driven orbital evolution.

Ensuring the consistency of our models is critical to extract statistically realistic estimates of the moons' rotational and tidal parameters from their orbits (which is at the core of the JUICE and Europa Clipper's scientific objectives, see discussion in Section 10.1). In particular, radio science measurements will be sensitive to the combined effects of tides and rotations both on the moons' orbits and on their gravity fields, which in turn influence the spacecraft's dynamics. This two-level sensitivity makes the full consistency of the moons' and spacecraft's dynamics even more critical, a requirement further strengthened by the fact that the moons' librations and tidal responses will also be detectable from other spacecraft-based data sets (e.g., altimetry, radar, see Section 10.1.2). Precisely modelling the moons' librations will be a particularly complex problem for the Galilean icy moons: unlike for completely rigid bodies, the decoupling of their deep interior, liquid layer, and icy crust will generate distinct librations, to which JUICE's instruments will moreover be sensitive in different ways (Section 10.1.2).

Critically, we should therefore carefully analyse whether tidal-rotational mismodelling can be absorbed in the estimation, possibly yielding erroneous estimates of dissipation parameters. If, on the contrary, they lead to incompressible, non-flat residuals, we should assess whether we could confidently map such residuals back to potential modelling inconsistencies (see discussion in Section 2.4.1).

9.2. ASSESSING THE POTENTIAL OF NOVEL OBSERVATION STRATEGIES

The first part of this dissertation (Chapters 4 and 5) focussed on the expected contribution of JUICE and Europa Clipper radio science to the Galilean satellites' ephemerides. However, as discussed in Section 3.4, present solutions primarily rely on astrometric observations. While the long time span over which classical astrometry observations have been collected is invaluable to constrain the moons' long-term dynamics, more recent techniques have revolutionised the field of astrometry for moons' ephemerides determination. Our work specifically investigated two of the currently most promising types of astrometric observations: mutual approximations (Chapter 6) and stellar occultations (Chapter 7).

9.2.1. MAIN RESULTS AND FINDINGS

As mentioned in Section 3.3.1, mutual approximations offer a promising alternative to mutual events to constrain natural satellites' ephemerides. They indeed yield as accurate measurements as for mutual events, but occur much more frequently. In light of the recent mutual approximation campaigns for the Galilean moons (Morgado et al., 2016, 2019b) and of their expected potential for moons' ephemerides in general, we developed the missing framework necessary to properly include these observables in the state estimation, answering the following research question:

How should mutual approximation observations between two moons be used in the estimation to reconstruct the moons' dynamics?

The primary observable of a mutual approximation is the time at which the distance between the two targets reaches a minimum in the plane-of-the-sky, referred to as central instant. We developed the missing analytical formulation for the observation partials of these central instants (Section 6.2), circumventing the need for the alternative observables traditionally used as substitutes (i.e., derivative of the apparent distance, Emelyanov, 2017). Advantageously, using the mutual approximation's central instant ensures that the full signature of the moons' dynamics encoded in the observation is also automatically captured and exploited in the estimation. Alternative observables, on the other hand, only contain the kinematic part of the observation's information content.

Despite this important difference in the nature of the two types of observables, we showed that directly using central instants in the estimation only yields a small improvement compared to the solution achieved with alternative observables. When simulating mutual approximations for the Galilean satellites over the 2020–2029 period and subsequently estimating the moons' states (using these observations only), the improvement in formal position errors achieved with central instant observables over the alternative option does not exceed 20% (Fig. 6.4). However, this only holds if the alternative observables are carefully and adequately weighted in the inversion. Formal error differences otherwise reach a factor 1.5 to 4 in favour of the central instants (see Section 6.4.4). When adopting the alternative observable approach, appropriate weighing accounting for the geometry of the close encounter is therefore indispensable, but also requires considering each observation separately. This information is, on the contrary, automatically included in the central instant.

The potential of mutual events and approximations for ephemerides determination has nonetheless been somewhat shadowed by the exceptional accuracy reached with stellar occultations which, unfortunately, occur very rarely (Morgado et al., 2019a, 2022, see Section 3.3.1). Recent improvements of the stellar catalogues' quality thanks to the Gaia mission (e.g., Brown et al., 2018, 2021) have made stellar occultations the most accurate ground-based technique to measure the moons' positions in the plane-of-the-sky. However, the kilometre accuracy level reached by stellar occultation observations implies that their error budget can effectively be dominated by the uncertainty in the central planet's ephemeris. To mitigate this, Chapter 7 proposed a novel experiment relying on VLBI tracking of an in-system spacecraft to *locally* reduce the planet's position uncertainty, specifically addressing the following:

How can spacecraft tracking contribute to further reducing the error budget of the most accurate ground-based astrometry observations?

We demonstrated the potential of the proposed experiment by using two occultations, by Ganymede and Callisto, as test cases, leveraging the presence of the Juno spacecraft in the Jovian system at the time of the occultations. Our results showed that VLBI tracking of the Juno spacecraft during the perijoves preceding and following each stellar occultation manages to *locally* reduce the Jovian ephemeris error to sub-kilometre level, below the nominal accuracy of a stellar occultation measurement (see Table 7.3). By reducing the error budget of such observations, this directly enhances their contribution to moons' ephemerides solutions.

Since this experiment was initially proposed, the two stellar occultations and their corresponding Juno perijoves have already taken place. While the first occultation could unfortunately not be positively recorded, partially due to poor meteorological conditions, both the second occultation and the VLBI tracking of Juno during the four perijoves were successful. The analyses of the occultation observation's results and the processing of the Juno tracking sessions are still ongoing, and will eventually allow us to confirm the simulation results reported in Chapter 7.

More generally, our results highlighted the potential of synergistic experiments capitalising on the strengths of various tracking and observation techniques to eventually benefit the moons' ephemerides determination. It should be noted that the proposed experiment is not only valid for the two specific test cases highlighted in Chapter 7. It is applicable to any stellar occultation with similar spacecraft tracking opportunity in its temporal proximity, as will be available during the upcoming JUICE and Europa Clipper mission phases.

9.2.2. OUTLOOK

In the following, we first present interesting research perspectives specific to mutual approximations and to the proposed stellar occultations experiment, respectively, before addressing more general considerations regarding promising astrometric observation techniques for Galilean moons' ephemerides.

CENTRAL INSTANTS AS PROMISING OBSERVABLES

First, it must be noted that the central instant concept used in Chapter 6 as the prime observable for mutual approximations is not restricted to this type of observations only. The same observable formulation could be considered for mutual events, to complement the relative tangential coordinates of the satellites typically used for these observations (see Section 3.3.1). Interestingly, the central instant contains different, *dynamical* information on the moon's motion, as opposed to the *kinematic* constraint extractable from the satellite's position at the time of the event. The potential benefit of including this observable in addition to the nominal position measurements should therefore be further investigated. This could indeed enhance the contribution of mutual events to the ephemerides solution by exploiting the full information captured in these observations. The analytical formulation developed in Chapter 6 to use central instants instead of alternative, simplified observables in the estimation is equally suited and directly applicable to mutual events. It is moreover interesting to note that the configurations for which using central instant observables proved the most beneficial correspond to mutual event observations (i.e., low impact parameter, see Chapter 6). The methodology initially developed for mutual approximations could thus prove even more valuable for mutual events.

Stellar occultations during the JUICE-Europa Clipper timeline

Coming back to the stellar occultation experiment presented in Chapter 7, it will also serve as a test experiment for the quality of planetary ephemerides. Differences between the two main Jovian ephemeris solutions currently available can indeed reach up to almost 5 km for the out-of-plane position component, indicating that their accuracy is at this level in this specific direction (Fig. 7.1). Circling back to the joint JUICE-Europa Clipper radio science results presented in Chapter 5, the very low position uncertainty levels predicted by our simulations will, as already discussed in Section 9.1, require to consider the influence of such Jupiter's position uncertainty on the estimation.

Bringing together the results and considerations presented in Chapters 5 and 7 regarding the Jovian ephemeris error leads to the following observations. When including Jupiter in the estimation, JUICE and Europa Clipper tracking data alone can bring the planet's position uncertainty down to about 200-300 m, 10 m and 1-10 m for the normal, tangential, and normal components, respectively (see Fig. 5.4e). Depending on the direction, these results are lower or comparable to what our simulations predict can be achieved locally with VLBI tracking of the Juno spacecraft. This result can be exploited in two different ways. First, a stellar occultation by a Galilean moon observed during the JUICE and Europa Clipper missions will benefit from a similarly reduced error budget as the one obtained in Chapter 7 from the Juno tracking experiment. Second, including Jupiter's normal points based on Juno measurements could possibly further reduce the Jovian position uncertainty (with respect to what is shown in Fig. 5.4e). This would limit the impact of the central planet's ephemeris error impact on the moons' solution, and at least limit the risk of erroneously absorbing other effects, such as range biases, in Jupiter's state.

Exploiting astrometry's potential

Nonetheless, neither Chapter 6 nor Chapter 7 quantified the contribution of mutual approximations or stellar occultations to the Galilean moons' ephemerides solution achievable *after* the JUICE and Europa Clipper missions. However, based on the very high accuracy levels attainable with radio science, these astrometric observations are not expected to significantly contribute to the post-mission estimation. This is further supported by the preliminary analyses of the contribution of future astrometry (classical astrometry and mutual events observations only) conducted in Chapter 8 (see Section 8.4.2). The radio science-derived constraints will indeed dominate the solution in the temporal vicinity of the JUICE and Europa Clipper mission. However, improving the moons' ephemerides prior to the missions is also critical. Reduced position uncertainties limit the need for pre- and post-flyby corrective manoeuvres, effectively reducing the statistical Delta-V budget required for such orbit corrections. This pre-mission improvement should be carefully assessed, to further motivate and prioritise future observation campaigns.

Furthermore, the promising observation strategies discussed in Chapters 6 and 7 will also be beneficial to refine the ephemerides solutions of other moon systems, in particular those for which radio science measurements of dedicated missions are not yet, or only scarcely, available (unlike e.g., the Saturnian system which benefits

9

from Cassini data). The growing interest in the icy giant planetary systems currently elevate Uranian moons, and to a lesser Neptune's, as high-priority mission targets (see detailed discussion in Sections 10.2.3 and 10.2.4, respectively). Improving the ephemerides of these satellites is therefore critical to facilitate the orbital design of potential upcoming mission(s), and is scientifically relevant in its own right (see Section 10.2). Tighter constraints on these systems' dynamics might also help refine the scientific objectives prior to the mission(s), and/or adjust the chosen mission design to best address them. In this perspective, the respective advantages of both mutual approximations and stellar occultations with respect to classical astrometry techniques make them particularly appealing, and future observation opportunities for such events are under investigation (e.g., Santos-Filho et al., 2019; Marques Oliveira et al., 2022; French and Souami, 2023).

9.3. Exploiting inter-data sets synergies

Chapters 4, 5, 6, and 7 each focussed on a specific type of observations. Even though the latter investigated VLBI's potential to benefit stellar occultations, it still considered these two kinds of measurements independently, first processing the simulated VLBI observables to eventually reduce the occultations' error budget. Chapters 4 and 5, on the other hand, demonstrated that JUICE and Europa Clipper radio science will bring the moons' ephemerides down to unprecedented accuracy levels. The relatively short time span of this data set (about five years, as opposed to more than one century of astrometry) will however not be sufficient to reconstruct the long-term dynamics of the Galilean system and may limit the quality of the dissipation parameters estimation. The robustness of the solution is moreover further degraded by the imbalance of the radio science data set, and specifically by the lack of direct constraints on Io's orbit. Merging different data sets is therefore key to overcoming their individual limitations, and ensuring that the ephemerides solution benefits from their respective strengths and complementarities.

9.3.1. Main results and findings

9

In this perspective, Chapter 8 performed a global inversion of existing astrometric observations and simulated radio science from both JUICE and Europa Clipper, addressing the following question:

How would adding existing astrometry data improve the JUICE-Europa Clipper radio science solution?

Our estimations showed that combining radio science and astrometry can yield a small reduction of Io's in-mission position uncertainty (about 50% in the tangential direction, see Fig. 8.5). A more significant improvement is obtained for the estimation of Io's and Jupiter's tidal dissipation quality factors (~30–35%[3] for Io's and a factor 2–4[4] for Jupiter, see Table 8.1). This will be extremely valuable to

[3]This range encompasses two solutions obtained using different software (see Chapter 8).
[4]see footnote 3

characterise the thermal-orbital evolution of Io, but also of the entire Galilean system as the strong tidal interaction between Io and Jupiter drives the evolution of the Laplace resonance, and thus the orbital migration of Europa and Ganymede (see Section 10.1.1). The state estimation solutions for the other moons, on the other hand, remain primarily constrained by the radio science data, and do not show any noticeable improvement when adding astrometry.

Our results also indicate that increasing the observation time span by including older data sets to the inversion helps constraining the long-term dynamics of the system. Adding astrometry to the joint JUICE-Europa Clipper radio science estimation indeed notably improved the stability of the solution: the moons' formal position errors progressively converge towards the astrometry-only solution accuracy (i.e., ~ 10 km in the along-track direction) when propagated backwards, away from the JUICE-Europa Clipper missions period (see Fig. 8.6). On the contrary, relying only on radio science data yields a comparatively poor and unstable characterisation of Io's orbit and of the dissipation between Io and Jupiter, which prevents robustly mapping the estimation results to the long-term evolution of the Galilean system.

Analysing the above results further, our global inversion setup allowed us to assess the respective contribution of the different astrometric measurements to the solution, thus examining the following:

Which existing astrometric observations will be most beneficial to combine with JUICE and Europa Clipper radio science data sets?

Old classical astrometric observations of Io (i.e., before 1960) were found to contribute to the solution the most. They respectively account for 40% and 64% of the total improvement in Jupiter and Io's dissipation estimates achieved when using all astrometric observations (see Table 8.2). This confirms the strong influence of the lack of direct radio science data for Io, in the absence of any flyby around that moon by JUICE or Europa Clipper. In the radio science estimation, Io's orbit is only indirectly constrained, through the Laplace resonance, by our accurate knowledge of Europa and Ganymede's dynamics. This is, however, insufficient to obtain a robust solution. Adding direct astrometric observations of Io nonetheless proved effective in complementing the radio science data set. This is further supported by the improved determination of Io's orbit and of the dissipation parameters characterising the tidal interaction between Io and Jupiter with respect to the radio science-only solution.

Besides the key importance of constraining Io's motion, these results confirmed the crucial role of old astrometric data, and thus of an increased observation time span, in the solution improvement described above. As mentioned in Chapter 8, this is even more remarkable considering that old classical astrometric observations are significantly less accurate than more recent measurements (both in timing and position). Our results however demonstrate that radio science data dominate the solution close to the missions' timelines, in such a way that the more recent astrometry cannot further improve the solution. On the other hand, the short time span of the radio science data set (about five years) makes older astrometry extremely valuable to improve the long-term robustness of the estimation solution.

9.3.2. Outlook

Our analyses clearly confirmed the global inversion of various data sets as the way forward for natural satellites' ephemerides determination. For the Galilean moons specifically, such data merging strategies are key to achieving a statistically consistent and robust solution from JUICE and Europa Clipper radio science, as well as to fully exploiting existing data sets. In the following, we discuss both the challenges and opportunities awaiting on this path, before future global inversion analyses can eventually bring current ephemerides solutions down to exceptional accuracy levels.

Data merging challenges

A number of challenges will arise specifically from dealing with real radio science data. The analysis presented in Chapter 8 included real existing astrometric observations, but simulated JUICE and Europa Clipper radio science measurements. We moreover limited ourselves to a covariance analysis. In full estimations based on real data, however, obtaining a statistically balanced solution will require adopting appropriate weighing strategies and bias representations to realistically represent the measurement errors and the information contained in each data set.

Current natural satellites' ephemerides already rely on the combination of different astrometric data sets and/or data types, with extremely different accuracy levels (e.g., Jacobson, 2010, 2022; Jacobson et al., 2022; Lainey et al., 2007, 2009, 2012, 2017, see Section 3.4). As discussed in Section 3.2.2, the weights assigned to each data set are typically adjusted to be in agreement with the RMS of the residuals (see e.g., Lainey et al., 2019). However, in existing global inversion of radio science and astrometry, with extremely contrasted data volume and quantity, the lack of available details on the exact weighting methodology makes current data merging strategies rather untransparent (e.g., Jacobson et al., 2006; Jacobson, 2010, 2022).

We will nonetheless be able to draw inspiration from other fields of study, where combined inversions of highly diverse and heterogeneous data sets are common, such as precise orbit determination and physical parameters estimation for e.g., Earth or lunar gravity missions (Kusche, 2003; Lemoine et al., 2013). A possible weight adjustment strategy consists in fine-tuning the weighting scheme to ensure that the differences between full and partial least-squares estimations (the former being based on a subset of the observations) are consistent with the estimated error bounds (Lerch, 1991). More rigorous approaches, widely used in gravity field analyses, rely on variance component estimation (VCE) to ensure that the adopted weights are consistent with the weighted residual variances (e.g., Lemoine et al., 2013, 2014; Goossens et al., 2023). These variance determination strategies have also been applied to planetary radio science analyses (Bertone et al., 2021; Goossens et al., 2022), and should be perfectly suited for global inversions of radio science and astrometry in the context of natural satellites' ephemerides estimation.

More complex noise whitening filters, such as the ones commonly applied for Earth gravity field determination (e.g., Pail and Plank, 2002; Schuh, 2003; Siemes, 2008), could moreover also be considered rather than the averaging approach mentioned in Section 3.2.2. Such whitening processes could help decorrelate the measurements, rather than accounting for the observation correlations in the weight matrix (e.g., by introducing non-zero diagonal components in Eq. 3.12).

Other complementary data sets

In addition to the existing astrometric observations considered in Chapter 8, other data sets could efficiently complement JUICE and Europa Clipper radio science. As hinted at by our previous analyses and confirmed by our combined astrometry and radio science estimation (Chapter 8), the lack of constraints on Io's orbit currently represents the main avenue of improvement for the Galilean moons' ephemerides. An obvious complementary data set to consider is the radio science measurements collected during the two Io flybys performed by Juno during its extended mission phase. Preliminary analyses, either as a standalone radio science data set or combined with JUICE and Europa Clipper (simulated) tracking measurements, already hinted at possible improvement of the estimation of Io and Jupiter's dissipation parameters (Filice et al., 2023; Magnanini et al., 2023).

In parallel to the work conducted in this dissertation, a comparative analysis of JUICE simulated radio science and radiometric navigation data has been performed in Hener et al. (2024). This study was originally initiated to investigate possible in-mission ephemerides improvements for the Galilean moons based on JUICE radio science data, as opposed to the radiometric measurements of lesser accuracy, but more widely spread out in time, on which the navigation solution relies. The results, however, did not confirm these initial expectations. While radio science will yield more accurate *post-mission* ephemerides, the *in-mission* solution achieved with navigation data seems competitive with what can be achieved with radio science. Partial radio science estimations relying on the limited - and thus imbalanced - data set available at a certain time t before the end of Jovian tour severely suffer from instability issues. The long navigation tracking arcs, on the other hand, proved very valuable to extract the signature of Io's orbit in the spacecraft's dynamics, and could therefore help constrain Io's state.

More detailed follow-up analyses will be required to confirm these unexpected conclusions. In particular, the accumulating effects of non-conservative perturbations acting on the spacecraft over the long navigation arcs and the possible mismodelling of such effects (see Sections 9.1.1 and 9.1.2) should be properly accounted for. It must moreover be noted that this analysis was conducted in a JUICE-only configuration. The radio science solution thus did not benefit from the complementarity of the JUICE and Europa Clipper data sets, which significantly improves both the robustness and the quality of the ephemerides estimation (see Chapters 4 and 5). Nonetheless, these considerations would only affect how the radio science and navigation *in-mission* solutions compare to each other, but not diminish the potential of JUICE's navigation data to constrain Io's orbit. This should be further investigated, by combining both nominal radio science and navigation data in a single inversion, and carefully investigating the resulting improvement for Io's estimated state.

In addition to radio science-derived constraints, either via rare direct flybys (Juno) or indirect sensitivity to dynamical coupling (JUICE, Europa Clipper), other space-based - yet more direct - observations of Io can be exploited to refine its ephemeris. JUICE's navigation and science cameras will indeed take optical images of Io throughout the mission. The potential of space-based astrometry for moons' ephemerides has already clearly been demonstrated in the context of the Cassini mission, where invaluable improvements of the Saturnian moons' ephemerides have been achieved thanks to ISS (Imaging Science Subsystem) images (e.g., Lainey et al., 2017, 2019, 2024). For the specific case of the Galilean system's dynamics in the JUICE-Europa Clipper context, such imaging observations can greatly help stabilise the solution by directly constraining Io's motion (e.g., Dirkx et al., 2017, for the JUICE-only case), similarly to what was observed in Chapter 8 with classical astrometry. Alternatively, space-based optical images of Io might also provide us with an independent, additional means to validate the radio science solution (see Section 9.1.1). Such validation opportunities are particularly critical for Io's orbit, given its indirect determination, but are also scarcer. The validation potential of the PRIDE VLBI data set, highlighted in Chapter 5, will for instance be much reduced for Io, specifically because of the absence of direct radiometric spacecraft tracking close to that moon. Zenk et al. (2024) investigated the possible role of space astrometry in that respect, assuming reasonable deviations between the true estimation errors for Io's orbit and the formal uncertainties obtained in this dissertation. These preliminary simulation analyses promisingly indicate that space imaging of Io could non-negligibly contribute to improving, or at least meaningfully validating, Io's radio science-based solution.

JUICE and Europa Clipper's instrument suites moreover offer an additional opportunity to further constrain Io's orbit (Van Hoolst et al., 2024). Both spacecraft carry similar UVS (UltraViolet Spectrograph) instruments, intended to study the atmospheres of Jupiter and its moons. The exceptional timing accuracy (about 1 ms, Davis et al., 2021) with which JUICE-UVS will record stellar occultations by Io can translate into a measurement of the moon's position with respect to the starry background with a accuracy of a few hundreds of metres. In addition to constraining Io's instantaneous shape - sensitive to both librations and tidal deformation - with the same accuracy level, these unique observations can thus notably contribute to the reconstruction of Io's orbit. UVS observations actually present the same advantages as space astrometry with respect to the radio science data set, providing independent and direct constraints on Io's motion, but show much better accuracy. The limited number of planned observations (about 60 occultations by Io[5]), combined with the influence of JUICE's orbit error and Io's topography uncertainties, will be the main limiting factors of UVS occultations' contribution to Io's ephemeris. Their promising potential and complementarity with the space astrometry data set should nonetheless be further investigated.

[5]https://www.cosmos.esa.int/web/juice/science-opportunity-analysis

10

Scientific implications

Chapter 9 presented the main conclusions of this dissertation, as well as derived recommendations and future research avenues, focussing specifically on the determination of the Galilean moons' ephemerides after the JUICE and Europa Clipper missions. In the following, we widen the scope of our discussion to consider the implications of a refined estimation methodology and improved solution for natural satellites' ephemerides. We will start with the Galilean system, to which this dissertation was originally bound to, before discussing possible applications to other planetary systems.

10.1. Implications for the Galilean satellites

This work has investigated the quality and robustness of the Galilean moons' ephemerides solution achievable in the wake of the upcoming JUICE and Europa Clipper missions to the Jovian system. The JUICE-Europa Clipper radio science data set, complemented by various other observations (Section 9.3.2) and most notably by existing and future astrometry (Chapter 8), will provide the most accurate picture of the system's present-day dynamics. Additionally, an improved ephemerides solution for the Galilean moons offers the opportunity to extract the tidal dissipation signal from their orbits. The determination of such dissipation parameters will bring invaluable insights into the satellites' current orbital migration rate and thermal state, critical to our understanding of the system's long-term thermal-orbital evolution. This will be complemented by other constraints on the moons' interiors derived from radio science (gravity fields and rotations, estimated alongside the moons' dynamics), but also altimetry, magnetic field, radar, and optical measurements (e.g., Petricca et al., 2023; Roberts et al., 2023; Van Hoolst et al., 2024). The following sections therefore discuss ephemerides-based insights, in the broader context of the JUICE and Europa Clipper's objectives and expected findings.

10.1.1. Constraining the system's evolution

We will first consider the characterisation of the moons' present-day orbits and dissipation-driven migration rates, before examining possible implications for our understanding of the system's long-term history.

Present orbital migration rates

The current orbital expansion rates of the Galilean moons result from the combined effects of the tides raised both on Jupiter and on the moons themselves, which have a very similar influence on their orbits (see Eq. 2.68–2.72). This is a major challenge when attempting to disentangle the contributions of the dissipation in Jupiter and in the moons based on measurements of the moons' orbits. Distinguishing between the two effects is then only possible because the eccentricity change is primarily caused by dissipation inside the satellite (e.g., Lainey et al., 2009, and Eqs. 2.69 and 2.72).

However, radio science tracking of JUICE and Europa Clipper offers the possibility to naturally separate both effects. The spacecraft's dynamics are indeed primarily sensitive to tidal effects via the variations induced in the satellite's gravity field (see Fig. 10.1, and more detailed discussion in Section 2.3.1). The tidal signature in the spacecraft's orbit is thus dominated by the tides raised on the moon, and can be extracted in gravity-focussed inversion without the need to reconstruct a global state solution for the moon (e.g., Durante et al., 2019; De Marchi et al., 2022). Natural satellites' state estimations from radio science data, on the other hand, are sensitive to both the effect of tidal dissipation on the spacecraft's dynamics and on the moon's orbit (Fig. 10.1), the latter being influenced by the dissipation in both Jupiter and the moon. These different sensitivities facilitate distinguishing between the real and imaginary parts of the Love number k_2, but also between the dissipation occurring within the central planet and within its moons. This, in turn, is critical to reliably determine not only the moons' orbital migration, but also the tidal heating rate of their interiors (see discussion in Section 10.1.2).

Distinguishing between the different dissipation signals in the moons' dynamics still requires accurately modelling the small secular effect that the tides on a given moon cause on its own orbit (see Section 2.3.4). It moreover assumes that a fully statistically consistent dynamical solution can be reconstructed for the moons over the course of the two missions, and beyond (to fit other data sets, see Chapter 3). Provided that the two above conditions are met, however, it will be possible not only to distinguish between tidal dissipation in Jupiter and its moons, but also to estimate a frequency-dependent dissipation in the planet, following refined dissipation models and recent results for the Saturnian system (Lainey et al., 2020). Existing simulations predict that, for the three outermost Galilean moons, JUICE and Europa Clipper radio science will indeed allow us to discriminate between dissipation in Jupiter and in the moons (e.g., Magnanini et al., 2024). This is of particular importance for the dissipation in Jupiter at Callisto's frequency: a joint inversion of JUICE and Europa Clipper radio science data will help us determine whether Callisto is caught in a resonant locking mechanism, and thus differentiate between the widely different long-term orbital evolutions that this would entail for the Galilean system (Lari et al., 2023), as well as for Jupiter's obliquity (Dbouk and Wisdom, 2023).

Our results, however, showed that only relying on JUICE and Europa Clipper radio science cannot yield an unambiguous estimation of the tidal dissipation in Io, and in Jupiter at Io's frequency. Not only the absence of direct flybys around this moon prevents us from distinguishing between moon and planet tides, but their combined signature in Io's orbit is only extracted from its indirect effect on the dynamics of the other moons (mostly on Europa's) via the Laplace resonance. This results in strong correlations between dissipation in Io, and dissipation in Jupiter at Io and Europa's frequencies (e.g., Magnanini et al., 2024). As highlighted by the results in Chapter 8, including direct observations of Io will therefore be crucial to overcome this issue and determine the moon's current orbital migration and tidal heating rate (see Section 9.3.2 for a more detailed discussion on promising complementary data sets). This is in turn essential to provide robust constraints on the long-term evolution of the system and of the Laplace resonance, as will be further discussed in the following.

Long-term evolution scenarios

In addition to a picture of the Jovian system's present-day dissipation, the JUICE-Europa Clipper ephemerides solution will help us investigate possible long-term evolution scenarios for the Galilean moons. The latter typically requires the coupled integration of thermal and dynamical models (e.g., Showman et al., 1997; Hussmann and Spohn, 2004; Bland et al., 2009), whose initialisation will directly benefit from tighter constraints on the moons' orbits and of the system's tidal dissipation parameters.

Our results, however, highlighted that the instability of Io's solution effectively limits the quality of the moons' orbital solution outside of the JUICE-Europa Clipper missions time bounds. Io's orbit indeed influences the entire system's orbital history via the Laplace resonance. Therefore, the lack of direct observations for this moon

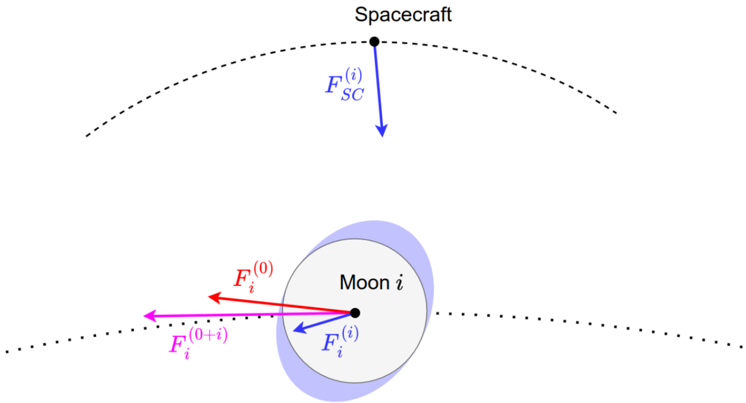

Figure 10.1.: Tidal forces acting on the spacecraft and moon i, due to tides raised in the moon (blue) and in the planet 0 (red). Tidal effects in the spacecraft's dynamics primarily originate from the moon's gravitational deformation (solid blue ellipsoid), but are also affected by the moon's orbital expansion (purple) under both planet and moon tides.

would overall loosen the constraints placed on long-term evolution models, and require the careful incorporation of all relevant correlations when exploring the parameter space. This again emphasises the need to include other data sets in the estimation, and give priority to direct observations of Io prior, during, and right after the two missions. Recent observation techniques developed for Earth-based astrometry (see Section 9.2.2), as well as complementary space data (Juno mission, or different JUICE-Europa Clipper data sets, see Section 9.3.2), are particularly promising.

Provided that the above solution instability is solved, which the results of this dissertation will facilitate, invaluable constraints will be available to refine our understanding of the system long-term evolution. Possible evolutionary paths should indeed be consistent with the moons' current orbits, but also with their internal structures, properties, and thermal states derived from ephemerides, gravity field, tidal deformation, magnetic field, and radar measurements, as well as geological features and estimates of the surfaces' heat outputs. Bridging the gap between the system's current and past states will nonetheless require developing a fully consistent model for the moons' interiors and dynamical evolution, coherently accounting for the intricate feedback between the moons' rotation, orbital migration, and tidal heating of their interiors. Such a model is however not yet available for the Galilean system, for which past thermal-orbital studies were limited to one or two satellites, assumed the Laplace resonance as locked, and did not consider the influence of rotational dynamics (e.g., Fischer and Spohn, 1990; Hussmann and Spohn, 2004).

Refined evolution scenarios for the Galilean moons will eventually bring invaluable insights into the yet poorly constrained history of the Laplace resonance, compared to existing, astrometry-based estimates of the resonance's current evolution (Lainey et al., 2009). Such constraints will help discriminate between a primordial origin or a later capture (Yoder and Peale, 1981; Canup and Ward, 2002), and investigate possible past periods of enhanced eccentricities. This will shed light onto the different thermal evolution processes undergone by Europa, Ganymede, and Callisto, explaining why these moons exhibit such different surface features and differentiation levels (e.g., Van Hoolst et al., 2024). The past tidal heating rate experienced by the Galilean satellites, driven by the moons' past eccentricities, will moreover be a key ingredient in better understanding the formation, history, and stability of their subsurface oceans (Section 1.1). This is particularly critical to explain how an ocean could have formed and subsisted until present day on Ganymede and even Callisto, despite current tidal heating being insufficient (see Section 10.1.2). Successive melting and freezing phases would moreover have affected the interactions between the trapped ocean and the moon's surface and/or deep interior (e.g., Běhounková et al., 2021), with consequences for possible chemical processes in the ocean, and thus for astrobiology.

10.1.2. Peeking at the moons' interiors

Our ability to extract the tidal quality factors Q of the Galilean satellites and of Jupiter from a refined, radio science-based dynamical solution offers another means to constrain the moons' dissipative and thermal states, opening a window onto their interior structure and properties. In the following, we discuss direct ephemerides-related insights into the moons' present-day interiors. We furthermore put them in perspective with other constraints derived from other instruments and/or data sets, some of which will also benefit from the modelling improvement required by the ephemerides determination process (see Section 9.1.2).

Thermal state

Refining our understanding of the Galilean moons' heat budget is key to answering some of the top scientific questions about these icy moons: how could subsurface oceans of liquid water form and subsist on these distant satellites until present-day? Besides radiogenic heating, tidal heating is the other main possible contributor to the heat budget of icy satellites (e.g., Hussmann et al., 2006). In the Galilean system, it is presently a significant heat source for both Io and Europa. This is enhanced, for the case of the more distant Europa, by the transfer of energy from Io via the Laplace resonance. Quantifying the satellites' tidal heating rate, defined by the phase lag of the complex Love number k_2[1], is thus crucial to characterise their current thermal and dissipative states. As shown in Section 2.3.4, this information can directly be extracted from the dissipation-driven evolution of the moons' orbits (Eqs. 2.68–2.72). For Europa and Ganymede, this is essential to investigate the present state of their internal oceans (freezing or in thermal equilibrium?). As mentioned in Section 10.1.1, exploiting current constraints to characterise this over long timespans is moreover key to investigate the stability and evolution of the subsurface oceans.

JUICE's GCO radio science will allow us to retrieve Ganymede's tidal phase lag with remarkable precision, providing invaluable insights into the moon's dissipative state. Constraining Callisto's $\text{Im}(k_2)$, on the other hand, is expected to be challenging (Mazarico et al., 2023; Magnanini et al., 2024). The current tidal heating rate inside Callisto is anyway estimated to be too small to explain the survival of a putative internal ocean until present-day, which should instead be linked to the moon's thermal-orbital history (Section 10.1.1). Finally, our ability to detect Europa's tidal phase lag, mostly from Europa Clipper radio science, will depend on the effective phase lag amplitude, and thus on the moon's interior (Magnanini et al., 2024). Current models predict a phase lag up to 1 degree (Moore and Schubert, 2000), at the limit of detectability from JUICE and Europa Clipper radio science data (Magnanini et al., 2024). We should only be able to detect large Φ_{k_2} values (up to 25 degrees Hussmann et al., 2016), corresponding to an extremely hot and dissipative interior which is currently considered unlikely. Our (in)capacity to obtain a statistically significant estimate for Europa's phase lag will therefore allow us to firmly rule out or confirm such highly dissipative interior models. A negative detection would moreover help us put upper bounds on the phase lag value. The state estimation methods developed in this dissertation will facilitate the robust estimation of Φ_{k_2} from the moons' orbits. However, the results in Chapter 2 evidence the risk for possible modelling consistency issues to affect the estimation when extracting Φ_{k_2} from both the spacecraft and moons' dynamics. This provides

[1] A large phase lag of the moon's tidal response Φ_{k_2} indicates a highly dissipative interior.

clear avenues for necessary model refinement to improve the characterisation of the moons' dissipative states from radio science.

Constraining Φ_{k_2} is nevertheless not enough to unambiguously determine whether the dissipation mostly occurs in a moon's outer ice shell or deep interior. Firmer insights into the dissipative state of the deep layers can be gained through the phase lag difference $\Delta\Phi = \Phi_{k_2} - \Phi_{h_2}$, where Φ_{h_2} designates the phase-lag of the radial shape deformation due to tides (Hussmann et al., 2016). Assuming that the outer icy shell is mostly decoupled from the deep interior, Φ_{h_2} will be primarily driven by dissipation in the former. The phase lag of the tidal potential Φ_{k_2}, on the other hand, depends on the moon's entire mass distribution. Large phase lag differences would therefore indicate a strong dissipation in the moons' deep interiors, i.e., in Ganymede's high pressure ice shell or Europa's silicate mantle, while similar Φ_{k_2} and Φ_{h_2} values would imply that most of the dissipation takes place in the outer shell. For Ganymede, large phase lag differences would however only be detectable for low-viscosity values of its high pressure ice layer (i.e., very hot deep interior, Hussmann et al., 2016; Van Hoolst et al., 2024). Constraining Europa's phase lag difference, on the other hand, might help detect a potential dissipation in its hot silicate mantle (Hussmann et al., 2016; Běhounková et al., 2021). Combining Φ_{k_2} and Φ_{h_2} would thus provide crucial information on the moons' internal viscosity and thermal states. The robustness of our estimates and interpretations, however, is again contingent upon the perfectly consistent modelling of the moon's rotation and tidal response, as well as spacecraft's dynamics. Linking together the spacecraft orbit and moon ephemerides errors with the resulting h_2 estimate uncertainties could nevertheless be achieved via a concurrent determination of orbital dynamics and shape deformation using altimetry crossovers, which are sensitive to both (Villamil et al., 2021).

Interior structure and properties

An accurate and consistent solution for the Galilean moons' ephemerides will moreover provide invaluable insights into the satellites' internal structure and properties. In the following, we specifically address how this will help characterising Europa and Ganymede's hydrospheres, thus contributing to some of JUICE and Europa Clipper's core scientific objectives.

The moons' internal structure and properties define both their rotational and tidal responses to external forcing (via Eq. 2.16 and 2.39, respectively). Despite their intricate feedback on the moons' orbits, all relevant internal properties cannot be unambiguously extracted from their signature in the satellites' dynamics, as discussed in Section 2.4.2. Reconstructing an accurate and detailed picture of the moons' interiors thus requires capitalising on synergistic constraints derived from different data sets and analyses. In particular, further insights can be gained by exploiting the different sensitivities of the spacecraft and moons' orbits to various manifestations of the moons' interiors (e.g., gravity, libration, tidal response). Obtaining physically reliable and robust estimates from such a concurrent estimation, however, requires the consistent modelling of orbits, tides, and rotations, and of their combined effects on both the spacecraft and the moons' dynamics. The extreme sensitivity of the moons' dynamics to the modelling of their tidal and rotational responses, underlined in Chapter 2, can in turn be exploited to verify the statistical realism and physical consistency of spacecraft-based estimates. In the following, we therefore take a broader view by examining both moon- and spacecraft-derived quantities together. This is essential to eventually maximise the information on the satellites' interiors which can be extracted from the moons' dynamics.

Starting with gravity-derived insights, JUICE and Europa Clipper solutions will confirm whether the three icy Galilean satellites are in hydrostatic equilibrium. Improved estimates of the moons' degree two gravity field coefficients, together with their rotational state, will help refine our current knowledge of their moments of inertia (see Section 2.1.2 and 2.2.1), providing constraints on their internal structure (Cappuccio et al., 2022). JUICE's orbital phase makes the radio science investigation at Ganymede a special case, as measurements acquired during the GCO will bring remarkably detailed insights into the moon's interior. Simulations indeed predict that Ganymede's gravity field could be estimated up to degree and order 30 to 50, depending on the adopted interior model (Cappuccio et al., 2020a; De Marchi et al., 2021). Low-degree coefficients will, as for the other moons, constrain Ganymede's internal structure. The higher degree part of the gravity field spectrum, on the other hand, can be compared with the moon's detailed shape model to extract crucial information about Ganymede's ice shell's thickness, degree of isostatic compensation, and density distribution (e.g., De Marchi et al., 2021). Although gravity constraints will mostly come from the spacecraft's orbit(s), the estimation of the moons' states and gravity fields should still be done concurrently, as they both influence each other (Section 2.1.1). It is nonetheless interesting to note that results in Chapter 4 showed very limited degradation in gravity field reconstruction when estimating the moons' states in an arc-wise manner instead of a coupled approach.

As described in Section 2.3.4, the moon tides signature in its own orbit depends on the ratio k_2/Q (Eqs. 2.68–2.72). Obtaining separate and reliable estimates for k_2's real and imaginary parts thus requires extracting the former from the spacecraft's dynamics. Once combined with dissipation estimates derived from the moon's ephemeris, powerful constraints can be placed on the moons' visco-elastic properties. The estimate of Callisto's k_2[2] from JUICE flybys should for instance be accurate enough to confirm the presence of an internal ocean (Cappuccio et al., 2022). Thanks to JUICE's GCO, we will moreover be able to determine Ganymede's k_2 at various forcing frequencies, providing tight constraints on its ocean layer's thickness (De Marchi et al., 2022). Furthermore, a recent model developed by Rovira-Navarro et al. (2023) expands the existing Love number formalism to account for lateral heterogeneities in the moon's interior, expected to arise from icy shell variations. The determination of Ganymede's k_2 should be accurate enough to distinguish between the respective contribution of radial and lateral heterogenities to the moon's tidal response, providing unique constraints onto possible icy shell variations. Promisingly, Ganymede's k_2 will still have an effect, albeit small, on its own dynamics. Although this signature can be very effectively absorbed in

[2]Here and the following, k_2 will by default refer to the real part of the Love number.

other parameters, the exceptionally accurate radio science constraints from JUICE's GCO will complicate such absorption. The consistent modelling of tides in the ephemerides solution could therefore be used to validate the refined spacecraft-based k_2 estimates mentioned above.

In addition to constraining the subsurface ocean's depth (achievable for Ganymede from its k_2 frequency spectrum, as discussed above), determining the thickness of the moons' outer icy shells is another key to characterising their hydrospheres. While this cannot be achieved with k_2 only, combining the Love numbers k_2 and h_2 can yield a less ambiguous estimate (Wahr et al., 2006; Cappuccio et al., 2020a; Mazarico et al., 2023). The ice shell's thickness can also be extracted from the moons' librations, offering a great opportunity to validate our results (Van Hoolst et al., 2024). As demonstrated in Section 2.3.4, the effect of the moon's main once-per-orbit libration on its own orbit is indistinguishable from that of the dissipation induced by moon tides (see Eqs. 2.118–2.119). The librations are therefore extracted from the spacecraft's dynamics, which sense the librational response of the moon's entire interior via the time-varying orientation of its static gravity field (Eq. 2.120). Nonetheless, this does not reduce the importance of proceeding to a concurrent estimation of the spacecraft and moons' dynamics, tidal dissipation, and librations, which is twofold. First, the constraints on librations originating from the spacecraft's orbit are crucial to obtain a reliable and robust estimate of tidal dissipation from the moon's orbital solution (Section 2.4.2). Second, the sensitivity of the latter to rotational parameters offers a powerful means of validation for the spacecraft-derived libration estimate.

In addition to the ice shell thickness, further insights could be gained from the detailed characterisation of Ganymede's librations enabled by GCO radio science. The respective contribution of the outer icy shell and deep interior to the librational response sensed by gravity field measurements will indeed depend on the degree of the spherical harmonics coefficient under consideration[3]. Using an expanded parametrisation accounting for the (partially) decoupled librations of the moon's different layers could therefore allow us to discriminate between librational contributions from different parts of Ganymede's interior. This disentanglement could moreover be facilitated by measurements from other instruments (e.g., imaging, altimetry, radar), sensitive to the librations of the satellite's outer icy shell. Eventually isolating the librational response of the icy shell, which depends on the shell's rigidity and thickness (Van Hoolst et al., 2013), could help us constrain both of these quantities. The comparison of the full body and icy shell's librations will also bring insights into the level of decoupling between the shell and the moon's deep interior. Such a detailed model for the moon's librations might, however, come at the risk of over-parametrising the inversion problem. This again highlights the need for a unified, full consistent dynamical model concurrently integrating both the rotational and translational dynamics. Such a coupled modelling approach - whose importance for moons' ephemerides specifically was strongly underlined in

[3]By construction of the spherical harmonics expansion of the gravity field, the coefficients $\bar{C}_{nm}$ and $\bar{S}_{nm}$ depend less on the density distribution of the moon's deep interior and, inversely, more on that of its outer layers, as the order n increases (see Section 2.1.2).

10

this dissertation (Chapters 2, 4, and 9) - would therefore also benefit estimated quantities primarily extracted from the spacecraft's dynamics.

As described above, the detailed characterisation of a moon's rotation and tidal response (using synergistic constraints from both spacecraft and moons' dynamics) can help us determine the thicknesses of its icy shell and underlying ocean layer. This is foreseen to be at least achievable for Ganymede (e.g., Van Hoolst et al., 2024). Interestingly, constraints on Ganymede's icy shell thickness and ocean depth can also be inferred from a joint inversion of JUICE's gravity and magnetic field measurements (Petricca et al., 2023). Such a synergistic approach proved successful in overcoming the individual limitations and ambiguities of the inversion solutions typically obtained separately from gravity and magnetic field data. Comparing the results of such a global inversion with the insights derived from the moon's rotation and tidal deformation offers invaluable cross-validation opportunities.

10.1.3. Future exploration

While the JUICE and Europa Clipper missions will revolutionise our knowledge and understanding of the Galilean satellites, both for each moon independently and for the entire system as a whole, they are but one step in our continued exploration of this fascinating system.

A key future mission target is the still enigmatic volcanic world Io, currently under-explored by space missions because of its extremely hostile radiation environment. As highlighted on numerous occasions in this work, a better characterisation of Io's present state is critical to complete the very accurate picture of Europa, Ganymede, and Callisto that will be available in the post-JUICE and Europa Clipper era. Io is moreover an extremely interesting object in its own right, offering the perfect opportunity to further our understanding of tidal heating and heat transport in planetary interiors (Keane et al., 2021a,b, 2022; Steinke, 2021). The Io Volcanic Explorer (IVO) mission proposed as part of NASA's Discovery Program was precisely designed to fill this knowledge gap, with multiple low altitude flybys (below 100 km) planned around Io (e.g., McEwen et al., 2023). This mission's core objectives include a deeper understanding of Io's extreme volcanism, via a better characterisation of the moon's present thermal state and heat , combined with detailed investigation of Io's interior via magnetic field measurements and refined characterisation of the moon's Love number k_2 and librations. It may allow Io's k2/Q to be determined directly, disentangling it from Jupiter's k2/Q and increasing the robustness of the ephemerides solution. However, due to the proximity to Jupiter, the tidal-orbital-rotational modelling consistency will be even more important. In addition to IVO, various Io-focussed New Frontiers mission concepts were proposed (McEwen et al., 2023). While the decadal strategy survey gave preference to other moon systems for New Frontiers missions (see Section 10.2), it nonetheless reiterated the critical importance of Io's exploration (Decadal strategy survey, 2022).

Furthermore, future steps in icy worlds exploration look beyond remote-sensing techniques to envision in-situ measurements. A lander mission on Europa is considered as a promising follow-up to the Europa Clipper mission (e.g., Hendrix et al., 2019; Blanc et al., 2021; Phillips et al., 2021; Hand et al., 2022). Together with the tiny Saturnian moon Enceladus (also a core future mission target, see Section 10.2.2), Europa appears to be an active ocean world: the interactions between its internal ocean and icy surface, as well as with its rocky seafloor (Běhounková et al., 2021), are indeed critical for ocean chemistry. Combined with the detailed orbit-based characterisation of this moon that will be available after completion of the Europa Clipper mission, this designates Europa as a prime candidate for a lander mission. Such a mission indeed represents the next step in investigating Europa's habitability, through a refined characterisation of the moon's surface, icy shell, and internal ocean. In particular, radio science tracking of a Europan lander would allow us to precisely determine the rotation and deformation of the moon's icy shell under the effects of tides, while in-situ measurements would bring invaluable constraints on the thermal state of the moon's icy shell (e.g., Blanc et al., 2021; Hand et al., 2022). Lander-based tracking measurements would moreover greatly benefit the ephemerides solution. Critically, such a mission would build on the JUICE and Europa Clipper scientific heritage, but also directly benefit from ensuing advances in modelling and estimation methodology (see Chapter 9).

10.2. Coda: application to other planetary systems

The above discussion summarised the main scientific implications of the methodologies developed in this dissertation, for our investigation of the Galilean moons specifically. However, the application of this work is not limited to our upcoming investigation of these four satellites. We will thus now take on a more top-level tour spanning from the Martian to the Neptunian moon systems. We will discuss the science case for refined ephemerides of their natural satellites, as key scientific questions pertain to our knowledge of the moons' present and past dynamics. The methodologies and findings presented in this dissertation, equally applicable to other systems, will therefore also directly contribute to achieving these science objectives. With the moons of our Solar System as key mission targets, future exploration perspectives will moreover rely on similar mission configurations and/or resulting data products as JUICE and Europa Clipper. The insights and advances achieved in the specific context of the preparation for these two missions are thus of great relevance for upcoming exploration steps, beyond the frontiers of the Jovian system.

10.2.1. The Martian system

Our neighbour planet Mars is the only other terrestrial planet in our Solar System to also possess natural satellites, Phobos and Deimos. Despite its proximity to Earth and the various missions that explored the Martian system, much is left to learn about these unique and fascinating moons. In particular, our current knowledge of their interiors and orbits could not yet yield firm conclusions regarding these satellites' origin and evolution. Three different scenarios - capture, disk accretion and post-impact accretion - are still disputed, implying widely different histories for the Martian system (e.g., Burns, 1978; Rosenblatt, 2011; Rosenblatt et al., 2016; Bagheri et al., 2021; Miranda et al., 2023). As in the Galilean system case, a better understanding of the Martian moons' formation and evolution would moreover bring further insights into planetary evolution processes in general.

A much refined dynamical solution for the Martian satellites would greatly help discriminating between these different evolution scenarios. Tighter constraints on Phobos and Deimos' still poorly characterised interiors (Le Maistre et al., 2019; Yang et al., 2020) would also provide invaluable insights, and are therefore key objectives for future Martian moons-dedicated missions. In particular, a better determination of these moons' orbits, gravity fields, rotations, and tidal responses would provide us with a natural way to refine our knowledge of Phobos and Deimos' current internal structure and properties (e.g., Le Maistre et al., 2019). As will be discussed below, this is achievable through direct tracking of future orbiters and/or landers, but also requires an improved reconstruction of the dynamics of the Martian moons themselves. Phobos' ephemeris error was indeed identified as an important limiting factor to the proper interpretation of the MEX flybys radio science (Yang et al., 2020).

The long-lasting interest in the Martian moons and plethora of remaining open questions regarding their origin and history inspired many attempted and/or proposed mission concepts in the past (e.g., Marov et al., 2004; Oberst et al., 2012; Murchie et al., 2014; Oberst et al., 2018). This includes the upcoming Martian Moons eXploration (MMX) JAXA-led mission, expected to be launched in 2026 and the first one to ever enter orbit around Phobos (Ogohara et al., 2022). Radio science simulations for MMX promisingly indicate that Phobos' degree and order 2 coefficients could be recovered with very good accuracy (0.1% of the value assumed in Yamamoto et al., 2023), bringing valuable constraints on the moon's moments of inertia (Eqs. 2.19 and 2.20). Beyond the MMX mission horizon, one of the most promising next steps in the exploration of the Martian moons (and of Phobos in particular) would rely on a lander to perform in-situ measurements. Tracking measurements from such a landing segment, as opposed to an orbiter, would be directly sensitive to Phobos' rotation and deformation, bringing invaluable insights into the moon's ephemeris and interior (Le Maistre et al., 2013; Dirkx et al., 2014).

The dynamical configuration of the Martian moon system is however particularly complex, as the close proximity of Phobos' orbit with Mars induces a strong coupling of Phobos' translational and rotational dynamics. Phobos' dynamics are indeed affected by its mutual gravitational interaction with Mars, which is in turn sensitive to the moon's rotation (Borderies and Yoder, 1990). This coupling between Phobos' orbit and rotation (including its librations, Rambaux et al., 2012), combined with the significant tidal torques exerted on Phobos' elongated shape, imposes a strict requirement on the consistency of our dynamical model(s) (Chapter 2), as also required for upcoming JUICE and Europa Clipper real data analyses (see Section 9.1.2). More precisely, in light of novel architectures and tracking techniques expected for future missions, the Martian moons' rotation and translational dynamics cannot be handled separately (Dirkx et al., 2014), and should be concurrently integrated in a unified, coupled model (Martinez and Dirkx, 2024). While modelling advances in preparation for JUICE and Europa Clipper will therefore directly benefit Martian system analyses, the synergy will actually be mutual. Phobos indeed offers the perfect test case for the development of refined, fully coherent dynamical models:

the modelling of its tidal and rotational response is significantly simpler than for an icy layered satellite (see Section 10.1.2) and its resonance-free orbit environment is a lot easier to model than the Galilean system.

In addition to these modelling aspects, improving the reconstruction of the Martian moons' dynamics also shares many of the state estimation and data merging challenges identified in the Galilean system case. Current estimation solutions for Phobos and Deimos' orbits and physical parameters indeed rely on diverse data sets, including long-term and space astrometry (Lainey et al., 2007, 2021), radio science from Phobos' flybys (Rosenblatt et al., 2008; Yang et al., 2019), or both (Jacobson, 2010, 2014). Similarly as what JUICE and Europa Clipper will achieve for the Galilean moons, accurate radio science tracking measurements of the MMX spacecraft will moreover radically improve the estimation solution in the coming decade. The state estimation methodology developed in this dissertation for the JUICE-Europa Clipper case will therefore be equally suited to the determination of Phobos' dynamics from MMX tracking radio science. The potential data merging strategies outlined in Section 9.1.2 for global inversions of the Galilean moons' dynamics will furthermore be (at least partially) applicable to the Martian case as well.

10.2.2. THE SATURNIAN SYSTEM

The Saturnian system is home to at least 82 moons, forming a very diverse set of icy and rocky worlds which the Voyager 1, 2 and Pioneer 11 missions started to reveal (Smith et al., 1981, 1982) . Most of our current knowledge of this system, however, comes from the Cassini mission which spent 13 years studying Saturn and its satellites before its final dive in the planet's atmosphere. Saturn possesses eight major satellites: Mimas, Enceladus, Tethys, Dione, Rhea, Titan, Hyperion, and Iapetus (by increasing distance to the planet, see Fig. 10.2). These moons form a unique system dominated by the massive Titan (accounting for 95% of the system's total mass), and exhibiting several orbital resonances, specifically a 4:2 MMR between Mimas and Tethys, a 2:1 MMR between Enceladus and Dione MMR, and a 4:3 MMR between Titan and Hyperion (see Fig. 10.2). The crossing of other MMRs in the past moreover plays an essential role in explaining the system's present orbital configuration (e.g., Iapetus' eccentric and inclined orbit, Polycarpe et al., 2018), and the potential formation of sub-surface oceans through past enhancements of eccentricity, and thus tidal heating (e.g., for Mimas, Lainey et al., 2024).

One of the ground-breaking results from Cassini is the strong and frequency-dependent dissipation occurring inside Saturn, estimated from the Saturnian moons' orbits (Lainey et al., 2012, 2017, 2020, see Section 1.1). Evidence for such a frequency-dependency was separately obtained from astrometry (ground- and space-based) and Cassini radio science, and predicts a fast outward orbital migration for the major Saturnian moons. In addition to suggesting a resonant locking mechanism at play in the Saturnian system (Fuller et al., 2016; Lainey et al., 2020)[4], these rapid migration rates, and that of Titan in particular, suggest different

[4]The rapid migrations of the Saturnian moons could also be reconciled with the energy dissipation model in Saturn's convective envelopes proposed in Terquem (2023), except for Titan and Rhea.

evolution scenarios for the Saturnian system (see detailed discussion in Section 1.1). Despite a good agreement for all the other moons, an independent study however reported an order of magnitude weaker dissipation for Saturn at Titan's frequency, based on a combined analysis of astrometry and Cassini radio science (Jacobson, 2022). This discrepancy has not yet been explained, and its origin remains difficult to identify given the complexity of the global inversion and the stability issues of the Cassini radio science solution, at present mostly ascribed to dynamical mismodelling (Durante et al., 2019; Zannoni et al., 2020; Jacobson, 2022). Combined with the present inconsistency between estimates of Saturn's dissipation at Titan's frequency, this calls for a re-analysis of Cassini data, for which the methodologies outlined in this dissertation would be ideally suited.

The complementarities between the state estimation strategies developed for future Galilean system missions (including the work initiated in this dissertation) and those needed to re-analyse Cassini data set(s) are bilateral. Both require combined aspects of data merging, global inversions, and dynamical modelling (see Chapter 2). Advances in any of the above in preparation for the JUICE and Europa Clipper missions will directly benefit the re-analysis of Cassini data for natural satellites' dynamics applications. On the other hand, the data set available for the Saturnian system - a diverse mix of astrometry (ground- and space-based) and radio science from multiple flybys at different moons - represents the best opportunity to apply and refine the global inversion methodologies developed for the Galilean moons' ephemerides.

Looking beyond the legacy of the Cassini mission, the Saturnian system is moreover still a very high priority for future missions, ever since Cassini brought evidence of the presence of sub-surface oceans on some of its icy moons, together

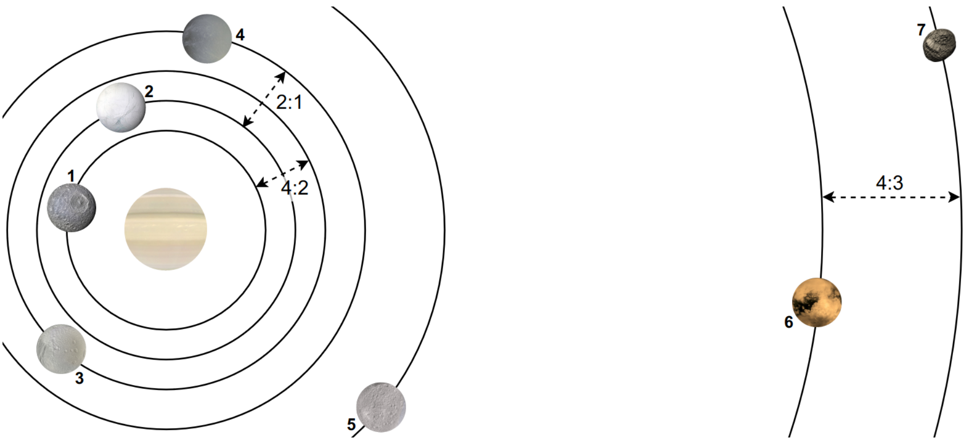

Figure 10.2.: Saturn's major satellites (excluding the outermost Iapetus) with 1:Mimas, 2:Enceladus, 3:Tethys, 4:Dione, 5:Rhea, 6:Titan, 7:Hyperion, including the Mimas-Tethys, Enceladus-Dione, Titan:Hyperion MMRs. The moons' sizes are not to scale, but their orbits are.

10

with hydrocarbon surface oceans on Titan. Enceladus and Titan are particularly interesting targets (Hendrix et al., 2019). The latter is a large, organics-rich moon, with a dense atmosphere and a unique methane cycle, possibly harbouring an internal ocean (Iess et al., 2012; Durante et al., 2019), thus showing great promises for habitability perspectives. Our interest in Mimas has also lately been renewed, as the rotation of this tiny moon indicates the surprising presence of a young sub-surface ocean (Tajeddine et al., 2014; Rhoden and Walker, 2022; Lainey et al., 2024). Nevertheless, the tiny ocean satellite Enceladus (Iess et al., 2014b; McKinnon, 2015; Thomas et al., 2016) remains the most fascinating of Saturn's moons. The detection of plumes (Porco et al., 2006), combined with the moon's mix of young and old surface features, makes Enceladus the most (tidally) active ocean world in the Solar System, but also the one offering the easiest access to its internal ocean, opening exciting exploration opportunities.

Most of our open questions about Enceladus are related to our limited understanding of tidal dissipation in the Saturnian system, which improved ephemerides can help furthering. In particular, solving Enceladus' heat budget enigma requires determining how much dissipation the moon experiences (Nimmo et al., 2018, 2023) and where dissipation occurs in its interior, which is still much disputed (Roberts and Nimmo, 2008; Chen and Nimmo, 2011; Beuthe, 2016; Choblet et al., 2017; Beuthe, 2019; Hay and Matsuyama, 2019; Rovira-Navarro et al., 2019; Souček et al., 2019; Rovira-Navarro et al., 2022). Determining the above is a key scientific objective of future Enceladus missions (see discussion below), and involves similar characterisation strategies as those presented in this dissertation for the JUICE-Europa Clipper case (see overview in Section 10.1).

Our limited knowledge of the tidal dissipation mechanisms at play in the Saturnian system also has implications for our understanding of the moons' origin and evolution. Presently, different formation scenarios co-exist for Saturn's mid-sized moons (mostly divided between circumplanetary disk and ring formations), predicting different moon ages and thermal-orbital evolutionary histories (e.g., Charnoz et al., 2011; Ćuk et al., 2016; Hyodo et al., 2017; Salmon and Canup, 2017). A better characterisation of Saturn's dissipation spectrum, aided by the methodologies developed in this dissertation, is key to discriminating between these different scenarios (e.g., Castillo-Rogez et al., 2018). Existing thermal-orbital evolution studies (e.g., Neveu and Rhoden, 2019) should moreover be revisited in light of our refined estimates of tidal dissipation in the system (Lainey et al., 2020).

In light of the strong science case exposed above, various mission concepts have been proposed for further explorations of the Saturnian moons (Barnes et al., 2021; Choblet et al., 2021; Mitri et al., 2021; Sulaiman et al., 2021; Mousis et al., 2022; Rodriguez et al., 2022). In particular, a strong case can be made for a single or dual orbiter around Enceladus (e.g., Ermakov et al., 2021; Marusiak et al., 2021), leveraging similar measurement and synergistic estimation strategies as JUICE and Europa Clipper for the Galilean system (see Section 10.1). In particular, the Enceladus mission concept investigated in Genova et al. (2024) shows strong similarities with the orbital phase of the JUICE mission. It could allow the estimation of the moon's gravity field up to degree 30, along with the determination of its k_2 and tidal dissipation. The dynamical model requirements, both in terms of accuracy and consistency, will also be similar to JUICE's. This again shows that modelling and state estimation advances achieved in the JUICE-Europa Clipper context will be directly transposable to future Saturnian system missions.

10.2.3. THE URANIAN SYSTEM

Succeeding to a decade of outer Solar System exploration strongly focussed on the Galilean satellites, the Uranian moon system is now at the centre of future mission plans. The decadal strategy survey outlining NASA's exploration program for the coming 2023-2032 period ranked the Uranus Orbit and Probe (UOP) mission highest among six flagship mission candidates (Decadal strategy survey, 2022). On the European side, the moons of the giant planets of the Solar System - including those of the icy giants Uranus and Neptune (see Section 10.2.4 for the latter) - were selected as one of three exploration themes for ESA's Voyage 2050 plan.

Improving the ephemerides of Uranus' five main satellites and precisely quantifying their accuracy (e.g., Lainey, 2008) is essential in preparation for a potential upcoming mission. The benefit of a pre-mission ephemerides improvement is twofold. It will first directly facilitate the mission's orbital design, but might also bring additional insights into the Uranian moons' dynamics, possibly helping us refine current evolution scenarios and related mission scientific objectives (see discussion below). The present ephemerides for Uranus' satellites primarily rely on classical astrometry and mutual events (Arlot et al., 2006a), but also include images from Voyager 2 (Lainey, 2008; Emelyanov and Nikonchuk, 2013) and HST (Jacobson, 2014). Nonetheless, the accuracy of these ephemerides remains limited to a few hundreds of kilometres (Lainey, 2008; Jacobson, 2014). To improve the current solutions, mutual approximations are a promising substitute to mutual events, which only occur every 42 years in the distant Uranian system. Mutual approximations between the major Uranian moons have already been successfully observed (Santos-Filho et al., 2019), with an accuracy far exceeding that of classical astrometry.

Many of the proposed mission concepts place Uranus' five major satellites Miranda, Ariel, Umbriel, Titania, and Oberon (see Fig. 10.3) at the core of their

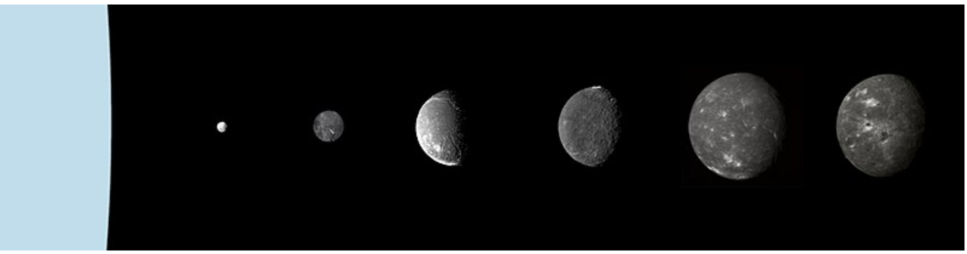

Figure 10.3.: Uranus' major satellites: Miranda, Arial Umbriel, Titania, and Oberon (in increasing distance from Uranus). Courtesy for the moons' images: NASA.

scientific objectives (Fletcher et al., 2020; Cartwright et al., 2021; Leonard et al., 2021). These objectives actually gravitate around these two main foci: 1) the exploration of the Uranian moons as ocean worlds whose interior, origin, and evolution are yet poorly constrained (Hendrix et al., 2019; Fletcher et al., 2020), 2) the use of Uranus' primordial satellite system as a laboratory for studying long-term evolution processes (Fletcher et al., 2020; Cartwright et al., 2021; Leonard et al., 2021; Castillo-Rogez et al., 2023). Both investigation avenues pertain to a refined understanding of the system's past and present orbital configuration, including an improved characterisation of tidal dissipation. These objectives are extremely similar to those of the JUICE and Europa Clipper missions, and will leverage analogous merging strategies of historical data sets and upcoming radio science from future missions. In the following, we examine more precisely open research questions related to the evolution of the Uranian moons' orbits and interiors, in light of the methodology advances outlined in this dissertation for the Galilean moons case.

Potential internal oceans, if they survived until present-day, most likely subsist in the form of residual, shallow oceans. Both Hussmann et al. (2006) and Bierson and Nimmo (2022) nevertheless showed that the thermal-orbital evolution of the two outermost major moons Titania and Oberon might be consistent with the subsistence of sub-surface oceans of liquid water. A better determination of the past and present orbital migration rate of these satellites from their ephemerides (Eqs. 2.68–2.72) would be - just as for the Galilean system - a powerful means to refine our knowledge of these moons' dissipation history, and shed new light on the evolution and stability of their subsurface oceans. Following the approach investigated in this dissertation, this will be facilitated by similarly exploiting the strengths and synergies of the various data sets available, namely combining ground astrometry and radio science from a future spacecraft.

At present, the orbital history of the Uranian moons remains poorly constrained. This partially follows from our poor knowledge of Uranus' dissipation, possibly both frequency- and time-dependent (Nimmo, 2023), which drives the orbital migration of these satellites and thus the crossing of past MMRs. These are crucial to explain both the present orbital configuration of the system, including Miranda's high inclination ($\sim$4 deg), and evidence of past intense tidal heating episodes on Miranda and Ariel's surfaces (e.g., Beddingfield et al., 2015; Peterson et al., 2015). However, the resonance overlap between the significant moon-moon interactions and the effects of the central planet's oblateness complicate the picture (e.g., Dermott et al., 1988): past capture(s) in MMR, secular and/or spin-orbit resonances may have induced chaotic motion (Laskar and Jacobson, 1987; Dermott et al., 1988). Despite many attempts to reconcile the present thermal and orbital constraints with various past resonances (e.g., Tittemore and Wisdom, 1989, 1990; Ćuk et al., 2020; Gomes and Correia, 2023), obtaining a consistent solution for all major Uranian satellites proved extremely challenging.

Most of these past dynamical analyses - both analytical and numerical - relied on a classical constant Q assumption for Uranus' dissipation. However, a recent study demonstrated that a low tidal quality factor in Uranus' recent past could explain the satellites' high surface heat flux (Nimmo, 2023). Such a strong dissipation could still be in agreement with an ancient formation of the Uranian moons if we assume a time-dependent Q, as suggested by the resonance locking mechanism (Fuller et al., 2016). Discriminating between the different orbital evolution scenarios presented above, while critical to our understanding of the system's thermal-orbital evolution, is nevertheless extremely difficult to achieve from dynamical simulations only. In particular, the determination of a variable Q would directly benefit from the combination of old astrometry and in-situ measurements from a dedicated mission (e.g., Filice et al., 2024). The methodologies developed in this dissertation to reconstruct accurate ephemerides and extract reliable dissipation estimates from various data sets are therefore particularly valuable in the perspective of a future mission to Uranus' moons.

It must be noted that the fast orbital migration of a former, now disrupted satellite driven by a strong dissipation in the past has moreover been recently suggested as a possible explanation for Uranus' tilting (Saillenfest et al., 2022). This offers an alternative to existing scenarios relying either on a slow tilting process of the planet's axis (Boué and Laskar, 2010) or, more commonly, on collisional event(s) (Morbidelli et al., 2012). Characterising dissipation in Uranus - which this dissertation will facilitate - therefore also holds the key to the origin of the planet's tilted axis.

While the above discussion focussed on Uranus' five major moons, the Uranian system also hosts nine irregular satellites (i.e., small satellites far away from the central planet on highly eccentric orbits). These are extremely faint objects and thus very difficult to observe. The lack of observations, combined with their highly perturbed dynamics, make the dynamics of the irregular satellites particularly difficult to constrain (e.g., Jacobson et al., 2012; Brozović and Jacobson, 2022). While challenging to achieve, an improved ephemerides solution for these moons, which are likely to be captured objects, would nonetheless be invaluable to shed light on their dynamical history.

10.2.4. The Neptunian system

Comparing the satellites of the Solar System's two icy giants, the Neptunian moon system is wildly different from its Uranian counterpart. While the latter is supposed to be primordial, the history and current state of the Neptunian system has been re-shaped by the capture of its largest satellite, Triton, a former Kuiper Belt Object (KBO). Triton's retrograde, yet almost circular, orbit indeed advocates against an in-situ formation. It can be better reconciled with the capture of a transneptunian object (McKinnon, 1984; Goldreich et al., 1989), possibly a binary as suggested in Agnor and Hamilton (2006). The capture would be followed by the tidal-driven circularisation of Triton's initially highly eccentric orbit (McCord, 1966; McKinnon, 1984; Goldreich et al., 1989; Correia, 2009), yielding strong internal dissipation and intense tidal heating (e.g., McKinnon, 1984; Ross and Schubert, 1990; Correia, 2009). The uniqueness of Triton's orbital history reinforces the scientific implications of an improved dynamical solution for this moon, and for the entire Neptunian system.

Our interest in Triton - the unique Solar System representative of a new class of moons comparable to dwarf planets of the trans-Neptunian region - is indeed deeply linked to its thermal-orbital history, primarily accessible to us via a refined determination of its ephemeris. First identified as a potential ocean world in Hussmann et al. (2006), the intense heating Triton experienced in the past due to eccentricity tides strengthens the likelihood of this moon retaining a liquid subsurface ocean until present-day. The discovery by Voyager 2 of plumes emerging from Triton's Southern polar cap (Soderblom et al., 1990), combined with the moon's extremely young surface and puzzling geological features, further contributed to raising interest in this singular satellite. Triton's is indeed the youngest icy surface in the Solar System, being evaluated to be at most 100 Myr, but probably much closer to 10 Myr (Schenk and Zahnle, 2007). Reconciling this estimate with Triton's thermal-orbital history is however difficult.

Triton's surface features, witnesses of a recent heating process, first appear rather inconsistent with its postulated dynamical evolution given the short eccentricity damping timescales (1 Gyr, Correia 2009; Nogueira et al. 2011). Nonetheless, Triton is the most likely natural satellite in the Solar System to currently experience significant ocean tidal dissipation, due to its very low eccentricity and highly inclined orbit (Chen et al., 2014; Nimmo and Spencer, 2015). The moon's high inclination (Fig. 10.4) could indeed be consistent with a rather large obliquity (0.7 deg, Chen et al. 2014; Nimmo and Spencer 2015), and the resulting tidal dissipation in Triton's ocean could account for its recent resurfacing. Distinguishing between the dissipation occurring in different layers of the moon's interior is however challenging, as discussed in Section 10.1.2 for the Galilean moons case. It would require combined measurements of the dynamics of both Triton and an in-situ spacecraft, and be difficult to achieve with a flyby mission only. The detectability of ocean tides from

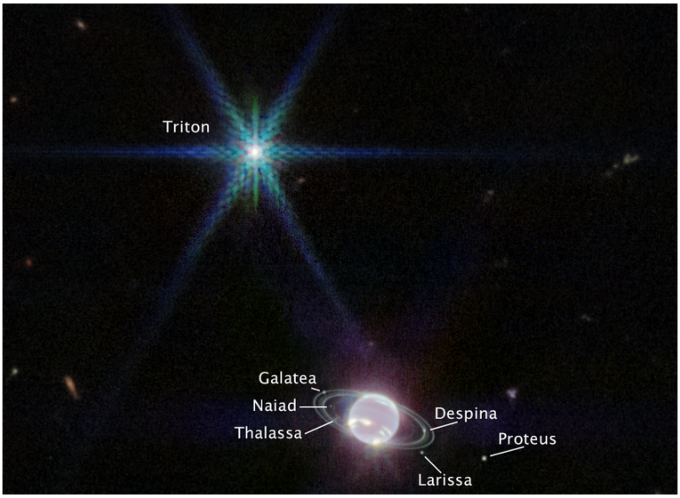

Figure 10.4.: Neptune and its moons (labelled) observed by the James Webb Space Telescope. The high inclination of Triton with respect to the rest of Neptune's moon system can be clearly observed. Courtesy: NASA, ESA, CSA, STScI.

an orbiting spacecraft furthermore remains to be investigated.

In addition to Triton, seven regular satellites are found inside Triton's orbit (Smith et al., 1989; Showalter et al., 2019). Interestingly, these satellites might not be primordial, but could have formed after Triton's capture. The circularisation of Triton's orbit is likely to have severely perturbed the orbits of Neptune's primordial regular satellites, possibly leading to their destruction through collisions and/or disruptions (e.g., Banfield and Murray, 1992; Rufu and Canup, 2017). Similarly, different explanations co-exist for the presence of the remaining six outer, irregular Neptunian satellites, found on highly eccentric and distant orbits (Holman et al., 2004): they were either captured after the circularisation of Triton's orbit (Nogueira et al., 2011) or leftovers of the chaotic, system-wide perturbations caused by Triton's capture (e.g., for Nereid, Goldreich et al., 1989; Rufu and Canup, 2017).

As just underlined, the origin and history of Neptune's satellites is still poorly understood, and a more accurate ephemerides solution would greatly help discriminate between different evolution scenarios. In particular, tighter constraints on the system's present-day dynamics are essential to investigate possible past orbital resonances, which are in turn critical to explain the system's present orbital configuration (e.g., Zhang and Hamilton, 2007, 2008; Brozović et al., 2020b). The dynamical history of the Neptunian moon system, and of past orbital resonances in particular, is moreover deeply linked to that of Neptune's ring arcs. Being able to exclude or confirm the previous crossing or capture in specific resonances via an improved solution of the moons' current orbits would thus also shed some light on the origin of such rings (e.g., Goldreich et al., 1989; De Pater et al., 2018), or on the possible formation of natural satellites from these rings (Crida and Charnoz, 2012).

The various singularities mentioned above make the Neptunian system, and more specifically its largest satellite, a fascinating mission target (e.g., Hendrix et al., 2019; Fletcher et al., 2020; Frazier et al., 2020; Hansen et al., 2021; Rymer et al., 2021). In particular, the opportunity to indirectly investigate icy dwarf planets formed in the Kuiper belt by studying Triton is especially appealing (e.g., Masters et al., 2014). Key scientific objectives of these proposed missions include a further characterisation of this moon, both as a captured KBO and candidate ocean world, as well a refined understanding of the system's thermal-orbital evolution and of interactions between Neptune's small inner satellites and the ring arcs. As highlighted in the above discussion, these open questions are deeply linked to our presently limited knowledge of the past and present dynamical state of the Neptunian moon system.

In this perspective, measurements to be collected by future missions will be invaluable to refine the ephemerides of the Neptunian satellites, currently based on Earth-based, Hubble Space Telescope, and Voyager 2 observations (Jacobson, 2009; Brozović et al., 2020b), with an accuracy ranging from several tens to hundreds of kilometres. The absence of tighter constraints on the moons' current orbits is precisely what prevents us from drawing firmer conclusions on their origin and history. Bringing the ephemerides accuracy to the kilometre level or below, which should be achievable with a dedicated mission, would translate into much refined initial conditions for critically-needed long-term dynamical simulations. Again, the methodologies developed in this dissertation for the Galilean system will help capitalising on the availability of both old astrometric observations and highly accurate radio science data to attain the best possible solution.

Expected challenges in the reconstruction of accurate ephemerides for Neptunian satellites will be of different nature than those faced in the Jovian system. While the Galilean moons' comparable masses cause significant moon-moon interactions, the dynamics of the Neptunian satellites will be, in this respect, much simpler to reconstruct. Additional difficulties will however arise from the very chaotic orbital history of this moon system, the highly perturbed orbits of Neptune's irregular satellites, and the much more limited available set of ground observations. Although the underlying causes will differ, similar inversion instabilities as those highlighted in this dissertation for the Galilean system are thus also likely to affect the ephemerides determination of the Neptunian moons. Possible mitigation strategies to stabilise the inversion developed in the JUICE-Europa Clippper context might therefore be relevant for future investigations of the Neptunian system's dynamics.

10.3. A NEW ERA FOR MOONS' EPHEMERIDES AND THEIR IMPLICATIONS

Our fascination for the icy moons of giant planets has only grown stronger and stronger since the discovery of their internal liquid water oceans, starting with Galileo's findings in the Galilean system. The coming decade will initiate a new exploration phase of these ocean worlds, with JUICE and Europa Clipper specifically targeting the Galilean satellites, while other icy satellites, now labelled as prime mission targets, await for their own dedicated mission (see Section 10.2). Unlike what was done for previous missions, whose data products could be analysed separately, this new era, with much more ground- and space-based data available, will require adopting a different analysis philosophy, relying more heavily on intra- and inter-mission synergies to maximise the science return.

At the core of our investigation of icy satellites lies the characterisation of their internal oceans' long-term stability and potential habitability, which requires a better understanding of the thermal-orbital history of these moons. This is, however, an extremely intricate problem, due to the coupling between the evolution of the moons' interiors and of their orbits, both driven by and driving tidal dissipation mechanisms. Exploiting the information contained in various data sets, and the complementarity of the different missions' foci and strengths, will thus be essential in this respect.

This work has clearly demonstrated the need for exploiting such synergies for the Galilean moons specifically, started to investigate some of them, and highlighted prioritisation avenues for the remaining candidate data sets. During the long time between launch and actually receiving JUICE and Europa Clipper's first data from the Galilean system, our focus should be on assessing the potential of merging these different data sets, and exploring new ways to extract information on the moons' orbits and interiors. Actively preparing ourselves for the data merging and dynamical modelling challenges that await is essential.

In the Jovian system and beyond, the next generation of ground- and space-based measurements, accompanied by parallel advances of our interior and dynamical models, will push back the current limits of the field. These developments offer new opportunities to further explore the link between the present state of the moons' orbits and interiors, and to better constrain their long-term thermal-orbital evolution. This will eventually revolutionise our understanding of these fascinating worlds, paving the way for future, possibly in-situ, exploration.

A

USEFUL CONIC MOTION EXPRESSIONS

This appendix provides relevant orbital motion and conic expressions used in the rest of the dissipation (in Chapter 2 and Appendix B specifically). Those are considered an input to the calculations presented in this work, and we therefore do not elaborate on the underlying derivations leading to these expressions. The interested reader is referred to Murray and Dermott (2000) or other astrodynamics textbooks.

Starting with fundamental conic motion definitions, the distance between a natural satellite and its central planet can equivalently be obtained as

$$r_i = \frac{a\left(1-e^2\right)}{1+e\cos\theta}, \tag{A.1}$$

$$r_i = a\left(1-e\cos E\right) \tag{A.2}$$

with a, e, θ, and E respectively referring to the moon's semi-major axis, eccentricity, true anomaly, and eccentricity anomaly. Consequently, the partial derivatives of r_i with respect to the true and eccentric anomalies are

$$\frac{dr}{d\theta} = \frac{ae\left(1-e^2\right)\sin\theta}{(1+e\cos\theta)^2}, \tag{A.3}$$

$$\frac{dr}{dE} = a\left(1+e\sin E\right). \tag{A.4}$$

The time derivative of r_i can moreover be expressed as

$$\dot{r}_i = nae\left(1-e^2\right)^{-\frac{1}{2}}\sin\theta. \tag{A.5}$$

The time derivative of the true anomaly θ, on the other hand, is

$$\dot{\theta} = \frac{n\left(1+e\cos\theta\right)^2}{\left(1-e^2\right)^{\frac{3}{2}}}. \tag{A.6}$$

A

As some of the calculations presented in Chapter 2 and Appendix A make use of the relations between the satellite's true, eccentric, and mean anomalies, the following partials are also particularly useful:

$$\frac{dM}{d\theta} = \frac{\left(1-e^2\right)^{\frac{3}{2}}}{(1+e\cos\theta)^2}, \tag{A.7}$$

$$\frac{d\theta}{dE} = \frac{\left(1-e^2\right)^{\frac{1}{2}}}{1-e\cos E}. \tag{A.8}$$

Furthermore, the orbital energy E_{orb} and angular momentum h are also useful quantity to define. The former is given by

$$E_{\text{orb}} = -\frac{Gm_0 m_i}{2a}, \tag{A.9}$$

and its time derivative can therefore be expressed as follows:

$$\frac{dE_{\text{orb}}}{dt} = \frac{Gm_0 m_i}{2a^2}\frac{da}{dt}. \tag{A.10}$$

The angular momentum h, on the other hand, is

$$h = \frac{Gm_0 m_i}{na}\left(1-e^2\right)^{\frac{1}{2}}, \tag{A.11}$$

leading to the following expression for the time derivative of the eccentricity:

$$\frac{de}{dt} = \frac{1-e^2}{2ae}\frac{da}{dt} - \frac{na\left(1-e^2\right)^{\frac{1}{2}}}{Gm_0 m_i e}\frac{dh}{dt}. \tag{A.12}$$

If the angular momentum is conserved, the above simplifies into:

$$\frac{de}{dt} = \frac{1-e^2}{2ae}\frac{da}{dt}. \tag{A.13}$$

Finally, the mean motion n and orbital period T are directly related, and defined as follows:

$$n = \left(\frac{G(m_0+m_i)}{a^3}\right)^{\frac{1}{2}}, \tag{A.14}$$

$$T = \frac{2\pi}{n} = 2\pi\left(\frac{a^3}{G(m_0+m_i)}\right)^{\frac{1}{2}}, \tag{A.15}$$

where m_0 and m_i designate the masses of the central planet and satellite, respectively.

B

ORBITAL ELEMENTS EVOLUTION: ADDITIONAL CALCULATIONS

As done in Section 2.3.4, the notations used in this appendix have been simplified for the sake of conciseness. By default and unless this could be a source of ambiguity, the absence of subscript and/or superscript refers to satellite-related properties. $\boldsymbol{r}$ represents the position vector of satellite i with respect to the central planet 0. Since we focus on satellite tides, Δt denotes the time lag associated with tides raised by the planet 0 on satellite i (i.e., $\Delta t_i^{(0)}$).

B.1. EFFECT OF SATELLITE TIDES ON a FROM GAUSS' PLANETARY EQUATIONS

In Section 2.3.4, we derive the secular evolution of the satellite's semi-major axis caused by satellite tides by quantifying the change in orbital and rotational energy due to dissipation. In light of the inconsistencies observed in the literature (specifically for the change in a due to satellite tides), we here take an alternative derivation route to verify the validity of the analytical results presented in Section 2.3.4. In the following, we use Gauss' form of the planetary equations to evaluate the drift in semi-major axis.

RADIAL TIDE CONTRIBUTION

Following the planetary equations, the evolution of the semi-major axis due to the radial component of the tidal force, F_r, is given by

$$\frac{da}{dt} = \frac{2}{n}\left(1-e^2\right)^{-\frac{1}{2}} e \sin\theta \frac{F_r}{m_i}. \tag{B.1}$$

From Eq. 2.73, and replacing r and $\dot{r}$ by Eq. A.1 and A.5, respectively, the radial tidal force can be re-written as

$$F_r = -9Gm_0^2 k_2 \Delta t R^5 a^{-7}\left(1-e^2\right)^{-\frac{17}{2}} n e \sin\theta \left(1+e\cos\theta\right)^8. \tag{B.2}$$

B

Substituting Eq. B.2 into Eq. B.1 and computing the average semi-major axis variation rate over one orbital period leads to the following:

$$\left|\frac{da}{dt}\right|_r = -\frac{9n}{\pi}\frac{Gm_0^2}{m_i}k_2\Delta t R^5 a^{-4}\left(1-e^2\right)^{-9}e^2\int_0^{2\pi}\sin\theta\,(1+e\cos\theta)^8\,\frac{d\theta}{dM}d\theta, \tag{B.3}$$

which after using Eq. A.7 and performing the integration gives

$$\left|\frac{da}{dt}\right|_r = -9\frac{m_0}{m_i}k_2\Delta t R^5 a^{-4}n^2e^2 + O(e^4). \tag{B.4}$$

After replacing the tidal time lag Δt by its definition in Eq. 2.42, we finally find the same expression as our previous result in Section 2.3.4 (Eq. 2.79):

$$\left|\frac{da}{dt}\right|_r = -9\frac{m_0}{m_i}\frac{k_2}{Q}\Delta t R^5 a^{-6}ne^2 + O(e^4), \tag{B.5}$$

thereby further verifying the consistency of our result.

Librational tide contribution

The planetary equations define the contribution of the tangential force component, F_t, to the change in semi-major axis as follows:

$$\frac{da_i}{dt} = \frac{2}{n}\frac{1}{r}\left(1-e^2\right)^{-\frac{1}{2}}(1+e\cos\theta)\,\frac{F_t}{m_i}. \tag{B.6}$$

Similar to what was done for the radial component, the force defining the librational tide, initially expressed as Eq. 2.81, can be expanded into

$$F_t = 3Gm_0^2k_2\Delta R^5 a^{-7}\left(1-e^2\right)^{-7}n\left[\left(1+\alpha e^2\right)-\left(1-e^2\right)^{-\frac{3}{2}}(1+e\cos\theta)^2\right](1+e\cos\theta)^7, \tag{B.7}$$

where the above is obtained by substituting r and $\dot{\theta}$ by Eq. A.1 and A.6, respectively. The satellite's rotational rate is again expressed as a function of the factor α (Eq. 2.87). Using B.7 in Eq. B.6 and averaging the change in semi-major axis over one orbital period yields

$$\begin{aligned}\left|\frac{da}{dt}\right|_t &= \frac{3}{\pi}G\frac{m_0^2}{m_i}k_2\Delta t R^5 a^{-7}\left(1-e^2\right)^{-\frac{15}{2}}\\ &\cdot\left[\left(1+\alpha e^2\right)\int_0^{2\pi}(1+e\cos\theta)^8\,\frac{d\theta}{dM}dM-\left(1-e^2\right)^{-\frac{3}{2}}\int_0^{2\pi}(1+e\cos\theta)^8\,\frac{d\theta}{dM}dM\right].\end{aligned} \tag{B.8}$$

Substituting Eq. A.7 in the above and performing the integration gives

$$\left|\frac{da}{dt}\right|_t = 3\frac{m_0}{m_i}k_2\Delta t R^5 a^{-4}n^2\left[\left(1+\alpha e^2\right)\left(2+15e^2\right)-\left(1+\frac{3}{2}e^2\right)\left(2+28e^2\right)\right]+O(e^4). \tag{B.9}$$

After some simplfications and replacing the tidal time lag Δt by Eq. 2.42, we finally arrive at the same analytical expression as the one obtained in Section 2.3.4 (Eq. 2.89):

$$\left|\frac{da}{dt}\right|_t = -6\frac{m_0}{m_i}\frac{k_2}{Q}R^5 a^{-4} n e^2 (8-\alpha) + O(e^4). \tag{B.10}$$

B

B.2. PHYSICAL LIBRATION

For the sake of clarity, we recall the modified formulation for the tidal force accounting for the once-per-orbit physical libration, γ, (Eq. 2.116):

$$\boldsymbol{F}_i^{(i)} = -\frac{3Gm_0^2 k_2^i R_i^5}{r_i^7}\left(\left(1+3\Delta t_i^{(0)}\frac{\hat{\mathbf{r}}_i\cdot\dot{\mathbf{r}}_i}{r_i}\right)\hat{\mathbf{r}}_i - \Delta t_i^{(i)}\left(1+\frac{\mathscr{A}}{2e}\right)(n_i-\dot{\theta}_i)\right). \tag{B.11}$$

The physical libration's contribution to the orbital energy dissipation caused by librational tides can thus directly be obtained from the case with no physical libration (Eq. 2.85)[1]:

$$(\Delta E_{\text{orb}})_{t,\gamma} = -24\pi G m^2 k_2 \Delta t R^5 n a^{-6}\mathscr{A} e. \tag{B.12}$$

The total amount of rotational energy dissipated by librational tides in the presence of the physical libration can furthermore be calculated as

$$(\Delta E_{\text{rot}})_t = -\int_0^{2\pi}\omega r F_t \frac{d\theta}{\dot{\theta}} \tag{B.13}$$

$$= -3Gk_2\Delta t m_0^2 R^5\left(1+\frac{\mathscr{A}}{2e}\right)\int_0^{2\pi}\left(\frac{1}{r}\right)^6\omega(n-\dot{\theta})\frac{d\theta}{\dot{\theta}}. \tag{B.14}$$

Replacing the satellite's rotation rate by Eq. 2.115 yields

$$(\Delta E_{\text{rot}})_t = -3Gk_2\Delta t m^2 R^5\left(1+\frac{\mathscr{A}}{2e}\right)\int_0^{2\pi}\left(\frac{1}{r}\right)^6\left(n+\frac{\mathscr{A}}{2e}(n-\dot{\theta})\right)(n-\dot{\theta})\frac{d\theta}{\dot{\theta}} \tag{B.15}$$

$$= -3Gk_2\Delta t m^2 R^5\left(1+\frac{\mathscr{A}}{2e}\right)\int_0^{2\pi}\left(\frac{1}{r}\right)^6\left[\left(1+\frac{\mathscr{A}}{2e}\right)\frac{n^2}{\dot{\theta}} - \left(1+\frac{\mathscr{A}}{e}\right)n + \frac{\mathscr{A}}{2e}\dot{\theta}\right]d\theta.$$

Expressing both $\dot{\theta}$ and r as function of θ using Eq. A.6 and A.1, respectively, the above becomes

$$\begin{aligned}(\Delta E_{\text{rot}})_t = {} & -3Gk_2\Delta t m^2 R^5 a^{-6}(1-e^2)^{-6}\left(1+\frac{\mathscr{A}}{2e}\right)\\ & \cdot\left[n\left(1+\frac{\mathscr{A}}{2e}\right)\left(1-\frac{3}{2}e^2\right)\int_0^{2\pi}(1+e\cos\theta)^4\,d\theta\right.\\ & \left.-n\left(1+\frac{\mathscr{A}}{e}\right)\int_0^{2\pi}(1+e\cos\theta)^6\,d\theta + \frac{\mathscr{A}}{2e}\left(1+\frac{3}{2}e^2\right)\int_0^{2\pi}(1+e\cos\theta)^8\,d\theta\right].\end{aligned} \tag{B.16}$$

[1]The derivation is analogous to the one presented in Section 2.3.4 for the no libration case.

B

After integration, we obtain

$$(\Delta E_{\mathrm{rot}})_t = -6\pi G k_2 \Delta t m^2 R^5 n a^{-6} \left(1+\frac{\mathscr{A}}{2e}\right) \cdot \left[\left(1+\frac{\mathscr{A}}{2e}\right)\left(1+\frac{3}{2}e^2\right)-\left(1+\frac{\mathscr{A}}{e}\right)\left(1+\frac{15}{2}e^2\right)+\frac{\mathscr{A}}{2e}\left(1+\frac{31}{2}e^2\right)\right]+O(e^3), \tag{B.17}$$

which after simplification gives

$$(\Delta E_{\mathrm{rot}})_t = -6\pi G k_2 \Delta t m^2 R^5 n a^{-6} \left(1+\frac{\mathscr{A}}{2e}\right)\left(-6e^2+\mathscr{A}e\right)+O(e^3) \tag{B.18}$$

$$= -6\pi G k_2 \Delta t m^2 R^5 n a^{-6} \left(-6e^2-2\mathscr{A}e+\frac{\mathscr{A}^2}{2}\right)+O(e^3). \tag{B.19}$$

Subtracting the rotational energy dissipated by librational tides for a fully synchronous satellite ($\gamma = 0$, Eq. 2.85) from the above provides the contribution of the physical libration specifically:

$$(\Delta E_{\mathrm{rot}})_{t,\gamma} = 6\pi G m^2 k_2 \Delta t R^5 n a^{-6} \left(2\mathscr{A}e-\frac{\mathscr{A}^2}{2}\right)+O(e^3). \tag{B.20}$$

The additional dissipation due to the physical libration over one orbit is finally given by

$$(\Delta E)_\gamma = (\Delta E_{\mathrm{orb}})_{t,\gamma} + (\Delta E_{\mathrm{rot}})_{t,\gamma} \tag{B.21}$$

$$= -3 G m^2 k_2 \Delta t R^5 n a^{-6}\left(4\mathscr{A}e+\mathscr{A}^2\right) \tag{B.22}$$

Recalling that the total amount of energy dissipated due to tides over one orbit in the absence of physical libration is (Eq. 2.107)

$$(\Delta E)_{\gamma=0} = -21\pi G m^2 k_2 \Delta t R^5 a^{-9} e^2, \tag{B.23}$$

the physical libration's contribution can finally be expressed as a factor of $(\Delta E)_{\gamma=0}$:

$$(\Delta E)_\gamma = \left(\frac{4}{7}\frac{\mathscr{A}}{e}+\frac{\mathscr{A}^2}{7e^2}\right)(\Delta E)_{\gamma=0}. \tag{B.24}$$

From the above derivatives, we can furthermore derive modified expressions for the secular evolution of the semi-major axis and eccentricity accounting for the physical libration effects. The semi-major axis rate is again derived from the total change in orbital energy (Eq. A.10), leading to

$$\left|\frac{da}{dt}\right|_\gamma = \left|\frac{da}{dt}\right|_{r,\gamma=0} + \left(1+\frac{\mathscr{A}}{2e}\right)\left|\frac{da}{dt}\right|_{t,\gamma=0} \tag{B.25}$$

$$= \left(-57-24\frac{\mathscr{A}}{e}\right)\frac{m_0}{m_i}\frac{k_2}{Q}R^5 a^{-4} n e^2. \tag{B.26}$$

Determining the eccentricity damping rate, on the other hand, first requires computing the angular momentum rate:

$$\left|\frac{dh}{dt}\right|_{t,\gamma} = \left(1+\frac{\mathscr{A}}{2e}\right)\left|\frac{dh}{dt}\right|_{t,\gamma=0}, \tag{B.27}$$

which similarly yields

$$\left|\frac{de}{dt}\right|_{\gamma} = \left|\frac{de}{dt}\right|_{r,\gamma=0} + \left(1+\frac{\mathscr{A}}{2e}\right)\left|\frac{de}{dt}\right|_{t,\gamma=0} \tag{B.28}$$

$$= -\left(\frac{21}{2}+\frac{9\mathscr{A}}{4e}\right)\frac{m_0}{m_i}\frac{k_2}{\Delta t}R^5 a^{-5} ne. \tag{B.29}$$

B.3. NON-ZERO S_{22} COEFFICIENT

Using Newton's third law, the force acting on the satellite due to its own S_{22} gravity coefficient is defined as (Eq. 2.14)

$$\mathbf{F}_{S_{22}} = -\frac{3}{2}Gm_0 m_i R^2 \left(\frac{1}{r}\right)^4 \left(6\bar{S}_{22}\sin(2\lambda)\hat{\boldsymbol{r}} - 4\bar{S}_{22}\cos(2\lambda)\hat{\boldsymbol{t}}\right). \tag{B.30}$$

Taking the most general formulation for the satellite's rotation accounting for both optical and physical librations 2.23, the satellite-fixed longitude of the central planet is

$$\lambda = \mathscr{B} e \sin E + O(e^2). \tag{B.31}$$

As a reminder, the amplitude $\mathscr{B}$ of the total libration angle is the sum of the optical and physical libration contributions (Eq. 2.23). $\mathscr{B}$ would therefore still be non-zero in the absence of physical libration (but then equal to -2, see Eq. 2.29).

Evaluating the effect of the satellite's S_{22} on its own orbit requires exploiting the Jacobi-Anger expansion (Weisstein, 2002a), leading to the following series expansions:

$$\sin(2\lambda) = \sin(2\mathscr{B} e \sin E) = 2\sum_{n=1}^{\infty} J_{2n-1}(2\mathscr{B} e)\sin((2n-1)E), \tag{B.32}$$

$$\cos(2\lambda) = \cos(2\mathscr{B} e \sin E) = J_0(2\mathscr{B} e) + 2\sum_{n=1}^{\infty} J_{2n}(2\mathscr{B} e)\cos(2\mathscr{B} e), \tag{B.33}$$

where J_k are Bessel functions of the first kind. Given that $2\mathscr{B} e = -4e + 2\mathscr{A} \ll 1$, use can be made of the following approximations (for $x \ll 1$):

$$J_0(x) \approx 1 - \left(\frac{x}{2}\right)^2 \tag{B.34}$$

$$J_k(x) \approx \frac{1}{k!}\left(\frac{x}{2}\right)^k. \tag{B.35}$$

Including only the terms up to e^2, Eq. B.32 and B.33 can be re-written as

$$\sin(2\lambda) = \mathscr{B} e \sin E + O(e^3) \tag{B.36}$$

$$\cos(2\lambda) = \left(1 - \mathscr{B}^2 e^2\right) + \mathscr{B}^2 e^2 \cos(2E). \tag{B.37}$$

B

Making use of the above expansions, the S_{22} force given by Eq. B.30 can be re-written as

$$\mathbf{F}_{S_{22}} = -\frac{3}{2} G m_0 m_i R^2 \left(\frac{1}{r}\right)^4 \cdot \left(6\bar{S}_{22}\mathscr{B} e \sin E \hat{\boldsymbol{r}} - 4\bar{S}_{22}\left[\left(1-\mathscr{B}^2 e^2\right) + \mathscr{B}^2 e^2 \cos(2E)\right]\hat{\boldsymbol{t}}\right) + O(e^3). \tag{B.38}$$

In the rest of this appendix, we will derive expressions for the secular drifts that a non-zero S_{22} coefficient induces in the satellite's semi-major axis and eccentricity, following a similar methodology as in Section 2.3.4.

Tangential effect

Considering Eq. B.30, the force exerted by the satellite S_{22} mostly acts in the tangential direction. The average variation in orbital energy that this tangential component induces over one orbit can be obtained as:

$$\left|\frac{dE_{\text{orb}}}{dt}\right|_t = \frac{n}{2\pi}\int_0^{2\pi} r F_t \frac{d\theta}{dE} dE, \tag{B.39}$$

which after substituting Eq. B.38, Eq. A.2, and A.8 becomes

$$\left|\frac{dE_{\text{orb}}}{dt}\right|_t = -\frac{6n}{\pi} G m_0 m_i R^2 \bar{S}_{22} a^{-3}\left(1-e^2\right)^{\frac{1}{2}} \cdot \left(1-\mathscr{B}^2 e^2\right)\int_0^{2\pi} (1-e\cos E)^{-4} dE + \mathscr{B}^2 e^2 \int_0^{2\pi} \cos(2E)\,(1-e\cos E)^{-4} dE. \tag{B.40}$$

After performing the integration and simplifying the resulting expression, we finally obtain

$$\left|\frac{dE_{\text{orb}}}{dt}\right|_t = -6nGm_0 m_i R^2 \bar{S}_{22} a^{-3}\left(1+\frac{9-\mathscr{B}}{2}e^2\right), \tag{B.41}$$

causing the following drift in semi-major axis:

$$\left|\frac{da}{dt}\right|_t = 12n\frac{R^2}{a}\bar{S}_{22}\left(1+\frac{9-\mathscr{B}}{2}e^2\right). \tag{B.42}$$

The average change in angular momentum, equivalent to the average torque exerted by the S_{22} coefficient, can further be derived as follows:

$$\left|\frac{dh}{dt}\right|_t = \frac{n}{2\pi}\int_0^{2\pi} r F_t \frac{d\theta}{\dot{\theta}}. \tag{B.43}$$

Expressing the term inside the integral as a function of the eccentric anomaly, E, instead of the true anomaly (using Eq. A.1, A.2, A.6, and A.8) eventually gives the following (after simplification):

$$\left|\frac{dh}{dt}\right|_t = \frac{3}{\pi} G m_0 m_i R^2 \bar{S}_{22} a^{-3} \cdot \left[\left(1-\mathscr{B}^2 e^2\right)\int_0^{2\pi} (1-e\cos E)^{-2} dE + \mathscr{B}^2 e^2 \int_0^{2\pi} \cos(2E) dE\right] + O(e^4). \tag{B.44}$$

Performing the integration leads to the following average S_{22} torque:

$$\left|\frac{dh}{dt}\right|_t = \Gamma_{S_{22}} = 6Gm_0 m_i R^2 \bar{S}_{22} a^{-3}\left(1 - \left(\mathscr{B} + \frac{3}{2}\right)e^2\right). \tag{B.45}$$

Using the relation between semi-major axis, eccentricity, and angular momentum, we can then derive the eccentricity drift caused by the S_{22} torque, using Eq. A.12. This eventually results in

$$\left|\frac{de}{dt}\right|_t = 6n\frac{R^2}{a^2}\bar{S}_{22} e\left(\frac{9-\mathscr{B}}{2} + \mathscr{B}^2\right). \tag{B.46}$$

RADIAL EFFECT

For the sake of completeness, we also derive the contribution of the radial component of the S_{22} force, even if its effect on the satellite's orbit is much less significant than the one acting in the tangential direction.

The orbital energy rate caused by the radial S_{22} effect is computed as

$$\left|\frac{dE_{\mathrm{orb}}}{dt}\right|_r = \frac{n}{2\pi}\int_0^{2\pi} F_r \frac{dr}{dE} dE, \tag{B.47}$$

which after substituting Eq. A.2 and A.8 becomes

$$\left|\frac{dE_{\mathrm{orb}}}{dt}\right|_r = -\frac{9n}{\pi} G m_0 m_i R^2 \bar{S}_{22} a^{-3} \mathscr{B} e \int_0^{2\pi} (1 - e\cos E)^{-4}(1 + e\sin E)\sin E dE \tag{B.48}$$

$$= -\frac{9}{n} G m_0 m_i R^2 \bar{S}_{22} a^{-3} \mathscr{B} e^2 + O(e^4). \tag{B.49}$$

The resulting secular variation of the semi-major axis can then be derived from Eq. A.10 and gives the following:

$$\left|\frac{da}{dt}\right|_r = -18n\frac{R^2}{a}\bar{S}_{22}\mathscr{B}e^2. \tag{B.50}$$

Finally, the effect on the eccentricity evolution is obtained using the conservation of the angular momentum (Eq. A.13):

$$\left|\frac{de}{dt}\right|_r = -9n\frac{R^2}{a^2}\bar{S}_{22}\mathscr{B}e. \tag{B.51}$$

As expected, the contribution of the S_{22} radial force to the semi-major axis evolution is very small with respect to that caused by the tangential forcing (Eq. B.42). In particular, the torque exerted by a non-zero S_{22} coefficient can counter-balance the residual, non-cancelling tidal torque acting on a fully synchronous satellite (see Sections 2.3.3 and 2.3.4).

Bibliography

Abbot, R. I., Shelus, P. J., Mulholland, J. D., and Silverberg, E. C. (1973). Laser observations of the Moon: Identification and construction of normal points for 1969-1971. *Astronomical Journal, Vol. 78, p. 784 (1973)*, 78:784.

Acton Jr, C. H. (1996). Ancillary data services of NASA's navigation and ancillary information facility. *Planetary and Space Science*, 44(1):65–70.

Agnor, C. B. and Hamilton, D. P. (2006). Neptune's capture of its moon Triton in a binary–planet gravitational encounter. *Nature*, 441(7090):192–194.

Aksnes, K. and Franklin, F. (1976). Mutual phenomena of the Galilean satellites in 1973. III-Final results from 91 light curves. *The Astronomical Journal*, 81:464–481.

Aksnes, K. and Franklin, F. (2001). Secular acceleration of Io derived from mutual satellite events. *The Astronomical Journal*, 122(5):2734.

Alessi, E. M., Cicalo, S., Milani, A., and Tommei, G. (2012). Desaturation manoeuvres and precise orbit determination for the BepiColombo mission. *Monthly Notices of the Royal Astronomical Society*, 423(3):2270–2278.

Anderson, J., Jacobson, R., McElrath, T., Moore, W., Schubert, G., and Thomas, P. (2001a). Shape, mean radius, gravity field, and interior structure of Callisto. *Icarus*, 153(1):157–161.

Anderson, J., Lau, E., Sjogren, W., Schubert, G., and Moore, W. (1996). Gravitational constraints on the internal structure of Ganymede. *Nature*, 384(6609):541–543.

Anderson, J., Schubert, G., Jacobson, R., Lau, E., Moore, W., and Sjogren, W. (1998). Europa's differentiated internal structure: Inferences from four Galileo encounters. *Science*, 281(5385):2019–2022.

Anderson, J. D., Jacobson, R. A., Lau, E. L., Moore, W. B., and Schubert, G. (2001b). Io's gravity field and interior structure. *Journal of Geophysical Research: Planets*, 106(E12):32963–32969.

Andreoli, F. and Zannoni, M. (2018). *Improvement of Jupiter's Satellites Ephemerides Using Stellar Occultation Observations*. PhD thesis, Master's thesis. University of Bologna.

Antreasian, P., Ardalan, S., Criddle, K., Ionasescu, R., Jacobson, R., Jones, J., MacKenzie, R., Parcher, D., Pelletier, F., Roth, D., et al. (2008). Orbit determination processes for the navigation of the Cassini-Huygens mission. In *SpaceOps 2008 conference*, page 3433.

Archinal, B., Acton, C., A'hearn, M., Conrad, A., Consolmagno, G., Duxbury, T., Hestroffer, D., Hilton, J., Kirk, R. L., Klioner, S., et al. (2018). Report of the IAU working group on cartographic coordinates and rotational elements: 2015. *Celestial Mechanics and Dynamical Astronomy*, 130:1–46.

Arlot, J. (2019). Four centuries of observations of the Galilean satellites of Jupiter: increasing the astrometric accuracy. *Journal of Astronomical History and Heritage*, 22:78–92.

Arlot, J.-E., Bernard, A., Merlin, P., Bouchet, P., Daguillon, J., Dourneau, G., Figer, A., Helmer, G., Meyer, C., Lecacheux, J., et al. (1982). The results of the PHEMU79 observations of phenomena common to Galilean satellites of Jupiter in 1979. *Astronomy and Astrophysics, vol. 111, no. 1, July 1982, p. 151-170. In French.*, 111:151–170.

Arlot, J.-E. and Emelyanov, N. (2019). Natural satellites mutual phenomena observations: achievements and future. *Planetary and Space Science*, 169:70–77.

Arlot, J.-E., Emelyanov, N., Varfolomeev, M., Amossé, A., Arena, C., Assafin, M., Barbieri, L., Bolzoni, S., Bragas-Ribas, F., Camargo, J., et al. (2014). The PHEMU09 catalogue and astrometric results of the observations of the mutual occultations and eclipses of the Galilean satellites of Jupiter made in 2009. *Astronomy & Astrophysics*, 572:A120.

Arlot, J.-E., Lainey, V., and Thuillot, W. (2006a). Predictions of the mutual events of the Uranian satellites occurring in 2006–2009. *Astronomy & Astrophysics*, 456(3):1173–1179.

Arlot, J.-E., Thuillot, W., Ruatti, C., Akasawa, H., Baroni, S., Beisker, W., Berthier, J., Blanco, C., Boonstra, J., Bourgeois, J., et al. (2006b). The PHEMU97 catalogue of observations of the mutual phenomena of the Galilean satellites of Jupiter. *Astronomy & Astrophysics*, 451(2):733–737.

Asmar, S., Armstrong, J., Iess, L., and Tortora, P. (2005). Spacecraft Doppler tracking: Noise budget and accuracy achievable in precision radio science observations. *Radio Science*, 40(2):1–9.

Bagheri, A., Khan, A., Efroimsky, M., Kruglyakov, M., and Giardini, D. (2021). Dynamical evidence for Phobos and Deimos as remnants of a disrupted common progenitor. *Nature Astronomy*, 5(6):539–543.

Baland, R.-M., Yseboodt, M., and Van Hoolst, T. (2012). Obliquity of the Galilean satellites: The influence of a global internal liquid layer. *Icarus*, 220(2):435–448.

Baland, R.-M., Yseboodt, M., and Van Hoolst, T. (2016). The obliquity of Enceladus. *Icarus*, 268:12–31.

Banfield, D. and Murray, N. (1992). A dynamical history of the inner Neptunian satellites. *Icarus*, 99(2):390–401.

Barnes, J. W., Turtle, E. P., Trainer, M. G., Lorenz, R. D., MacKenzie, S. M., Brinckerhoff, W. B., Cable, M. L., Ernst, C. M., Freissinet, C., Hand, K. P., et al. (2021). Science goals and objectives for the Dragonfly Titan rotorcraft relocatable lander. *The Planetary Science Journal*, 2(4):130.

Beddingfield, C., Burr, D., and Emery, J. (2015). Fault geometries on Uranus' satellite Miranda: Implications for internal structure and heat flow. *Icarus*, 247:35–52.

Běhounková, M., Tobie, G., Choblet, G., Kervazo, M., Melwani Daswani, M., Dumoulin, C., and Vance, S. D. (2021). Tidally induced magmatic pulses on the oceanic floor of Jupiter's moon Europa. *Geophysical Research Letters*, 48(3):e2020GL090077.

Bellerose, J., Nandi, S., Roth, D., Tarzi, Z., Boone, D., Criddle, K., and Ionasescu, R. (2016). Cassini Navigation: The Road to Consistent Subkilometer Accuracy Satellite Encounters. In *AAS Annual Guidance and Control Conference*, number AAS 16-142.

Bertone, S., Mazarico, E., Barker, M., Goossens, S., Sabaka, T., Neumann, G., and Smith, D. E. (2021). Deriving Mercury geodetic parameters with altimetric crossovers from the Mercury Laser Altimeter (MLA). *Journal of Geophysical Research: Planets*, 126(4):e2020JE006683.

Beuthe, M. (2016). Crustal control of dissipative ocean tides in Enceladus and other icy moons. *Icarus*, 280:278–299.

Beuthe, M. (2019). Enceladus's crust as a non-uniform thin shell: II tidal dissipation. *Icarus*, 332:66–91.

Bierson, C. J. and Nimmo, F. (2022). A note on the possibility of subsurface oceans on the uranian satellites. *Icarus*, 373:114776.

Blanc, M., Prieto-Ballesteros, O., André, N., Gomez-Elvira, J., Jones, G., Sterken, V., Desprats, W., Gurvits, L. I., Khurana, K., Balmino, G., et al. (2021). Joint Europa Mission (JEM): A Multiscale, Multi-Platform Mission to Characterize Europa's Habitability and Search for Extant Life. A White Paper prepared for the NAS 2023-2032 Decadal Survey for Planetary Science and Astrobiology August 15th, 2020. *Bulletin of the American Astronomical Society*, 53(4):e–id.

Bland, M. T., Showman, A. P., and Tobie, G. (2009). The orbital–thermal evolution and global expansion of Ganymede. *Icarus*, 200(1):207–221.

Bocanegra Bahamon, T. (2019). Planetary Radio Interferometry and Doppler Experiment (PRIDE) for radio occultation studies; A Venus Express test case. *Ph. D. Thesis.*

Bocanegra-Bahamón, T., Calvés, G. M., Gurvits, L., Cimò, G., Dirkx, D., Duev, D., Pogrebenko, S., Rosenblatt, P., Limaye, S., Cui, L., et al. (2019). Venus Express radio occultation observed by PRIDE. *Astronomy & Astrophysics*, 624:A59.

Bocanegra-Bahamón, T., Calvés, G. M., Gurvits, L., Duev, D., Pogrebenko, S., Cimò, G., Dirkx, D., and Rosenblatt, P. (2018). Planetary radio interferometry and Doppler experiment (PRIDE) technique: a test case of the mars express phobos flyby-II. Doppler tracking: formulation of observed and computed values, and noise budget. *Astronomy & Astrophysics*, 609:A59.

Bolton, S. J., Adriani, A., Adumitroaie, V., Allison, M., Anderson, J., Atreya, S., Bloxham, J., Brown, S., Connerney, J., DeJong, E., et al. (2017). Jupiter's interior and deep atmosphere: The initial pole-to-pole passes with the Juno spacecraft. *Science*, 356(6340):821–825.

Boone, D., Bellerose, J., and Roth, D. (2017). Resolution of orbit determination prediction instabilities at titan during cassini's solstice mission. In *26th International Symposium on Space Fight Dynamics, Matsuyama, Japan.*

Borderies, N. and Yoder, C. (1990). Phobos' gravity field and its influence on its orbit and physical librations. *Astronomy and Astrophysics (ISSN 0004-6361), vol. 233, no. 1, July 1990, p. 235-251.*, 233:235–251.

Boué, G., Correia, A. C., and Laskar, J. (2016). Complete spin and orbital evolution of close-in bodies using a Maxwell viscoelastic rheology. *Celestial Mechanics and Dynamical Astronomy*, 126:31–60.

Boué, G. and Efroimsky, M. (2019). Tidal evolution of the Keplerian elements. *Celestial Mechanics and Dynamical Astronomy*, 131:1–46.

Boué, G. and Laskar, J. (2010). A collisionless scenario for Uranus tilting. *The Astrophysical Journal Letters*, 712(1):L44.

Brown, A., Vallenari, A., Prusti, T., De Bruijne, J., Babusiaux, C., Bailer-Jones, C., Biermann, M., Evans, D. W., Eyer, L., Jansen, F., et al. (2018). Gaia data release 2-summary of the contents and survey properties. *Astronomy & astrophysics*, 616:A1.

Brown, A. G., Vallenari, A., Prusti, T., De Bruijne, J., Babusiaux, C., Biermann, M., Creevey, O., Evans, D., Eyer, L., Hutton, A., et al. (2021). Gaia early data release 3-summary of the contents and survey properties. *Astronomy & Astrophysics*, 649:A1.

Brozović, M. and Jacobson, R. A. (2022). Orbits of the Irregular Satellites of Uranus and Neptune. *The Astronomical Journal*, 163(5):241.

Brozović, M., Nolan, M. C., Magri, C., Folkner, W. M., Jacobson, R. A., Harcke, L. J., McMichael, J. G., Richardson, J. E., Harmon, J. K., Taylor, P. A., et al.

(2020a). Arecibo Radar Astrometry of the Galilean Satellites from 1999 to 2016. *The Astronomical Journal*, 159(4):149.

Brozović, M., Showalter, M. R., Jacobson, R. A., French, R. S., Lissauer, J. J., and de Pater, I. (2020b). Orbits and resonances of the regular moons of Neptune. *Icarus*, 338:113462.

Bruzzone, L. et al. (2024). RIME. *To be submitted to Space Science Reviews.*

Burns, J. A. (1978). The dynamical evolution and origin of the Martian moons. *Vistas in Astronomy*, 22:193–210.

Canup, R. M. and Ward, W. R. (2002). Formation of the Galilean satellites: Conditions of accretion. *The Astronomical Journal*, 124(6):3404.

Canup, R. M. and Ward, W. R. (2009). Origin of Europa and the Galilean satellites. *Europa*, pages 59–83.

Cappuccio, P., Di Benedetto, M., Durante, D., and Iess, L. (2022). Callisto and Europa Gravity Measurements from JUICE 3GM Experiment Simulation. *The Planetary Science Journal*, 3(8):199.

Cappuccio, P., Hickey, A., Durante, D., Di Benedetto, M., Iess, L., De Marchi, F., Plainaki, C., Milillo, A., and Mura, A. (2020a). Ganymede's gravity, tides and rotational state from JUICE's 3GM experiment simulation. *Planetary and Space Science*, 187:104902.

Cappuccio, P., Notaro, V., di Ruscio, A., Iess, L., Genova, A., Durante, D., di Stefano, I., Asmar, S. W., Ciarcia, S., and Simone, L. (2020b). Report on first inflight data of BepiColombo's Mercury orbiter radio science experiment. *IEEE Transactions on Aerospace and Electronic Systems*, 56(6):4984–4988.

Cartwright, R. J., Beddingfield, C. B., Nordheim, T. A., Elder, C. M., Castillo-Rogez, J. C., Neveu, M., Bramson, A. M., Sori, M. M., Buratti, B. J., Pappalardo, R. T., et al. (2021). The science case for spacecraft exploration of the Uranian satellites: Candidate ocean worlds in an ice giant system. *The Planetary Science Journal*, 2(3):120.

Castillo-Rogez, J., Hemingway, D., Rhoden, A., Tobie, G., and McKinnon, W. (2018). Origin and evolution of Saturn's mid-sized moons. *Enceladus and the Icy Moons of Saturn*, pages 285–306.

Castillo-Rogez, J., Weiss, B., Beddingfield, C., Biersteker, J., Cartwright, R., Goode, A., Melwani Daswani, M., and Neveu, M. (2023). Compositions and interior structures of the large moons of Uranus and implications for future spacecraft observations. *Journal of Geophysical Research: Planets*, 128(1):e2022JE007432.

Celletti, A., Karampotsiou, E., Lhotka, C., Pucacco, G., and Volpi, M. (2022). The Role of Tidal Forces in the Long-term Evolution of the Galilean System. *Regular and Chaotic Dynamics*, 27(4):381–408.

Charlot, P., Jacobs, C., Gordon, D., Lambert, S., de Witt, A., Böhm, J., Fey, A., Heinkelmann, R., Skurikhina, E., Titov, O., et al. (2020). The third realization of the International Celestial Reference Frame by very long baseline interferometry. *Astronomy & Astrophysics*, 644:A159.

Charnoz, S., Crida, A., Castillo-Rogez, J. C., Lainey, V., Dones, L., Karatekin, Ö., Tobie, G., Mathis, S., Le Poncin-Lafitte, C., and Salmon, J. (2011). Accretion of Saturn's mid-sized moons during the viscous spreading of young massive rings: Solving the paradox of silicate-poor rings versus silicate-rich moons. *Icarus*, 216(2):535–550.

Chen, E. and Nimmo, F. (2011). Obliquity tides do not significantly heat Enceladus. *Icarus*, 214(2):779–781.

Chen, E., Nimmo, F., and Glatzmaier, G. A. (2014). Tidal heating in icy satellite oceans. *Icarus*, 229:11–30.

Choblet, G., Tobie, G., Buch, A., Čadek, O., Barge, L. M., Běhounková, M., Camprubi, E., Freissinet, C., Hedman, M., Jones, G., et al. (2021). Enceladus as a potential oasis for life: Science goals and investigations for future explorations. *Experimental Astronomy*, pages 1–39.

Choblet, G., Tobie, G., Sotin, C., Běhounková, M., Čadek, O., Postberg, F., and Souček, O. (2017). Powering prolonged hydrothermal activity inside Enceladus. *Nature Astronomy*, 1(12):841–847.

Colombo, G., Franklin, F., and Shapiro, I. (1974). On the formation of the orbit-orbit resonance of Titan and Hyperion. *Astronomical Journal, Vol. 79, p. 61 (1974)*, 79:61.

Combrinck, L. (2012). General relativity and space geodesy. In *Sciences of Geodesy-II: Innovations and Future Developments*, pages 53–95. Springer.

Connerney, J., Timmins, S., Oliversen, R., Espley, J., Joergensen, J., Kotsiaros, S., Joergensen, P., Merayo, J., Herceg, M., Bloxham, J., et al. (2022). A new model of Jupiter's magnetic field at the completion of Juno's Prime Mission. *Journal of Geophysical Research: Planets*, 127(2):e2021JE007055.

Correia, A. C. (2009). Secular evolution of a satellite by tidal effect: application to Triton. *The Astrophysical Journal*, 704(1):L1.

Crida, A. and Charnoz, S. (2012). Formation of regular satellites from ancient massive rings in the solar system. *Science*, 338(6111):1196–1199.

Ćuk, M., Dones, L., and Nesvornỳ, D. (2016). Dynamical evidence for a late formation of Saturn's moons. *The Astrophysical Journal*, 820(2):97.

Ćuk, M., El Moutamid, M., and Tiscareno, M. S. (2020). Dynamical history of the Uranian system. *The Planetary Science Journal*, 1(1):22.

Curkendall, D. W. and Border, J. S. (2013). Delta-DOR: The one-nanoradian navigation measurement system of the deep space network—History, architecture, and componentry. *The Interplanetary Network Progress Report*, 42:193.

Davis, M. W., Gladstone, G. R., Retherford, K. D., and Persyn, S. C. (2021). The JUICE ultraviolet spectrograph: a next-generation compact UVS for ESA's JUICE mission. In *International Conference on Space Optics—ICSO 2020*, volume 11852, pages 919–929. SPIE.

Dbouk, R. and Wisdom, J. (2023). The Origin of Jupiter's Obliquity. *The Planetary Science Journal*, 4(10):188.

De Filippis, U., Lefevre, C., Lucente, M., Magnafico, C., Santoli, F., Cappuccio, P., di Stefano, I., Zurria, A., and Iess, L. (2024). Pseudo-Drag-Free System Simulation for Bepicolombo Radio Science Using Accelerometer Data. *Journal of Guidance, Control, and Dynamics*, pages 1–12.

De Marchi, F., Cappuccio, P., Mitri, G., and Iess, L. (2022). Frequency-dependent Ganymede's tidal Love number k2 detection by JUICE's 3GM experiment and implications for the subsurface ocean thickness. *Icarus*, 386:115150.

De Marchi, F., Di Achille, G., Mitri, G., Cappuccio, P., Di Stefano, I., Di Benedetto, M., and Iess, L. (2021). Observability of Ganymede's gravity anomalies related to surface features by the 3GM experiment onboard ESA's JUpiter ICy moons Explorer (JUICE) mission. *Icarus*, 354:114003.

De Pater, I., Renner, S., Showalter, M., Sicardy, B., Tiscareno, M., and Murray, C. (2018). Planetary Ring Systems. *Properties, Structure, and Evolution.*

De Sitter, W. (1931). Jupiter's Galilean satellites (George Darwin Lecture). *Monthly Notices of the Royal Astronomical Society, Vol. 91, p. 706-738*, 91:706–738.

Decadal strategy survey (2022). Origins, worlds, and life: a decadal strategy for planetary science and astrobiology 2023-2032. *National Academies of Sciences, Engineering, and Medicine and others.*

Dehant, V. and Mathews, P. M. (2015). *Precession, nutation and wobble of the Earth*. Cambridge University Press.

Deienno, R., Nesvorný, D., Vokrouhlický, D., and Yokoyama, T. (2014). Orbital perturbations of the Galilean satellites during planetary encounters. *The Astronomical Journal*, 148(2):25.

Dermott, S. F., Malhotra, R., and Murray, C. D. (1988). Dynamics of the Uranian and Saturnian satelite systems: A chaotic route to melting Miranda? *Icarus*, 76(2):295–334.

Desmars, J., Arlot, S., Arlot, J.-E., Lainey, V., and Vienne, A. (2009). Estimating the accuracy of satellite ephemerides using the bootstrap method. *Astronomy & Astrophysics*, 499(1):321–330.

Di Benedetto, M., Cappuccio, P., Molli, S., Federici, L., and Zavoli, A. (2021). Analysis of 3GM Callisto Gravity Experiment of the JUICE Mission. *arXiv preprint arXiv:2101.03401*.

Di Ruscio, A. (2021). *Use of radio science and navigation data for the construction of planetary ephemerides*. PhD thesis, Université Côte d'Azur; Università degli studi La Sapienza (Rome).

Di Ruscio, A., Fienga, A., Durante, D., Iess, L., Laskar, J., and Gastineau, M. (2020). Analysis of Cassini radio tracking data for the construction of INPOP19a: A new estimate of the Kuiper belt mass. *Astronomy & Astrophysics*, 640:A7.

di Stefano, I., Cappuccio, P., and Iess, L. (2023). Precise Modeling of Non-Gravitational Accelerations of the Spacecraft BepiColombo During Cruise Phase. *Journal of Spacecraft and Rockets*, 60(5):1625–1638.

Dias-Oliveira, A., Vieira-Martins, R., Assafin, M., Camargo, J., Braga-Ribas, F., da Silva Neto, D., Gaspar, H., Pires dos Santos, P., Domingos, R., Boldrin, L., et al. (2013). Analysis of 25 mutual eclipses and occultations between the Galilean satellites observed from Brazil in 2009. *Monthly Notices of the Royal Astronomical Society*, 432(1):225–242.

Dirkx, D., Gurvits, L. I., Lainey, V., Lari, G., Milani, A., Cimò, G., Bocanegra-Bahamon, T., and Visser, P. N. (2017). On the contribution of PRIDE-JUICE to Jovian system ephemerides. *Planetary and Space Science*, 147:14–27.

Dirkx, D., Lainey, V., Gurvits, L., and Visser, P. (2016). Dynamical modelling of the Galilean moons for the JUICE mission. *Planetary and Space Science*, 134:82–95.

Dirkx, D., Mooij, E., and Root, B. (2019a). Propagation and estimation of the dynamical behaviour of gravitationally interacting rigid bodies. *Astrophysics and Space Science*, 364:1–22.

Dirkx, D., Prochazka, I., Bauer, S., Visser, P., Noomen, R., Gurvits, L. I., and Vermeersen, B. (2019b). Laser and radio tracking for planetary science missions—a comparison. *Journal of Geodesy*, 93(11):2405–2420.

Dirkx, D., Vermeersen, L., Noomen, R., and Visser, P. (2014). Phobos laser ranging: Numerical Geodesy experiments for Martian system science. *Planetary and Space Science*, 99:84–102.

Dougherty, M. et al. (2024). J-MAG. *To be submitted to Space Science Reviews.*

Downey, B. G., Nimmo, F., and Matsuyama, I. (2020). Inclination damping on Callisto. *Monthly Notices of the Royal Astronomical Society*, 499(1):40–51.

Duev, D. A., Calvés, G. M., Pogrebenko, S. V., Gurvits, L. I., Cimo, G., and Bahamon, T. B. (2012). Spacecraft VLBI and Doppler tracking: algorithms and implementation. *Astronomy & Astrophysics*, 541:A43.

Duev, D. A., Pogrebenko, S. V., Cimò, G., Calvés, G. M., Bahamón, T. B., Gurvits, L. I., Kettenis, M. M., Kania, J., Tudose, V., Rosenblatt, P., et al. (2016). Planetary Radio Interferometry and Doppler Experiment (PRIDE) technique: A test case of the Mars Express Phobos fly-by. *Astronomy & Astrophysics*, 593:A34.

Durante, D., Guillot, T., Iess, L., Stevenson, D. J., Mankovich, C. R., Markham, S., Galanti, E., Kaspi, Y., Zannoni, M., Gomez Casajus, L., et al. (2022). Juno spacecraft gravity measurements provide evidence for normal modes of Jupiter. *Nature communications*, 13(1):4632.

Durante, D., Hemingway, D., Racioppa, P., Iess, L., and Stevenson, D. (2019). Titan's gravity field and interior structure after Cassini. *Icarus*, 326:123–132.

Durante, D., Parisi, M., Serra, D., Zannoni, M., Notaro, V., Racioppa, P., Buccino, D., Lari, G., Gomez Casajus, L., Iess, L., et al. (2020). Jupiter's gravity field halfway through the Juno mission. *Geophysical Research Letters*, 47(4):e2019GL086572.

Efroimsky, M. (2018). Dissipation in a tidally perturbed body librating in longitude. *Icarus*, 306:328–354.

Efroimsky, M. and Lainey, V. (2007). Physics of bodily tides in terrestrial planets and the appropriate scales of dynamical evolution. *Journal of Geophysical Research: Planets*, 112(E12).

Efroimsky, M. and Makarov, V. V. (2013). Tidal friction and tidal lagging. Applicability limitations of a popular formula for the tidal torque. *The Astrophysical Journal*, 764(1):26.

Efroimsky, M. and Makarov, V. V. (2014). Tidal dissipation in a homogeneous spherical body. I. Methods. *The Astrophysical Journal*, 795(1):6.

Efroimsky, M. and Williams, J. G. (2009). Tidal torques: a critical review of some techniques. *Celestial Mechanics and Dynamical Astronomy*, 104:257–289.

Emelyanov, N. (2017). Precision of natural satellite ephemerides from observations of different types. *Monthly Notices of the Royal Astronomical Society*, 469(4):4889–4898.

Emelyanov, N. (2018). Influence of tides in viscoelastic bodies of planet and satellite on the satellite's orbital motion. *Monthly Notices of the Royal Astronomical Society*, 479(1):1278–1286.

Emelyanov, N. (2021). 5 - Observations of planetary satellites. In *The Dynamics of Natural Satellites of the Planets*, pages 173–200. Elsevier.

Emelyanov, N., Arlot, J., Anbazhagan, P., André, P., Bardecker, J., Canaud, G., Coliac, J., De Elias Cantalapiedra, J., Ellington, C., Fernandez, J., et al. (2022). The PHEMU21 catalogue and astrometric results of the observations of the mutual occultations and eclipses of the Galilean satellites of Jupiter made in 2021. *Monthly Notices of the Royal Astronomical Society*, 516(3):3685–3691.

Emelyanov, N. and Nikonchuk, D. (2013). Ephemerides of the main Uranian satellites. *Monthly Notices of the Royal Astronomical Society*, 436(4):3668–3679.

Emelyanov, N. V. (2009). Mutual occultations and eclipses of the Galilean satellites of Jupiter in 2002–2003: final astrometric results. *Monthly Notices of the Royal Astronomical Society*, 394(2):1037–1044.

Emelyanov, N. V., Andreev, M., Berezhnoi, A., Bekhteva, A., Vashkovyak, S., Velikodskii, Y. I., Vereshchagina, I., Gorshanov, D., Devyatkin, A., Izmailov, I., et al. (2011). Astrometric results of observations at Russian observatories of mutual occultations and eclipses of Jupiter's Galilean satellites in 2009. *Solar System Research*, 45:264–277.

Ermakov, A. I., Park, R. S., Roa, J., Castillo-Rogez, J. C., Keane, J. T., Nimmo, F., Kite, E. S., Sotin, C., Lazio, T. J. W., Steinbrügge, G., et al. (2021). A recipe for the geophysical exploration of Enceladus. *The Planetary Science Journal*, 2(4):157.

ESOC (2017–2019). JUICE: Navigation Analysis of the Jupiter Tour. Technical Report v1.1–v2.2, ESA.

Evans, S., Taber, W., Drain, T., Smith, J., Wu, H.-C., Guevara, M., Sunseri, R., and Evans, J. (2018). MONTE: the next generation of mission design and navigation software. *CEAS Space Journal*, 10:79–86.

Fayolle, M., Dirkx, D., Cimo, G., Gurvits, L. I., Lainey, V., and Visser, P. N. (2024). Contribution of PRIDE VLBI products to the joint JUICE-Europa Clipper moons' ephemerides solution. *Icarus*, under revision.

Fayolle, M., Dirkx, D., Lainey, V., Gurvits, L., and Visser, P. (2022). Decoupled and coupled moons' ephemerides estimation strategies application to the JUICE mission. *Planetary and Space Science*, 219:105531.

Fayolle, M., Dirkx, D., Visser, P., and Lainey, V. (2021). Analytical framework for mutual approximations-Derivation and application to Jovian satellites. *Astronomy & Astrophysics*, 652:A93.

Fayolle, M., Lainey, V., Dirkx, D., Gurvits, L. I., Cimo, G., and Bolton, S. (2023a). Spacecraft VLBI tracking to enhance stellar occultations astrometry of planetary satellites. *Astronomy & Astrophysics*, 676:L6.

Fayolle, M., Magnanini, A., Lainey, V., Dirkx, D., Zannoni, M., and Tortora, P. (2023b). Combining astrometry and JUICE–Europa Clipper radio science to improve the ephemerides of the Galilean moons. *A&A*, 677:A42.

Fienga, A., Deram, P., Di Ruscio, A., Viswanathan, V., Camargo, J., Bernus, L., Gastineau, M., and Laskar, J. (2021a). INPOP19a planetary ephemerides.

Fienga, A., Deram, P., Di Ruscio, A., Viswanathan, V., Camargo, J., Bernus, L., Gastineau, M., and Laskar, J. (2021b). INPOP21a planetary ephemerides.

Filice, V., Le Maistre, S., Baland, R.-M., Cascioli, G., Mazarico, E., and Goossens, S. J. (2024). Exploring the Uranian system with the Uranus Orbiter & Probe Radio Science experiment: expected performance and possible enhancements. *Authorea Preprints*.

Filice, V., Le Maistre, S., Dehant, V., and Van Hoolst, T. (2023). How well can we measure io's librations, tides and obliquity from the upcoming juno flybys? *Poster presentation, Origins and Habitability of the Galilean Moons workshop*.

Fischer, H.-J. and Spohn, T. (1990). Thermal-orbital histories of viscoelastic models of Io (J1). *Icarus*, 83(1):39–65.

Fletcher, L. N., Helled, R., Roussos, E., Jones, G., Charnoz, S., André, N., Andrews, D., Bannister, M., Bunce, E., Cavalié, T., et al. (2020). Ice Giant Systems: The scientific potential of orbital missions to Uranus and Neptune. *Planetary and Space Science*, 191:105030.

Floberghagen, R. (2001). The Far Side: Lunar Gravimetry into the Third Millenium.

Fomalont, E., Martin-Mur, T., Border, J., Naudet, C., Lanyi, G., Romney, J., Dhawan, V., and Geldzahler, B. (2010). Spacecraft navigation using the VLBA. In *10th European VLBI Network Symposium and EVN Users Meeting: VLBI and the new generation of radio arrays*, volume 10, page 66.

Frazier, W., Bearden, D., Mitchell, K. L., Lam, T., Prockter, L., and Dissly, R. (2020). Trident: The Path to Triton on a Discovery Budget. In *2020 IEEE Aerospace Conference*, pages 1–12. IEEE.

French, R. G. and Souami, D. (2023). Earth-based Stellar Occultation Predictions for

Jupiter, Saturn, Uranus, Neptune, Titan, and Triton: 2023–2050. *The Planetary Science Journal*, 4(11):202.

Fuller, J., Luan, J., and Quataert, E. (2016). Resonance locking as the source of rapid tidal migration in the Jupiter and Saturn moon systems. *Monthly Notices of the Royal Astronomical Society*, 458(4):3867–3879.

Gaia, C., Brown, A., Vallenari, A., Prusti, T., De Bruijne, J., Babusiaux, C., Juhász, Á., Marschalkó, G., Marton, G., Molnár, L., et al. (2018). Gaia Data Release 2 Summary of the contents and survey properties. *Astronomy & Astrophysics*, 616(1).

Genova, A., Hussmann, H., Van Hoolst, T., Heyner, D., Iess, L., Santoli, F., Thomas, N., Cappuccio, P., Di Stefano, I., Kolhey, P., et al. (2021). Geodesy, geophysics and fundamental physics investigations of the BepiColombo mission. *Space science reviews*, 217(2):31.

Genova, A., Parisi, M., Gargiulo, A. M., Petricca, F., Andolfo, S., Torrini, T., Del Vecchio, E., Glein, C. R., Cable, M. L., Phillips, C. B., et al. (2024). Gravity Investigation to Characterize Enceladus's Ocean and Interior. *The Planetary Science Journal*, 5(2):40.

Gill, E. and Montenbruck, O. (2013). *Satellite orbits: Models, methods and applications*. Springer.

Goldreich, P., Murray, N., Longaretti, P., and Banfield, D. (1989). Neptune's story. *Science*, 245(4917):500–504.

Goldreich, P. and Peale, S. (1966). Spin-orbit coupling in the solar system. *Astronomical Journal, Vol. 71, p. 425 (1966)*, 71:425.

Goldreich, P. and Soter, S. (1966). Q in the Solar System. *Icarus*, 5(1-6):375–389.

Gomes, S. R. and Correia, A. C. (2023). Effect of the inclination in the passage through the 5/3 mean motion resonance between Ariel and Umbriel. *Astronomy & Astrophysics*, 674:A111.

Gomez Casajus, L., Ermakov, A., Zannoni, M., Keane, J., Stevenson, D., Buccino, D., Durante, D., Parisi, M., Park, R., Tortora, P., et al. (2022). Gravity Field of Ganymede after the Juno Extended Mission. *Geophysical Research Letters*, 49(24):e2022GL099475.

Gomez Casajus, L., Zannoni, M., Modenini, D., Tortora, P., Nimmo, F., Van Hoolst, T., Buccino, D., and Oudrhiri, K. (2021). Updated Europa gravity field and interior structure from a reanalysis of Galileo tracking data. *Icarus*, 358:114187.

Goossens, S., Genova, A., James, P. B., and Mazarico, E. (2022). Estimation of crust and lithospheric properties for Mercury from high-resolution gravity and topography. *The Planetary Science Journal*, 3(6):145.

Goossens, S., van Noort, B., Mateo Aguaron, A., Mazarico, E., and van der Wal, W. (2023). Enceladus Gravity and Titan Gravity and Tides from Cassini Tracking Data. *LPI Contributions*, 2806:1528.

Grasset, O., Dougherty, M., Coustenis, A., Bunce, E., Erd, C., Titov, D., Blanc, M., Coates, A., Drossart, P., Fletcher, L., et al. (2013). JUpiter ICy moons Explorer (JUICE): An ESA mission to orbit Ganymede and to characterise the Jupiter system. *Planetary and Space Science*, 78:1–21.

Green, A., Elder, C., Bland, M., Tackley, P., and Byrne, P. (2024). No Magmatic Driving Force for Europan Seafloor Volcanism. *LPI Contributions*, 3040:1481.

Greenberg, R. (1987). Galilean satellites: Evolutionary paths in deep resonance. *Icarus*, 70(2):334–347.

Greenberg, R. (2010). The icy Jovian satellites after the Galileo mission. *Reports on Progress in Physics*, 73(3):036801.

Greenberg, R., Geissler, P., Hoppa, G., Tufts, B. R., Durda, D. D., Pappalardo, R., Head, J. W., Greeley, R., Sullivan, R., and Carr, M. H. (1998). Tectonic processes on Europa: Tidal stresses, mechanical response, and visible features. *Icarus*, 135(1):64–78.

Gurvits, L., Bahamon, B., Cimò, G., Duev, D., Molera Calvés, G., Pogrebenko, S., De Pater, I., Vermeersen, L., Rosenblatt, P., Oberst, J., et al. (2013). Planetary radio interferometry and Doppler experiment (PRIDE) for the JUICE mission. In *European Planetary Science Congress*, pages EPSC2013–357.

Gurvits, L. I., Cimò, G., Dirkx, D., Pallichadath, V., Akins, A., Altobelli, N., Bocanegra-Bahamon, T. M., Cazaux, S. M., Charlot, P., Duev, D. A., et al. (2023). Planetary Radio Interferometry and Doppler Experiment (PRIDE) of the JUICE mission. *Space Science Reviews*, 219(8):79.

Hand, K. P., Phillips, C. B., Murray, A., Garvin, J., Maize, E., Gibbs, R., Reeves, G., San Martin, A., Tan-Wang, G., Krajewski, J., et al. (2022). Science goals and mission architecture of the Europa lander mission concept. *The Planetary Science Journal*, 3(1):22.

Hansen, C., Bolton, S., Sulaiman, A., Duling, S., Bagenal, F., Brennan, M., Connerney, J., Clark, G., Lunine, J., Levin, S., et al. (2022). Juno's close encounter with Ganymede—an overview. *Geophysical Research Letters*, 49(23):e2022GL099285.

Hansen, C. J., Bolton, S. J., Matson, D. L., Spilker, L. J., and Lebreton, J.-P. (2004). The Cassini–Huygens flyby of Jupiter. *Icarus*, 172(1):1–8.

Hansen, C. J., Castillo-Rogez, J., Grundy, W., Hofgartner, J., Martin, E., Mitchell, K., Nimmo, F., Nordheim, T., Paty, C., Quick, L. C., et al. (2021). Triton: fascinating moon, likely ocean world, compelling destination! *The Planetary Science Journal*, 2(4):137.

Haw, R., Antreasian, P., McElrath, T., and Lewis, G. (2000). Galileo prime mission navigation. *Journal of Spacecraft and Rockets*, 37(1):56–63.

Hay, H. C. and Matsuyama, I. (2019). Non-linear tidal dissipation in the subsurface oceans of Enceladus and other icy satellites. *Icarus*, 319:68–85.

Hay, H. C., Trinh, A., and Matsuyama, I. (2020). Powering the Galilean satellites with moon-moon tides. *Geophysical Research Letters*, 47(15):e2020GL088317.

Heller, R., Marleau, G.-D., and Pudritz, R. E. (2015). The formation of the Galilean moons and Titan in the Grand Tack scenario. *Astronomy & Astrophysics*, 579:L4.

Hendrix, A. R., Hurford, T. A., Barge, L. M., Bland, M. T., Bowman, J. S., Brinckerhoff, W., Buratti, B. J., Cable, M. L., Castillo-Rogez, J., Collins, G. C., et al. (2019). The NASA roadmap to ocean worlds. *Astrobiology*, 19(1):1–27.

Hener, J., Fayolle, M., and Dirkx, D. (2024). JUICE: In-mission synergy of science and navigation ephemeris products. Application to potential benefits for statistical Delta-V expenditure. *Re-submitted to Planetary and Space Science.*

Henrard, J. (1983). Orbital evolution of the Galilean satellites: Capture into resonance. *Icarus*, 53(1):55–67.

Holman, M. J., Kavelaars, J., Grav, T., Gladman, B. J., Fraser, W. C., Milisavljevic, D., Nicholson, P. D., Burns, J. A., Carruba, V., Petit, J.-M., et al. (2004). Discovery of five irregular moons of Neptune. *Nature*, 430(7002):865–867.

Horner, J., Kane, S. R., Marshall, J. P., Dalba, P., Holt, T., Wood, J., Maynard-Casely, H., Wittenmyer, R., Lykawka, P., Hill, M., et al. (2020). Solar system physics for exoplanet research. *Publications of the Astronomical Society of the Pacific*, 132(1016):102001.

Hussmann, H. et al. (2024). GALA. *To be submitted to Space Science Reviews.*

Hussmann, H., Lingenauber, K., Kallenbach, R., Enya, K., Thomas, N., Lara, L. M., Althaus, C., Araki, H., Behnke, T., Castro-Marin, J. M., et al. (2019). The Ganymede laser altimeter (GALA): key objectives, instrument design, and performance. *CEAS space journal*, 11:381–390.

Hussmann, H., Shoji, D., Steinbrügge, G., Stark, A., and Sohl, F. (2016). Constraints on dissipation in the deep interiors of Ganymede and Europa from tidal phase-lags. *Celestial Mechanics and Dynamical Astronomy*, 126:131–144.

Hussmann, H., Sohl, F., and Spohn, T. (2006). Subsurface oceans and deep interiors of medium-sized outer planet satellites and large trans-neptunian objects. *Icarus*, 185(1):258–273.

Hussmann, H. and Spohn, T. (2004). Thermal-orbital evolution of Io and Europa. *Icarus*, 171(2):391–410.

Hut, P. (1981). Tidal evolution in close binary systems. *Astronomy and Astrophysics, vol. 99, no. 1, June 1981, p. 126-140.*, 99:126–140.

Hyodo, R., Charnoz, S., Ohtsuki, K., and Genda, H. (2017). Ring formation around giant planets by tidal disruption of a single passing large Kuiper belt object. *Icarus*, 282:195–213.

Iafolla, V., Fiorenza, E., Lefevre, C., Morbidini, A., Nozzoli, S., Peron, R., Persichini, M., Reale, A., and Santoli, F. (2010). Italian Spring Accelerometer (ISA): a fundamental support to BepiColombo radio science experiments. *Planetary and Space Science*, 58(1-2):300–308.

Idini, B. and Stevenson, D. J. (2021). Dynamical tides in Jupiter as revealed by Juno. *The Planetary Science Journal*, 2(2):69.

Iess, L., Di Benedetto, M., James, N., Mercolino, M., Simone, L., and Tortora, P. (2014a). Astra: Interdisciplinary study on enhancement of the end-to-end accuracy for spacecraft tracking techniques. *Acta Astronautica*, 94(2):699–707.

Iess, L. et al. (2024). The 3GM instrument for JUICE. *To be submitted to Space Science Reviews.*

Iess, L., Folkner, W., Durante, D., Parisi, M., Kaspi, Y., Galanti, E., Guillot, T., Hubbard, W., Stevenson, D., Anderson, J., et al. (2018). Measurement of Jupiter's asymmetric gravity field. *Nature*, 555(7695):220–222.

Iess, L., Jacobson, R. A., Ducci, M., Stevenson, D. J., Lunine, J. I., Armstrong, J. W., Asmar, S. W., Racioppa, P., Rappaport, N. J., and Tortora, P. (2012). The tides of Titan. *Science*, 337(6093):457–459.

Iess, L., Militzer, B., Kaspi, Y., Nicholson, P., Durante, D., Racioppa, P., Anabtawi, A., Galanti, E., Hubbard, W., Mariani, M., et al. (2019). Measurement and implications of Saturn's gravity field and ring mass. *Science*, 364(6445):eaat2965.

Iess, L., Stevenson, D., Parisi, M., Hemingway, D., Jacobson, R., Lunine, J., Nimmo, F., Armstrong, J., Asmar, S., Ducci, M., et al. (2014b). The gravity field and interior structure of Enceladus. *Science*, 344(6179):78–80.

Imperi, L., Iess, L., and Mariani, M. J. (2018). An analysis of the geodesy and relativity experiments of BepiColombo. *Icarus*, 301:9–25.

Jacobson, R. (2009). The orbits of the Neptunian satellites and the orientation of the pole of Neptune. *The Astronomical Journal*, 137(5):4322.

Jacobson, R. (2010). The orbits and masses of the Martian satellites and the libration of Phobos. *The Astronomical Journal*, 139(2):668.

Jacobson, R. (2014). The orbits of the Uranian satellites and rings, the gravity field of the Uranian system, and the orientation of the pole of Uranus. *The Astronomical Journal*, 148(5):76.

Jacobson, R., Brozović, M., Gladman, B., Alexandersen, M., Nicholson, P., and Veillet, C. (2012). Irregular satellites of the outer planets: Orbital uncertainties and astrometric recoveries in 2009–2011. *The Astronomical Journal*, 144(5):132.

Jacobson, R., Haw, R., McElrath, T., and Antreasian, P. (2000). A comprehensive orbit reconstruction for the Galileo prime mission in the J2000 system. *The Journal of the Astronautical Sciences*, 48:495–516.

Jacobson, R. A. (2004). The orbits of the major saturnian satellites and the gravity field of Saturn from spacecraft and Earth-based observations. *The Astronomical Journal*, 128(1):492.

Jacobson, R. A. (2022). The Orbits of the Main Saturnian Satellites, the Saturnian System Gravity Field, and the Orientation of Saturn's Pole. *The Astronomical Journal*, 164(5):199.

Jacobson, R. A., Antreasian, P., Bordi, J., Criddle, K., Ionasescu, R., Jones, J., Mackenzie, R., Meek, M., Parcher, D., Pelletier, F., et al. (2006). The gravity field of the Saturnian system from satellite observations and spacecraft tracking data. *The Astronomical Journal*, 132(6):2520.

Jacobson, R. A., Brozović, M., Mastrodemos, N., Riedel, J. E., and Sheppard, S. S. (2022). Ephemerides of the Irregular Saturnian Satellites from Earth-based Astrometry and Cassini Imaging. *The Astronomical Journal*, 164(6):240.

Jacobson, R. A. and French, R. G. (2004). Orbits and masses of Saturn's coorbital and F-ring shepherding satellites. *Icarus*, 172(2):382–387.

Jones, D., Folkner, W., Park, R., and Dhawan, V. (2021). VLBA Astrometry of Juno. In *American Astronomical Society Meeting Abstracts*, volume 53, pages 142–05.

Jones, D. L., Folkner, W. M., Jacobson, R. A., Jacobs, C. S., Romney, J., and Dhawan, V. (2020). Very long baseline array astrometry of Cassini: the final epochs and an improved orbit of Saturn. *The Astronomical Journal*, 159(2):72.

Jones, D. L., Folkner, W. M., Jacobson, R. A., Jacobs, C. S., Romney, J., Dhawan, V., and Fomalont, E. B. (2015). Update on VLBA astrometry of Cassini. In *American Astronomical Society Meeting Abstracts# 225*, volume 225, pages 137–12.

Jones, D. L., Fomalont, E., Dhawan, V., Romney, J., Folkner, W. M., Lanyi, G., Border, J., and Jacobson, R. A. (2010). Very long baseline array astrometric observations of the Cassini spacecraft at Saturn. *The Astronomical Journal*, 141(2):29.

Jones, D. L., Romney, J. D., Folkner, W. M., Park, R. S., Jacobs, C. S., and Dhawan, V. (2019). The First Two Years of juno Spacecraft Astrometry with the Very Long Baseline Array. In *2019 IEEE Aerospace Conference*, pages 1–6. IEEE.

Kaspi, Y. e., Galanti, E., Hubbard, W. B., Stevenson, D., Bolton, S., Iess, L., Guillot, T., Bloxham, J., Connerney, J., Cao, H., et al. (2018). Jupiter's atmospheric jet streams extend thousands of kilometres deep. *Nature*, 555(7695):223–226.

Kaula, W. M. (1966). Tesseral harmonics of the earth's gravitational field from camera tracking of satellites. *Journal of Geophysical research*, 71(18):4377–4388.

Keane, J., Ahern, A. A., Bagenal, F., Barr Mlinar, A. C., Basu, K., Becerra, P., Bertrand, T., Beyer, R. A., Bierson, C. J., Bland, M. T., et al. (2021a). Recommendations for addressing priority Io science in the next decade. *Bulletin of the American Astronomical Society*, 53(4):179.

Keane, J., Ahern, A. A., Bagenal, F., Barr Mlinar, A. C., Basu, K., Becerra, P., Bertrand, T., Beyer, R. A., Bierson, C. J., Bland, M. T., et al. (2021b). The science case for Io exploration. *Bulletin of the American Astronomical Society*, 53(4):178.

Keane, J. T., de Kleer, K., and Spencer, J. (2022). Perspective: the future exploration of Io. *Elements: An International Magazine of Mineralogy, Geochemistry, and Petrology*, 18(6):399–404.

Khurana, K., Kivelson, M., Stevenson, D., Schubert, G., Russell, C., Walker, R., and Polanskey, C. (1998). Induced magnetic fields as evidence for subsurface oceans in Europa and Callisto. *Nature*, 395(6704):777–780.

Khurana, K. K., Jia, X., Kivelson, M. G., Nimmo, F., Schubert, G., and Russell, C. T. (2011). Evidence of a global magma ocean in Io's interior. *Science*, 332(6034):1186–1189.

Kiseleva, T., Izmailov, I., Kiselev, A., Khrutskaya, E., and Khovritchev, M. Y. (2008). The astrometric observations of planetary satellites, close approaches and occultations of stars by asteroids and mutual events in the systems of planetary satellites with the 26-in. refractor of Pulkovo observatory in 1995–2006. *Planetary and Space Science*, 56(14):1908–1912.

Kivelson, M., Khurana, K., Russell, C., Walker, R., Warnecke, J., Coroniti, F., Polanskey, C., Southwood, D., and Schubert, G. (1996). Discovery of Ganymede's magnetic field by the Galileo spacecraft. *Nature*, 384(6609):537–541.

Kivelson, M., Khurana, K., and Volwerk, M. (2002). The permanent and inductive magnetic moments of Ganymede. *Icarus*, 157(2):507–522.

Kivelson, M. G. (2004). Moon–magnetosphere interactions: a tutorial. *Advances in Space Research*, 33(11):2061–2077.

Kivelson, M. G., Khurana, K. K., Russell, C. T., Volwerk, M., Walker, R. J., and Zimmer, C. (2000). Galileo magnetometer measurements: A stronger case for a subsurface ocean at Europa. *Science*, 289(5483):1340–1343.

Konopliv, A. S., Asmar, S. W., Folkner, W. M., Karatekin, Ö., Nunes, D. C., Smrekar, S. E., Yoder, C. F., and Zuber, M. T. (2011). Mars high resolution gravity fields from MRO, Mars seasonal gravity, and other dynamical parameters. *Icarus*, 211(1):401–428.

Konopliv, A. S., Park, R. S., Yuan, D.-N., Asmar, S. W., Watkins, M. M., Williams, J. G., Fahnestock, E., Kruizinga, G., Paik, M., Strekalov, D., et al. (2013). The JPL lunar gravity field to spherical harmonic degree 660 from the GRAIL Primary Mission. *Journal of Geophysical Research: Planets*, 118(7):1415–1434.

Kuchynka, P., Folkner, W. M., Konopliv, A. S., Parker, T. J., Park, R. S., Le Maistre, S., and Dehant, V. (2014). New constraints on Mars rotation determined from radiometric tracking of the Opportunity Mars Exploration Rover. *Icarus*, 229:340–347.

Kusche, J. (2003). Noise variance estimation and optimal weight determination for GOCE gravity recovery. *Advances in Geosciences*, 1:81–85.

Lainey, V. (2002). *Théorie dynamique des satellites galiléens*. PhD thesis, Observatoire de Paris.

Lainey, V. (2008). A new dynamical model for the Uranian satellites. *Planetary and Space Science*, 56(14):1766–1772.

Lainey, V. (2016). Quantification of tidal parameters from Solar System data. *Celestial Mechanics and Dynamical Astronomy*, 126:145–156.

Lainey, V., Arlot, J.-E., Karatekin, Ö., and Van Hoolst, T. (2009). Strong tidal dissipation in Io and Jupiter from astrometric observations. *Nature*, 459(7249):957–959.

Lainey, V., Arlot, J.-E., and Vienne, A. (2004a). New accurate ephemerides for the Galilean satellites of Jupiter-II. Fitting the observations. *Astronomy & Astrophysics*, 427(1):371–376.

Lainey, V., Casajus, L. G., Fuller, J., Zannoni, M., Tortora, P., Cooper, N., Murray, C., Modenini, D., Park, R. S., Robert, V., et al. (2020). Resonance locking in giant planets indicated by the rapid orbital expansion of Titan. *Nature Astronomy*, 4(11):1053–1058.

Lainey, V., Dehant, V., and Pätzold, M. (2007). First numerical ephemerides of the Martian moons. *Astronomy & Astrophysics*, 465(3):1075–1084.

Lainey, V., Duriez, L., and Vienne, A. (2004b). New accurate ephemerides for the Galilean satellites of Jupiter-I. Numerical integration of elaborated equations of motion. *Astronomy & Astrophysics*, 420(3):1171–1183.

Lainey, V., Duriez, L., and Vienne, A. (2006). Synthetic representation of the Galilean satellites' orbital motions from L1 ephemerides. *Astronomy & Astrophysics*, 456(2):783–788.

Lainey, V., Jacobson, R. A., Tajeddine, R., Cooper, N. J., Murray, C., Robert, V., Tobie, G., Guillot, T., Mathis, S., Remus, F., et al. (2017). New constraints on Saturn's interior from Cassini astrometric data. *Icarus*, 281:286–296.

Lainey, V., Karatekin, Ö., Desmars, J., Charnoz, S., Arlot, J.-E., Emelyanov, N., Le Poncin-Lafitte, C., Mathis, S., Remus, F., Tobie, G., et al. (2012). Strong tidal dissipation in Saturn and constraints on Enceladus' thermal state from astrometry. *The Astrophysical Journal*, 752(1):14.

Lainey, V., Noyelles, B., Cooper, N., Rambaux, N., Murray, C., and Park, R. (2019). Interior properties of the inner Saturnian moons from space astrometry data. *Icarus*, 326:48–62.

Lainey, V., Pasewaldt, A., Robert, V., Rosenblatt, P., Jaumann, R., Oberst, J., Roatsch, T., Willner, K., Ziese, R., and Thuillot, W. (2021). Mars moon ephemerides after 14 years of Mars Express data. *Astronomy & Astrophysics*, 650:A64.

Lainey, V., Rambaux, N., Tobie, G., Cooper, N., Zhang, Q., Noyelles, B., and Baillié, K. (2024). A recently formed ocean inside Saturn's moon Mimas. *Nature*, 626(7998):280–282.

Lainey, V. and Tobie, G. (2005). New constraints on Io's and Jupiter's tidal dissipation. *Icarus*, 179(2):485–489.

Lambeck, K. (1988). Geophysical geodesy-The slow deformations of the Earth. *Research supported by CNES and Universite de Paris VI. Oxford and New York.*

Lari, G. (2018). A semi-analytical model of the Galilean satellites' dynamics. *Celestial Mechanics and Dynamical Astronomy*, 130(8):50.

Lari, G. and Milani, A. (2018). The Galilean Satellites' Dynamics and the Estimation of the Jovian System's Dissipation from JUICE Data. *Univeritá di Pisa*.

Lari, G. and Milani, A. (2019). Chaotic orbit determination in the context of the JUICE mission. *Planetary and Space Science*, 176:104679.

Lari, G., Saillenfest, M., and Fenucci, M. (2020). Long-term evolution of the Galilean satellites: the capture of Callisto into resonance. *Astronomy & Astrophysics*, 639:A40.

Lari, G., Saillenfest, M., and Grassi, C. (2023). Dynamical history of the Galilean satellites for a fast migration of Callisto. *Monthly Notices of the Royal Astronomical Society*, 518(2):3023–3035.

Lari, G., Zannoni, M., Durante, D., Park, R. S., and Tommei, G. (2024). Determination of Jupiter's Pole Orientation from Juno Radio Science Data. *Aerospace*, 11(2):124.

Laskar, J. and Jacobson, R. (1987). GUST86-an analytical ephemeris of the Uranian satellites. *Astronomy and Astrophysics (ISSN 0004-6361), vol. 188, no. 1, Dec. 1987, p. 212-224.*, 188:212–224.

Le Maistre, S., Rivoldini, A., and Rosenblatt, P. (2019). Signature of Phobos' interior structure in its gravity field and libration. *Icarus*, 321:272–290.

Le Maistre, S., Rosenblatt, P., Rambaux, N., Castillo-Rogez, J. C., Dehant, V., and Marty, J.-C. (2013). Phobos interior from librations determination using Doppler and star tracker measurements. *Planetary and Space Science*, 85:106–122.

Lemoine, F. G., Goossens, S., Sabaka, T. J., Nicholas, J. B., Mazarico, E., Rowlands, D. D., Loomis, B. D., Chinn, D. S., Caprette, D. S., Neumann, G. A., et al. (2013). High–degree gravity models from GRAIL primary mission data. *Journal of Geophysical Research: Planets*, 118(8):1676–1698.

Lemoine, F. G., Goossens, S., Sabaka, T. J., Nicholas, J. B., Mazarico, E., Rowlands, D. D., Loomis, B. D., Chinn, D. S., Neumann, G. A., Smith, D. E., et al. (2014). GRGM900C: A degree 900 lunar gravity model from GRAIL primary and extended mission data. *Geophysical research letters*, 41(10):3382–3389.

Leonard, E. J., Elder, C., Nordheim, T. A., Cartwright, R., Patthoff, D. A., Beddingfield, C., Cochrane, C., Brooks, S., Tiscareno, M., Strange, N., et al. (2021). UMaMI: A New Frontiers-style Mission Concept to Explore the Uranian System. *The Planetary Science Journal*, 2(5):174.

Lerch, F. J. (1991). Optimum data weighting and error calibration for estimation of gravitational parameters. *Bulletin géodésique*, 65:44–52.

Levrard, B. (2008). A proof that tidal heating in a synchronous rotation is always larger than in an asymptotic nonsynchronous rotation state. *Icarus*, 193(2):641–643.

Li, C., Ingersoll, A., Bolton, S., Levin, S., Janssen, M., Atreya, S., Lunine, J., Steffes, P., Brown, S., Guillot, T., et al. (2020). The water abundance in Jupiter's equatorial zone. *Nature Astronomy*, 4(6):609–616.

Lieske, J. (1980). Improved ephemerides of the Galilean satellites. *Astronomy and Astrophysics, vol. 82, no. 3, Feb. 1980, p. 340-348.*, 82:340–348.

Lieske, J. (1987). Galilean satellite evolution - Observational evidence for secular changes in mean motions. *Astronomy and Astrophysics (ISSN 0004-6361), vol. 176, no. 1, April 1987, p. 146-158.*, 176:146–158.

Lieske, J. (1998). Galilean satellite ephemerides E5. *Astronomy and Astrophysics Supplement Series*, 129(2):205–217.

Lieske, J. H. (1977). Theory of motion of Jupiter's Galilean satellites. *Astronomy and Astrophysics, vol. 56, no. 3, Apr. 1977, p. 333-352.*, 56:333–352.

Lindegren, L. (1977). Meridian observations of planets with a photoelectric multislit micrometer. *Astronomy and Astrophysics, vol. 57, no. 1-2, May 1977, p. 55-72.*, 57:55–72.

Lopes, R. M., de Kleer, K., and Keane, J. T. (2023). *Io: A New View of Jupiter's Moon*, volume 468. Springer Nature.

Lunine, J. I. (2017). Ocean worlds exploration. *Acta Astronautica*, 131:123–130.

Lunine, J. I. and Atreya, S. K. (2008). The methane cycle on Titan. *Nature Geoscience*, 1(3):159–164.

Lynam, A. E. and Longuski, J. M. (2012). Preliminary analysis for the navigation of multiple-satellite-aided capture sequences at Jupiter. *Acta Astronautica*, 79:33–43.

Magnanini, A. (2021). Estimation of the ephemerides and gravity fields of the galilean moons through orbit determination of the JUICE mission. *Aerotecnica Missili & Spazio*, 100(3):195–206.

Magnanini, A., Zannoni, M., Gomez Casajus, L., and Tortora, P. (2023). Estimation of dissipation in Jupiter system through joint analysis of JUICE, Europa Clipper and Juno radio science data. *Poster presentation, Origins and Habitability of the Galilean Moons workshop.*

Magnanini, A., Zannoni, M., Gomez Casajus, L., Tortora, P., Lainey, V., Mazarico, E., and Iess, L. (2024). Joint Analysis of JUICE and Europa Clipper Tracking Data to Study the Jovian System Ephemerides and Dissipative Parameters. *Under revision for publication in Astronomy & Astrophysics.*

Majid, W. and Bagri, D. (2007). In-beam phase referencing with the deep space network array. *IPN Progress Report*, pages 42–169.

Makarov, V. V. and Efroimsky, M. (2013). No pseudosynchronous rotation for terrestrial planets and moons. *The Astrophysical Journal*, 764(1):27.

Malhotra, R. (1991). Tidal origin of the Laplace resonance and the resurfacing of Ganymede. *Icarus*, 94(2):399–412.

Marion, G. M., Fritsen, C. H., Eicken, H., and Payne, M. C. (2003). The search for life on Europa: limiting environmental factors, potential habitats, and Earth analogues. *Astrobiology*, 3(4):785–811.

Mariotti, G. and Tortora, P. (2013). Experimental validation of a dual uplink multifrequency dispersive noise calibration scheme for Deep Space tracking. *Radio Science*, 48(2):111–117.

Marov, M. Y., Avduevsky, V., Akim, E., Eneev, T., Kremnev, R., Kulikov, S., Pichkhadze, K., Popov, G., and Rogovsky, G. (2004). Phobos-Grunt: Russian sample return mission. *Advances in Space research*, 33(12):2276–2280.

Marques Oliveira, J., Sicardy, B., Gomes-Júnior, A. R., Ortiz, J. L., Strobel, D. F., Bertrand, T., Forget, F., Lellouch, E., Desmars, J., Berard, D., et al. (2022). Constraints on the structure and seasonal variations of Triton's atmosphere from the 5 October 2017 stellar occultation and previous observations. *Astronomy & Astrophysics*, 659:A136.

Martinez, J. and Dirkx, D. (2024). Translational-rotational couplings in the dynamics of Phobos. *To be submitted to Astronomy & Astrophysics.*

Marusiak, A. G., Vance, S., Panning, M. P., Běhounková, M., Byrne, P. K., Choblet, G., Daswani, M. M., Hughson, K., Journaux, B., Lobo, A. H., et al. (2021). Exploration of icy ocean worlds using geophysical approaches. *The Planetary Science Journal*, 2(4):150.

Masters, A., Achilleos, N., Agnor, C., Campagnola, S., Charnoz, S., Christophe, B., Coates, A. J., Fletcher, L., Jones, G. H., Lamy, L., et al. (2014). Neptune and Triton: Essential pieces of the Solar System puzzle. *Planetary and Space Science*, 104:108–121.

Mathis, S. and Le Poncin-Lafitte, C. (2009). Tidal dynamics of extended bodies in planetary systems and multiple stars. *Astronomy & Astrophysics*, 497(3):889–910.

Mazarico, E., Buccino, D., Castillo-Rogez, J., Dombard, A. J., Genova, A., Hussmann, H., Kiefer, W. S., Lunine, J. I., McKinnon, W. B., Nimmo, F., et al. (2023). The Europa Clipper Gravity and Radio Science Investigation. *Space Science Reviews*, 219(4):30.

Mazarico, E., Genova, A., Neumann, G. A., Smith, D. E., and Zuber, M. T. (2015). Simulated recovery of Europa's global shape and tidal Love numbers from altimetry and radio tracking during a dedicated flyby tour. *Geophysical Research Letters*, 42(9):3166–3173.

Mazarico, E., Rowlands, D. D., Sabaka, T. J., Getzandanner, K. M., Rubincam, D. P., Nicholas, J. B., and Moreau, M. C. (2017). Recovery of Bennu's orientation for the OSIRIS-REx mission: implications for the spin state accuracy and geolocation errors. *Journal of Geodesy*, 91:1141–1161.

McCord, T. B. (1966). Dynamical evolution of the Neptunian system. *Astronomical Journal, Vol. 71, p. 585 (1966)*, 71:585.

McEwen, A. S., Haapala, A. F., Keszthelyi, L. P., and Mandt, K. E. (2023). Outstanding Questions and Future Observations of Io. In *Io: A New View of Jupiter's Moon*, pages 349–370. Springer.

McKinnon, W. B. (1984). On the origin of Triton and Pluto. *Nature*, 311(5984):355–358.

McKinnon, W. B. (2015). Effect of Enceladus's rapid synchronous spin on interpretation of Cassini gravity. *Geophysical Research Letters*, 42(7):2137–2143.

Mignard, F. (1980). The evolution of the lunar orbit revisited, II. *The Moon and the planets*, 23(2):185–201.

Milani, A. and Gronchi, G. (2010). *Theory of orbit determination*. Cambridge University Press.

Milani, A., Rossi, A., Vokrouhlickỳ, D., Villani, D., and Bonanno, C. (2001). Gravity field and rotation state of Mercury from the BepiColombo Radio Science Experiments. *Planetary and Space Science*, 49(14-15):1579–1596.

Miranda, C., Patel, M., Berberan-Santos, M. N., Hormigo, T., Correia, A., Pedras, B., and Martins, Z. (2023). The importance of Phobos simulants: a review on our current knowledge. *Frontiers in Astronomy and Space Sciences*, 10.

Mitri, G., Barnes, J., Coustenis, A., Flamini, E., Hayes, A., Lorenz, R. D., Mastrogiuseppe, M., Orosei, R., Postberg, F., Reh, K., et al. (2021). Exploration of Enceladus and Titan: investigating ocean worlds' evolution and habitability in the Saturn system. *Experimental astronomy*, pages 1–34.

Molera Calvés, G., Pogrebenko, S. V., Wagner, J. F., Cimò, G., Gurvits, L. I., Bocanegra-Bahamón, T. M., Duev, D. A., and Nunes, N. V. (2021). High spectral resolution multi-tone Spacecraft Doppler tracking software: Algorithms and implementations. *Publications of the Astronomical Society of Australia*, 38:e065.

Moore, K., Cao, H., Bloxham, J., Stevenson, D., Connerney, J., and Bolton, S. (2019). Time variation of Jupiter's internal magnetic field consistent with zonal wind advection. *Nature Astronomy*, 3(8):730–735.

Moore, K. M., Yadav, R. K., Kulowski, L., Cao, H., Bloxham, J., Connerney, J. E., Kotsiaros, S., Jørgensen, J. L., Merayo, J. M., Stevenson, D. J., et al. (2018). A complex dynamo inferred from the hemispheric dichotomy of Jupiter's magnetic field. *Nature*, 561(7721):76–78.

Moore, W. B. and Schubert, G. (2000). The tidal response of Europa. *Icarus*, 147(1):317–319.

Morbidelli, A., Tsiganis, K., Batygin, K., Crida, A., and Gomes, R. (2012). Explaining why the uranian satellites have equatorial prograde orbits despite the large planetary obliquity. *Icarus*, 219(2):737–740.

Morgado, B., Assafin, M., Vieira-Martins, R., Camargo, J., Dias-Oliveira, A., and Gomes-Júnior, A. (2016). Astrometry of mutual approximations between natural satellites. Application to the Galilean moons. *Monthly Notices of the Royal Astronomical Society*, 460(4):4086–4097.

Morgado, B., Benedetti-Rossi, G., Gomes-Júnior, A., Assafin, M., Lainey, V., Vieira-Martins, R., Camargo, J., Braga-Ribas, F., Boufleur, R., Fabrega, J., et al. (2019a). First stellar occultation by the Galilean moon Europa and upcoming events between 2019 and 2021. *Astronomy & Astrophysics*, 626:L4.

Morgado, B., Gomes-Júnior, A., Braga-Ribas, F., Vieira-Martins, R., Desmars, J., Lainey, V., D'aversa, E., Dunham, D., Moore, J., Baillié, K., et al. (2022). Milliarcsecond astrometry for the Galilean moons using stellar occultations. *The Astronomical Journal*, 163(5):240.

Morgado, B., Vieira-Martins, R., Assafin, M., Machado, D., Camargo, J., Sfair, R., Malacarne, M., Braga-Ribas, F., Robert, V., Bassallo, T., et al. (2019b). APPROX–mutual approximations between the Galilean moons: the 2016–2018 observational campaign. *Monthly Notices of the Royal Astronomical Society*, 482(4):5190–5200.

Morrison, L. V. and Gilmore, G. F. (1994). *Galactic and Solar System Optical Astrometry*. Cambridge University Press.

Mousis, O., Bouquet, A., Langevin, Y., André, N., Boithias, H., Durry, G., Faye, F., Hartogh, P., Helbert, J., Iess, L., et al. (2022). Moonraker: enceladus multiple flyby mission. *The planetary science journal*, 3(12):268.

Moyer, T. D. (2005). *Formulation for observed and computed values of Deep Space Network data types for navigation*. John Wiley & Sons.

Murchie, S., Eng, D., Chabot, N., Guo, Y., Arvidson, R., Yen, A., Trebi-Ollennu, A., Seelos, F., Adams, E., and Fountain, G. (2014). MERLIN: Mars-Moon Exploration, Reconnaissance and Landed Investigation. *Acta Astronautica*, 93:475–482.

Murray, C. D. and Dermott, S. F. (2000). *Solar system dynamics*. Cambridge university press.

Murrow, D. and Jacobson, R. (1988). Galilean satellite ephemeris improvement using Galileo tour encounter information. In *Astrodynamics Conference*, page 4249.

Musotto, S., Varadi, F., Moore, W., and Schubert, G. (2002). Numerical simulations of the orbits of the Galilean satellites. *Icarus*, 159(2):500–504.

Neveu, M. and Rhoden, A. R. (2019). Evolution of Saturn's mid-sized moons. *Nature astronomy*, 3(6):543–552.

Nimmo, F. (2023). Strong Tidal Dissipation at Uranus? *The Planetary Science Journal*, 4(12):241.

Nimmo, F., Barr, A. C., Behounková, M., and McKinnon, W. B. (2018). The thermal and orbital evolution of Enceladus: observational constraints and models. *Enceladus and the icy moons of Saturn*, 475:79–94.

Nimmo, F., Neveu, M., and Howett, C. (2023). Origin and Evolution of Enceladus's Tidal Dissipation. *Space Science Reviews*, 219(7):57.

Nimmo, F. and Pappalardo, R. T. (2016). Ocean worlds in the outer solar system. *Journal of Geophysical Research: Planets*, 121(8):1378–1399.

Nimmo, F. and Spencer, J. (2015). Powering Triton's recent geological activity by obliquity tides: Implications for Pluto geology. *Icarus*, 246:2–10.

Nogueira, E., Brasser, R., and Gomes, R. (2011). Reassessing the origin of Triton. *Icarus*, 214(1):113–130.

Noyelles, B., Vienne, A., and Descamps, P. (2003). Astrometric reduction of lightcurves observed during the PHESAT95 campaign of Saturnian satellites. *Astronomy & Astrophysics*, 401(3):1159–1175.

Oberst, J., Lainey, V., Poncin-Lafitte, C. L., Dehant, V., Rosenblatt, P., Ulamec, S., Biele, J., Spurmann, J., Kahle, R., Klein, V., et al. (2012). GETEMME — A mission to explore the Martian satellites and the fundamentals of Solar System physics. *Experimental Astronomy*, 34:243–271.

Oberst, J., Wickhusen, K., Willner, K., Gwinner, K., Spiridonova, S., Kahle, R., Coates, A., Herique, A., Plettemeier, D., Díaz-Michelena, M., et al. (2018). DePhine–the Deimos and Phobos interior explorer. *Advances in Space Research*, 62(8):2220–2238.

Ogohara, K., Nakagawa, H., Aoki, S., Kouyama, T., Usui, T., Terada, N., Imamura, T., Montmessin, F., Brain, D., Doressoundiram, A., et al. (2022). The Mars system revealed by the Martian Moons eXploration mission. *Earth, Planets and Space*, 74:1–32.

Ojakangas, G. W. and Stevenson, D. (1986). Episodic volcanism of tidally heated satellites with application to Io. *Icarus*, 66(2):341–358.

Pail, R. and Plank, G. (2002). Assessment of three numerical solution strategies for gravity field recovery from GOCE satellite gravity gradiometry implemented on a parallel platform. *Journal of Geodesy*, 76:462–474.

Pappalardo, R., Becker, T., Blaney, D., Blankenship, D., Burch, J., Christensen, P., Craft, K., Daubar, I., Gudipati, M., Hayes, A., et al. (2021). The Europa Clipper Mission: understanding icy world habitability and blazing a path for future exploration. *Bulletin of the American Astronomical Society*, 53(4):255.

Pappalardo, R. T., Belton, M. J., Breneman, H., Carr, M., Chapman, C. R., Collins, G., Denk, T., Fagents, S., Geissler, P. E., Giese, B., et al. (1999). Does Europa have a subsurface ocean? Evaluation of the geological evidence. *Journal of Geophysical Research: Planets*, 104(E10):24015–24055.

Park, R. S., Folkner, W. M., Williams, J. G., and Boggs, D. H. (2021). The JPL planetary and lunar ephemerides DE440 and DE441. *The Astronomical Journal*, 161(3):105.

Parkinson, C. D., Liang, M.-C., Yung, Y. L., and Kirschivnk, J. L. (2008). Habitability of Enceladus: planetary conditions for life. *Origins of Life and Evolution of Biospheres*, 38:355–369.

Peale, S. (1999). Origin and evolution of the natural satellites. *Annual Review of Astronomy and Astrophysics*, 37(1):533–602.

Peale, S. and Lee, M. H. (2002). A primordial origin of the Laplace relation among the Galilean satellites. *Science*, 298(5593):593–597.

Peale, S. J. (1969). Generalized Cassini's laws. *Astronomical Journal, Vol. 74, p. 483 (1969)*, 74:483.

Peale, S. J., Cassen, P., and Reynolds, R. T. (1979). Melting of Io by tidal dissipation. *Science*, 203(4383):892–894.

Peng, Q., He, H., Lainey, V., and Vienne, A. (2012). Precise CCD positions of Galilean satellite-pairs. *Monthly Notices of the Royal Astronomical Society*, 419(3):1977–1982.

Peng, Q. Y., Vienne, A., Wu, X., Gan, L., and Desmars, J. (2008). CCD positions of Saturn and its major satellites from 2002–2006. *The Astronomical Journal*, 136(5):2214.

Peterson, G., Nimmo, F., and Schenk, P. (2015). Elastic thickness and heat flux estimates for the uranian satellite Ariel. *Icarus*, 250:116–122.

Petit, G., Luzum, B., et al. (2010). IERS technical note no. 36. *IERS conventions*, 179.

Petricca, F., Genova, A., Castillo-Rogez, J. C., Styczinski, M. J., Cochrane, C. J., and Vance, S. D. (2023). Characterization of icy moon hydrospheres through joint inversion of gravity and magnetic field measurements. *Geophysical Research Letters*, 50(17):e2023GL104016.

Phillips, C., Hand, K., Scully, J., Pitesky, J., Craft, K., Cameron, M., Nordheim, T., Hofmann, A., Tan-Wang, G., Hofgartner, J., et al. (2021). An exploration strategy for Europa. *Bulletin of the American Astronomical Society*, 53(4):207.

Pitjeva, E. V. (2009). EPM ephemerides and relativity. *Proceedings of the International Astronomical Union*, 5(S261):170–178.

Pogrebenko, S., Gurvits, L., Campbell, R., Avruch, I., Lebreton, J.-P., and van't Klooster, C. (2004). VLBI tracking of the Huygens probe in the atmosphere of Titan. In *Planetary Probe Atmospheric Entry and Descent Trajectory Analysis and Science*, volume 544, pages 197–204.

Polycarpe, W., Saillenfest, M., Lainey, V., Vienne, A., Noyelles, B., and Rambaux,

N. (2018). Strong tidal energy dissipation in Saturn at Titan's frequency as an explanation for Iapetus orbit. *Astronomy & Astrophysics*, 619:A133.

Porco, C. C., Helfenstein, P., Thomas, P., Ingersoll, A., Wisdom, J., West, R., Neukum, G., Denk, T., Wagner, R., Roatsch, T., et al. (2006). Cassini observes the active south pole of Enceladus. *Science*, 311(5766):1393–1401.

Pradel, N., Charlot, P., and Lestrade, J.-F. (2006). Astrometric accuracy of phase-referenced observations with the VLBA and EVN. *Astronomy & Astrophysics*, 452(3):1099–1106.

Rambaux, N. and Castillo-Rogez, J. (2013). Tides on satellites of giant planets. In *Tides in astronomy and astrophysics*, pages 167–200. Springer.

Rambaux, N., Castillo-Rogez, J., Le Maistre, S., and Rosenblatt, P. (2012). Rotational motion of Phobos. *Astronomy & Astrophysics*, 548:A14.

Rambaux, N., Castillo-Rogez, J. C., Williams, J. G., and Karatekin, Ö. (2010). Librational response of Enceladus. *Geophysical Research Letters*, 37(4).

Raofi, B., Guman, M., and Potts, C. (2000). Preliminary statistical Delta V analysis for a representative Europa Orbiter Mission. In *Astrodynamics Specialist Conference*, page 4035.

Renaud, J. P., Henning, W. G., Saxena, P., Neveu, M., Bagheri, A., Mandell, A., and Hurford, T. (2021). Tidal dissipation in dual-body, highly eccentric, and nonsynchronously rotating systems: Applications to Pluto–Charon and the exoplanet TRAPPIST-1e. *The Planetary Science Journal*, 2(1):4.

Rhoden, A. R. and Walker, M. E. (2022). The case for an ocean-bearing Mimas from tidal heating analysis. *Icarus*, 376:114872.

Robert, V., De Cuyper, J.-P., Arlot, J.-E., De Decker, G., Guibert, J., Lainey, V., Pascu, D., Winter, L., and Zacharias, N. (2011). A new astrometric reduction of photographic plates using the DAMIAN digitizer: improving the dynamics of the Jovian system. *Monthly Notices of the Royal Astronomical Society*, 415(1):701–708.

Robert, V., Saquet, E., Colas, F., and Arlot, J.-E. (2017). CCD astrometric observations of Amalthea and Thebe in the Gaia era. *Monthly Notices of the Royal Astronomical Society*, 467(1):694–698.

Roberts, J. H., McKinnon, W. B., Elder, C. M., Tobie, G., Biersteker, J. B., Young, D., Park, R. S., Steinbrügge, G., Nimmo, F., Howell, S. M., et al. (2023). Exploring the Interior of Europa with the Europa Clipper. *Space Science Reviews*, 219(6):46.

Roberts, J. H. and Nimmo, F. (2008). Tidal heating and the long-term stability of a subsurface ocean on Enceladus. *Icarus*, 194(2):675–689.

Rodriguez, S., Vinatier, S., Cordier, D., Tobie, G., Achterberg, R. K., Anderson, C. M., Badman, S. V., Barnes, J. W., Barth, E. L., Bézard, B., et al. (2022). Science goals and new mission concepts for future exploration of Titan's atmosphere, geology and habitability: titan POlar scout/orbitEr and in situ lake lander and DrONe explorer (POSEIDON). *Experimental Astronomy*, 54(2-3):911–973.

Rosenblatt, P. (2011). The origin of the Martian moons revisited. *The Astronomy and Astrophysics Review*, 19:1–26.

Rosenblatt, P., Charnoz, S., Dunseath, K. M., Terao-Dunseath, M., Trinh, A., Hyodo, R., Genda, H., and Toupin, S. (2016). Accretion of Phobos and Deimos in an extended debris disc stirred by transient moons. *Nature Geoscience*, 9(8):581–583.

Rosenblatt, P., Lainey, V., Le Maistre, S., Marty, J.-C., Dehant, V., Pätzold, M., Van Hoolst, T., and Häusler, B. (2008).

Accurate Mars Express orbits to improve the determination of the mass and ephemeris of the Martian moons. *Planetary and Space science*, 56(7):1043–1053.

Ross, M. N. and Schubert, G. (1990). The coupled orbital and thermal evolution of Triton. *Geophysical research letters*, 17(10):1749–1752.

Roth, L., Saur, J., Retherford, K. D., Blöcker, A., Strobel, D. F., and Feldman, P. D. (2017). Constraints on Io's interior from auroral spot oscillations. *Journal of Geophysical Research: Space Physics*, 122(2):1903–1927.

Rovira-Navarro, M., Katz, R. F., Liao, Y., van der Wal, W., and Nimmo, F. (2022). The tides of Enceladus' porous core. *Journal of Geophysical Research: Planets*, 127(5):e2021JE007117.

Rovira-Navarro, M., Matsuyama, I., and Berne, A. (2023). A Spectral Method to Compute the Tides of Laterally-Heterogeneous Bodies. *arXiv preprint arXiv:2311.15710*.

Rovira-Navarro, M., Rieutord, M., Gerkema, T., Maas, L. R., van der Wal, W., and Vermeersen, B. (2019). Do tidally-generated inertial waves heat the subsurface oceans of Europa and Enceladus? *Icarus*, 321:126–140.

Rufu, R. and Canup, R. M. (2017). Triton's evolution with a primordial Neptunian satellite system. *The Astronomical Journal*, 154(5):208.

Rymer, A. M., Runyon, K. D., Clyde, B., Núñez, J. I., Nikoukar, R., Soderlund, K. M., Sayanagi, K., Hofstadter, M., Quick, L. C., Stern, S. A., et al. (2021). Neptune odyssey: A flagship concept for the exploration of the neptune–triton system. *The Planetary Science Journal*, 2(5):184.

Saillenfest, M., Lari, G., and Boué, G. (2021a). The large obliquity of Saturn explained by the fast migration of Titan. *Nature Astronomy*, 5(4):345–349.

Saillenfest, M., Lari, G., Boué, G., and Courtot, A. (2021b). The past and future obliquity of Saturn as Titan migrates. *Astronomy & Astrophysics*, 647:A92.

Saillenfest, M., Rogoszinski, Z., Lari, G., Baillié, K., Boué, G., Crida, A., and Lainey, V. (2022). Tilting Uranus via the migration of an ancient satellite. *Astronomy & Astrophysics*, 668:A108.

Salmon, J. and Canup, R. M. (2017). Accretion of Saturn's inner mid-sized moons from a massive primordial ice ring. *The Astrophysical Journal*, 836(1):109.

Sampson, R. A. (1921). Theory of the four great satellites of Jupiter. *Memoirs of the Royal Astronomical Society, Vol. 63, p. 1*, 63:1.

Samuel, H., Lognonné, P., Panning, M., and Lainey, V. (2019). The rheology and thermal history of Mars revealed by the orbital evolution of Phobos. *Nature*, 569(7757):523–527.

Santos-Filho, S., Assafin, M., Morgado, B., Vieira-Martins, R., Camargo, J., Gomes-Júnior, A., and Benedetti-Rossi, G. (2019). Mutual approximations between the five main moons of Uranus. *Monthly Notices of the Royal Astronomical Society*, 490(3):3464–3475.

Saur, J., Duling, S., Roth, L., Jia, X., Strobel, D. F., Feldman, P. D., Christensen, U. R., Retherford, K. D., McGrath, M. A., Musacchio, F., et al. (2015). The search for a subsurface ocean in Ganymede with Hubble Space Telescope observations of its auroral ovals. *Journal of Geophysical Research: Space Physics*, 120(3):1715–1737.

Schenk, P. M. and Zahnle, K. (2007). On the negligible surface age of Triton. *Icarus*, 192(1):135–149.

Schettino, G., Cicalo, S., Di Ruzza, S., and Tommei, G. (2015). The relativity experiment of MORE: Global full-cycle simulation and results. In *2015 IEEE*

Metrology for Aerospace (MetroAeroSpace), pages 141–145. IEEE.

Schubert, G., Anderson, J., Spohn, T., and McKinnon, W. (2004). Interior composition, structure and dynamics of the Galilean satellites. *Jupiter: The planet, satellites and magnetosphere*, 1:281–306.

Schuh, W.-D. (2003). The processing of band-limited measurements; filtering techniques in the least squares context and in the presence of data gaps. *Space Science Reviews*, 108:67–78.

Serra, D., Spoto, F., and Milani, A. (2018). A multi-arc approach for chaotic orbit determination problems. *Celestial Mechanics and Dynamical Astronomy*, 130:1–17.

Showalter, M. R., de Pater, I., Lissauer, J. J., and French, R. S. (2019). The seventh inner moon of Neptune. *Nature*, 566(7744):350–353.

Showman, A. P., Stevenson, D. J., and Malhotra, R. (1997). Coupled orbital and thermal evolution of Ganymede. *Icarus*, 129(2):367–383.

Siemes, C. (2008). *Digital filtering algorithms for decorrelation within large least squares problems*. PhD thesis, Institute of Geodesy and Geoinformation, University of Bonn.

Smith, B. A., Soderblom, L., Batson, R., Bridges, P., Inge, J., Masursky, H., Shoemaker, E., Beebe, R., Boyce, J., Briggs, G., et al. (1982). A new look at the Saturn system: The Voyager 2 images. *Science*, 215(4532):504–537.

Smith, B. A., Soderblom, L., Beebe, R., Boyce, J., Briggs, G., Bunker, A., Collins, S. A., Hansen, C. J., Johnson, T. V., Mitchell, J. L., et al. (1981). Encounter with Saturn: Voyager 1 imaging science results. *Science*, 212(4491):163–191.

Smith, B. A., Soderblom, L. A., Banfield, D., Barnet, C., Basilevsky, A., Beebe, R., Bollinger, K., Boyce, J., Brahic, A., Briggs, G., et al. (1989). Voyager 2 at Neptune: Imaging science results. *Science*, 246(4936):1422–1449.

Smith, B. A., Soderblom, L. A., Beebe, R., Boyce, J., Briggs, G., Carr, M., Collins, S. A., Cook, A. F., Danielson, G. E., Davies, M. E., et al. (1979a). The Galilean satellites and Jupiter: Voyager 2 imaging science results. *Science*, 206(4421):927–950.

Smith, B. A., Soderblom, L. A., Johnson, T. V., Ingersoll, A. P., Collins, S. A., Shoemaker, E. M., Hunt, G., Masursky, H., Carr, M. H., Davies, M. E., et al. (1979b). The Jupiter system through the eyes of Voyager 1. *Science*, 204(4396):951–972.

Soderblom, L. A., Kieffer, S., Becker, T., Brown, R., Cook, A., Hansen, C., Johnson, T., Kirk, R. L., and Shoemaker, E. (1990). Triton's geyser-like plumes: Discovery and basic characterization. *Science*, 250(4979):410–415.

Sotin, C., Tobie, G., Wahr, J., McKinnon, W. B., McKinnon, W., and Khurana, K. (2009). Tides and tidal heating on Europa. *Europa*, 11.

Souček, O., Běhounková, M., Čadek, O., Hron, J., Tobie, G., and Choblet, G. (2019). Tidal dissipation in Enceladus' uneven, fractured ice shell. *Icarus*, 328:218–231.

Spohn, T. and Schubert, G. (2003). Oceans in the icy Galilean satellites of Jupiter? *Icarus*, 161(2):456–467.

Steinke, T. (2021). The Curious Case of Io-Connections Between Interior Structure, Tidal Heating and Volcanism.

Stone, R. C. (1996). An accurate method for computing atmospheric refraction. *Publications of the Astronomical Society of the Pacific*, 108(729):1051.

Stone, R. C. (2001). Positions for the outer planets and many of their satellites. V. FASTT observations taken in 2000-2001. *The Astronomical Journal*, 122(5):2723.

Sulaiman, A. H., Achilleos, N., Bertucci, C., Coates, A., Dougherty, M., Hadid, L., Holmberg, M., Hsu, H.-W., Kimura, T., Kurth, W., et al. (2021). Enceladus and Titan: emerging worlds of the Solar System. *Experimental Astronomy*, pages 1–28.

Tajeddine, R., Rambaux, N., Lainey, V., Charnoz, S., Richard, A., Rivoldini, A., and Noyelles, B. (2014). Constraints on Mimas' interior from Cassini ISS libration measurements. *Science*, 346(6207):322–324.

Terquem, C. (2023). On the energetics of a tidally oscillating convective flow. *Monthly Notices of the Royal Astronomical Society*, 525(1):508–526.

Thomas, P., Tajeddine, R., Tiscareno, M., Burns, J., Joseph, J., Loredo, T., Helfenstein, P., and Porco, C. (2016). Enceladus's measured physical libration requires a global subsurface ocean. *Icarus*, 264:37–47.

Thornton, C. L. and Border, J. S. (2005). *Radiometric tracking techniques for deep-space navigation*. John Wiley & Sons.

Throop, H., Porco, C., West, R., Burns, J., Showalter, M., and Nicholson, P. (2004). The jovian rings: new results derived from Cassini, Galileo, Voyager, and Earth-based observations. *Icarus*, 172(1):59–77.

Tittemore, W. C. and Wisdom, J. (1989). Tidal evolution of the Uranian satellites: II. An explanation of the anomalously high orbital inclination of Miranda. *Icarus*, 78(1):63–89.

Tittemore, W. C. and Wisdom, J. (1990). Tidal evolution of the Uranian satellites: III. Evolution through the Miranda-Umbriel 3: 1, Miranda-Ariel 5: 3, and Ariel-Umbriel 2: 1 mean-motion commensurabilities. *Icarus*, 85(2):394–443.

Van Hoolst, T., Baland, R.-M., and Trinh, A. (2013). On the librations and tides of large icy satellites. *Icarus*, 226(1):299–315.

Van Hoolst, T., Baland, R.-M., Trinh, A., Yseboodt, M., and Nimmo, F. (2020). The librations, tides, and interior structure of Io. *Journal of Geophysical Research: Planets*, 125(8):e2020JE006473.

Van Hoolst, T. et al. (2024). Geophysical characterization of the interiors of Ganymede, Callisto and Europa by ESA's JUpiter ICy moons Explorer. *Re-submitted to Space Science Reviews*.

Van Hoolst, T., Rambaux, N., Karatekin, Ö., Dehant, V., and Rivoldini, A. (2008). The librations, shape, and icy shell of Europa. *Icarus*, 195(1):386–399.

Vance, S. D., Panning, M. P., Stähler, S., Cammarano, F., Bills, B. G., Tobie, G., Kamata, S., Kedar, S., Sotin, C., Pike, W. T., et al. (2018). Geophysical investigations of habitability in ice-covered ocean worlds. *Journal of Geophysical Research: Planets*, 123(1):180–205.

Vasavada, A. R. and Showman, A. P. (2005). Jovian atmospheric dynamics: An update after Galileo and Cassini. *Reports on Progress in Physics*, 68(8):1935.

Veeder, G. J., Davies, A. G., Matson, D. L., Johnson, T. V., Williams, D. A., and Radebaugh, J. (2012). Io: Volcanic thermal sources and global heat flow. *Icarus*, 219(2):701–722.

Verma, A. K. and Margot, J.-L. (2018). Expected precision of Europa Clipper gravity measurements. *Icarus*, 314:35–49.

Villamil, S., Dirkx, D., Stark, A., and Hussmann, H. (2021). Improvement of orbit determination using laser altimeter crossovers: JUICE mission case study. *Acta Astronautica*, 182:587–598.

Wahr, J., Zuber, M., Smith, D. E., and Lunine, J. (2006). Tides on Europa, and the thickness of Europa's icy shell. *Journal of Geophysical Research: Planets*, 111(E12).

Weber, T., Moore, K., Connerney, J., Espley, J., DiBraccio, G., and Romanelli, N.

Yoder, C. F. and Peale, S. J. (1981). The tides of Io. *Icarus*, 47(1):1–35.

Young, B., Nandi, S., Mastrodemos, N., Boone, D., and Tarzi, Z. (2019). Orbit determination sensitivity analysis for the Europa Clipper Mission tour.

Zannoni, M., Hemingway, D., Casajus, L. G., and Tortora, P. (2020). The gravity field and interior structure of Dione. *Icarus*, 345:113713.

Zannoni, M. and Tortora, P. (2013). Numerical error in interplanetary orbit determination software. *Journal of Guidance, Control, and Dynamics*, 36(4):1008–1018.

Zenk, K., Dirkx, D., and Fayolle, M. (2024). Constraining the Ephemeris and Interior Structure of Io using Space-Based Astrometry by JUICE. *To be submitted to Astronomy & Astrophysics*.

Zhang, K. and Hamilton, D. P. (2007). Orbital resonances in the inner neptunian system: I. The 2: 1 Proteus–Larissa mean-motion resonance. *Icarus*, 188(2):386–399.

Zhang, K. and Hamilton, D. P. (2008). Orbital resonances in the inner neptunian system: II. Resonant history of Proteus, Larissa, Galatea, and Despina. *Icarus*, 193(1):267–282.

Curriculum Vitæ

Sam Liam Fayolle

05-04-1997	Born in Pierre-Benite, France.

Education

2010–2013 Secondary Education
Lycee Champagnat, Saint Symphorien sur Coise, France

2013–2015 Classes Preparatoires aux Grandes Ecoles (CPGE)
Lycee aux Lazaristes, Lyon, France

2015-2020 Engineering School (specialisation in aerospace engineering)
Ecole Centrale de Nantes, Nantes, France

2017-2020 Master of Science in Aerospace Engineering (cum laude)
Delft University of Technology, Delft, The Netherlands
Thesis: Geodetic parameter estimation for small-satellite small-body missions – An uncertainty-driven approach

2020-2024 PhD Aerospace Engineering
Delft University of Technology, Delft, The Netherlands
Thesis: Natural satellites ephemerides – The Galilean moons' dynamics in the JUICE-Europa Clipper era

List of Publications

Journal papers

13. Zenk, K., Dirkx, D., **Fayolle, M.** (2024) Constraining the ephemeris and interior structure of Io using space-based astrometry by JUICE. To be submitted to Astronomy & Astrophysics.
12. Pallichadath, V., Gurvits, L.I., Dirkx, D., Boven, P., Cimo, G., **Fayolle, M.**, Fogasy, J., Frey, S., Molera Calvés, G., Perger, K., Said, N.M.M., & Vermeersen, L.L.A. (2023). Planetary Radio Interferometry and Doppler Experiment as an operational component of the Jupiter Icy Moons Explorer mission. To be submitted to CEAS Space Journal.
11. **Fayolle, M.**, Dirkx, D., Cimo, G., Gurvits, L.I., Lainey, V., & Visser, P.N.A.M. (2024). Contribution of PRIDE VLBI products to the joint JUICE-Europa Clipper moons' ephemerides solution. Icarus, under revision.
10. Hener, J., **Fayolle, M.**, & Dirkx, D. (2024). JUICE: In-mission synergy of science and navigation ephemeris products. Application to potential benefits for statistical Delta-V expenditure. Planetary and Space Science, re-submitted.
9. Van Hoolst, T. , Tobie, G., Vallat, C., Altobelli, N., Bruzzone, L., Cao, H., Dirkx, D., Genova, A., Hussmann, H., Iess, L., Kimura, J., Khurana, K., Lucchetti, A., Mitri, G., Moore, W., Saur, J., Stark, A., Vorburger, A., Wieczorek, M., Aboudan, A., Bovolo, F., Breuer, D., Cappuccio, P., Carrer, L., Choblet, G., De Marchi, F., **Fayolle, M.**, Fienga, A., Hauber, E., Lainey, V., Plaut, J., Retherford, K., Seignovert, B., Steinbrügge, G., Thakur, S., Zannoni, M., Barabash, S., Dougherty, M., Gladstone, R., Gurvits, L.I., Hartogh, P., Palumbo, P., Poulet, F., Wahlund, J.-E., Grasset, O., & Witasse, O. (2023). Geophysical characterization of the interiors of Ganymede, Callisto and Europa by ESA's JUpiter ICy moons Explorer. Space Science Reviews, re-submitted.
8. Gurvits, L.I, Cimo, G., Dirkx, D., Pallichadath, V., Akins, A., Altobelli, N., Bocanegra Bahamon, T., Cazaux, S., Charlot, P., Duev, D., **Fayolle, M.**, Fogasy, J., Frey, S., Lainey, V., Molera Calves, G., Perger, K., Pogrebenko, S., Said, N.M.M., Vallat, C., Vermeersen, L.L.A., Visser, P.N.A.M., Wang, K-W., & Willner, K. (2023). Planetary Radio Interferometry and Doppler Experiment (PRIDE) of the JUICE mission. Space Science Reviews, 219(8):79.
7. **Fayolle, M.**, Magnanini, A., Lainey, V., Dirkx, D., Zannoni, M., & Tortora, P. (2023). Combining astrometry and JUICE–Europa Clipper radio science to improve the ephemerides of the Galilean moons. Astronomy & Astrophysics, 677, A42.
6. **Fayolle, M.**, Lainey, V., Dirkx, D., Gurvits, L.I., Cimo, G., & Bolton, S. J. (2023). Spacecraft VLBI tracking to enhance stellar occultations astrometry of planetary satellites. Astronomy & Astrophysics, 676, L6.
5. Hu, X., Stark, A., Dirkx, D., Hussmann, H., Fienga, A., Briaud, A., Memin, A., Melini, D., **Fayolle, M.**, Rambaux, N., Baguet, D., & Oberst, J. (2023). Sensitivity analysis of polar orbiter motion to lunar viscoelastic tidal deformation. Celestial Mechanics and Dynamical Astronomy, 135(2), 16.

4. **Fayolle, M.**, Dirkx, D., Lainey, V., Gurvits, L.I., & Visser, P.N.A.M. (2022). Decoupled and coupled moons' ephemerides estimation strategies - application to the JUICE mission. Planetary and Space Science, 219, 105531.
3. **Fayolle, M.**, Dirkx, D., Visser, P.N.A.M., & Lainey, V. (2021). Analytical framework for mutual approximations - Derivation and application to Jovian satellites. Astronomy & Astrophysics, 652, A93.
2. **Fayolle, M.**, Quirico, E., Schmitt, B., Jovanovic, L., Gautier, T., Carrasco, N., Grundy, W., Vuitton, V., Poch, O., Protopapa, S., Young, L., Cruikshank, D., Dalle Ore, C., Bertrand, T., Stern, A., & the New Horizons Surface Composition Science Theme Team. (2021). Testing tholins as analogues of the dark reddish material covering Pluto's Cthulhu region. Icarus, 367, 114574.
1. Jovanović, L., Gautier, T., Broch, L., Protopapa, S., Bertrand, T., Rannou, P., **Fayolle, M.**, Quirico, E., Johann, L., En Naciri, A., & Carrasco, N. (2021). Optical constants of Pluto aerosol analogues from UV to near-IR. Icarus, 362, 114398.

SELECTED CONFERENCE CONTRIBUTIONS

7. **Fayolle, M.**, Magnanini, A., Lainey, M., Dominic, D., Zannoni, M., & Tortora, T. (2023). Merging ground-based astrometry with JUICE and Clipper radio-science to improve the estimation of the Galilean moons' dynamics. Complex Planetary Systems II – Kavli-IAU Symposium 382 – July 3-7, 2023.
6. **Fayolle, M.**, Dirkx, D., Cimò, G., Gurvits, L.I., Lainey, V., Calvés, G. M., Pallichadath, V., Vermeersen, L.L.A. & Visser, P.N.A.M. (2022, September). Contribution of simultaneous PRIDE observations of JUICE and Clipper spacecraft to the Galilean satellites' ephemerides. In Europlanet Science Congress 2022 (EPSC 2022).
5. Dirkx, D., **Fayolle, M.**, Garrett, G., Avillez, M., Cowan, K., Cowan, S., Encarnacao, J., Fortuny Lombrana, C., Gaffarel, J., Hener, J., Hu, X., van Nistelrooij, M., Oggionni, F., & Plumaris, M. (2022). The open-source astrodynamics Tudatpy software – Overview for planetary mission design and science analysis. In Europlanet Science Congress 2022 (EPSC 2022).
4. **Fayolle, M.**, Dirkx, D., Garrett, G., Gurvits, L.I., Hener, J., Lainey, V., Magnanini, A., & Visser, P.N.A.M. (2022, May). An open-source multi-mission, multi-observation estimation tool for natural satellites' dynamics-Application to Jupiter's Galilean moons. In EGU General Assembly Conference Abstracts (pp. EGU22-7933).
3. Magnanini, A., **Fayolle, M.**, Gomez Casajus, L., Zannoni, M., Tortora, P., Lainey, V., Dirkx, D., Gurvits, L.I., Mazarico, E., & Park, R. (2022, May). Combining JUICE and Europa Clipper range, range-rate and VLBI observables to improve the Galilean moons ephemerides. In EGU General Assembly Conference Abstracts (pp. EGU22-7836).
2. **Fayolle, M.**, Dirkx, D., Lainey, V., Gurvits, L., & Visser, P.N.A.M. (2021). Coupled and decoupled strategies for spacecraft's and natural bodies' state estimation - Application to the JUICE mission. In Europlanet Science Congress 2021 (EPSC 2021).
1. **Fayolle, M.**, Quirico, E., Schmitt, B., Jovanovic, L., Gautier, T., Carrasco, N., Grundy, W., Vuitton, V., Poch, O., Gabasova, L., Protopapa, S., & Young, L. (2019, September). Testing tholins as analogs of the dark reddish material covering the Cthulhu region. In EPSC-DPS Joint Meeting 2019.

Afterword

The first time I got exposed to satellite ephemerides was in the form of a thick mysterious book filled with numbers, lying on the desk of my grandfather's garden shed. Not convinced by the idea that his life was influenced by the moon's phases (a common belief among men of his generation and background), he was attempting to derive an alternative strategy to base his cropping schedule on lunar tides instead. Throughout my childhood, space kept exerting a complex fascination on me, fuelled by my grandfather's folkloric investigations, but also somewhat mixed with some childish resentment at the asteroid which wiped out the dinosaurs. More than 20 years later, not much has changed. My sense of awe and wonder is intact, and it is sometimes hard not to feel that my understanding of natural satellites' dynamics is still as rudimentary as my grandfather's back then.

Nevertheless, embracing a career in space did not cross my mind until very late, as I could never have envisioned this to be a realistic option. When I finally ended up at Delft more than seven years ago, a bit disillusioned with the aeronautics engineering career path I had chosen so far, I had never seen an orbit equation and the only thing I knew was that I did not like planes that much after all. I still vividly remember how it felt to open the timetable for the first quarter of the academic year and see courses like "Astrodynamics I" and "Planetary Sciences" waiting for me. I could never have dreamed back then to be one day embarking on a PhD journey within such an amazing research team. I would like to deeply thank everyone at the Space Engineering department who has in some way contributed to this adventure. I have learned so much from all of you, first as a student and later as a colleague. Thank you for sparking my interest on such a variety of topics, for feeding my curiosity, and overall for having made TU Delft feel like home for so many years now.

I would like to express a few special thanks. To my promotors Pieter and Bert, thank you for entrusting me with this project. I really appreciated that you gave me a lot of freedom about how to conduct my research, while still making me feel that I could always come to you for advice. To Erwin, who helped so much during this PhD and especially at the beginning. Thank you for all the fun chats and for haunting the 9th floor corridor together with EJO and me during the Covid period. To Bart, for all the existentialism chats we had (I am truly sorry, but I still do not believe in free will), for your support and wisdom, and for being such a "Camusian role model" in academia to me. To the French gang, thanks for all the love, laughs and raclette dinners. Nothing cheers you up like friends and melted cheese combined. To Marc, thank you very much for taking the time to read this thesis and provide very helpful feedback (and for writing such a great dissertation to draw inspiration from). I always enjoy our little chats and I am really happy to start working more closely together now! To all the PhDs of the department, who have also become my friends, many thanks for sharing this journey with me and making it so much fun! Special mention to Livio and Rania, who started their PhD trajectory almost at the same time as I did, and with whom I shared so many 4-year PhD hugs and breakdowns. And to Andrea for all the discussions on work, the universe, and everything (you will always remain the little brother though). To all of you guys, many thanks!

During the course of my PhD, I had the opportunity to work with amazing scientists outside TU Delft who have contributed so much to this project and to my own scientific trajectory. I would like to start with Valery Lainey, thank you for welcoming me for three months at Paris Observatory and for a couple of shorter visits since then. I always felt welcome in your research group and I have learned so much from you and your team. You always made time for me, whether it was to explain something, discuss future projects, or help me write research proposals. I am really looking forward to continuing to work with you in the coming years. To all the PhDs at the Observatory, thank you so much for the wonderful months I spent there. It always makes me very happy whenever we get the chance to meet again.

To Olivier Witasse who was my point of contact at ESA during the entire project. I really enjoyed each of our meetings and discussions, whether about JUICE or trail running. And, of course, thank you for welcoming me very recently at ESTEC! To Leonid, Giuseppe, and the PRIDE team in general. I feel very lucky that I could work on an actual mission experiment, and I am really grateful for this opportunity! To Gabriel and Tim, many thanks for welcoming me to the JUICE working group 1. To every member of the ZENITH consortium, thank you so much for the interesting discussions and feedback. It was amazing to be able to meet the moons' ephemerides community very early on in my PhD, especially in the difficult conditions of the Covid years. Special mention to Marco, Paolo, and especially Andrea with whom I got the chance to collaborate closely. More generally, I want to thank my co-authors and all the inspiring people I got the chance to talk to over the last years. Thank you for the additional understanding, insight, motivation, and creativity that spawned from our discussions. Finally, many thanks to my committee members for accepting to be part of my jury and for taking the time to read this dissertation.

Last but definitely not least. To my supervisor Dominic, thinking about how influential our random meeting at a conference in Berlin six years ago was is a bit vertiginous. Your teaching shaped the scientist that I am trying to become, the way I think, and how I choose to do science. Starting with the obvious, I could not have carried out this research without access to the powerful and versatile tool that Tudat is. With time I keep growing more impressed by the amount of work and thinking behind this software. I am so happy to see how this project has developed over the years and that your efforts and dedication are paying off. Thank you for involving me in this journey since I was a MSc student. Being part of the Tudat team definitely accounts for a significant part of my learning trajectory at TU Delft. As your student, I have learned so much from you over the years, and I still do just as much as I did on day one. Your ability to provide insightful and detailed feedback on a wide variety of topics and to always come up with relevant questions and comments is something I really admire. Entering your office with a question, I know that I will always leave with a better understanding of the problem, oftentimes with a direct solution, but anyway with a fruitful and insightful discussion that leaves me better armed to tackle whatever issue I am facing. I really enjoyed how open our meetings and discussions were, and I am so grateful that you always made me feel valued in those. Maybe even more important than your great technical support, thank you for always being so patient and considerate, for supporting me through numerous existential crises (however severe), and for believing in me when I do not. I would not have completed this without your support. After so many years working together and with the "director-directee" relation progressively coming to an end, I feel very privileged to count you among my friends.

After living in Delft for so many years, I still got so much support from my friends outside of my current little space bubble. Whether we met as kids, during my studies in Nantes or in the Delft MSc program, thank you so much to all of you. To Vincent, you have been my best friend for almost 10 years now and we have shared each other lives, both highs and lows, every single day since. Your presence at my side has been an intrinsic part not only of this journey but of my life in general. Thank you for everything.

I would like to finish by mentioning my family. Thanks to all of you for your support, either loud or quiet. To my grandmother, who has followed the progress of this PhD adventure week after week and came up with the concept of "thesis director". Thank you for gently reminding me of who I am and what truly matters. To both you and grandpa, thank you for your unconditional love and support. To my siblings, Agathe and Louis, finding the right words has always been really difficult, especially when one understands each other without the need for speaking. Maybe it is enough to say that having you as paranymphs means everything to me. You have always been there for me and having you in my life is the greatest gift I ever got.

Sam Fayolle
Delft, December 2024